

SU-SEL-67-039

Photoemission Studies of the Noble Metals, the Cuprous Halides, and Selected Alkali Halides

by

Walter F. Krolikowski

May 1967

GPO PRICE \$ _____
 CFSTI PRICE(S) \$ _____
 Hard copy (HC) 300
 Microfiche (MF) .60

Technical Report No. 5218-1

Prepared under
 National Aeronautics and Space Administration
 Grant NGR-05-020-066,
 Center for Materials Research Contract SD-87 and
 National Science Foundation Grant GP-1033

ff 653 July 65

(THRU) _____
 (CODE) 126
 (CATEGORY) _____

(ACCESSION NUMBER) N68-15118
 (PAGES) _____
 (NASA CR OR TMX OR AD-NUMBER) CP-92521

FACILITY FORM 602

SOLID-STATE ELECTRONICS LABORATORY
STANFORD ELECTRONICS LABORATORIES
 STANFORD UNIVERSITY • STANFORD, CALIFORNIA



PHOTOEMISSION STUDIES OF THE NOBLE METALS,
THE CUPROUS HALIDES, AND SELECTED ALKALI HALIDES

by

Walter F. Krolikowski

May 1967

Reproduction in whole or in part
is permitted for any purpose of
the United States Government.

Technical Report No. 5218-1

Prepared under
National Aeronautics and Space Administration
Grant NGR-05-020-066
Center for Materials Research Contract SD-87
National Science Foundation Grant GP-1033

Solid State Laboratory
Stanford Electronics Laboratories
Stanford University Stanford, California



PHOTOEMISSION STUDIES OF THE NOBLE METALS,
THE CUPROUS HALIDES, AND SELECTED ALKALI HALIDES

by Walter F. Krolikowski

ABSTRACT

The possible presence of the copper d band in the valence band of the cuprous halides has been largely ignored in the recent literature, and structure in the optical spectrum of the cuprous halides has been associated with direct transitions between symmetry points in a germanium-like band structure. In order to test the validity of these explanations for the optical spectrum of the cuprous halides, the electronic properties of the cuprous halides have been investigated in detail by use of experimental photoemission techniques. The quantum yield and photoemission data resulting from these photoemission measurements have been interpreted in terms of the electronic structure of the cuprous halides, and it is found that the copper d band plays a significant role in the valence band of the cuprous halides.

In order to distinguish the copper d band from the halogen p bands in the cuprous halides, it was found useful to extend the photoemission studies to the noble metals and the alkali halides. Consequently, this report includes not only studies of the cuprous halides (CuCl, CuBr, CuI), but also detailed studies of the noble metals (Cu, Ag, Au) and certain alkali halides (CsCl, CsBr, CsI, and KI). Some of the most important results of this work are summarized below:

- (1) The experimental quantum yield and photoelectric energy distributions have been measured for all the materials in the range of photon energies below 11.6 eV. In several cases, the measurements have been extended to photon energies as high as 21.2 eV.
- (2) For nearly all of the materials, the optical density of states has been determined in the range of energies between 11.6 eV below the fermi level and 11.6 eV above the fermi level.
- (3) Nondirect transitions are found to dominate the optical absorption process in the noble metals and the cuprous halides. Direct transitions are found to have secondary importance compared with nondirect transitions.

- (4) For the noble metals and the cuprous halides, a simple mathematical model is found to account quantitatively for the quantum yield, the photoelectric energy distributions, the electron-electron scattering length, and $\epsilon_2(\omega)$. This mathematical model is based upon the model of nondirect transitions.

The new information presented in this report should be useful to theorists making future energy band calculations, and may be helpful in leading to a unified theory for the optical absorption process in solids.

CONTENTS

	<u>Page</u>
I. INTRODUCTION	1
II. EXPERIMENTAL METHODS	5
A. The Basic Measurements	5
B. Light Source and Vacuum Monochromator	5
C. The Vacuum System	7
D. The Photodiode	10
E. The Sealed Glass Phototube	14
F. The Photoemission Chamber	18
G. The Knock-Off Tube	25
H. Preparation of Films	33
1. Copper, Silver, and Gold	33
2. Cuprous Chloride, Cuprous Bromide, and Cuprous Iodide	34
3. Cesium Chloride, Cesium Bromide, Cesium Iodide, and Potassium Iodide	37
I. Measurement of Photoelectric Energy Distributions	38
J. Measurement of the Quantum Yield	38
K. Measurement of Reflectivity	43
III. ANALYSIS AND INTERPRETATION OF PHOTOEMISSION DATA	45
A. The Free Electron Model	46
B. Semiclassical Escape Function, $T_f(E)$	48
C. The Electron-Electron Scattering Length $L(E)$	50
D. Direct and Nondirect Transitions	61
E. The Photoemission Process	75
F. Methods for Obtaining the Density of States and Other Parameters from Photoemission and Optical Data	88
G. The "Optical Density of States"	101
H. Analysis of Photoemission Data for Free Electron Metals	102
IV. PHOTOEMISSION FROM COPPER	115
A. The Optical Density of States for Copper	116
B. Comparison of the Optical Density of States for Copper with Other Experimental Data	120
C. Comparison of the Optical Density of States for Copper with Theoretical Calculations	122
D. The Photoelectric Yield from Clean Copper	124
E. Photoelectric Energy Distributions from Clean Copper	127
F. The Electron-Electron Scattering Length $L(E)$ for Copper	138
G. The Threshold Function and the Effective Threshold Function for Copper	140

CONTENTS (CONTD)

	<u>Page</u>
H. The Imaginary Part of the Dielectric Constant $\epsilon_2(\omega)$ for Copper	141
I. The Specific Heat for Copper	149
J. The Rigid Band Model and the Density of States for Nickel	150
K. Comparison of the Present Work on Clean Copper with Earlier Work on Cesium Copper	152
L. Conclusions	157
V. PHOTOEMISSION FROM GOLD	159
A. The Optical Density of States for Gold	159
B. The Photoelectric Yield from Gold	162
C. Photoelectric Energy Distributions from Gold	164
D. The Electron-Electron Scattering Length in Gold	175
E. Comparison of Calculated and Experimental Values of $\epsilon_2(\omega)$ for Gold	177
F. The Specific Heat for Gold	181
G. Conclusions	182
VI. PHOTOEMISSION FROM SILVER	185
A. The Optical Density of States for Silver	185
B. The Photoelectric Yield for Clean Silver	188
C. The Photoelectric Energy Distribution Curves for Clean Silver	189
D. The Electron-Electron Scattering Length for Silver.	201
E. The Specific Heat for Silver	202
F. The Imaginary Part of the Dielectric Constant $\epsilon_2(\omega)$ for Silver	202
G. The Photoelectric Yield from Cesium Silver	204
H. Photoelectric Energy Distributions from Cesium Silver	209
I. The Direct Transition in Silver	220
J. Conclusions	227
VII. COMPARISON OF COPPER, SILVER, AND GOLD	229
VIII. THE CUPROUS HALIDES	231
A. Historical Background, Some Physical Properties, and a Bonding Model for the Cuprous Halides	231
B. Photoemission and Optical Studies of Cuprous Iodide	240
1. The Optical Density of States for Cuprous Iodide	240
2. Optical Data for Cuprous Iodide	246
3. The Quantum Yield for Cuprous Iodide	251
4. Photoelectric Energy Distribution Curves from Cuprous Iodide	254

CONTENTS (CONTD)

	<u>Page</u>
5. The Electron-Electron Scattering Length $L(E)$ for Cuprous Iodide	274
6. The Location of the Fermi Level in Cuprous Iodide	276
7. Comparison with Energy-Band Calculations	278
C. Photoemission Studies of Cuprous Bromide	281
D. Photoemission Studies of Cuprous Chloride	295
E. A Comparison of CuCl, CuBr, and CuI	307
IX. PHOTOEMISSION STUDIES OF CESIUM CHLORIDE, CESIUM BROMIDE, CESIUM IODIDE, AND POTASSIUM IODIDE	317
A. Photoemission Studies of Cesium Bromide	317
B. Photoemission Studies of Cesium Chloride	329
C. Photoemission Studies of Cesium Iodide	338
D. Photoemission Studies of Potassium Iodide	353
E. Conclusion	361
X. A COMPARISON OF THE NOBLE METALS, THE CUPROUS HALIDES, AND THE ALKALI HALIDES	367
APPENDIX A. UNIQUENESS OF THE PHOTOEMISSION ANALYSIS	371
APPENDIX B. COMPUTER PROGRAM FOR ANALYZING PHOTOEMISSION DATA	383
APPENDIX C. A PRACTICAL METHOD FOR NORMALIZING ENERGY DISTRIBUTION CURVES (EDCs)	395
REFERENCES	401



TABLES

<u>No.</u>	<u>Page</u>
1. Analysis of photoemission data for Case III	99
2. Origin of peaks in the calculated $\epsilon_2(\omega)$ for copper	142
3. Assignment to major structure in the calculated $\epsilon_2(\omega)$ for gold if the proposed peak (P) exists	180
4. Identification of structure in $\epsilon_2(\omega)$ for silver	206
5. Comparison of certain properties of copper, silver and gold	230
6. Some properties of the cuprous halides	232
7. Goldschmidt's ionic radii (\AA)	234
8. A portion of the periodic table	235
9. Exciton splittings for the cuprous and silver halides compared to the halogen spin-orbit splitting	239
10. Location of structure in the energy bands of the cuprous halides	308
11. Experimental optical data and identification of structure for the cuprous halides	310



ILLUSTRATIONS

<u>No.</u>	<u>Title</u>	<u>Page</u>
1.	Measurement of photoelectric energy distributions and quantum yield at photon energies less than 11.8 eV	6
2.	Block diagram of vacuum system	8
3.	Time required to form a monolayer of gas on a surface	9
4.	The basic pumping unit evacuating an apparatus for purifying cuprous bromide	10
5.	The basic pumping unit and associated control units mounted on a mobile frame	11
6.	Evacuating a phototube	12
7.	Bell jar used in conjunction with the basic pump unit	13
8.	The photoemission chamber (Section F) being continuously pumped during a photoemission experiment performed as in Fig. 1b	14
9.	Geometry and dimensions of collector and emitter of the photodiode	15
10.	Sealed glass phototube used to check the effect of the collector light hole on energy distribution curves for cuprous bromide	16
11.	Schematic of the photoemission chamber	20
12.	Schematic of the emitter assembly	23
13.	The photoemission chamber as seen from the glass viewpoint side	26
14.	Schematic of the knock-off tube showing basic features	29
15.	Schematic of the experiment using knock-off tube	30
16.	Experimental knock-off tube in holder	31
17.	Knock-off tube and guillotine after an experiment	32
18.	Evaporation of copper, gold, and silver	34
19.	Preparation of cuprous halide films	35

ILLUSTRATIONS (CONTD)

<u>No.</u>	<u>Title</u>	<u>Page</u>
20.	X-ray powder pattern of an evaporated film of cuprous bromide	36
21.	Thickness measurements of cuprous halide films	37
22.	Circuit used for measuring energy distribution curves	39
23.	Photograph of an actual energy distribution curve being traced on an x-y recorder during a photoemission experiment on cuprous iodide	40
24.	Measurement of quantum yield	41
25.	Free electron model of a metal	47
26.	Velocity cone used in calculation of semiclassical escape function	49
27.	Semiclassical escape function, $T_f(E)$, for a free electron model	51
28.	Calculation of electron-electron scattering length $L(E)$ from the density of states	52
29.	Hypothetical density of states with a free electron conduction band and delta function valence band	55
30.	Density of states models approximated by the model of Fig. 29	57
31.	Brillouin zone for face-centered cubic lattice	58
32.	Free electron energy bands for a face-centered cubic structure with lattice parameter $a = 4.07 \text{ \AA}$, the lattice constant for gold and silver	59
33.	Identifying characteristics of direct and nondirect transitions	71
34.	The photoemission process	77
35.	Correction factor $C[\alpha(\omega)L(E), T_f(E)]$ for various values of (αL) and T_f	83
36.	Example showing how density of states can be deduced from energy distribution curves for case of $\alpha L \gg 1$	92

ILLUSTRATIONS (CONTD)

<u>No.</u>	<u>Title</u>	<u>Page</u>
37.	Simple example showing two arbitrary choices of $\epsilon_2(\omega)$ that can be made consistent with the photoemission energy distribution curves of Fig. 36 by a proper choice of $ M(\omega) ^2$	94
38.	Density of states parameters for two examples of free electron metals	102
39.	Calculated shape of ϵ_2 for free electron metal of Fig. 38a	103
40.	Calculated electron-electron length $L(E)$ for free electron metal of Fig. 38a	105
41.	Threshold function $T_F(E)$ and effective threshold function $EFFTH(E)$ for free electron metal of Fig. 38a	106
42.	Calculated energy distributions for free electron metals of Fig. 38a (primary electrons only)	107
43.	Comparison of energy distribution with shape of valence band density of states for free electron metal of Fig. 38a	108
44.	Photoelectric yield for free electron metal of Fig. 38a (primary electrons only)	109
45.	Calculated electron-electron scattering length $L(E)$ for the sodium model of Fig. 38b	110
46.	Calculated energy distributions for sodium-like free electron metal of Fig. 38b (primary electrons only)	110
47.	Estimated energy distribution for sodium-like free electron metal of Fig. 38b (including scattered electrons)	111
48.	Calculated photoelectric yield for sodium-like free electron metal of Fig. 38b (primary electrons only)	112
49.	Optical density of states for copper	117
50.	Calculated band structure of copper	118
51.	Comparison of the optical density of states of Fig. 49 with the density of states determined from ion neutralization experiments (Hagstrum, Ref. 41)	120

ILLUSTRATIONS (CONTD)

<u>No.</u>	<u>Title</u>	<u>Page</u>
52.	Comparison of shape of optical density of states for copper with the soft x-ray emission spectrum from copper [Ref. 42]	121
53.	Comparison of the optical density of states with the density of states of Ref. 43 in the region between 2 and 6 eV below the fermi level	122
54.	Comparison of optical density of states for copper with calculated density of states for nickel (Ref. 44) . .	123
55.	Comparison of experimental yield and calculated yield for copper	125
56.	Photoelectric energy distributions from clean copper . . .	128
57.	Uncertainty ΔE due to lifetime broadening	135
58.	Comparison of the shapes of the energy distribution curves from several different samples of copper	137
59.	Effect of inadequate vacuum on copper energy distribution curves	138
60.	Calculated electron-electron scattering length $L(E)$ for copper	139
61.	Semiclassical threshold function for copper calculated from Eq. (3.11)	140
62.	Comparison of semiclassical threshold $T_f(E)$ to effective threshold function $EFFTH(E)$ for copper	141
63.	ϵ_2 calculated from optical density of states of copper (Ref. 49)	142
64.	Comparison of calculated ϵ_2 for copper with the results of Ref. 45 and Ref. 46	143
65.	Comparison of calculated ϵ_2 for copper with Beaglehole's ϵ_2 (Ref. 47)	144
66.	Comparison of calculated ϵ_2 for copper with the ϵ_2 of Garfinkel et al (Ref. 48b)	144
67.	Different optical densities of states used to calculate ϵ_2 for copper (see Fig. 49)	147

ILLUSTRATIONS (CONTD)

<u>No.</u>	<u>Title</u>	<u>Page</u>
68.	Comparison of shapes of ϵ_2 calculated from density of states I and from density of states II (see Fig. 67) . . .	147
69.	Adjustment of the optical density of states for copper to agree with the value derived from the specific heat	150
70.	Comparison of Blodgett's (Ref. 13) optical density of states for nickel with the density of states derived from the optical density of states of copper using the rigid band model and an exchange splitting of 0.6 eV	151
71.	Comparison of Hagstrum's (Ref. 41) nickel density of states with the density of states derived from the optical density of states of copper using the rigid band model and an exchange splitting of 0.6 eV	151
72.	Comparison of calculated vs experimental photoelectric yield for copper with a surface monolayer of cesium	153
73.	Calculated and experimental energy distribution curves for copper	154
74.	Optical density of states for gold	160
75.	Comparison of experimental and calculated yield for gold . . .	163
76.	Family of experimental energy distribution curves for gold (normalized to yield)	164
77.	Plot of peak energy (E_p) vs photon energy for the energy distributions of Fig. 76 and Fig. 77	165
78a.	Energy distribution curves showing deterioration with time shortly after LiF window had been knocked off	167
78b.	Experimental energy distribution curve for gold obtained using a "knock-off tube"	167
78c.	Experimental energy distribution curve for gold obtained using a "knock-off tube"	168
79.	Energy distribution curves before and after gold sample was exposed to air	169
80.	Comparison of shapes of energy distribution curves for different samples of gold	170

ILLUSTRATIONS (CONTD)

<u>No.</u>	<u>Title</u>	<u>Page</u>
81.	Comparison of calculated and experimental energy distribution curves for gold	171
82.	Calculated electron-electron scattering length $L(E)$ for gold	176
83a.	ϵ_2 for gold calculated from the optical density of states of Fig. 74	178
83b.	Comparison of calculated ϵ_2 with the ϵ_2 of Garfinkel, Tiemann, and Engeler (Ref. 48b)	178
83c.	Comparison of calculated ϵ_2 with the ϵ_2 of Refs. 50a, 46	178
83d.	Comparison of calculated ϵ_2 with Beaglehole's ϵ_2 (Ref. 47)	178
84.	Adjustment of optical density of states to agree with the value derived from the specific heat (at the fermi level)	182
85.	Optical density of states for silver	186
86.	Calculated band structure of silver	187
87.	Comparison of experimental and calculated photoelectric yield for silver	189
88.	Photoelectric energy distribution curves for clean silver	190
89.	Energy distribution curve for silver sample with an anomalously low vacuum level	198
90.	Calculated electron-electron scattering length for silver	201
91.	Adjustment of density of states of silver at the fermi level to agree with the density of states calculated from heat	203
92.	Comparison of calculated ϵ_2 for silver with the ϵ_2 obtained from reflectivity measurements	205
93.	Discrepancy in ϵ_2 for silver ($h\nu > 4$ eV) compared with $(\epsilon_2)_{\text{plasma}}$ for photassium, as calculated by Hopfield [Ref. 65]	207

ILLUSTRATIONS (CONTD)

<u>No.</u>	<u>Title</u>	<u>Page</u>
94.	Comparison of calculated yield with experimental yield for silver with a surface monolayer of cesium	208
95.	Photoelectric energy distribution curves for cesiated silver	210
96.	Experimental energy distribution curves of cesiated silver normalized to Berglund's yield [Ref. 7]	218
97.	Experimental energy distribution curves of cesiated silver [Ref. 7], normalized to yield B of Fig. 94.	219
98.	Experimental energy distribution curves of cesiated silver [Ref. 7], normalized to Berglund's yield	220
99.	Evidence for direct transitions in silver	221
100.	Evidence of direct transitions in a silver sample with an anomalously low vacuum level	222
101.	Direct transitions in silver	223
102.	Energy of initial and final states for the direct transition in silver	224
103.	Determination of effective masses in silver	226
104.	Parabolic bands explaining the direct transition in silver in the range of photon energies between 4 and 7 eV	227
105.	Proposed model of the chemical bonding for the zinc sulfide phase of cuprous bromide	233
106.	Optical energy gap vs λ^2 for horizontal sequences in the periodic table [Ref. 79]	236
107.	Optical energy gaps vs λ for the diagonal sequences in the periodic table [Ref. 79]	236
108.	Exciton spectrum of cuprous bromide [Ref. 68]	238
109.	Exciton spectrum of a cuprous bromide film evaporated on cleaved sodium chloride and annealed at various temperatures [Ref. 69]	238
110.	Estimated optical density of states for cuprous iodide	242
111.	Threshold function for cuprous iodide	245

ILLUSTRATIONS (CONTD)

<u>No.</u>	<u>Title</u>	<u>Page</u>
112.	Reflectivity for cuprous iodide	247
113.	Absorption coefficient $\alpha(\omega)$ of cuprous iodide	248
114.	Comparison of calculated and experimental values of $\epsilon_2(\omega)$ for cuprous iodide	249
115.	Effect of the matrix element $ M_{14} ^2$ on $\epsilon_2(\omega)$ for cuprous iodide	251
116.	The quantity $\omega\sigma(\omega) = \omega^2\epsilon_2(\omega)$ for cuprous iodide	252
117.	Comparison of absorption coefficient of cuprous iodide and silver iodide	253
118.	Photoelectric yield for cuprous iodide	255
119.	Comparison of experimental and calculated energy distribution curves for cuprous iodide	256
120.	Experimental energy distribution curves for cuprous iodide in the range of photon energies between 7.8 and 8.6 eV . .	270
121.	Experimental energy distribution curves for cuprous iodide in the range of photon energies between 11.0 and 11.8 eV .	270
122.	Comparison of experimental energy distribution curves for several samples of cuprous iodide	271
123.	Experimental energy distribution curves for one cuprous iodide sample that had no pronounced structure when freshly evaporated, but did show pronounced structure upon aging .	272
124.	E_p vs $h\nu$ plot for cuprous iodide	273
125.	Calculated $L(E)$ for cuprous iodide compared with experimental data of Pong [Ref. 71], which is for cuprous bromide	275
126.	Location of fermi level from energy distribution curves for cuprous iodide	277
127.	Comparison of optical density of states for cuprous iodide with adjusted band structure of silver bromide	279
128.	Photoelectric yield for cuprous bromide	282
129.	Energy distribution curves for cuprous bromide	283

ILLUSTRATIONS (CONTD)

<u>No.</u>	<u>Title</u>	<u>Page</u>
130.	Energy distribution curves for cuprous bromide indicating structure in the conduction band	287
131.	Energy distribution curves for cuprous bromide indicating structure in the conduction band	288
132.	ΔE_p vs $\Delta h\nu$ plot for cuprous bromide	289
133.	Estimated optical density of states for cuprous bromide . .	290
134.	Reflectivity $R(\omega)$ for cuprous bromide, from Cardona [Ref. 68]	291
135.	Absorption coefficient $\alpha(\omega)$ for cuprous bromide, from Cardona [Ref. 68]	292
136.	Comparison of optical density of states for cuprous bromide with adjusted band structure of silver bromide . . .	293
137.	Effect of temperature on energy distribution curves from cuprous bromide	294
138.	Energy distribution curves for cuprous bromide before and after heating	294
139.	Relative photoelectric yield for cuprous chloride	295
140.	Experimental energy distribution curves for cuprous chloride	296
141.	ΔE_p vs $\Delta h\nu$ plot for cuprous chloride	300
142.	Estimated optical density of states for cuprous chloride . .	302
143.	Reflectivity for cuprous chloride [Ref. 68]	303
144.	Absorption coefficient $\alpha(\omega)$ for cuprous chloride.	303
145.	Comparison of optical density of states for cuprous chloride with adjusted band structure of silver chloride . .	306
146.	Location of structure in the energy bands of the cuprous halides	312
147.	Comparison of experimental energy distribution curves for cuprous chloride, cuprous bromide, and cuprous iodide .	314

ILLUSTRATIONS (CONTD)

<u>No.</u>	<u>Title</u>	<u>Page</u>
148.	Relative quantum yield for cesium bromide	318
149.	Energy distribution curves for cesium bromide in the range of photon energies between 7.2 and 7.4 eV	318
150.	Energy distribution curves for cesium bromide in the range of photon energies between 7.2 and 7.7 eV	319
151.	Energy distribution curves for cesium bromide in the range of photon energies between 7.7 and 8.4 eV	319
152.	Energy distribution curves for cesium bromide in the range of photon energies between 8.4 and 9.2 eV	320
153.	Energy distribution curves for cesium bromide in the range of photon energies between 8.4 and 9.8 eV	320
154.	Energy distribution curves for cesium bromide in the range of photon energies between 10.0 and 10.2 eV	321
155.	Energy distribution curves for cesium bromide in the range of photon energies between 10.3 and 10.5 eV	321
156.	Energy distribution curves for cesium bromide in the range of photon energies between 10.6 and 10.9 eV	322
157.	Energy distribution curves for cesium bromide in the range of photon energies between 11.0 and 11.8 eV	322
158.	Comparison of the present work with the energy distribution curve obtained by Phillipp et al [Ref. 85] for CsBr	323
159.	E_p vs $h\nu$ for cesium bromide	324
160.	Estimated optical density of cesium bromide	325
161.	Optical density for cesium bromide	326
162.	Quantum yield for cesium chloride	330
163.	Energy distribution curves for cesium chloride at 7.5 and 7.7 eV	331
164.	Energy distribution curves for cesium chloride in the range of photon energies between 7.7 and 9.2 eV	331

ILLUSTRATIONS (CONTD)

<u>No.</u>	<u>Title</u>	<u>Page</u>
165.	Energy distribution curves in the range of photon energies between 9.2 and 10.2 eV	332
166.	Energy distribution curves for cesium chloride in the range of photon energies between 10.2 and 11.9 eV	333
167.	Comparison of shapes of energy distribution curves	334
168.	E_p vs $h\nu$ for cesium chloride	334
169.	Estimated optical density of states for cesium chloride	335
170.	Optical density of cesium chloride	336
171.	Quantum yield for cesium iodide at room temperature	338
172.	Relative quantum yield of cesium iodide at 80°K	339
173.	Energy distribution curves for cesium iodide in the range of photon energies between 6.7 and 8.8 eV	340
174.	Energy distribution curves for cesium iodide in the range of photon energies between 8.8 and 9.4 eV	340
175.	Energy distribution curves for cesium iodide in the range of photon energies between 9.4 and 9.7 eV	341
176.	Energy distribution curves for cesium iodide in the range of photon energies between 9.7 and 10.0 eV	341
177.	Energy distribution curves for cesium iodide in the range of photon energies between 10.0 and 10.6 eV	342
178.	Energy distribution curves for cesium iodide in the range of photon energies between 10.6 and 11.0 eV	342
179.	Energy distribution curves for cesium iodide in the range of photon energies between 11.0 and 11.4 eV	343
180.	Energy distribution curves for cesium iodide in the range of photon energies between 11.4 and 11.8 eV	343
181.	Comparison of the shapes of the energy distribution curves from several samples of cesium iodide	344
182.	Comparison of shapes of energy distribution curves for cesium chloride	345

ILLUSTRATIONS (CONTD)

<u>No.</u>	<u>Title</u>	<u>Page</u>
183.	E_p vs $h\nu$ plot for cuprous iodide	346
184.	Estimated optical density of states for cesium iodide . . .	347
185.	Optical data and identification of structure for cesium iodide	348
186.	Location of fermi level in cesium iodide	350
187.	Energy distribution curves from the cesium iodide knock-off-tube experiment	350
188.	Energy distribution curves for cesium iodide (knock-off-tube experiment)	351
189.	Energy distribution curves from the cesium iodide knock-off-tube experiment	351
190.	Quantum yield for potassium iodide	354
191.	Energy distribution curves for potassium iodide in the range of photon energies between 7.7 and 8.5 eV	355
192.	Energy distribution curves for potassium iodide in the range of photon energies between 8.3 and 8.9 eV	356
193.	Energy distribution curves for potassium iodide in the range of photon energies between 8.9 and 9.5 eV	356
194.	Energy distribution curves for potassium iodide in the range of photon energies between 9.5 and 10.4 eV	357
195.	Energy distribution curves for potassium iodide in the range of photon energies between 10.4 and 11.9 eV	357
196.	Comparison of present work with the work of Phillipp, Taft, and Apker	358
197.	E_p vs $h\nu$ for potassium iodide	359
198.	Estimated optical density of states of potassium iodide . .	359
199.	Optical density of potassium iodide [Teegarden and Baldini, Ref. 86]	361
200.	Energy distribution curves for insulating potassium iodide in the range of photon energies between 7.6 and 9.2 eV . .	362

ILLUSTRATION (CONTD)

<u>No.</u>	<u>Title</u>	<u>Page</u>
201.	Energy distribution curves for insulating potassium iodide in the range of photon energies between 9.5 and 10.6 eV . . .	363
202.	Energy distribution curves for insulating potassium iodide in the range of photon energies between 11.0 and 11.8 eV . .	364
203.	Comparison of energy distribution curves before and after potassium iodide sample became insulating	365
204.	A comparison of the optical density of states $N(E)$ for Cu, CuI, CsI, and KI	369
C-1.	Schematic of normalizing apparatus	396



PRECEDING PAGE BLANK NOT FILMED.

SYMBOLS

B.Z.	Brillouin zone
C	constant
$C[\alpha L, T_f]$	correction factor accounting for angular distribution of electrons
c	velocity of electromagnetic radiation in free space
c.b.	conduction band
E	energy of an electron
EDC(s)	energy distribution curve(s)
E_f	energy of fermi level
EFFTH(E)	shape factor (or effective value of threshold function)
E_p	energy of a peak or a shoulder in the experimental EDCs
e	magnitude of electron charge
fcc	face-centered cubic
$f_{vc}(\vec{k})$	interband oscillator strength
$G(x, \omega)$	generation rate of electrons
h	Planck's constant
\hbar	$h/2\pi$
h ν	energy of a photon
I_o	incident photon flux
K	constant
K	constant
\vec{k}	wave vector
$k(\omega)$	extinction coefficient
L(E)	electron-electron scattering length
L_o	normalizing constant for electron-electron scattering length

M	momentum matrix element
m	electron mass
N_c	conduction-band density of states
$N(E)$	density of states
N_v	valence-band density of states
$n(E, \omega)$	energy distribution of photoemitted electrons
n	index of refraction
$R(\hbar\omega)$	magnitude of reflection coefficient
R_s	total number of electrons that are first reflected at the surface, next suffer an inelastic electron-electron collision, and are then photoemitted
R_{tot}	total number of once-scattered electrons that are photoemitted
r	position vector
S	scale factor
$T(E)$	escape function
$T_f(E)$	semi-classical escape function
V	voltage
V_p	phase velocity of electromagnetic radiation
$v.b.$	valence band
v_g	electron group velocity
v_p	electron phase velocity
$y(\hbar\omega)$	quantum yield
$\alpha(\omega)$	absorption coefficient
γ	electronic specific heat
δ	delta function

ϵ	dielectric susceptibility
ϵ_1	real part of dielectric susceptibility
ϵ_2	imaginary part of dielectric susceptibility
θ_0	angle defining escape cone
λ	wavelength
ν	frequency of electromagnetic radiation
σ_b	optical conductivity
τ	electron lifetime
ϕ	work function (energy difference between fermi level and vacuum level)
χ	electron affinity (energy difference between bottom of conduction band and vacuum level)
ψ	wave function describing the state of an electron
ω	$2\pi f$
∇_k	differential vector operator with respect to k

I. INTRODUCTION

The energy band structures of silicon and germanium have been rather well understood for a number of years (Herman, 1955), but accurate energy band calculations for the zincblende III-V, II-VI, and I-VII compounds are just becoming available. However, germanium and silicon crystallize in a diamond lattice, which has essentially the same symmetry as the zincblende lattice. Because of the similarity between the diamond and zincblende lattices, peaks in the reflectivity and absorption spectra of the zincblende III-V, II-VI, and I-VII compounds have been interpreted in terms of a germanium-like energy band structure (Cardona, 1963; Phillips, 1964). In explaining the optical data in terms of a germanium-like band structure, a starting approximation was used in which the atomic nature of the constituent atoms was disregarded; J. C. Phillips (1964) has stated that "A wide range of experimental data now indicates that uv structure depends primarily upon crystal structure and only secondarily on atomic composition." In this manner, a certain amount of success has been achieved in explaining the optical data of the III-V and the II-VI zincblende compounds.

Since the cuprous halides are I-VII compounds that crystallize in a zincblende lattice, peaks in the optical spectra of these materials have also been identified (Cardona, 1963; Phillips, 1964) with direct transitions between symmetry points in a germanium-like band structure. In making these identifications, it has been assumed that the copper 3d band does not play an important role in the valence band structure of the cuprous halides. However, an examination of the outer electron configurations of the atoms making up the cuprous halides indicates that the copper 3d bands could be intimately involved in the construction of the valence bands of the cuprous halides. For example, in CuBr, the outer electron configuration of the copper atom is $3d^{10}4s^1$, and the outer electron configuration of the bromine atom is $4p^5$. Thus, without a detailed energy band calculation or experimental information other than reflectivity, it would seem presumptuous to ignore the possible presence of the copper 3d band in explaining the optical spectra of the cuprous halides.

The main objective of this work has been to use experimental photoemission techniques to study the electron structure of the cuprous

halides, and thereby to determine whether or not the copper 3d band is involved in the valence band structure of the cuprous halides. To have a sound basis for distinguishing between the copper 3d bands and the halogen p bands in the photoelectric energy distributions, the photoemission studies were extended to include the noble metals and certain alkali halides. The studies of the noble metals provided information on the character of d bands in photoelectric energy distributions, and the studies of the alkali halides provided information on the characteristic features of halogen p bands in photoelectric energy distributions. Because the photoemission studies of the noble metals and the alkali halides revealed a wealth of new information about the electronic structure of these materials, a significant portion of this report has been devoted to the noble metals and the alkali halides.

The photoemission experiments consisted of measuring the quantum yield and the photoelectric energy distributions from evaporated films of the material under study. These films were prepared and measured in an oil-free vacuum of typically 2×10^{-9} torr at photon energies up to 11.9 eV, the high energy cutoff of the LiF window. In several cases, windowless low vacuum measurements were made at photon energies up to 21.2 eV. In addition to the photoemission studies, reflectivity measurements were made in cases where adequate experimental data were not available in the literature. The photoemission data provided much more useful information than the reflectivity data, for the following reasons: The energy of a peak in the reflectivity corresponds to the energy difference between electronic levels in the valence band and electronic levels in the conduction band; however, the absolute energy of these levels cannot be determined from the reflectivity data. The photoelectric energy distributions, on the other hand, provide information on the initial and final states involved in an optical transition. For the purposes of this study, the photoelectric energy distributions were by far the single most important piece of experimental data.

Reliable photoelectric energy distributions and quantum yield data were obtained by essentially eliminating the possibility of contamination due to foreign gases. This was done by constructing an oil-free vacuum system in which the samples could be prepared and tested at a vacuum of

typically 2×10^{-9} torr. At such a low pressure, at least one photoelectric energy distribution curve could be measured before a monolayer of foreign gas could condense on the surface of freshly prepared samples. Nearly all of the photoemission measurements were carried out in a versatile stainless steel and glass photoemission chamber, which was designed to provide rapid changeover from experiment to experiment, an impossibility with conventional glass phototubes.

The experimental techniques and equipment are described in Chapter II, and the mathematical formalism that is used in later chapters as a basis for interpreting the photoemission data is developed in Chapter III. A portion of the formalism presented in Chapter III can be found in the literature, but this material has been included for the sake of continuity and convenience to the reader. Chapter III also includes the description of a simple model that describes quantitatively the photoemission process, the optical data, and the electron-electron scattering length in terms of the optical density of states. This model is based upon nondirect transitions, and uses a semiclassical threshold function and a modified free-electron-like conduction band. As an example, this model is used in Chapter III to predict the photoemission properties of simple metals. This model is used in the subsequent chapters on the noble metals and the cuprous halides to deduce the optical density of states, the electron-electron scattering length, and $\epsilon_2(\omega)$ from the experimental photoemission data. The studies of Cu, Ag, and Au are presented in Chapters IV, V, and VI, and the properties of these noble metals are compared in Chapter VII. The studies of the cuprous halides are presented in Chapter VIII, and the studies of the alkali halides are presented in Chapter IX. In Chapter X, the optical densities of states of the cuprous halides are compared with the optical densities of states of copper and the alkali halides, and it is shown that the electronic structure of the cuprous halides seems to be composed of distinct contributions from the copper and the halogen atoms. A mathematical discussion concerning the uniqueness of the model used in analyzing the photoemission data and an outline of the computer programs used in processing the photoemission data are included in the Appendixes.

II. EXPERIMENTAL METHODS

The experimental techniques and methods used by the author in studying photoemission from a number of different materials are outlined in this chapter. The innovations made by the author are emphasized; the reader is referred to the literature for details on equipment and techniques described earlier by other workers.

A. THE BASIC MEASUREMENTS

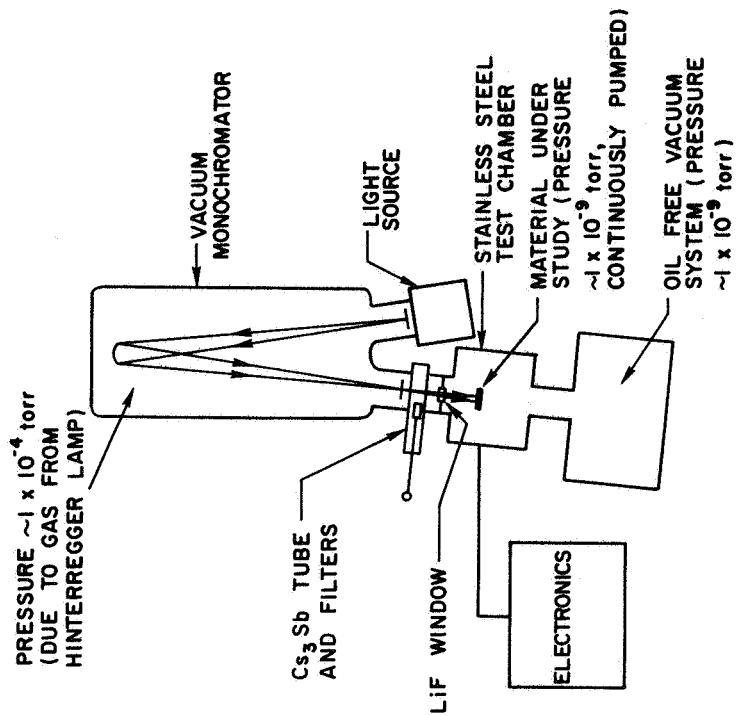
Three types of measurements are presented in this report:

- (1) Photoelectric energy distribution (EDCs) - $n(E, \omega)$.
- (2) Quantum yield - $Y(h\nu)$.
- (3) Reflectivity - $R(h\nu)$.

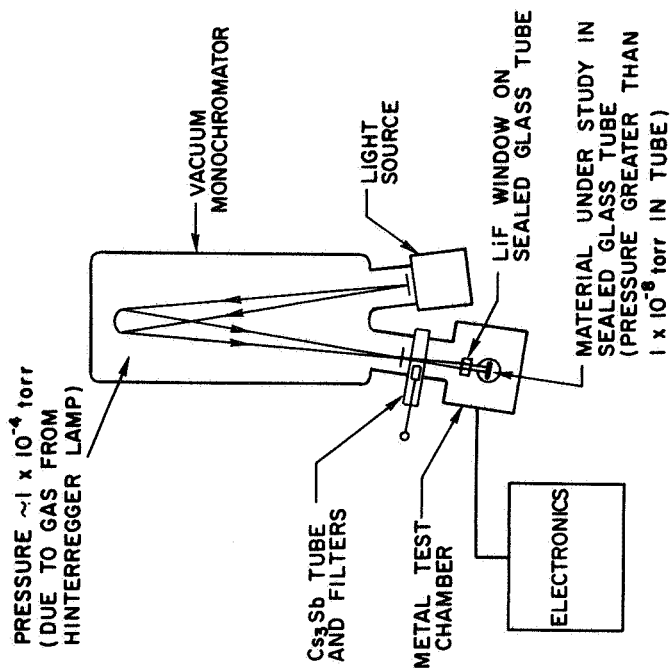
Figure 1 is a block diagram of the apparatus used to measure the energy distributions and the quantum yield. In Fig. 1a, the material under study is sealed in a glass photodiode with a LiF single crystal window. The high energy cutoff of the LiF window is 11.8 eV, which sets the upper limit for high vacuum measurements in our laboratory. In Fig. 1b, the material under investigation is prepared and studied in a continuously pumped, oil-free vacuum. Almost all of the experimental data presented in this investigation has been obtained with the use of the continuously pumped system sketched in Fig. 1b. The amount of light incident upon the LiF window is measured by the photocurrent from a calibrated Cs_3Sb tube, which can be moved in and out of the light beam. The instruments used to measure the EDCs and the quantum yield are schematically labeled "electronics" in Fig. 1b.

B. LIGHT SOURCE AND VACUUM MONOCHROMATOR

The light source is a Hinterregger-type gas discharge lamp, and the monochromator is a McPherson Model 225 Vacuum Ultraviolet Monochromator with a 600-line/mm reflection grating blazed at 1500 \AA . Details concerning the discharge lamp and the monochromator can be found in the report of Kindig [Ref. 1]. The light source and monochromator used in the present



b. Continuously pumped method



a. Sealed glass tube method

FIG. 1. MEASUREMENT OF PHOTOELECTRIC ENERGY DISTRIBUTIONS AND QUANTUM YIELD AT PHOTON ENERGIES LESS THAN 11.8 eV.

experiment were essentially the same as those described by Kindig except that the gas for the discharge lamp was passed through a liquid nitrogen trap, so as to condense any oil vapors that might be present in the compressed gas tanks.

The range of photon energies used in the experiment varied from 3 to 21.2 eV. The experiments using photon energies greater than 11.9 eV were done with no window between the sample chamber and the monochromator. Thus, they were made in a vacuum of no better than 1×10^{-5} torr. Hydrogen, neon, and helium were used as gases in the Hinterregger lamp to provide radiation in the spectral region indicated below:

Hydrogen	3 to 14 eV (continuous spectrum)
Neon	16.8 eV (strong line)
Helium	21.2 eV (strong line).

Because the output slits of the monochromator were never made less than 0.1 mm, the resolution was not sufficient to resolve lines in the hydrogen spectrum, resulting in an effective continuum.

C. THE VACUUM SYSTEM

The possibility of oil vapor contamination of the material under study was eliminated by the construction of the vacuum system shown in the block diagram, Fig. 2. The pumps and the valves are standard components purchased from Varian Associates, Palo Alto, California. The entire system was constructed of stainless steel, glass, and other low-vapor pressure materials. All vacuum joints were made by compressing a soft copper gasket in a Varian Conflat Flange, and no rubber or viton seals were used in the ultrahigh vacuum section. After bakeout of the experimental chamber and the pump system, an ultimate pressure of 5×10^{-10} torr could be achieved in the experimental chamber. (In this case, an additional titanium sublimation pump was built into the experimental chamber.) The ultimate pressure of 5×10^{-10} torr was reached only after many days of pumping, but pressures of 1 or 2×10^{-9} torr were routinely achieved after several days of pumping. After the pressure reached about 2×10^{-9} torr, the material under investigation was evaporated and studied.

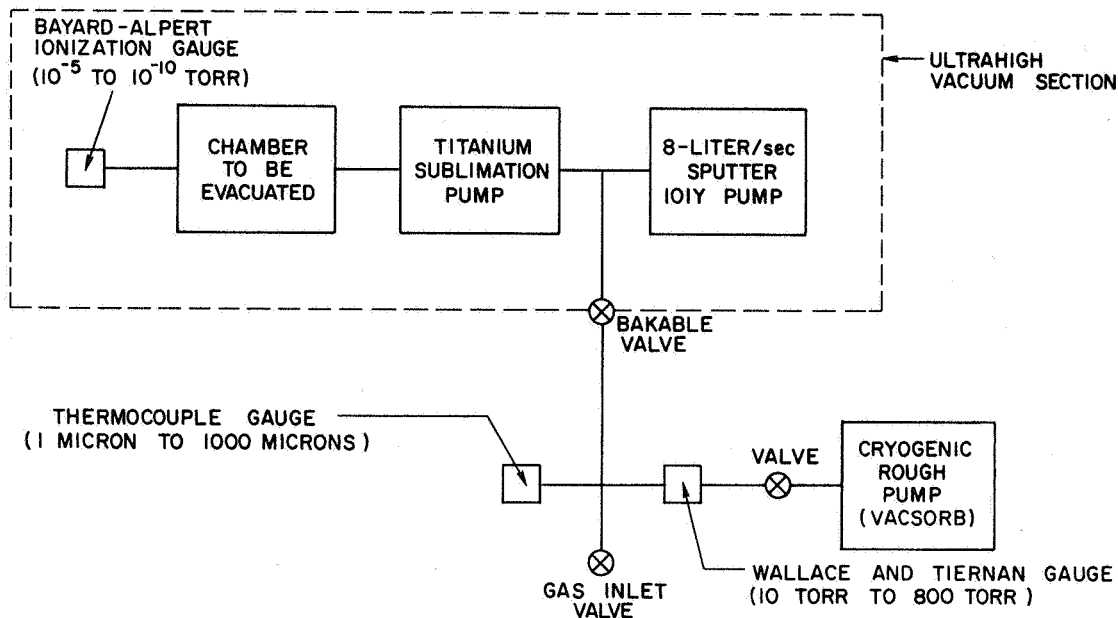


FIG. 2. BLOCK DIAGRAM OF VACUUM SYSTEM. Varian Associates vacuum components used throughout.

The motivation for building a vacuum system that attains a pressure of less than 2×10^{-9} torr stems from the desirability of being able to measure at least one EDC between the time of evaporation of a film and the time required for a monolayer of foreign gas to condense on the surface. Thus, the effect of the foreign gas on the EDCs would be determinable. Figure 3 shows the time required to form a monolayer as a function of pressure for several common gases. The curves in Fig. 3 were calculated assuming unity sticking coefficient and the molecular diameters given [Ref. 2]. Since the minimum practical time between evaporation and completion of one EDC measurement was 6 or 7 minutes, reference to Fig. 3 shows that, for a total pressure of 2×10^{-9} torr, an EDC could be measured before gases such as H_2O , CO_2 , N_2 , and O_2 could form a monolayer. Note, however, that for unity sticking coefficient, it is necessary to have a partial pressure of H_2 less than 2.3×10^{-10} torr. (During the course of this research, the partial pressure of the gases constituting the 2×10^{-9} torr total pressure was not determined. However, recent partial pressure measurements [Ref. 3] of a similar system indicate the partial pressures of light gases such as H_2 and He to

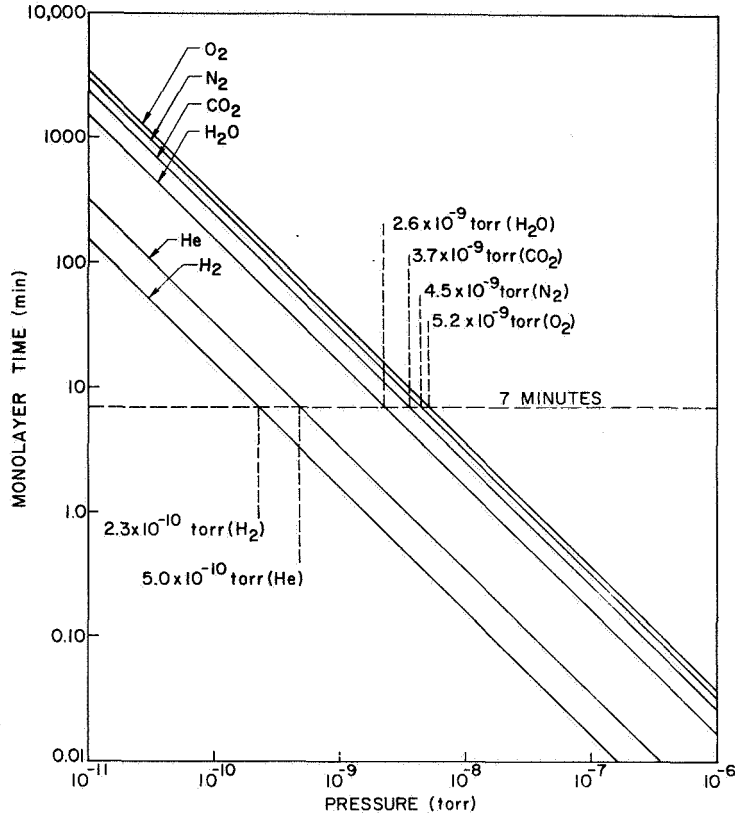


FIG. 3. TIME REQUIRED TO FORM A MONOLAYER OF GAS ON A SURFACE. Unity sticking coefficient has been assumed.

be considerably less than 2.3×10^{-10} torr at a total pressure of 2×10^{-9} torr.) The vacuum system (Fig. 2) was constructed by the author with the intent of routinely achieving an oil-free vacuum of less than 2×10^{-9} torr, under the restriction of minimum cost for vacuum components.

Figure 4 is a picture of the basic pumping unit. For maneuverability, the basic pumping unit and the electronics (necessary to operate the vacuum pumps, bakeout units, and evaporators) were mounted on a mobile frame, as shown in Fig. 5. Note in Fig. 4 that the experimental chamber is attached to the basic pump unit with a single Varian Conflat Flange. This flange can be quickly unbolted, and a new experiment can be rapidly attached and evacuated. The mobility of the pump station and the convenience of the Conflat Flange made the vacuum system a versatile and flexible unit that was used for many applications in the course of this research. Several of these applications are shown in Figs. 6, 7, and 8.

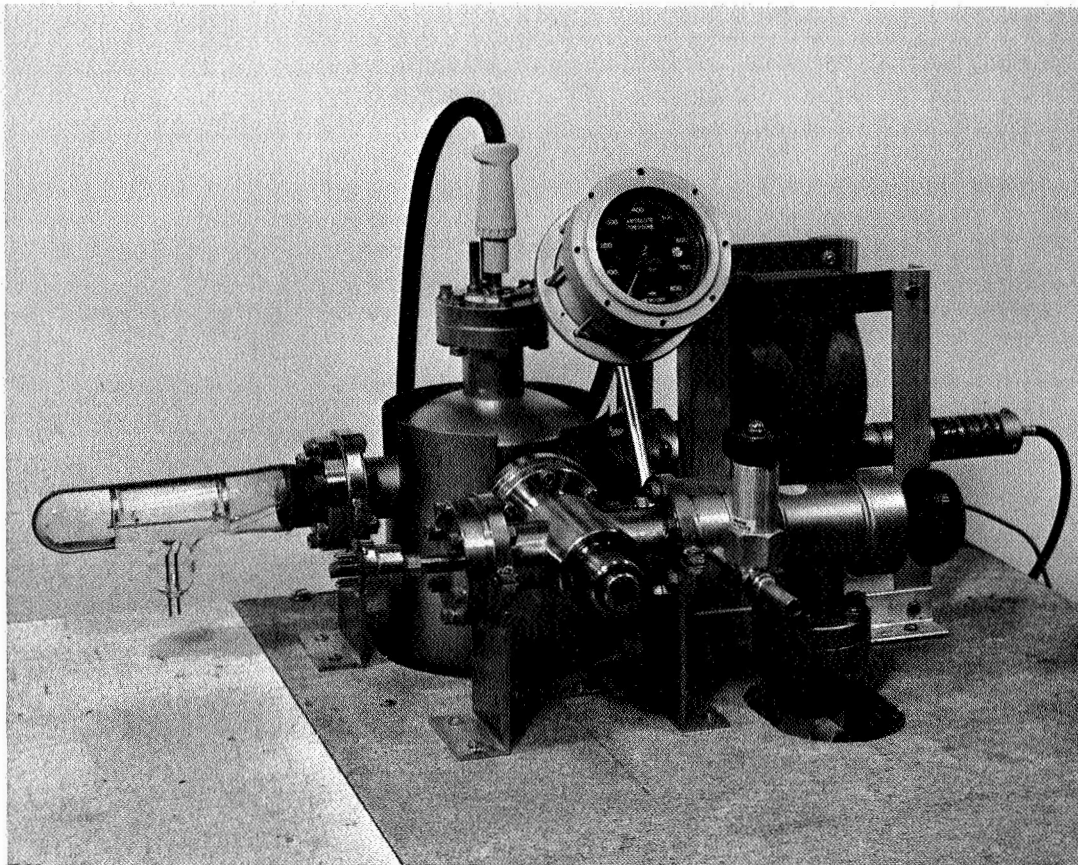


FIG. 4. THE BASIC PUMPING UNIT EVACUATING AN APPARATUS FOR PURIFYING CUPROUS BROMIDE.

D. THE PHOTODIODE

The photodiodes used to measure the velocity distributions and the quantum yield were of the simple cylindrical type described by Apker et al [Ref. 4] and Spicer [Ref. 5]. The geometry and dimensions of the collector and emitter are shown in Fig. 9. Although this configuration is quite different from the ideal geometry of a small emitter in a large spherical collector with a small light hole, Spicer [Ref. 6] found little difference in the EDCs obtained from either geometry. Because the cylindrical collector is much easier to manufacture than the spherical collector, the cylindrical collector was used in all the experiments reported here.

The emitter was usually a highly polished piece of copper that was hydrogen-fired before it was used as a substrate for an evaporated film.

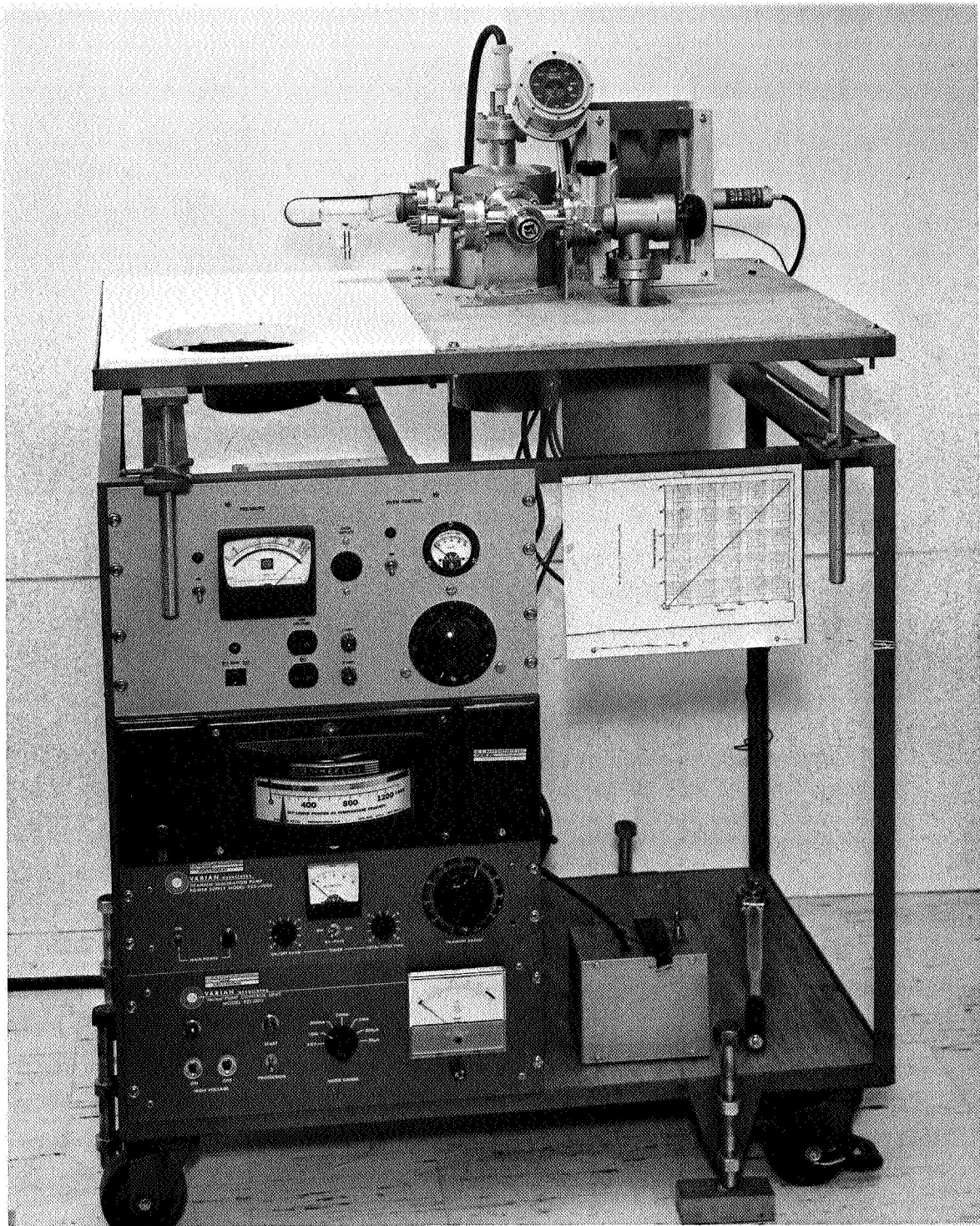


FIG. 5. THE BASIC PUMPING UNIT AND ASSOCIATED CONTROL UNITS MOUNTED ON A MOBILE FRAME.

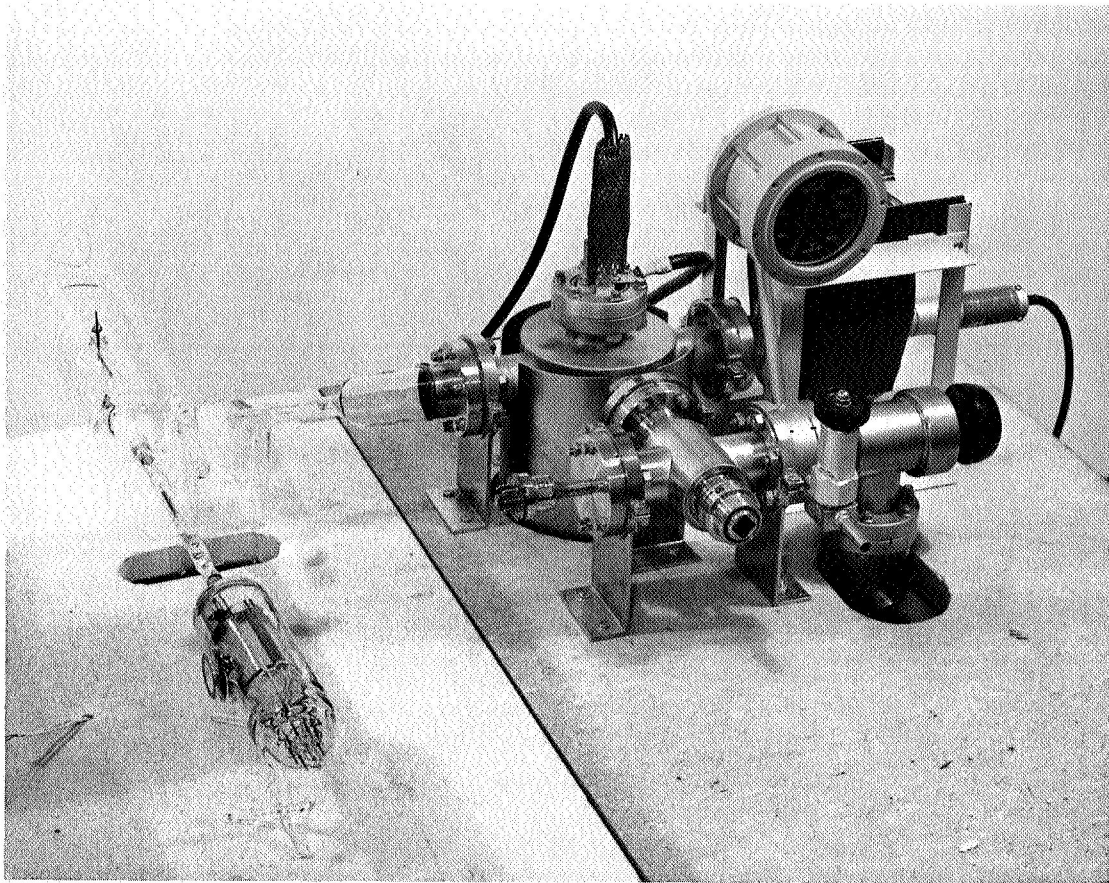


FIG. 6. EVACUATING A PHOTOTUBE. The phototube is continuously pumped while the material under investigation is being evaporated. The phototube is then sealed off, and photo-emission studies are made as in Fig. 1.

For the materials studied, identical results were obtained for copper, silver, or gold substrates. The collector can (in glass photodiodes) was usually made of molybdenum, although no difference was found between molybdenum and nickel collector cans. (Nickel is ferromagnetic and can have a small residual magnetic field. Kindig [Ref. 1] showed that a magnetic field of a few gauss can be detrimental to accurate measurement of EDCs, so the use of magnetic materials was strictly avoided by the author whenever possible.)

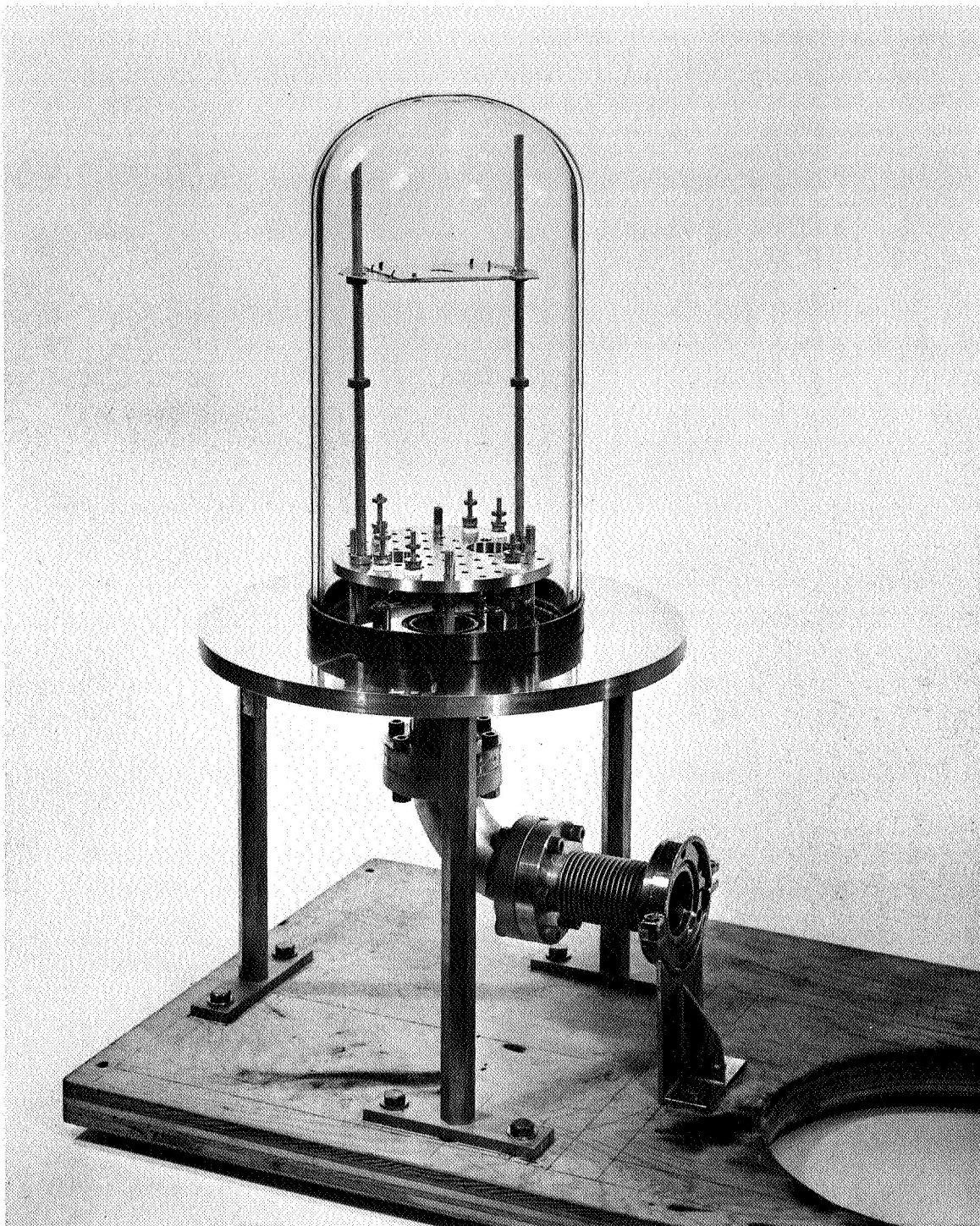


FIG. 7. BELL JAR USED IN CONJUNCTION WITH THE BASIC PUMP UNIT. This bell jar was used for many experiments of a minor nature that required an oil-free vacuum, but did not require a pressure less than 5×10^{-8} torr. The gasket was made of viton, and the base was a machined (not polished) monel plate.

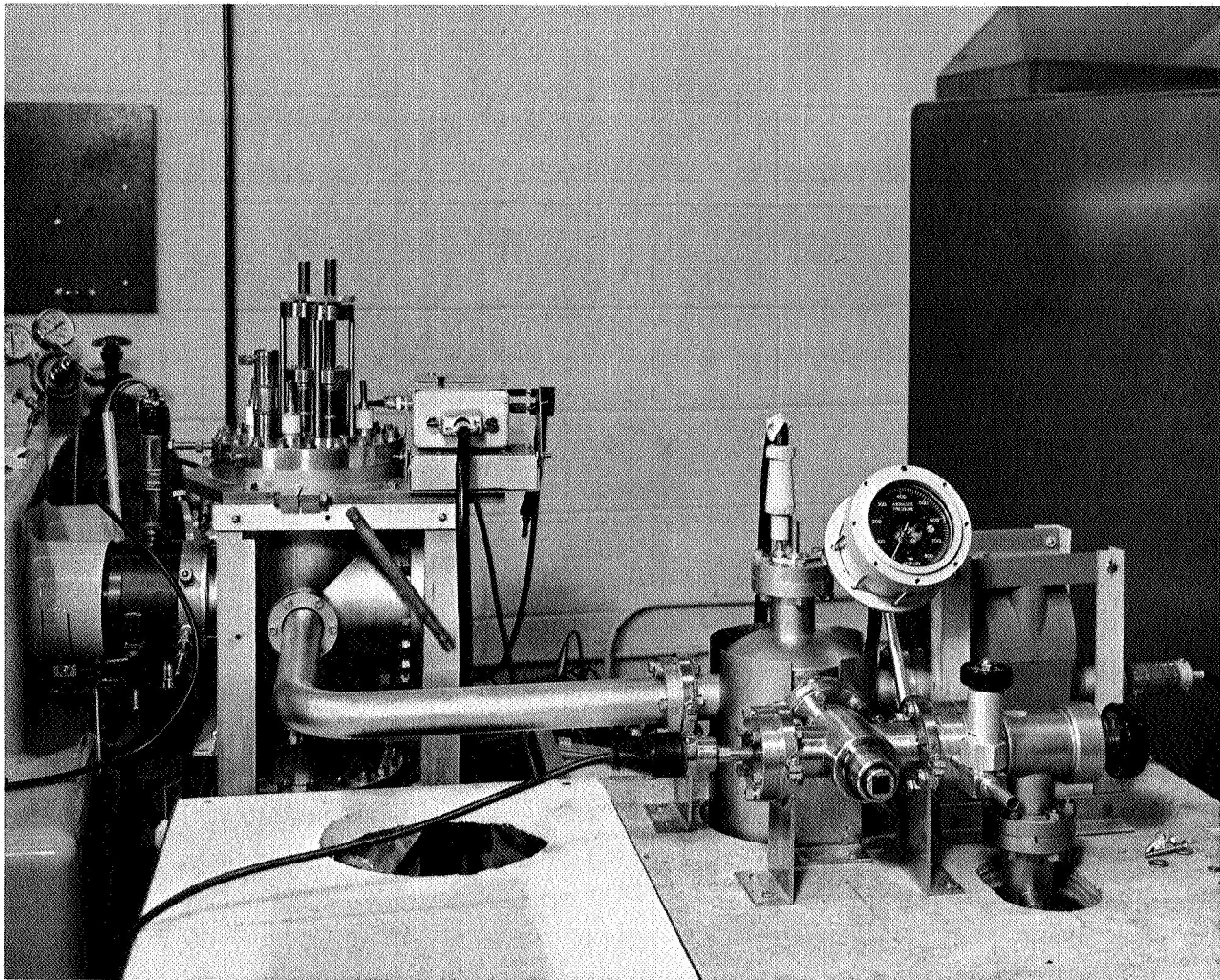


FIG. 8. THE PHOTOEMISSION CHAMBER (SECTION F) BEING CONTINUOUSLY PUMPED DURING A PHOTOEMISSION EXPERIMENT PERFORMED AS IN FIG. 1b.

E. THE SEALED GLASS PHOTOTUBE

In a limited number of cases, EDC and quantum yield measurements were made with a sealed glass phototube such as that shown in Fig. 10. The glass phototube consists basically of an emitter substrate and a collector can mounted in a glass envelope with a LiF window.

The LiF window, a single crystal of cleaved LiF purchased from the Harshaw Chemical Company, is transparent to ultraviolet radiation for photon energies less than 11.9 eV. Lithium fluoride was used because it has the highest cutoff frequency of any practical material known.

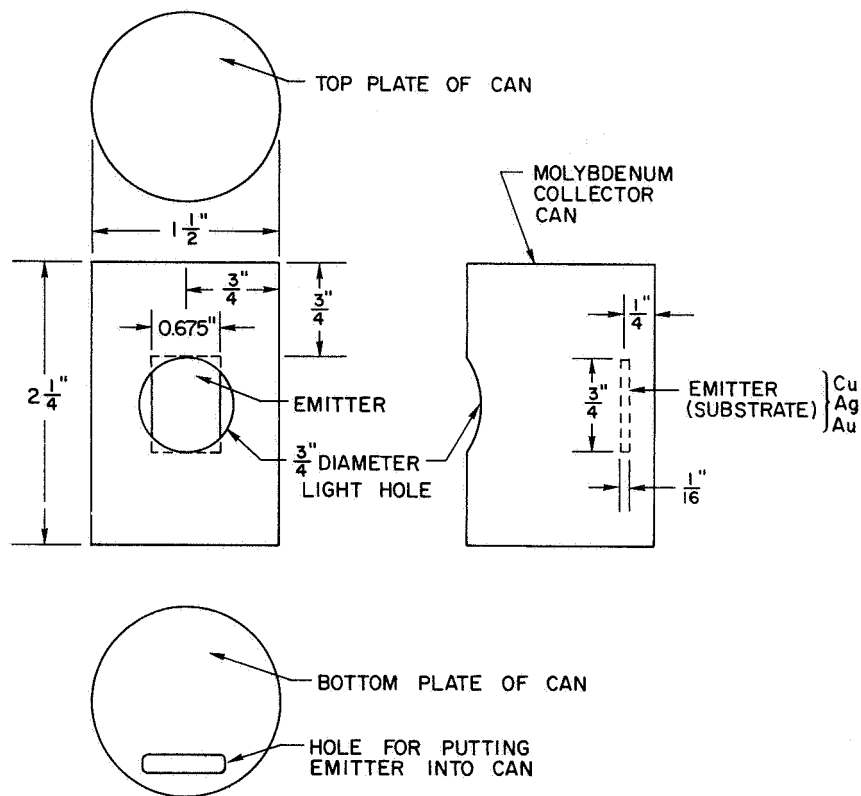


FIG. 9. GEOMETRY AND DIMENSIONS OF COLLECTOR AND EMITTER OF THE PHOTODIODE.

Using a process described earlier by Berglund [Ref. 7], the LiF crystal was sealed by a silver chloride "glue" to a silver flange that was sealed into the glass body of the tube. Such seals are vacuum-tight and have a very low vapor pressure. The use of a LiF window permits preparation and study of a material under ultrahigh vacuum at photon energies up to 11.9 eV. Exposure to the atmosphere has a severe effect on the EDCs and the quantum yield of most materials; therefore, ultrahigh vacuum is essential for meaningful photoemission studies. Structure in the EDCs was found to be much more sensitive to contamination than the quantum yield, and the smearing of such structure in the EDCs was usually interpreted as a sign of an inadequate high vacuum.

The tube shown in Fig. 10 was used to measure EDCs and quantum yield from CuBr. The CuBr powder was evaporated onto the polished metal substrate outside the collector can. The substrate was mounted on a rail,

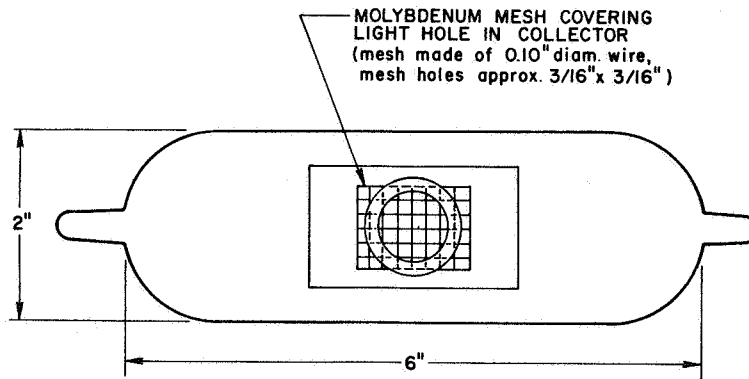
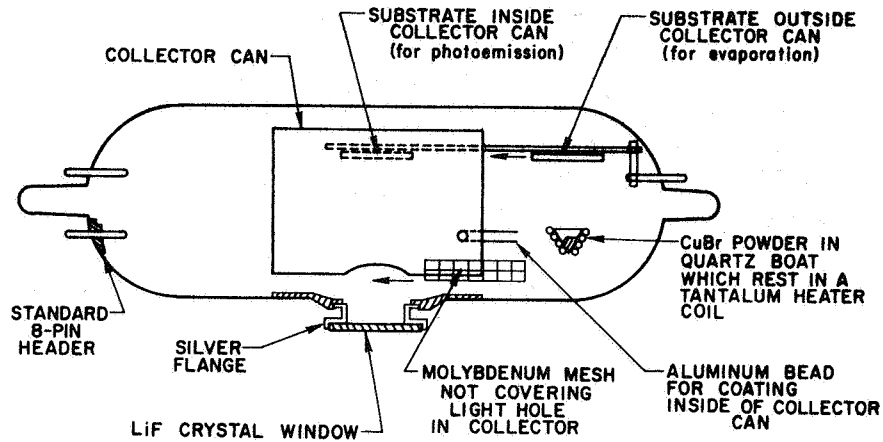


FIG. 10. SEALED GLASS PHOTOTUBE USED TO CHECK THE EFFECT OF THE COLLECTOR LIGHT HOLE ON ENERGY DISTRIBUTION CURVES FOR CUPROUS BROMIDE.

so that it could slide into the collector can for the photoemission experiment. To assure uniformity of the work function on the inside of the collector can, an aluminum bead was evaporated inside the collector can.

Note that in this "typical" phototube, the light hole in the collector is quite large and that the LiF window is quite close to the collector. To test the effect of the large light hole and the close

proximity of the LiF window on the experimental EDCs, the tube in Fig. 10 was fitted with a molybdenum wire mesh that could be moved over the light hole. The mesh served, in effect, to make the collector light hole electrically much smaller, since the mesh was in good electrical contact with the collector can, and the potential of the collector was essentially extended over the light hole. The fine wire minimized the photoemission of electrons from the mesh. The result of the experiment was that the same EDCs were measured with or without the mesh over the light hole. This result suggests that the LiF window and the glass tube had charged up to such a potential that all the electrons that were photoemitted through the open light hole were repelled by the glass envelope and eventually collected by the collector can. Whatever the detailed nature of the charging phenomenon, the experiment with the mesh supports the contention that the cylindrical diode geometry used in the photoemission experiments does not distort the EDC or the quantum yield measurements. In some phototubes, however, distortion occurred in the EDCs because the LiF window did not (apparently) charge up sufficiently. This effect was corrected by using a 15-V battery to bias the silver flange negative with respect to the collector can.

The tube of Fig. 10 was prepared in the following manner: Purified CuBr powder was placed in the quartz boat, and the tube was sealed to the high vacuum pump station in the manner of Fig. 6. After bakeout at about 175°C and several days of pumping, the pressure in the pump system was less than 5×10^{-9} torr. (The pressure inside the phototube was not monitored.) At this time, the CuBr was evaporated onto the substrate, the aluminum bead was evaporated inside the collector can, and the tube was sealed off with a torch. During the seal-off process, the pressure inside the phototube was not monitored, but any possible pressure rise had been minimized by heating the glass at the seal-off point to its softening temperature prior to the evaporation of the CuBr. After seal-off, photoemission studies were made and found to be stable for six months, after which the structure in the EDCs became smeared, indicating contamination due to a poor vacuum within the phototube. The poor vacuum after six months appeared to be due to diffusion of air through the silver chloride seal, since the life of a tube could be extended far beyond six

months by coating the silver chloride seal with "glyptol" (as suggested by W. E. Spicer).

The sealed glass phototube described above was not used extensively to study the materials presented in this study because of the following disadvantages:

- (1) During evaporation, the pressure in the phototube may be much higher than the pressure in the vacuum pumps, due to the small size of the glass tubulation at the seal-off point.
- (2) The torch seal-off might contaminate the sample before it is studied.
- (3) The tube is sealed, so that the pressure inside the tube cannot be monitored during photoemission measurements.
- (4) Construction of the tube is time-consuming and difficult, especially if a number of evaporators, heaters, baffles, and motions must be incorporated into the tube.

Because of these disadvantages,¹ it was decided to abandon the use of glass phototubes for general photoemission studies and to construct a versatile, continuously pumped photoemission chamber that would have none of the above disadvantages of a glass phototube. Such a chamber was constructed (see Section F).

F. THE PHOTOEMISSION CHAMBER

Nearly all of the photoemission data presented in this report has been obtained with the use of the continuously pumped photoemission

¹Several of the disadvantages enumerated above can be overcome to a certain extent by the use of special techniques. For example, the pressure rise at seal-off can be eliminated by use of a soft copper "pinch-off" instead of a glass seal, as described in Section G. Also, the phototube can be used to study photoemission while being continuously pumped, by use of a technique developed by Eden [Ref. 8]. In this method, a vacuum-tight LiF window is placed at the exit slit of the vacuum monochromator, and the phototube is aligned on the pump station so that light can pass out of the monochromator, through a few centimeters of air and into the phototube. Because air severely attenuates the ultraviolet light, the region between the phototube and the monochromator is filled with He gas, which is sufficiently transparent to ultraviolet radiation to permit a significant amount of light to reach the phototube. Eden has been successful in making photoemission measurements by use of this technique.

chamber sketched in Fig. 11. This versatile chamber consists basically of a photodiode mounted in a large stainless steel chamber with a LiF window. The schematic of Fig. 11 is intended to portray the basic features of the photoemission chamber, and does not include all of the electrical feedthroughs, liquid nitrogen feedthroughs, and linear motions that exist in the actual chamber. For a more detailed description of the chamber and the design concepts, the reader is advised to contact either the author or W. E. Spicer, Stanford Electronics Laboratories. The major features of the photoemission chamber are described below:

- (1) Rapid changeover from experiment to experiment is easily accomplished. The entire photoemission apparatus is attached to the top flange, which is a Varian Conflat Flange sealed by compressing a soft copper gasket. A new experiment can be installed in the chamber in a matter of hours, compared with the weeks or months required to build a glass phototube. The substrate clips into its holder (see Fig. 12) with four wires, and a new polished substrate can be mounted in the emitter assembly in a matter of minutes.
- (2) Ultrahigh vacuum is readily achieved. All components are stainless steel, glass, and other low vapor-pressure materials. No organic materials are used in the chamber. All seals are made with soft copper gaskets and Varian Conflat Flanges that can be quickly assembled and disassembled. The system is pumped externally by use of the basic pump station of Fig. 2, as shown in Fig. 8. In addition, a titanium sublimation pump is built into the chamber, as shown in Fig. 11. With the use of these pumps, a pressure of 2×10^{-9} torr is routinely attained in the chamber after a two-day bakeout at a temperature of 150°C . The pressure is measured with a Bayard-Alpert ionization gauge that is mounted in the side of the photoemission chamber (not shown in Fig. 11). The ultimate pressure of 5×10^{-10} torr can be reached only after many days of pumping. (Future use of larger pumps should lower the ultimate pressure and decrease the pumpdown time.)
- (3) Two linear motions, each with a travel of more than 2 inches, were built into the top flange of Fig. 11. One linear motion is used to move the substrate in and out of the collector can, and the other linear motion is (usually) used to move a metal evaporator bead in and out of the collector can.
- (4) The temperature of the substrate can be varied from 77°K (liquid nitrogen temperature) to over 900°K . As seen from Figs. 11 and 12, the substrate is directly connected

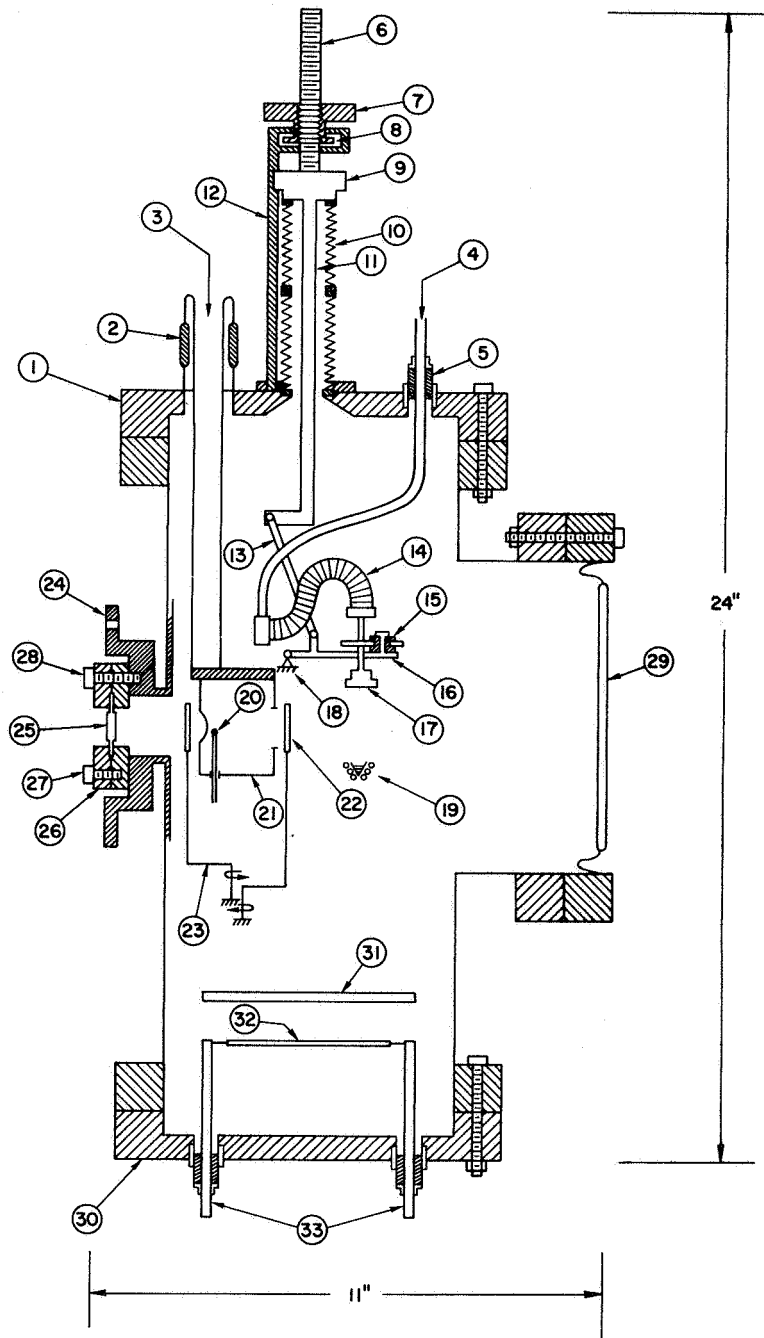


FIG. 11. SCHEMATIC OF THE PHOTOEMISSION CHAMBER.

PHOTOEMISSION CHAMBER COMPONENTS (FIG. 11)

- ① Top Flange
- ② Glass insulator.
- ③ Stainless steel liquid nitrogen pipe for cooling the collector.
- ④ Liquid nitrogen tube for cooling the substrate. This is a copper tube that is brazed (in place of a solid conductor) into a Varian 150 ampere current feedthrough.
- ⑤ Ceramic insulator.

Linear Motion

- ⑥ Screw.
- ⑦ Rotary disk (rotating this disk causes the screw to move up and down. The disk turns freely in the teflon bearing)
- ⑧ Teflon bearing (removable for bakeout).
- ⑨ Alignment plunger.
- ⑩ Stainless steel bellows (welded diaphragm type, purchased from Varian Associates, Palo Alto, Calif.).
- ⑪ Stainless steel rod.
- ⑫ Rigid support rod (three of these guide the alignment plunger).

Movable Emitter Assembly

- ⑬ Linkage arm.
- ⑭ Liquid nitrogen bellows (stainless steel, welded diaphragm type, purchased from "Metal Bellows Corporation, 20977 Knapp St., Chatsworth, Calif.).
- ⑮ Ceramic insulator (to insulate emitter from linear motion).
- ⑯ Support arm.
- ⑰ Emitter assembly (in position for evaporation outside the collector can) (see Fig. 12 for details).
- ⑱ Fixed pivot point.
- ⑲ Evaporator outside collector can (example shown: CuBr powder in quartz cone in tantalum heater coil).
- ⑳ Metal bead evaporator inside collector can (after evaporation, this bead is taken out of the collector can with the second linear motion not shown in Fig. 11).
- ㉑ Collector can (1/8-in. thick, for good heat conduction).
- ㉒ Evaporator shield covering hole in back of collector can (a small piece of soft iron is connected to the shield mechanism. After evaporation, the shield is rotated away from the hole using a magnet external to the photoemission chamber.)

PHOTOEMISSION CHAMBER COMPONENTS (FIG. 11) (CONTD)

②③ Evaporator shield covering hole in front of collector (magnetically actuated in the same manner as ②②).

②④ Flange that is bolted to the vacuum monochromator.

LiF Window Assembly

②⑤ LiF window in silver flange, which is clamped between two conflat flanges ②⑥ .

②⑥ Assembly of two conflat flanges which hold LiF window. This assembly can be removed from the photoemission chamber without breaking the vacuum seal on the silver flange. (The LiF window is removed and the transmission measured for each photoemission experiment.)

②⑦ Bolt that clamps two conflat flanges around silver ring which holds the LiF window.

②⑧ Bolt that attaches assembly ②⑥ to the photoemission chamber.

②⑨ Glass viewport.

③⑩ Bottom flange.

③① Copper plate to shield photoemission apparatus from Ti filament.

③② Ti filament (used as a titanium sublimation pump in the chamber).

③③ Current feedthroughs for Ti filament.

NOTE: EMITTER AND LIQUID N₂ RESERVOIR ARE MADE OF OFHC COPPER.

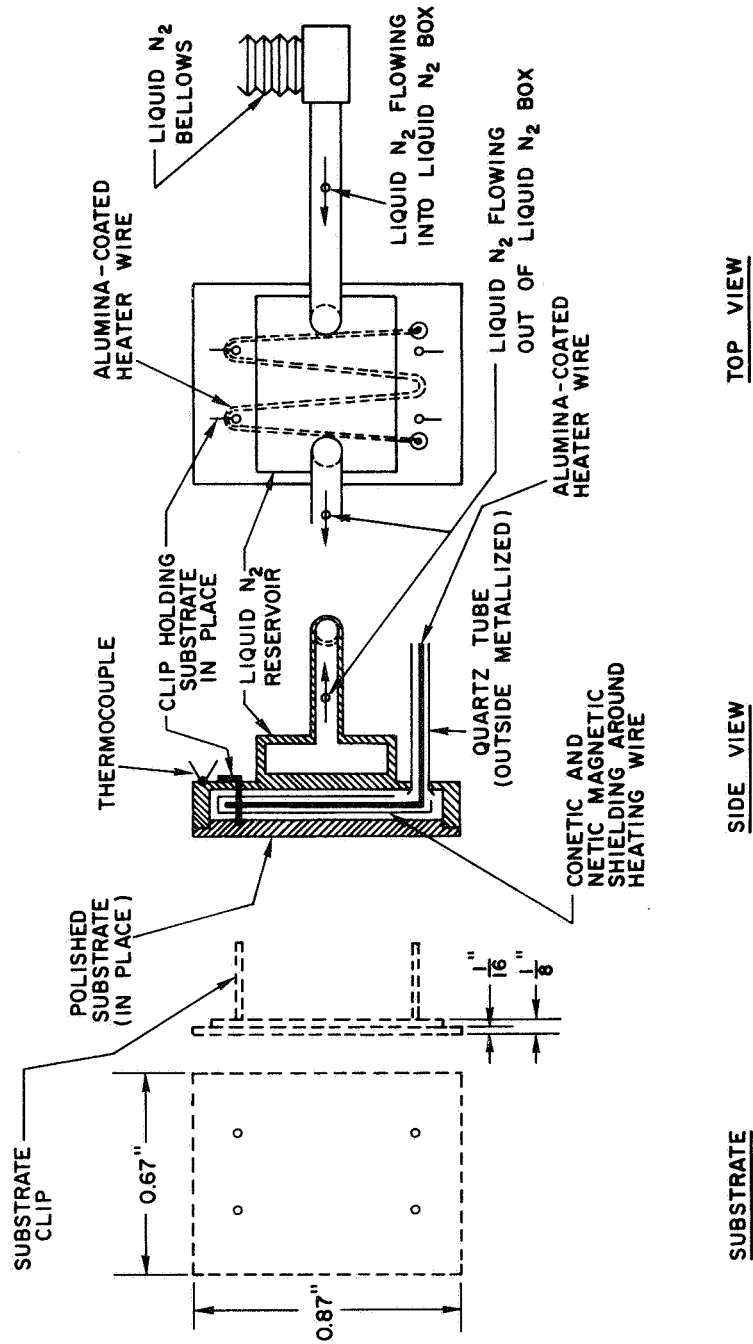


FIG. 12. SCHEMATIC OF THE EMITTER ASSEMBLY.

to a small liquid nitrogen reservoir. The problem of possible nitrogen gas buildup in the liquid nitrogen reservoir has been avoided by constructing the liquid nitrogen reservoir with an input and an output pipe. Liquid nitrogen under slight pressure can thus be made to flow through the reservoir. The problem of getting liquid nitrogen to a movable substrate under ultrahigh vacuum was solved by the use of stainless steel bellows. These bellows were strong enough to withstand atmospheric pressure, yet flexible enough so that the substrate could be moved with liquid nitrogen in the bellows. As shown in Fig. 11, the copper pipes carrying the liquid nitrogen to the bellows were connected to the top flange by means of a novel, compact, and very inexpensive liquid nitrogen feedthrough that was insulated from the top flange. This feedthrough consists simply of a Varian medium-current feedthrough whose solid center conductor has been replaced by a hollow copper pipe.

The substrate can be heated to a temperature of over 900°K by passing current through the alumina-coated heater wire embedded in the "substrate box" shown in Fig. 12. To prevent magnetic fields from distorting the EDCs, this heater wire is surrounded with "netic" and "conetic" magnetic shielding material. Since the curie point of these materials is only about 700°K, they provide no magnetic shielding above this temperature.

The collector can is also coolable to liquid nitrogen temperature, since it consists of a massive copper cylinder connected to a rigid liquid nitrogen feedthrough. This feedthrough is insulated from the top flange, as shown in Fig. 11.

- (5) Evaporated films and materials that can be fashioned into the form of a substrate are easily studied in the photoemission chamber. Since the substrate can be moved out of the collector can for evaporation, there is little space limitation on the type of evaporator that can be used to deposit a film onto the substrate. The author has used quartz boats and filament evaporators, and Yu [Ref. 9] has used an electron gun for very high temperature evaporations.
- (6) Because of the large number of electrical feedthroughs and the movable substrate, several photoemission experiments can be made during a single pumpdown. For example, during the course of this research, the author made it a practice to study photoemission from a metal and from an insulator on each pumpdown. The procedure was as follows: The first experiment was made by moving the substrate into the collector can and by evaporating the metal bead in the collector can. This evaporation served two purposes: to evaporate the metal under study onto the substrate and to coat the collector can with a fresh metal, thus assuring a uniform

collector work function. After photoemission studies were made on the metal, the substrate was moved out of the collector can, and an insulator (such as CsI) was evaporated from a quartz boat onto the substrate. After photoemission studies were made on the insulator film, the top flange of the photoemission chamber was removed, and a new experiment was prepared simply by washing the insulator off the old substrate (which was usually still highly polished), and installing new evaporators. In a matter of hours after the previous photoemission experiments, the chamber was being pumped down for another set of experiments.

- (7) The photoemission chamber was mounted on a mobile table that could be rigidly bolted to the vacuum pump station; thus, a single unit could be rolled up to the vacuum monochromator for photoemission measurements, as shown in Fig. 8.

The stainless steel body of the chamber was built by Varian, but the rest of the chamber was constructed in the facilities of the Stanford Electronics Laboratories. The author is indebted to P. McKernan of the Stanford Electronics Laboratories Tube Shop for his assistance in the construction and assembly of the photoemission chamber. Mr. McKernan is responsible for the many construction details that made the chamber a reality. Also, the author would like to thank Barry Schechtman for his assistance in building the mobile table and in designing the removable LiF window flange.

Figure 13 is a photograph of the photoemission chamber.

G. THE KNOCK-OFF TUBE

As discussed earlier in this chapter, ultrahigh vacuum photoemission experiments are limited in our laboratory to photon energies less than 11.9 eV, the high energy cutoff of the LiF window. In many instances, it is desirable to obtain photoemission data at photon energies higher than 11.9 eV. One solution would be to construct a windowless light source-monochromator-test chamber apparatus in which the test chamber could be maintained at a pressure of 10^{-9} torr and the lamp pressure maintained at 10^{-3} torr. Unfortunately, a rather elaborate differential pumping scheme [Ref. 10] would probably have to be used to realize such a system, and this is not presently feasible in our laboratory. In this section, an alternative solution is described; it has, in many cases,

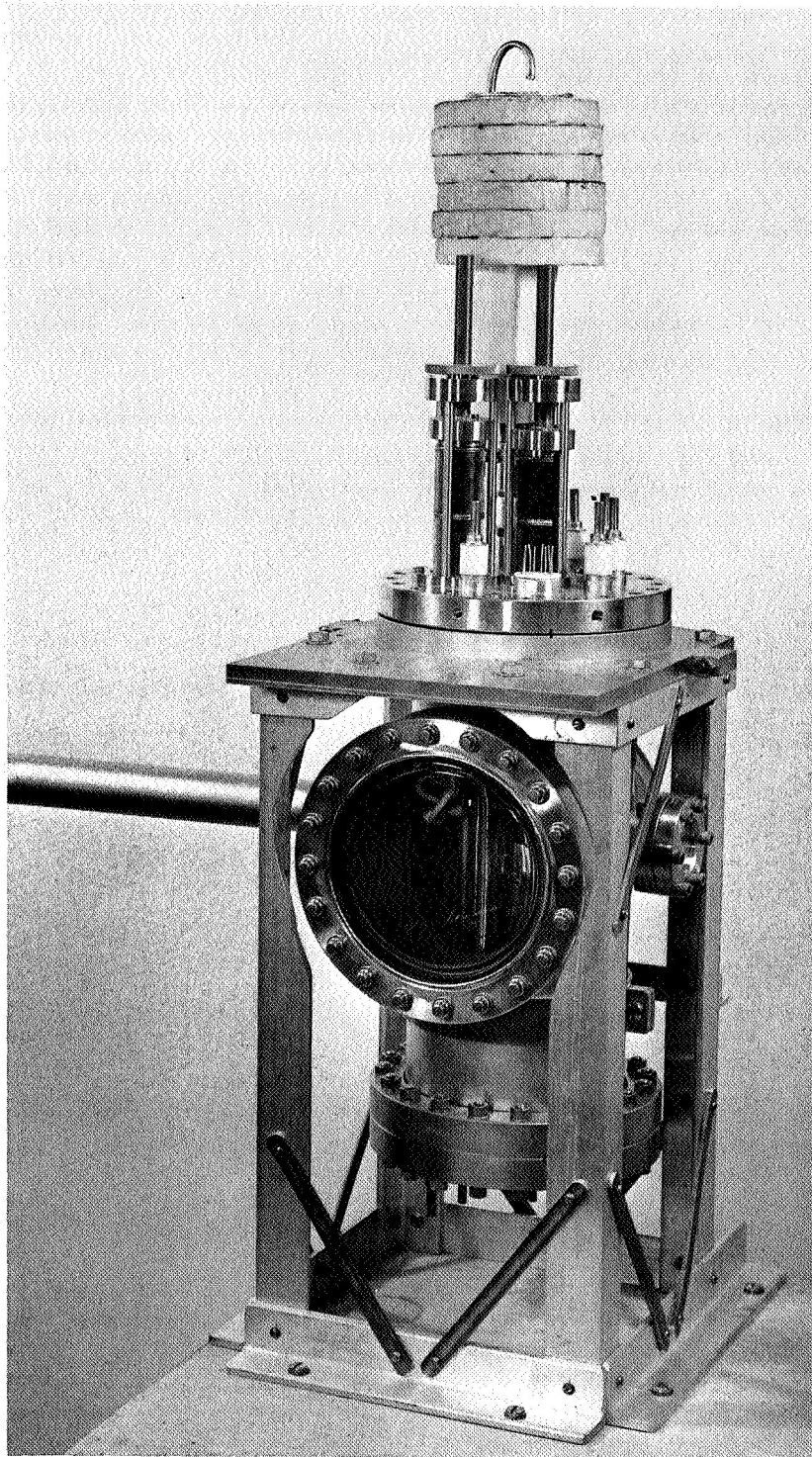


FIG. 13. THE PHOTOEMISSION CHAMBER AS SEEN FROM THE GLASS VIEWPOINT SIDE. The LiF window on the opposite side cannot be seen in this photograph. The exotic apparatus on the top of the chamber is a simple system for recirculating liquid nitrogen through the emitter assembly.

resulted in good photoemission data from evaporated films at photon energies greater than 11.9 eV.

This alternative solution, called a knock-off tube, is a specially constructed photodiode with a LiF window that will allow a material to be prepared and studied in ultrahigh vacuum, in the usual manner. However, the knock-off tube has the additional feature that the LiF window part is connected to the tube body by a neck of very thin glass, so that the LiF window can be broken off, and photoemission studies can be made at photon energies greater than 11.9 eV. Figure 14 is a sketch of this tube. Note that the glass in the neck of the tube is only about 0.010 inch thick. Thicknesses between 0.005 and 0.020 inch have been found strong enough to withstand the pressure of the surrounding atmosphere, yet fragile enough for the LiF window to be broken off easily. Note also that the tube has a soft copper "pinch-off" (made by Palmer Larson Co., Redwood City, Calif.). By use of this pinch-off, the tube can be sealed off with a single stroke of a bolt cutter, thus avoiding any gas contamination that might occur if the tube were sealed off in the conventional manner of melting the glass tubulation with a torch.

The knock-off tube is used in the following manner: First, the tube (Fig. 14) is evacuated to a pressure of typically 5×10^{-9} torr, and then the material under study is evaporated onto the substrate. This processing is done with the oil-free ion pump system described in Section C, to insure that the material under study is free of oil and contaminants. The tube is then placed in a chamber that is attached to the vacuum monochromator, as shown in Fig. 15. When gas is not flowing through the lamp, the pressure in the vacuum monochromator is less than 1×10^{-7} torr. When the gas (H_2 , Ne, or He) flows through the lamp into the monochromator, the pressure rises to 1×10^{-4} torr in the monochromator. The only connection between the chamber surrounding the knock-off tube and the interior of the vacuum monochromator is the slit opening, which is typically $1 \text{ cm} \times 1 \text{ mm}$. Thus, if no auxiliary pump is used (dashed lines in Fig. 15), the pressure in the chamber around the knock-off tube is about 2×10^{-4} torr. If the auxiliary pump is used, the pressure in the chamber falls to about 2×10^{-5} torr. Note that both the vacuum monochromator pump and the auxiliary pump systems have liquid nitrogen traps and

molecular sieve traps. The purpose of these traps is to minimize the amount of oil vapor in the vacuum monochromator and the experimental chamber. Note also the large "cold finger" that replaces a "hatch-cover" in the monochromator. This cold finger is filled with liquid nitrogen several hours before the experiment, and is intended to condense any oxygen and oil vapor that may be in the monochromator.

In the actual experiment, photoemission data are first taken at photon energies up to 11.9 eV, while the LiF window is still intact and the material under study is in an oil-free ultrahigh vacuum. Then, with all measuring equipment in readiness, the plunger in the top of the experimental chamber is pushed down, and the guillotine (which should have a sharp point) chops off the LiF window. Energy distribution curves are then quickly taken, because the sample will often tend to contaminate rapidly in a vacuum of 1×10^{-4} torr. In practical cases, it appears that the best data are obtained in the time between knock-off and 5 to 30 minutes after knock-off. In addition, contamination effects are apparently most severe when the hydrogen gas is used. This may occur because the small hydrogen atoms (or ions) can diffuse interstitially into the material under study, thus increasing the internal scattering of electrons photoexcited in the bulk of the substrate. Thus, it is recommended that the LiF window be chopped off in the presence of neon (a line at 16.8 eV) or helium (a line at 21.2 eV), rather than in the presence of hydrogen (continuum up to 14 eV). The quality of the data in the "windowless" experiment can be checked by comparison with the high vacuum data taken with the LiF window intact at energies less than 11.9 eV.

This knock-off method has the advantage that a high quality film is first prepared in ultrahigh vacuum, and then studied in a poor vacuum, often before gas diffusion and other contaminating effects occur. If the material was not first prepared in ultrahigh vacuum but was prepared in the vacuum of the monochromator, foreign gas would be included in the film, and the material would be contaminated to start with.

Figure 16 is a photograph of an experimental knock-off tube in its holder before placement in the experimental chamber, and Fig. 17 is a photograph of the knock-off tube and the guillotine apparatus after the experiment.

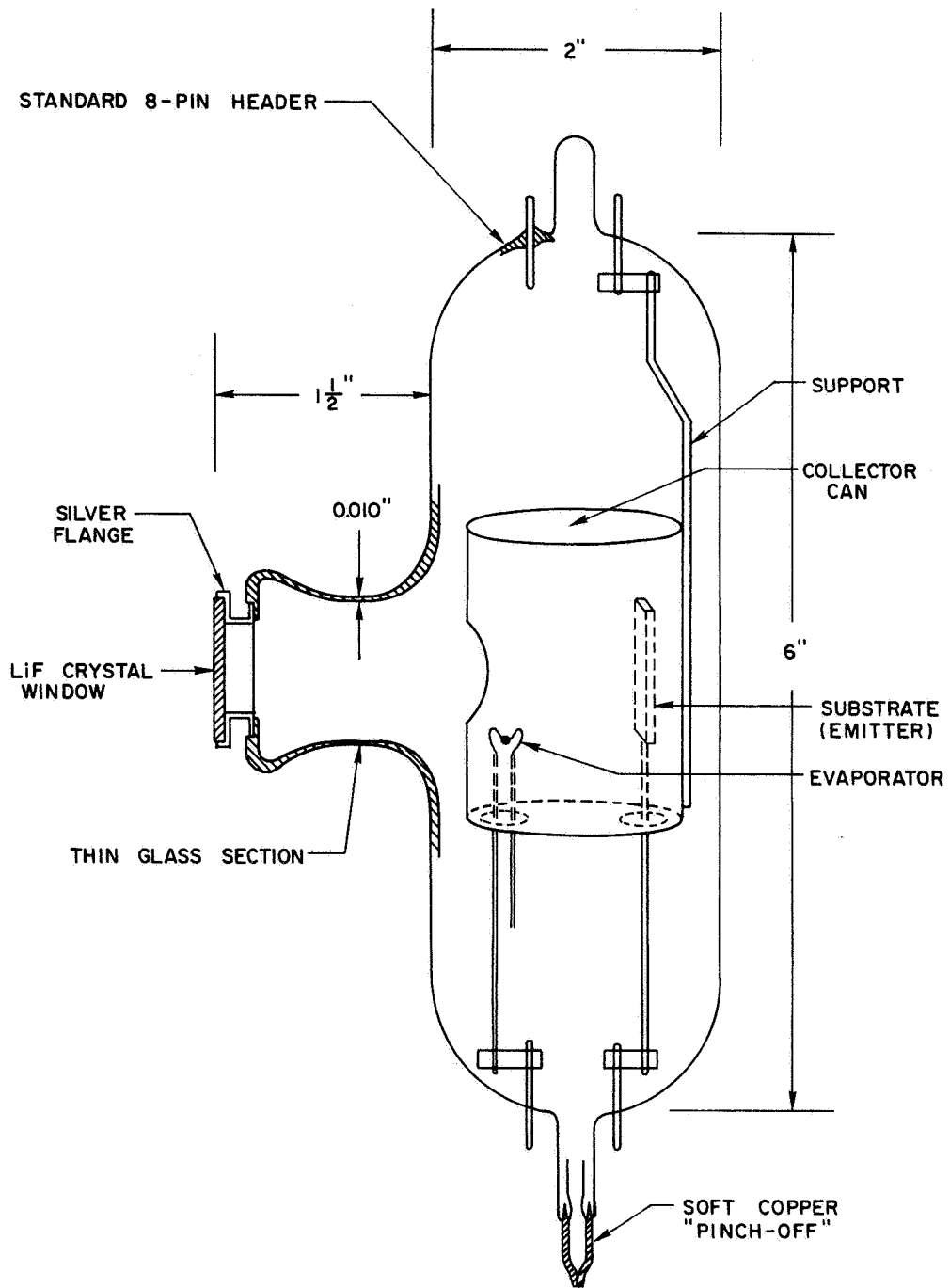
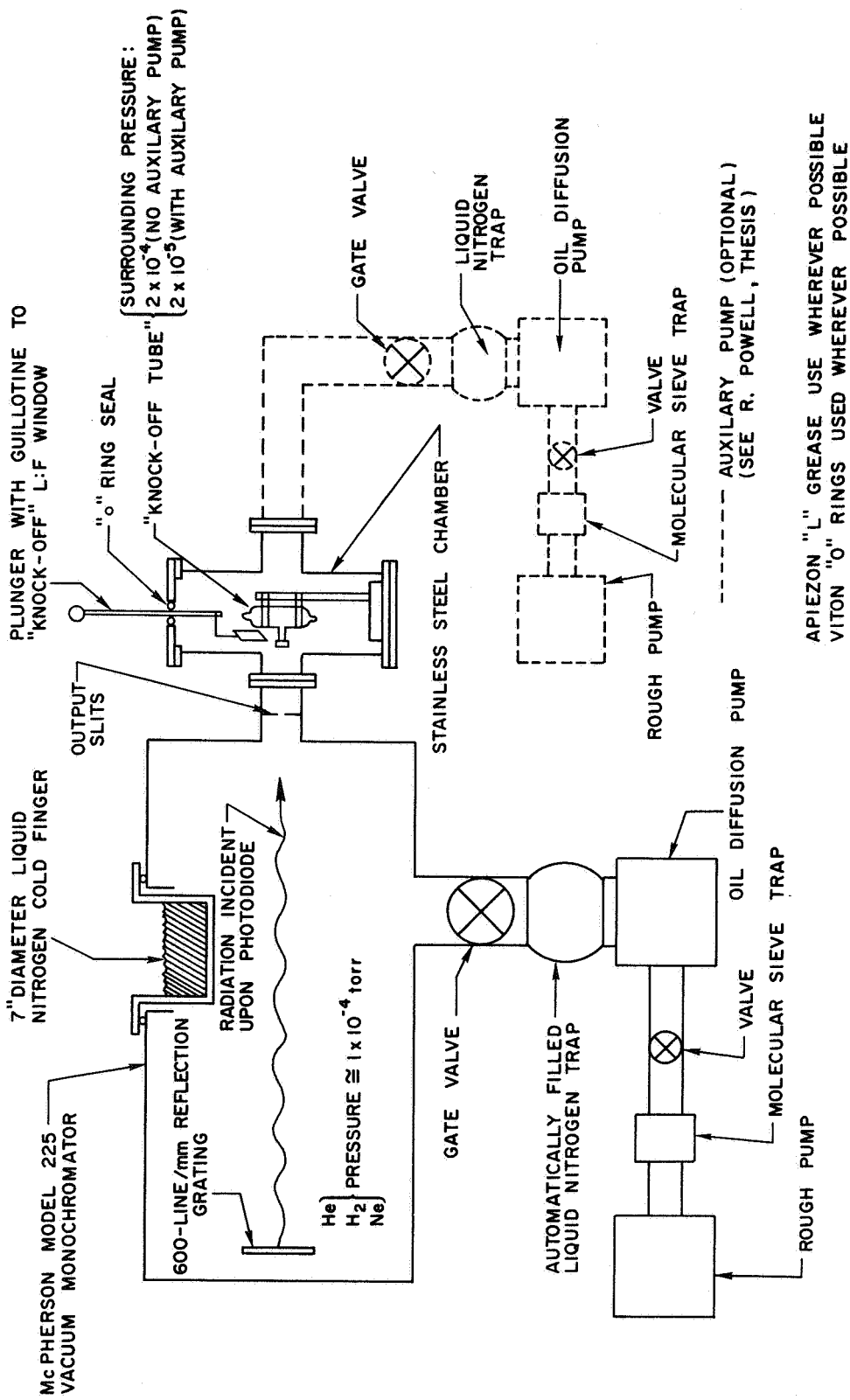


FIG. 14. SCHEMATIC OF THE KNOCK-OFF TUBE SHOWING BASIC FEATURES.
 The actual tubes are more complicated.



APIEZON "L" GREASE USE WHEREVER POSSIBLE
VITON "O" RINGS USED WHEREVER POSSIBLE

FIG. 15. SCHEMATIC OF THE EXPERIMENT USING KNOCK-OFF TUBE.

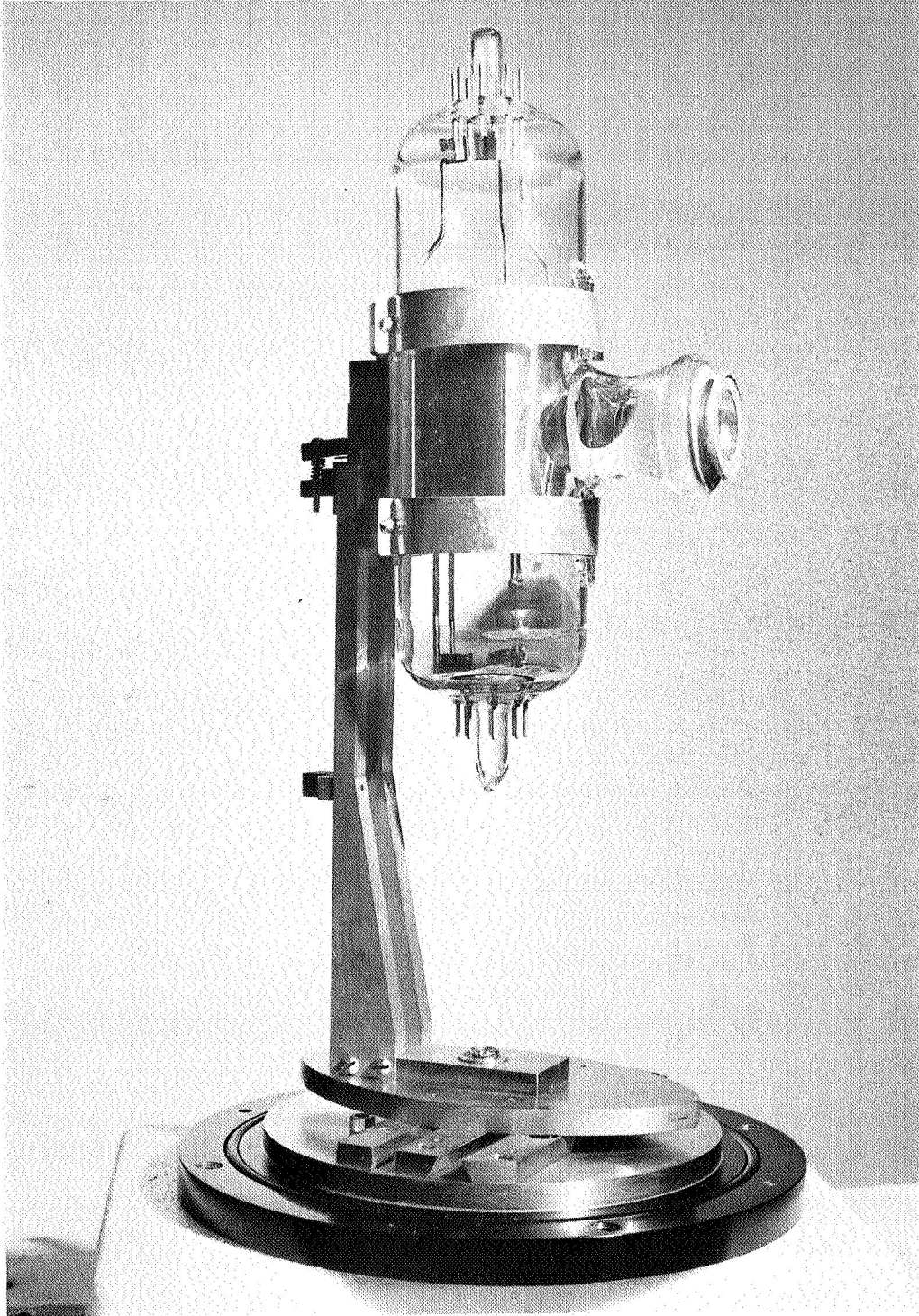


FIG. 16. EXPERIMENTAL KNOCK-OFF TUBE IN HOLDER.

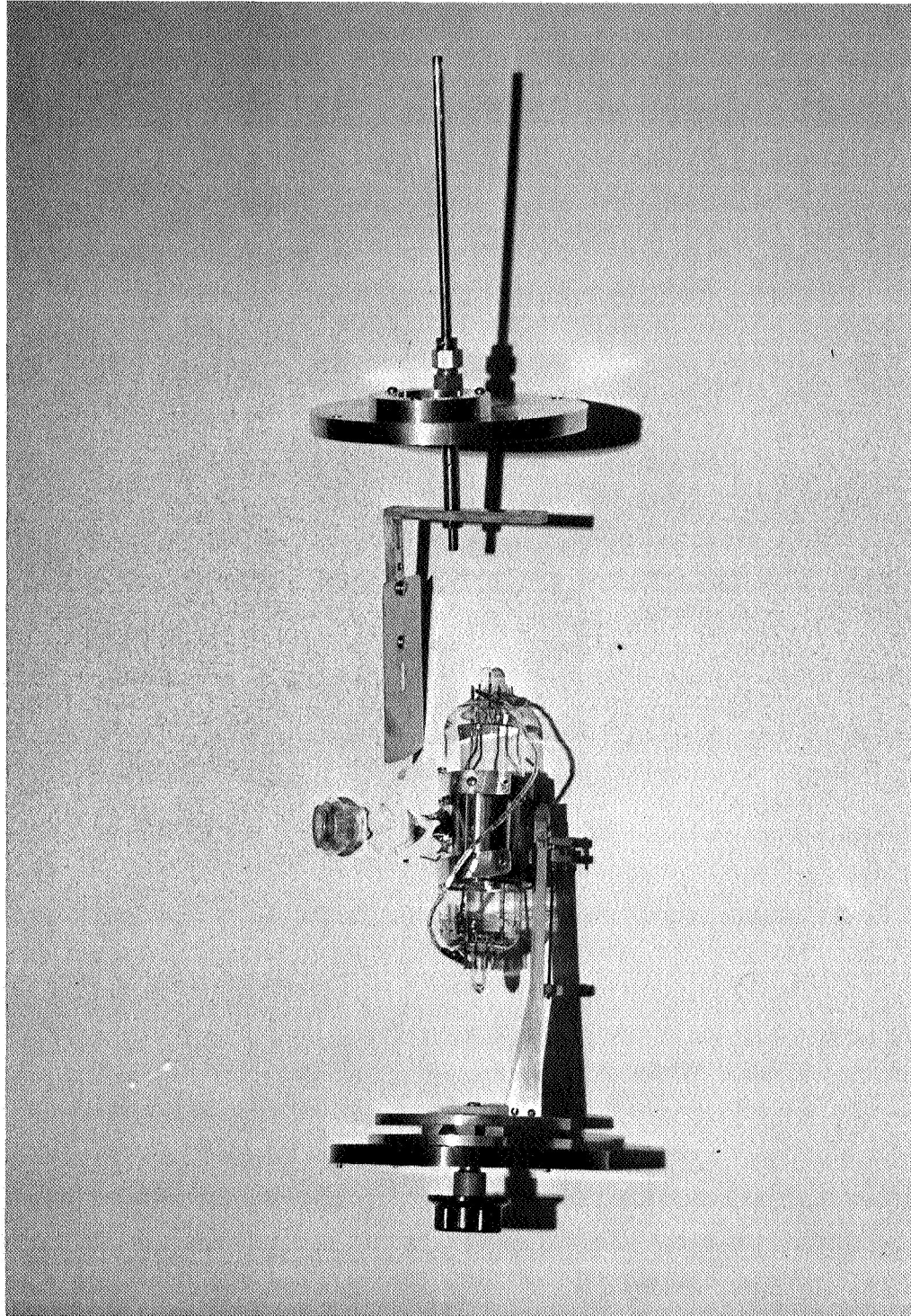


FIG. 17. KNOCK-OFF TUBE AND GUILLOTINE AFTER AN EXPERIMENT.
Note that the glass has broken at the neck of the LiF
window port.

The author is indebted to Frank Peters and David F. Mosher of the Stanford Electronics Laboratories Tube Shop for developing the techniques necessary for the construction of the delicate knock-off tube. Without their skills, the important results deduced from knock-off experiments would never have been obtained by the author.

H. PREPARATION OF FILMS

All of the photoemission experiments presented in this paper were made on evaporated films several thousand angstroms thick. The methods used to evaporate these materials are described in this section. In all cases, these materials were evaporated onto a polished substrate of either copper, silver, or gold. The substrate was at room temperature. In all cases, the photoemission data were independent of the substrate material.

1. Copper, Silver, and Gold

Copper, silver, and gold beads were formed by wrapping wire of at least 99.99 percent purity onto a 0.010-inch-diameter molybdenum wire, and then melting the wire into a bead in a vacuum bell jar. The resulting bead and molybdenum wire took the shape shown in Fig. 18a.

Before evaporation of these beads for photoemission studies in the stainless steel chamber, the pressure was typically 1.5 to 2.0×10^{-9} torr, and during evaporation, the pressure rose to a maximum of about 5.0×10^{-9} torr. The following technique resulted in films that had more detailed structure in the photoelectric energy distribution curves than did other methods: The current through the bead was increased a few tenths of an ampere at a time, and there was a small pressure rise associated with each current increase. The current was then held at a constant level for several minutes, until the pressure had dropped back to nearly its original value. This procedure was continued slowly and gradually until the bead began to evaporate slightly (at a current of 3 or 4 amperes). At this time, the current was increased abruptly to 5 or 6 amperes, so that the bead evaporated very rapidly. In about 30 seconds to 1 minute, about 90 percent of the bead had been evaporated. At this point, the heater current was shut off, leaving a small bead still

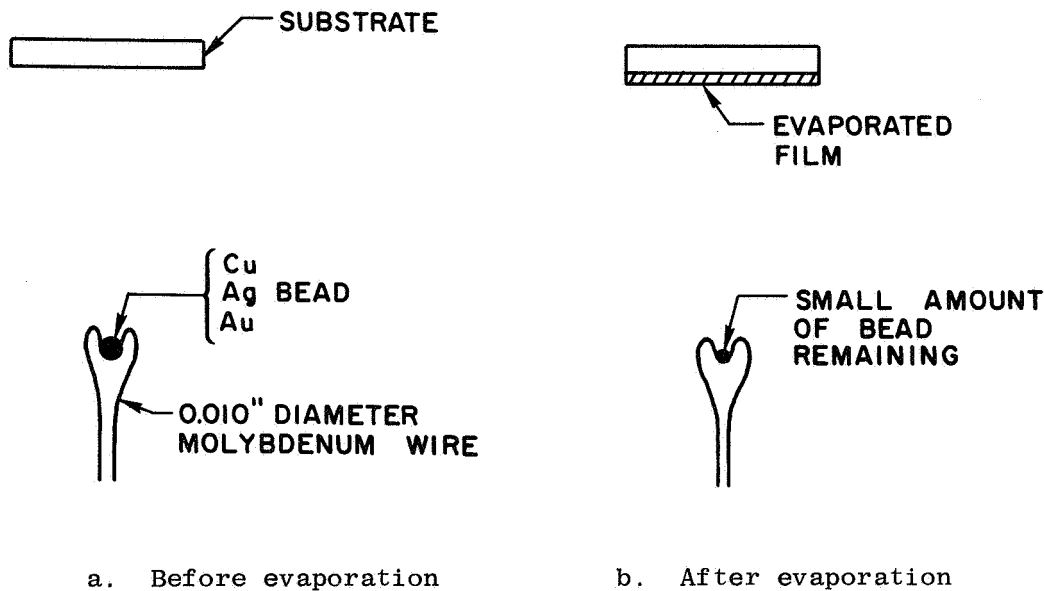


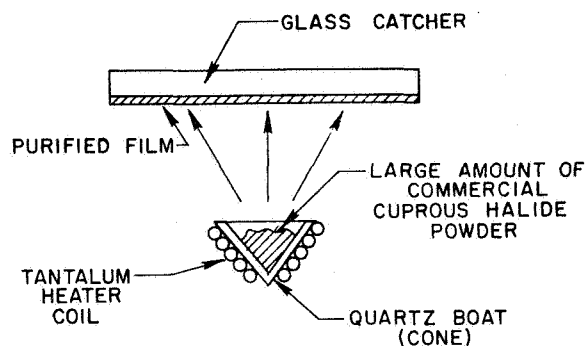
FIG. 18. EVAPORATION OF COPPER, GOLD, AND SILVER.

on the molybdenum wire, as shown in Fig. 18b. Inferior photoemission data sometimes resulted when the bead was entirely evaporated. The inferior results may have been due to material that was evaporated from within the molybdenum filament. The purpose of the rapid evaporation was to insure that only a small amount of foreign gas could be buried in the metal film. After the evaporation, the pressure fell rapidly to its original value.

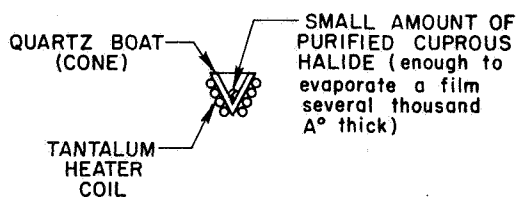
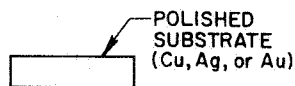
2. Cuprous Chloride, Cuprous Bromide, and Cuprous Iodide

The cuprous halide materials were purchased in powder form from two sources: (1) Fisher Scientific Co., U.S.A.; (2) B. D. H.

Laboratory Chemicals Division, Poole, England. As purchased, the cuprous halide powders were only about 98-99 percent pure, and were greenish-brown-white. Before use in an experiment, these powders were purified by the sublimation technique (Fig. 19). Using the oil-free pumping



a. Purification of commercial cuprous halide



b. Evaporation of film for photoemission studies

FIG. 19. PREPARATION OF CUPROUS HALIDE FILMS.

station described in Section C, a large amount of the powder was sublimated from the quartz cone onto the glass "catcher" at a vacuum of about 5×10^{-7} torr. A pure white film (with a faint yellowish tinge) was found to condense on the "catcher," leaving a dark residue in the quartz cone. X-Ray powder patterns indicated that the purified films consisted of crystallites with a zinblende (ZnS) crystal structure (see, for example, Fig. 20). For use in a photoemission experiment, the purified cuprous halide was quickly scraped from the glass catcher and placed in the quartz cone (Fig. 19). To minimize the amount of water vapor absorbed

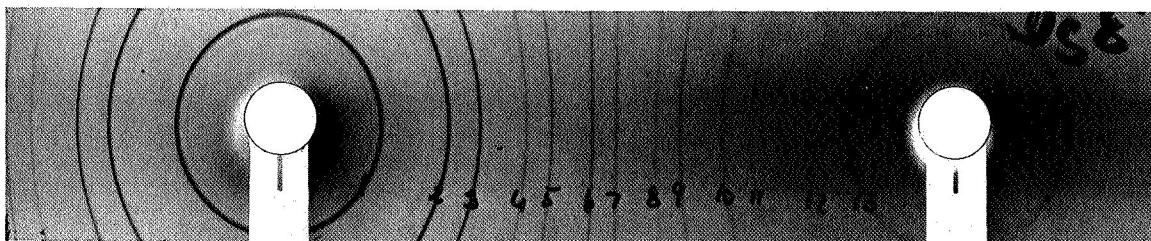


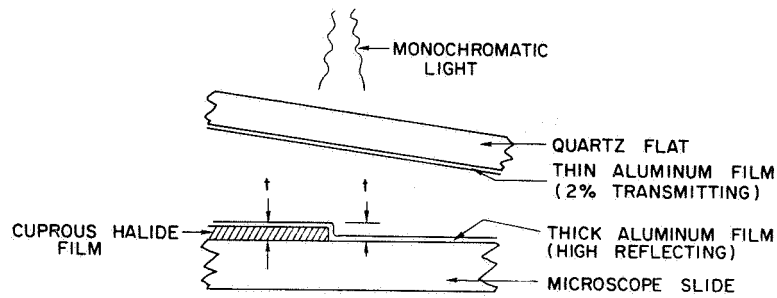
FIG. 20. X-RAY POWDER PATTERN OF AN EVAPORATED FILM OF CUPROUS BROMIDE. The pattern identifies the evaporated film as polycrystalline cuprous bromide with a zinblende structure.

by the hygroscopic cuprous halides, the stainless steel photoemission chamber (Section F) was immediately evacuated. As shown in Fig. 19, the cuprous halides were evaporated from a quartz cone onto a polished Cu, Ag, or Au substrate in a vacuum between 2.0×10^{-9} and 5.0×10^{-9} torr. The current through the tantalum heater coil was increased slowly in increments of a few tenths of an ampere; after an hour or two, a current of several amperes would be reached, and the cuprous halide would evaporate. The rate of evaporation was quite slow, and typically 15 to 30 minutes of evaporation time was necessary to deposit a layer several thousand angstroms thick. The thickness of the film could be estimated during the evaporation by counting interference fringes.

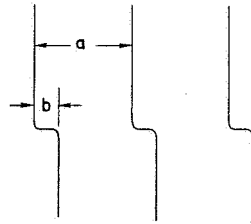
Earlier bell jar experiments had determined the film thickness that would result from a given volume of packed cuprous halide powder. In these experiments, a cuprous halide film was evaporated onto half of a glass microscope slide, and the resulting step aluminized, as shown in Fig. 21. The thickness of the film was determined by placing an aluminized (2 percent transmission) quartz flat on the step, and observing the interference fringes, which were similar to those shown in Fig. 21. If the monochromatic light was of wavelength λ , the height of the step (and consequently the thickness of the film) was found from the relationship

$$t = \left(\frac{\lambda}{2}\right)\left(\frac{b}{a}\right) \quad (2.1)$$

where b and a are defined in Fig. 21. Details of this process can be found in Tolansky [Ref. 11] and Beck [Ref. 12].



a. Enlarged view of step in film



b. Observed interference fringes used to determine step heights (t)

FIG. 21. THICKNESS MEASUREMENTS OF CUPROUS HALIDE FILMS USING THE TOLANSKY METHOD.

3. Cesium Chloride, Cesium Bromide, Cesium Iodide, and Potassium Iodide

Cesium chloride, cesium bromide, and cesium iodide were purchased in powder (small crystallite) form from Electronic Space Products, Inc., Los Angeles, Calif. The potassium iodide was purchased in small crystallite form from Baker and Adamson, General Chemical Division, Allied Chemical Division, New York. These materials were evaporated without additional purification from a quartz boat (Fig. 19). The temperature of the heater coil was increased very slowly until the evaporating temperature was reached. (This time was typically one hour.) When the material began to evaporate, the heater current was increased to accelerate the evaporation, which took place at a pressure of about 5×10^{-9} torr (in the stainless steel chamber). About five minutes were necessary to evaporate a film several thousand angstroms thick.

I. MEASUREMENT OF PHOTOELECTRIC ENERGY DISTRIBUTIONS

The most important measurements presented in this report are the energy distribution curves (EDCs) of the photoemitted electrons. These EDCs were measured by use of a method in which the EDCs were recorded directly by differentiating the I-V characteristic with a small ac voltage superimposed on a retarding potential between the collector and emitter. The circuit used to make these measurements is shown in Fig. 22, where the EDCs are plotted directly on a x-y recorder. Figure 23 is a photograph showing an EDC being recorded.

This ac method has at least two significant advantages over the conventional method of making a dc measurement of the I-V characteristic, and then mechanically differentiating to obtain the EDC:

- (1) To obtain good resolution in the EDCs by the dc method, the I-V characteristic must be known to great precision. This precision is limited by noise in the electronics and light fluctuations. In practice, the noise limitation is probably orders of magnitude less in the ac method than in the dc method.
- (2) Using the ac method, the experimentalist has immediate access to the EDCs and can immediately investigate phenomena that might be of a transient nature.

A more complete description of this ac method can be found in Refs. 13, 14, and 15.

J. MEASUREMENT OF THE QUANTUM YIELD

During the course of this research, measurement of the quantum yield proved to be considerably more difficult than measurement of the EDCs. Because of the small amount of light available from the vacuum monochromator, the total photocurrent was small, typically between 10^{-9} and 10^{-12} amperes. However, these small currents were routinely measured by use of the circuits of Fig. 24.

The difficulty in measuring quantum yield in the vacuum ultraviolet lies not in measuring the small photocurrents but in measuring the very small number of photons in the light beam. During the earlier stages of this research, the relative quantum yield in the region between 4 and

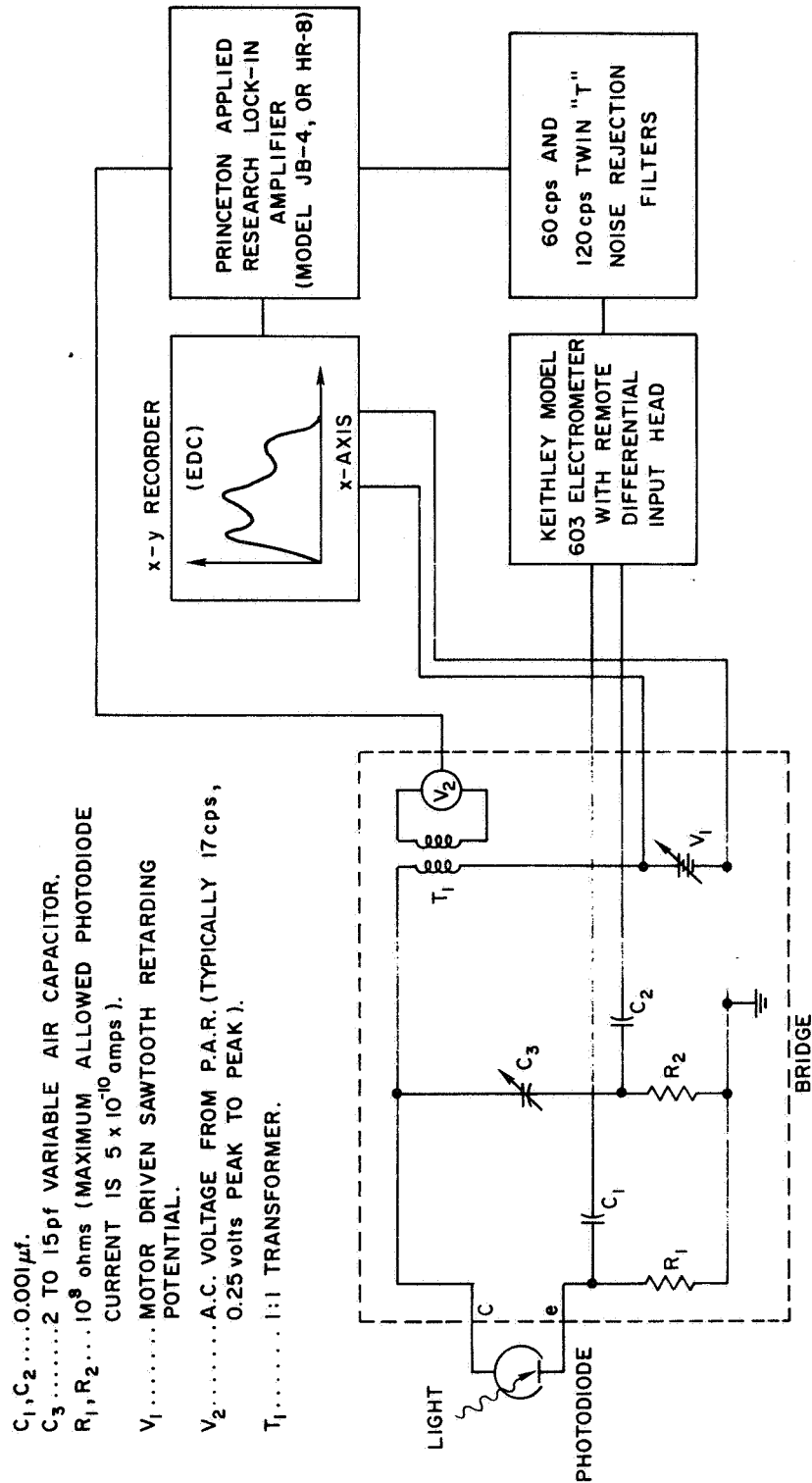


FIG. 22. CIRCUIT USED FOR MEASURING ENERGY DISTRIBUTION CURVES. The EDC is directly plotted on an x-y recorder.

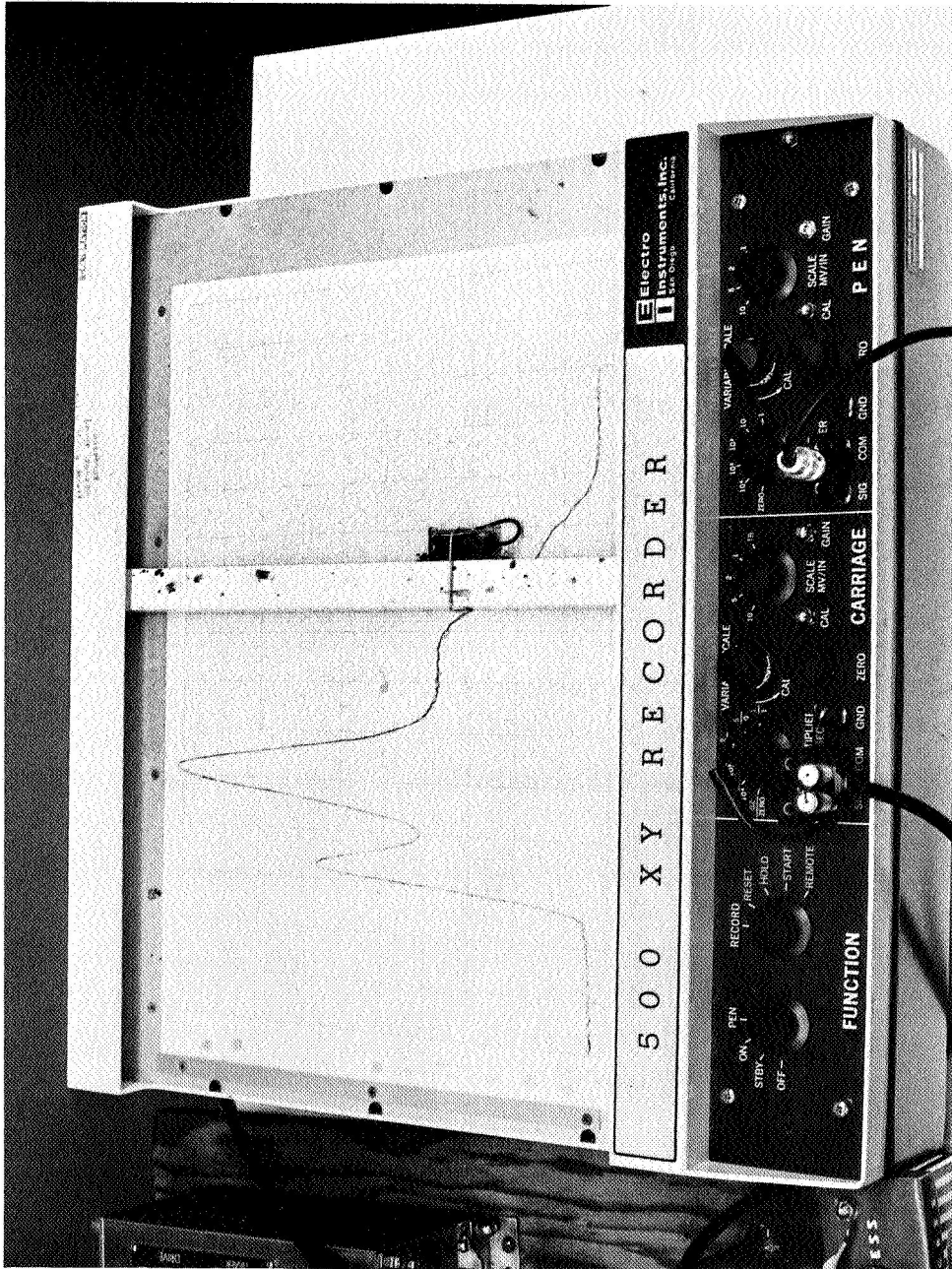


FIG. 23. PHOTOGRAPH OF AN ACTUAL ENERGY DISTRIBUTION CURVE
 BEING TRACED ON AN X-Y RECORDER DURING A PHOTOEMISSION
 EXPERIMENT ON CUPROUS IODIDE.

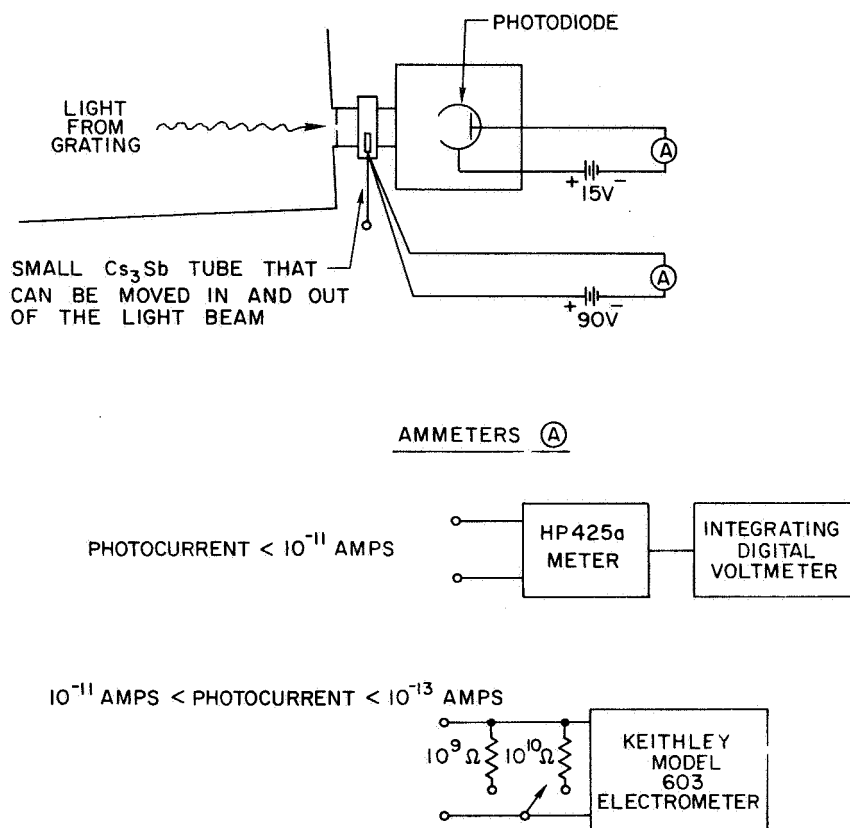


FIG. 24. MEASUREMENT OF QUANTUM YIELD.

11.9 eV was based upon the assumption of constant quantum efficiency from a layer of sodium salicylate mounted on a photomultiplier. Sodium salicylate is a material that fluoresces with (supposedly) constant quantum efficiency at a wavelength of 4300 \AA for incident radiation in the region of photon energies between 3000 and 500 \AA . In the actual measurement of photoelectric yield, the sodium salicylate was not used directly. Instead, the number of photons in the incident light beam was determined by measuring the photocurrent from a conveniently small Cs_3Sb tube, which could be moved in and out of the light beam, as shown in Fig. 24. The Cs_3Sb tube did not have a constant quantum efficiency, but the relative quantum efficiency of the Cs_3Sb tube could be calibrated by comparison with the fluorescence from a sodium salicylate film. The absolute quantum efficiency of the Cs_3Sb tube was obtained by comparison with bolometers and "standard" tubes at photon energies less than 5 eV.

In addition to the calibration of the Cs₃Sb tube, corrections were made for the reflectivity of the material under study and the transmission of the LiF window on the experimental phototube (or on the photoemission chamber). Thus, the absolute quantum yield $Y(h\nu)$ was experimentally determined using the relation

$$Y(h\nu) = \text{quantum yield (electrons photoemitted per absorbed photon)}$$

$$= \frac{I_M(h\nu)}{I_{\text{Cs}_3\text{Sb}}(h\nu)} \times \frac{1}{1 - R(\omega)} \times \frac{1}{T(\omega)} \times Q_{\text{Cs}_3\text{Sb}} \quad (2.2)$$

where

$I_M(\omega)$ = measured photocurrent from the material under study

$I_{\text{Cs}_3\text{Sb}}(\omega)$ = measured photocurrent from the Cs₃Sb tube

$R(\omega)$ = reflectivity of the material under study

$T(\omega)$ = transmission of the LiF window

$Q_{\text{Cs}_3\text{Sb}}$ = absolute quantum efficiency of the Cs₃Sb tube.

During the course of experimentation, the various Cs₃Sb tubes used were calibrated vs the sodium salicylate layers. A definite aging effect was found in some of the Cs₃Sb tubes, so occasional calibration was necessary.

Unfortunately, an exhaustive study of sodium salicylate layers by Koyama [Ref. 16] has shown that the sodium salicylate layers do not necessarily have constant quantum efficiency and that the characteristics of these layers vary with time and with such variables as exposure to atmosphere and methods of preparation.

During the latter part of this research, Koyama successfully calibrated a Cs₃Sb tube and several sodium salicylate films with a thermopile. Those quantum yields that have been made using these standards are probably quite accurate. The accuracy of some of the earlier measurements is subject to some doubt; this uncertainty is pointed out wherever such data are presented in this report.

Additional information concerning the measurement of quantum yield in the vacuum ultraviolet can be found in Refs. 1, 7, 13, and 16.

K. MEASUREMENT OF REFLECTIVITY

A limited number of reflectivity measurements were made where reliable data were not available in the literature. Both high vacuum and windowless measurements were made using the light pipe apparatus described by Yu [Ref. 9]. The optical constants were deduced from this reflectivity data by use of a Kramers-Kronig analysis. The Kramers-Kronig analysis was done on the Burroughs B5500 computer using a computer program written by Shay [Ref. 17].



PRECEDING PAGE BLANK NOT FILMED.

III. ANALYSIS AND INTERPRETATION OF PHOTOEMISSION DATA

The material presented in this study can be divided into two main categories: (1) the experimental measurement of new photoemission and optical data and (2) the analysis and interpretation of these data in terms of the electronic structure of the material.

The new experimental data consist largely of photoelectric yield and photoelectric energy distributions for a number of metals, semiconductors, and insulators. In addition, reflectivity measurements have been made where good measurements were not available in the literature. The techniques used in obtaining these measurements have already been presented (Chapter II).

This chapter is devoted to presenting several methods of analysis that can be used to interpret these photoemission and optical data in terms of the electronic structure of the material. These analytical methods rely heavily upon the availability of good photoemission and optical data that are representative of the bulk material. Relevant background material is condensed and reviewed in the first part of the chapter. Using this background information and several important simplifications, an analytical model is then constructed; this relates the experimentally measured photoemission data to other electronic and optical properties of the material. The importance of the electron-electron scattering length is emphasized in this model; several cases are given in which the relative magnitude of the electron-electron scattering length permits simplification of the analytic equations and subsequent interpretation of the photoemission data. This model is applied without simplification to the important case where the envelope of the conduction band¹ can be approximated by a free electron density of states that has a E energy dependence.² With a minimum

¹ In this report, the term "valence band" will be used to refer to filled electron states, and the term "conduction band" will be used to refer to the empty electron states. Thus, a metal will be described as having a "conduction band" and a "valence band," even though there is no energy gap.

² In this important case, the conduction band density of states consists of experimentally observed peaks superimposed upon an envelope that has a \sqrt{E} energy dependence.

number of arbitrary parameters, this model permits quantitative calculation of the photoelectric yield, the photoelectric energy distributions, the electron-electron scattering length, and the imaginary part of the dielectric constant (ϵ_2) from the density of states. The density of states is determined by an iterative technique, in which the final density of states must be consistent with these experimentally observed quantities. For the special case of a free-electron-like metal, the density of states is theoretically specified, and the quantities listed above can be calculated in an a priori manner if experimental data are available for (1) the absorption coefficient at all photon energies of interest and (2) the electron-electron scattering length at one energy several electron-volts above the fermi level.

The model described above is obtained from a conventional analysis of optical transitions by making two very important assumptions: (1) the momentum matrix elements are constant; (2) the "conservation of the wave vector \vec{k} " is not an important selection rule. When these two approximations are made, it is found that the relative probability of an optical transition is determined solely from the density of states, and is not dependent upon the wave vector \vec{k} . The conventional analysis of optical transitions that is used as a starting point is based upon a one-electron approximation, in which it is assumed that an optical transition involves only a single electron and a single photon; the possible many-body interactions with the other electrons and the phonons are neglected. In this sense, the simplified model used in this chapter can be considered to be consistent with the one-electron model for optical absorption.

Thus, any successes of the analysis will tend to support the validity of the assumptions made and the one-electron approximation. Any failures must then be attributed to either (1) erroneous simplifications of the one-electron model or (2) inapplicability of the simple one-electron model to the process of optical absorption.

A. THE FREE ELECTRON MODEL

The "nearly free electron approximation" of an electron in a crystalline solid states that the electron wavefunction has the periodicity of the lattice, but that the potential experienced by the electron is nearly constant, as approximated by the potential well of Fig. 25a. This simple potential

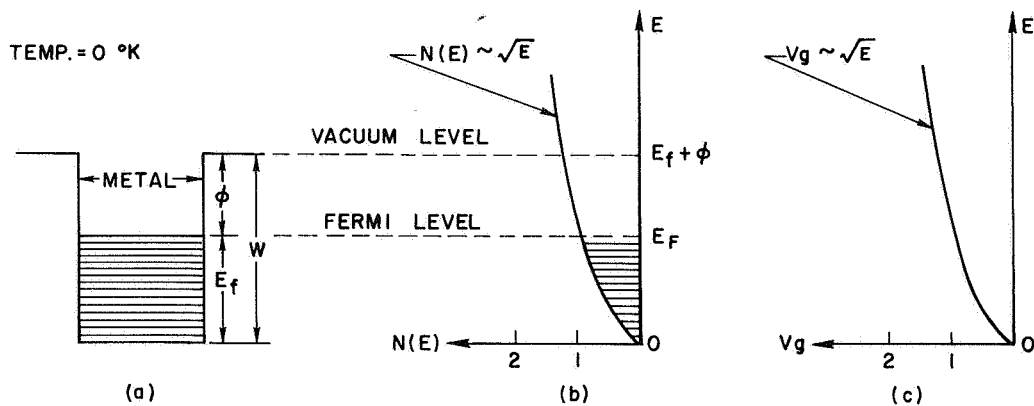


FIG. 25. FREE ELECTRON MODEL OF A METAL. (a) Potential well; (b) density of states; (c) group velocity.

well, called the Sommerfeld model, will be adequate to demonstrate the free electron characteristics that will be useful in subsequent analyses.¹

Let us consider a cube of edge L that is described by the potential well of Fig. 25. The solution of Schrodinger's equation for the energy of an electron in such a well is given by Dekker [Ref. 18].

$$E = \frac{\hbar^2 k^2}{2m} = \frac{\hbar^2}{2m} (k_x^2 + k_y^2 + k_z^2) \quad (3.1)$$

where

$$k_i = \frac{n_i \pi}{L}, \quad n_i = \text{integer} \quad (3.2)$$

We see that in k -space, the surfaces of constant energy are spheres. Each set of integers (n_x, n_y, n_z) defines an allowed wavefunction, which can accept two possible electrons, when spin is taken into account. The number

¹ Later on in this chapter, the \sqrt{E} energy dependence of the free electron density of states will be used to analyze photoemission data from simple "free-electron" metals such as sodium and potassium. In addition, the \sqrt{E} energy dependence will be used to approximate the envelope of the conduction band density of states in a number of materials that are not strictly "free-electron metals." The functional form of the threshold function and the group velocity appropriate to a free electron metal will also be used in the analysis of photoemission data from metals such as Cu, Ag, and Au.

of allowed states in the energy range between E and $E+dE$ is called the "density of states," $N(E)$, and is given by

$$N(E)dE = CE^{1/2} dE \quad (3.3)$$

where C is a constant:

$$C = \frac{4\pi L^3 (2m)^{3/2}}{h^3} \quad (3.4)$$

The functional dependence of $N(E)$ is sketched in Fig. 25b. For the purposes of this analysis and all subsequent analyses, we shall assume that all the states below the fermi level are filled and that all the states above the fermi level are empty. This approximation corresponds to solving the problem at a temperature of $T = 0^\circ K$, but for the phenomena of interest, the error is negligible even at $300^\circ K$. The shaded areas of Figs. 25a and 25b indicate the occupied states. The group velocity of an electron wave packet at energy E is given by

$$|v_g(E)| = \left| \frac{\partial w}{\partial k} \right| = \left| \frac{1}{h} \frac{\partial E}{\partial k} \right| = \left| \frac{\hbar \vec{k}}{m} \right| = \sqrt{\frac{2}{m}} \sqrt{E} \quad (3.5)$$

For a free electron metal, the group velocity has the same energy dependence as the phase velocity, v_p , since

$$|v_p(E)| = \left| \frac{\omega}{k} \right| = \sqrt{\frac{1}{2m}} \sqrt{E} \quad (3.6)$$

B. SEMICLASSICAL ESCAPE FUNCTION, $T_f(E)$

If an electron is excited to an energy E that is greater than $(E_f + \phi)$ in the model of Fig. 25, then the electron can escape if the energy associated with the velocity component normal to the surface is greater than $(E_f + \phi)$, or

$$\frac{m(v_g)_{\text{normal}}}{2} \geq (E_f + \phi) \quad (3.7)$$

For the purpose of our discussion, we shall not be interested in the nature of the work function ϕ , but shall consider ϕ as a phenomenological potential that must be overcome for the electron to escape the metal. For the case of a parabolic conduction band, the energy distribution of the electron is spherical in velocity space, so only a fraction of electrons at energy $E \geq (E_f + \phi)$ satisfy the escape criterion of Eq. (3.7), as shown in Fig. 26. Choosing the x-direction to be normal to the surface, we require that

$$(v_g)_x \geq (v_g)_x^0 = \sqrt{2m(E_f + \phi)} \quad (3.8)$$

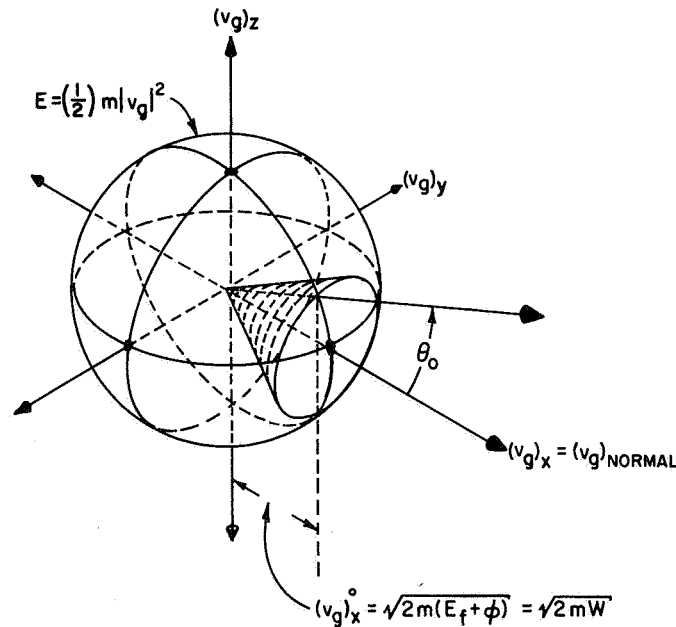


FIG. 26. VELOCITY CONE USED IN CALCULATION OF SEMI-CLASSICAL ESCAPE FUNCTION. The surface of the material is in the positive x-direction.

The fraction of electrons at energy E that satisfy Eq. (3.8) is given by the fraction of the surface that is intersected by the velocity cone of Fig. 26. Defining θ_0 as the maximum angle with respect to the x-axis that will still permit escape, we find that

$$\cos \theta_o = \frac{(v_g)_x}{|v_g|} = \sqrt{\frac{E_f + \phi}{E}}, \quad E \geq (E_f + \phi) \quad (3.9)$$

$T_f(E)$ = fraction of electrons with $(v_g)_x \geq (v_g)_x^o$

$$T_f(E) = \frac{1}{2} (1 - \cos \theta_o) \quad 0 \leq \theta_o \leq 90^\circ \quad (3.10)$$

$$T_f(E) = \frac{1}{2} \left(1 - \sqrt{\frac{E_f + \phi}{E}} \right) \quad E \geq (E_f + \phi) \quad (3.11)$$

The quantity $T_f(E)$ is the semiclassical threshold function for electrons in a parabolic (free electron) band. Thus, if the electrons encounter no scattering processes on the way to the surface, $T_f(E)$ gives the fraction of electrons excited to energy E (at any depth x) that can escape the solid. The $(\frac{1}{2})$ factor occurs because one-half of the electrons are going away from the surface, and the solid is assumed to be infinitely thick in the minus x -direction. Once the electron escapes the solid into vacuum, it has a velocity given by

$$(v_g)_{\text{vacuum}} = \sqrt{2m (E - E_f - \phi)} \quad (3.12)$$

Those electrons not in the escape cone but with a component of velocity in the positive x -direction may eventually strike the surface. These electrons will then be reflected back into the solid. The cases of specular and diffuse reflection from the surface have been treated by Spicer et al [Ref. 19].

$T_f(E)$ is plotted as a function of $[E/(E_f + \phi)]$ in Fig. 27. Note that even at $E = 2(E_f + \phi)$, $T_f(E)$ is only about (0.15). This small value helps to explain the small photoelectric yield of metals such as Cu, Ag, and Au.

C. THE ELECTRON-ELECTRON SCATTERING LENGTH $L(E)$

To begin, let us assume that an electron is somehow excited to a state in the conduction band above the fermi level. The excitation mechanism could be light, an applied electric field, hot electron injection, or any

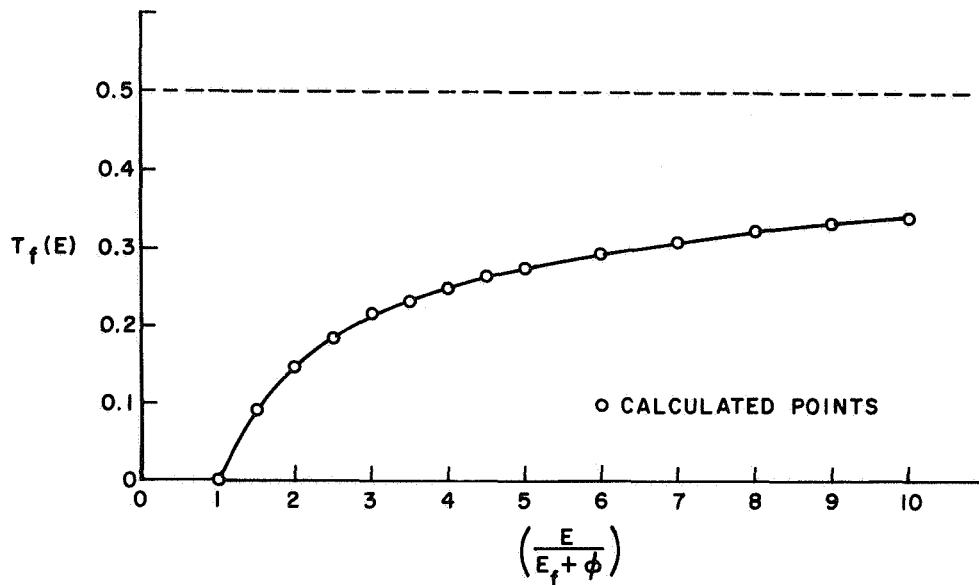


FIG. 27. SEMICLASSICAL ESCAPE FUNCTION, $T_f(E)$, FOR A FREE ELECTRON MODEL.

other means. This analysis will be restricted to the case in which the number of "hot" electrons in the conduction band is very small compared with the number of electrons in the filled valence band. The excited electron, or wave packet, will assume some state of the crystal, and move through the crystal with a group velocity v_g . For the case of a free electron metal, Eq. (3.5) shows that $v_g \sim \sqrt{E}$. Eventually, the electron will have an interaction or "collision" with another electron, a phonon, an impurity, or a vacancy. In this analysis, we shall assume that the electron-electron interaction dominates in the region of interest, which is from 1.5 to 12 eV above the fermi level. Thus, we shall consider only the case of electron-electron scattering.

The detailed nature of the electron-electron interaction in solids is not well known, and the wavefunctions describing the interacting electrons are difficult to formulate. However, a good deal can still be said about the interaction if a number of simplifying approximations are made. With reference to Fig. 28, let us assume that an electron at energy E in the conduction band "collides" inelastically with an electron at energy E_v^0 in the valence band. If the conduction electron at energy E loses an amount of energy, ΔE , then the valence electron at E_v^0 must gain an energy, ΔE , if energy is to be conserved.

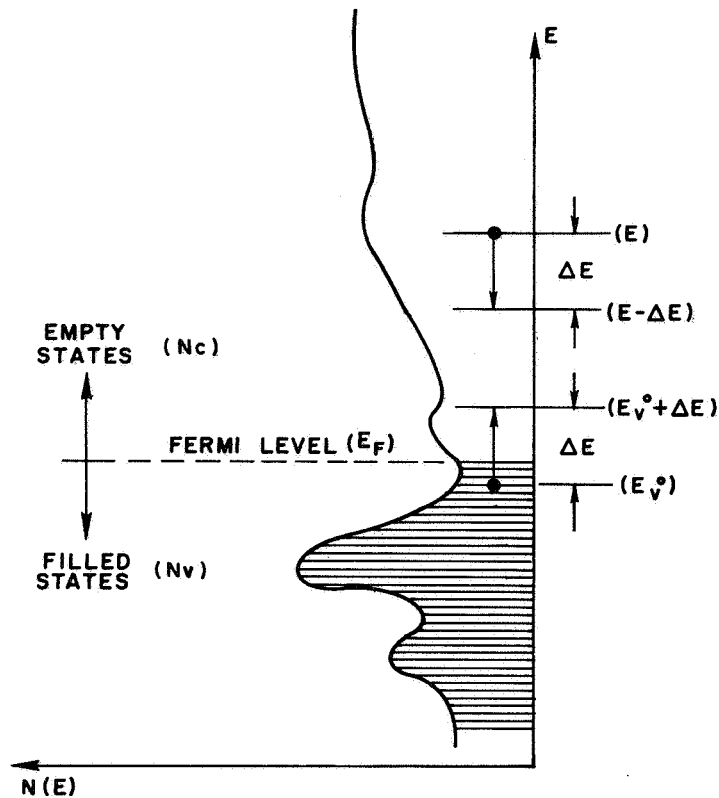


FIG. 28. CALCULATION OF ELECTRON-ELECTRON SCATTERING LENGTH $L(E)$ FROM THE DENSITY OF STATES.

Let us now consider the relative probability of a collision of a "hot" electron at energy E with a valence electron at energy E_V^0 . If the energy loss of the collision is given by ΔE , the relative probability of collision is given by $P'(E, E_V^0, \Delta E)$, where

$$\begin{aligned}
 P'(E, E_V^0, \Delta E) &= (K_1) \text{ (number of valence electrons at } E_V^0) \\
 &\times \text{ (number of conduction band states at } (E-\Delta E) \text{ to which the electron at } E \text{ can fall)} \\
 &\times \text{ (number of conduction band states at } (E_V^0 + \Delta E) \text{ to which the electron at } E_V^0 \text{ can be excited)} \\
 &= (K_1) N_V(E_V^0) N_C(E-\Delta E) N_C(E_V^0 + \Delta E) \quad (3.13)
 \end{aligned}$$

In Eq. (3.13),¹ K_1 is a proportionality constant, N_v is the valence band density of states, and N_c is the conduction band density of states. Equation (3.13) states that the relative probability of a collision with energy loss, ΔE , is simply proportional to the total number of possible collisions that conserve energy. Since the nature of the interaction is not well known, no constraint is put upon quantum mechanical selection rules; only the density of states is involved in the analysis. For materials such as silicon, a detailed analysis [Ref. 21] involving quantum mechanical selection rules seems to reduce to the approximation of Eq. (3.13). To obtain the total relative probability of collision for an electron at energy E , we must sum $P'(E, E_v^0, \Delta E)$ over all possible E_v^0 and ΔE . We shall call this total probability $P(E)$, which is given by

$$P(E) = K_1 \int_{E_f}^{2E_f - E} d(E_v^0) \int_{E_f - E_v^0}^{E - E_f} d(\Delta E) N_v(E_v^0) N_c(E - \Delta E) N_c(E_v^0 + \Delta E) \quad (3.14)$$

Since the "hot" electron from energy E and the valence electron from energy E_v^0 are indistinguishable after the interaction, we need only sum values of ΔE from $(E_f - E_v^0)$ to $\frac{1}{2}(E - E_v^0)$, or

$$P(E) = 2K_1 \int_{E_f}^{2E_f - E} d(E_v^0) \int_{E_f - E_v^0}^{\frac{1}{2}(E - E_v^0)} d(\Delta E) N_v(E_v^0) N_c(E - \Delta E) N_c(E_v^0 + \Delta E) \quad (3.15)$$

Equation (3.15) is the form most useful for computer calculation, since this equation involves half as many terms as Eq. (3.14). The limits on Eq. (3.14) and Eq. (3.15) are relevant to the notation of Fig. 28.

The lifetime, $\tau(E)$, of a "hot" electron is the inverse of the collision probability per unit time, or

$$\tau(E) = \frac{1}{P(E)} \quad (3.16)$$

¹ Note that Eq. (3.13) is of the same form as given earlier by Berglund and Spicer [Ref. 20].

Defining the electron-electron scattering length, $L(E)$, as the mean distance an electron travels before colliding inelastically with another electron, we have

$$L(E) = \langle |v_g(E)| \rangle \tau \quad (3.17)$$

where the brackets indicate an average overall directions. Using Eq. (3.16) and Eq. (3.15) in Eq. (3.17), we obtain for the electron-electron scattering length

$$L(E) = L_0 \frac{\langle |v_g(E)| \rangle}{\int_{E_f}^{2E_f - E} d(E_v^0) \int_{E_f - E_v^0}^{\frac{1}{2}(E - E_v^0)} d(\Delta E) N_v^0(E_v^0) N_c(E - \Delta E) N_v^0(E_v^0 + \Delta E)} \quad (3.18)$$

where L_0 is a normalizing constant. The same expression has been obtained independently by Berglund [Ref. 7]. Equation (3.18) gives only the shape of $L(E)$, and not the magnitude. The magnitude of $L(E)$ must be obtained by adjusting the constant L_0 so that $L(E)$ agrees with an experimental point at some energy E .

As an example of Eq. (3.18), let us calculate $L(E)$ for the model density of states shown in Fig. 29. This simplified model, which is actually a rough approximation to many practical cases¹ consists of a narrow valence band of filled core states at energy $E = 0$, and a free-electron conduction band at energies $E > 0$. The electron velocity is given by Eq. (3.5) for a free-electron conduction band, so Eq. (3.18) becomes

$$L(E) = L_0' \frac{\sqrt{E}}{\int_0^{-\delta} d(E_v^0) \int_{-E_v^0}^{\frac{1}{2}(E - E_v^0)} d(\Delta E) N_v^0(E_v^0) \sqrt{E - \Delta E} \sqrt{E_v^0 + \Delta E}} \quad (3.19)$$

¹ In actual practice, Eq. (3.18) is evaluated using a digital computer, and no approximations are made. The simple model of Fig. 29 is presented solely for the purpose of illustrating the basic physics of the calculation for $L(E)$.

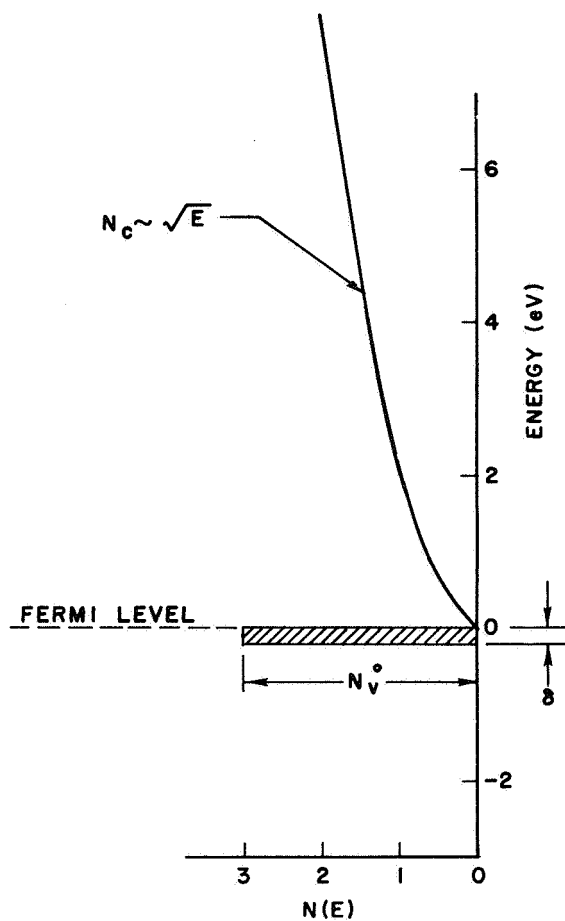


FIG. 29. HYPOTHETICAL DENSITY OF STATES WITH A FREE ELECTRON CONDUCTION BAND AND DELTA FUNCTION VALENCE BAND.

where L'_0 is a normalizing constant. Since δ is very small, the valence band density of states is essentially an impulse function, and we can approximate Eq. (3.19) by

$$L(E) = L'_0 \frac{\sqrt{E}}{(N_v^0)(\delta) \int_0^{\frac{E}{2}} d(\Delta E) \sqrt{E-\Delta E} \sqrt{\Delta E}} \quad (3.20)$$

Changing variables, let $\Delta E = (\Delta E' + E/2)$, so that

$$L(E) = L'_0 \frac{\sqrt{E}}{(N_v^0)(\delta) \int_{E/2}^0 d(\Delta E') \sqrt{\left(\frac{E}{2}\right)^2 - (\Delta E')^2}} \quad (3.21)$$

Using integral (109) of Ref. 22, we can evaluate the integral in the denominator of Eq. (3.21) and obtain

$$L(E) = \left[\frac{L'_O}{(N_V^O)(\delta)(\pi/16)} \right] \frac{1}{(E)^{3/2}} \quad (3.22)$$

Thus, we see that for the model of Fig. 29, $L(E) \sim E^{-3/2}$, and that the magnitude of $L(E)$ is inversely proportional to the total number of valence electrons $[(N_V^O)(\delta)]$.

Equation (3.22) has practical significance, since it gives an analytic expression for a simple model that approximates several real cases at energies well above the fermi level. Three of these cases are shown in Fig. 30, where curve (a) shows a free electron metal, curve (b) shows a metal with a free electron conduction band but with a highly structured valence band, and curve (c) shows a semiconductor with a free electron conduction band. One would expect that Eq. (3.22) would be a fairly good approximation in cases (a) and (b) for $E > |W|$, and in case (c) for $E > (|W| + |E_g|)$, where W denotes the width of the valence band, and E_g the energy gap. Thus, at energies well above the fermi level, Eq. (3.22) would predict an $(E)^{-3/2}$ dependence for $L(E)$ in metals and semiconductors that have a free electron-like conduction band. At energies close to the fermi level, Eq. (3.22) will be very inaccurate. In addition, Eq. (3.22) predicts that a material with more electrons in the valence band should have a shorter scattering length, all other factors being equal.

These conclusions rest on the assumption that only conservation of energy and the total number of possible collisions are important in determining the electron-electron scattering length.¹ However, the validity of Eq. (3.18) and the specific example of Eq. (3.22) can be tested when the difficult task of actually measuring $L(E)$ as a function of energy in the energy range between the fermi level and 10 or 12 eV above the fermi level is performed in future experiments.

¹ E. O. Kane [Ref. 21] has found that, for the case of silicon, the $L(E)$ calculated from Eq. (3.18) is in remarkably close agreement with the $L(E)$ calculated from an analysis based upon \vec{k} -conservation and the detailed band structure of silicon.

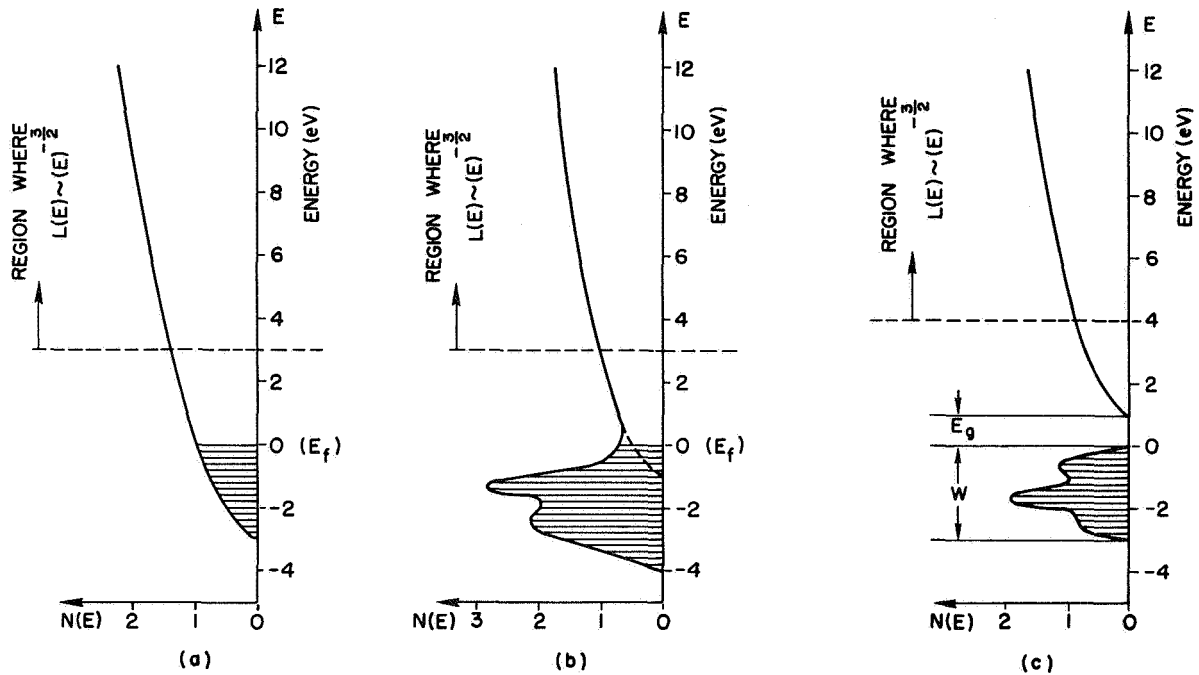


FIG. 30. DENSITY OF STATES MODELS APPROXIMATED BY THE MODEL OF FIG. 29. (a) free electron metal; (b) metal with a free electron conduction band; (c) semiconductor with a free electron conduction band. At energies above the solid dotted line the energy dependence of $L(E)$ is given approximately by $L(E) \sim (E)^{-3/2}$.

At this writing, the only reliable experimental values for $L(E)$ known to the author are for gold [Ref. 24]. These values are in excellent agreement with the predictions of Eq. (3.18), as will be discussed in Chapter V.

Equation (3.18) gives the hot electron mean free path in terms of only electron-electron scattering. As we shall see from numerical examples of metals in later chapters, electron-phonon and/or electron-impurity scattering will tend to dominate over electron-electron scattering in the energy range between the fermi level and about 1 eV above the fermi level. At energies greater than 2 eV above the fermi level, electron-electron scattering tends to dominate; it is in this region that the net electron mean free path is described by Eq. (3.18) alone. In the intermediate region between 1 and 2 eV, the magnitude of the electron-electron scattering length will be found to be comparable to the magnitude of typical electron-phonon scattering length. In this intermediate region, the net electron mean free path is determined by a combination of electron-phonon and electron-electron scattering lengths. This problem has been treated at length in Ref. 19.

At energies several volts above the fermi level, there is another possible electron scattering mechanism--that of electron diffraction at the edges of the Brillouin zone. As a specific example, let us consider the case of gold, which has a face-centered cubic lattice. The first Brillouin zone for a material with a fcc lattice is shown in Fig. 31.

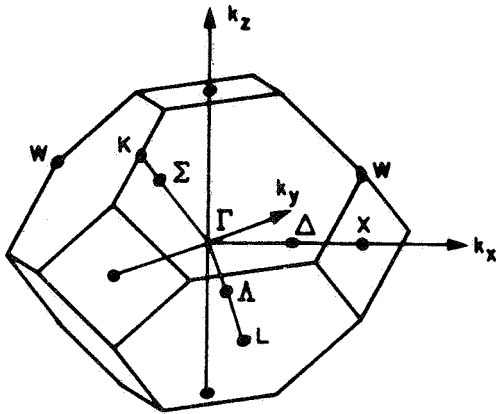


FIG. 31. BRILLOUIN ZONE FOR FACE-CENTERED CUBIC LATTICE. Points and lines of symmetry are indicated.

If we consider the Γ point to be at $(0,0,0)$, then the reciprocal lattice vector in the X-direction is given by [Ref. 25] $[(2\pi/a)(1,0,0)]$, in the L direction by $[(2\pi/a)(\frac{1}{2},\frac{1}{2},\frac{1}{2})]$, and in the W direction by $[(2\pi/a)(1,\frac{1}{2},0)]$, where a is the lattice constant. The surface of the first Brillouin zone bisects each of these reciprocal lattice vectors; thus, for example, at the X point we find $|k| = \frac{1}{2}|(2\pi/a)(1,0,0)| = (\pi/a)$. Let us now assume that the conduction bands of gold can be approximated by nearly free electron bands. The solution of Schrodinger's equation is given in this case by [Ref. 25]:

$$E = \frac{\hbar^2}{2m} |\vec{k} + \vec{K}_n|^2 \quad (3.23)$$

where k has the form

$$\vec{k} = \frac{2\pi}{a} (x, y, z) \quad (3.24)$$

and where \vec{K}_n is any reciprocal lattice vector given by

$$\vec{k}_n = \left(\frac{2\pi}{a}\right)(n_1, n_2, n_3) \quad \begin{matrix} (n_1, n_2, n_3 \\ \text{are integers}) \end{matrix} \quad (3.25)$$

The lattice constant for gold is tabulated [Ref. 26] to be $a = 4.07 \text{ \AA}$. With this information and the use of Eq. (3.24) and Eq. (3.25), we can solve Eq. (3.23) for the free electron conduction bands of gold. The results of such a calculation are shown in Fig. 32 for several principal

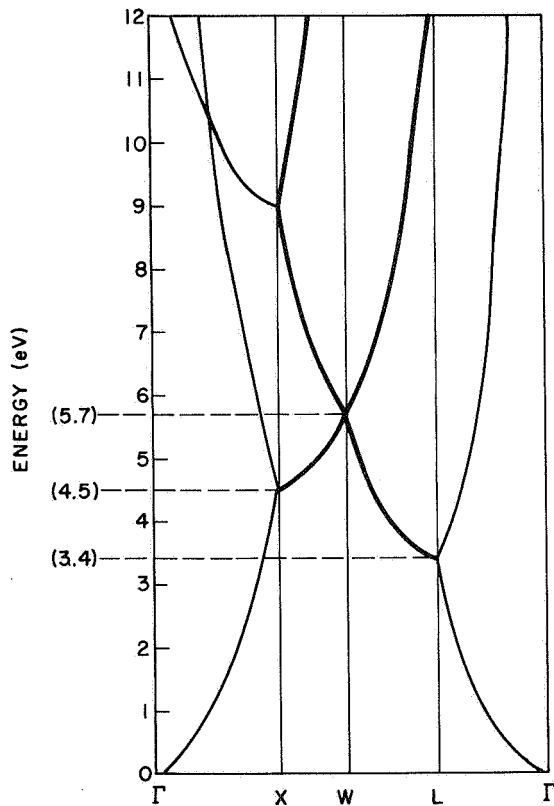


FIG. 32. FREE ELECTRON ENERGY BANDS FOR A FACE-CENTERED CUBIC STRUCTURE WITH LATTICE PARAMETER $a = 4.07 \text{ \AA}$, THE LATTICE CONSTANT FOR GOLD AND SILVER. [Ref. 96] The heavy bands correspond to points on the surface of the Brillouin zone.

symmetry directions. The heavy lines indicate the points where a surface of energy E intersects the edge of the Brillouin zone. In the real case of a periodic potential, the bands would split at the zone edges, and the slope of the E vs $(\vec{k})_{\text{normal}}$ curves would be zero at the edge of the Brillouin zone, and not finite, as in Fig. 32; however, the deviation from the parabolic curves (Fig. 32) is quite small. Thus, the heavy lines (Fig. 32) indicate the energies at which diffraction from the edges of the Brillouin zone occurs, since

$$(v_g)_{\text{normal}} = \frac{1}{\hbar} \left(\frac{\partial E}{\partial k}\right)_{\text{normal}} = 0 \quad (3.26)$$

at the edge of the Brillouin zone.

Equation (3.26) tells us that if an electron is excited to an energy E on the surface of the Brillouin zone, the electron will not have a group velocity given by $v_g = \sqrt{2mE}$, but will have $v_g = 0$, and will not propagate through the crystal. For these electrons, the electron-electron scattering length will be zero, since $L(E) = v_g(E)\tau(E) = 0$. This could have a profound effect on the electron-electron scattering length as calculated from Eq. (3.18), if a significant portion of the free electron sphere at energy E intersected the edge of the Brillouin zone. $L(E)$ would be different in different crystallographic directions, but the average value of $L(E)$ would not change appreciably if only a small portion of the constant energy surface intersected the Brillouin zone edge. If we imagine the bottom of the free electron bands in gold to be at the fermi level, then Fig. 32 shows that the spherical energy surfaces do not intersect the Brillouin zone for energies less than 3.4 eV above the fermi level. At energies above 3.4 eV, the heavy lines indicate that the energy surfaces do indeed intersect the Brillouin zone in the region of interest, which extends up to 12 eV. Thus, one might expect some change in $L(E)$ due to diffraction effects at energies above 3.4 eV. The most significant effect seems to be in the energy range from 4.5 to 6.0 eV, where the free electron sphere tends to merge with the faces of the Brillouin zone. In the actual case of gold, it is possible for this effect to be accentuated if the constant energy surface is not a sphere, but is fairly close to the truncated octahedron shape of the Brillouin zone. At energies higher than about 6 eV, the diffraction effect seems to be smaller, since it appears (at first glance) that a smaller portion of a constant energy sphere intersects the edge of the Brillouin zone.

In the analysis of photoemission data later in this study, Eq. (3.18) will be used to calculate the electron-electron scattering length; other effects, such as the electron diffraction discussed above, will not be included in the formal analysis. The possible presence of these other effects will be pointed out where anomalous deviation from the predictions of Eq. (3.18) seems to occur.

D. DIRECT AND NONDIRECT TRANSITIONS

The optical conductivity $\sigma_b(\omega)$ is the number of photons absorbed per unit time per unit volume, and is given in terms of the dielectric susceptibility by [Ref. 27]:

$$\sigma_b(\omega) = \omega \epsilon_2(\omega) \quad (3.27)$$

Here, $\epsilon_2(\omega)$ is the imaginary part of the dielectric susceptibility $\epsilon(\omega)$, which is given by Eq. (3.28), where we follow the notation of Refs. 28 and 29:

$$\epsilon(\omega) = \epsilon_f(\omega) + \epsilon_b(\omega) \quad (3.28)$$

The quantity $\epsilon_f(\omega)$ is conventionally called the intraband or free-charge contribution, given by

$$\epsilon_f(\omega) = 1 - \frac{\omega_p^2}{\omega \left[\omega + i \left(\frac{1}{\tau} \right) \right]} \quad (3.29)$$

$$\epsilon_f(\omega) = \left(1 - \frac{\omega_p^2}{\omega^2 + 1/\tau^2} \right) + i \frac{\omega_p^2}{\omega \tau (\omega^2 + 1/\tau^2)} \quad (3.30)$$

For angular frequencies, (ω) , corresponding to photon energies greater than about 2 eV, the interband contribution $\epsilon_b(\omega)$ tends to dominate over $\epsilon_f(\omega)$. The quantity $\epsilon_b(\omega)$ is given in Ref. 30 as

$$\epsilon_b(\omega) = - \frac{1}{m} \left(\frac{e}{\pi} \right)^2 \sum_{v,c,k} f_{vc}(\vec{k}) \left[\omega_{vc} + i \left(\frac{1}{\tau} \right) - \omega \right]^{-1} \left[\omega_{vc} + i \left(\frac{1}{\tau} \right) + \omega \right]^{-1} \quad (3.31)$$

where

c = a conduction band

v = a valence band

$\omega_{vc} = \omega_v - \omega_c$

$f_{vc}(\vec{k})$ = interband oscillator strength, which is given by

$$f_{vc}(\vec{k}) = \frac{2}{3m} \frac{|\langle \psi_{k,v} | \nabla | \psi_{k,c} \rangle|^2}{E_v(\vec{k}) - E_c(\vec{k})} \quad (3.32)$$

Equation (3.31) is usually solved by assuming that the relaxation time τ is long enough so that the condition

$$\omega_{vc} \tau \gg 1 \quad (3.33)$$

In obtaining Eq. (3.31), the relaxation time τ was artificially introduced into the time-dependent perturbation theory by assuming that the coefficient of the wavefunction ψ_j is given by [Ref. 29, pp. 223 and 646]

$$-\frac{\hbar}{i} \frac{\partial a_c(t)}{\partial t} \cong H_{co} e^{-\frac{i}{\hbar}(E_o - E_c)t} e^{-\frac{t}{\tau}} \quad (3.34)$$

Thus, we see that the occupancy $|a_c(t)|^2$ is associated with the lifetime τ . In a later chapter, we shall find that, in a free-electron-like conduction band, the electron-electron scattering length at an energy of 10 eV above the bottom of the free electron band is typically about 10 Å. At 10 eV,

$$\omega = \frac{E}{\hbar} = \frac{10 \text{ eV}}{\hbar} = 1.5 \times 10^{16} \text{ sec}^{-1} \quad (3.35a)$$

$$\tau = \frac{L}{v_g} = \frac{10 \text{ Å}}{\sqrt{2E/m}} = 5.3 \times 10^{-16} \text{ sec} \quad (3.35b)$$

$$\omega\tau \cong 8 \quad (3.36)$$

Now, the largest terms in the sum of Eq. (3.31) are for $\omega_{vc} \approx \omega$, so we can say that as far as Eq. (3.31) is concerned,

$$\omega_{vc} \tau \cong 8 \quad (3.37)$$

Thus, we see that at 10 eV the approximation of Eq. (3.33) is not very good when the lifetime for inelastic collisions is evaluated. In addition, it

is conceivable that the electron interacts in an inelastic manner with the electrons of each atom that it passes, so that the effective inelastic scattering length would be on the order of a lattice constant, or $L \cong 2\text{\AA}$. If it is this value of L that determines the lifetime τ to be used in Eq. (3.31), then $\omega\tau \cong 1.5$, and the approximation $\omega_{vc} \tau \gg 1$ is indeed incorrect. However, it is difficult to say exactly how a relaxation time τ should be incorporated into the quantum mechanical expressions without any accurate knowledge of the mechanism that determines τ , so with tongue in cheek, let us assume that the approximation $\omega_{vc} \tau \gg 1$ is valid, and proceed in the conventional manner. With a certain amount of manipulation, the imaginary part of Eq. (3.31) can be written as [Ref. 31]

$$\epsilon_{2b}(\omega) = \frac{4\pi^2 e^2 \hbar}{3m^2 \omega^2} \sum_{v,c} \int_{\text{B.Z.}} \left\{ \frac{2}{(2\pi)^3} |\langle \mu_{k,v} | \nabla | \mu_{k,c} \rangle|^2 \delta(\vec{k}_c - \vec{k}_v) \delta\left(\frac{E_c}{\hbar} - \frac{E_v}{\hbar} - \omega\right) \right\} dk^3 \quad (3.38)$$

In obtaining the delta function $\delta(\vec{k}_c - \vec{k}_v)$, it was assumed that the electron in the initial state is described by a Bloch function of the form

$$\psi_{k,v} = \mu_{k,v}(\vec{r}) e^{i(\vec{k}_v) \cdot \vec{r}},$$

and in the final state by a Bloch function of the form

$$\psi_{k,c} = \mu_{k,c}(\vec{r}) e^{i(\vec{k}_v) \cdot \vec{r}}.$$

(The photon momentum is neglected, since it is small compared to the range of \vec{k} .) If these functions are indeed the proper description of the electron wavefunction during the optical absorption process, then the matrix element $\langle \psi_{k,v} | \nabla | \psi_{k,c} \rangle$ is zero unless

$$\vec{k}_v \cong \vec{k}_c \quad (3.39)$$

Equation (3.39) corresponds to a "vertical" transition in the Brillouin zone, and is called a "DIRECT TRANSITION." If, for the moment, we neglect the matrix element in the integral of Eq. (3.38), then the contribution

from a given pair of bands to $\epsilon_{2b}(\omega)$ is given by the joint density of states $J_{c,v}(\omega)$, where

$$J_{c,v}(\omega) = \int_{\text{B.Z.}} \frac{2}{(2\pi)^3} \delta(\vec{k}_c - \vec{k}_v) \delta\left(\frac{E_c}{\hbar} - \frac{E_v}{\hbar} - \omega\right) dk^3 \quad (3.40)$$

The quantity $J_{c,v}(\omega)$ is called the joint density of states for bands indexed c and v . The quantity $J_{c,v}(\omega)\Delta\omega$ is equal to the number of pairs of states in bands c and v that have the same \vec{k} value and are separated by an energy E_{cv} , where $[(\hbar\omega) - (\Delta\omega/2)] \leq E_{cv} \leq [(\hbar\omega) + (\Delta\omega/2)]$. One can imagine that the joint density of states is calculated by searching the Brillouin zone with a "vertical" arrow of length E_{cv} , at each point multiplying the number of states at the tip by the number of states at the tail, and then summing these products over the entire Brillouin zone.

Brust [Ref. 31] has found that for a pair of bands (c,v) in silicon and germanium, the momentum matrix element is approximately independent of k , or

$$\langle \mu_{k,v} | \nabla | \mu_{k,c} \rangle \cong \langle \mu_v | \nabla | \mu_c \rangle \quad (3.41)$$

Thus, Brust pointed out that a knowledge of the properties of $J_{c,v}(\omega)$ is all that is necessary to understand the properties of $\epsilon_{2b}(\omega)$ for Si and Ge.

Another approach to evaluating $\epsilon_{2b}(\omega)$ has been suggested by W. E. Spicer, who has been led to his conclusions by a number of convincing photoemission experiments. In some materials [Ref. 32], Spicer has found that the photoelectric energy distribution curves (EDCs) are inconsistent with Eq. (3.39), which states that "conservation of the wave vector \vec{k} " is an important optical selection rule. This implies that the initial valence state and/or the excited conduction state of the electron are not well described by simple Bloch functions of the form $\mu_k(r) e^{i\vec{k}\cdot\vec{r}}$. This would be the case if the electron was very localized, or if the lifetime was very short. In both of these cases, the periodicity of the wavefunction would be destroyed. Consequently, Spicer has proposed that the "conservation of the wave vector \vec{k} " as described by Eq. (3.39) is not an important selection rule, and we can rewrite Eq. (3.38) as follows:

$$\epsilon_{2b}(\omega) = \frac{4\pi e^2 \hbar}{3m^2 \omega^2} \sum_{v,c} \int_{B.Z.} \left\{ \frac{2}{(2\pi)^3} |\langle \psi_{v,k} | \nabla | \psi_{c,k} \rangle|^2 \delta \left(\frac{E_c}{\hbar} - \frac{E_v}{\hbar} - \omega \right) \right\} d\vec{k}^3 \quad (3.42)$$

where $\psi_{v,k}$ and $\psi_{c,k}$ are the (unspecified) wavefunctions describing the electron in the initial valence state and in the final conduction state. Let us define the momentum matrix element $M(v,c,k)$ as

$$M(v,c,k) = \langle \psi_{v,k} | \nabla | \psi_{c,k} \rangle \quad (3.43)$$

Since we are uncertain as to the exact description of $\psi_{v,k}$ and $\psi_{c,k}$, let us now make two basic assumptions concerning the matrix element $|M|^2$: (1) $|M|^2$ is independent of \vec{k} and of the band indices c and v ; (2) $|M|^2$ is only a function of ω , the energy difference between states. (In a later chapter, we shall see that this assumption is in accord with the photoemission experiments for certain materials.) We now have

$$|M(v,c,k)|^2 = |M(\omega)|^2 \quad (3.44)$$

and

$$\epsilon_{2b}(\omega) = \frac{4\pi e^2 \hbar}{3m^2 \omega^2} |M(\omega)|^2 \sum_{v,c} \int_{B.Z.} \frac{2}{(2\pi)^3} \delta \left(\frac{E_c}{\hbar} - \frac{E_v}{\hbar} - \omega \right) d\vec{k}^3 \quad (3.45)$$

Let us now rewrite Eq. (3.45) in terms of an energy integral: Expanding the sum in Eq. (3.45),

$$\sum_{v,c} \int_{B.Z.} \frac{2}{(2\pi)^3} \delta \left(\frac{E_c}{\hbar} - \frac{E_v}{\hbar} - \omega \right) d\vec{k}^3 = \frac{2}{(2\pi)^3} \int_{B.Z.} d\vec{k}_1^3 \sum_i N_i^v(\vec{k}) \int_{B.Z.} d\vec{k}_j^3 \sum_j N_j^c(\vec{k}) \delta \left(\frac{E_c}{\hbar} - \frac{E_v}{\hbar} - \omega \right) \quad (3.46)$$

In Eq. (3.46), $N_i^v(\vec{k})$ means the number of states in the volume $d\vec{k}^3$ that come from the valence band labeled "i." Thus, Eq. (3.46) equals

$$\frac{2}{(2\pi)^3} \int_{E_f}^{E_f + \hbar\omega} dE \int_{B.Z.} d\vec{k}_j^3 \sum_j N_j^c(E, \vec{k}) \int_{B.Z.} d\vec{k}_i^3 \sum_i N_i^v(E - \hbar\omega, \vec{k}) \quad (3.47)$$

Now, the conduction band density of states $N_c(E)$ gives the number of states per unit volume between energies E and $E + dE$, or

$$N_c(E) = \frac{2}{(2\pi)^3} \int_{\text{B.Z.}} d\vec{k}_j \sum_j N_i^c(E, \vec{k}) \quad (3.48)$$

Similarly,

$$N_v(E - \hbar\omega) = \frac{2}{(2\pi)^3} \int_{\text{B.Z.}} d\vec{k}_i \sum_i N_i^v(E - \hbar\omega, \vec{k}) \quad (3.49)$$

Using Eq. (3.46), Eq. (3.47), Eq. (3.48), and Eq. (3.49) in Eq. (3.45), we obtain

$$\epsilon_{2b}(\omega) = \frac{32\pi^3}{3} \frac{e^2 \hbar}{m^2 \omega^2} |M(\omega)|^2 \int_{E_f}^{E_f + \hbar\omega} N_c(E) N_v(E - \hbar\omega) dE \quad (3.50)$$

Equation (3.50) is a very important relationship for the purpose of this investigation, since it describes a type of transition called a nondirect transition, as first coined by W. E. Spicer.

The density of states $N(E)$ can be found from an integral over a surface of constant energy, and is given by [Ref. 33]:

$$N(e) = \frac{2}{(2\pi)^3} \oint_S \frac{dS}{|\nabla_k E(k)|} \quad (3.51)$$

Note that $N(E)$ will be large where $|\nabla_k E(k)|$ is small.

In the approximation of Eq. (3.50), we know that $|M(\omega)|^2$ cannot be independent of ω , but must decrease as ω increases, since a sum rule states that [Ref. 99]:

$$\int_0^\infty \omega \epsilon_2(\omega) d\omega = \frac{1}{2} \pi \omega_p^2 \quad (3.52)$$

where ω_p is the plasma frequency for the total electron density of the system. If $|M(\omega)|^2$ was a constant, then the integral of Eq. (3.52) would diverge for the $\epsilon_2(\omega)$ given by Eq. (3.50).

The interband optical conductivity is given by Eq. (3.27), so

$$\sigma_b(\omega) = \frac{32\pi^3}{3} \frac{e^2 \hbar}{m^2 \omega} |M(\omega)|^2 \int_{E_f}^{E_f + \hbar\omega} N_c(E) N_v(E - \hbar\omega) dE \quad (3.53)$$

The differential conductivity, $\sigma_b(\omega, E)dE$, represents the portion of the conductivity due to transitions to energy E , or

$$\sigma_b(\omega, E)dE = \frac{32\pi^3}{3} \frac{e^2 \hbar}{m^2 \omega} |M(\omega)|^2 N_c(E) N_v(E - \hbar\omega) dE \quad (3.54)$$

For nondirect transitions, $\sigma_b(\omega, E)dE$ gives the probability per unit time that a photon will be absorbed by a valence electron at energy $(E - \hbar\omega)$. The functional dependence of this transition probability is stressed in Eq. (3.55):

$$\left(\begin{array}{l} \text{transition probability} \\ \text{for nondirect transitions} \end{array} \right) \sim \frac{1}{\omega} |M(\omega)|^2 N_c(E) N_v(E - \hbar\omega) \quad (3.55)$$

The fractional number of electrons excited to energy E for nondirect transitions is thus

$$\left(\begin{array}{l} \text{fractional number of} \\ \text{electrons excited to} \\ \text{energy } E \end{array} \right) = \frac{\sigma_b(\omega, E)}{\sigma_b(\omega)} = \frac{N_c(E) N_v(E - \hbar\omega)}{\int_{E_f}^{E_f + \hbar\omega} N_c(E) N_v(E - \hbar\omega) dE} \quad (3.56)$$

Thus, if N photons are absorbed by N electrons per unit time per unit volume, then Eq. (3.56) gives the fractional number that are excited to energy E . Note that for a given $\hbar\omega$, the number of electrons excited to energy E is proportional to $N_c(E) N_v(E - \hbar\omega)$. This proportionality characterizes the type of optical transition called a nondirect transition.

The characteristics of DIRECT and NONDIRECT optical transitions are summarized below:

Nondirect Transitions

a. Theoretical implications

- (1) All electron states involved in the optical absorption process are not well described by Bloch waves.
- (2) Conservation of the wave vector \vec{k} is not an important selection rule.
- (3) The momentum matrix element $|M|^2$ is independent of \vec{k} and band indices, but may be a function of ω .

b. Photoemission characteristics (energy distributions)

- (1) At photon energy $\hbar\omega_1$, a peak in the valence band density of states at energy $(E_1 - \hbar\omega_1)$ will cause a peak in the EDC at energy E_1 . If the photon energy is increased to $\hbar\omega_2$, the peak in the EDC will appear at energy

$$E_2 = E_1 + \hbar(\omega_2 - \omega_1) \quad \text{or}$$
$$\underbrace{(E_2 - E_1)}_{\text{peak}} = \hbar(\omega_2 - \omega_1)_{\text{photon}}$$

Thus, an increment $(\hbar\Delta\omega)$ in photon energy will result in an equal increment in the energy of a peak in the EDC, if the peak is due to structure in the valence band density of states.¹

- (2) Structure in the conduction band density of states remains at the same energy E for all values of photon energy.²

¹ These statements apply if there is no structure in the conduction band density of states. If there is structure in the conduction band, this structure will modulate the EDCs, and in the region of the conduction band peak, $\Delta E_p \neq \Delta\hbar\omega$, as seen by the example of Fig. (33a) and Fig. (33b).

² A stationary peak in the EDCs can also be due to electron-electron scattering. A scattering peak is often characterized by a large number of slow electrons that appear in the EDCs at high photon energies. An example of such scattering can be seen in the case of silver covered with a monolayer of cesium, as will be discussed in Chapter VI.

Direct Transitions

a. Theoretical implications

- (1) $\vec{k}_v \cong \vec{k}_c$
- (2) Simple Bloch waves adequately describe valence and conduction electrons involved in the optical transitions.

b. Photoemission characteristics (energy distributions)

- (1) Characteristic b(1) (nondirect transitions) is observed from a very narrow valence band that has the same energy for all values of k .
- (2) In other cases, an increment ($\hbar\Delta\omega$) in photon energy will cause peaks in EDC to move in increments that are either larger than ($\hbar\Delta\omega$) or smaller than ($\hbar\Delta\omega$).
- (3) Peaks can appear or disappear with small changes in photon energy.

The measurement of photoelectric energy distributions over a wide range of photon energies can be a very important technique in determining whether the optical transitions in a material are of a direct or a nondirect nature, since the two types of transitions have such different characteristics in the EDCs.

We have not discussed another possible type of transition, which involves the emission or absorption of a phonon. This type of transition is commonly called an indirect transition,¹ and is thoroughly discussed in a number of texts [Refs. 34]. Phonons typically have energies less than 0.1 eV, but can have any value of \vec{k} . Thus, indirect transitions could cause the same effects as nondirect transitions, except that there would be a pronounced temperature dependence, since the probability of emission or absorption² of a phonon becomes very small as the temperature decreases. Such temperature dependences have not yet been observed in

¹ It should be emphasized that direct and nondirect transitions are a first-order process, whereas indirect transitions are a second-order process, with a smaller probability of occurrence.

² Neglecting the zero-point vibration.

photoelectric energy distributions, so we shall restrict our attention to direct and nondirect transitions.

The illustrative example of Fig. 33 serves to depict the characteristic differences between direct and nondirect transitions as seen in the photoelectric energy distributions. A hypothetical energy band diagram of Fig. 33a will serve as the basis for this example. Note that in the $(\vec{k}_1 - \vec{k}_0)$ direction, there are no bands between energies 5 and 15 eV above the fermi level, and in the $(\vec{k}_2 - \vec{k}_0)$ direction, there are no bands below 5 eV above the fermi level. Let us assume that 10 electrons occupy the filled valence bands in the energy range between 0 and (-)6 eV. The density of states $N(E)$ that corresponds to this energy band diagram is shown in Fig. 33b. Note that there is a valence band peak of height 5 electrons/photon/eV in the region 0 to (-)1 eV below the fermi level, and a conduction band peak of height 6 electrons/photon/eV in the region 15 to 16 eV above the fermi level. These peaks are due to the "flat" bands in the $(\vec{k}_1 - \vec{k}_0)$ direction. The density of states is easily obtained from the energy band diagram, since in this simple case, Eq. (3.51) reduces to

$$N(E) = \sum_i \left(\frac{dE}{dk_i} \right)^{-1} \quad (3.57)$$

where the sum is over all bands (i) at energy E, and the units of \vec{k} are given in Fig. 33a. In the photoemission process, let us assume that all electrons excited to an energy E above the vacuum level will escape the surface of the solid and be measured in the EDC. Let us also assume that all electrons excited to an energy E below the vacuum will not escape the solid, and will not be measured in the EDCs.

First, we shall consider the case of direct transitions shown in Fig. 33c. The optical transitions are governed by Eq. (3.39), which says that only "vertical" transitions in which $k_{\text{initial}} = k_{\text{final}}$ are allowed. Thus, the threshold for photoemission is at a photon energy $h\nu = 2.4$ eV, as indicated by the transition (1d) in Fig. 33a. At a photon energy of 2.4 eV, electrons at

$$\vec{k} = 3 \left(\frac{\vec{k}_1 - \vec{k}_0}{|\vec{k}_1 - \vec{k}_0|} \right)$$

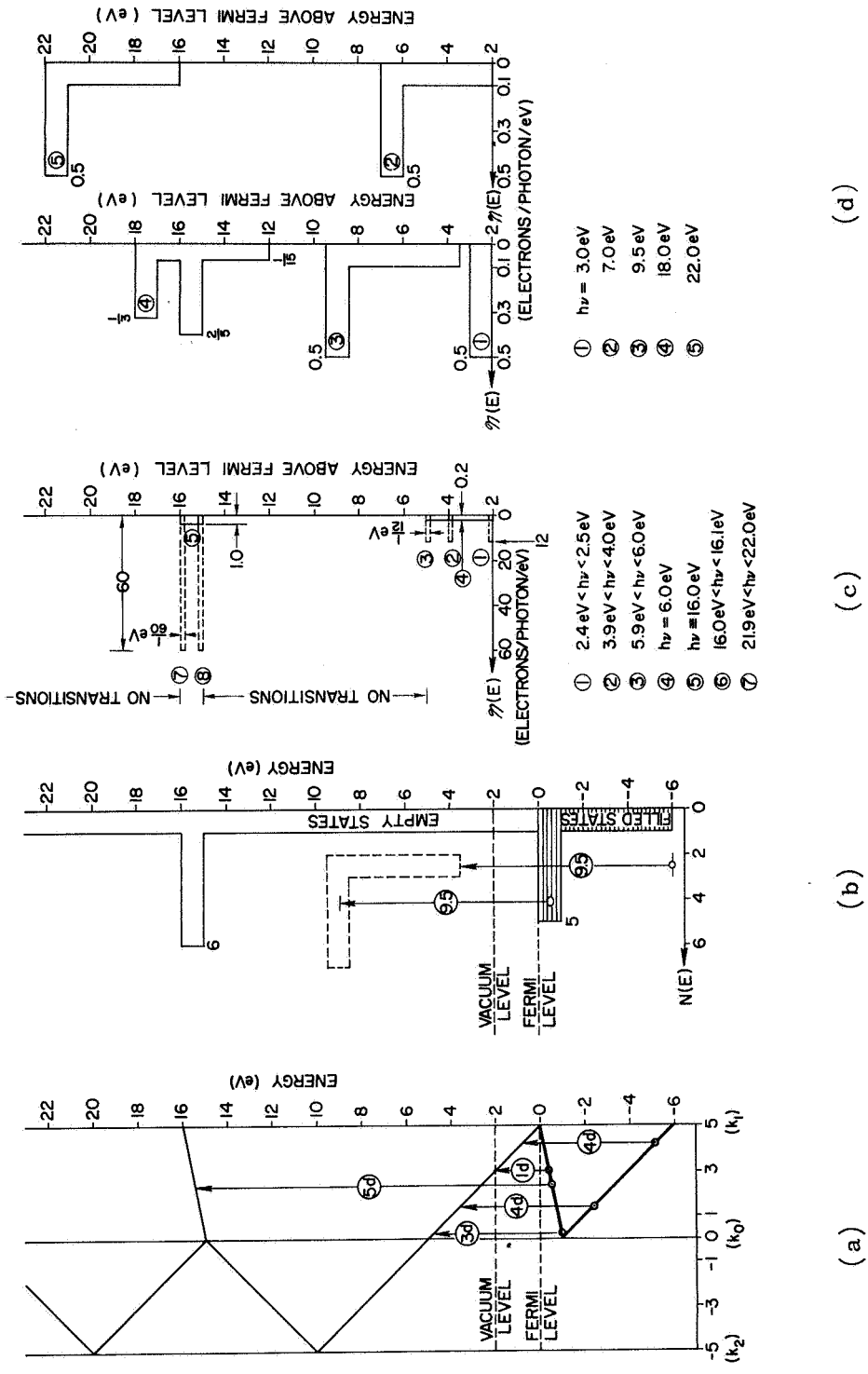
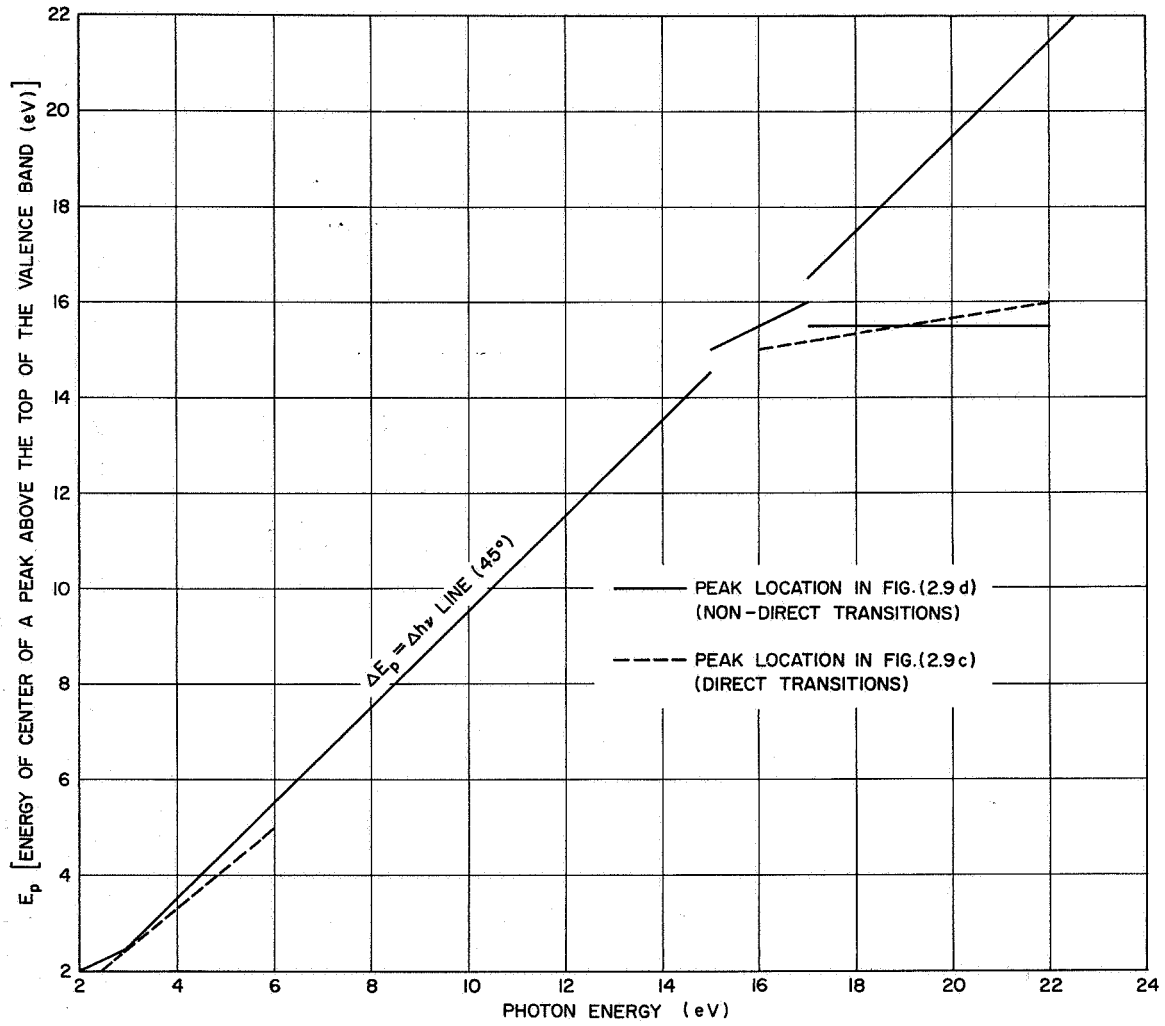


FIG. 33. IDENTIFYING CHARACTERISTICS OF DIRECT AND NONDIRECT TRANSITIONS: (a) hypothetical E vs k diagram; (b) density of states corresponding to (a); (c) energy distributions for direct transitions; (d) energy distributions for nondirect transitions; (e) ΔE_p vs $\Delta h\nu$ plot for direct and nondirect transitions.



(e)

FIG. 33. CONTINUED.

are excited from the valence band to a conduction band at 2 eV above the fermi level. Let us assume that the bandwidth of the incident light is not zero, but is 0.1 eV, and that the incident photons are evenly distributed such that $2.4 \text{ eV} < h\nu < 2.5 \text{ eV}$. If all the excited electrons get out, then the measured EDC is that indicated by (1) in Fig. 33c. The width of this EDC occurs because of the finite bandwidth. Note that the area under EDC (1) is one electron/photon, which is the case since all the excited electrons are at energy E greater than the vacuum level and will be photoemitted. If we increase the photon energy to $3.9 \text{ eV} < h\nu < 4.0 \text{ eV}$, the EDC is given by curve (2) in Fig. 33c. At a still higher photon energy, $5.9 \text{ eV} < h\nu < 6.0 \text{ eV}$, the direct transition occurs at \vec{k}_0 , as seen by transition (3d) in Fig. 33a, and there is a corresponding peak of photoemitted electrons at $E = 5 \text{ eV}$, as shown by EDC (3) in Fig. 33c. Observe that while the photon energy has increased by an increment of 4.0 eV from EDC (1) to EDC (3), the peaks in the EDC have increased in energy by only $(E_{(3)} - E_{(1)}) = 3.0 \text{ eV}$. Thus, the increment in peak energy is not equal to the increment in photon energy, as pointed out earlier. At a photon energy of exactly 4.0 eV, the only possible transition is between two parallel bands, as shown in Fig. 33a by transitions (4d). Note that in this case, all values of k between \vec{k}_1 and \vec{k}_0 are possible. The resulting EDC is flat and extends between $E = 2 \text{ eV}$ and $E = 5 \text{ eV}$, as shown by EDC (4) in Fig. 33c. Note that the area of EDC (4) is only 0.6 electrons/photon, since 40 percent of the electrons are excited to energies below the vacuum level.

In the range of photon energies between 6.0 and 16.0 eV, no direct transitions are possible, so no electrons are photoemitted, and there are no EDCs. At a photon energy of exactly 16.0 eV, transitions can occur between two parallel bands, as indicated by transition (5d) in Fig. 33a. This transition corresponds to EDC (5) in Fig. 33c, which has a width of 1.0 eV and an area of one electron per photon. As the photon energy is increased to $16.0 \text{ eV} < h\nu < 16.1 \text{ eV}$, a narrow peak suddenly appears in the EDC at an energy of 15 eV, as shown by EDC (6) in Fig. 33c. The width of this EDC is only $1/60 \text{ eV}$, but the area is one electron/photon. As the photon energy is increased, the energy of the EDC peak slowly increases, and at a photon energy $21.9 \text{ eV} < h\nu < 22.0 \text{ eV}$, the peak is at 16 eV. Note that the photon energy has increased an increment of 6.0 eV

in going from EDC (6) to EDC (7), but the peak in the EDC has moved only an increment $(E_{(7)} - E_{(6)}) = 1.0$ eV. Again, we see that the increment in peak energy does not equal the increment in photon energy. For photon energies greater than 22.0 eV, there are no possible direct transitions, and the peak in the EDC disappears.

The EDCs for the case of nondirect transitions are quite different from the EDCs for direct transitions, as seen from Fig. 33d, which shows EDCs for nondirect transitions. First, let us focus our attention on the dashed curve, Fig. 33b, which is for a photon energy of $h\nu = 9.5$ eV. The fractional number of electrons excited to energy E is given by Eq. (3.56). Since the denominator of Eq. (3.56) is constant for a given $h\nu$, then the number of electrons excited to energy E is $\eta'(E)$, where

$$\eta'(E) = (\text{constant})N_c(E)N_v(E - h\nu) \quad (3.58)$$

for all E . This calculation is equivalent to raising the valence band density of states by an energy $h\nu$, and at each energy E , multiplying by $N_c(E)$. The result is the energy distribution of excited electrons in the material, and is indicated by the dashed curve in Fig. 33b for $h\nu = 9.5$ eV. Since $N_c(E) = 1$ for $0 < E < 15$ eV, the dashed curve of Fig. 33b is an exact replica of the valence band density of states. Since all the electrons are excited to energies higher than the vacuum level, all are photoemitted, and the corresponding energy distribution curve EDC (3) of Fig. 33d is also an exact replica of the valence band density of states.

Figure 33d shows EDCs for several photon energies. In contrast to the case of direct transitions, the photoemission threshold is at 2.0 eV for the nondirect transitions, whereas it was 2.4 eV for the direct transitions. Note that for a photon energy of 3.0 eV, the leading edge of the EDC is at 3.0 eV, and that for a photon energy of 22.0 eV, the leading edge of the EDC is at 22.0 eV. Thus, we see that for nondirect transitions, the increment in photon energy is equal to the increment in peak energy, in contrast to the direct transitions. Note that for $h\nu = 18$ eV, EDC (4) of Fig. 33d is modulated by the peak in the

conduction band density of states. This modulation remains fixed in energy for all photon energies, a characteristic of nondirect transitions.

The effect of the modulation of the conduction band density of states on the location of a peak in the EDCs is shown in Fig. 33d, where the energy E_p of the center of a peak is plotted as a function of photon energy for both the direct and the nondirect transition. In the range of photon energies between 3 and 15 eV and above 17 eV, the nondirect transition follows the rule $\Delta E_p = \Delta \hbar \omega$. However, near the vacuum level ($\hbar \nu < 3$ eV) and in the vicinity of a conduction band (15 eV $< \hbar \nu < 17$ eV), the location of the peak does not follow the rule $\Delta E_p = \Delta \hbar \omega$, and the distinction between the direct transition curve and the nondirect transition is not very great.

Later in this paper, ΔE_p vs $\Delta \hbar \omega$ plots of the type shown in Fig. 33d will be found to be quite useful in the analysis of EDCs from real materials.

Figure 33 has been used to illustrate some of the major features that distinguish direct from nondirect transitions in the EDCs. Thus, we see that experimental measurement of the photoelectric EDC at different photon energies can tell us whether direct or nondirect transitions occur in a specific material. Unfortunately, the photoemission process in a real material is quite complex, and all the excited electrons are not photoemitted, as was assumed in the model of Fig. 33d. In the next section, we shall attempt to describe the photoemission process in a more realistic manner.

E. THE PHOTOEMISSION PROCESS

In this section, we derive a mathematical model describing the photoemission process for a material with a free-electron-like conduction band and a semiclassical threshold function. The model is based upon nondirect transitions. The method of analysis will proceed as follows:

- (1) Calculate the probability of exciting an electron at a depth x from the surface;
- (2) Calculate the probability that the electron will then be excited to an energy E in the conduction band;

- (3) Calculate the probability that the electron excited to energy E will then travel to the surface without suffering an inelastic electron-electron scattering event, and escape into the vacuum.

The result will yield the photoelectric energy distributions and the photoelectric yield for nonscattered electrons in terms of the density of states, the electron-electron scattering length, and other physical parameters.

Let us begin the analysis by assuming that a monochromatic beam of photon energy $h\nu$ travels through vacuum and is normally incident upon a solid or liquid surface, as shown in Fig. 34a. Some of the light will be reflected and some of the light will be absorbed within the material; we assume that the sample is much thicker than the optical absorption length $(\frac{1}{\alpha})$, so that we need not consider reflections from a back surface. Let us consider only light of energy $h\nu$ such that

- (1) The photon energy is high enough so that band-to-band transitions dominate over other optical absorption mechanisms;
- (2) The wavelength λ is appreciably longer than the lattice spacing.

If the incident photon flux is given by $I_0^i(\omega)$, then the flux that penetrates the surface is given by $I_0(\omega)$, where

$$I_0(\omega) = [1 - R(\omega)] I_0^i(\omega) \quad (3.59)$$

In Eq. (3.59), $R(\omega)$ is the magnitude of the reflection coefficient, $I_0(\omega)$ represents the total number of photons per unit area per unit time that are absorbed in the material. The electromagnetic wave propagates into the material with a phase velocity $V_p(\omega) = c/n(\omega)$, where $n(\omega)$ is the index of refraction. However, in the energy range corresponding to band-to-band absorption, the photons are strongly absorbed. The probability of absorption per unit time is given by the optical conductivity $\sigma(\omega)$, and is a property of the material. Thus, at any point x in the material [Ref. 27],

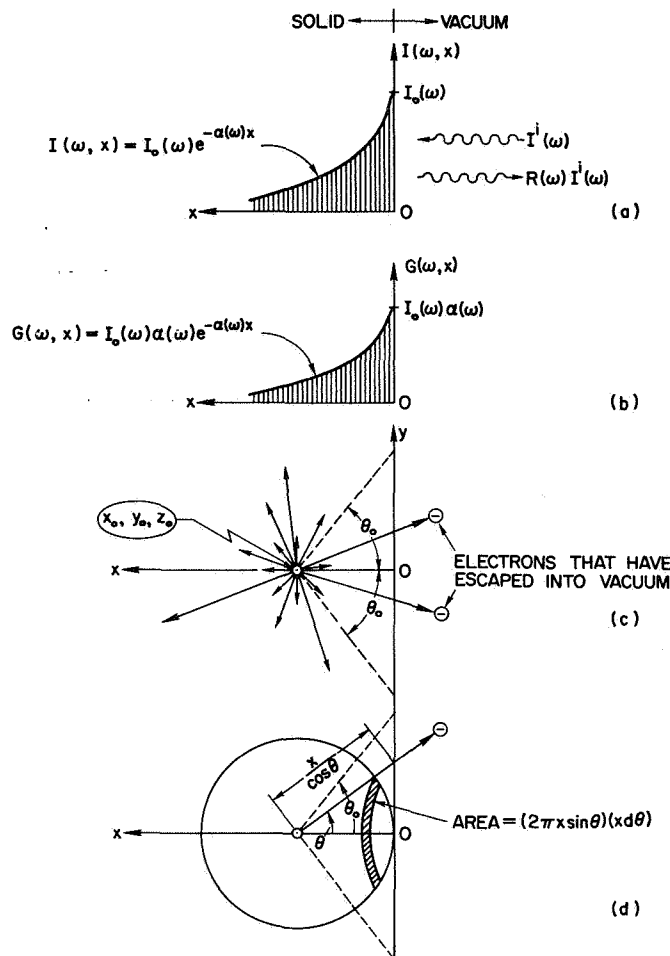


FIG. 34. THE PHOTOEMISSION PROCESS: (a) DISTRIBUTION OF PHOTON FLUX IN THE MATERIAL; (b) TOTAL GENERATION RATE OF ELECTRONS $G(x, \omega)$ AS A FUNCTION OF DEPTH x FROM THE SURFACE; (c) MOVEMENT OF ELECTRONS GENERATED AT POINT (x_0, y_0, z_0) TO AN ENERGY e ABOVE THE VACUUM LEVEL. The direction of an arrow represents the direction of the velocity, and the tip of the arrow indicates where the electron scatters with another electron. The dashed line shows the velocity cone. Electrons in the velocity cone can escape from the solid if they do not scatter before reaching the surface. (d) Geometry used in calculating the escape probability.

$$\sigma(\omega) = 2\omega n(\omega)k(\omega) \quad (3.60)$$

where $k(\omega)$ is called the extinction coefficient. The permittivity of free space ϵ_0 has been set equal to unity in obtaining Eq. (3.60). (For a discussion of the optical constants and their interrelations, see Ref. 27.) The absorption coefficient per unit $\alpha(\omega)$ is related to $k(\omega)$ by

$$\alpha(\omega) = \frac{4\pi k(\omega)}{\lambda} \quad (3.61)$$

and

$$n(\omega) = \frac{c}{v_p(\omega)} \quad (3.62)$$

$$\lambda\nu = c \quad (3.63)$$

Using Eq. (3.61), Eq. (3.62), and Eq. (3.63) in Eq. (3.60), we obtain

$$\alpha(\omega) \cdot v_p(\omega) = \sigma(\omega) \quad (3.64)$$

or

$$\left(\begin{array}{c} \text{Probability of Absorption} \\ \text{per unit length} \end{array} \right) \left(\text{Phase Velocity} \right) = \left(\begin{array}{c} \text{Probability of Absorption} \\ \text{per unit time} \end{array} \right) \quad (3.65)$$

Thus, the probability of absorption per unit length $\alpha(\omega)$ is directly related to the optical conductivity $\sigma(\omega)$. Since the probability of absorption per unit length $\alpha(\omega)$ is the same at every point x , the number of photons absorbed per unit area between x and $x+dx$ is proportional to (the number of photons in the increment dx) times (the probability of absorption per unit length), or

$$dI(x, \omega) = -\alpha(\omega)I(x, \omega) \quad (3.66)$$

so

$$I(x, \omega) = I_0(\omega)e^{-\alpha x} \quad (3.67)$$

where $x = 0$ is taken at the surface as in Fig. 34. The spatial distribution of the flux $I(x, \omega)$ is sketched in Fig. 34a. If we assume that each absorbed photon corresponds to an excited electron, then the spatial distribution of excited electrons $G(x, \omega)$ is given by

$$G(x, \omega) = - \frac{dI(x, \omega)}{dx} = I_0(\omega) \alpha(\omega) e^{-\alpha(\omega)x} \quad (3.68)$$

$G(x, \omega)$ is a generation rate, giving the number of electrons generated in the increment between x and $(x+dx)$ per unit area per unit time, and is sketched in Fig. 34b. The electrons represented by $G(x, \omega)$ are excited from filled states in the valence band to empty states in the conduction band. According to the model of nondirect transitions, the fractional number of electrons excited to an energy E in the conduction band is given by Eq. (3.56). Thus, if we denote the total number of electrons excited to energy E by the quantity $G(E, x, \omega)$, we have

$$G(E, x, \omega) = \frac{N_c(E)N_v(E - \hbar\omega)}{\int_{E_f}^{E_f + \hbar\omega} N_c(E)N_v(E - \hbar\omega) dE} \cdot G(x, \omega) \quad (3.69a)$$

or

$$G(E, x, \omega) = I_0(\omega) \alpha(\omega) e^{-\alpha(\omega)x} \frac{N_c(E)N_v(E - \hbar\omega)}{\int_{E_f}^{E_f + \hbar\omega} N_c(E)N_v(E - \hbar\omega) dE} \quad (3.69b)$$

Equation (3.69) gives a mathematical expression for the generation rate of electrons to the state E in the conduction band at depth x from the surface. $G(E, x, \omega)$ is sketched in Fig. 34b. Once these electrons are excited to energy E , they take on some state $\psi(E)$ of the crystal, and move in various directions through the crystal. It is difficult to proceed further than Eq. (3.69) unless we can say something about how these excited electrons move through the crystal.

In the discussion to follow, we shall restrict the analysis to the case where the final state in the conduction band is a spherical band,

so that all directions are equivalent. Thus, electrons originating at the point (x_o, y_o, z_o) in Fig. 34c will travel in all directions with a group velocity appropriate to a free electron band, as given by Eq. (3.5) to be

$$|v_g(E)| = \sqrt{\frac{2}{m}} \sqrt{E - E_B}, \quad (E > E_B) \quad (3.70)$$

where the quantity E_B denotes the energy of the bottom of the free electron band.

Let us now proceed to calculate the number of electrons that will travel to the surface, overcome the potential barrier (W), and escape into the vacuum. The velocity cone of Fig. 26 gives the fractional number of electrons at energy E that are moving toward the surface and have $\frac{1}{2}m(v_g)_x^2 \geq W$. Thus, according to Eq. (3.9), all those electrons in the solid angle

$$\theta_o = \cos^{-1} \sqrt{\frac{W}{E}}, \quad E \geq W \quad (3.71)$$

are candidates for escape into vacuum. However, some of these electrons will suffer inelastic electron-electron collisions on the way to the surface. We shall calculate the number of electrons that reach the surface without encountering such a scattering event.

An electron, starting at point $r_o(x_o, y_o, z_o)$ and traveling at an angle θ with respect to the x-axis must travel a distance $(\vec{r} - \vec{r}_o)$ before reaching the surface, where

$$|\vec{r} - \vec{r}_o| = \frac{x}{\cos \theta} \quad (3.72)$$

as seen from Fig. 34d. The probability that an electron does not scatter before reaching the surface is given by

$$\left(\begin{array}{l} \text{probability of not colliding} \\ \text{before reaching surface} \end{array} \right) = e^{-\frac{-(|\vec{r} - \vec{r}_o|)}{L(E)}} = e^{-\frac{x}{L(E) \cos \theta}} \quad (3.73)$$

where $L(E)$ is the electron-electron scattering length. From Fig. 34d, the fraction of the electrons in the solid angle between θ and $(\theta+d\theta)$ is given by the ratio of the area of the sphere between θ and $(\theta+d\theta)$ to the total area of the sphere, or

$$\frac{\text{area between } \theta \text{ and } \theta+d\theta}{\text{area of sphere}} = \frac{2\pi x^2 \sin \theta d\theta}{4\pi x^2} = \frac{1}{2} \sin \theta d\theta \quad (3.74)$$

Thus, the fraction of electrons from (x, y_0, z_0) that can escape is given by $F(E, x)$, where

$$F(E, x) = \left(\begin{array}{l} \text{fraction of electrons} \\ \text{at } E \text{ and depth } x \text{ that} \\ \text{escape without scattering} \end{array} \right) = \int_{\theta=0}^{\theta_0} \frac{1}{2} \sin \theta e^{-\frac{x}{L(E) \cos \theta}} d\theta \quad (3.75)$$

The generation rate at depth x and energy E is $G(E, x, \omega)$ so the total number of nonscattered electrons that escape is given by $\mathcal{N}'(E, x, \omega)$, where

$$\mathcal{N}'(E, x, \omega) = G(E, x, \omega) \int_{\theta=0}^{\theta_0} \frac{1}{2} \sin \theta e^{-\frac{x}{L(E) \cos \theta}} d\theta \quad (3.76)$$

Summing up contributions from all possible values of x , we obtain

$$\mathcal{N}'(E, \omega) = \int_{x=0}^{\infty} dx G(E, x, \omega) \int_{\theta=0}^{\theta_0} \frac{1}{2} \sin \theta e^{-\frac{x}{L(E) \cos \theta}} d\theta \quad (3.77)$$

where $\mathcal{N}'(E, \omega)$ is the number of electrons photoemitted at energy E due to the light flux $I_0(\omega)$. Substituting Eq. (2.69) for $G(E, x, \omega)$, Eq. (3.77) becomes

$$\mathcal{N}'(E, \omega) = I_0(\omega) \frac{1}{2} \alpha(\omega) \frac{N_c(E) N_v(E - \hbar\omega)}{\int_{E_f}^{E_f+E} N_c(E) N_v(E - \hbar\omega) dE} \int_{x=0}^{\infty} dx \int_{\theta=0}^{\theta_0} \sin \theta e^{-\left[\alpha(\omega) + \frac{1}{L(E) \cos \theta}\right] x} d\theta \quad (3.78)$$

We now let

$$\mathcal{N}(E, \omega) = \frac{\mathcal{N}'(E, \omega)}{I_0(\omega)} \quad (3.79)$$

where $\mathcal{N}(E, \omega)$ is the number of electrons photoemitted at energy E per absorbed photon per eV. By making the substitution $\beta = \cos \theta$, and

changing the order of integration, Eq. (3.78) becomes

$$\eta(E, \omega) = \frac{1}{2} \alpha(\omega) \frac{N_c(E)N_v(E - \hbar\omega)}{\int_{E_f}^{E_f + \hbar\omega} N_c(E)N_v(E - \hbar\omega) dE} \int_{\cos \theta_0}^1 \left\{ \int_{x=0}^{\infty} e^{-\left[\alpha(\omega) + \frac{1}{L(E)\beta}\right] x} dx \right\} d\beta \quad (3.80)$$

The integrals are easily evaluated with the use of integral 47 of Ref. 22, and we obtain

$$\eta(E, \omega) = \frac{1}{2} \left\{ 1 - \cos \theta_0 - \frac{1}{\alpha(\omega)L(E)} \ln \left[\frac{\alpha(\omega)L(E) + 1}{\alpha(\omega)L(E) \cos \theta_0 + 1} \right] \right\} \cdot \left[\frac{N_c(E)N_v(E - \hbar\omega)}{\int_{E_f}^{E_f + \hbar\omega} N_c(E)N_v(E - \hbar\omega) dE} \right] \quad (3.81)$$

Equation (3.81) is actually the final objective of this derivation, but the expression can be put into a more understandable form if we factor out the quantity $\frac{1}{2}(1 - \cos \theta_0) \left(\frac{\alpha L}{\alpha L + 1}\right)$, to obtain

$$\eta(E, \omega) = \left\{ \left[\frac{1}{2}(1 - \cos \theta_0) \frac{\alpha L}{\alpha L + 1} \right] \left[\frac{\alpha L + 1}{\alpha L} - \frac{1}{\alpha L(1 - \cos \theta_0)} \frac{\alpha L + 1}{\alpha L} \ln \left(\frac{\alpha L + 1}{\alpha L \cos \theta_0 + 1} \right) \right] \frac{N_c(E)N_v(E - \hbar\omega)}{\int_{E_f}^{E_f + \hbar\omega} N_c(E)N_v(E - \hbar\omega) dE} \right\} \quad (3.82)$$

The quantity $\frac{1}{2}(1 - \cos \theta_0)$ is just the semiclassical threshold function $T_f(E)$ given by Eq. (3.10), so we can rewrite Eq. (3.82) as

$$\eta(E, \omega) = C \left[\alpha(\omega)L(E), T_f(E) \right] \left(\frac{\alpha(\omega)L(E)}{\alpha(\omega)L(E) + 1} \right) \frac{N_c(E)N_v(E - \hbar\omega)}{\int_{E_f}^{E_f + \hbar\omega} N_c(E)N_v(E - \hbar\omega) dE} \quad (3.83)$$

where the correction factor $C \left[\alpha(\omega)L(E), T_f(E) \right]$ is given by

$$C \left[\alpha(\omega)L(E), T_f(E) \right] = \left[\frac{\alpha L + 1}{\alpha L} + \frac{\alpha L + 1}{2(T_f)(\alpha L)^2} \ln \left(\frac{\alpha L + 1}{\alpha L + 1 - 2\alpha L T_f} \right) \right] \quad (3.84)$$

The factor $T_f(E) \frac{\alpha(\omega)L(E)}{\alpha(\omega)L(E) + 1}$ in Eq. (3.83) is just what would be obtained if all the electrons in the velocity cone had velocities directed normal to the surface. The correction factor C of Eq. (3.84) gives the

adjustment that must be made when the actual angular distribution of electrons is taken into account. Figure 35 gives a plot of the correction

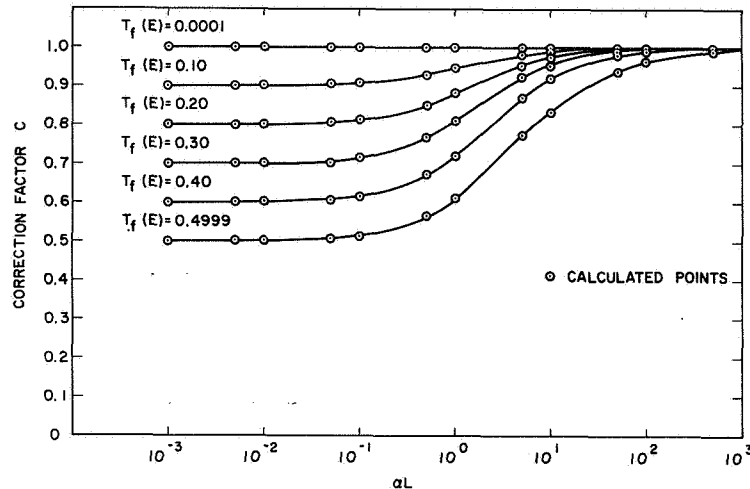


FIG. 35. CORRECTION FACTOR $C [\alpha(\omega)L(E), T_f(E)]$ FOR VARIOUS VALUES OF (αL) AND T_f .

factor C as a function of the quantities (αL) and T_f . Note that for any αL , the magnitude of C can vary only between 0.5 and 1.0. In many cases of interest, the range of E is such that the semiclassical threshold function T_f is always small, say $T_f(E) \lesssim 0.2$. In this case, the range of the correction factor C is $0.8 \leq C \leq 1.0$ for any value of $\alpha(\omega)L(E)$ whatsoever. Thus, for cases near the threshold, the velocity cone is sufficiently small so that it is a good approximation to assume that the velocity component of all the electrons that escape is essentially normal to the surface. Setting $C \cong 1$, we obtain for the case of the "small angle approximation"¹

¹ It is to be emphasized that the correction factor C does not include the effect of phonons. In the cases where the electron-phonon scattering length is shorter than the electron-electron scattering length, Eq. (3.85) would not apply.

$$\eta(E, \omega) \cong T_f(E) \left(\frac{\alpha(\omega)L(E)}{\alpha(\omega)L(E)+1} \right) \frac{N_c(E)N_v(E - h\omega)}{\int_{E_f}^{E_f+h\omega} N_c(E)N_v(E - h\omega) dE} \quad (3.85)$$

Equation (3.83), the important equation we have sought to derive, gives the energy distribution of nonscattered electrons in terms of the density of states, $N_c(E)$ and $N_v(E)$, the electron-electron scattering length $L(E)$, the absorption coefficient $\alpha(\omega)$, and the semiclassical threshold function $T_f(E)$. It must be emphasized that Eq. (3.83) applies to the case of a material with a free-electron-like conduction band, and is based upon the theory of nondirect transitions.

The total photoelectric yield $Y(\omega)$ is given by finding the area under the EDC, or

$$Y(\omega) = \int_{\phi}^{\hbar\omega} \eta(E, \omega) dE \quad (3.86)$$

where ϕ is the vacuum level, and the energy zero is taken at the top of the valence band. Equation (3.86) gives the quantum yield $Y(\omega)$ in terms of the total number of electrons photoemitted per absorbed photon of angular frequency ω .

Equations (3.83) and (3.86) give two quantities that can be measured by experiment. In the next section, we shall describe several methods by which the quantities $N_c(E)$, $N_v(E)$, $L(E)$ and $\epsilon_2(\omega)$ can be calculated from an experimental knowledge of $\eta(E, \omega)$ and $Y(\omega)$.

The results of this section appear to be consistent with the relations of Berglund [Ref. 7], which were derived earlier.

In the analysis thus far, we have considered only the electrons that escape without suffering a scattering event. Berglund [Ref. 7] has calculated the number of electrons that escape after one electron-electron scattering event to be $R'(E', E, \omega) dE$, where E is the energy at which the electrons escape, and E' is the energy of the primary electrons. Berglund finds that [see Eq. 80, Ref. 7]

$$R'(E', E, \omega) dE \cong \left\{ \left[(C[\alpha(\omega)L(E), T(E)]) T(E) G_0(E', \omega) \frac{\alpha(\omega)}{\alpha(\omega)+1/L(E)} \frac{P_s(E', E)}{P_s(E')} \right] \right. \\ \left. \cdot \left[\frac{1}{\alpha(\omega)L(E')} \ln [1+\alpha(\omega)L(E')] + \frac{L(E)}{L(E')} \ln \left(1 + \frac{L(E')}{L(E)} \right) \right] \right\} dE \quad (3.87)$$

where

$G_0(E', \omega) = I_0(\omega) \cdot$ (probability of being excited to energy E')

$p_s(E', E) =$ number of primary electrons that scatter from E' to E

$P_s(E') =$ total number of electrons at energy E' that scatter before reaching the surface

In the case of nondirect transitions, the quantity (probability of being excited to energy E') is given by Eq. (3.56). Berglund has pointed out that the term

$$\left\{ \frac{L(E)}{L(E')} \ln \left[1 + \frac{L(E')}{L(E)} \right] \right\}$$

is due to those electrons initially excited to E' which are moving away from the surface.

Equation (3.87) accounts for those electrons that originate in the bulk of the material. In addition, there may be a large number of electrons that do reach the surface without scattering, but are reflected from the surface because their velocity direction is not in the velocity cone. Thus, if we assume spherical scattering from the surface, these electrons act as a source of primary (unscattered) electrons generated at the surface. The total number of electrons that arrive at the surface without scattering is given by setting the velocity cone equal to 90° , or setting $T_f(E) = 0.5$ in Eq. (3.83). Thus, the total number of unscattered electrons incident upon the surface is given by

$$I_0(\omega) \mathcal{N}(E', \omega, T_f = 0.5)$$

or

$$I_0(\omega)n(E', \omega, T_f = 0.5) = C[\alpha(\omega)L(E'), T_f = 0.5] \left(\frac{1}{2}\right) \frac{\alpha L}{\alpha L + 1} G_0(E', \omega) \quad (3.88)$$

The total number of reflected electrons $[I_0(\omega)n^R(E', \omega)]$ is found by substituting the number of photoemitted electrons from the total number of electrons incident upon the surface, or

$$I_0(\omega)n^R(E', \omega) = \left(\frac{\alpha L'}{\alpha L' + 1}\right) G_0(E', \omega) \left\{ \left(\frac{1}{2}\right) C[\alpha L', T_f = 0.5] - T_f(E') C[\alpha L', T_f(E')] \right\} \quad (3.89)$$

where $L' = L(E')$ and $\alpha = \alpha(\omega)$. Now, Eq. (3.87) can be adapted to take into account these reflected electrons by letting $\alpha \rightarrow \infty$. This corresponds to the case where all the electrons are excited very near the surface. In addition, we must replace the generation rate $G_0(E', \omega)$ in Eq. (3.87) by $[I_0(\omega)n^R(E', \omega)]$ of Eq. (3.89). Letting $R'_s(E', E, \omega)dE$ denote the number of electrons that are photoemitted at energy E due to primary electrons at energy E' that have been reflected from the surface, the adaptation of Eq. (3.87) gives

$$\begin{aligned} R'_s(E', E, \omega)dE = & \left\{ \left(C[\alpha L, T_f(E)] T_f(E) G_0(E', \omega) \frac{p_s(E', E)}{P_s(E')} \right) \right. \\ & \cdot \left(\frac{1}{2} C[\alpha L', T_f = 0.5] - T_f(E') C[\alpha L', T_f(E')] \right) \\ & \left. \cdot \left(\frac{L(E)}{L(E')} \ln \left[1 + \frac{L(E')}{L(E)} \right] \right) \right\} dE \quad (3.90) \end{aligned}$$

The total number of once-scattered electrons that are photoemitted at energy E due to primaries at E' is thus $R'_{tot}(E', E, \omega)$, where

$$R'_{tot}(E', E, \omega)dE = [R'(E', E, \omega) + R'_s(E', E, \omega)] dE \quad (3.91)$$

To obtain the total number of once-scattered electrons that are photoemitted at energy E , we must sum Eq. (3.91) over all energies $E' > E$.

Let us compare the magnitude of $R'_s(E', E, \omega)dE$ to the magnitude of $R'(E', E, \omega)$ for the case of a free electron metal with the work

function $\phi = 4$ eV, and the bottom of the band at 4 eV below the fermi level. We shall use the parameters below:

$$E' = 8 \text{ eV above fermi level (primary electrons)}$$

$$E = 5 \text{ eV above fermi level (once-scattered electrons)}$$

$$\frac{L(E)}{L(E')} \cong \left(\frac{8}{5}\right)^{3/2} = 2.03$$

$$\alpha(\omega)L(E') = 0.125$$

$$\alpha(\omega)L(E) = 0.254$$

$$C[\alpha(\omega)L(E), T_f(E)] \cong 0.91$$

$$C[\alpha(\omega)L(E'), T_f(E')] \cong 0.99$$

$$C[\alpha(\omega)L(E'), T_f = 0.5] \cong 0.63$$

$$T_f(E) = 0.029$$

$$T_f(E') = 0.092$$

Using the above parameters, the result is

$$\frac{R'_s(E', E, \omega)}{R'(E', E, \omega)} \cong 0.51$$

where R'_s denotes the electrons that have been reflected from the surface. Thus, we see that for typical values, Eq. (3.91) provides about a 50 percent correction to Eq. (80) of Berglund. Most of the once-scattered electrons are photoemitted at energies considerably lower than the primary electrons, and the majority of the once-scattered electrons will tend to appear near the threshold of the EDC. In the photoemission studies of this investigation, secondary electrons are seen in the EDCs only for photon energies greater than 11 or 12 eV. Thus, the once-scattered electrons will not be included in the formal analysis of photoemission data in this report.

However, in cases where secondary electrons are observed, the energy distribution of once-scattered electrons can easily be obtained by evaluating Eq. (3.91) on a computer. The scattering probability $p_s(E', E)/P(E')$

could be obtained by the theory of electron-electron scattering presented in Section C, which involves only the density of states and conservation of energy. One would calculate

$$\frac{p_s(E', E)}{P_s(E')} = \frac{\left(\begin{array}{l} \text{total number of ways an electron can be} \\ \text{scattered from } E' \text{ to a specific energy } E \end{array} \right)}{\left(\begin{array}{l} \text{total number of ways an electron can be} \\ \text{scattered from } E' \text{ to any energy } E \end{array} \right)} \quad (3.92)$$

The total number of once-scattered electrons at energy E is proportional to $[2p_s(E', E)/P_s(E')]$ where the factor (2) is due to excited valence electrons. The EDC, including primary and once-scattered electrons, is given by

$$[n(E, \omega)]_{\substack{\text{primary and} \\ \text{once scattered}}} = \int_E^{E_f + \hbar\omega} R'_{\text{tot}}(E', E, \omega) dE' + [n(E, \omega)]_{\text{primary}} \quad (3.93)$$

where (E, ω) is given by Eq. (3.83), and $R'_{\text{tot}}(E', E, \omega)$ is given by Eq. (3.91).

F. METHODS FOR OBTAINING THE DENSITY OF STATES AND OTHER PARAMETERS FROM PHOTOEMISSION AND OPTICAL DATA

In this section, we describe several methods of obtaining the density of states and other parameters from experimental photoemission data. In all cases, the analysis is based upon nondirect transitions, and can be applied to any metal, semiconductor, or insulator that satisfies the conditions of the specific method. In no case is any restriction put upon the nature of the valence band. In all cases phonon scattering effects on the excited electrons are neglected.

Case I.

$$[\alpha(\omega)L(E) \gg 1; \text{ ISOTROPIC CONDUCTION BAND}]$$

In this case, one half of the electrons excited to energy E above the vacuum level will have velocities in the direction of the surface, and all of these will eventually strike the surface. In this case, the nature of $T(E)$ and $N_c(E)$ are unspecified, except that the velocity distribution of electrons excited to energy E is spherical. (A more

complicated analysis would be necessary for the case in which the photo-emission data depend strongly upon the crystal orientation.) Instead of Eq. (3.83), the EDC curve is

$$\eta(E, \omega) = T(E) \frac{N_c(E)N_v(E - \hbar\omega)}{\int_{E_f}^{E_f + \hbar\omega} N_c(E)N_v(E - \hbar\omega) dE} \quad (3.94)$$

where $T(E)$, $N_c(E)$, and $N_v(E)$ are to be determined from the experimental $\eta(E, \omega)$. Using Eq. (3.50), we can rewrite Eq. (3.94) as

$$\eta(E, \omega) = \frac{(K) T(E) |M(\omega)|^2 N_c(E)N_v(E - \hbar\omega)}{(\omega)^2 \epsilon_{2b}(\omega)} \quad (3.95)$$

where (K) is a constant described by Eq. (3.50). To proceed further, we assume that $|M(\omega)|^2$ is a constant in the region of interest, and that $\epsilon_{2b}(\omega)$ has been obtained from experimental reflectivity measurements. Let us now fix the variable E , and measure the EDCs at many different photon energies. Next, we take the ratio for two different photon energies $(\hbar\omega_1)$ and $(\hbar\omega_2)$ as

$$\frac{\eta(E, \omega_1)}{\eta(E, \omega_2)} = \frac{N_v(E - \hbar\omega_1)}{N_v(E - \hbar\omega_2)} \cdot \frac{\epsilon_{2b}(\omega_2)}{\epsilon_{2b}(\omega_1)} \cdot \frac{(\omega_2)^2}{(\omega_1)^2} \quad (3.96)$$

which is obtained from Eq. (3.95). Solving Eq. (3.96) for the ratio of valence band density of states,

$$\frac{N_v(E - \hbar\omega_2)}{N_v(E - \hbar\omega_1)} = \frac{\epsilon_{2b}(\omega_2)}{\epsilon_{2b}(\omega_1)} \cdot \frac{(\omega_2)^2}{(\omega_1)^2} \cdot \frac{\eta(E, \omega_2)}{\eta(E, \omega_1)} \quad (3.97)$$

All the quantities on the right hand side of Eq. (3.97) are experimentally obtained, so we can determine the ratio of two different points in the valence band. If we use $N_v(E - \hbar\omega_1)$ as a "base," and let (ω_2) be any other photon energy, then Eq. (3.97) can be used to plot out the

shape of the valence band density of states N_v . The same shape must result for any value of E , if the theory behind the method is correct. The closer to the threshold we choose E , the deeper into the valence band we can calculate N_v .

Having determined the shape of the valence band density of states, the conduction band density of states can be calculated by the use of Eq. (3.50), which states that

$$\epsilon_{2b}(\omega) = \frac{K|M|^2}{\omega^2} \int_{E_f}^{E_f + \hbar\omega} N_c(E)N_v(E - \hbar\omega) dE \quad (3.98)$$

Knowing $\epsilon_{2b}(\omega)$ and $N_v(E)$, we can "unfold" Eq. (3.98) and determine the shape of $N_c(E)$. For the sake of example, let us consider a semiconductor with band gap E_g and energy zero at the top of the valence band. At the edges of the gap, we set $N_c(E_g) = N_v(0) = 0$. We solve Eq. (3.98) by dividing the energy scale E into small increments ΔE , and solving in a cumulative manner, starting with $\omega = \hbar(E_g + 2\Delta E)$, and increasing ω in steps of $\hbar\Delta E$, in the following manner: (We let $(K|M|^2)/(\hbar^2) = K = \text{constant}$)

$$K(E_g + 2\Delta E)^2 \epsilon_{2b}[\hbar(E_g + 2\Delta E)] = N_c(E_g + \Delta E)N_v(-\Delta E) \quad (3.99a)$$

$$K(E_g + 3\Delta E)^2 \epsilon_{2b}[\hbar(E_g + 3\Delta E)] = N_c(E_g + 2\Delta E)N_v(-\Delta E) + N_c(E_g + \Delta E)N_v(-2\Delta E) \quad (3.99b)$$

$$K(E_g + 4\Delta E)^2 \epsilon_{2b}[\hbar(E_g + 4\Delta E)] = N_c(E_g + 3\Delta E)N_v(-\Delta E) + N_c(E_g + 2\Delta E)N_v(-2\Delta E) + N_c(E_g + \Delta E)N_v(-3\Delta E) \quad (3.99c)$$

$$K(E_g + N\Delta E)^2 \epsilon_{2b}[\hbar(E_g + N\Delta E)] = \sum_{m=1}^N N_c(E_g + m\Delta E)N_v[(m-N)\Delta E] \quad (3.99N)$$

We first solve for $N_c(E_g + \Delta E)$ using Eq. (3.99a), next solve for $N_c(E_g + 2\Delta E)$ using Eq. (3.99b), and continue until we have covered the range of interest. Equation (3.99) can be easily solved by computer for arbitrarily small values of (ΔE) . Note that Eq. (3.99) is in the form of a matrix equation with all the elements above one diagonal set equal

to zero. Thus, Eq. (3.99) could be solved in a straightforward manner by use of a "library computer program" for a matrix equation. [However, a "cumulative" solution in which the computer first solves Eq. (3.99a), then uses the result to solve Eq. (3.99b), etc., would probably be much less time-consuming.] Since the solution is of a cumulative nature, it is possible that small errors in $\epsilon_{2b}(\omega)$ near the band gap could cause large errors in the final $N_c(E)$.

Having now obtained $N_c(E)$ and $N_v(E)$, we can obtain $T(E)$ from Eq. (3.94), and the analysis is complete, if the deduced values of $N_c(E)$, $N_v(E)$, and $T(E)$ are consistent with Eq. (3.94) for all the different EDCs.

An example of how the method explained above can be used to deduce the density of states and the threshold function from the experimental EDCs and $\epsilon_2(\omega)$ is shown in Fig. 36. The EDCs must be normalized, and in units of (electrons photoemitted/absorbed photon/eV). In the range $5 \text{ eV} < \hbar\omega < 12 \text{ eV}$, the experimental EDCs are described by $\eta(E) = (.08)(E-5)$, $E \leq \hbar\omega$, as shown in Fig. 35c for several values of $\hbar\omega$. The experimental $\epsilon_2(\omega)$ is given in Fig. 35e. The procedure of analysis is as follows:

- (1) Assume $|M(\omega)|^2 = \text{CONSTANT} = 1$.
- (2) From the EDCs of Fig. 35c and $\omega^2 \epsilon_2(\omega)$ from Fig. 35e the use of Eq. (3.97) yields the valence band density of states $N_v(E)$ as shown in Fig. 35a; note that in this case, the shape of $N_v(E)$ is very different from the shape of the EDCs.
- (3) Next, the conduction band density of states $N_c(E)$ is obtained by unfolding Eq. (3.98) by the technique of Eq. (3.99), using the experimental $\epsilon_2(\omega)$ and the valence band density of states $N_v(E)$.
- (4) $T(E)$ is obtained from Eq. (3.94) or from Eq. (3.95), testing all of the experimental EDCs for consistency, and making sure that agreement is achieved for both shape and magnitude of the EDCs. If such a $T(E)$ exists, then a consistent solution for $N_c(E)$, $N_v(E)$, and $T(E)$ has been obtained. Since the magnitude of

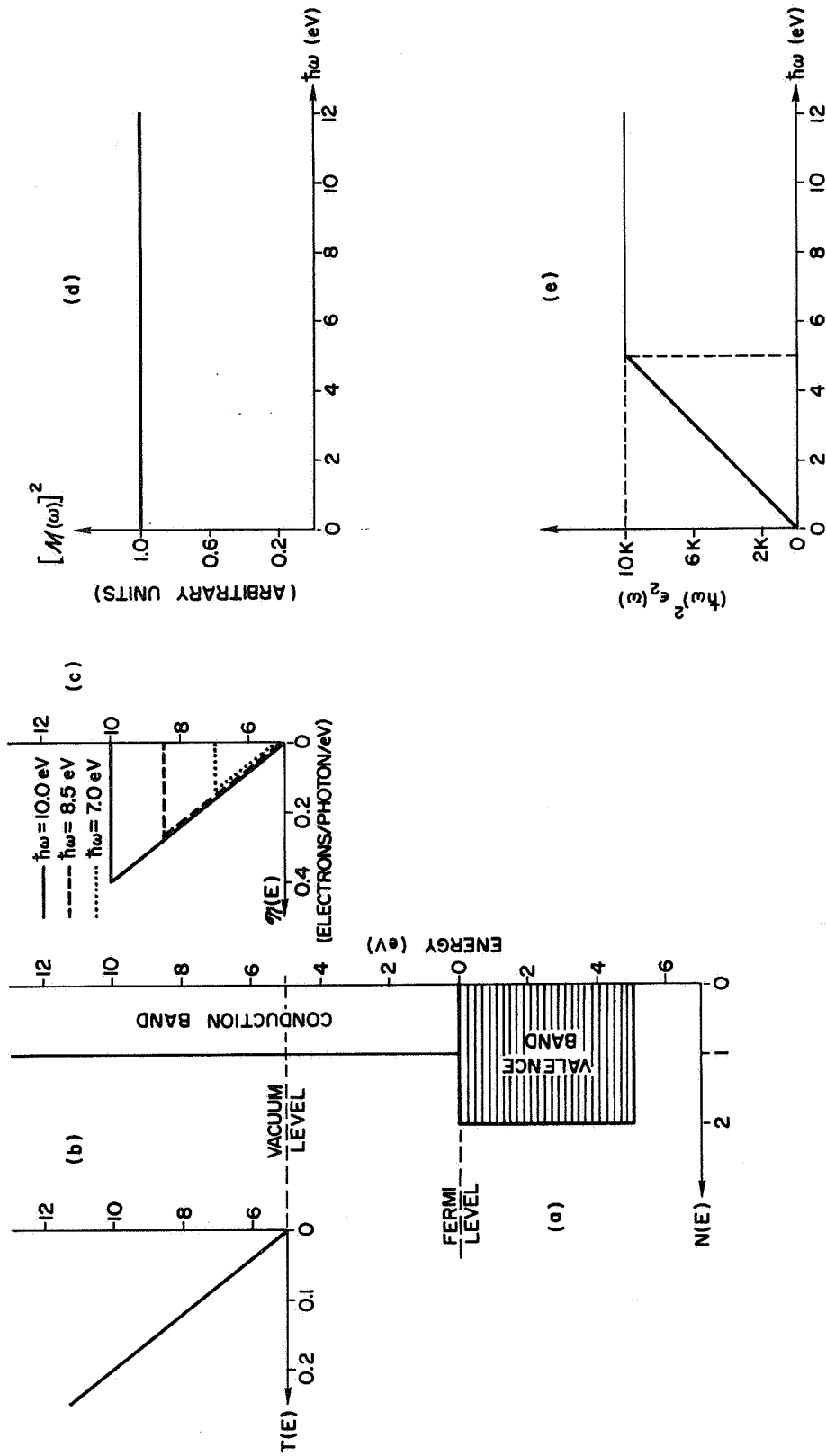


FIG. 36. EXAMPLE SHOWING HOW DENSITY OF STATES CAN BE DEDUCED FROM EDCs FOR CASE OF $\omega L \gg 1$.
 (a) Density of states; (b) threshold function; (c) experimental EDCs; (d) $|M(\omega)|^2$; (e) experimental $\epsilon_2(\omega)$. If $|M(\omega)|^2$ is constant, $N_C(E)$, $N_V(E)$, and $T(E)$ are unique.

$|M(\omega)|^2$ is arbitrary, we can only determine the shape of $N_c(E)$. In the special case of a metal, we can match $N_c(E)$ to $N_v(E)$ at the fermi level, and thus obtain the magnitude of $N_c(E)$ as well as the shape. The magnitude of $N_v(E)$ can be obtained by normalizing $N_v(E)$ to contain the total number of valence electrons.

In the case in which $|M(\omega)|^2$ is a constant, the experimental value of $\epsilon_2(\omega)$ puts a constraint upon $N_c(E)$ and $N_v(E)$, with the result that if a set $[N_c(E), N_v(E), T(E)]$ is found that is consistent with Eq. (3.94) and Eq. (3.50), then such a solution is unique. A proof of this statement is presented in some detail in Appendix A.

Although the method outlined above involves the use of $\epsilon_2(\omega)$ to obtain $N_c(E)$ and $N_v(E)$, the photoemission process depends only upon $N_c(E)$ and $N_v(E)$, as seen from Eq. (3.94). Agreement with $\epsilon_2(\omega)$ is not required to find a set $[N_c(E), N_v(E), T(E)]$ that satisfies Eq. (3.94). Thus, instead of using a systematic technique, we could have first approached the problem by guessing both $N_c(E)$ and $N_v(E)$, and then taking the ratio

$$\frac{\eta(E, \omega_1)}{\eta(E, \omega_2)} = \frac{N_v(E - \hbar\omega_1)}{N_v(E - \hbar\omega_2)} \cdot \frac{\int_{E_f}^{E_f + \hbar\omega_2} N_c(E) N_v(E - \hbar\omega_2) dE}{\int_{E_f}^{E_f + \hbar\omega_1} N_c(E) N_v(E - \hbar\omega_1) dE} \quad (3.100)$$

A trial and error procedure might eventually yield an $N_c(E)$ and an $N_v(E)$ that satisfies Eq. (3.100), and then $T(E)$ could be calculated from Eq. (3.94). However, this set $[N_c(E), N_v(E), T(E)]$ would not be unique, unless agreement was obtained with the experimental $\epsilon_2(\omega)$, using $|M(\omega)|^2 = \text{constant}$ in Eq. (3.50).

It may occur that the assumption $|M(\omega)|^2 = \text{constant}$ does not lead to consistent results with the photoemission equation (3.94). The problem may be that $|M(\omega)|^2$ is not a constant, but is a function of frequency. In this case, we must use a trial and error method to see if we can find a set $[N_c(E), N_v(E), T(E)]$ that is consistent with

Eq. (3.100) and Eq. (3.94). If we are indeed successful, then we can calculate the frequency dependence of $|M(\omega)|^2$ from Eq. (3.50) using the experimental value of $\epsilon_2(\omega)$. Thus if $|M(\omega)|^2$ is not a constant, then a knowledge of $\epsilon_2(\omega)$ is of no assistance in the analysis of photoemission data. In fact, an $|M(\omega)|^2$ can be chosen to make Eq. (3.50) agree with an arbitrary $\epsilon_2(\omega)$, as shown in Fig. 37. Unfortunately, if $|M(\omega)|^2$

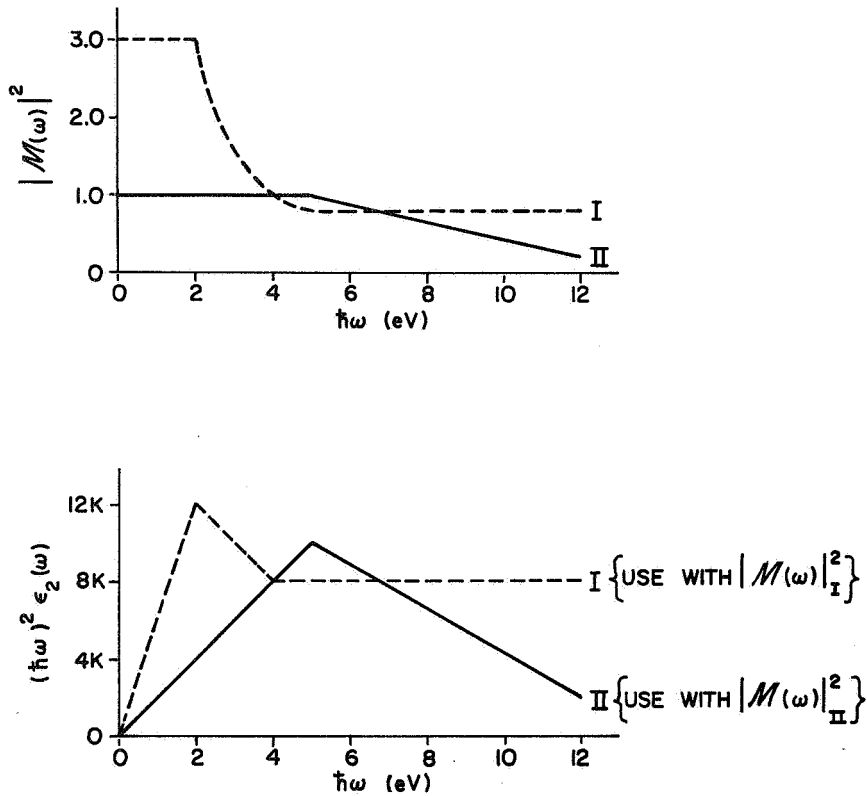


FIG. 37. SIMPLE EXAMPLE SHOWING TWO ARBITRARY CHOICES OF $\epsilon_2(\omega)$ THAT CAN BE MADE CONSISTENT WITH THE PHOTOEMISSION EDCs OF FIG. 36 BY A PROPER CHOICE OF $|M(\omega)|^2$.

is not a constant, then the experimental $\epsilon_2(\omega)$ does not sufficiently constrain $N_c(E)$ and $N_v(E)$, and the set $[N_c(E), N_v(E), T(E), |M(\omega)|^2]$ is not a unique solution. This conclusion is proved in Appendix A, where it is found that if $[N_c(E), N_v(E), T(E), |M(\omega)|^2]$ is one solution, then an infinite set of solutions can be generated by the formulas

$$N_v^\beta(E) = g(0) e^{-\beta(E)} N_v(E) \quad (3.101a)$$

$$N_c^\beta(E) = \frac{K}{g(0)} e^{-\beta(E)} N_c(E) \quad (3.101b)$$

$$T^\beta(E) = T(E) \quad (3.101c)$$

$$|M^\beta(\omega)|^2 = \frac{1}{K} e^{-\beta\hbar\omega} |M(\omega)|^2 \quad (3.101d)$$

where β is a real number (positive or negative). The reader can satisfy himself that the above relations are true by substituting into Eq. (3.94) and Eq. (3.50) or by using the specific example of Figs. 36 and 37 where $|M(\omega)|^2$ is not a constant.

However, it must be emphasized that a great deal of information can still be obtained from the model of nondirect transitions even in the cases where the matrix elements are not constant. The location of the peaks in the valence band and conduction band density of states can still be determined, the only uncertainty being in the relative strength of these peaks. In many practical cases, the nature of the individual problem may very well put a limit on the uncertainty in the relative peak heights, so that even though the density of states is not unique, the uncertainty in the density of states falls within certain well defined limits. The analysis of the cuprous halides (Chapter VIII) is a good example of such a situation.

A severe problem can arise in the systematic method discussed above if $\epsilon_2(\omega)$ is composed of both band-to-band transitions and other types of transitions (such as excitons or "free electron" transitions). In this case, $\epsilon_{2b}(\omega)$ may be difficult to separate from the total $\epsilon_2(\omega)$ at low energies near the band-to-band threshold. If $\epsilon_{2b}(\omega)$ cannot be obtained accurately enough to "unfold" Eq. (3.98), then we cannot calculate $N_c(E)$. Consequently, we have no check on $|M(\omega)|^2$, and the assumption that $|M(\omega)|^2 = \text{constant}$ cannot be verified, at least in the threshold region for band-to-band transitions. A possible approach would be to guess an $N_c(E)$ in this difficult region, and then use this $N_c(E)$ in the unfold process of Eq. (3.99) to obtain an estimate of $N_c(E)$ for energies above this difficult region.

If no values of $N_c(E)$ and $N_v(E)$ can be found that are consistent with Eq. (3.94), and if we are confident that either (1) the model of nondirect transitions as formulated in Section D does not apply, or (2) the one electron approximation is not appropriate for analyzing photoemission data in the case at hand. However, if the peaks in the EDCs move in increments of energy equal to the increments in photon energy, the optical transitions are of the nondirect type, and we can still locate the positions (but not the relative heights) of peaks in the valence band density of states. Similarly, we can still locate the positions of peaks in the conduction band density of states.

Case II.

[$\alpha(\omega)L(E) \ll 1$; ISOTROPIC CONDUCTION BAND,
SMALL "VELOCITY CONE"]

In this case, the electron group velocity $v_g(E)$ is unspecified, except that the velocity distribution is spherical in real space at every energy E above the vacuum level. If only those electrons that are going in a direction normal to the surface escape, then the EDCs are given by

$$\eta(E, \omega) \cong \frac{\alpha(\omega)L(E)}{\alpha(\omega)L(E) + 1} T(E) \frac{N_c(E)N_v(E - \hbar\omega)}{\int_{E_f}^{E_f + \hbar\omega} N_c(E)N_v(E - \hbar\omega) dE} \quad (3.102)$$

where $T(E)$ is to be determined. Equation (3.102) is found in the same manner as Eq. (3.83), except that no restriction is put upon the nature of $N_c(E)$ and $T(E)$. If we assume $\alpha(\omega)L(E) \ll 1$, then Eq. (3.102) becomes

$$\eta(E, \omega) = \alpha(\omega) [L(E)T(E)] \frac{N_c(E)N_v(E - \hbar\omega)}{\int_{E_f}^{E_f + \hbar\omega} N_c(E)N_v(E - \hbar\omega) dE} \quad (3.103)$$

Using Eq. (3.50), Eq. (3.103) becomes

$$\eta(\mathbf{E}, \omega) = \frac{\alpha(\omega) |M(\omega)|^2 [L(\mathbf{E})T(\mathbf{E})] N_c(\mathbf{E})N_v(\mathbf{E} - \hbar\omega)}{\omega^2 \epsilon_2(\omega)} \quad (3.104)$$

Since the absorption coefficient $\alpha(\omega)$ can be obtained from experiment, we can proceed just as in the method of Case I for the condition $|M(\omega)|^2 = \text{constant}$, since $L(\mathbf{E})$ will cancel out in Eq. (3.96). The only difference from the method of Case I is that we can calculate only the product $[L(\mathbf{E})T(\mathbf{E})]$, and cannot calculate $T(\mathbf{E})$ unless we have additional information for the energy dependence of $L(\mathbf{E})$.

If an independent measurement of $L(\mathbf{E})$ is available, then we can calculate the threshold function $T(\mathbf{E})$, and all the quantities of interest will have been determined.

Just as in Case I, if a consistent solution can be found for the shapes of $N_c(\mathbf{E})$, $N_v(\mathbf{E})$, and $T(\mathbf{E})$, then the solution is unique, as shown in Appendix A.

Case III.

FREE ELECTRON CONDUCTION BAND, SEMICLASSICAL THRESHOLD FUNCTION

We now consider the case in which the following restrictions apply: (1) the conduction band density of states consists of occasional peaks superimposed upon a free-electron conduction band with an $(\mathbf{E})^{1/2}$ energy dependence; (2) the threshold function is the semiclassical escape function $T_f(\mathbf{E})$ given by Eq. (3.11). From the nature of these restrictions, this case is probably most applicable to metals with a free electron-like conduction band, and will be applied to the analysis of Cu, Au, and Ag later in this study. By specifying the functional form of $N_c(\mathbf{E})$ and $T(\mathbf{E})$ from theories that are simple but that retain the basic physical character of the problem, we have essentially specified two independent variables in the equation describing the photoemission process.

The energy distributions for a material with a free electron conduction band and a semiclassical threshold function have already been derived, and are given by Eq. (3.83). Although the nature of $N_c(\mathbf{E})$

and $T_f(E)$ have been specified, the position of the bottom of this "average free electron band" will be considered as an arbitrary parameter in the analysis. In practice, we shall find that the position of the bottom of this "free electron band" is not completely arbitrary, but must be placed above flat bands that represent tightly bound electrons. In the sense used in this investigation, this "free electron band" is not to be associated with any individual band in the actual energy band diagram, but should be located so that it can represent in an "averaging" or "smoothing" manner the nature of bands that tend to be free-electron-like. Thus, for example, in the cases of copper, silver, and gold, we shall find it reasonable to place the bottom of this free electron band a few eV above the flat d-bands (see Chapters IV, V, and VI).

For cases of practical interest, we shall find later that the quantity $\alpha(\omega)L(E)$ is typically of the order of unity for $E \cong 4$ eV, but may vary by nearly two orders of magnitude in the region between 1 and 12 eV above the fermi level due to the rapid variation in $L(E)$. Thus, it is of primary importance that no approximation be made in the quantity $(\alpha L/\alpha L+1)$ that appears in Eq. (3.83). Since the electron-electron scattering length plays such an important part in the analysis, it would be best to use good experimental values for $L(E)$. However, the measurement of $L(E)$ is a difficult task in the region 1 to 12 eV above the fermi level, and no reliable experimental curves of $L(E)$ are presently available in this energy region for most metals. Thus, we shall calculate the shape of $L(E)$ from the density of states using Eq. (3.18), and adjust the magnitude of $L(E)$ by arbitrarily adjusting the constant L_0 . In actual practice, it may be found convenient to adjust L_0 to fit the experimental quantum yield at one photon energy. In the event a good experimental value for $L(E)$ becomes available at even one energy, $L(E)$ as calculated from Eq. (3.18) can be normalized to agree with this single point, and a degree of arbitrariness can be removed.

The method of analysis is an iterative approach that involves the use of a maximum of three arbitrary parameters. The approach that applies if $|M(\omega)|^2$ is a constant is outlined in Table 1.

The lower the work function of the material, the better the conduction band structure can be specified from the EDCs, and the smaller the

TABLE 1. ANALYSIS OF PHOTOEMISSION DATA FOR CASE III.

Step	Procedure	Consequences and Comments
1	Locate peak positions from EDCs. Peaks that "move with $h\nu$ " correspond to peaks in the valence band at energy $(E-h\nu)$. Peaks that stay fixed correspond to peaks in the conduction band if not due to electron-scattering.	Peak positions fixed to within roughly ± 0.1 eV by experimental EDCs.
2	Adjust relative peak heights; sketch the valence band density of states. A good first guess might be to duplicate the EDCs in the region 3 to 8 eV above the vacuum level, as EDCs in this region often tend to be replicas of $N_v(E)$.	Arbitrary parameter No. 1 introduced.
3	Choose position for bottom of free electron band. This specifies $N_c(E)$ and $T_f(E)$. Choose this point above any core-like states in the valence band. Good energy band calculations can be useful as a qualitative guide.	Arbitrary parameter No. 2 introduced.
4	Superimpose conduction band peaks on free electron envelope. Make a smooth curve.	
5	Pick an arbitrary value for L_o in Eq. (3.18). This value is usually chosen to obtain proper agreement with the photoelectric yield $Y(h\nu)$ at one photon energy. If a good experimental value of $L(E)$ is available at some point, adjust L_o to make $L(E)$ agree with the experimental value.	Arbitrary parameter No. 3 introduced (this parameter is not arbitrary if an experimental point is used).
6	<p>Calculate the following quantities, using the computer program of Appendix B:</p> <p>A. Shape and magnitude of $L(E)$. [Use Eq. (3.18) and free electron group velocity.]</p> <p>B. Shape and magnitude of EDCs (Eq. 3.83).</p> <p>C. Shape and magnitude of $Y(h\nu)$ (Eq. 3.86).</p> <p>D. Shape of $\epsilon_{2b}(\omega)$. (Eq. 3.98), assuming $M ^2 = 1$.</p>	<p>B. This calculation for nonscattered electrons only. Use Eq. (3.93) to include first scattered electrons.</p>
7	<p>Compare calculated quantities of Step 6 with experiment. Separate "free electron" and "exciton" effects from experimental $\epsilon_2(\omega)$ before comparison with calculated $\epsilon_{2b}(\omega)$. If only fair agreement is obtained, go back to Step 2 and repeat iteration. If good agreement has been obtained for EDCs, yield $L(E)$, and $\epsilon_2(\omega)$, then calculation is finished.</p> <p>If no consistent solution is possible, then either (1) the free electron conduction band is not appropriate, or (2) the theory of nondirect transitions does not apply, or (3) the one-electron model for optical absorption does not apply.</p>	<p>Analysis must be <u>self-consistent</u> to be valid.</p> <p>If $\alpha(\omega)L(E) \gg 1$, then the analysis of EDCs and yield is insensitive to $L(E)$, and an accurate calculation of $L(E)$ is impossible by this method.</p> <p>If the final $N_c(E)$ and $N_v(E)$ are in agreement with the results of theoretical energy band calculations, this method of analysis and the theory of nondirect transitions are justified.</p>

uncertainty in the analysis outlined in Table 1. If the work function ϕ of a metal is high, and if there is structure in the conduction band a volt or two above the fermi level, it is unlikely that the method of Table 1 will require a priori inclusion of this structure to obtain a consistent solution, unless the structure is indeed large, because the integrals used to calculate the EDCs, yield, and electron-electron scattering length are rather insensitive to small structure in the conduction band. Thus, it is highly recommended that in cases of high work function ϕ , the work function be lowered by the careful application of a monolayer of a material such as Cs or Ba. If the Cs or Ba does not react with the material, then photoelectric energy distributions can reveal structure down to 1.5 eV above the fermi level (in the case of Cs on a metal). In a later chapter, the method of Table 1 will be applied to the analysis of photoemission data from Cu. In this case, we shall see that Berglund's photoemission data [Ref. 7] for Cu with a monolayer of Cs provides important information about conduction band structure near the fermi level.

In all cases, the method of Table 1 should be checked for uniqueness by changing important parameters, and seeing if a good fit can be made by more than one combination of parameters. Appendix A shows that if an exact solution is found, it is unique, if the conditions $\alpha L \gg 1$ and/or $\alpha L \ll 1$ prevail. However, in practice, it is unlikely that the adjustment of two or three parameters in a very simple model would result in an exact fit to experimental data, although in some cases, such as Cu, the success of the method of Table 1 is remarkable. If it is possible to get an equivalent "fairly good fit" with several quite different combinations of parameters, then the answers obtained by this method are of little consequence.

The amount of arbitrary adjustment afforded by the method of Table 1 is very little, as the assumptions of a free electron conduction band and a semiclassical threshold function almost completely specify the photoemission process. Any successes of this simple model and the method of Table 1 are no guarantee that the results are correct. It is possible that there exists a much more sophisticated theory and method of analysis that would also account for the photoemission data with a different density of states. However, it is likely that such a theory would have

many more than two or three adjustable parameters, and could be used to "fit an elephant." The present model has the virtue that it contains the basic physics of the problem, requires a straightforward analysis, and has a unique solution, all of which lend to the credence of the results.

G. THE "OPTICAL DENSITY OF STATES"

Thus far in the discussion, we have assumed that $N_c(E)$ and $N_v(E)$ indeed represent the "true" density of states that would be obtained by a one-electron energy band calculation. Under the assumption of nondirect transitions, the transition probability $\sigma(\omega)$ was found to depend upon the "true" density of states, $N_c(E)$ and $N_v(E)$, as seen from Eq. (3.53). Using these results, we have developed equations describing the photoemission process in terms of $N_c(E)$ and $N_v(E)$. These equations are consistent with the equations of the one-electron theory. If the momentum matrix element $|M(\omega)|^2$ is constant, we can assume that the density of states deduced from photoemission is the "true" density of states, and use Eq. (3.98) to calculate $\epsilon_{2b}(\omega)$. If agreement was obtained with the experimental $\epsilon_{2b}(\omega)$, then it would be likely that the density of states deduced from photoemission studies is indeed the "true" density of states, since Eq. (3.98) requires the use of the "true" $N_c(E)$ and $N_v(E)$.

It is possible that the one electron approximation does not properly describe the optical absorption process in all materials. Thus, the formalism used to obtain the expression describing the photoemission process would be inappropriate. However, it is possible that the equations describing the photoemission process [e.g. Eq. (3.94), Eq. (3.102), and Eq. (3.83)] still have the correct functional form for describing the experimental EDCs and the photoelectric yield. In such a case, $N_c(E)$ and $N_v(E)$ would not necessarily be the "true" density of states, but would be an effective or "optical density of states" describing the photoemission process. Since recent investigations [Ref. 35] have suggested that this is a distinct possibility, we shall henceforth refer to the density of states that is deduced from photoemission data as the "optical density of states," with the understanding that the "optical density of states" may also be the "true" density of states.

H. ANALYSIS OF PHOTOEMISSION DATA FOR FREE ELECTRON METALS

The use of Eq. (3.83) to analyze photoemission data is most easily done for the case of a free electron metal, such as Na or K. If the free electron mass is used to describe the density of states, as in Eq. (3.4), then the position E_f of the bottom of the free electron band is found from the relationship

$$N_{\text{tot}} = \int_0^{E_f} N(E) dE = \frac{2}{3} C E_f^{3/2} \quad (3.105)$$

where N_{tot} is the total number of electrons in the band, C is given by Eq. (3.4), and E_f is defined by Fig. 25b. Thus, the quantities $N_v(E)$, $N_c(E)$, and $T_f(E)$ are completely specified by the theory. (It is possible that the free electron mass is not appropriate; then the value of the effective mass would be used as an arbitrary parameter.) Equation (3.83) also requires a knowledge of $\alpha(\omega)$, the absorption coefficient. This quantity can be readily obtained from either direct measurement, or from reflectivity measurements, as discussed in Chapter II.

Thus, there remains only one unspecified quantity in Eq. (3.83)--the magnitude and energy dependence of the electron-electron scattering length $L(E)$. If reliable experimental data are available for the metal under study, then $L(E)$ is specified, and Eq. (3.83) must then predict the magnitude and shape of the EDCs and photoelectric yield for unscattered electrons, without any arbitrary parameters. If no good experimental values of $L(E)$ are available, then Eq. (3.18) can be used to calculate $L(E)$. The normalizing constant L_0 would then be taken as an arbitrary parameter. If one experimental point is available for $L(E)$, then Eq. (3.18) would be normalized to this point, leaving no arbitrary parameters.

Since there are at most one or two arbitrary parameters involved in the analysis of photoemission data from free electron metals, very good agreement must be obtained between the experimental photoemission data and those predicted by Eq. (3.83), if the theory upon which Eq. (3.83) rests is to have any validity. Thus, application of Eq. (3.83) to free electron metals is a strict test of the theory used to derive Eq. (3.83). In the event that scattered electrons will appear in the EDCs for free electron

metals with low work functions, Eq. (3.91) can be used in place of Eq. (3.83) to predict the EDCs.

Unfortunately, in the course of this investigation, time did not permit experimental photoemission data to be taken for a free electron metal, so Eq. (3.83) was not "put to the test." However, it is at this point instructive to see what Eq. (3.83) would predict for a hypothetical free-electron metal with "typical" parameters. The two examples that we shall consider are sketched in Fig. 38. The metal of Fig. 38a has a work

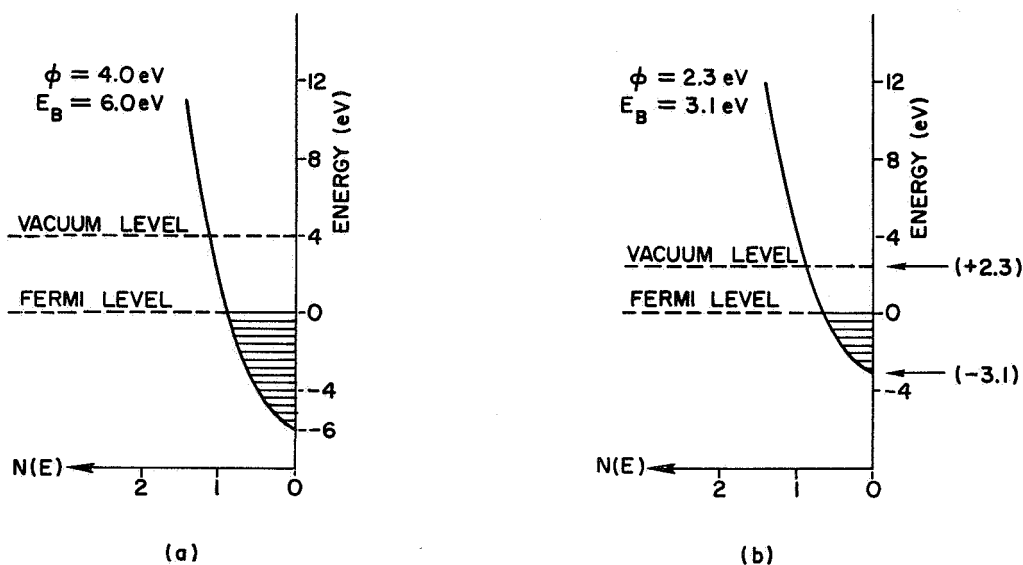


FIG. 38. DENSITY OF STATES PARAMETERS FOR TWO EXAMPLES OF FREE ELECTRON METALS. (a) A "typical" free electron metal; (b) Sodium.

function $\phi = 4.0$ eV, and a valence band depth $E_B = 6.0$ eV. These parameters are a numerical average of the parameters for different metals as given by Table 9-1 of Dekker [Ref. 18], and thus represent a "typical" free electron metal. The metal of Fig. 38b is intended to represent sodium (Na), which has parameters $\phi = 2.3$ eV, and $E_B = 3.1$ eV, according to Table 9-1 of Ref. 18.

Let us first consider the case of the "typical" metal of Fig. 38a. For the sake of example, let us choose $\alpha(\omega) = 5.0 \times 10^5 \text{ cm}^{-1}$ for all (ω) of interest, and let us normalize the electron-electron scattering length by choosing $L(8.6 \text{ eV}) = 25 \text{ \AA}$. Both of these values are typical of metals. Using these parameters in the computer program of Appendix B, we obtain

the shape and magnitude of the following quantities: the threshold function $T_f(E)$, the effective threshold function $EFFTH(E)$, the EDCs, and the photoelectric yield $Y(\omega)$. In addition, we obtain the relative shape of $\epsilon_{2b}(\omega)$, assuming that $|M(\omega)|^2$ is a constant.

The shape of $\epsilon_{2b}(\omega)$ is shown in Fig. 39, where $\epsilon_{2b}(\omega)$ is plotted in arbitrary units. This shape is compared to the $(\omega)^{-3}$ dependence expected from the Drude free electron model of Eq. (3.30). These two curves

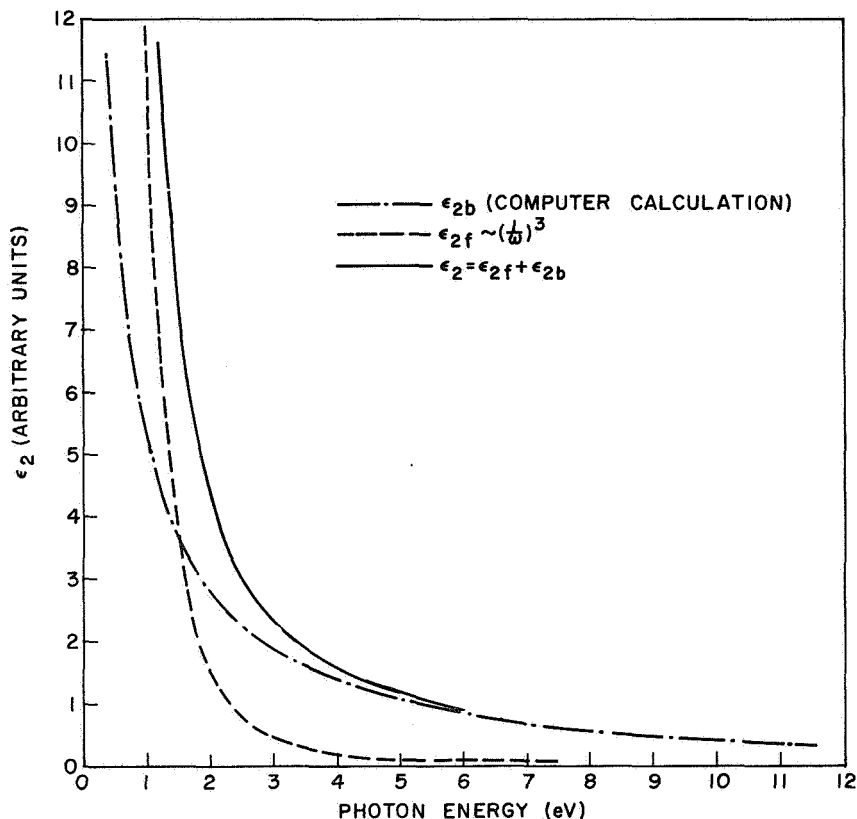


FIG. 39. CALCULATED SHAPE OF ϵ_2 FOR FREE ELECTRON METAL OF FIG. 38.a.

are arbitrarily chosen to intersect at a photon energy of 1.5 eV, which is a typical value. The total dielectric constant $\epsilon_2(\omega)$ is obtained by adding the free electron contribution $\epsilon_{2f}(\omega)$ to the density of states' contribution $\epsilon_{2b}(\omega)$, and is also sketched in Fig. 40. At lower photon energies, the free electron term dominates; at higher energies, the density of states term dominates. We note that the total $\epsilon_2(\omega)$ is a rather smooth curve, and that experiment gives only this value. To obtain an experimental $\epsilon_{2b}(\omega)$, one must fit an $(\omega)^{-3}$ curve to the

experimental $\epsilon_2(\omega)$ at low energies, and set $\epsilon_{2b}(\omega)$ equal to the difference between $\epsilon_2(\omega)$ and the fitted $(\omega)^{-3}$ curve. Such a procedure is likely to give a large error in $\epsilon_{2b}(\omega)$ at low photon energies, unless the experimental value of $\epsilon_2(\omega)$ is very accurately known. It is this experimental $\epsilon_{2b}(\omega)$ that is to be compared with the computer calculations of Appendix B in the analysis of a real material. Note that there is no pronounced structure in $\epsilon_{2b}(\omega)$. In many so-called "free electron" metals, Al, Cd, and Zn, there is considerable structure [Ref. 30] in $\epsilon_{2b}(\omega)$ in the vicinity of 1 to 2 eV. This may be due to direct transitions, deviations from a true free-electron nature, or some other factor.

At very high energies, Eq. (3.98) can be approximated by

$$\epsilon_{2b}(\omega) \cong \frac{K|M(\omega)|^2}{\omega^2} N_{\text{tot}} (\hbar\omega)^{1/2}$$

$$\epsilon_{2b}(\omega) \cong \hbar K N_{\text{tot}} \frac{|M(\omega)|^2}{\omega^{3/2}} \quad (3.106)$$

Thus, if $|M(\omega)|^2$ were a constant at large ω , then $\epsilon_{2b}(\omega)$ as given by Eq. (3.106) would cause the sum rule of Eq. (3.52) to diverge. Thus, we require that for large ω , the momentum matrix element $|M(\omega)|^2$ should decrease at least as fast as

$$|M(\omega)|^2 \sim (\omega)^{-(\frac{1}{2} + \Delta)} \quad (3.107)$$

where Δ is a positive number.

The calculated electron-electron scattering length $L(E)$ is plotted in Fig. 40. The shape of the curve is determined by the density of states of Fig. 38a, and in the region above 6 eV, is found to be closely approximated by an energy dependence of $(E)^{-3/2}$, just as predicted by the model of Fig. 29 and Eq. (3.22). We see that at 1 eV above the fermi level, the electron-electron scattering length is about 1500 Å, whereas at 11.6 eV above the fermi level, the electron-electron scattering length is only 16 Å. Note that $L(E)$ varies by a factor of about six between the vacuum level (4 eV) and 11.6 eV, the region of interest for photoemission studies. Since the mean free path for electron-phonon scattering is typically [Ref. 18]

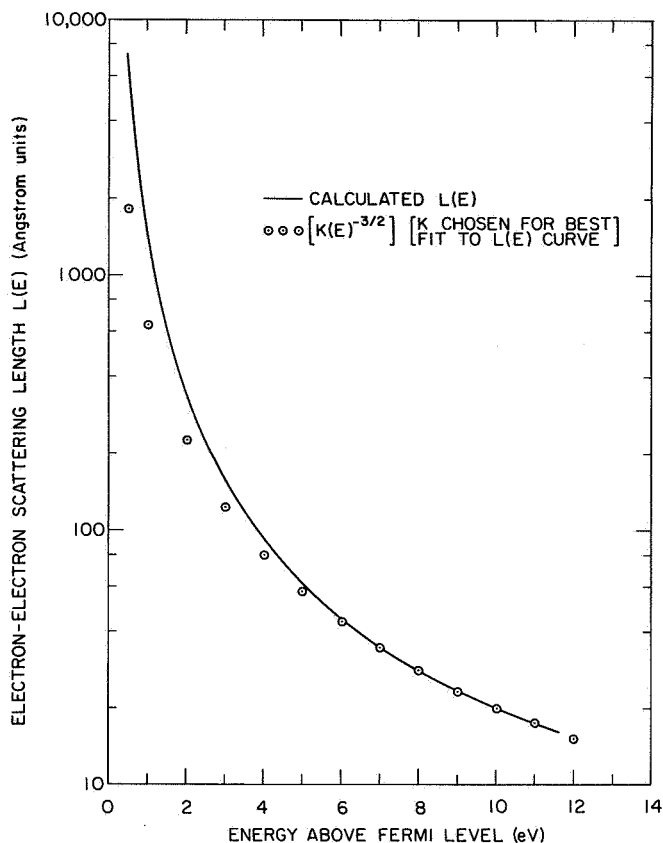


FIG. 40. CALCULATED ELECTRON-ELECTRON LENGTH $L(E)$ FOR FREE ELECTRON METAL OF FIG. 38a.

about 400 \AA , electron-phonon scattering tends to dominate over electron-electron scattering in the region between the fermi level and 1.5 eV above the fermi level. At energies higher than the 3 eV above the fermi level, the electron-electron scattering length is much shorter than the electron-phonon scattering length.

The free electron threshold function $T_f(E)$ is plotted in Fig. 41. Note that in the region of interest between 4 and 12 eV, $T_f(E)$ is well approximated by a straight line, and has a value of only 0.117 at 11 eV above the fermi level. Thus, most of the photoexcited electrons that strike the surface are reflected back into the bulk, and only a few are photoemitted. The small value of the free electron threshold function helps to explain why the photoelectric yield of many metals is so small, typically on the order of 1×10^{-2} electrons photoemitted per absorbed photon at a photon energy of 10 eV. Note that for the "typical" case at hand, the free electron function of Fig. 41 represents only the extreme left-hand portion of the curve in Fig. 27.

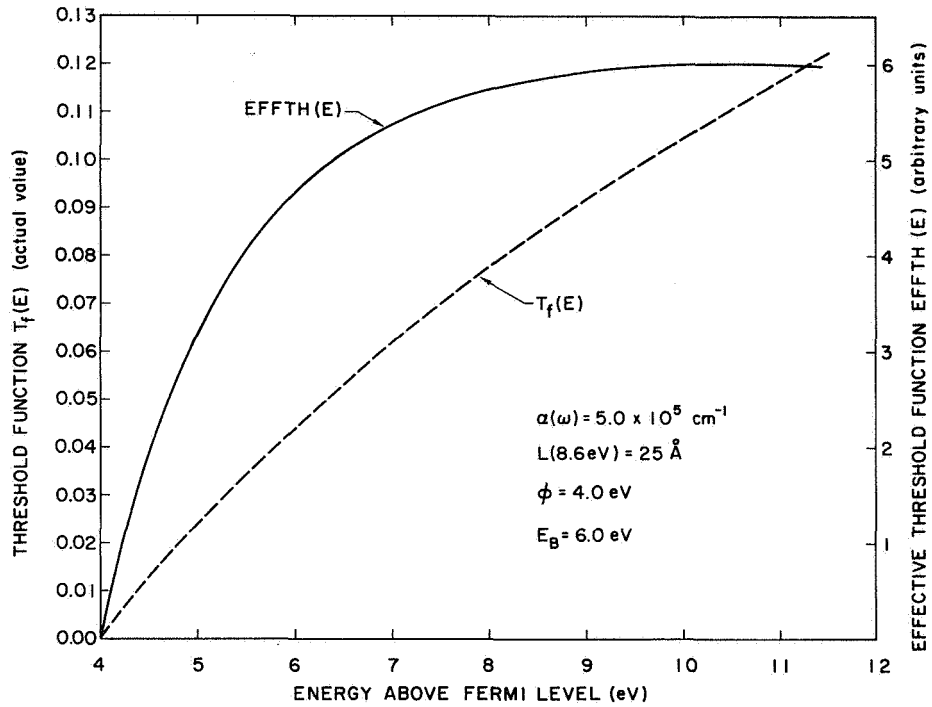


FIG. 41. THRESHOLD FUNCTION $T_f(E)$ AND EFFECTIVE THRESHOLD FUNCTION $EFFTH(E)$ FOR FREE ELECTRON METAL OF FIG. 38a.

Because of the severe modulation effects of a nearly linear threshold function in the region between 4 and 12 eV, it would seem at first glance that the EDCs would not closely resemble the valence band density of states. However, it is not the threshold function alone that determines the shape of the EDCs, but the "effective threshold function" $EFFTH(E)$, which is given by

$$EFFTH(E) = C[\alpha(\omega)L(E), T_f(E)] T_f(E) N_c(E) \frac{\alpha(\omega)L(E)}{\alpha(\omega)L(E)+1} \quad (3.108)$$

The "effective threshold function" or "shape factor" $EFFTH(E)$ is the factor that modulates the shape of $N_v(E-\hbar\omega)$ in Eq. (3.83), and is plotted in Fig. 41. We note that in the region between 4 and 5.5 eV, $EFFTH(E)$ is approximated by a straight line of steep slope, but in the region between 7 and 12 eV, $EFFTH(E)$ is nearly constant. Thus, we would expect that the portion of the EDCs in the region between 7 and 12 eV would be a faithful reproduction of the valence band density of states. That this

is indeed the case is seen from Fig. 42, which shows the calculated EDCs for a number of different photon energies. Note that the maximum peak height in the EDCs occurs at a photon energy of 8.5 eV. At higher energies,

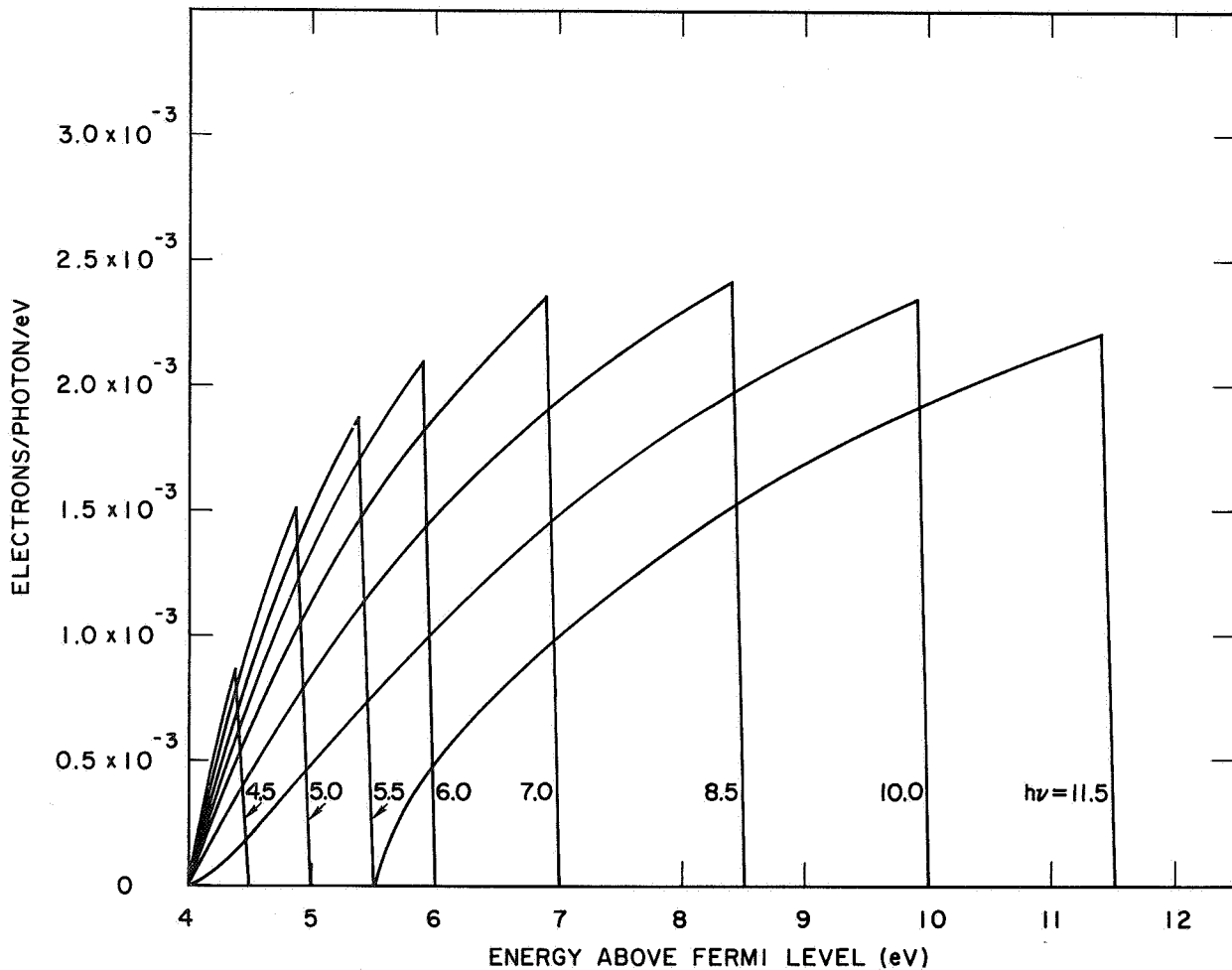


FIG. 42. CALCULATED ENERGY DISTRIBUTIONS FOR FREE ELECTRON METAL OF FIG. 38a (PRIMARY ELECTRONS ONLY).

the rapidly decreasing electron-electron scattering length prevents the peak height from increasing further. Figure 43 compares the EDC for a photon energy of 11.5 eV with the shape of the free electron density of states. The agreement is quite close, just as would be expected from the "shape factor" of Fig. 41.

The "flatness" of the shape factor at energies greater than 3 eV above the vacuum level may explain why, in some cases, successful analyses have been carried out by deducing a step-like threshold function, and finding the analysis to be consistent with such an assumption. Thus, one might expect that for many free-electron-like metals, that portion of the

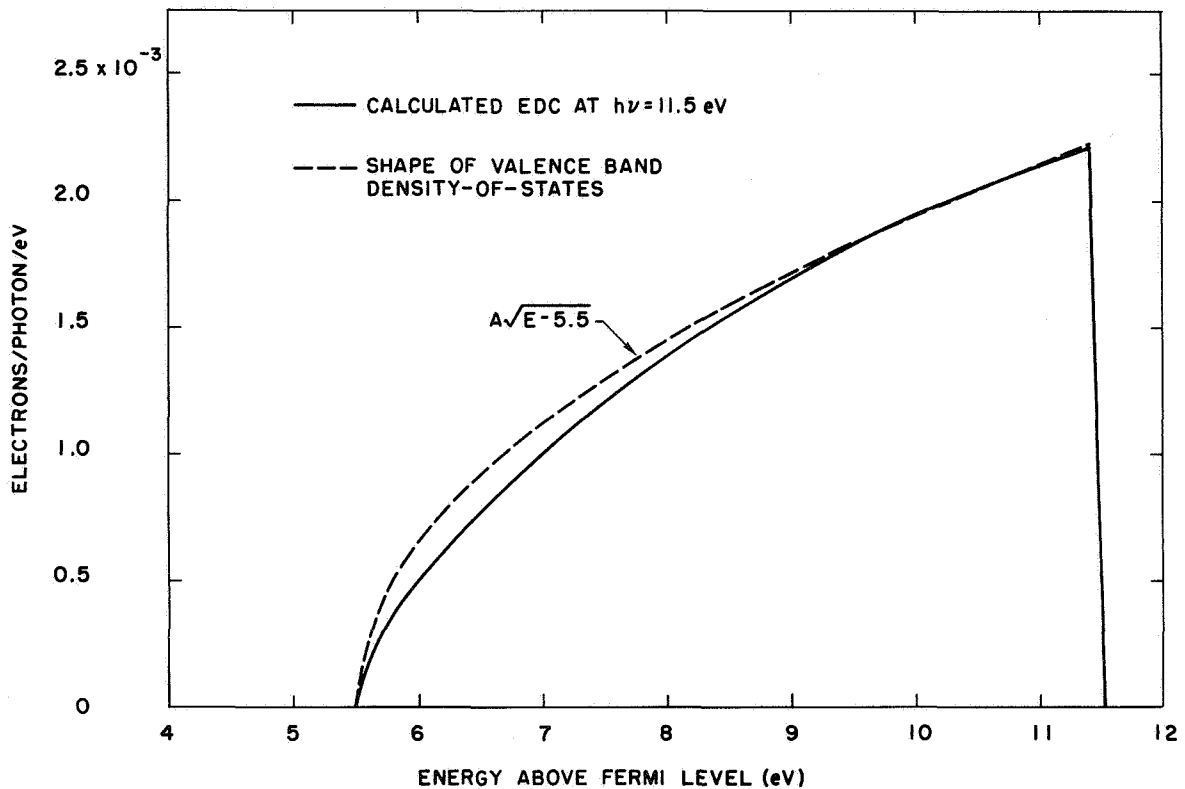


FIG. 43. COMPARISON OF ENERGY DISTRIBUTION WITH SHAPE OF VALENCE BAND DENSITY OF STATES FOR FREE ELECTRON METAL OF FIG. 38a.

experimental EDC that is more than several volts above the vacuum level would be a close replica of the valence band density of states. It is important to realize that a constant shape factor $EFFTH(E)$ determines the shape of the EDCs, but does not determine the magnitude of the EDCs. Strong transitions to points in the conduction band below the vacuum level could change the magnitude of the quantity

$$\int_{E_f}^{E_f + \hbar\omega} N_c(E)N_v(E - \hbar\omega) dE$$

in Eq. (3.83), and consequently change the magnitude of the EDCs. However, the shape of the EDCs would not be affected.

The photoelectric yield for primary electrons is shown in Fig. 44, and seems to saturate at slightly less than 10^{-2} electrons photoemitted per absorbed photon. This low quantum yield is a consequence of the 200 \AA

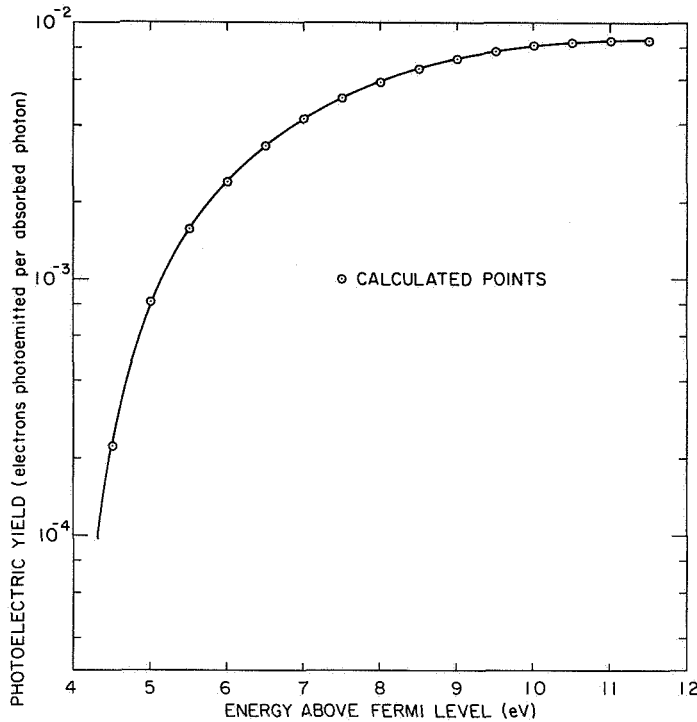


FIG. 44. PHOTOELECTRIC YIELD FOR FREE ELECTRON METAL OF FIG. 38a (PRIMARY ELECTRONS ONLY).

absorption depth $[1/\alpha(\omega)]$, the short electron-electron scattering length, and the small value of the threshold function $T_f(E)$.

As a final example, let us consider the case of sodium, which is shown in Fig. 38b. Let us assume that $\alpha(\omega) = 5.0 \times 10^5 \text{ cm}^{-1}$ for all ω , and normalize $L(E)$ by assuming that $L(8.6 \text{ eV}) = 25 \text{ \AA}$. A computer calculation using the program in Appendix B gives the results shown in Figs. 45 through 48.

The electron-electron scattering length is shown in Fig. 45, where $L(E)$ is very well approximated by an $(E)^{-3/2}$ energy dependence for $E > 3 \text{ eV}$, just as would be predicted by Eq. (3.23).

The calculated EDCs for primary electrons are shown in Fig. 46 for a number of different photon energies. A significant feature of the EDCs is that the maximum peak height occurs at a photon energy of only 5.0 eV. The peak height decreases at photon energies greater than 5.0 eV; at a photon energy of 11.5 eV, the peak height is only $2/3$ of the peak height for the curve at $h\nu = 5.0 \text{ eV}$.

Because of the low work function of only 2.3 eV, a large number of scattered electrons would be expected to appear in experimental EDCs.

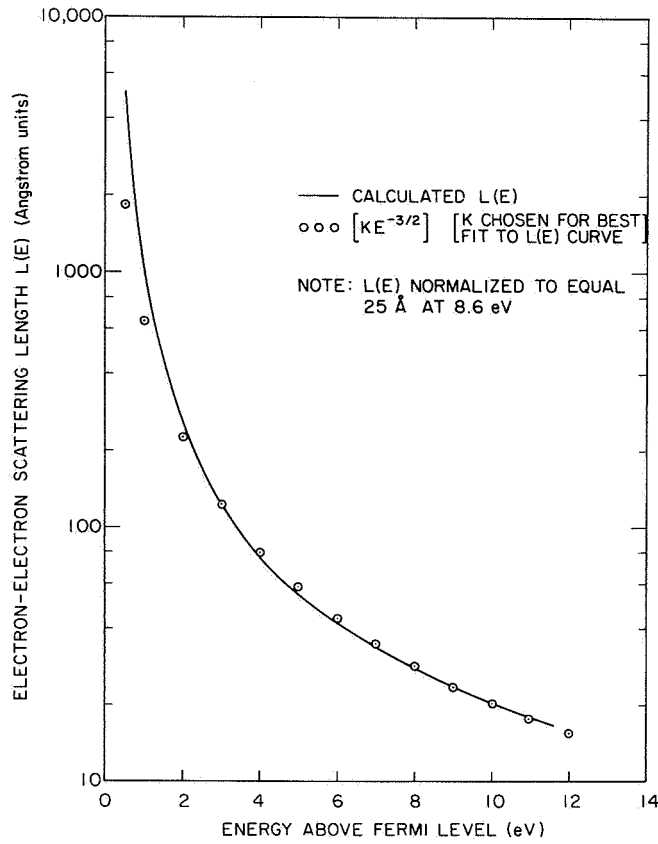


FIG. 45. CALCULATED ELECTRON-ELECTRON SCATTERING LENGTH $L(E)$ FOR THE SODIUM MODEL OF FIG. 38b.

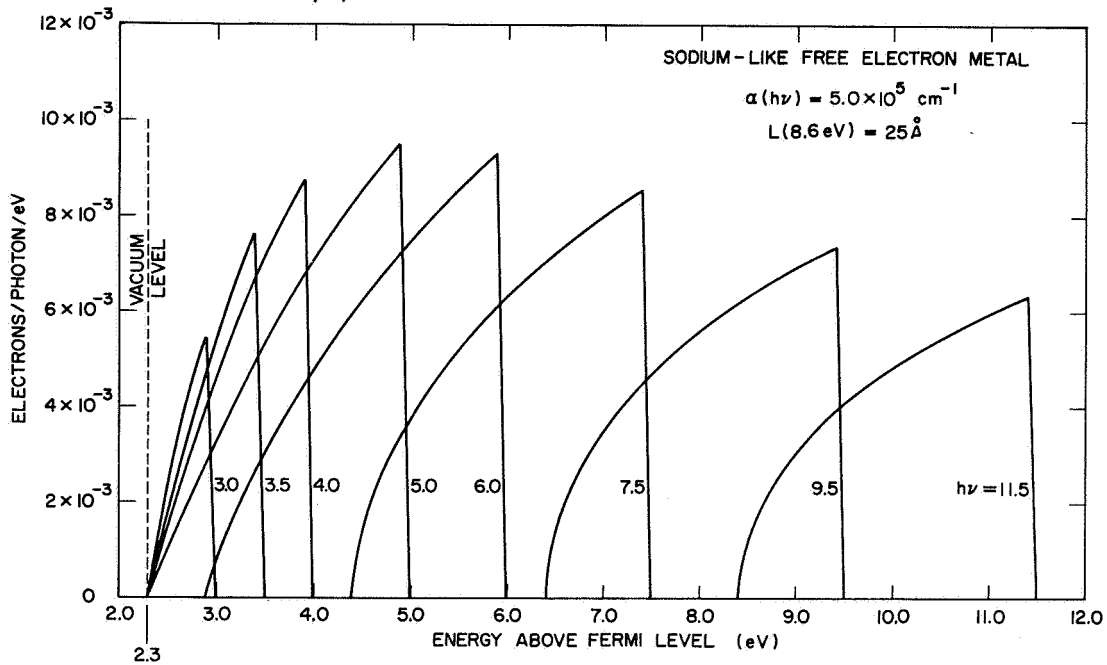


FIG. 46. CALCULATED ENERGY DISTRIBUTIONS FOR SODIUM-LIKE FREE ELECTRON METAL OF FIG. 38b (PRIMARY ELECTRONS ONLY).

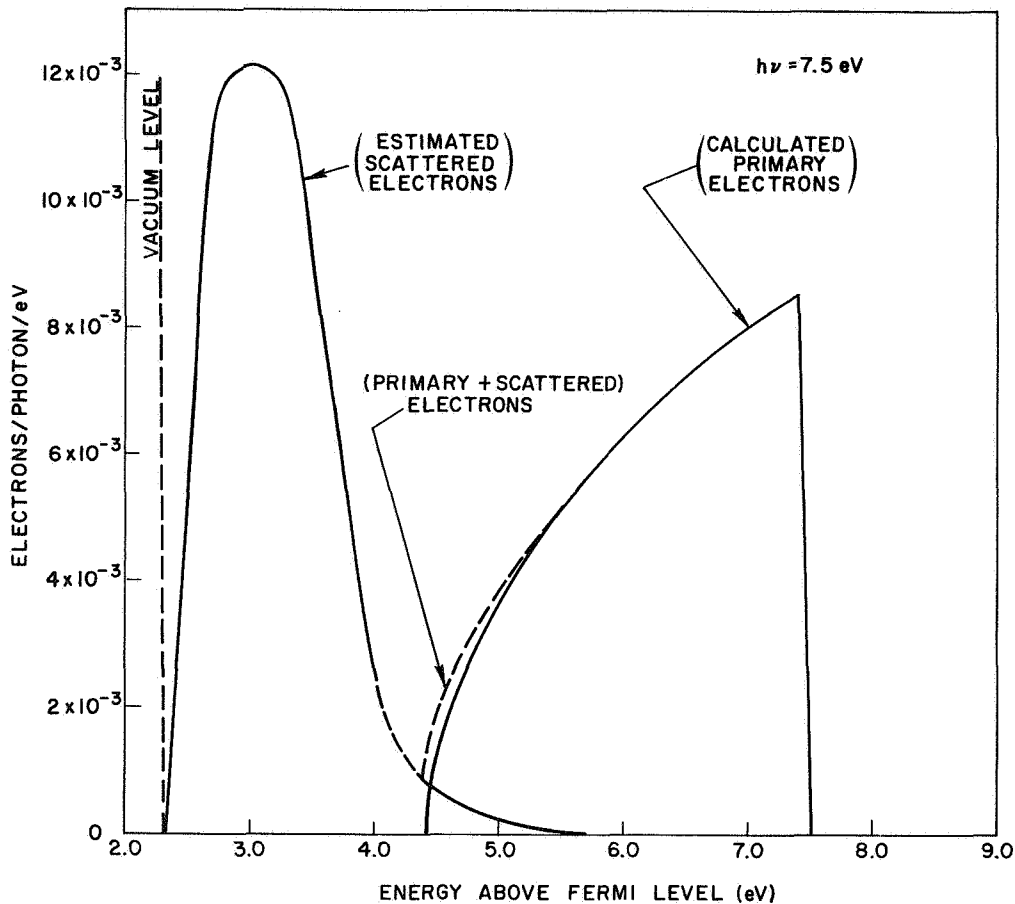


FIG. 47. ESTIMATED ENERGY DISTRIBUTION FOR SODIUM-LIKE FREE ELECTRON METAL OF FIG. 38b (INCLUDING SCATTERED ELECTRONS).

In this case, the total EDC would consist of the sum of the primary electrons and the scattered electrons, as shown in Fig. 47, where the number of scattered electrons is to be interpreted as no more than an educated guess. Secondary electrons might be expected to appear in the EDCs at photon energies greater than 4 or 5 eV. However, the width of the valence band density of states is only 3.1 eV, so it is likely that the energy distribution of scattered electrons will not overlap significantly with the EDC for the primary electrons. If this is the case, the analysis can be carried out in terms of the primary electrons alone. In the case of a wide valence band and a low work function, the scattered EDC would overlap the primary EDC, and Eq. (3.93) would have to be used in the analysis, rather than Eq. (3.83). [Eq. (3.90) includes the effects of only the

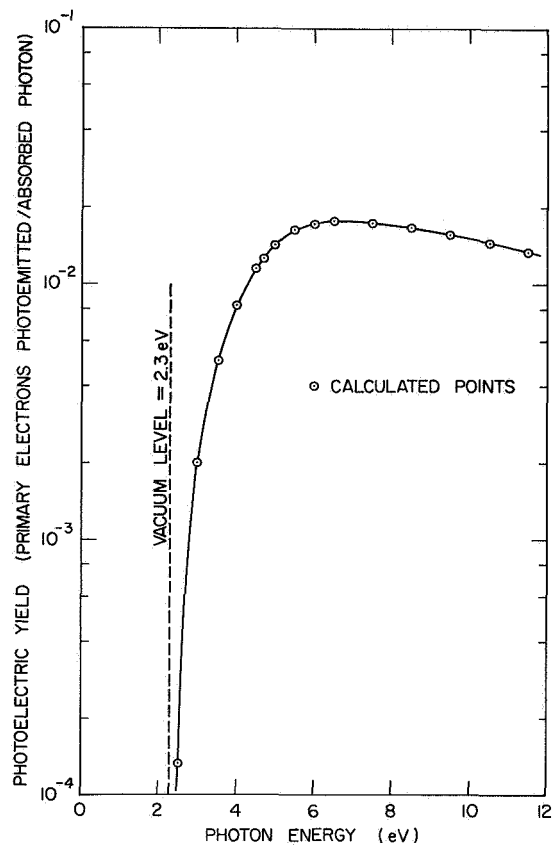


FIG. 48. CALCULATED PHOTOELECTRIC YIELD FOR SODIUM-LIKE FREE ELECTRON METAL OF FIG. 38b (PRIMARY ELECTRONS ONLY).

primary and the once-scattered electrons; a more complete analysis would include all orders of electron-electron scattering, and also phonon effects.]

Figure 48 gives the calculated photoelectric yield due to primary electrons for our hypothetical model of sodium. Note that the photoelectric yield peaks at a value of about 1.8×10^{-2} electrons photoemitted per absorbed photon for a photon energy $h\nu = 6.5$ eV. The magnitude of the yield is greater for sodium, the metal of Fig. 38b, than for the metal of Fig. 38a, because the work function is lower. The appearance of scattered electrons could cause an appreciable increase in the photoelectric yield of Fig. 48 for photon energies greater than 5 eV, and it is likely that the total photoelectric yield (primary + scattered electrons) would slowly increase with increasing photon energy, rather than decrease as in Fig. 48.

It has been recently called to the attention of the author that experimental EDCs have been obtained by Dickey [Ref. 36] for sodium.

These experimental data have been presented in Refs. 36-38. The similarity between the experimental data and the crude predictions of Fig. 46 and Fig. 47 is remarkable. Note that the EDCs predicted in Fig. 46 and Fig. 47 differ considerably from the "rectangular" distributions calculated by Berglund and Spicer [Ref. 37], which were obtained assuming a step-like threshold function.

J. C. Phillips [Ref. 39] has apparently interpreted the peak at the leading edge of the sodium EDCs as due to an "s-wave resonance" that cannot be explained by a one-electron density of states. However, the EDCs calculated in this chapter are based upon a simple one electron model, and are found to be in good qualitative agreement with the experimental EDCs for sodium. Thus, it appears unlikely that Phillips' "s-wave resonances" play a significant role in the EDCs from sodium.

IV. PHOTOEMISSION FROM COPPER

New photoemission data obtained from copper films evaporated and tested at a pressure of about 2×10^{-9} torr, using the oil-free vacuum system and the photoemission chamber described in Chapter II, are presented in this chapter. The possible effect of contamination has been essentially eliminated because, at such a low pressure, several EDCs could be measured on a freshly prepared film before a monolayer of gas could form on the surface. The EDCs taken within minutes after evaporation had slightly sharper features than the EDCs taken on the same film hours or days later. However, the difference in structure between a fresh film and an old film was on the order of 1 percent, a negligible amount of deterioration.

A considerable amount of structure is found in the experimental EDCs on clean copper, and this structure is found to differ in certain details from the earlier results of Berglund [Ref. 7] and Berglund and Spicer [Ref. 37]. This earlier work was done with a layer of cesium on the surface of the copper, and there may have been some interaction between the copper and the cesium in these experiments. However, the general features of the new photoemission data on clean copper are consistent with the earlier work on cesiated copper, and much of the data obtained from the experiments on cesiated copper is incorporated into the analysis presented in this chapter.

The photoemission data is analyzed according to the method outlined in Table 1 of Chapter III. From this analysis, which is based upon non-direct transitions, an optical density of states is deduced that is found to be in remarkably good agreement with the experimental EDCs, the experimental photoelectric yield, and the experimental ϵ_2 .

The optical density of states is one of the most important pieces of information that can be deduced from photoemission experiments, and many of the calculations presented in this chapter involve the optical density of states. Thus, the optical density of states for copper will be discussed first, in Section A of this chapter. In Section B, this optical density of states will be compared with the results deduced from experiments other than photoemission, and in subsequent sections, calculations based upon the optical density of states will be compared with experimental data.

A. THE OPTICAL DENSITY OF STATES FOR COPPER

Figure 49 shows the optical density of states for copper that has been deduced from the photoemission data, using the analysis described in Table 1 of Chapter III.

In the valence band, the location of the peaks labeled (5), (6), (7), and (8) has been obtained from the new photoemission data on clean copper. The location of peaks (4) and (9) is taken from the data of Berglund and Spicer [Ref. 37], which were obtained from cesiated copper. The location of all these peaks ((4) through (9)) is accurate to within about ± 0.1 eV. The experimental EDCs show that peaks (5) through (9) move in the manner of nondirect transitions, in which $\Delta E_p = \Delta h\nu$, where E_p is the energy of the peaks in the EDCs, and $h\nu$ is the photon energy. The direct transitions associated with peak (4) have been discussed in detail by Berglund and Spicer [Ref. 37]. The relative heights of peaks (4) through (8) were determined by direct comparison of the experimental EDCs with those calculated from the density of states of Fig. 49. The uncertainty in the relative heights is difficult to estimate, but is probably on the order of ± 10 percent. The strength of peak (9) was adjusted so that a close match was obtained between the calculated ϵ_2 and the experimental ϵ_2 in the region of photon energies between 7 and 11 eV. (Actually, a better fit would be obtained in this region if the strength of peak (9) was reduced, perhaps by about 25 percent.)

Reference to Fig. 50 strongly suggests that the valence band density of states in the region between 2 and 8 eV below the fermi level is associated with the "flat" bands that are derived largely from the 3d atomic wavefunctions, and that the region between the fermi level and 2 eV below the fermi level is associated with the bands that are derived largely from the 4s and 4p atomic wavefunctions. Having made this association, we shall find it convenient to refer to the valence band density of states corresponding to the "flat" bands as the "d-band optical density of states."

The conduction band consists of several peaks superimposed upon a free-electron-like conduction band envelope. The free-electron density of states has a \sqrt{E} energy dependence, and is labeled (1) in Fig. 49. As seen from the band structure of Fig. 50, most of the bands above the fermi level have a parabolic nature, which is characteristic of a nearly free

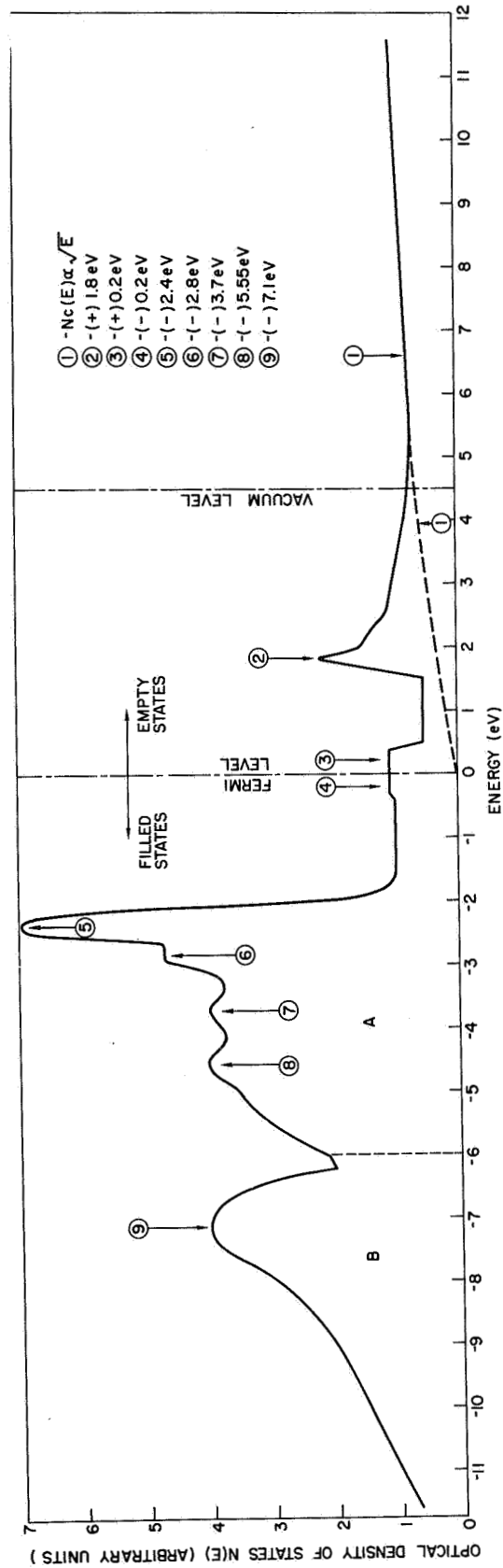


FIG. 49. OPTICAL DENSITY OF STATES FOR COPPER.

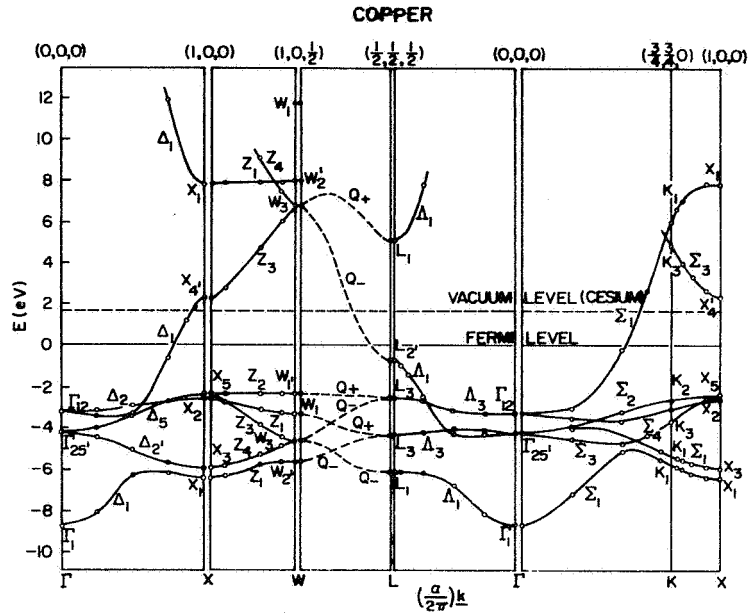


FIG. 50. CALCULATED BAND STRUCTURE OF COPPER.

electron metal. In the analysis presented in this chapter, the free-electron-like conduction band density of states is intended to represent in an "averaging" manner the character of the actual conduction band, which is composed largely of parabolic bands derived from the 4s and 4p atomic wavefunctions. The location of the bottom of the free electron band is arbitrarily chosen to be at the fermi level, which is about 2 eV above the top of the d-bands. Moving the location of the bottom of the free electron band by as much as ± 1 eV about the fermi level changes the magnitude of the free electron threshold functions by only about ± 20 percent in the region of interest, and does not significantly change any other parameter. The group velocity v_g used in calculating the electron-electron scattering length, $L(E)$, and the conduction band density of states are, of course, dependent upon the location of the bottom of the free electron band. However, at energies greater than about 4 eV, these parameters are not significantly changed by moving the bottom of the free electron band ± 1 eV about the fermi level. It is, however, important that the bottom of the free electron band be located at an energy that is "natural" for "averaging" the parabolic bands in the actual energy band calculation.

The large, sharp peak labeled (2) is taken from the work of Berglund and Spicer [Ref. 37]. In their data, this peak is clearly seen at an energy only a few tenths of a volt above the vacuum level; since only a very strong peak is likely to be seen so near the vacuum level, the "strength" attributed to peak (2) is justified. The peak labeled (3) is not a true peak; i.e., it is not experimentally observed, but is a histogram intended to represent a smooth transition between peak (4) and the free electron conduction band envelope. The effect of the presence of "peak" (3) on ϵ_2 is discussed in Section H of this chapter.

In the analysis used to determine the optical density of states, the magnitude of the entire conduction band density of states can be scaled by the same arbitrary constant without affecting any of the results. In Fig. 49 the conduction band density of states is scaled to match the valence band density of states at the fermi level.

The vacuum level of 4.5 eV shown in Fig. 49 is the vacuum level appropriate to the experimental data presented in this chapter. The vacuum level was found to vary by several tenths of an electron volt from sample to sample, but with no effect on the shape of the experimental EDCs. Hagstrum [Ref. 40] has suggested that the variations in vacuum level may be due to different crystalline orientations in different evaporated films.

An important question to consider in evaluating the density of states of Fig. 49 is its uniqueness. As can be seen from the discussions in Chapter III and in Appendix A, the analysis of the noble metals allows the adjustment of only a few parameters to fit many pieces of experimental data. Because of the excellent agreement with the available experimental data, the optical density of states of Fig. 49 is probably quite accurate, and changes of greater than about 20 percent in any single parameter or combination of parameters have resulted in poorer fits to the experimental data. The locations of all the peaks are accurate to within ± 0.1 eV, and in the region between the fermi level and 6 eV below the fermi level, the relative peak heights are probably correct to better than ± 10 percent. The greatest uncertainty lies in the strength of peak (9) and in the shape of the conduction band in the region between the fermi level and 1.5 eV above the fermi level, a region which cannot be directly investigated by photoemission.

In addition, the leading edge in the experimental EDCs is usually somewhat blurred, so that the valence band density of states cannot be accurately determined in the region between the fermi level and a few tenths of an eV below the fermi level.

For the case of copper, there are no good experimental data for the electron-electron scattering length $L(E)$ in the region several eV above the fermi level. However, the $L(E)$ that is calculated for copper is found to be quite close to the $L(E)$ calculated for gold, and the calculated $L(E)$ for gold is found to be in remarkably good agreement with available experimental data.

B. COMPARISON OF THE OPTICAL DENSITY OF STATES FOR COPPER WITH OTHER EXPERIMENTAL DATA

Figure 51 shows a comparison of the shape of the optical density of states obtained from photoemission data with the density of states obtained

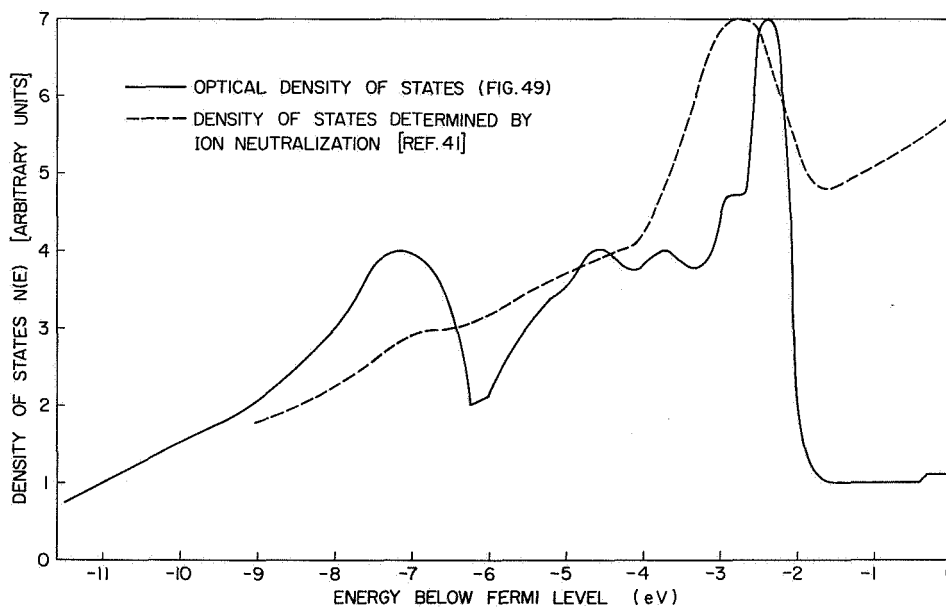


FIG. 51. COMPARISON OF THE OPTICAL DENSITY OF STATES OF FIG. 49 WITH THE DENSITY OF STATES DETERMINED FROM ION NEUTRALIZATION EXPERIMENTS (HAGSTRUM, REF. 41).

by Hagstrum [Ref. 41] using ion-neutralization spectroscopy with He^+ ions. Hagstrum has pointed out that the resolution of the ion-neutralization experiment is not better than several tenths of an electron volt, and that

the density of states due to the d-electrons is de-emphasized compared with the density of states due to the s and p electrons. This de-emphasis occurs because the localized nature of the tightly bound d electrons results in a smaller tunneling probability for the d electrons than for the less localized s and p electrons. Thus, in the region between the fermi level and 2 eV below the fermi level, Hagstrom's density of states should be reduced relative to the d band density of states, which seems to extend from 2 to 8 eV below the fermi level. If this adjustment is made, we see that the density of states obtained from ion-neutralization experiments is in fairly good qualitative agreement with the optical density of states obtained from photoemission experiments. In both cases, the most pronounced structure is a large peak located in the vicinity of 2.5 eV below the fermi level. However, the optical density of states contains much more detail, and is considerably more accurate than the density of states deduced from ion-neutralization experiments.

Figure 52 compares the optical density of states for copper with the soft X-ray emission spectrum for copper obtained by Clift et al [Ref. 42].

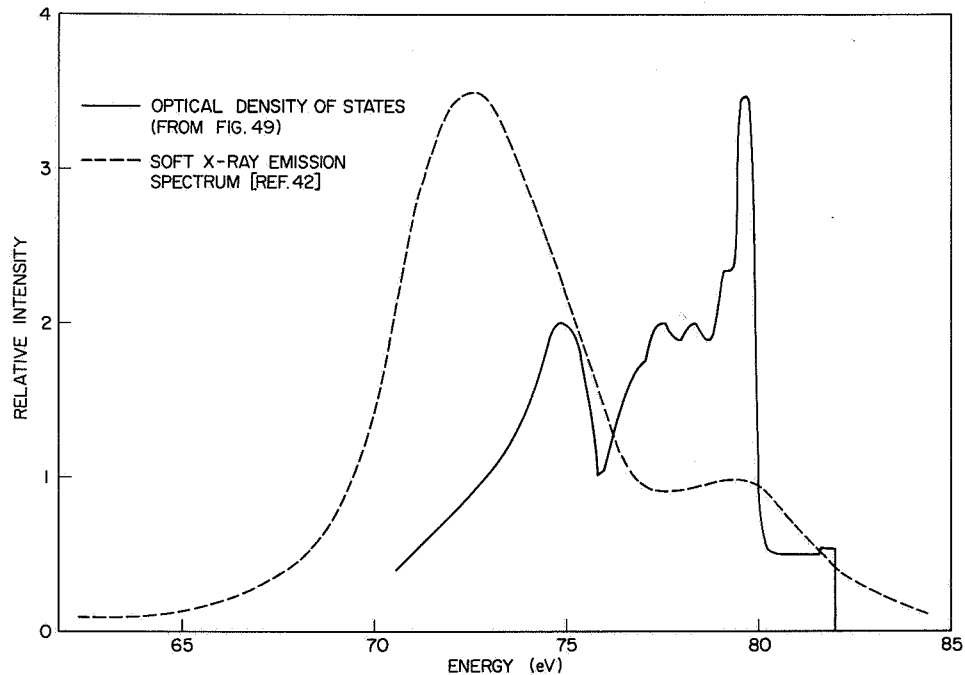


FIG. 52. COMPARISON OF SHAPE OF OPTICAL DENSITY OF STATES FOR COPPER WITH THE SOFT X-RAY EMISSION SPECTRUM FROM COPPER [REF. 42].

As seen from Fig. 52, the soft X-ray spectrum from copper does not even remotely resemble the shape of the optical density of states. Some authors [Ref. 51] have recently interpreted the soft X-ray spectrum from nickel as closely representative of the density of states in the valence band a few eV below the fermi level. However, in the soft X-ray experiment an electron is removed from a core level, thus causing a drastic change in the core potential, and probably a correspondingly drastic change in the energy band structure near the fermi level. For this reason, the soft X-ray emission spectrum is not likely to bear any close resemblance to the true unperturbed density of states.

C. COMPARISON OF THE OPTICAL DENSITY OF STATES FOR COPPER WITH THEORETICAL CALCULATIONS

Figure 53 compares the d-band optical density of states in the region between 2 and 6 eV below the fermi level with the density of states obtained

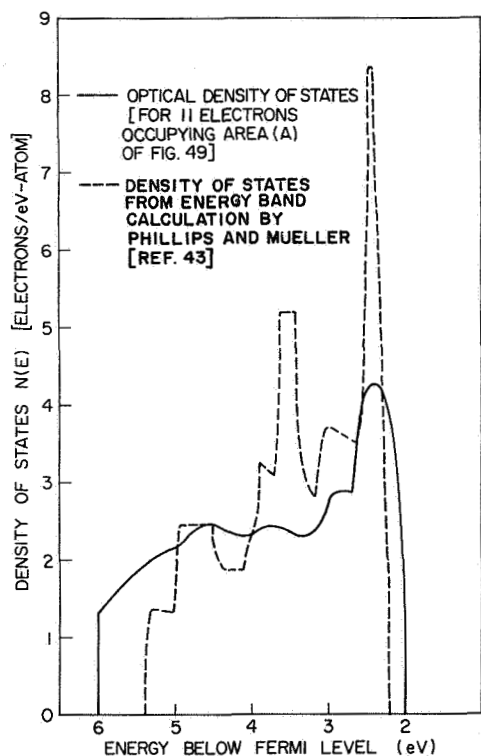


FIG. 53. COMPARISON OF THE OPTICAL DENSITY OF STATES WITH THE DENSITY OF STATES OF REF. 43 IN THE REGION BETWEEN 2 AND 6 eV BELOW THE FERMI LEVEL. Both curves are normalized to hold 10 electrons.

from an early tight binding calculation by J. C. Phillips and F. M. Mueller [Ref. 43]. Both curves are normalized to contain ten 3d electrons. The calculation of Phillips and Mueller was done by use of an interpolation scheme [Ref. 52], and the energy band calculations of Brudick [Ref. 53].

Because of the close agreement between the two curves in Fig. 53 in the region 2 to 6 eV below the fermi level, it was at first thought that the deeper lying peak (9) in the optical density of states of Fig. 49 was not representative of the true density of states, but might perhaps be due to a many-body resonance, as proposed by J. C. Phillips [Refs. 38, 39]. However, recent calculations [Refs. 44, 52, 54, 55] show that the width and character of the d bands can be changed by introduction of s-d hybridization into the energy band calculations. Figure 54 compares the optical density of states for copper with the density of states for paramagnetic

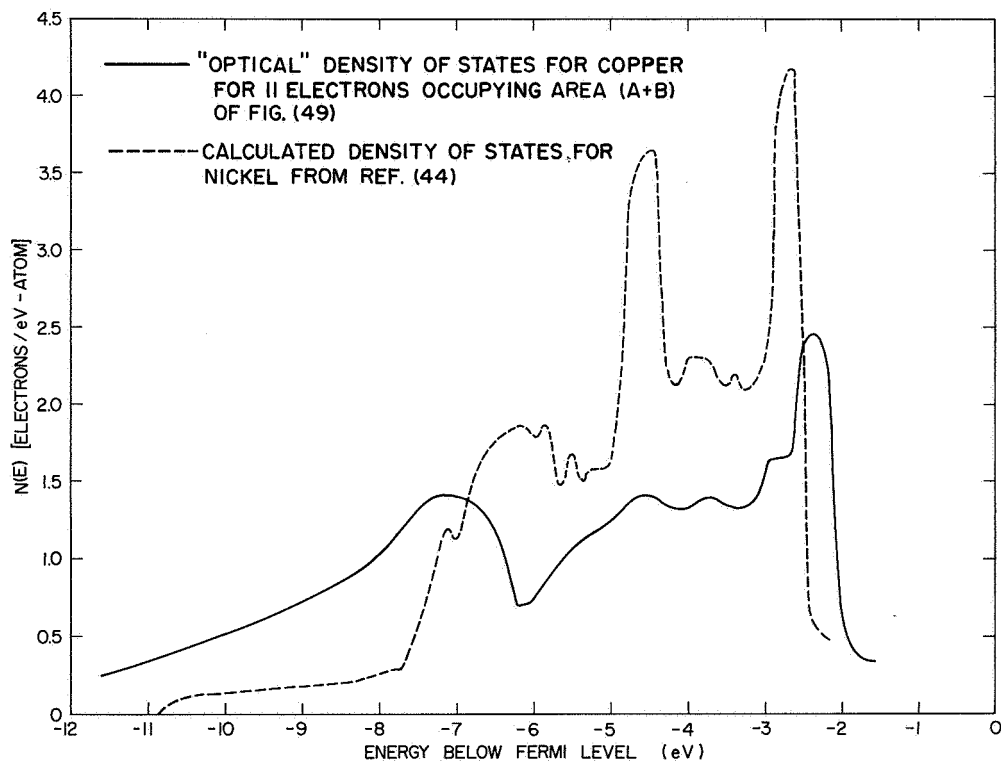


FIG. 54. COMPARISON OF OPTICAL DENSITY OF STATES FOR COPPER WITH CALCULATED DENSITY OF STATES FOR NICKEL (REF. 44).

nickel, as calculated by Hodges et al [Ref. 44] with the inclusion of s-d hybridization. (According to the rigid band model, the density of states for nickel should not differ appreciably from the density of states for copper.) Figure 54 shows a remarkable similarity between Hodges' [Ref. 44] nickel density of states and the optical density of states for copper. If Hodges' nickel density of states was uniformly "stretched" so as to

increase the overall bandwidth by about 1 eV, the similarity would be even closer. However, Marshall [Ref. 56] and Wood [Ref. 57] have recently found that the width of the d bands can be changed significantly by manipulating exchange terms in the potential used for energy band calculations. Consequently, it seems possible that by adjusting both exchange and s-d hybridization in the energy band calculations, the width of the d bands will be found to be somewhat wider than the nickel density of states in Fig. 54, and considerably closer to the optical density of states. Thus, it now seems likely that peak (9) of Fig. 49 is not due to many-body resonances, but may actually represent the true density of states. In fact, the striking similarity between the calculated nickel density of states in Fig. 54 and the optical density of states suggests that the entire optical density of states below the fermi level may be a very close replica of the true density of states.

However, because of the present activity in improving the band calculations for nickel and copper, it would seem to be too early to make a detailed comparison between the optical density of states for copper and the "best" energy band calculation presently available. A detailed comparison involving the bandwidth, peak locations, and relative peak heights will be significant only when the theoretical energy band calculations for these materials have improved considerably beyond the present state of sophistication.

D. THE PHOTOELECTRIC YIELD FROM CLEAN COPPER

The experimental photoelectric yield and the calculated photoelectric yield¹ are compared in Fig. 55. The experimental yield has been corrected for reflectivity and the transmission of the LiF window, and the calculated yield was obtained by use of the density of states of Fig. 49 and the analysis described in Table 1 of Chapter III. Both the magnitude and the shape of the calculated yield are in remarkably good agreement with the experimental results, attesting to the validity of the optical density of states and the simple model used to calculate the photoemission data. In the actual analysis, the magnitude of the electron-electron scattering length $L(E)$ was arbitrarily set equal to 22 Å at an energy 8.6 eV above the fermi level. No experimental value is available to use as a check on

¹See Chapter III for a description of this calculation.

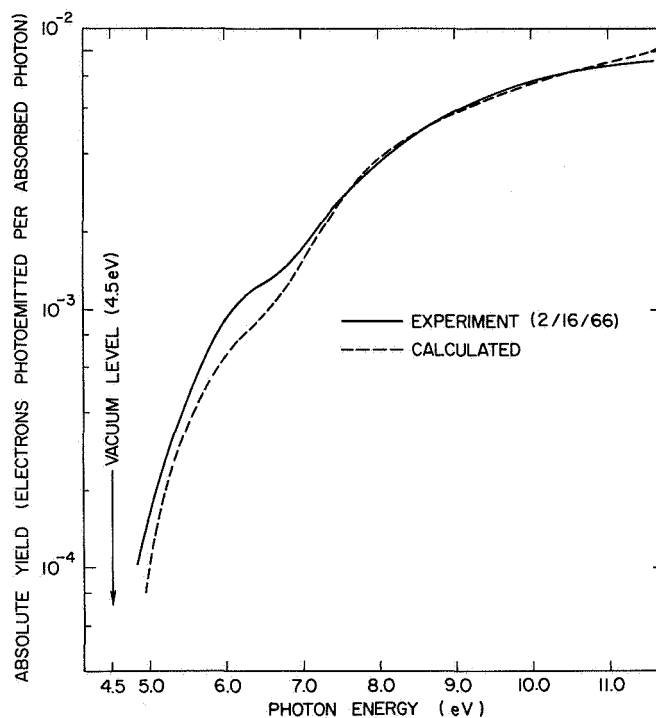


FIG. 55. COMPARISON OF EXPERIMENTAL YIELD AND CALCULATED YIELD FOR COPPER. For experimental curve, absolute yield at 7.7 eV was obtained by using a value of 22 percent for F-7 Cs₃Sb tube (from thermopile data of Shay Ref. 17). Relative yield was obtained by comparison with sodium salicylate (V-1), which was calibrated by thermopile measurements of Koyama [Ref. 16] above 8 eV.

$L(E)$ in copper, but the value of 22 \AA is very close to the value of 20 \AA which Kanter [Ref. 49] has experimentally observed to be the electron-electron scattering length in gold at 8.6 eV above the fermi level. Since the density of states for copper is very similar to the density of states for gold, the arbitrarily chosen value of 22 \AA for copper is probably very close to the actual value. The vacuum level pertinent to the calculation was 4.5 eV, which was determined by taking the energy difference between the photon energy and the well-defined width of the resulting EDC. No attempt was made to accurately measure the photoelectric yield in the threshold region between 4.5 and 5.0 eV above the fermi level, since the photoelectric current in this region was too low to measure EDCs.

One of the most significant features of the photoelectric yield for copper is that, even at a photon energy of 11.6 eV, the yield is only

1×10^{-2} electrons photoemitted per absorbed photon. At lower photon energies, the yield is even lower, showing that for a metal such as copper, more than 99 percent of the excited electrons are not photoemitted in the range of $h\nu$ used in this study. It is indeed remarkable that the small value of the free electron threshold function and the short electron-electron scattering length are able to account almost exactly for the very small magnitude of the photoelectric yield in the region of photon energies between 5 and 12 eV. The only significant structure in the yield curve is the rather sharp rise that occurs at a photon energy of 6.8 eV. This rise at 6.8 eV appears in both the experimental and calculated yield curves, and is due to the onset of photoemission from the large d band density of states peak labeled (5) in Fig. 49.

The absorption coefficient $\alpha(\omega)$ is used in calculating the EDCs from the optical density of states and the analysis described in Table 1 of Chapter III. The values of $\alpha(\omega)$ used in the calculations for copper were taken from Ref. 45. The reflectivity at normal incidence $R(\omega)$ is used to "normalize" the experimental EDCs (to units of electrons photoemitted per absorbed photon per eV), and is also taken from the experimental results of Ref. 45. Any error in the values of $\alpha(\omega)$ and $R(\omega)$ will result in errors in the analysis of the photoemission data. Ideally, $\alpha(\omega)$ and $R(\omega)$ should be measured at ultrahigh vacuum on the same films that are used to measure the EDCs and the quantum yield. However, such an ideal measurement was not feasible in our laboratory at the time of this investigation. Fortunately, in the study of photoemission from clean copper, the data of most interest occurred at photon energies in the region between 6 and 12 eV, where the reflectivity is typically about 10 percent. For such small values of $R(\omega)$, an error in $R(\omega)$ will result in a much smaller error in the quantity $\{1/[1-R(\omega)]\}$ which is the quantity used to correct the yield for reflectivity. As discussed in Chapter II, by far the greatest error in the photoelectric yield is due to calibration, and this error is estimated to be about ± 10 percent. The overall uncertainty in the magnitude and shape of the experimental yield curve for copper (Fig. 55) in the region of photon energies between 5 and 11.6 eV is estimated to be less than ± 15 percent.

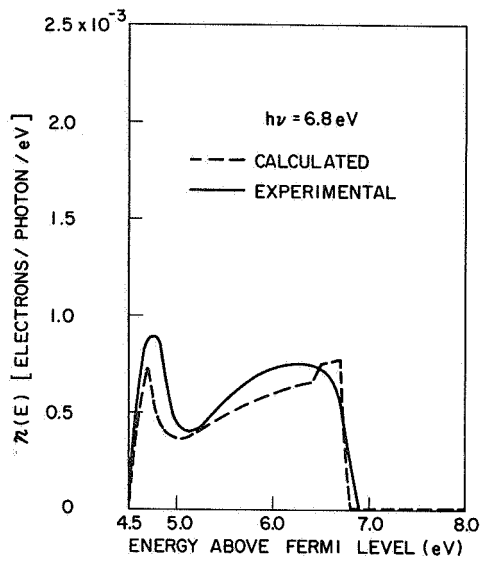
E. PHOTOELECTRIC ENERGY DISTRIBUTIONS FROM CLEAN COPPER

Sixteen experimental and calculated EDCs for clean copper in the range of photon energies between 6.8 and 11.6 eV are shown in Figs. 56a through 56p. The EDCs were calculated by use of the density of states of Fig. 49 in the analysis described in Table 1 of Chapter III. The most outstanding feature of these curves is the excellent agreement between all of the calculated and experimental EDCs, both in shape and in magnitude. It is amazing that the model used in calculating the EDCs is able to account so well for the experimental EDCs, especially since the transport of photoexcited electrons toward the surface and the threshold function are based upon such simple models. Apparently, these simple models are a good description of the basic physics involved in the photoemission process.

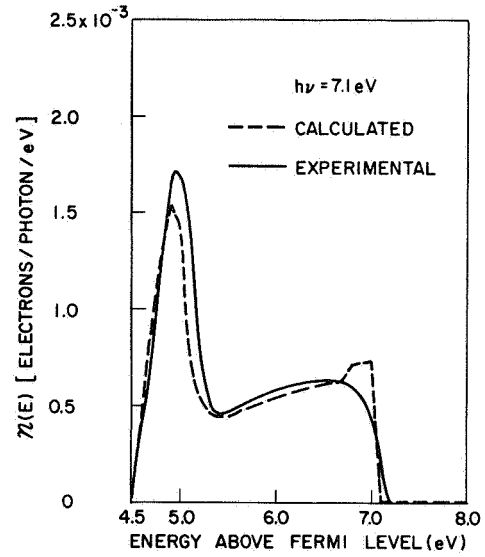
Another significant feature of the experimental EDCs is that the four d band peaks labeled ⑤, ⑥, ⑦, and ⑧ in Fig. 49 all move in the manner of nondirect transitions, where $\Delta E_p = \Delta h\nu$. These peaks are readily identified in the curves of Fig. 56, since the experimental EDCs bear a close resemblance to the valence band density of states. The non-direct nature of the d band peaks is convincing evidence that, in the range of photon energies below 11.6 eV, "k-conservation" is not an important selection rule for optical transitions from the d bands of copper. An interesting feature to be noted in Figs. 56d, 56e, and 56f is that even at 6 eV above the fermi level, the half-width of d band peak, ⑤, is only about 0.5 eV. At higher photon energies, the weaker peak ⑥ seems to merge into the side of the very strong peak ⑤, and for photon energies greater than about 9.6 eV, the weak peak ⑥ appears as a broadening in the side of the strong peak ⑤. The blurring of the relatively weak peak ⑥ may be due to lifetime broadening, which can be estimated from the uncertainty principle $\Delta E \Delta \tau \geq \hbar$. We can evaluate ΔE by setting

$$\Delta \tau = \tau(E) = \frac{L(E)}{|\mathbf{v}_g(E)|}$$

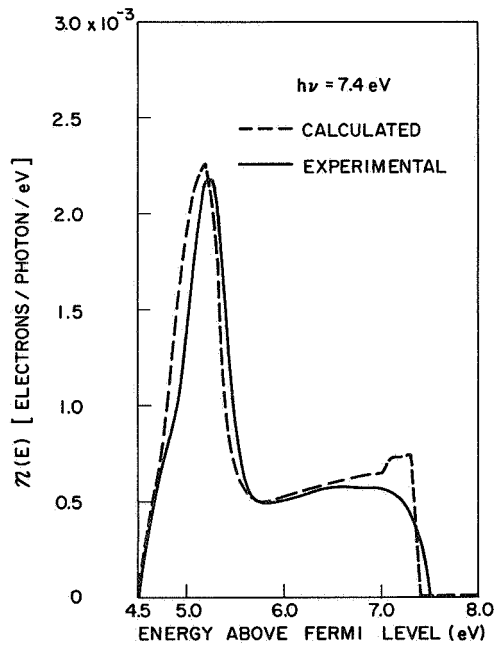
where $\frac{1}{2} m |\mathbf{v}_g|^2 = E(\text{eV})$.



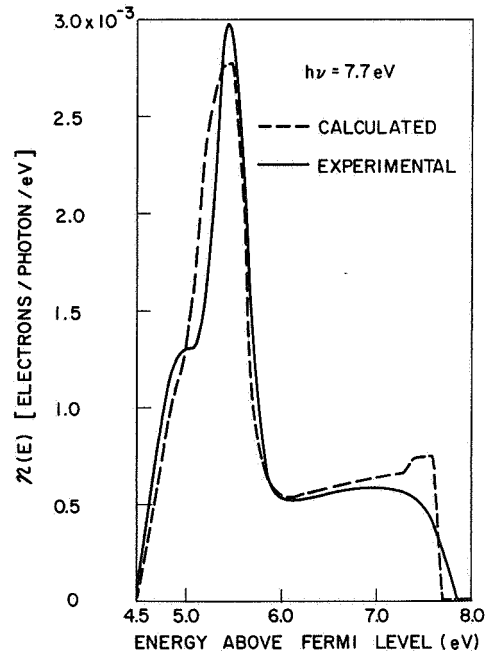
(a)



(b)

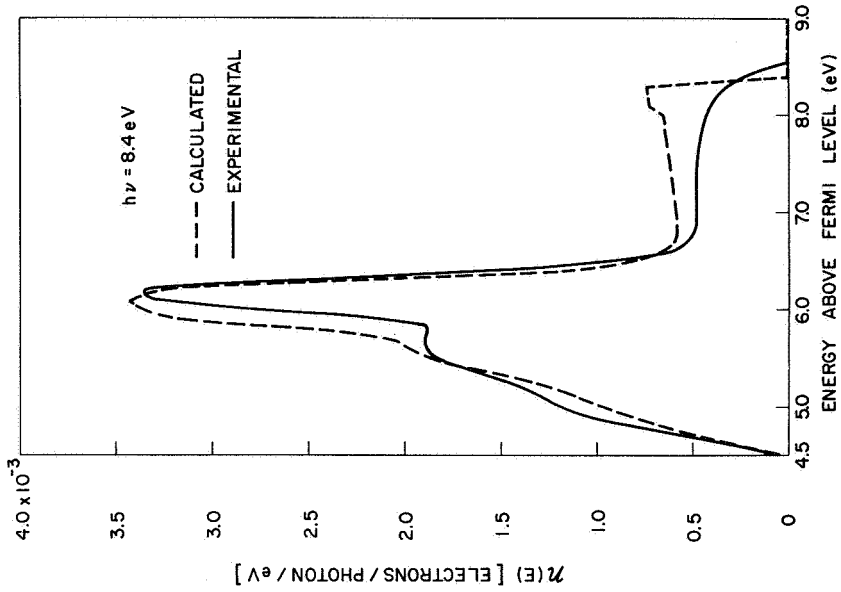


(c)

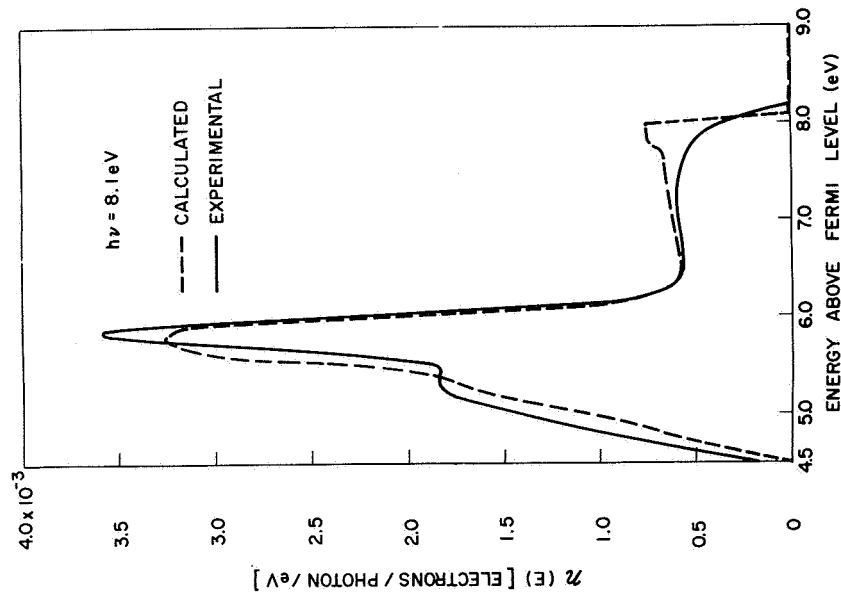


(d)

FIG. 56. PHOTOELECTRIC ENERGY DISTRIBUTIONS FROM CLEAN COPPER.

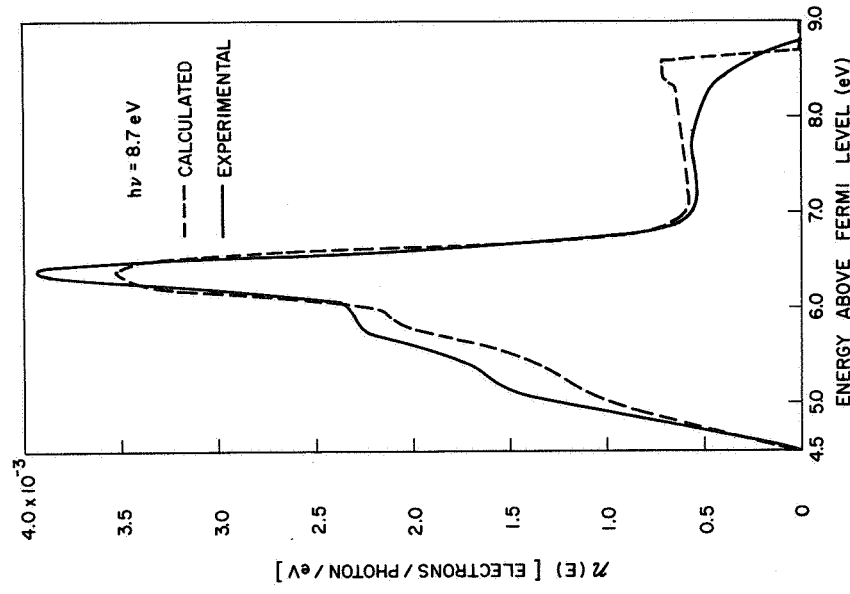


(f)

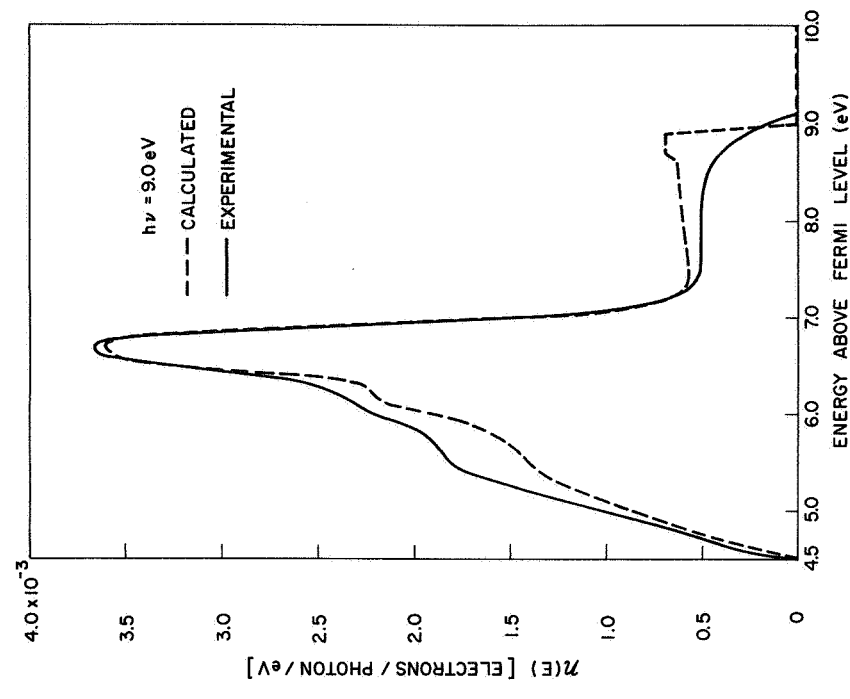


(e)

FIG. 56. CONTINUED.

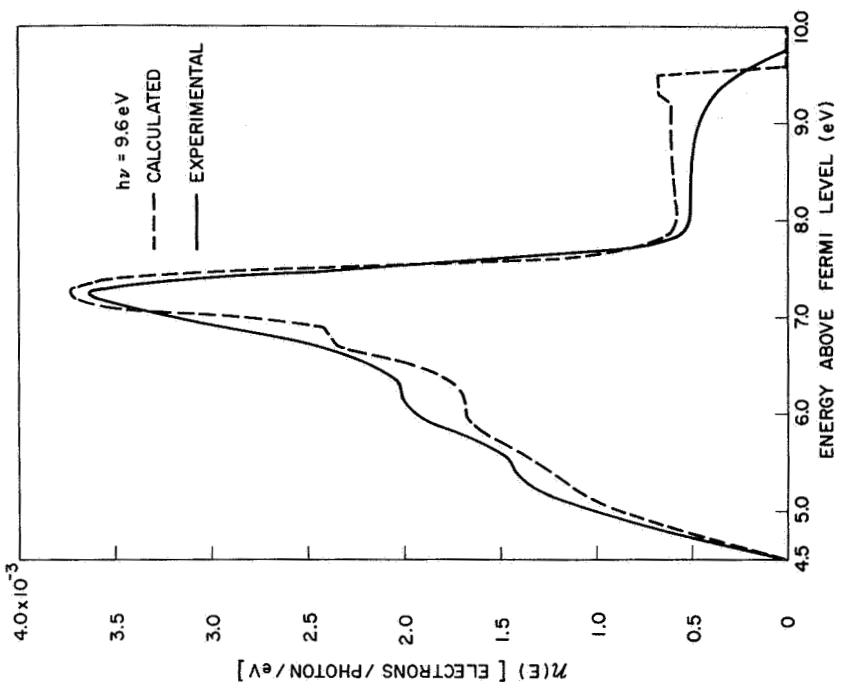


(g)

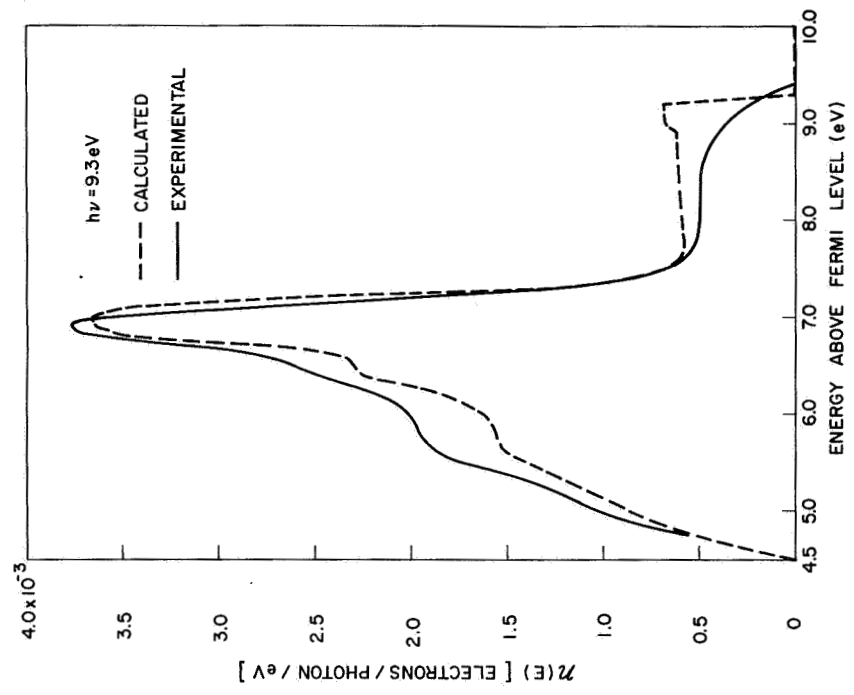


(h)

FIG. 56. CONTINUED.

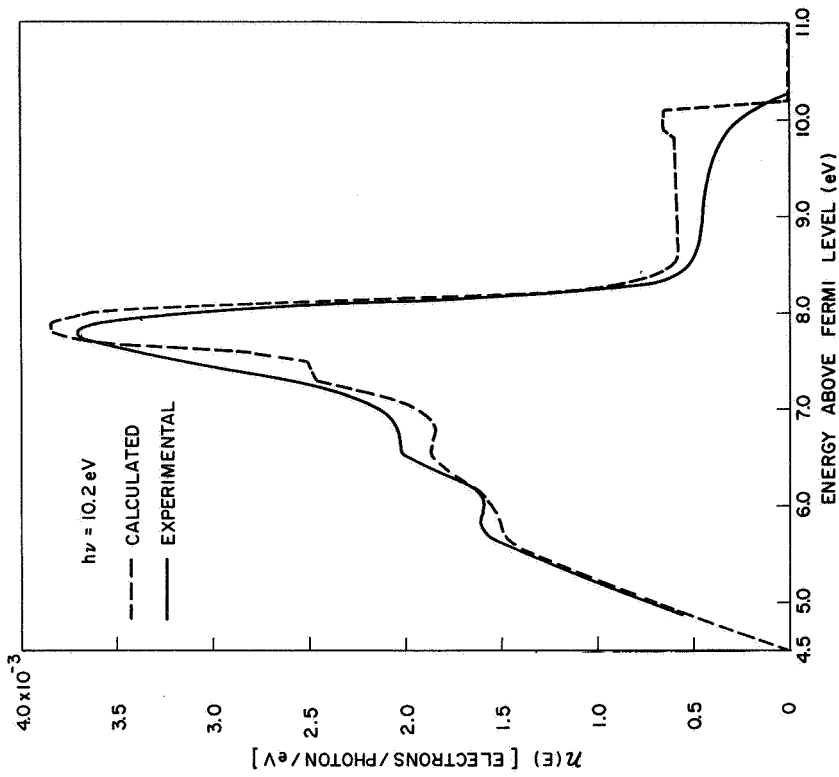


(j)

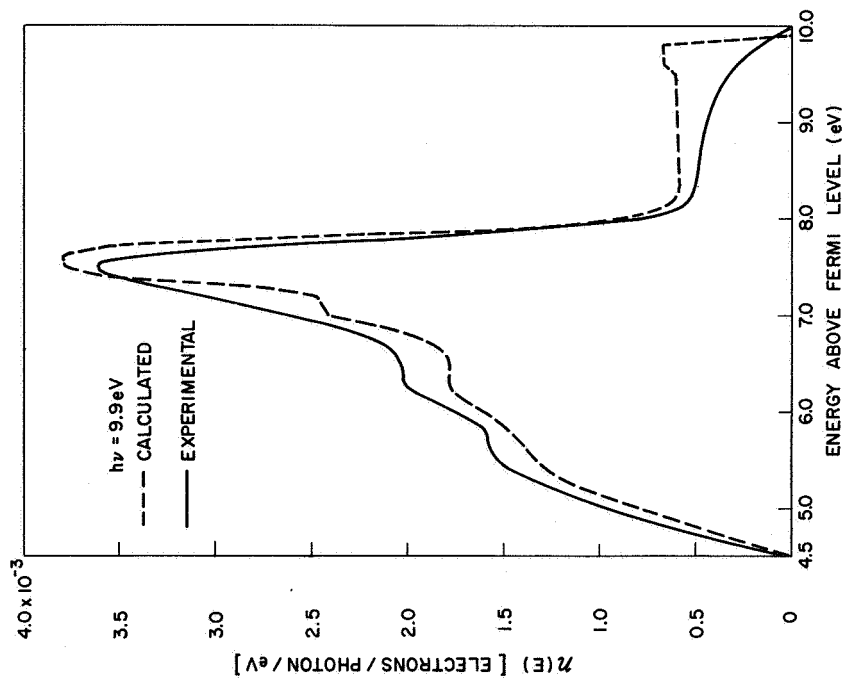


(i)

FIG. 56. CONTINUED.

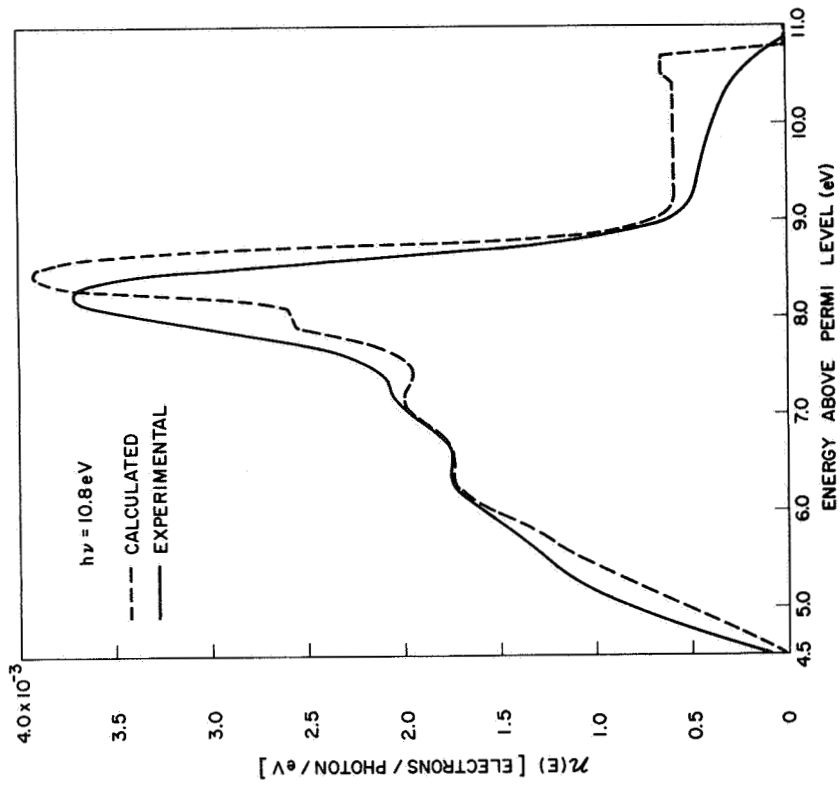


(l)

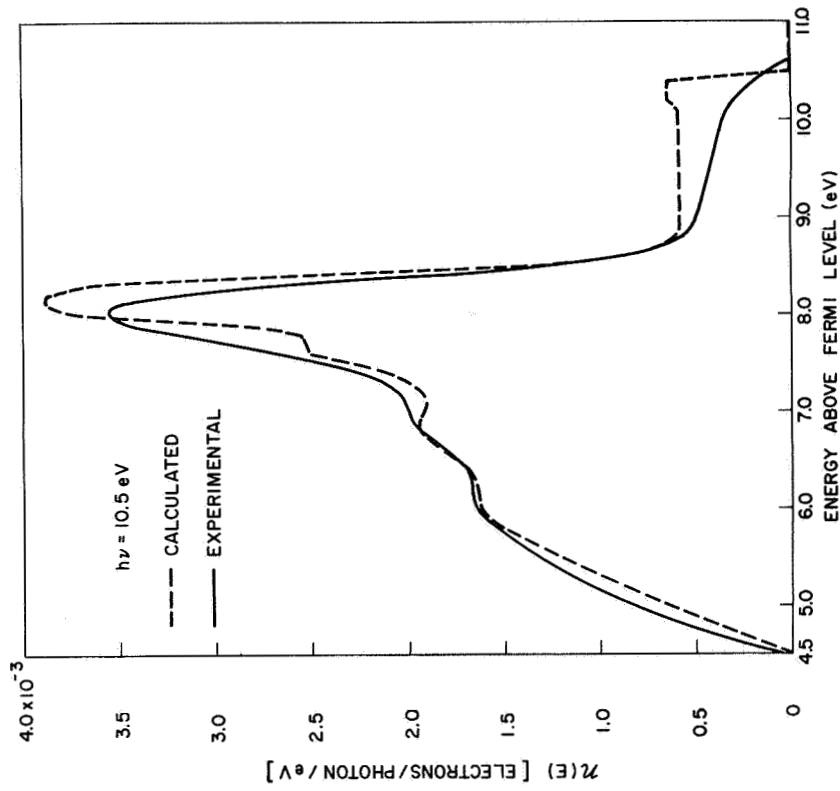


(k)

FIG. 56. CONTINUED.

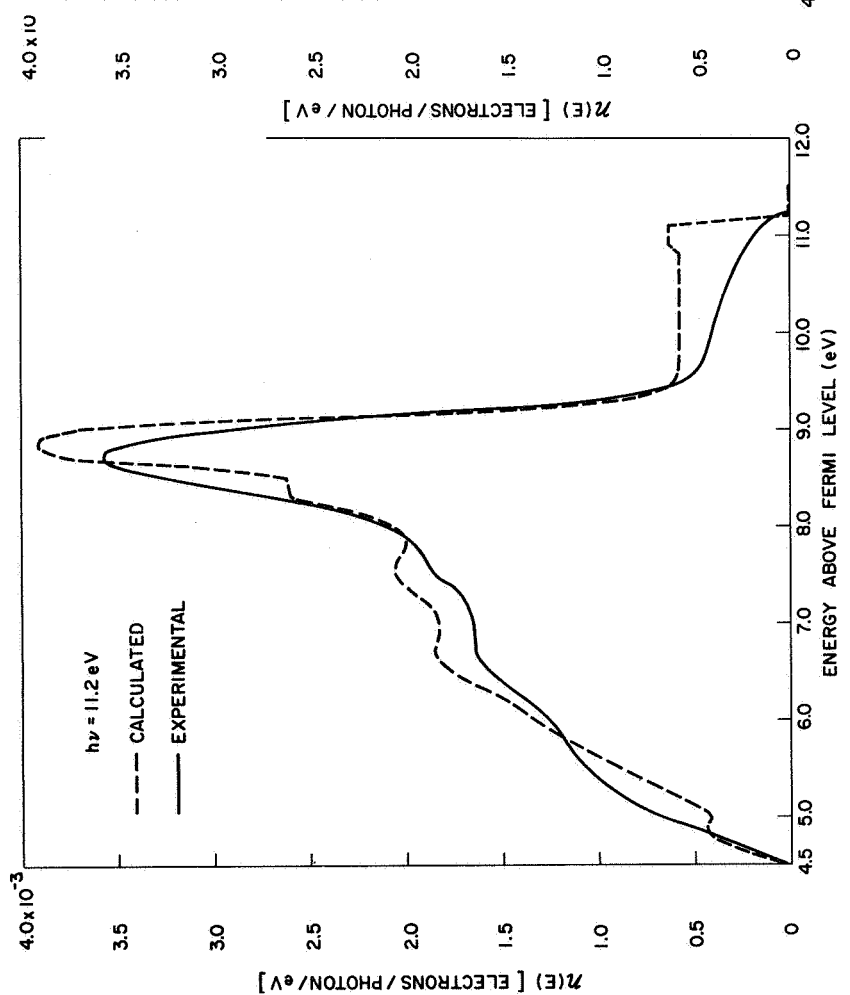


(n)

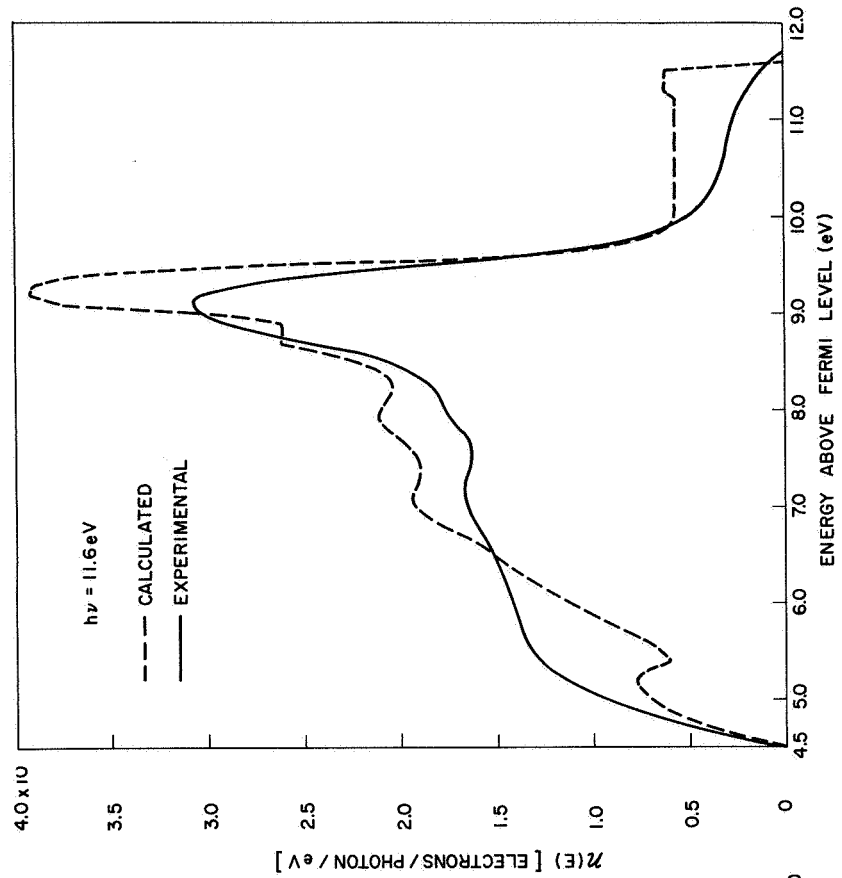


(m)

FIG. 56. CONTINUED.



(o)



(p)

FIG. 56. CONTINUED.

Using the free electron mass for m and measuring $E(\text{eV})$ from the bottom of the free electron conduction band in Fig. 49, the uncertainty ΔE is calculated to be as shown in Fig. 57. At 5.5 eV above the fermi

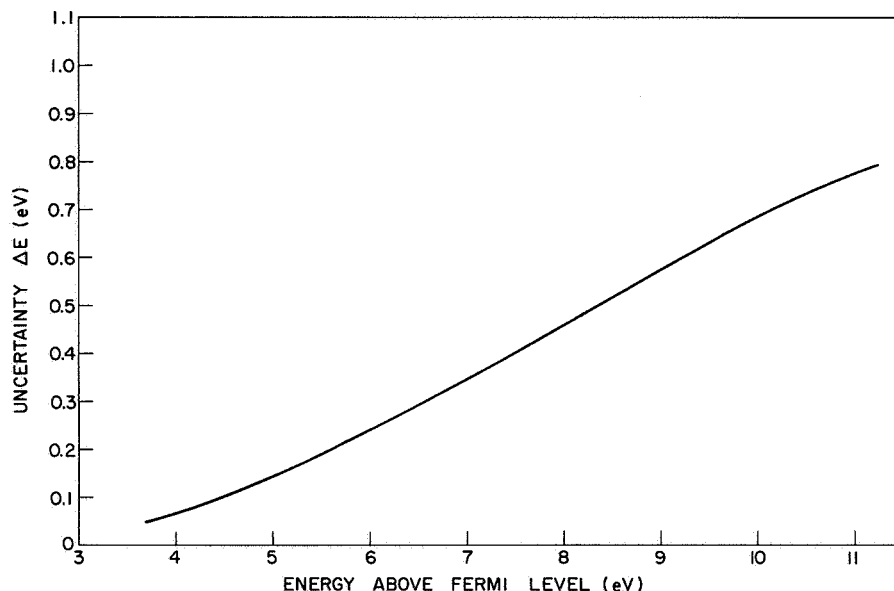


FIG. 57. UNCERTAINTY ΔE DUE TO LIFETIME BROADENING.

level, ΔE is only 0.19 eV, considerably less than the observed bandwidth of d-band peak (5). At 7 eV, however, $\Delta E = 0.35$ eV, just large enough to cause loss of resolution for the weak peak (6), which is separated from the strong peak (5) by only 0.4 eV. Thus, the broadening of the d band peaks is remarkably consistent with the uncertainty expected from a simple lifetime broadening calculation.

Another cause of broadening (or sharpening) of peak widths in the EDCs at energies higher than 9 eV above the fermi level might be due to the fact that at these energies $L(E)$ is less than 20 \AA , so that most of the photoemitted electrons come from within 20 \AA of the surface. Figure 60 shows that, at 9 eV above the fermi level, $L(E)$ is about 20 \AA , and that at 11.6 eV above the fermi surface, $L(E)$ is only about 15 \AA . The change in periodicity and/or the change in lattice constant that occurs so near the surface could conceivably result in changes in the energy level structure near the surface, which would result in EDCs that were not good, detailed representations of the bulk energy level structure. Because $L(E)$

is longer at lower energies, the electrons at lower energies originate (on the average) from deeper in the bulk than do the electrons at higher energies, and are probably more representative of the bulk material than those electrons that originate within a few atomic layers of the surface.

The calculated photoelectric yield of Fig. 55 and the calculated EDCs of Fig. 56 are for those electrons that have not suffered an inelastic electron-electron collision. As discussed by Berglund and Spicer [Ref. 37], photoemission from secondary (at least once scattered) electrons is usually characterized in the EDCs by a large, stationary peak of slow electrons just above the vacuum level. In the experimental EDCs for clean copper, most of the secondary electrons seem to fall to energies below the vacuum level, for there is no evidence of significant photoemission from secondary electrons in any of the EDCs at photon energies up to 11.6 eV. Thus, an analysis involving only primary electrons appears to be adequate in describing the photoemission from clean copper at photon energies up to 11.6 eV, and the equations of Chapter III that include both primary and secondary electrons need not be used. At photon energies of 11.2 and 11.6 eV, there is a small "bump" of electrons just above the vacuum level, but this bump may very well be due to the onset of photoemission from peak (9) in the valence band optical density of states.

At a photon energy of 11.6 eV, it appears that the height of the experimental d band peak labeled (5) has suddenly become somewhat smaller relative to the height of peak (7) than was the case at lower photon energies. This effect may be due to a dip in the conduction band density of states at about 9 eV above the fermi level. Unfortunately, the high energy cutoff of the LiF window was at about 11.8 eV, and good EDCs could not be measured at photon energies greater than about 11.6 eV, and the exact cause of the change in the peak height of d band peak (5) could not be established.

The EDCs for several different samples of clean copper are shown in Fig. 58. The curves are very similar; the only difference occurs in small variations in the vacuum level and in the height of d band peak (5).

As described in Chapter II, considerable care was taken in evaporating the copper films, and it was found that pressures in the vicinity of 2×10^{-9} torr were necessary to avoid contamination of the films and

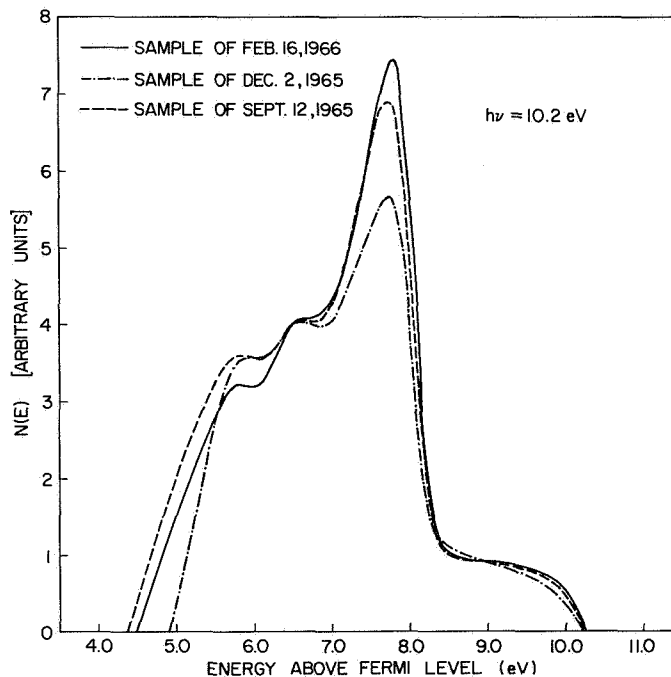


FIG. 58. COMPARISON OF THE SHAPES OF THE EDCs FROM SEVERAL DIFFERENT SAMPLES OF COPPER. The curves were fitted at 6.5 eV above the fermi level.

deterioration in the quality of the EDCs. Figure 59 shows the effect of evaporating a copper film at a pressure between 1×10^{-8} and 1×10^{-7} torr. Immediately after evaporation, the EDC at 10.2 eV closely resembled the stable EDCs that are obtained from films evaporated at a pressure of 2×10^{-9} torr. However, as time progressed, a large peak of slow electrons began to appear at low energies in the EDCs, causing the total yield to increase. It seemed as if a large peak of slow electrons was superimposed upon the electrons of EDC (1); as seen from EDC (3), which was taken two hours after evaporation, the lower energy peaks of EDC (1) appear as small shoulders superimposed upon a background of low energy electrons. During the contamination, the peak at 7.6 eV (due to d band peak (5)) did not appear to change in magnitude, as might be expected if the contamination merely shortened the electron-electron scattering length $L(E)$. The contamination effects shown in Fig. 59 indicate that EDCs from copper films are extremely sensitive to poor vacuum conditions, and that vacuums somewhat better than 1×10^{-9} torr are necessary for good photoemission

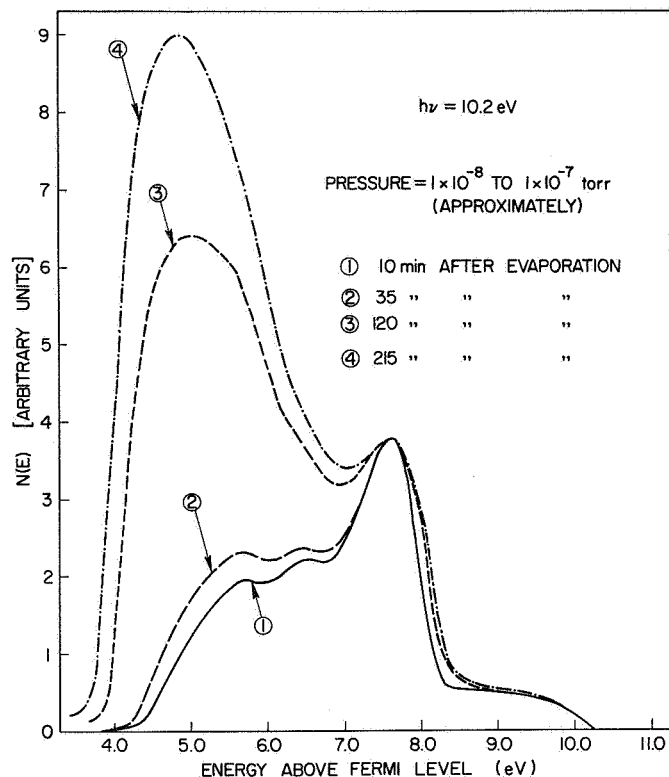


FIG. 59. EFFECT OF INADEQUATE VACUUM ON COPPER ENERGY DISTRIBUTION CURVES. These curves were not fitted, and the relative magnitudes were experimentally observed. Note that the peak at 7.6 eV above the fermi level did not change magnitude with time.

studies on copper. Silver and gold were found to be much less sensitive to vacuum conditions.

F. THE ELECTRON-ELECTRON SCATTERING LENGTH $L(E)$ FOR COPPER

The shape of the electron-electron scattering length $L(E)$ for copper was calculated from the optical density of states of Fig. 49 using the analysis discussed in Table 1 of Chapter III. The magnitude of $L(E)$ was arbitrarily set equal to 22 \AA at a photon energy 8.6 eV above the vacuum level. The calculated electron-electron scattering length $L(E)$ for copper is shown in Fig. 60. We see that in the region between 4.5 and 11.6 eV above the fermi level, $L(E)$ varies from 78 to 15 \AA . Thus, $L(E)$ changes considerably in the energy range of interest for photoemission studies from clean copper, and severely modulates the shape of the

experimental EDCs. Because the absorption coefficient $\alpha(\omega)$ is on the order of $7 \times 10^{-5} \text{ cm}^{-1}$ in the range of photon energies between 6 and 11 eV,

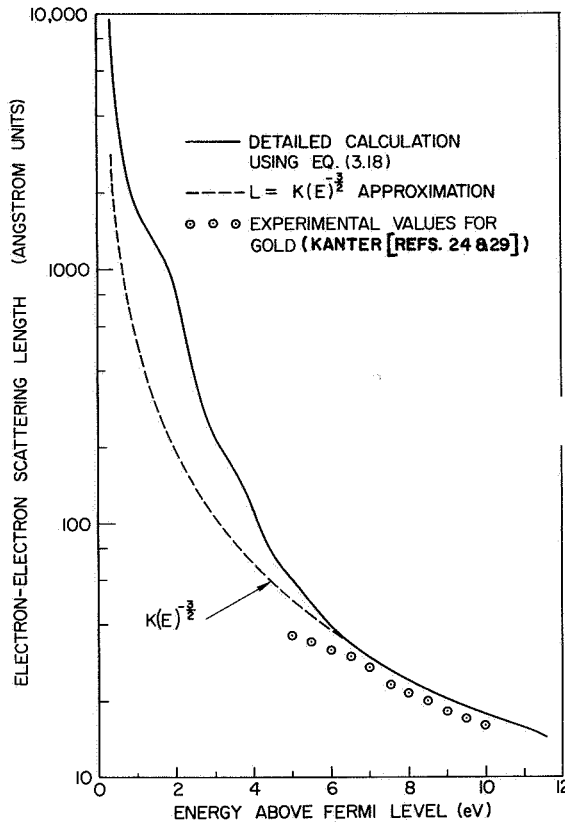


FIG. 60. CALCULATED ELECTRON-ELECTRON SCATTERING LENGTH $L(E)$ FOR COPPER. (Magnitude set equal to 22 Å at 8.6 eV above the fermi level to give experimental yield.)

His results for gold are compared to the calculated $L(E)$ for copper in Fig. 60, and the agreement is remarkably close, indicating that the calculated $L(E)$ for copper is probably not far from the actual value of $L(E)$ for copper.

Because of the contamination problems with copper (discussed in Section E of this chapter), future electron transmission measurements through copper films will have to be carried out with careful attention to cleanliness and vacuum pressure. Kanter's [Ref. 49] values for gold

the approximation $[\alpha(\omega) L(E) \ll 1]$ is valid only for energies greater than about 9 eV above the fermi level. No approximations were made in using Eq. (3.83) to calculate the EDCs on clean copper. For energies greater than 6 eV above the fermi level, $L(E)$ has an $E^{-1.5}$ energy dependence, just as expected from the discussion in Chapter III.

Unfortunately, no good experimental values for $L(E)$ are available to use as a check on the copper calculations. However, as we shall see in Chapter V, the density of states for gold is qualitatively similar to the density of states for copper, so that $L(E)$ for gold should not be appreciably different from $L(E)$ for copper. Kanter [Ref. 49] has recently determined $L(E)$ for gold in the energy range between 5 and 10 eV above the fermi level by measuring the transmission of a monoenergetic beam of electrons through a thin film of gold.

are probably reliable because of the insensitivity of gold to contamination, as will be discussed in Chapter V. Because of the contamination problem, equally reliable experimental values of $L(E)$ for copper will probably be extremely difficult to obtain.

G. THE THRESHOLD FUNCTION AND THE EFFECTIVE THRESHOLD FUNCTION FOR COPPER

The semiclassical threshold function $T_f(E)$ used in calculating the EDCs and yield for clean copper and cesiated copper are shown in Fig. 61.

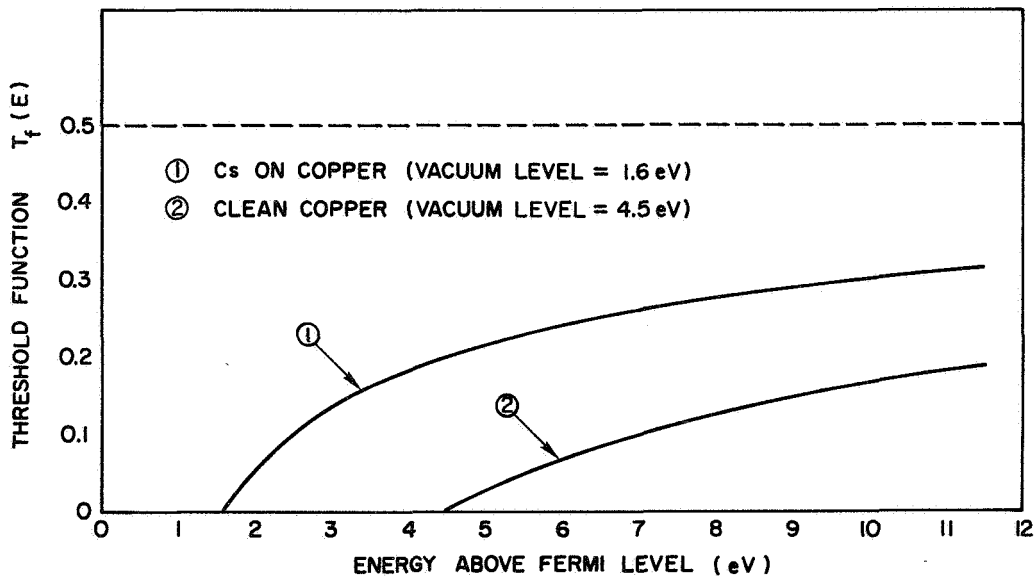


FIG. 61. SEMICLASSICAL THRESHOLD FUNCTION FOR COPPER CALCULATED FROM EQ. (3.11). The bottom of the conduction band is at the fermi level (see Fig. 49).

For the case of clean copper, $T_f(E)$ is fairly well described by a straight line in the region between 4.5 and 11.6 eV above the fermi level. The magnitude of $T_f(E)$ is small, being only 0.19 for clean copper at 11.6 eV above the fermi level. The small value of $T_f(E)$ helps to explain the small magnitude of the photoelectric yield from clean copper. Because $T_f(E)$ for clean copper is not too much different from a straight line, we see that $T_f(E)$ severely modulates the shape of the experimental EDCs from clean copper.

However, the factor that determines the shape of the experimental EDCs is not $T_f(E)$, but the effective threshold function $EFFTH(E)$, which is given by Eq. (3.108). $EFFTH(E)$ for clean copper is plotted in Fig. 62,

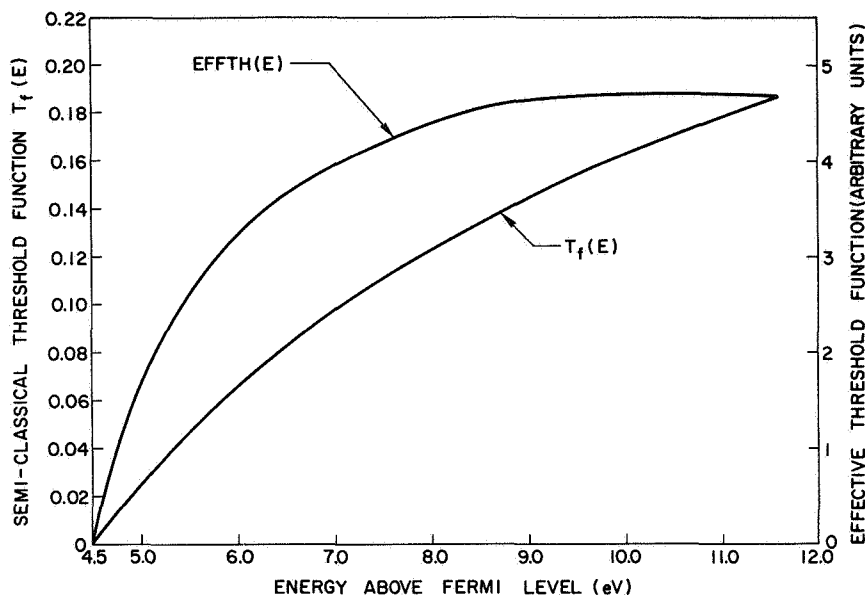


FIG. 62. COMPARISON OF SEMICLASSICAL THRESHOLD $T_f(E)$ TO EFFECTIVE THRESHOLD FUNCTION $EFFTH(E)$ FOR COPPER. The curve for $EFFTH(E)$ applies only in the region of photon energies between 7.7 eV and 11.6 eV.

and compared with the semiclassical threshold function $T_f(E)$. $EFFTH(E)$ has the character of a step function, in that $EFFTH(E)$ is nearly constant in the region between 7.0 and 11.6 eV above the fermi level. Thus, the shapes of the EDCs in this region are nearly replicas of the valence band density of states, as can be verified by comparing the shape of the experimental EDCs of Fig. 56 with the shape of the valence band density of states of Fig. 49.

H. THE IMAGINARY PART OF THE DIELECTRIC CONSTANT $\epsilon_2(\omega)$ FOR COPPER

By using Eq. (3.98) and assuming constant matrix elements, the shape of the imaginary part of the dielectric constant $\epsilon_2(\omega)$ can be calculated solely from the optical density of states of Fig. 49. "Conservation of the wave vector \vec{k} " is not considered to be an important selection rule

in these calculations. The results are shown in Fig. 63, where four major pieces of structure are evident. These peaks in $\epsilon_2(\omega)$ can be associated with well defined transitions between certain valence band states and conduction band states in Fig. 49. These identifications are presented in Table 2.

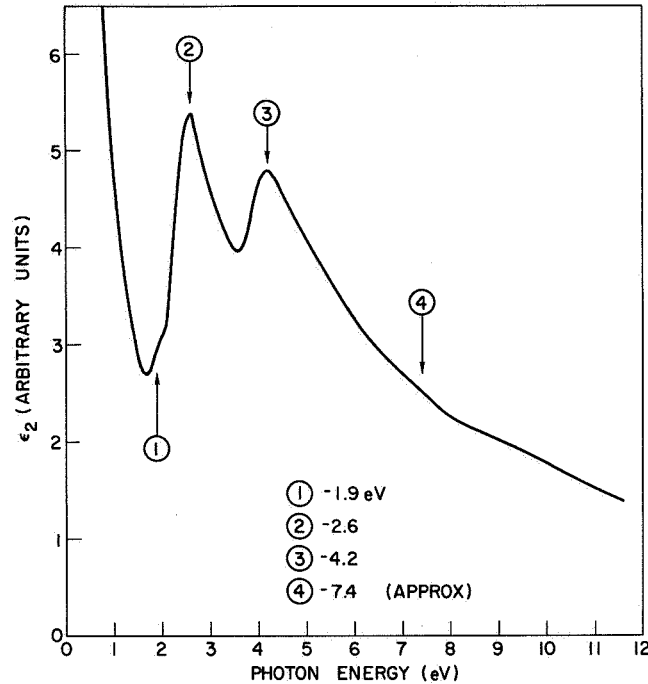


FIG. 63. ϵ_2 CALCULATED FROM OPTICAL DENSITY OF STATES OF COPPER (Fig. 49).

TABLE 2. ORIGIN OF PEAKS IN THE CALCULATED $\epsilon_2(\omega)$ FOR COPPER

Peak in $\epsilon_2(\omega)$ (Fig. 63)	Initial Valence Band State (Fig. 49)	Final Conduction Band State (Fig. 49)
①	④	②
②	⑤	③
③	⑤	②
④	⑨	③

Thus, we see that peaks ① and ③ in $\epsilon_2(\omega)$ are due to transitions to the experimentally observed conduction band peak ②, and that peaks ② and ④ in $\epsilon_2(\omega)$ are due to the onset of transitions from a high density of states in the valence band to empty states just above the fermi level.

The sharp rise in $\epsilon_2(\omega)$ at low photon energies is due to the $(1/\omega)^2$ factor in Eq. (3.98), and is not due to any strong optical transitions.

The shape of the calculated $\epsilon_2(\omega)$ is compared with the "experimental" values of $\epsilon_2(\omega)$ in Figs. 64 - 66. The experimental values of $\epsilon_2(\omega)$

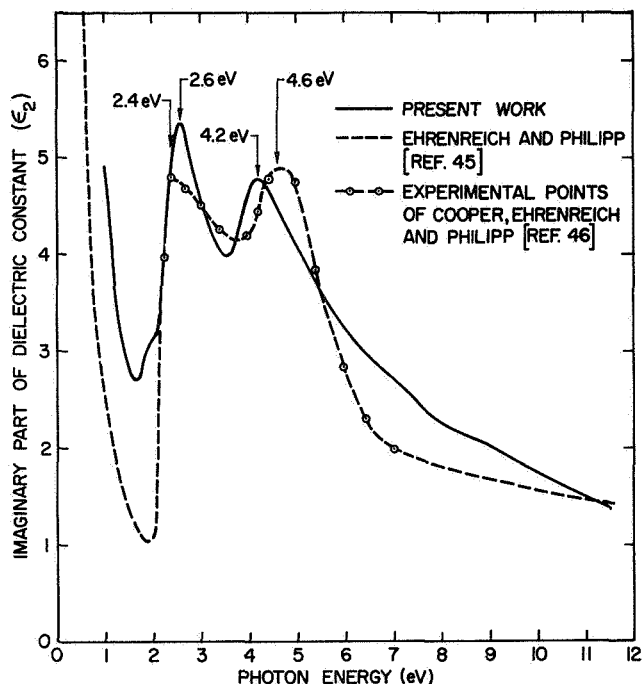


FIG. 64. COMPARISON OF CALCULATED ϵ_2 FOR COPPER WITH THE RESULTS OF REF. 45 AND REF. 46.

have all been deduced from various reflectivity measurements, but the results of different investigators are not completely consistent, resulting in the necessity to compare the calculated $\epsilon_2(\omega)$ with the results of several different experiments. As can be seen by inspection of Figs. 64 - 66, the agreement between the major features of the calculated $\epsilon_2(\omega)$ and the major features of the "experimental" $\epsilon_2(\omega)$ is indeed very good, indicating that the important structure in $\epsilon_2(\omega)$ between 1.5 and 11.6 eV can be accounted for in a "natural" way by an analysis based upon nondirect transitions and the optical density of states of Fig. 49.

In one of the experiments [Ref. 48b], the reflection at low energies was carefully measured, and a discrepancy between the expected free-electron behavior and the measurement occurred at an energy of about

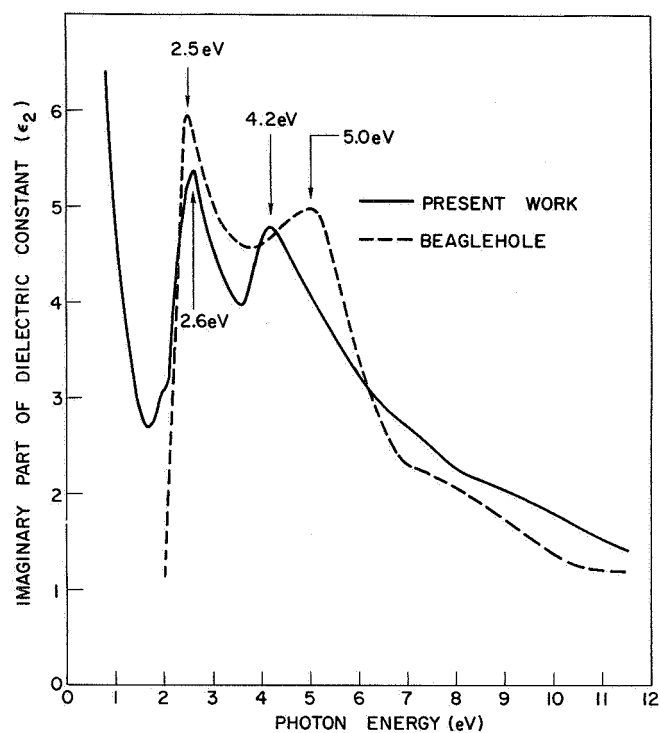


FIG. 65. COMPARISON OF CALCULATED ϵ_2 FOR COPPER WITH BEAGLEHOLE'S ϵ_2 (REF. 47).

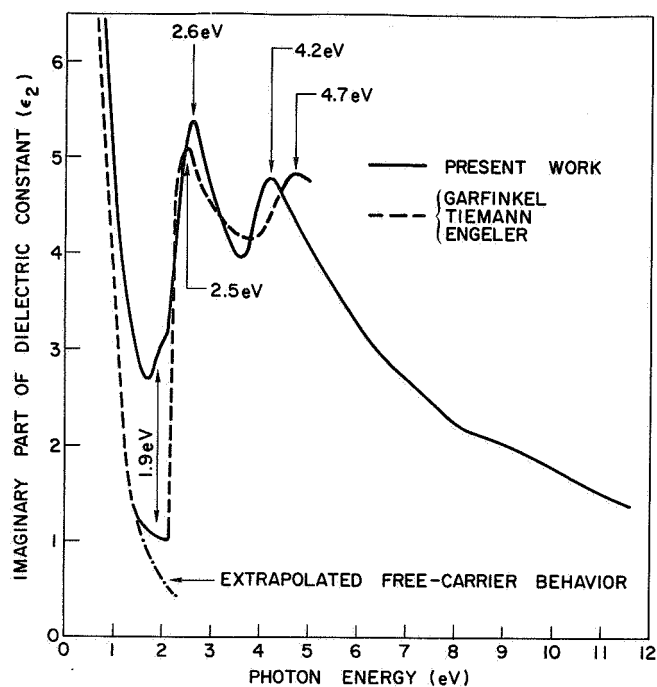


FIG. 66. COMPARISON OF CALCULATED ϵ_2 FOR COPPER WITH THE ϵ_2 OF GARFINKEL ET AL (REF. 48b).

1.9 eV, as can be seen in Fig. 66. The location of this discrepancy is in excellent agreement with the location of shoulder (1) in the calculated $\epsilon_2(\omega)$.

Peak (2) of the calculated $\epsilon_2(\omega)$ occurs at a photon energy of about 2.6 eV, which is within about ± 0.1 eV of all the experimental values. Again, there is excellent agreement between the calculated $\epsilon_2(\omega)$ and the "experimental" $\epsilon_2(\omega)$.

Peak (3) of the calculated $\epsilon_2(\omega)$ occurs at a photon energy of 4.2 eV, and the corresponding experimental peak is found by various investigators to occur between 4.6 and 5.0 eV. Thus, the calculated peak location appears to be several tenths of an eV below the experimental values. The location of peak (3) in the calculated $\epsilon_2(\omega)$ is determined largely by the location of peak (2) in the conduction band density of states of Fig. 49 which was experimentally found by Berglund and Spicer [Ref. 37] to occur at 1.8 eV above the fermi level. In Berglund and Spicer's experimental EDCs, a pronounced fixed peak appeared at about 0.15 eV above the vacuum level. Since the vacuum level was 1.65 eV, this peak in the EDCs was interpreted as a peak in the conduction band density of states at an energy 1.8 eV above the fermi level. Kane [Ref. 23], however, has recently pointed out that group velocity effects coupled with small energy losses due to inelastic electron-phonon collisions can cause a sharp peak in the conduction band density of states to appear as a peak in the photoelectric EDCs at an energy several tenths of an eV lower than the energy of the conduction band peak. Indeed, at an energy about 2 eV above the fermi level, electron-phonon scattering could very well be important, since the electron-electron scattering length $L(E)$ is about 800 \AA (Fig. 60) and the electron-phonon scattering length is estimated [Ref. 18] to be about 400 \AA . Thus, the electron-phonon scattering length is considerably shorter than the electron-electron scattering length, and electron-phonon scattering should be included in an accurate analysis of electrons that are photoemitted within a few eV above the fermi level. Consequently, it is conceivable that the observed photoemission peak at 1.8 eV above the fermi level corresponds to a peak in the conduction band density of states at 2.0 or 2.1 eV above the fermi level. If this small correction was made, the location of peak (3) in the calculated $\epsilon_2(\omega)$

would increase by several tenths of an electron volt, and would be in very close agreement with the corresponding "experimental" peak.

Much of the "strength" in $\epsilon_2(\omega)$ in the vicinity of peak (4) of Fig. 63 is due to transitions from the deep-lying valence band peak (9) of Fig. 49. In Figs. 64 and 65, the calculated $\epsilon_2(\omega)$ at energies between 6.5 and 10 eV is about 10 percent too high. A reduction of about 25 percent in the amplitude of valence band peak (9) would eliminate this discrepancy. If peak (9) was completely absent, the calculated $\epsilon_2(\omega)$ would fall below the experimental value, and the calculated photoelectric yield and EDCs would not be in good agreement with the experimental values.

In the region of photon energies between 1 and 2 eV, the magnitude of the calculated $\epsilon_2(\omega)$ is about a factor of two greater than the experimental $\epsilon_2(\omega)$. In this range of photon energies, the optical transitions are largely due to transitions between s- and p-derived wavefunctions, and it may be that the assumption of constant matrix elements is not valid. However, at higher photon energies between 2 and 11.6 eV, optical transitions from d band states dominate the absorption spectrum, and the assumption of constant matrix elements and nondirect transitions appears to be justified by the close agreement between the calculated $\epsilon_2(\omega)$ and the "experimental" $\epsilon_2(\omega)$.

Another point to be considered is the "blending" of the conduction band density of states to the valence band density of states at the fermi level, since the calculated $\epsilon_2(\omega)$ is sensitive to the value of the conduction band near the fermi level. Because there is evidence [Ref. 37] for a peak in the valence band density of states a few tenths of an eV below the fermi level, it is difficult to determine exactly how to match the conduction band and valence band at the fermi level. Figure 67 shows two possibilities that are intended to represent extreme cases bracketing any reasonable match at the fermi surface. In Curve I, the valence band peak just below the fermi level is extended about 0.4 eV into the conduction band, and in Curve II, it is assumed that the conduction band is perfectly flat near the fermi level. Figure 68 compares the values of $\epsilon_2(\omega)$ that are calculated from curves I and II of Fig. 67. The only major difference is that curve I results in an $\epsilon_2(\omega)$ with a peak height at 2.6 eV that is in good agreement with the data of Beaglehole [Ref. 47]

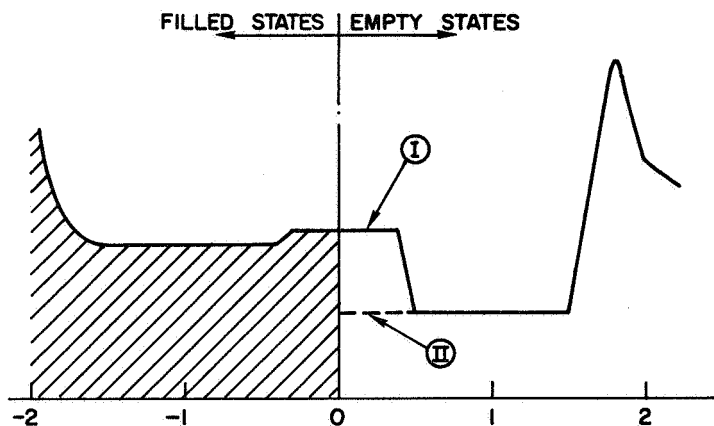


FIG. 67. DIFFERENT OPTICAL DENSITIES OF STATES USED TO CALCULATE ϵ_2 FOR COPPER (SEE FIG. 49).

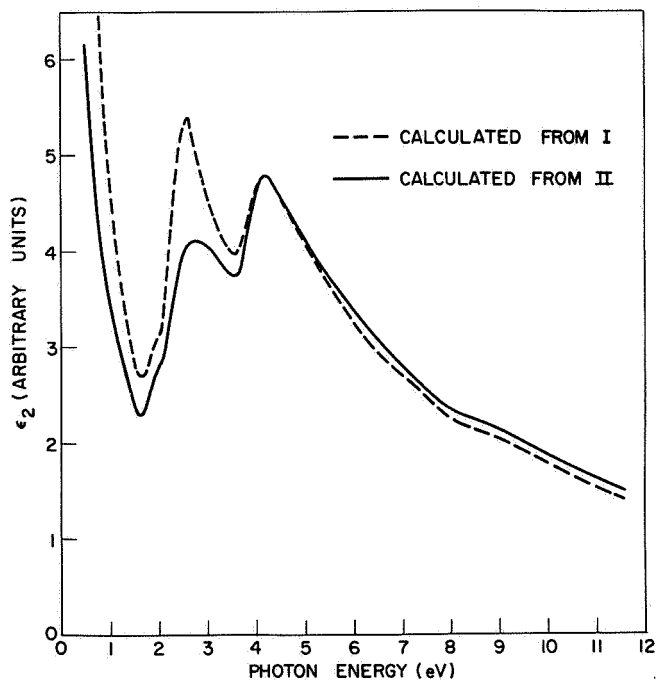


FIG. 68. COMPARISON OF SHAPES OF ϵ_2 CALCULATED FROM DENSITY OF STATES I AND FROM DENSITY OF STATES II (SEE FIG. 67).

and Garfinkel [Ref. 48] (Figs. 65 and 66), and that curve II results in a peak height at 2.6 eV that is in closer agreement with the data of Ehrenreich and Philipp [Ref. 45] (Fig. 64). Thus, the presently available experimental results for $\epsilon_2(\omega)$ are not consistent enough to determine whether or not there is a "peak" in the conduction band density of states just above the fermi level.

We have seen that a calculation based upon nondirect transitions and the optical density of states of Fig. 49 accounts in a "natural" way for all of the major features of $\epsilon_2(\omega)$ in the range of photon energies between about 1.5 and 11.6 eV. Cooper et al [Ref. 50a] and Phillips and Mueller [Ref. 43] have attempted to calculate $\epsilon_2(\omega)$ for copper by using Segall's [Ref. 58] and Burdick's [Ref. 53] energy bands in an analysis based upon " \vec{k} -conservation" and direct transitions, as described by Eq. (3.38). Both of these calculations give poor agreement with the shape of the experimentally determined $\epsilon_2(\omega)$, especially with regard to the peak in $\epsilon_2(\omega)$ at 2.6 eV. In both calculations, the peak at 2.6 eV is small by a factor of about three, and Phillips [Ref. 43] has hypothesized that the peak in $\epsilon_2(\omega)$ at 2.6 eV may be due to a "virtual exciton resonance." There remain the possibilities that such "resonances" do indeed exist, or that more accurate energy band calculations will result in "better" calculations of $\epsilon_2(\omega)$ based upon direct transitions. However, there exists the fact that the calculation of $\epsilon_2(\omega)$ based upon nondirect transitions can account very well for the major features in the experimental $\epsilon_2(\omega)$, and that the calculations based upon direct transitions have been notably unsuccessful.

Using the band structure of Fig. 50, Cooper et al [Ref. 50a] have associated the two major peaks in $\epsilon_2(\omega)$ with direct transitions between critical points. They have assigned the peak at 2.6 eV to be due to transitions from L_2' to L_{32} , and have assigned the peak at 4.6 eV to be due to transitions from X_5 to X_4' . Since peak (2) in the conduction band of Fig. 49 and the X_4' point lie at approximately the same energy, the assignment $X_5 \rightarrow X_4'$ appears to be consistent with the nondirect transition analysis of $\epsilon_2(\omega)$, as seen from Table 2. However, the critical point L_{32} lies below the fermi level, and there is no critical point in the joint density of states coupling L_3 to states above the fermi level.

This difficulty is not encountered in the nondirect transition analysis, which depends only upon the total density of states just above the fermi level. The energy band calculation of Fig. 50 is only for states along symmetry directions, and there exists the possibility that there may be important critical points off the symmetry lines. In addition, more accurate calculations of the energy band structure of copper in the future could conceivably change the energy of the X_4' critical point in the conduction band. For these reasons, the assignment $X_5 \rightarrow X_4'$ for the peak in $\epsilon_2(\omega)$ at 4.6 eV must be regarded with some reservation.

I. THE SPECIFIC HEAT FOR COPPER

The electronic specific heat can be related to the density of states at the fermi level by the expression [Ref. 59]

$$\gamma = \frac{k^2 \pi^2 N(E_f)}{3} \left[\frac{\text{millijoule}}{\text{mole } (^{\circ}\text{K})^2} \right] = (2.357) N \left[\frac{\text{electrons}}{\text{eV-atom}} \right] \quad (4.1)$$

where γ is the electronic specific heat (neglecting electron-phonon interactions) and where $N(E_f)$ is the density of states at the fermi level. The temperature dependence of the specific heat can be determined experimentally, and the coefficient of the linear term is given in Ref. 95 as

$$\gamma = 0.753 \left[\frac{\text{millijoule}}{\text{mole } (^{\circ}\text{K})^2} \right]$$

so that

$$N(E_f) = 0.32 \left[\frac{\text{electrons}}{\text{eV-atom}} \right]$$

This value of $N(E_f)$ can be used as a check on the optical density of states of copper.

Assuming that the deep-lying peak (9) in Fig. 49 represents the "true" density of states, we can normalize the optical density of states to the total number of electrons in the valence band. There are eleven electrons in the valence band of copper, since the outer electron configuration is $3d^{10}4s^1$. The resulting normalized optical density of states is shown as

the solid line labeled N_V^{AB} in Fig. 69, and the "a priori" optical density of states is found to be 0.38 electrons/eV-atom at the fermi surface, not far from the value of 0.32 electrons/eV-atom derived from the specific heat. The dashed line labeled N_V^{ABS} shows how the valence band optical density of states can be adjusted at the fermi level to agree exactly with the value derived from the specific heat. As can be seen from Fig. 69, the necessary adjustment is very small, and we find the "a priori" optical density of states that was determined from photoemission studies to be in amazingly close agreement at the fermi surface with the value derived from the specific heat.

The fact that use of the deep-lying peak ⑨ in the normalization led to good agreement in the density of states at the fermi surface is evidence that peak ⑨ does indeed represent a peak in the true density of states.

J. THE RIGID BAND MODEL AND THE DENSITY OF STATES FOR NICKEL

According to the rigid band model [Ref. 13], the density of states for ferromagnetic nickel can be obtained from the density of states for

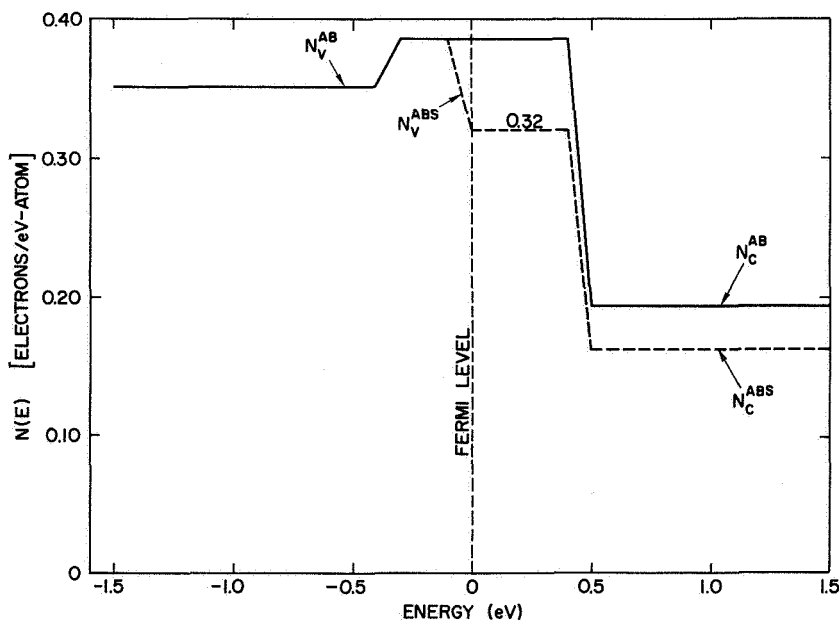


FIG. 69. ADJUSTMENT OF THE OPTICAL DENSITY OF STATES FOR COPPER TO AGREE WITH THE VALUE DERIVED FROM THE SPECIFIC HEAT.

copper by first assigning 5 spin-up and 5 spin-down electrons to two bands having the same density of states as for copper, then shifting one band relative to the other by the exchange energy, and then at each energy, summing the densities of states in the two bands. Blodgett [Ref. 13] has found that a reasonable "average" exchange splitting is about 0.6 eV. Using this value for the exchange energy, the rigid band model described above was used to calculate the density of states of ferromagnetic nickel from the optical density of states of copper. Before this was done, a magnitude was assigned to the optical density of states for copper by normalizing the valence band in the optical density of states of Fig. 49 to hold eleven electrons. The resulting "nickel" density of states is shown as the solid curve in Figs. 70 and 71, where the fermi level was

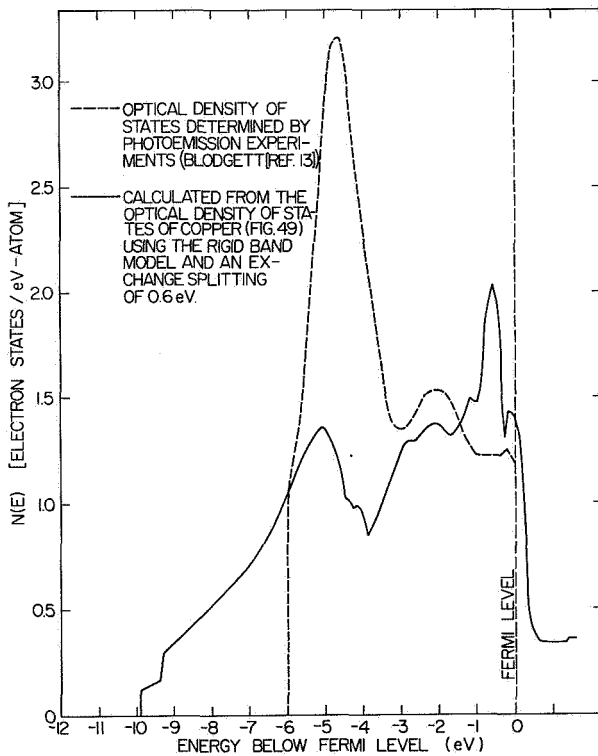


FIG. 70. COMPARISON OF BLODGETT'S [REF. 13] OPTICAL DENSITY OF STATES FOR NICKEL WITH THE DENSITY OF STATES DERIVED FROM THE OPTICAL DENSITY OF STATES OF COPPER USING THE RIGID BAND MODEL AND AN EXCHANGE SPLITTING OF 0.6 eV.

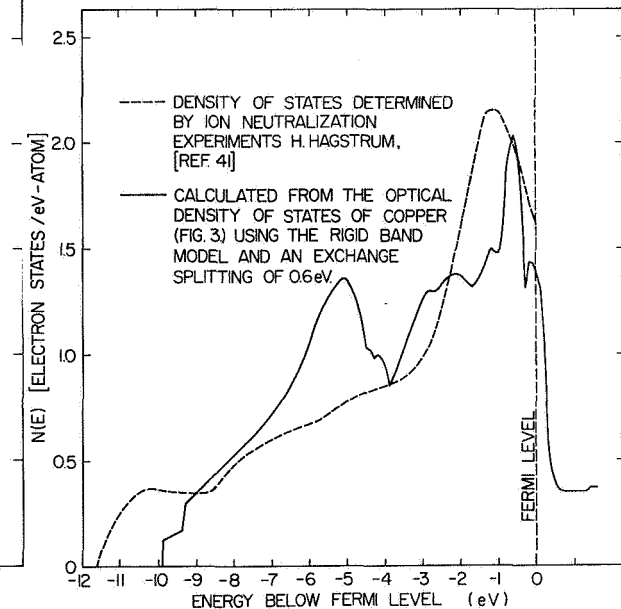


FIG. 71. COMPARISON OF HAGSTRUM'S [REF. 41] NICKEL DENSITY OF STATES WITH THE DENSITY OF STATES DERIVED FROM THE OPTICAL DENSITY OF STATES OF COPPER USING THE RIGID BAND MODEL AND AN EXCHANGE SPLITTING OF 0.6 eV.

positioned so that the valence band of nickel would hold ten $3d^8 4s^2$ electrons.

Figure 71 compares the "rigid-band" nickel density of states with the nickel density of states deduced by Hagstrum [Ref. 41] from ion-neutralization spectroscopy experiments. The two curves are in good qualitative agreement, in that the major structure in both cases is a strong peak at about 1 eV below the fermi level. There is a significant discrepancy between the two curves, in that the "rigid-band" density of states has a peak at about 5 eV below the fermi level, whereas no such peak appears in Hagstrom's results.

Figure 70 compares the "rigid-band" nickel density of states with the density of states derived by Blodgett [Ref. 13] from photoemission studies. The major structure in Blodgett's curve is a very strong peak at 5 eV below the fermi level and smaller peaks at 2 and 0.2 eV below the fermi level. By comparison, the "rigid-band" nickel density of states has small peaks at 5 and 2 eV below the fermi level and a relatively larger peak at about 0.5 eV below the fermi level. Thus, there is qualitative agreement in the location of the three major peaks and in the magnitudes of the peaks at 0.2 and 2 eV below the fermi level. However, the peak at 5 eV below the fermi level is much larger in Blodgett's optical density of states than in the "rigid-band" density of states derived from copper. A possible explanation is that matrix element effects enhanced the magnitude of the 5-eV peak in Blodgett's photoemission data, but such a hypothesis has yet to be verified, and should be treated with reservation until further studies on nickel have been carried out.

K. COMPARISON OF THE PRESENT WORK ON CLEAN COPPER WITH EARLIER WORK ON CESIATED COPPER

The experimental EDCs obtained from clean copper differ from the experimental EDCs obtained earlier from cesiated copper [Ref. 37] in two significant ways: (1) The EDCs from clean copper show fine structure not present in the EDCs from cesiated copper, and (2) the EDCs from clean copper show no evidence of a large d-band peak at 3.2 eV below the fermi level, which appeared in the EDCs from cesiated copper. These discrepancies were apparently caused by an interaction between the cesium and the copper in the photoemission experiments reported on by Berglund and Spicer [Ref. 37].

However, the general features of the new photoemission data on clean copper are consistent with the earlier work on cesiated copper. Because of the apparent cesium-copper interaction, the optical density of states of Fig. 49 is probably more representative of copper than the earlier results deduced from cesiated copper alone.

An attempt was made to calculate the photoelectric yield and the EDCs from cesiated copper by using the optical density of states of Fig. 49 and the same analysis that was used to calculate the yield and the EDCs for clean copper. The only difference was that the vacuum level was set to 1.5 eV, the appropriate value for copper covered with a surface monolayer of cesium; the magnitude of the electron-electron scattering length was the same as had been deduced from the photoemission experiments on clean copper. Since electron-phonon scattering was not included in the analysis, good results were not expected at energies only a few eV above the fermi level, where the electron-phonon scattering length is shorter than the

electron-electron scattering length.

Some of the results of the calculation are shown in Fig. 72 and in Figs. 73a through 73e. As seen from Fig. 72, the magnitudes of the calculated and experimental quantum yield are in good qualitative agreement just above the vacuum level and in the range of photon energies between 4 and 11.6 eV. However, there is a large discrepancy between 2 and 4 eV. This discrepancy may be due to such causes as electron-phonon scattering, inappropriateness of the free electron model in calculating transport effects and the threshold function, and copper-cesium interaction. Strangely enough, quite good agreement is obtained between the SHAPES of the calculated EDCs and the experimental EDCs, even

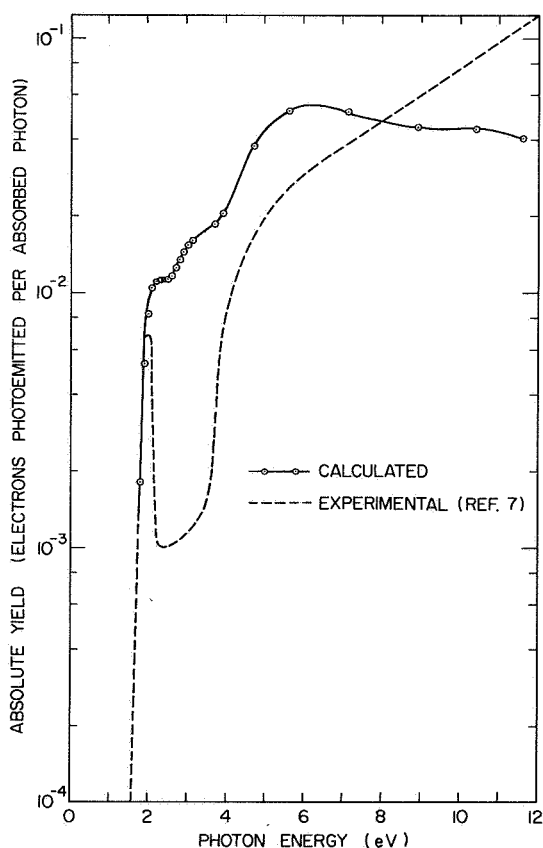
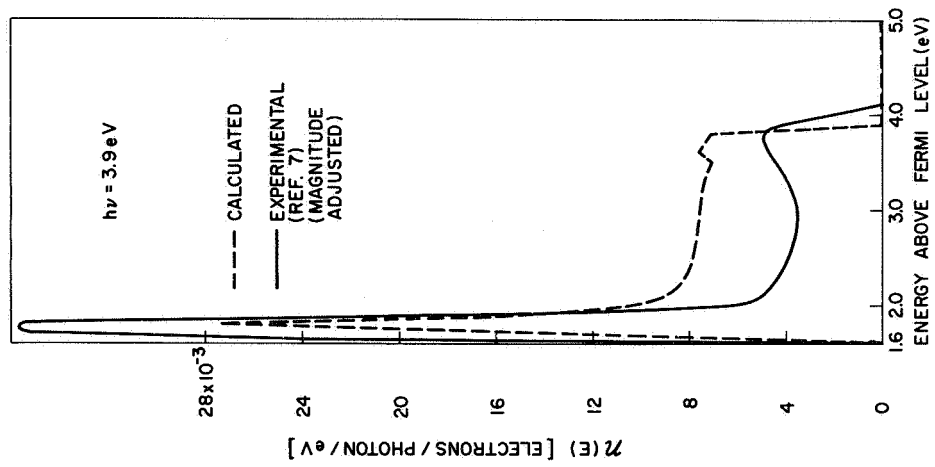
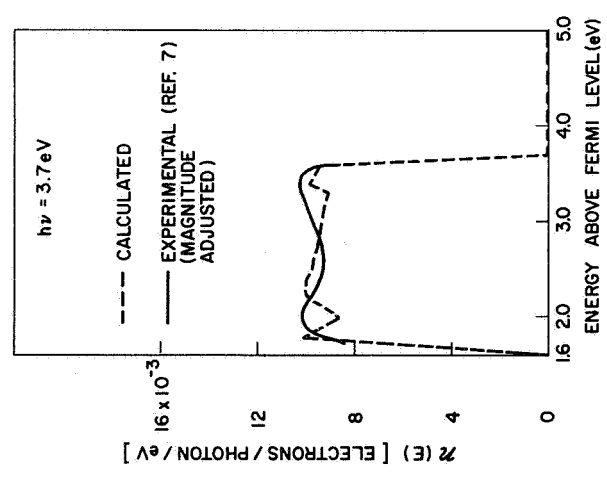


FIG. 72. COMPARISON OF CALCULATED VS EXPERIMENTAL PHOTOELECTRIC YIELD FOR COPPER WITH A SURFACE MONOLAYER OF CESIUM.

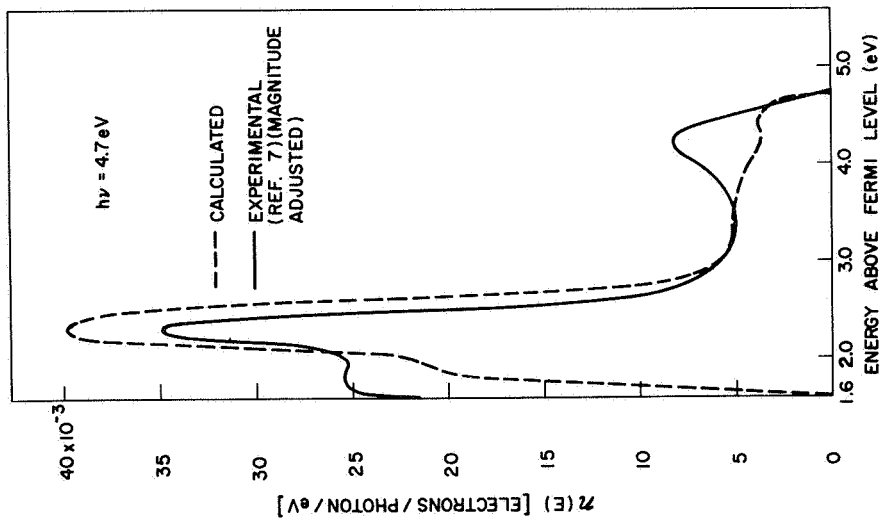


(a)

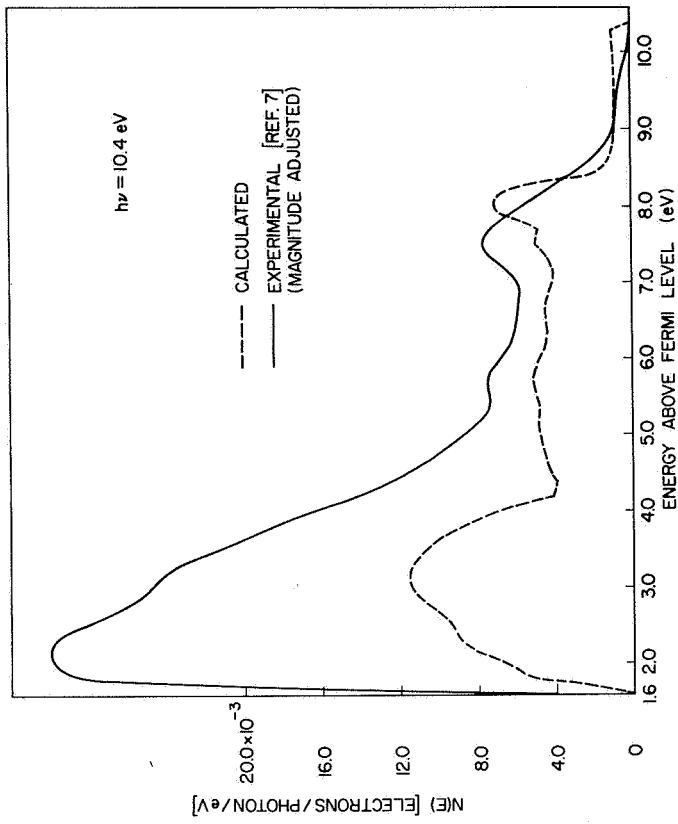


(b)

FIG. 73. CALCULATED AND EXPERIMENTAL ENERGY DISTRIBUTION CURVES FOR COPPER.



(c)



(d)

FIG. 73. CONTINUED.

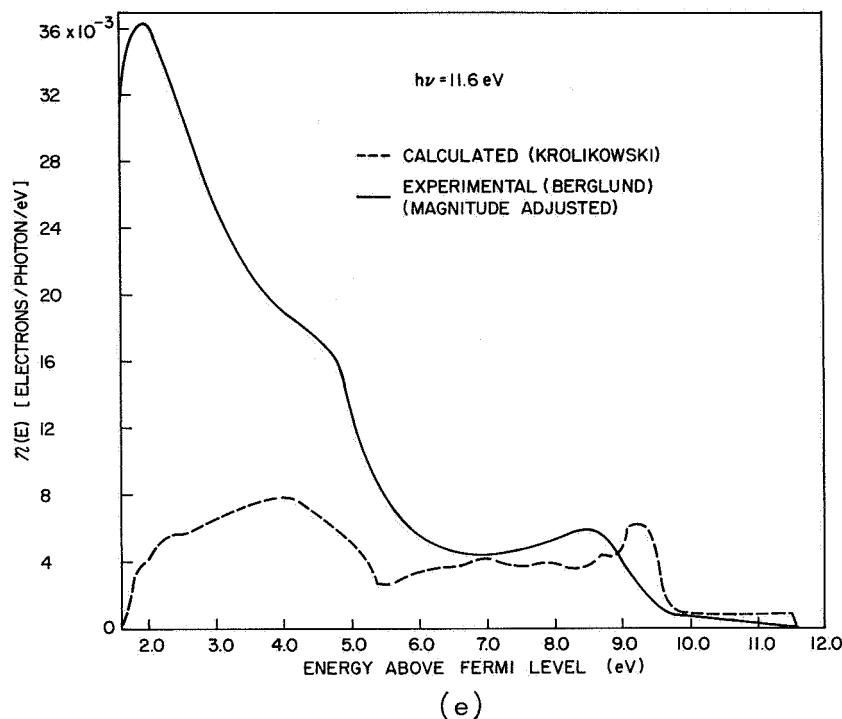


FIG 73. CONTINUED.

in the range of photon energies where there is a large discrepancy in the calculated yield. Figures 73a through 73e compare the shapes of the calculated and the experimental EDCs, and the agreement is seen to be quite good. The calculated curves do not include secondary electrons, which appear as a large, fixed peak of slow electrons in the experimental EDCs of Figs. 73d and 73e. Figures 73d and 73e also show evidence of photoemission from the deep-lying valence band peak 9, which is quite prominent in both the calculated and the experimental EDCs.

The calculated value of $\epsilon_2(\omega)$ obtained in the earlier work of Berglund and Spicer [Ref. 37] appears to be in somewhat better agreement with experiment than the $\epsilon_2(\omega)$ that is calculated from Fig. 49, as can be seen by comparing Fig. 27 of Ref. 37 with Fig. 64 of this chapter. However, it is difficult to see how Berglund and Spicer's calculated curve for $\epsilon_2(\omega)$ (Fig. 27, Ref. 37) can be derived from their density of states (Fig. 12, Ref. 37), and it appears that some rather serious errors were made in their calculation of $\epsilon_2(\omega)$. Thus, the excellent agreement between the calculated and the experimental $\epsilon_2(\omega)$ in Fig. 27 of Ref. 37 appears to be erroneous, and the subsequent conclusions based upon this

excellent agreement appear to be unjustified. However, it must be emphasized that the conclusions of Ref. 37 are not incorrect, but appear to be entirely consistent with the present work on clean copper.

L. CONCLUSIONS

This chapter has described experimental photoemission measurements on copper that have led to the construction of an optical density of states in the region ± 11.6 eV about the fermi level. An analysis based upon this optical density of states and nondirect transitions has been remarkably successful in calculating the magnitude and shape of the photoelectric yield, the magnitude and shape of the photoelectric energy distributions, the magnitude and shape of the electron-electron scattering length, and the shape of $\epsilon_2(\omega)$. In addition, the density of states at the fermi level is found to be consistent with the value derived from the specific heat, and the valence band optical density of states bears a close resemblance to certain energy band calculations. Nondirect transitions are found to dominate in the photoelectric energy distributions from copper, except for a small contribution of direct transitions from s- and p-derived states near L_2' to states near L_1 , as discussed earlier by Berglund and Spicer [Ref. 37]. Without exception, all of the optical transitions from d band states are well described by nondirect transitions, perhaps as a result of their localized character.

Because of the overwhelming success of the nondirect model in explaining a large number of different phenomena in copper, it must be concluded that in the range of photon energies between 1.5 and 11.6 eV, the optical absorption in copper is dominated by nondirect transitions, and that the direct transition model is inadequate in describing the optical absorption process.



PRECEDING PAGE BLANK NOT FILMED.

V. PHOTOEMISSION FROM GOLD

This chapter presents new photoemission data obtained from evaporated films of gold in the range of photon energies between 5 and 21.2 eV. The measurements between 5 and 11.6 eV were obtained from films evaporated and studied at a pressure of about 5×10^{-9} torr, using the oil-free vacuum system and the photoemission chamber described in Chapter II. The measurements at higher photon energies were made in low vacuum, using the "knock-off tube" technique described in Section G of Chapter II. Using these photoemission data, the analysis described in Table 1 of Chapter III has resulted in the construction of an optical density of states for gold in the region ± 11.6 eV above the fermi level. Gold is found to be qualitatively similar to copper, and the analysis for gold proceeded in much the same manner as the analysis used in studying copper. Because of the insensitivity of gold to contamination, reliable experimental values for the electron-electron scattering length in gold are available and these values are used as a check on the results deduced from photoemission studies.

A. THE OPTICAL DENSITY OF STATES FOR GOLD

The optical density of states for gold that has been deduced from photoemission studies using the analysis of Table 1 in Chapter III is shown in Fig. 74. The locations of the valence band peaks (3), (4), (5), and (6) have been deduced from the photoelectric EDCs, and the appearance of peaks (4), (5), and (6) in the EDCs is well described by the nondirect transition model, where $\Delta E_p = \Delta h\nu$. Because of the resemblance between the valence band optical density of states for gold and the valence band optical density of states for copper, it is not unreasonable to assume that peaks (4), (5), and (6) in Fig. 74 are to be associated with states derived largely from 5d-atomic wavefunctions, since the outer electron configuration of gold is $5d^{10}6s^1$ and the outer electron configuration of copper is $3d^{10}4s^1$.

The general appearance of the gold density of states in the vicinity of peak (3) in the region between the fermi level and 2 eV below the fermi level bears a close resemblance to the copper density of states in the

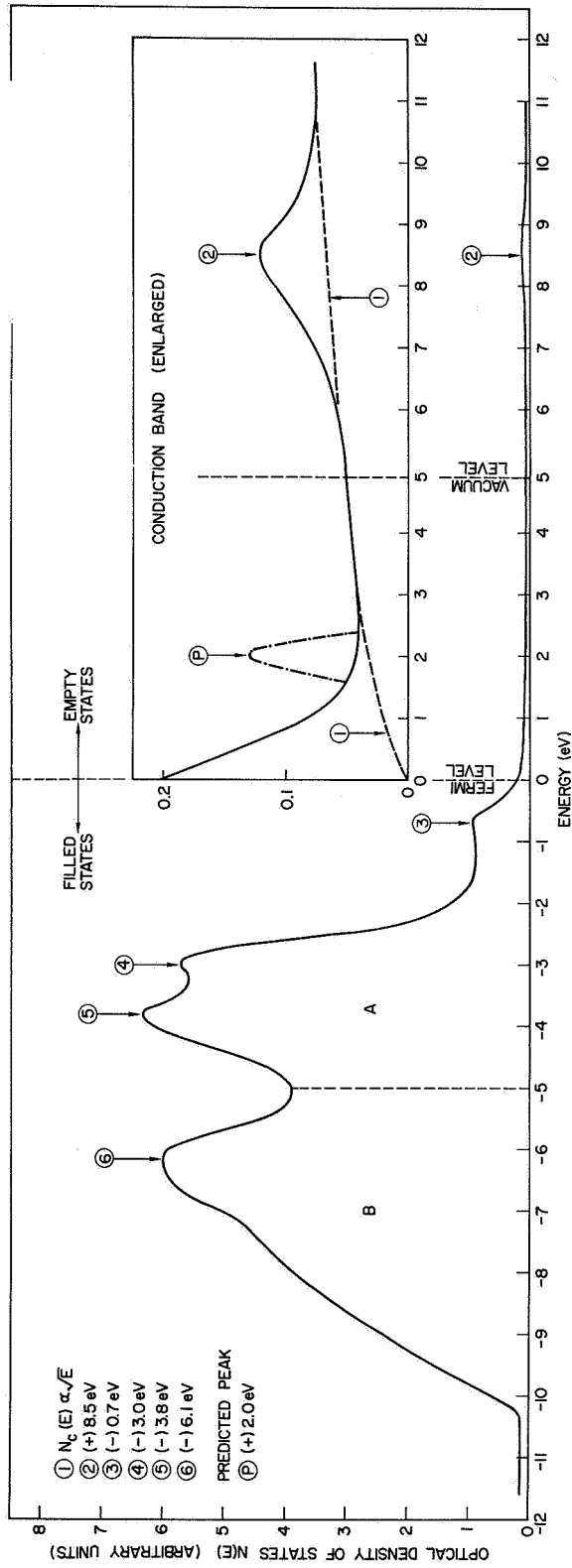


FIG. 74. OPTICAL DENSITY OF STATES FOR GOLD.

region between the fermi level and 2 eV below the fermi level. Since this region in the copper density of states is derived largely from s and p atomic wavefunctions, it seems reasonable to assume that the corresponding region in gold is also derived largely from s and p atomic wavefunctions. The correspondence between copper and gold in the region between the fermi level and 2 eV below the fermi level is even more striking because of the fact that a direct transition is seen in gold between the s- and p-derived states, and the initial states for this direct transition occur in the region between the fermi level and 2 eV below the fermi level, just as seen in copper by Berglund and Spicer [Ref. 37].

The shape of the valence band optical density of states for gold in the region between peak (3) of Fig. 74 and the fermi level has been sketched to represent the shape of the leading edge in the experimental EDCs at photon energies greater than about 7.5 eV. However, it is usually found that, at such high photon energies, the leading edge in the experimental EDCs is somewhat blurred relative to the sharpness of the leading edge seen at lower photon energies. Thus, the valence band optical density of states just below the fermi level should probably be adjusted to be considerably higher than the value indicated in Fig. 74. Such an adjustment would also make the density of states near the fermi surface agree more closely with the value calculated from the specific heat, as will be discussed later in this chapter. In addition, increasing the magnitude of the valence band density of states at the fermi surface would have the effect of increasing the magnitude of the entire conduction band density of states, which has been scaled to match the valence band density of states at the fermi level. As shown in Fig. 74, the magnitude of the conduction band optical density of states seems to be unreasonably small relative to the magnitude of the valence band optical density of states.

The conduction band optical density of states of Fig. 74 consists basically of a free-electron conduction band envelope, with the bottom of the free electron band placed at the fermi level, just as in the case of copper. In the region between the fermi level and 2 eV above the fermi level, the conduction band optical density of states has been blended to match the free electron density of states. In addition, there is a peak in the conduction band density of states at 8.5 eV above the fermi level.

The location of this peak has been deduced from the experimental photoelectric EDCs. Unfortunately, the vacuum level for gold was found to be about 4.9 eV above the fermi level, and no experimental information was available concerning structure that may very well exist in the region between the fermi level and about 4.9 eV above the fermi level.

Because cesium is known to react with gold to form the compound CsAu, it is likely that conventional [Ref. 37] "cesiating" in order to lower the vacuum level would also result in bulk-alloying between the cesium and the gold. DiStefano [Ref. 60] has suggested that a possible solution might be to cool the gold to very low temperatures, and then evaporate a monolayer of cesium onto the surface of the gold. By this technique, the low temperature could conceivably inhibit bulk-alloying between the cesium and the gold, and successful EDCs could be measured with a vacuum level of about 1.5 eV. Alternatively, a surface monolayer of barium could be applied to the gold, thereby lowering the vacuum level to about 2.0 eV above the fermi level. In any case, a future photoemission experiment on gold with a vacuum level lowered to about 2.0 eV above the fermi level would be exceedingly valuable by providing information about structure that may very well exist in the unexplored region between the fermi level and 4.9 eV above the fermi level.

B. THE PHOTOELECTRIC YIELD FROM GOLD

The experimental photoelectric yield measured at a pressure of 2×10^{-9} torr and the calculated photoelectric yield for gold are compared in Fig. 75. The experimental yield has been corrected for reflectivity and the transmission of the LiF window, and the calculated curve was obtained using the density of states of Fig. 74 and the analysis described in Table 1 of Chapter III. Both the magnitude and the shape of the calculated yield are in excellent agreement with the experimental results. One of the most significant features of the quantum yield is that it is very small, only about 2 percent at a photon energy of about 11.6 eV above the fermi level. This small value of the photoelectric yield is due mainly to the small value of the free electron threshold function and the short electron-electron scattering length. The values found for the free electron threshold function and the electron-electron scattering length in

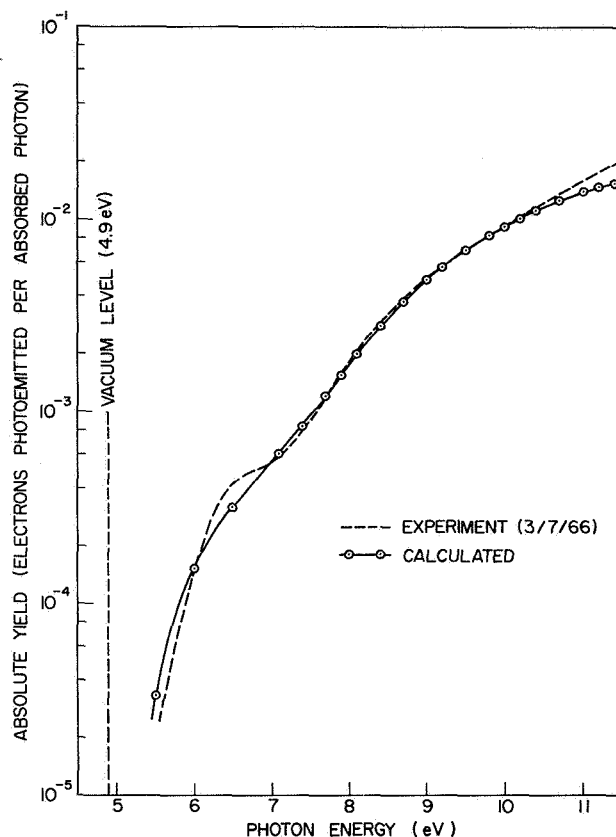


FIG. 75. COMPARISON OF EXPERIMENTAL AND CALCULATED YIELD FOR GOLD. The experimental yield was measured using the standards described in the caption of Fig. 55.

gold do not differ appreciably from the values found for copper in Chapter IV, and the yield for gold in Fig. 75 is seen to be quite similar to the yield for copper in Fig. 55. The only significant structure in the yield curve for gold is a fairly pronounced rise that begins at a photon energy of about 7.0 eV. This rise at 7.0 eV is evident in both the calculated and the experimental curves, and is due to the onset of photoemission from the d band density of states of Fig. 75.

In the calculation of the photoelectric yield and the EDCs from the density of states of Fig. 74, the electron-electron scattering length was set equal to 27 \AA at an energy 8.6 eV above the fermi level. This value is quite close to Kanter's [Ref. 49] experimental values of about 20 \AA at 8.6 eV above the fermi level, as will be discussed later in this chapter. The absorption coefficient $\alpha(\omega)$ used in calculating the yield and

the EDCs was taken from Ref. 61, and the reflection coefficient $R(\omega)$ used to correct the experimental yield for reflection was taken from the data of Refs. 46, 61, and 62.

Just as in the case of copper, the greatest error in the photoelectric yield was a ± 10 percent error due to uncertainty in the calibration standards. The overall uncertainty in the magnitude and the shape of the experimental yield curve of Fig. 75 is estimated to be less than ± 15 percent.

C. PHOTOELECTRIC ENERGY DISTRIBUTIONS FROM GOLD

Figure 76 shows a family of experimental photoelectric EDCs for gold in the range of photon energies between 7.4 and 11.6 eV above the fermi

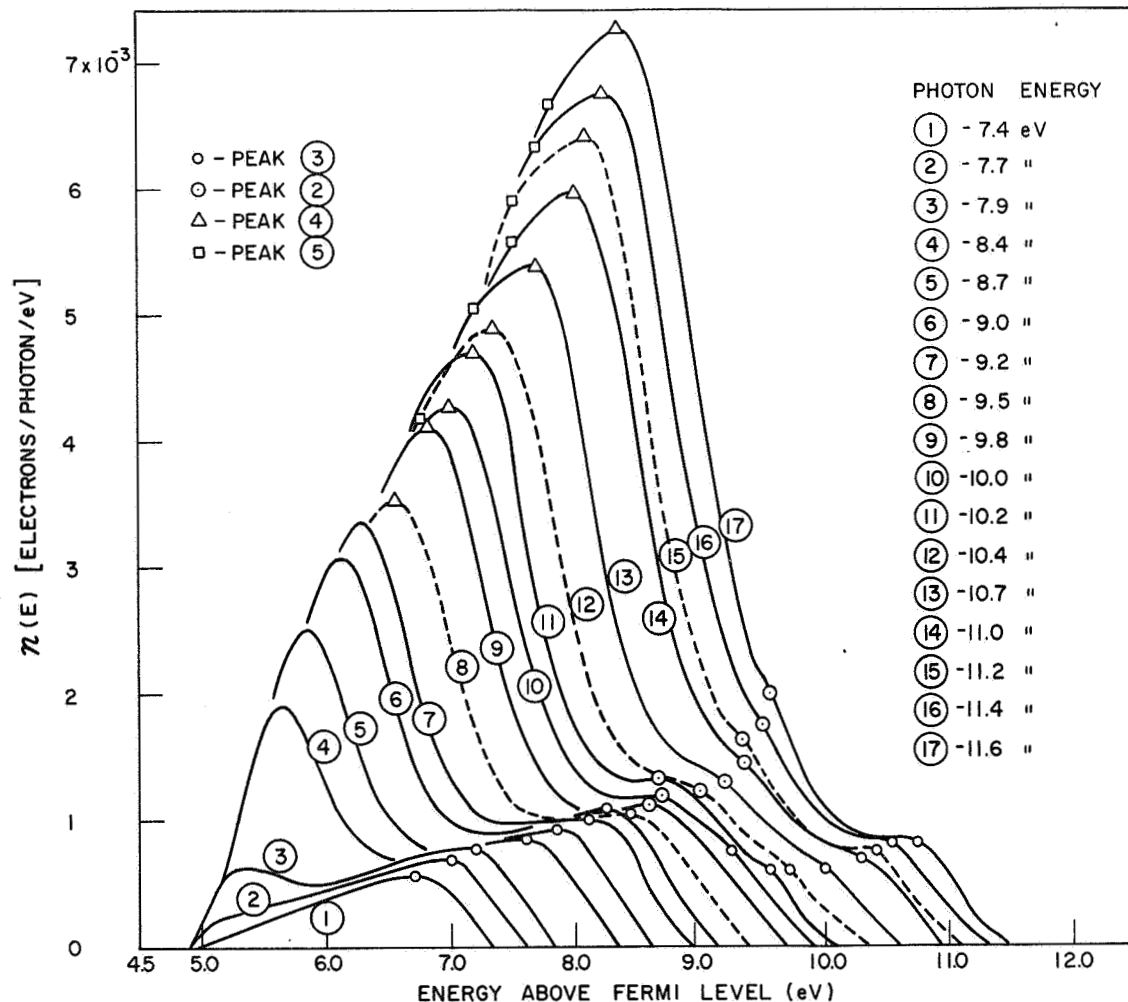


FIG. 76. FAMILY OF EXPERIMENTAL ENERGY DISTRIBUTION CURVES FOR GOLD (NORMALIZED TO YIELD).

level. These EDCs were obtained from a gold film prepared and tested in a vacuum of about 5×10^{-9} torr. Inspection of Fig. 76 shows that all the curves tend to increase in size in the vicinity of 8 to 9.5 eV above the fermi level, and this effect has been interpreted as being caused by a peak in the conduction band density of states in the vicinity of about 8.5 eV above the fermi level; this conduction band peak is labeled peak (2) in the optical density of states of Fig. 74.

The peaks in the experimental EDCs of Fig. 76 are labeled according to the notation of the optical density of states in Fig. 74. In Fig. 77, the energy E_p of these peaks is plotted as a function of photon energy in the range of photon energies between 7.4 and 21.2 eV. The points at

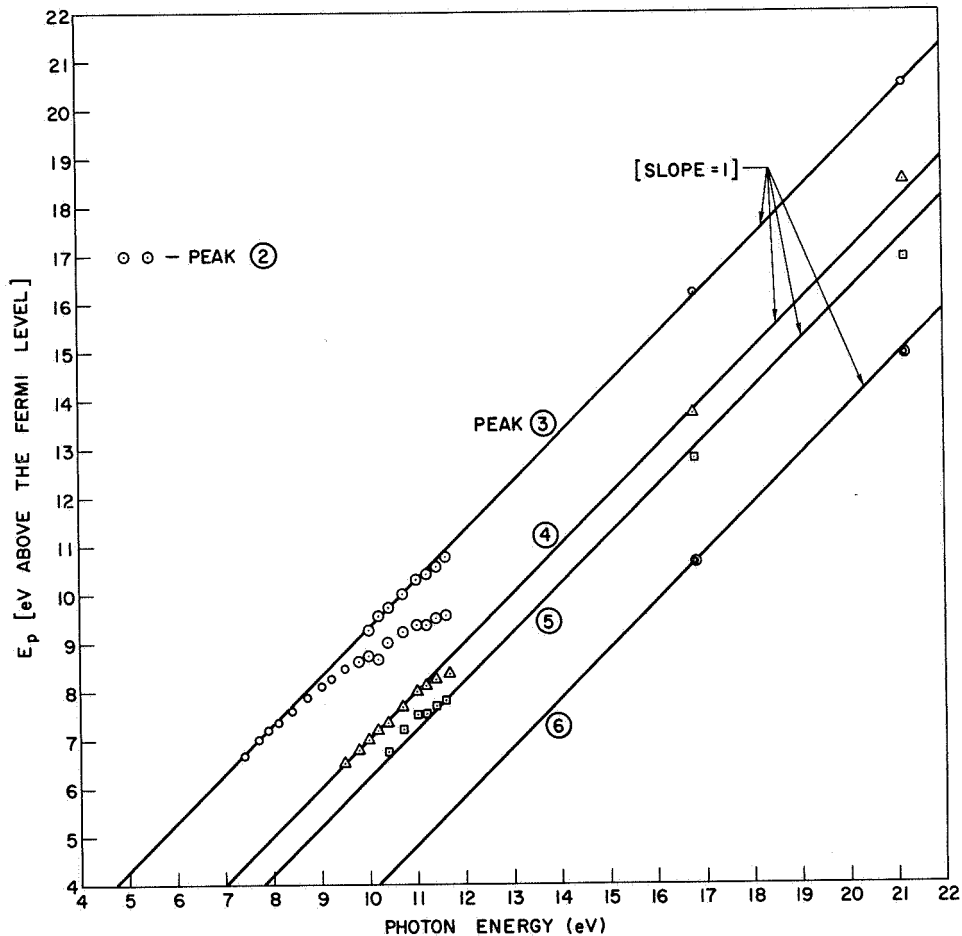


FIG. 77. PLOT OF PEAK ENERGY (E_p) VS PHOTON ENERGY FOR THE ENERGY DISTRIBUTIONS OF FIG. 76 AND FIG. 77. See Fig. 74 for identification of the peaks in terms of peaks in the density of states.

16.8 and 21.2 eV were obtained from low vacuum experiments, using the "knock-off-tube" technique described in Section H of Chapter II.

As seen from Figs. 76 and 77, the valence band peak (3) is seen to split into two peaks in the vicinity of 8 to 9.5 eV above the fermi level. One of the peaks (peak (3)) moves in the manner of nondirect transitions, where $\Delta E_p = \Delta h\nu$. The other peak, called peak (2) because it occurs in the vicinity of the conduction band peak (2) of Fig. 74, has the nature of a direct transition, where $\Delta E_p \neq \Delta h\nu$. The initial states for this direct transition are the s- and p-derived states in the range of energies between 1 and 2 eV below the fermi level, and the final states are in the range of energies between 8 and 9.5 eV above the fermi level. Thus, the s- and p-derived states in gold appear to be involved in a direct transition, just as in the case of copper, where Berglund and Spicer [Ref. 37] have made the assignment $L_2' \rightarrow L_2$ for the direct transition between s- and p-like states. The same assignment may also be appropriate for the direct transition in gold, but such an assignment can only be tentatively proposed, since no energy band calculations have yet been done for gold. As can be seen from Figs. 76 and 77, the valence band peaks (3), (4), (5), and (6) seem to move in the manner of nondirect transitions in the range of photon energies between 7.4 and 21.2 eV, indicating that the nondirect transition model dominates the optical absorption process in gold, with the exception of a single direct transition.

Peak (6) in the valence band optical density of states of Fig. 74 could not be clearly identified in the photoemission experiments from clean copper, because of the limitations of the LiF window. However, the location of peak (6) was experimentally observed by making low vacuum studies using the knock-off-tube technique described in Section G of Chapter II. In this experiment, a gold film was evaporated at ultrahigh vacuum in a knock-off-tube and the EDCs from this film were found to be identical to the EDCs shown in Fig. 76. The LiF window was then knocked-off in the low vacuum of the monochromator, which was at a pressure of about 1×10^{-4} torr. Nearly all of this pressure was due to the neon gas from the arc lamp, since the pressure in the monochromator was about 1×10^{-7} torr before the argon was allowed to flow through the arc lamp into the monochromator. The significant results of this experiment are shown in Fig. 78. The effect

of rapid contamination in the vacuum monochromator is seen in Fig. 78a, where curves completed within 5 minutes and 13 minutes after knock-off

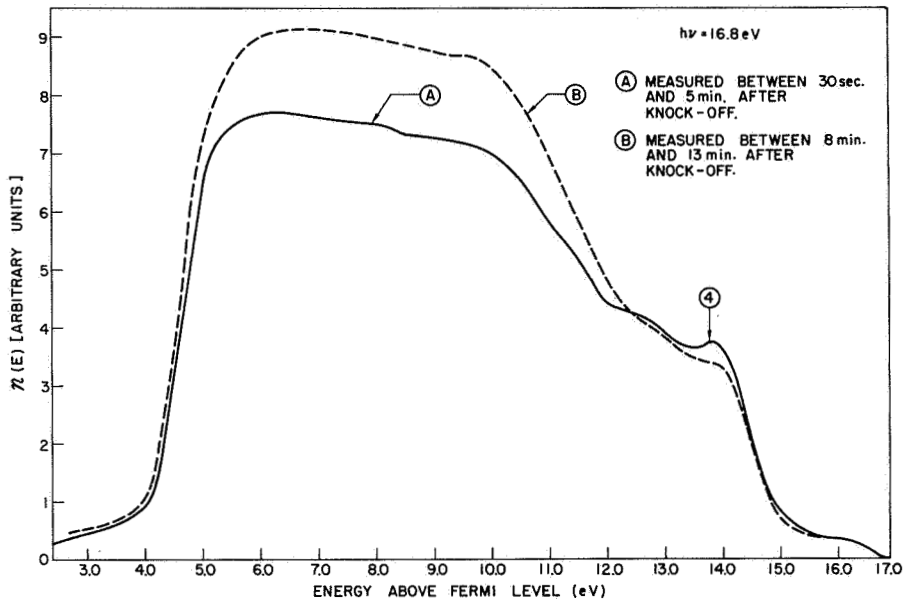


FIG. 78a. ENERGY DISTRIBUTION CURVES SHOWING DETERIORATION WITH TIME SHORTLY AFTER LiF WINDOW HAD BEEN KNOCKED OFF.

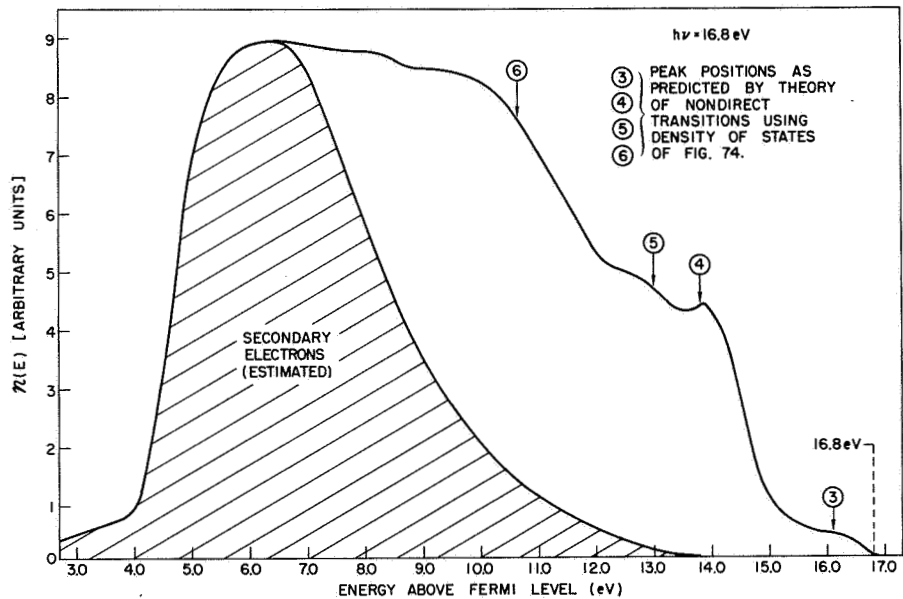


FIG. 78b. EXPERIMENTAL ENERGY DISTRIBUTION CURVE FOR GOLD OBTAINED USING A "KNOCK-OFF TUBE." The measurement of this curve was begun 30 seconds after knock-off, and completed within 5 minutes after knock-off.

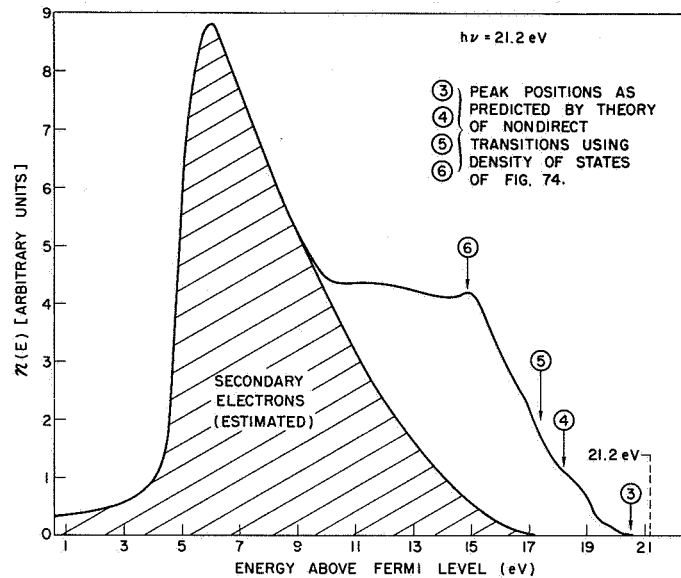


FIG. 78c. EXPERIMENTAL ENERGY DISTRIBUTION CURVE FOR GOLD OBTAINED USING A "KNOCK-OFF TUBE." The measurement was made 3 hours after the LiF window was knocked-off.

are compared. In the curve taken within 5 minutes after knock-off, peak (4) is quite distinct, whereas in the curve taken shortly afterwards, peak (4) appears only as a shoulder. Figure 78b again shows the "5-minute" curve of Fig. 78a, but with the addition of labels indicating the expected location of peaks using the optical density of states of Fig. 74 and the model of nondirect transitions. Note in Fig. 78b that the shape of the EDC in the region between 16.8 and 13.0 eV above the fermi level bears a close resemblance to the valence band optical density of states in the region between the fermi level and 3.8 eV below the fermi level, indicating that even at these high energies, the energy distribution of the primary electrons is very little distorted from the shape of the valence band optical density of states. Unfortunately, a large number of slow secondary (scattered) electrons are present in the EDC at a photon energy of 16.8 eV, and the location of peak (6) must be obtained by estimating the distribution of secondary electrons, and then subtracting the secondary distribution from the total distribution. If this is done, a peak in the "difference" distribution is found to occur at the location of label (6) in Fig. 78b. At photon energies higher than 16.8 eV, the

location of peak (6) becomes much more clearly defined as peak (6) moves farther away from the large, low energy peak of scattered electrons. At a photon energy of 21.2 eV, the location of peak (6) is very clearly defined, as shown in Fig. 78c. Thus, we see that the use of the knock-off-tube technique has resulted in the verification of the existence and the location of peak (6) in the valence band optical density of states of gold. In addition, the location of peaks (3), (4), (5), and (6) in the low vacuum EDCs shown in Figs. 78b and 78c provides evidence that nondirect transitions dominate in gold up to photon energies as high as 21.2 eV.

Although some contamination resulted in the gold films studied in the oil-pumped vacuum of the McPherson Vacuum Monochromater, the EDCs for gold appear to be quite insensitive to exposure to air. Figure 79 compares two

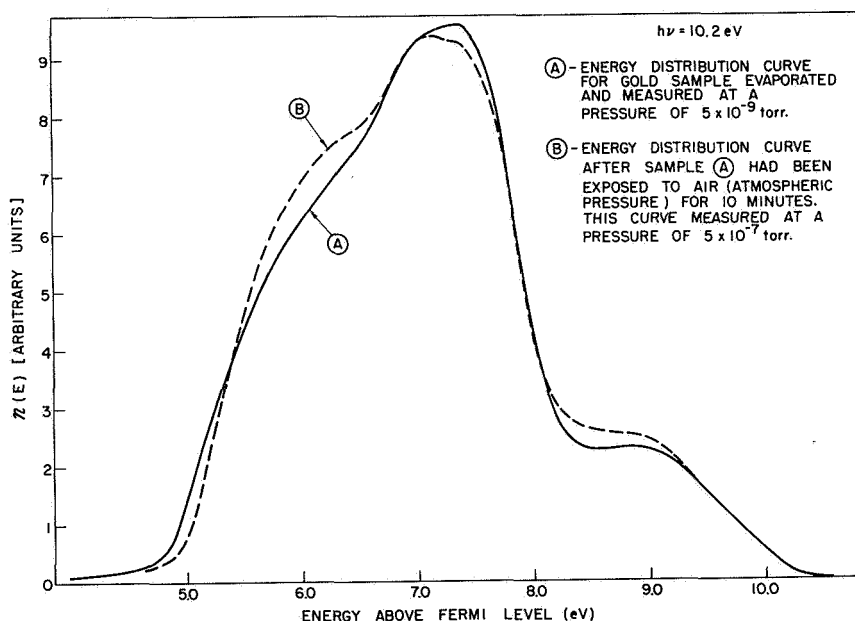


FIG. 79. ENERGY DISTRIBUTION CURVES BEFORE AND AFTER GOLD SAMPLE WAS EXPOSED TO AIR. Exposure to air caused the photoelectric yield to change by less than 1 percent at a photon energy of 10.2 eV.

EDCs at a photon energy of 11.6 eV: EDC (A) was measured from a freshly prepared film at ultrahigh vacuum, and EDC (B) was measured on the same gold film after it had been exposed to air at atmospheric pressure. Both measurements were made by use of the oil-free vacuum system and the photo-emission chamber described in Chapter II. As can be seen from the very

close agreement between the two curves, it must be concluded that EDCs from gold are very insensitive to exposure to air.

Figure 80 shows a comparison of different samples of gold; all the EDCs are quite similar. Note that in one case, the vacuum level was only about 4.5 eV, and that photoemission from the deep-lying valence band peak (6) of Fig. 74 is more evident than in the other two curves.

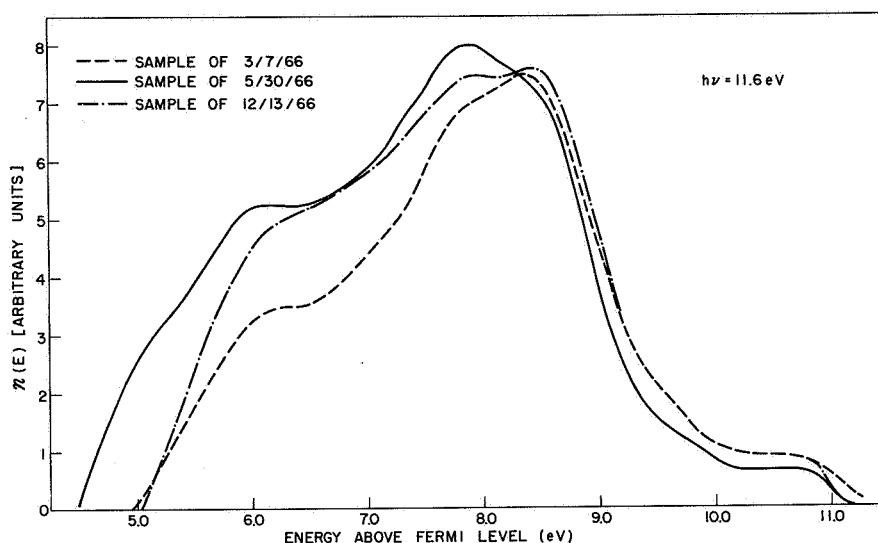


FIG. 80. COMPARISON OF SHAPES OF ENERGY DISTRIBUTION CURVES FOR DIFFERENT SAMPLES OF GOLD.

Figures 81a through 81r compare the calculated EDCs for gold with the experimental EDCs for gold in the range of photon energies between 7.4 and 11.6 eV. The calculated curves were obtained by use of the optical density of states of Fig. 74 and the analysis described in Table 1 of Chapter III. The curves of Fig. 81 show that the agreement between the calculated and the experimental curves is very good with regard to both shape and magnitude. However, the detailed agreement between theory and experiment is not quite as good as that obtained for copper. As seen from Fig. 81, the nondirect model does not explain the peak location for the direct transitions to final states in the conduction band between 8 and 9.5 eV above the fermi level. Nevertheless, the nondirect model and the optical density of states of Fig. 74 appear to account very well for the overall characteristics of the experimentally observed photoelectric EDCs

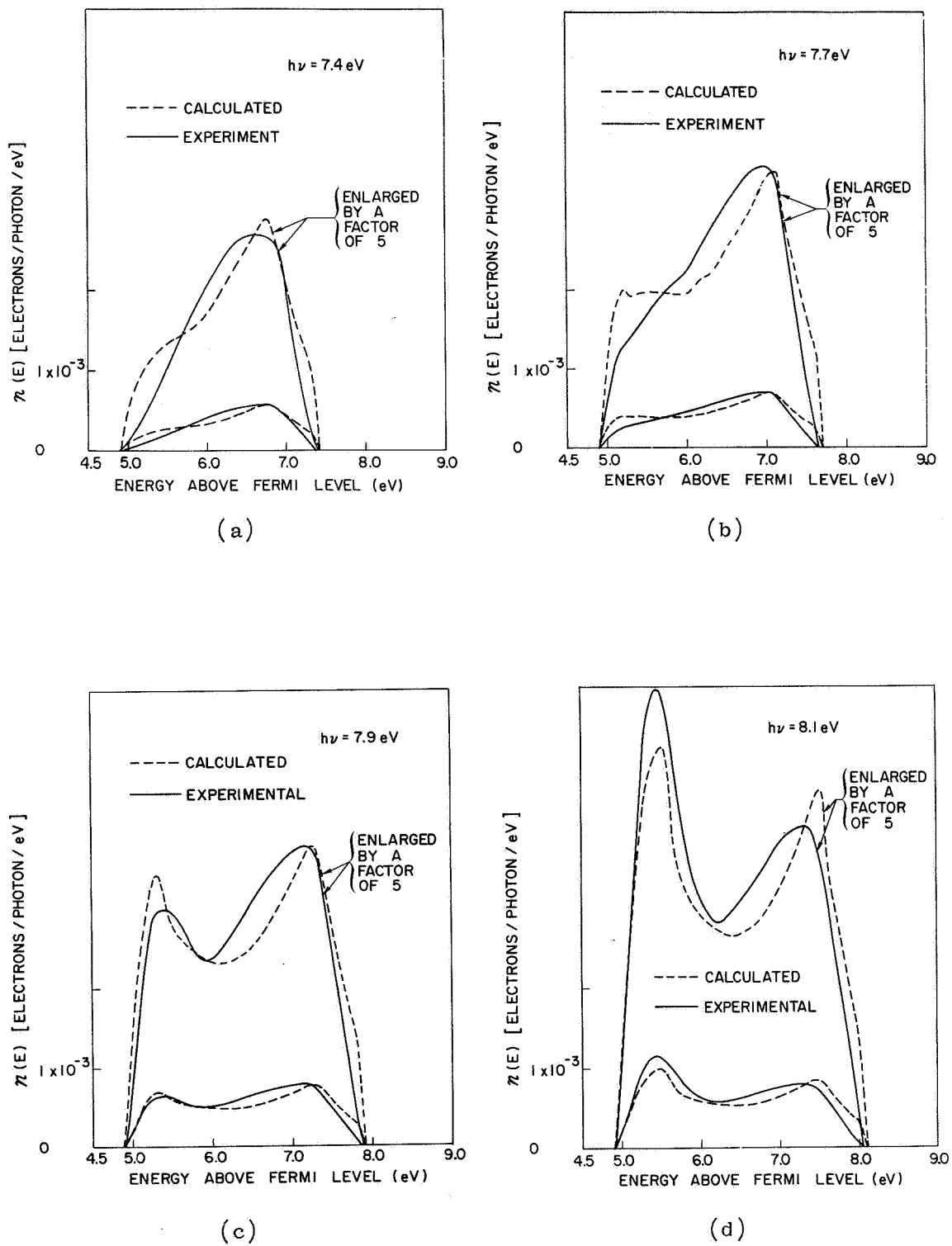
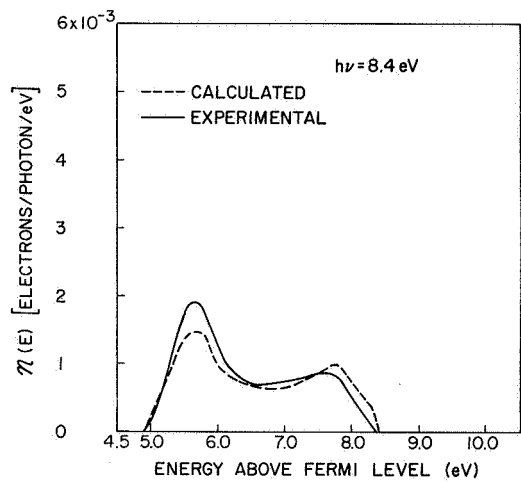
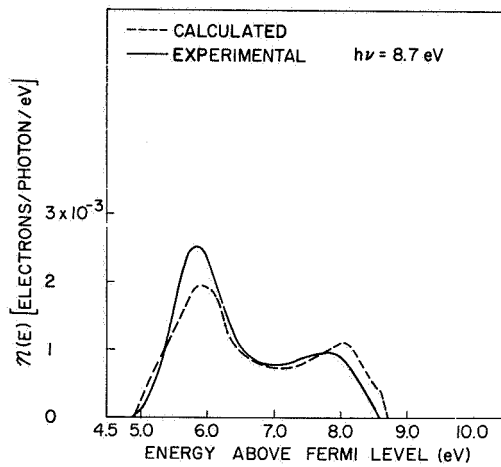


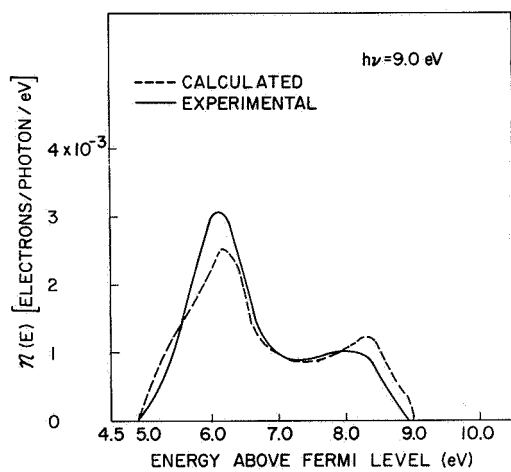
FIG. 81. COMPARISON OF CALCULATED AND EXPERIMENTAL ENERGY DISTRIBUTION CURVES FOR GOLD.



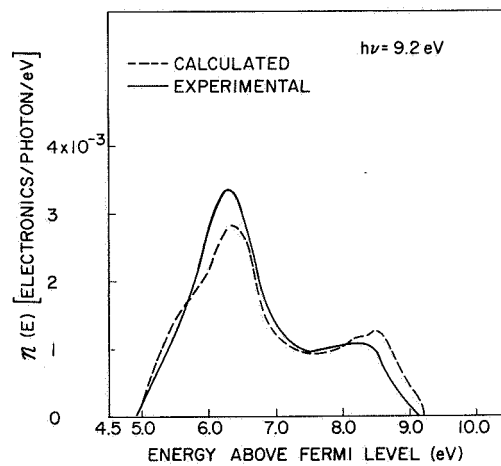
(e)



(f)

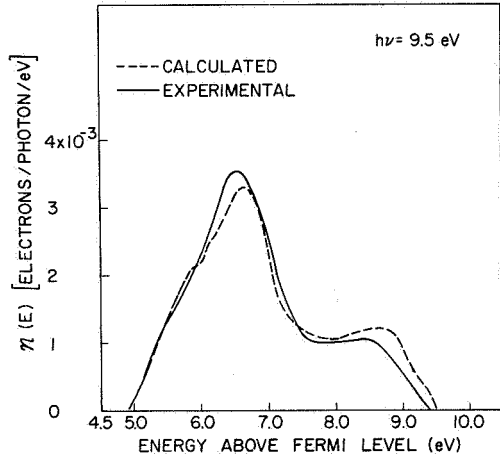


(g)

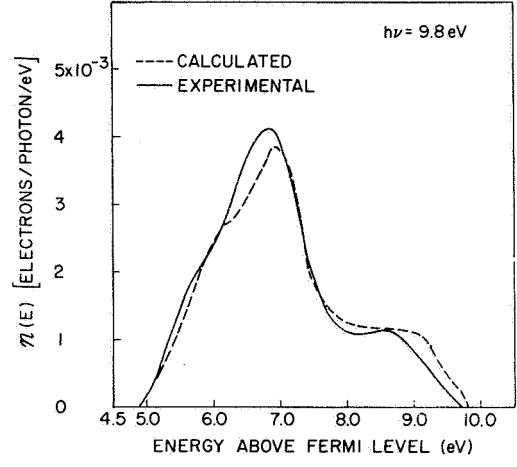


(h)

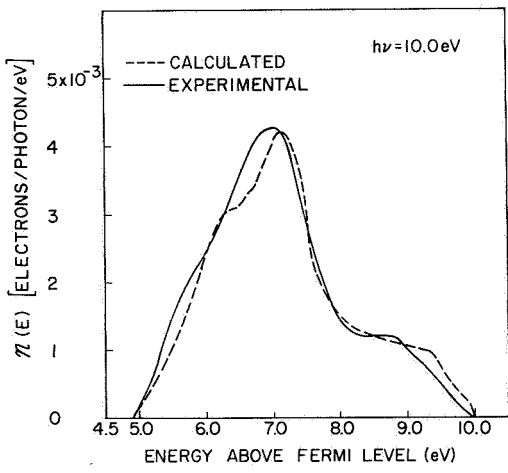
FIG. 81. CONTINUED



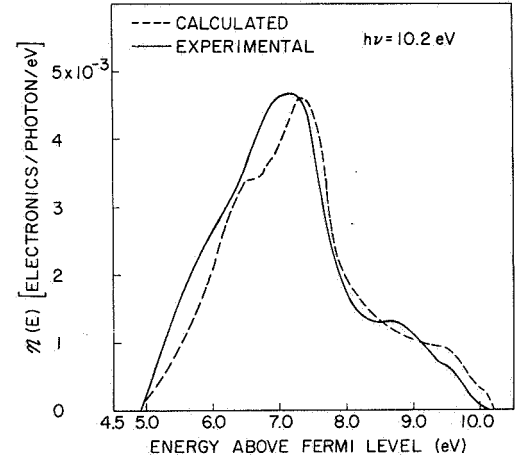
(i)



(j)

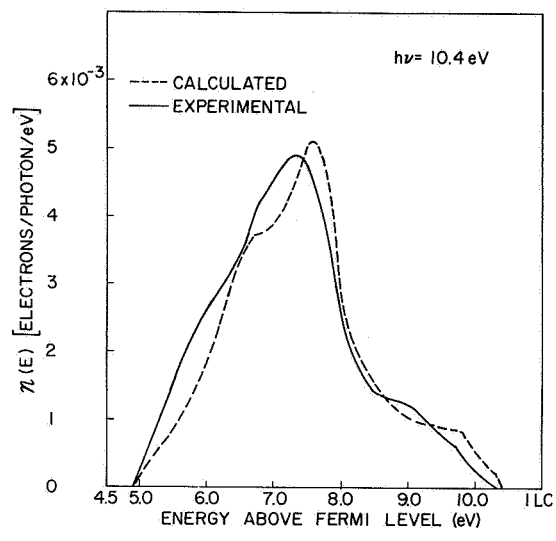


(k)

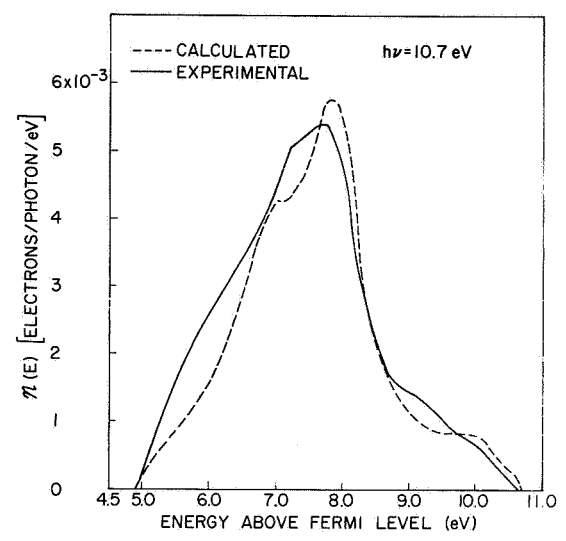


(l)

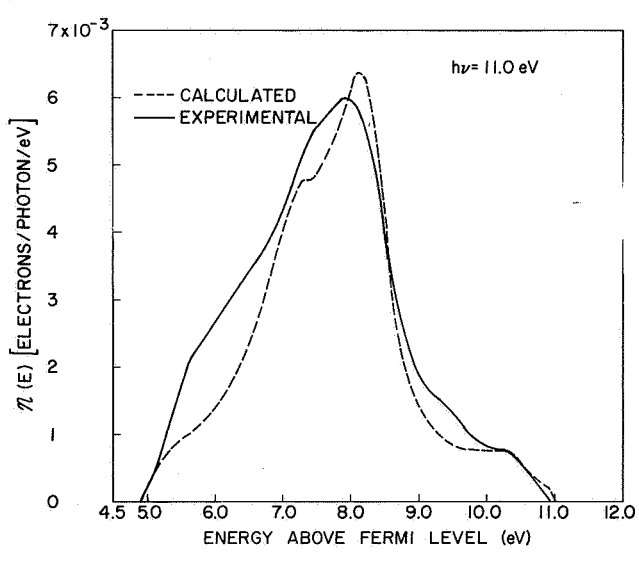
FIG. 81. CONTINUED.



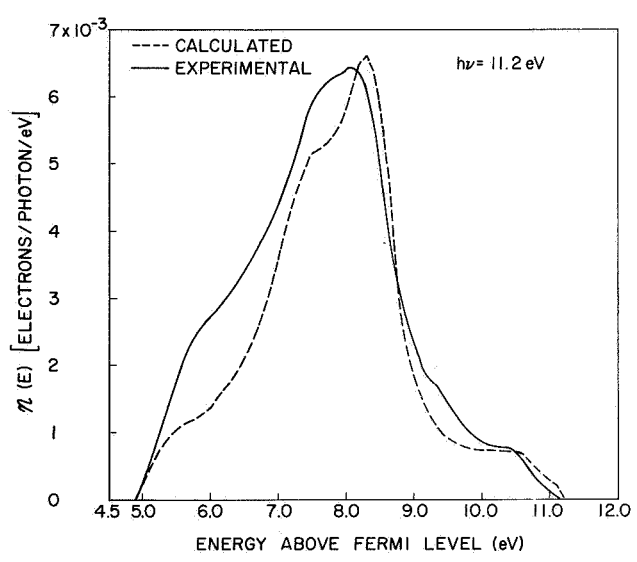
(m)



(n)



(o)



(p)

FIG. 81. CONTINUED.

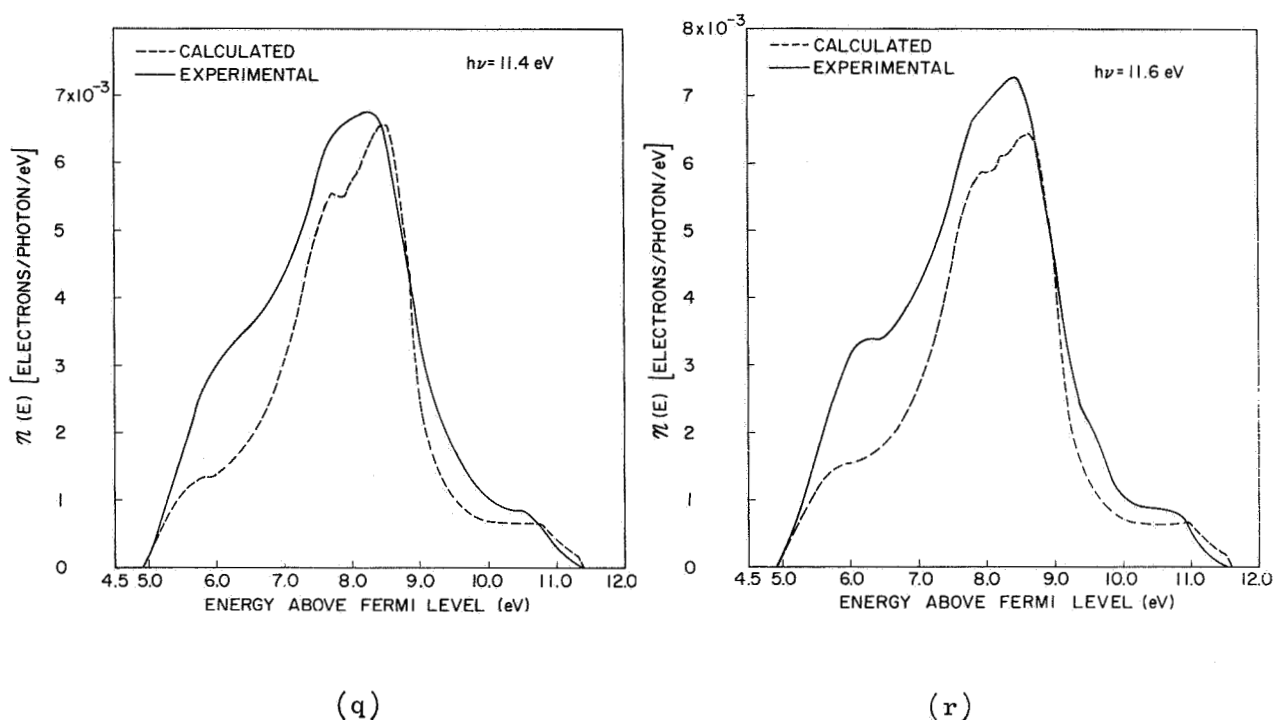


FIG. 81. CONTINUED.

in the range of photon energies between 7.4 and 11.6 eV above the fermi level.

D. THE ELECTRON-ELECTRON SCATTERING LENGTH IN GOLD

In the method of analyzing photoemission data described in Table 1 of Chapter III, the magnitude of the electron-electron scattering length is arbitrarily chosen at one energy, because no good experimental data are available for most materials. In the case of gold, however, several experimental measurements of the electron-electron scattering length have been made, and these measurements are probably very reliable, because gold is quite insensitive to contamination, as discussed in Section C of this chapter. The experimental values of $L(E)$ for gold are exceedingly important for the purposes of this investigation and for the analysis of copper, silver, and gold, since the experimental values for gold provide an exacting check on the method used to analyze photoemission data in this study.

Crowell [Ref. 48] has measured $L(E)$ in the vicinity of 1 eV above the fermi level by injecting hot electrons through thin films of gold, using various semiconductor-gold-semiconductor structures. This technique is described in detail in Refs. 63 and 64. Using a method that employs optical injection of electrons over a Schottky barrier, Sze, Moll, and Sugano [Ref. 50b] have determined the electron-electron scattering length for gold in the range of energies between 1 and 5 eV above the fermi level. Unfortunately, the methods of Crowell [Ref. 63] and Sze et al [Ref. 50b, 64] directly measure only the total electron-scattering length, and the effects of electron-phonon scattering must be accounted for in deducing the electron-electron scattering length from the experimental data. Since the electron-

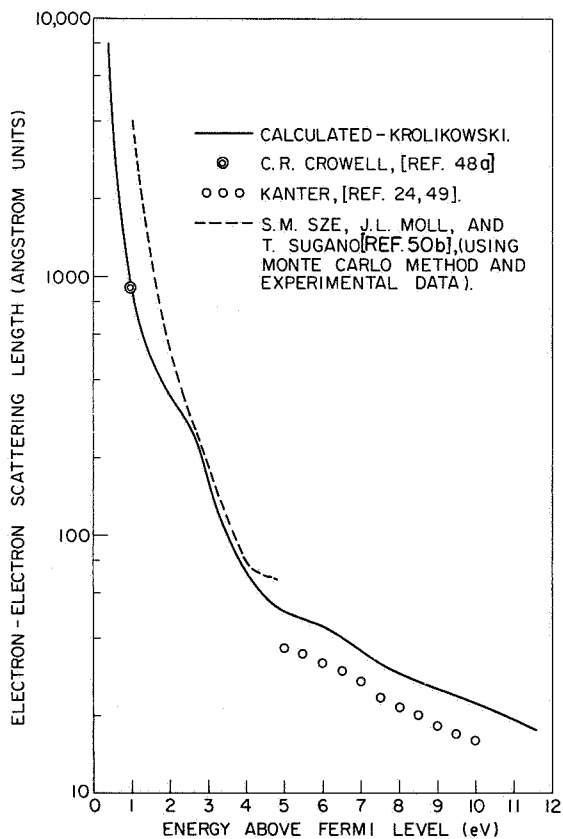


FIG. 82. CALCULATED ELECTRON-ELECTRON SCATTERING LENGTH $L(E)$ FOR GOLD. (Magnitude arbitrarily set equal to 27\AA at 8.6 eV above the fermi level.)

phonon scattering length is comparable to the electron-electron scattering length in the region of energies within a few eV of the fermi level, the uncertainty in the data of Crowell and Sze et al is probably quite large. In addition, the uncertainty in the calculated $L(E)$ of Fig. 82 is also quite large at energies only a few eV above the fermi level, since there may be unaccounted for structure in the conduction band optical density of states for gold in the region between the fermi level and 4.9 eV above the fermi level.

The calculated electron-electron scattering length $L(E)$ for gold is compared with a number of experimental data points in Fig. 82. The agreement between the calculated curve and the experimental data is seen to be amazingly good over a very wide range of energies; however, in the low energy range, this good agreement is probably fortuitous.

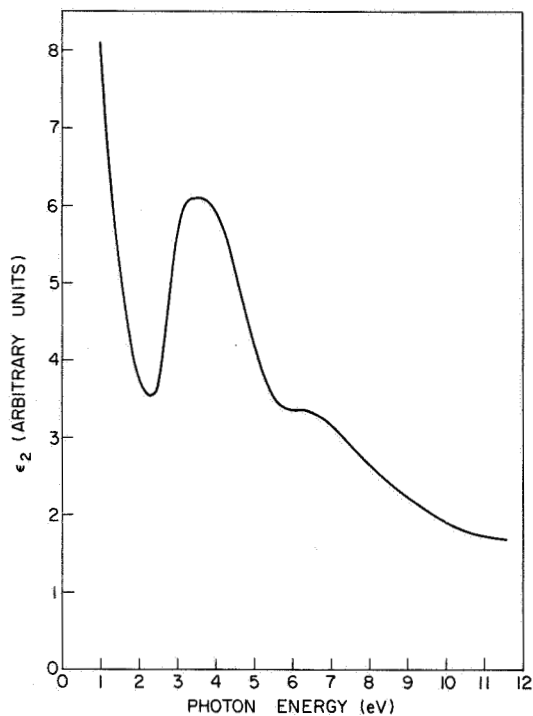
However, for the purposes of photoemission studies on clean gold, the most important region of energies is between 4.9 and 11.6 eV above the fermi level, and in this region, there is excellent agreement between the calculated $L(E)$ and the data points of Kanter. Kanter's data points have been deduced from transmission measurements of electron beams through thin gold films, and are probably quite reliable. Not only is the magnitude of the calculated $L(E)$ very close to Kanter's measurement, but there also appears to be detailed agreement between the shapes of the curves: In both the calculated curve and the experimental curve, $L(E)$ decreases suddenly at an energy of about 6.5 eV above the fermi level. As seen from the density of states of Fig. 74, this sudden decrease in $L(E)$ is due to the onset of scattering between the "hot" electrons and the valence band peak labeled (6).

The remarkable agreement between the calculated $L(E)$ and the experimental data points for gold lends great confidence to the validity of the method described in Table 1 of Chapter III, which is used in this study to analyze photoemission data from a number of different materials for which there are no reliable experimental values of $L(E)$.

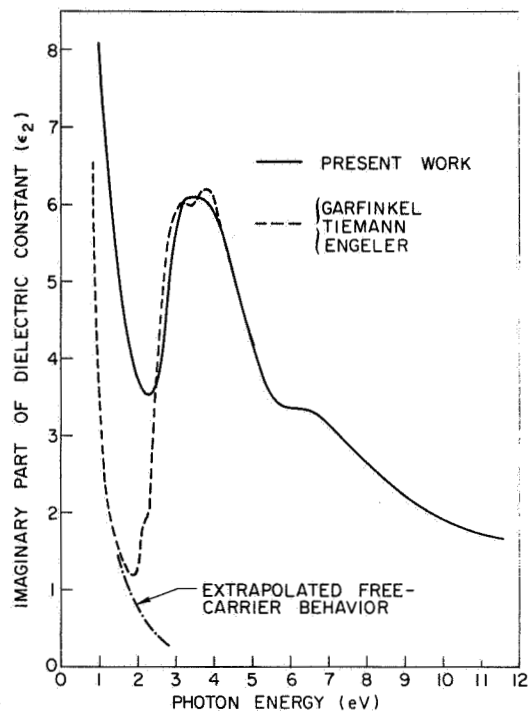
E. COMPARISON OF CALCULATED AND EXPERIMENTAL VALUES OF $\epsilon_2(\omega)$ FOR GOLD

The shape of $\epsilon_2(\omega)$ that is calculated for gold from the optical density of states of Fig. 74 and the theory of nondirect transitions is shown in Fig. 83a. The major features of this curve are the rather "flat" peak in the region between 3 and 4 eV and a strong shoulder at 6.5 eV. The flat peak between 3 and 4 eV is due to strong transitions between filled states in the vicinity of peaks (4) and (5) in the valence band of Fig. 74 to empty states just above the fermi level. The shoulder at 6.5 eV is due to strong transitions from peak (6) in the valence band to empty states just above the fermi level.

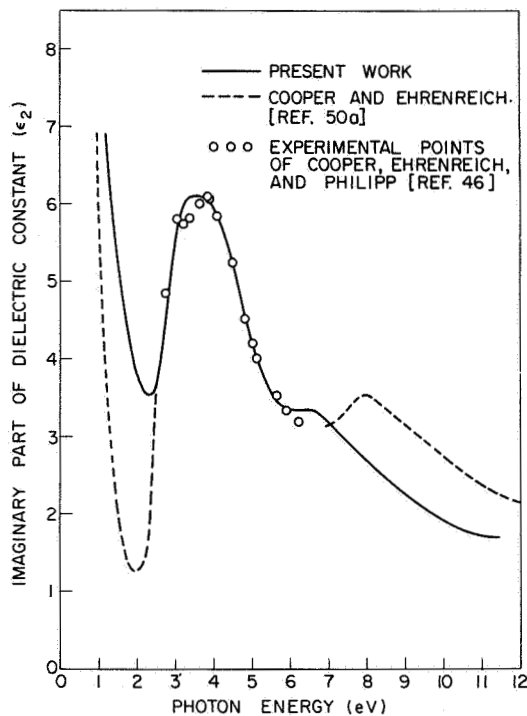
Just as the case of copper, the published values of $\epsilon_2(\omega)$ that have been deduced from experimental data are somewhat inconsistent, necessitating comparison of the calculated $\epsilon_2(\omega)$ with the "experimental" $\epsilon_2(\omega)$ of several different investigators. The comparisons are presented in Figs. 83b, 83c, and 83d.



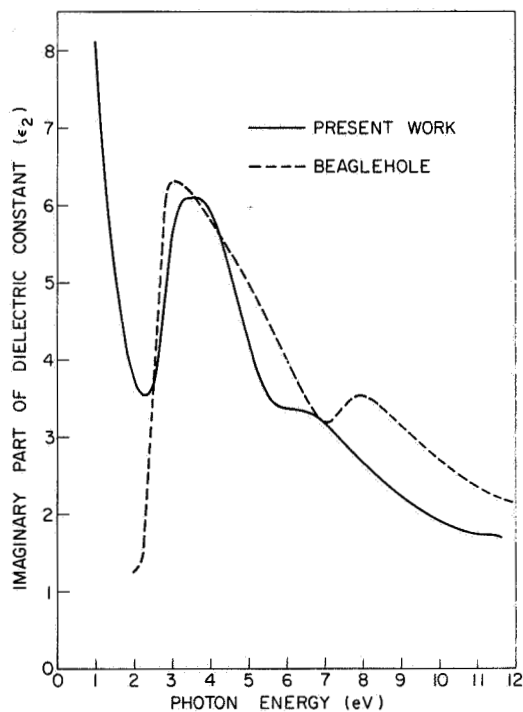
a. ϵ_2 FOR GOLD CALCULATED FROM THE OPTICAL DENSITY OF STATES OF FIG. 74.



b. COMPARISON OF CALCULATED ϵ_2 WITH THE ϵ_2 OF GARFINKEL, TIEMANN, AND ENGELER (REF. 48b)



c. COMPARISON OF CALCULATED ϵ_2 WITH THE ϵ_2 OF REFS. 50a, 46.



d. COMPARISON OF CALCULATED ϵ_2 WITH BEAGLEHOLE'S ϵ_2 (REF. 47).

FIG. 83.

Figure 83b shows that the "corners" of the "flat" calculated peak are in rather good agreement with the two experimentally observed peaks at 3.1 and 3.8 eV. However, the experimentally observed shoulder at 2.2 eV does not appear in the calculated $\epsilon_2(\omega)$. Note, however, the similarity between the experimental shoulder at 2.2 eV in gold and the calculated shoulder that occurs at 1.9 eV in copper (see Fig. 63).

In Fig. 83c, the agreement between the major features of $\epsilon_2(\omega)$ is again good in the vicinity of 2.5 to 6 eV, but there is a glaring discrepancy in that a large peak occurs in the experimental data at a photon energy of 8.0 eV, and no such peak appears in the calculated $\epsilon_2(\omega)$. This peak at 8.0 eV has also been experimentally observed by Beaglehole [Ref. 47], as seen in Fig. 83d.

Thus, we see that the optical density of states of Fig. 74 and the theory of nondirect transitions is able to account for the two peaks in $\epsilon_2(\omega)$ at 3.1 and 3.8 eV, but is not able to account for the shoulder at 2.2 eV and the very strong peak at 8.0 eV. This discrepancy may very well be due to the present lack of information about structure that could exist in the unexplored region between the fermi level and 4.9 eV above the fermi level. Because of the similarities in the EDCs from copper and gold, it is possible that there exists a peak in the conduction band density of states for gold at an energy about 2 eV above the fermi level, just as in the case of copper. Such a peak is sketched in Fig. 74; it is labeled \textcircled{P} (for proposed). If such a peak does exist, and if the density of states near the fermi level was adjusted to agree with the specific heat (see Section F of this chapter), then the $\epsilon_2(\omega)$ calculated from the optical density of states would account for all of the major features in the experimental data, including the peaks at 2.2 and 8.0 eV. Table 3 lists the results that would be obtained if a peak was to exist in the conduction band at about 2.0 eV above the fermi level. However, until photoemission studies are made on "cesiated" or "bariated" gold, or until a good energy band calculation is made, the existence of a peak in the conduction band optical density of states of gold at about 2.0 eV above the fermi level will remain a conjecture.

TABLE 3. ASSIGNMENT TO MAJOR STRUCTURE IN THE CALCULATED $\epsilon_2(\omega)$ FOR GOLD IF THE PROPOSED PEAK \textcircled{P} EXISTS

Photon Energy of Experimentally Observed Structure (eV)	Photon Energy of Calculated Structure (eV)	Location of Initial State in Valence Band (Fig. 74)	Location of Final State in Conduction Band (Fig. 74)
2.2 (Garfinkel only)	2.2	Filled states just below the fermi level	\textcircled{P}
3.1	3.1	$\textcircled{4}$	Empty states just above the fermi level
3.1	2.8	$\textcircled{3}$	\textcircled{P}
3.8	3.8	$\textcircled{5}$	Empty states just above the fermi level
Wide broadening between 5.0 and 6.5 eV (Beaglehole only)	6.5	$\textcircled{6}$	Empty states just above the fermi level
8.0	8.0	$\textcircled{6}$	\textcircled{P}

F. THE SPECIFIC HEAT FOR GOLD

Using the experimental results of Ref. 95 for the electronic specific heat of gold, the density of states at the fermi level can be calculated from Eq. (4.1). The result is found to be the same as for copper, $N(E_f) = 0.32$ electrons/eV-atom. The outer electron configuration of gold is $5d^{10}6s^1$ so it can be assumed that the valence band of gold holds eleven electrons. Normalizing the area (A+B) of Fig. 74 to hold eleven electrons, we can calculate the optical density of states near the fermi level. The results are shown as the solid curve labeled N_v^{AB} in Fig. 84, where it is seen that the optical density of states at the fermi level is 0.06 electrons/eV-atom, as compared with the value of 0.32 electrons/eV-atom calculated from the specific heat. This large discrepancy may be due to electron-phonon interactions, which have been neglected, but is more likely due to the uncertainty in the valence band optical density of states just below the fermi level. The shape of the optical density of states between the fermi level and 0.7 eV below the fermi level was sketched in the shape of the leading edge of the experimental EDCs measured at photon energies greater than 7.4 eV. Since the leading edge of experimental EDCs is usually found to be blurred at such high energies and much sharper at lower energies, it is likely that the valence band optical density of states near the fermi level is actually much higher than shown in Fig. 74 and in curve N_v^{AB} of Fig. 84. Thus, increasing the optical density of states near the fermi level to agree with the value derived from the specific heat does not seem to be an unreasonable adjustment. The result is shown as the dashed curve labeled N_v^{AB} in Fig. 84.

Increasing the valence band density of states near the fermi level to agree with the specific heat value necessitates scaling the entire conduction band optical density of states by a factor of about 5, if the conduction band is to match the valence band at the fermi level. This increase in the overall magnitude of the conduction band density of states makes the relative magnitude between the conduction band density of states and the valence band density of states seem more reasonable than is shown in Fig. 84, where the magnitude of the conduction band optical density of states seems unreasonably small compared with the valence band optical density of states.

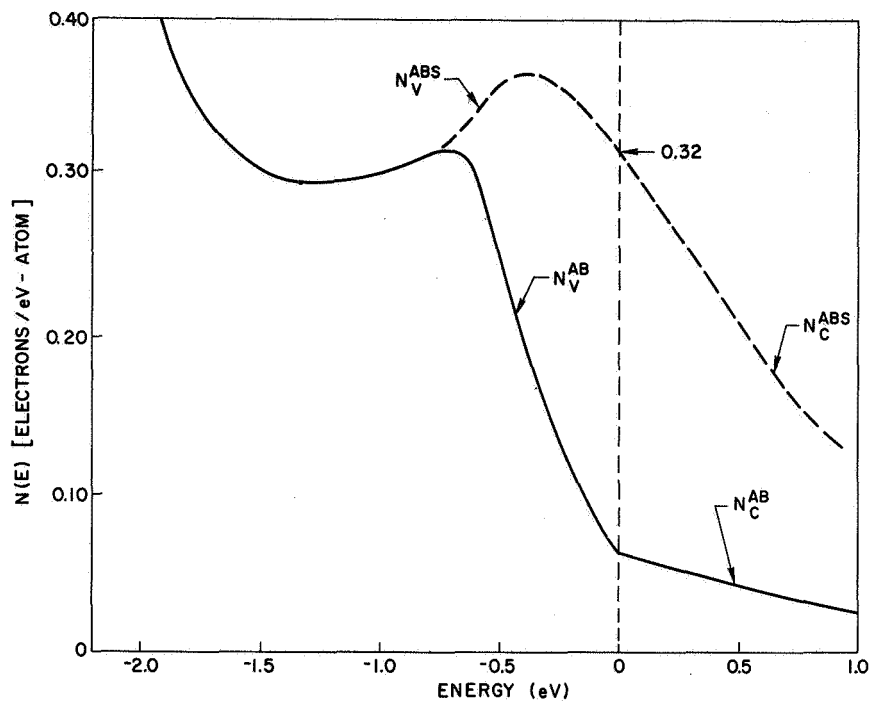


FIG. 84. ADJUSTMENT OF OPTICAL DENSITY OF STATES TO AGREE WITH THE VALUE DERIVED FROM THE SPECIFIC HEAT (AT THE FERMI LEVEL).

G. CONCLUSIONS

This chapter has presented new experimental photoemission data on gold in the range of photon energies between 7.4 and 21.2 eV. From these photoemission data, an optical density of states has been constructed in the region between the fermi level and 11.6 eV below the fermi level, and in the region between 4.9 and 11.6 eV above the fermi level. The conduction band density of states in the region between the fermi level and 4.9 eV above the fermi level could not be directly studied by photoemission measurements on clean gold, so the density of states in this region has been approximated by a smooth curve.

The bulk of the photoemission data is well described by the theory of nondirect transitions, except for a single direct transition, which bears some resemblance to the $L_2' \rightarrow L_1$ transition observed in copper by Berglund and Spicer [Ref. 37]. The optical density of states for gold is found to account for certain major features in the spectrum of $\epsilon_2(\omega)$, but is unable to account for all of the experimentally observed structure

in $\epsilon_2(\omega)$. This discrepancy may very well be due to structure in the as yet unexplored conduction band region between the fermi level and 4.9 eV above the fermi level.

The calculated electron-electron scattering length in gold is found to be in remarkably good quantitative agreement with experimental data points in the range of energies between 1 eV and 10 eV above the fermi level. This result is of great importance for the purposes of this study, since it is an exacting check on the method used by the author to analyze photoemission data.

A qualitative resemblance between copper and gold is observed to exist in the photoelectric EDCs, the photoelectric yield, the optical density of states, the electron-electron scattering length, $\epsilon_2(\omega)$, and the specific heat, indicating that considerable similarity may exist between the energy band structure of copper and gold in the range of energies ± 11.6 eV above the fermi level.



VI. PHOTOEMISSION FROM SILVER

This chapter presents new photoemission data obtained from clean silver films evaporated and tested at a pressure of about 2×10^{-9} torr using the oil-free vacuum system and the photoemission chamber described in Chapter II. The new photoemission data on clean silver are in excellent agreement with the photoemission data obtained earlier from cesiated silver by Berglund [Ref. 7] and Berglund and Spicer [Ref. 37].

The photoemission data are analyzed using the method outlined in Table 1 of Chapter III and an optical density of states in the region of energies ± 11.6 eV above the fermi level. This optical density of states incorporates the photoemission data from both clean silver and cesiated silver.

A. THE OPTICAL DENSITY OF STATES FOR SILVER

The optical density of states shown in Fig. 85 has been constructed using both the new photoemission data on clean silver and the earlier photoemission data on cesiated silver [Refs. 7 and 37], and is quite similar to the optical density of states presented earlier by Berglund and Spicer [Ref. 37]. The most outstanding feature of Fig. 85 is that the density of states is relatively large in the region between 4 and 7 eV below the fermi level, and relatively low and constant elsewhere. With reference to the energy band diagram of Fig. 86, we see that the high density of states between 4 and 7 eV below the fermi level corresponds closely to the "flat" bands derived largely from 5d atomic wavefunctions. Because of this correspondence, we shall refer to the region between 4 and 7 eV below the fermi level in Fig. 85 as the "d band" optical density of states for silver. In addition, comparison of Fig. 85 with the energy band diagram of Fig. 86 indicates that the valence band optical density of states between the fermi level and 4 eV below the fermi level is to be associated with bands that are largely derived from s and p atomic wavefunctions. It must be pointed out, however, that the location of the d bands in silver appears to be quite sensitive to the potential, and that Segall [Ref. 58] determined the location of the d-bands in Fig. 86 in an ad hoc way to agree with the experimental optical absorption data.

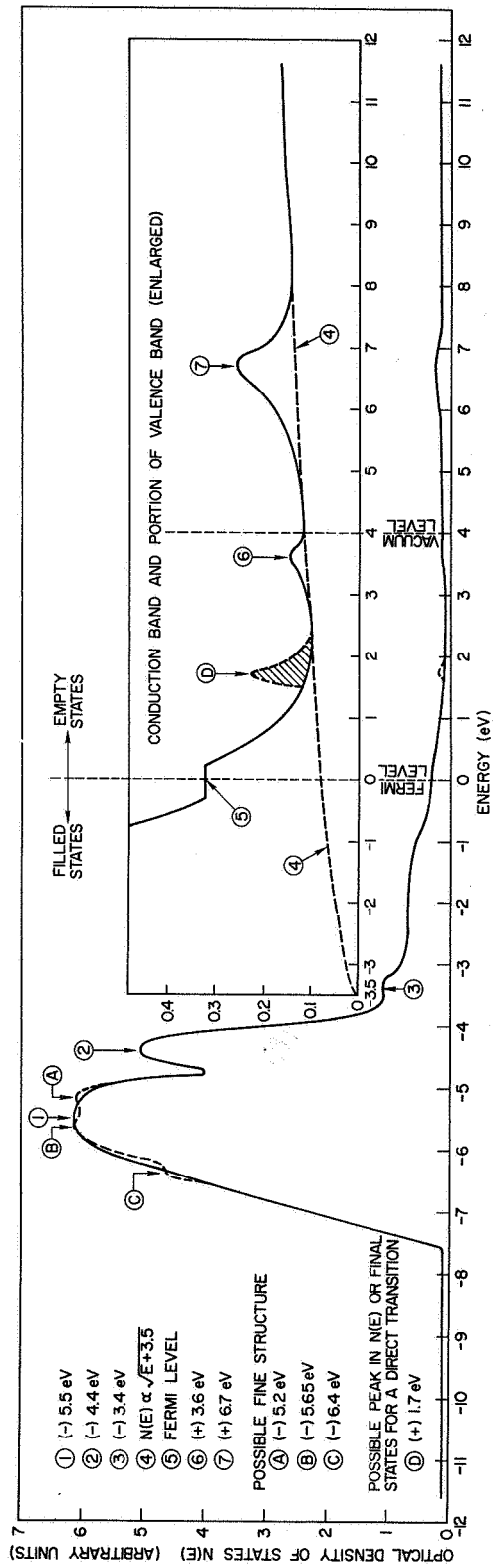


FIG. 85. OPTICAL DENSITY OF STATES FOR SILVER.

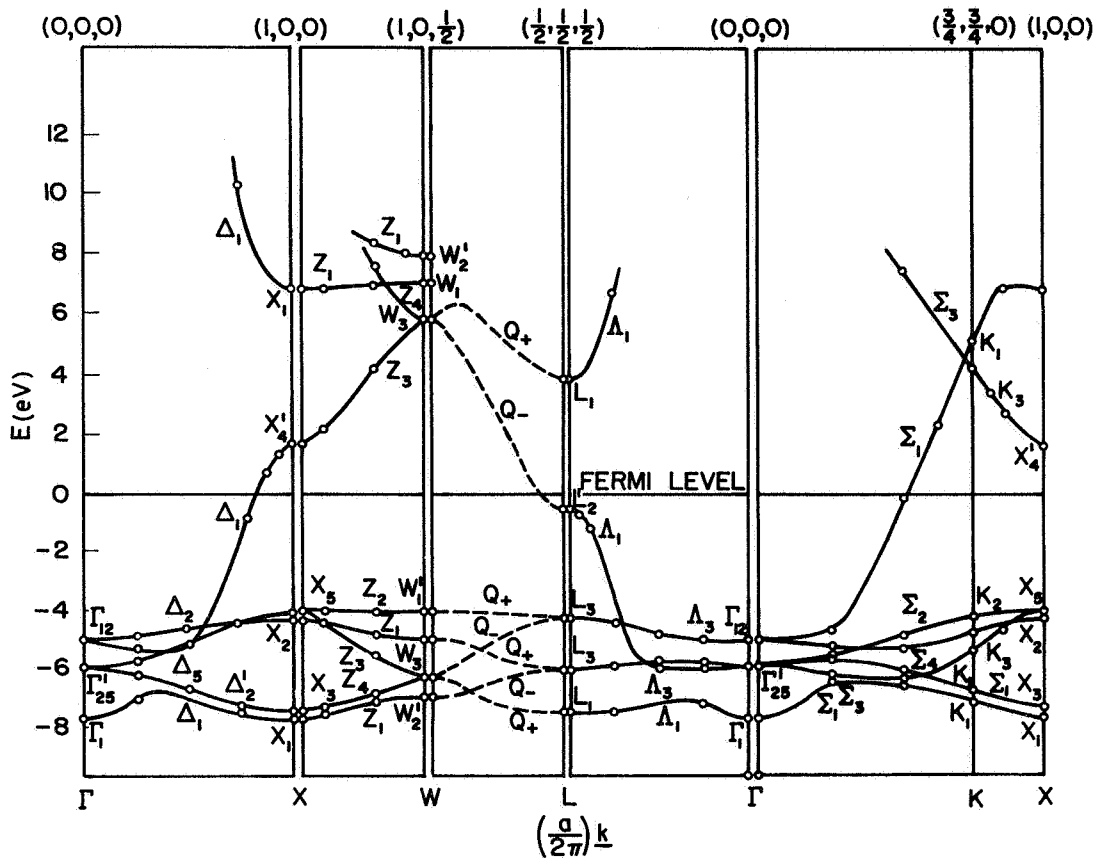


FIG. 86. CALCULATED BAND STRUCTURE OF SILVER.

Although the optical density of states for silver in Fig. 85 is very similar to that presented earlier by Berglund and Spicer [Ref. 37], there are several new features to be noted:

- (1) There exists a small peak in the valence band at about 3.4 eV below the fermi level.
- (2) There may be fine structure in the d band density of states. This fine structure is labeled (A), (B), and (C) in Fig. 85.
- (3) There is no sharp peak in the valence band a few tenths of an eV below the fermi level.
- (4) There is a peak in the conduction band at 6.7 eV above the fermi level.

- (5) There is a small peak in the conduction band at 3.6 eV above the fermi level, which can be seen in the earlier data of Berglund and Spicer [Ref. 37]. This peak may, however, be due to Auger electrons, as proposed earlier by Berglund and Spicer [Ref. 37].
- (6) There is structure in the conduction band at 1.7 eV above the fermi level. Evidence of this structure has been found by normalizing the raw data of Berglund [Ref. 7] and Berglund and Spicer [Ref. 37] to quantum yield, and observing the character of the EDCs at low energies near the vacuum level.

The bottom of the free electron conduction band was arbitrarily placed at 3.5 eV below the fermi level. This seemed to be a "natural" location for "averaging" the free-electron-like bands that exist above the d-bands in the energy band diagram of Fig. 86.

B. THE PHOTOELECTRIC YIELD FOR CLEAN SILVER

The calculated yield and the experimental quantum yield for silver are compared in Fig. 87. The calculated yield was obtained from the optical density of states of Fig. 85 and the analysis described in Table 1 of Chapter III. The experimental yield has been corrected for the transmission of the LiF window and the reflectivity. In calculating the quantum yield, the electron-electron scattering length was arbitrarily set equal to 44 \AA at 8.6 eV above the fermi level. As can be seen from Fig. 87, this choice of 44 \AA made the overall agreement between the calculated and the experimental yield quite good. Just as in the cases of copper and gold, the magnitude of the quantum yield is quite low, being only about 1 percent at a photon energy of 10.5 eV. The vacuum level was determined to be about 4.0 eV by taking the energy difference between the photon energy and the well defined width of the experimental EDCs. No attempt was made to carefully measure the quantum yield very close to the threshold.

The absorption coefficient $\alpha(\omega)$ used in calculating the photoelectric yield and the EDCs was taken from Ref. 45, as was the reflectivity $R(\omega)$ used in correcting the experimental yield.

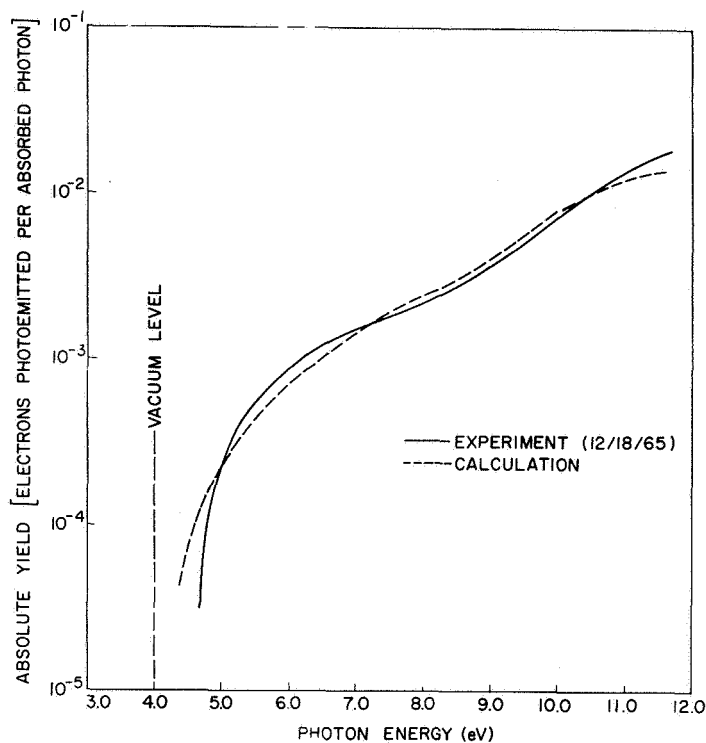


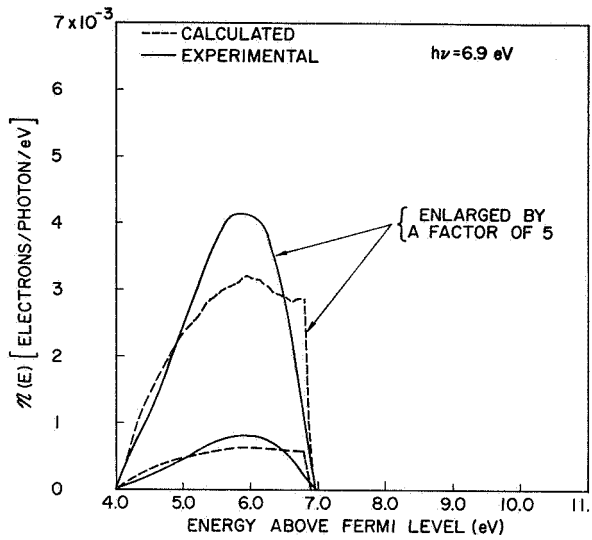
FIG. 87. COMPARISON OF EXPERIMENTAL AND CALCULATED PHOTOELECTRIC YIELD FOR SILVER. The experimental yield was measured according to the standards described in the caption of Fig. 31.

The overall uncertainty in the shape and magnitude of the experimental quantum yield in Fig. 87 is due to uncertainties in the standards used for calibration, in the reflectivity, and in the transmission of the LiF window. This overall uncertainty is estimated to be less than ± 20 percent.

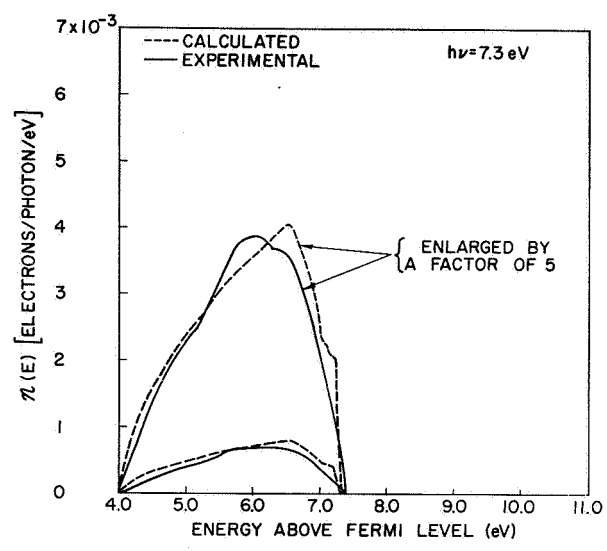
C. THE PHOTOELECTRIC ENERGY DISTRIBUTION CURVES FOR CLEAN SILVER

In Fig. 88 the calculated and experimental EDCs for clean silver are shown over a range of photon energies between 6.9 and 11.8 eV. It appears that the magnitude of the experimental EDCs increases in the vicinity of 6.5 eV above the fermi level, and this increase has been interpreted as caused by a peak in the conduction band density of states. This conduction band peak is labeled (7) in Fig. 85.

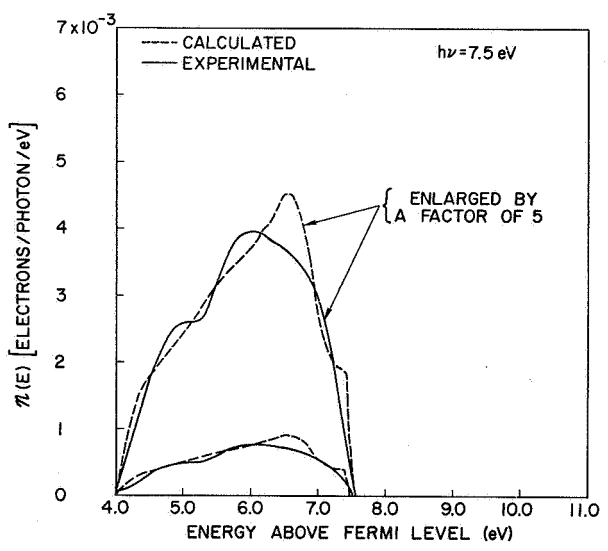
The agreement between the calculated and the experimental EDCs in Fig. 88 appears to be good in both shape and magnitude, indicating that



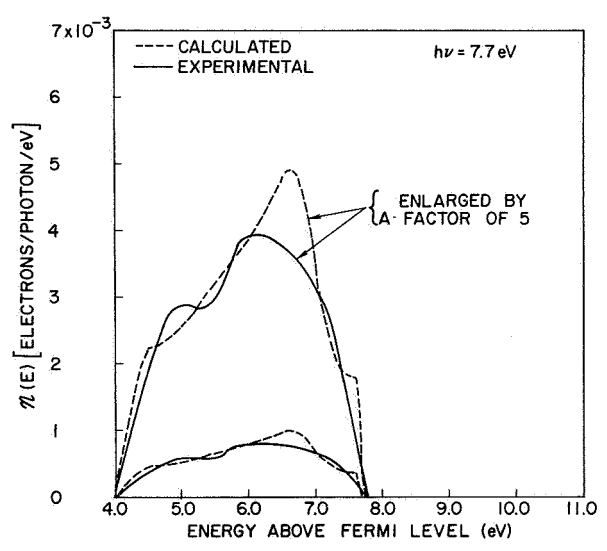
(a)



(b)

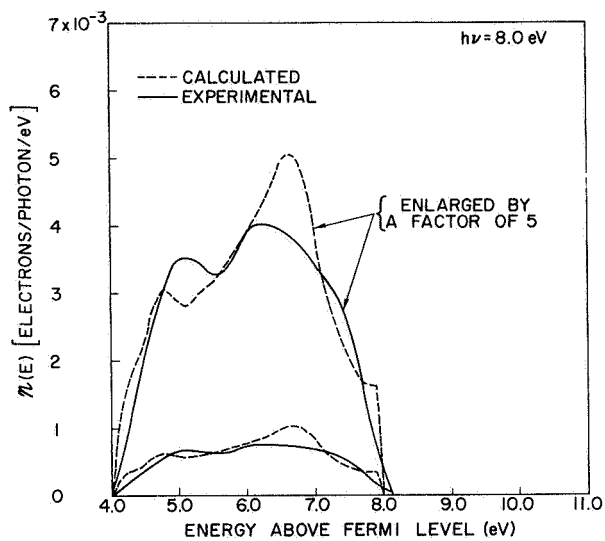


(c)

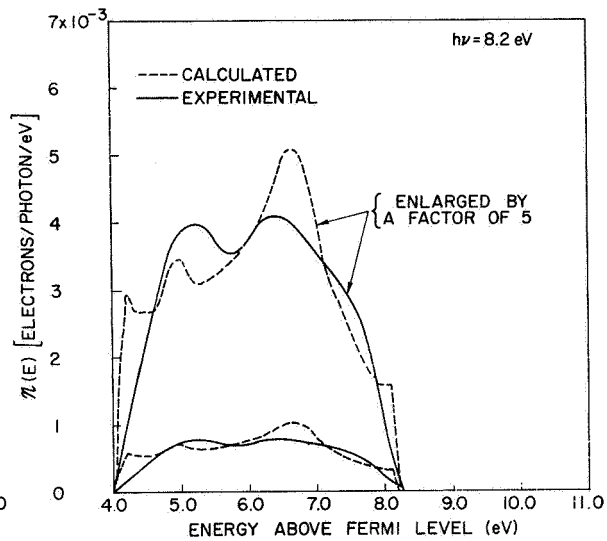


(d)

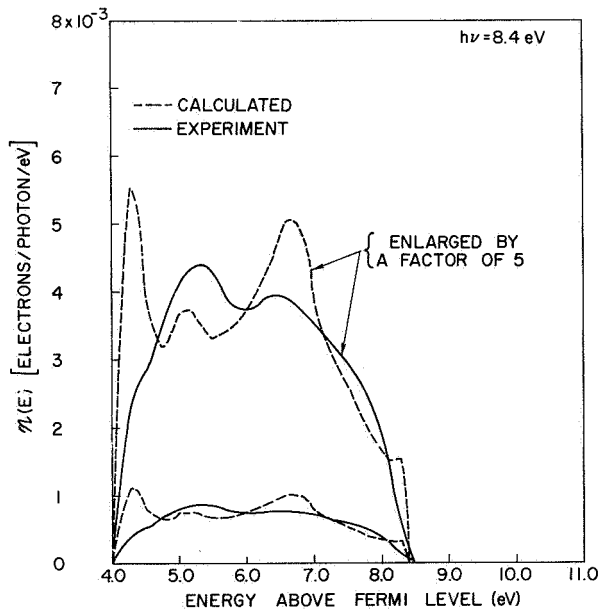
FIG. 88. PHOTOELECTRIC ENERGY DISTRIBUTION CURVES FOR CLEAN SILVER.



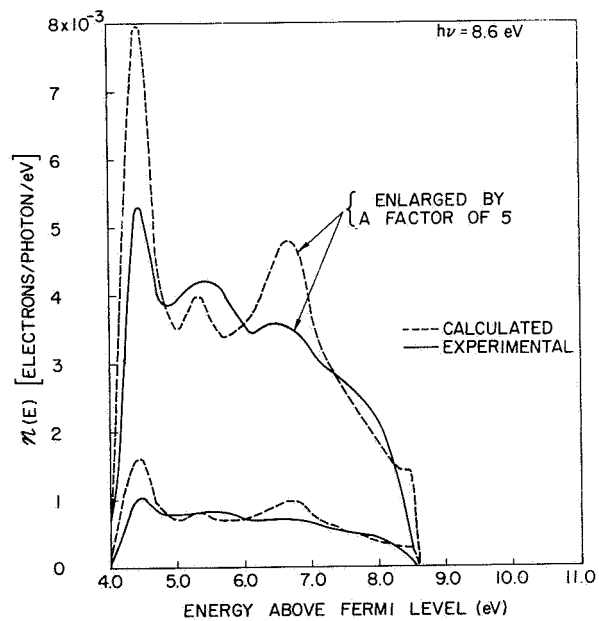
(e)



(f)

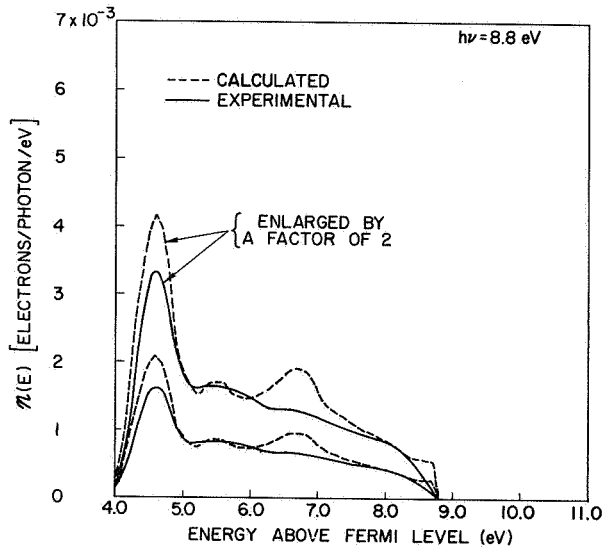


(g)

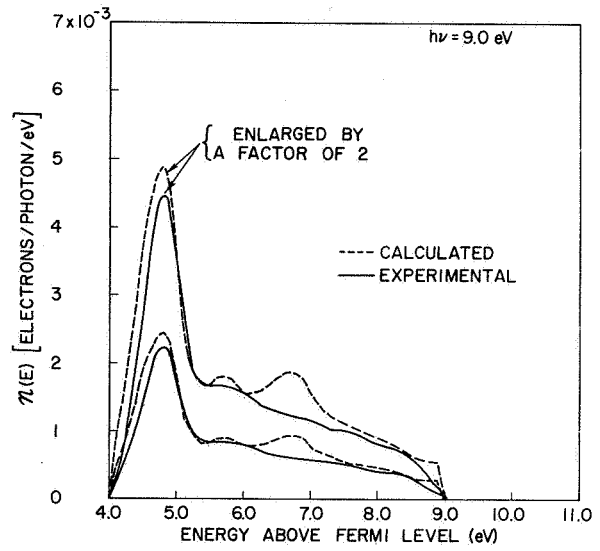


(h)

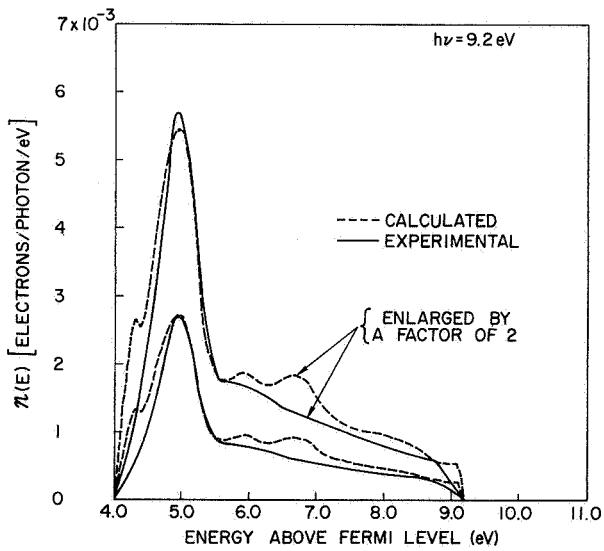
FIG. 88. CONTINUED.



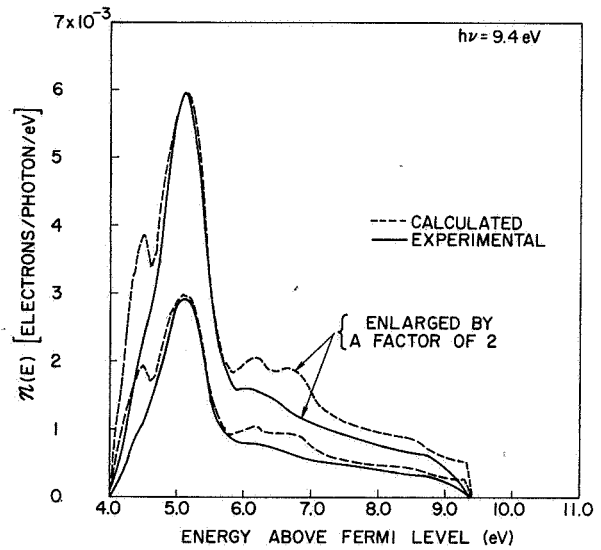
(i)



(j)



(k)



(l)

FIG. 88. CONTINUED.

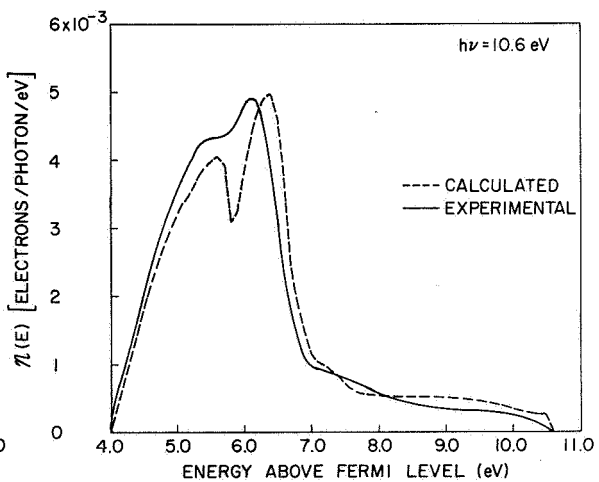
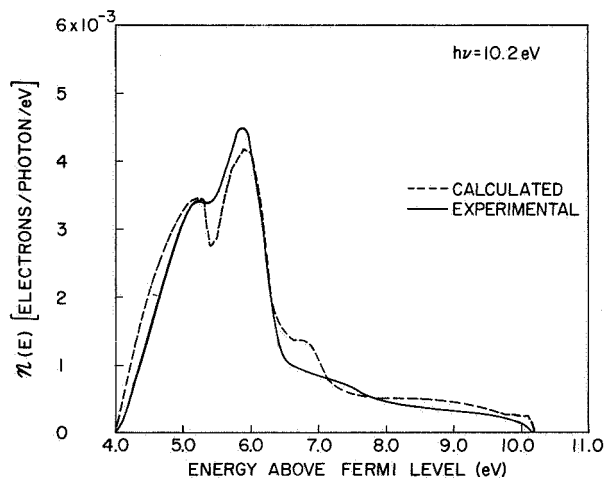
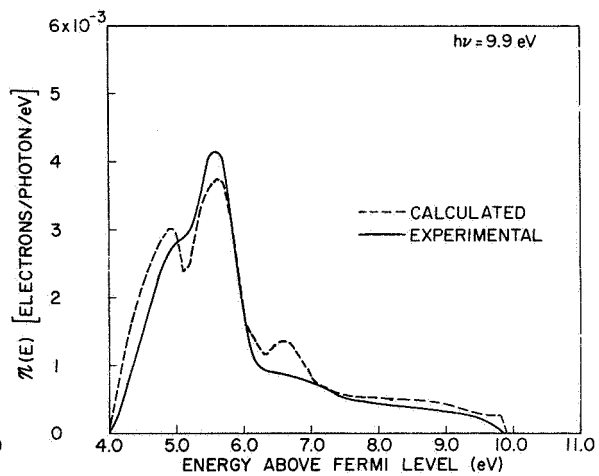
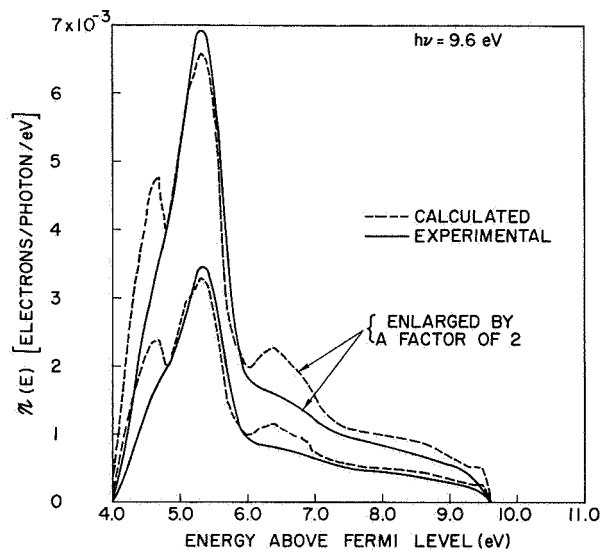
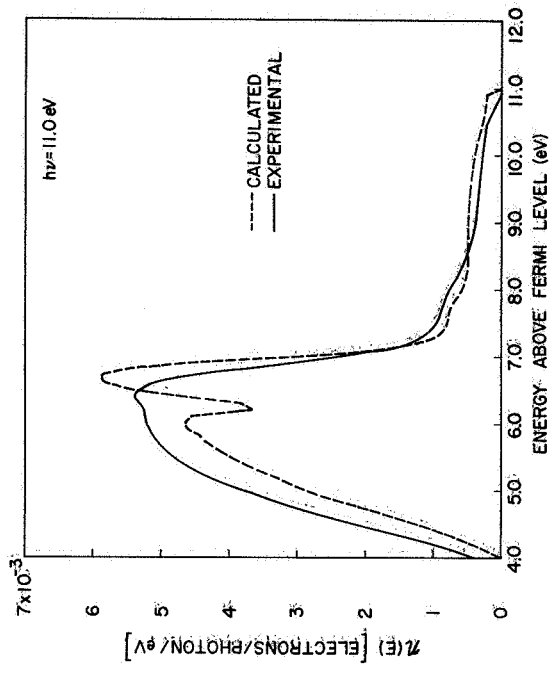
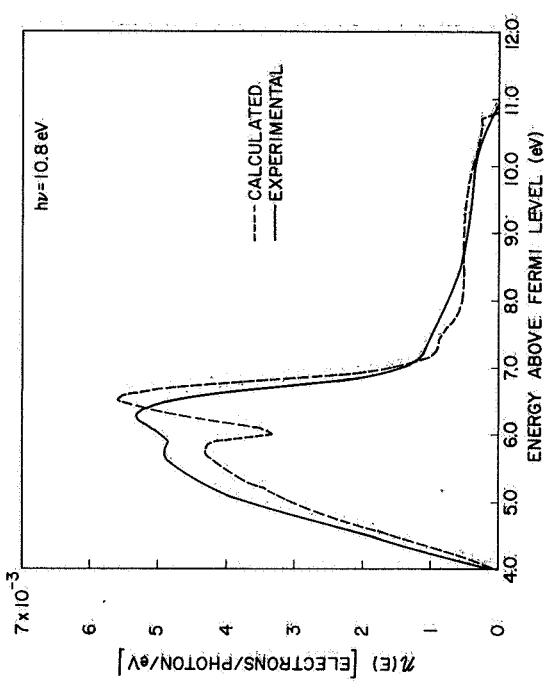


FIG. 88. CONTINUED.

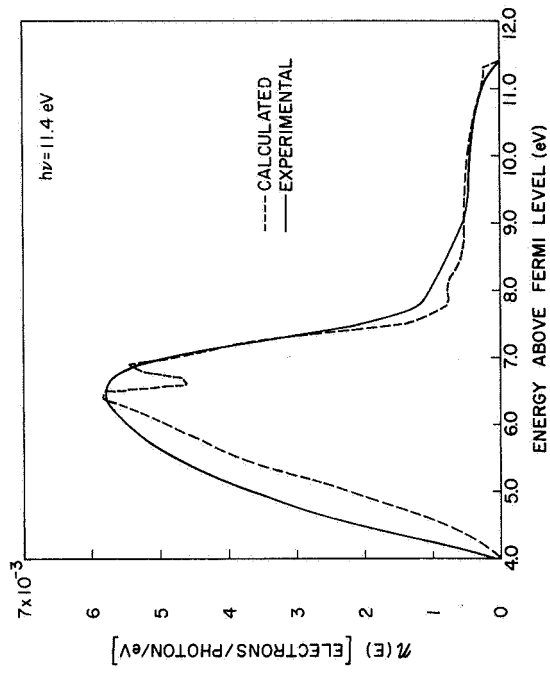


(r)

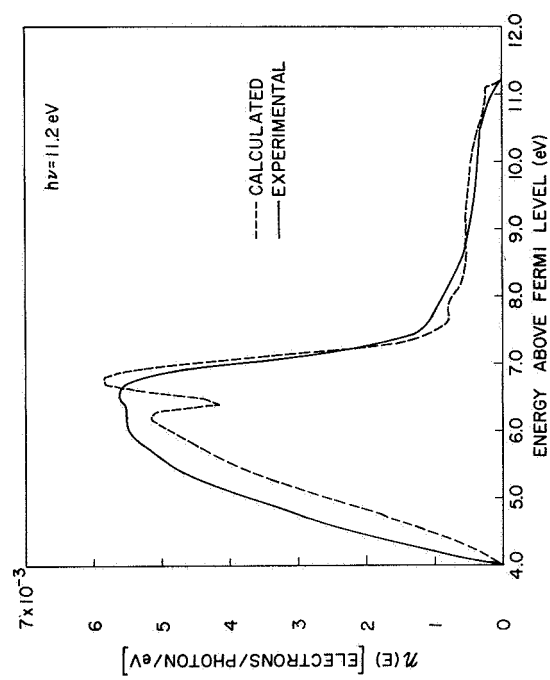


(q)

FIG. 88. CONTINUED.

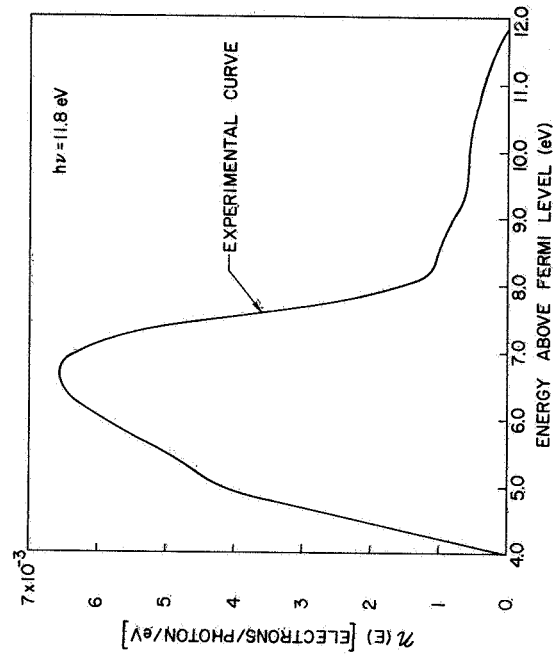


(t)

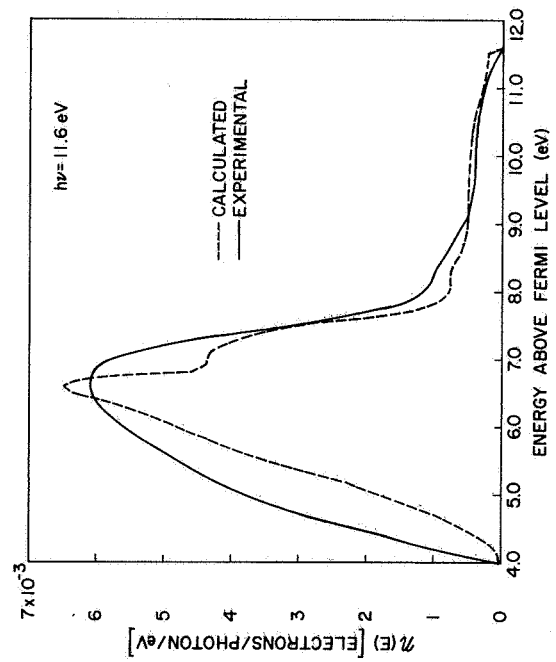


(s)

FIG. 88. CONTINUED.



(v)



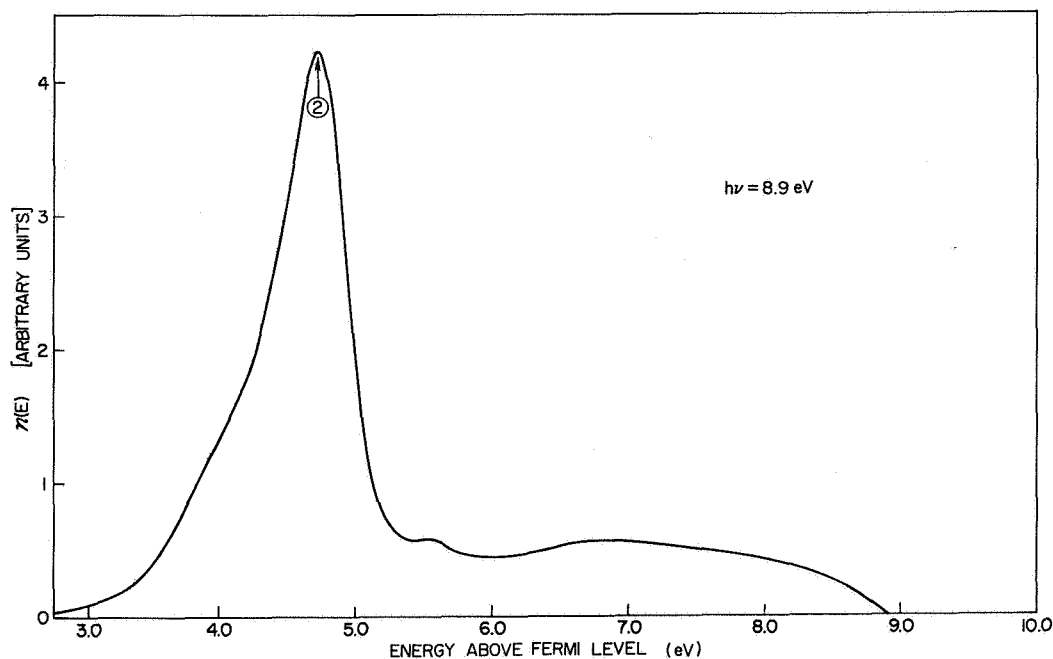
(u)

FIG. 88. CONTINUED.

the theory of nondirect transitions can account for the bulk of the photoemission data in silver for photon energies up to 11.8 eV. However, there are two features in the experimental EDCs that are not accounted for by the calculated EDCs: (1) A direct transition involving s- and p-derived states can be seen in the EDCs for clean silver. This direct transition can be seen in the experimental EDCs of Fig. 88 as a very slow-moving peak in the range of energies between 5.8 and 6.5 eV above the fermi level. (2) The sharp structure due to photoemission from peak ② in the valence band of Fig. 85 seems to be "blurred" in the region between 6 and 7 eV above the fermi level. The direct transition seen in the EDCs for clean silver appears to be the same direct transition that was seen earlier by Berglund and Spicer [Ref. 37] on cesiated silver, and will be discussed in considerable detail later in this chapter. The "blurring" of the sharp photoemission structure from d band peak ② seems to occur at the same energy as the "blurring" seen earlier by Berglund and Spicer [Ref. 37] on cesiated silver. No satisfactory explanation for this effect has yet been established, but the "blurring" may be due to lifetime broadening, or may perhaps be associated with the high density of states in the conduction band at 6.5 eV. The existence of the high density of states in the conduction band at 6.5 eV seems to account very well for the envelope of the experimental EDCs, but does not explain the apparent loss of structure. In addition, the direct transition is not observed at energies higher than 6.5 eV above the fermi level, and this might be somehow associated with the "blurring" of the d band peak ② that also occurs at 6.5 eV above the fermi level. However, this could just be a coincidence. Thus, there appears to be evidence for some structure in the conduction band density of states in the region between 6 and 7 eV above the fermi level, but the exact nature of this structure remains to be explained.

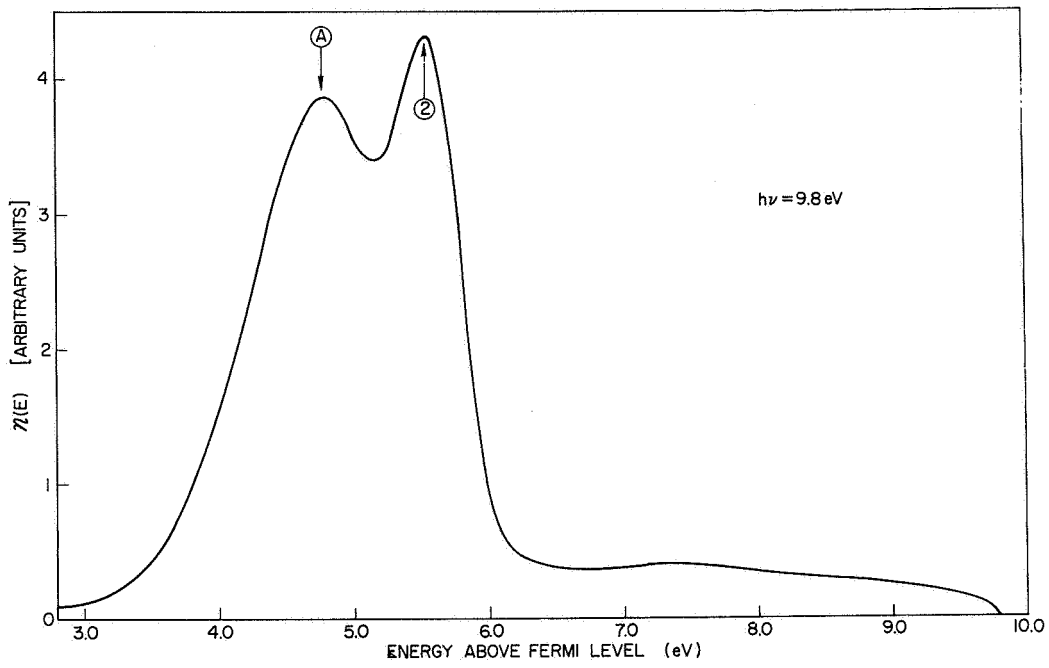
The calculated quantum yield of Fig. 87 and the calculated EDCs of Fig. 88 are for primary electrons only. As seen from the EDCs of Fig. 88, there is very little evidence of scattered electrons in the EDCs at photon energies below about 11.4 eV. However, the low energy "bulge" that begins to appear in the EDCs at photon energies of 11.4, 11.6, and 11.8 eV is probably due to the appearance of significant amounts of scattered electrons in the experimental EDCs.

Figures 89a through 89c show experimental EDCs obtained from a silver sample with an anomalously low vacuum level of about 3.0 eV. Because the EDCs do not rise abruptly at 3.0 eV, it seems possible that the surface of this silver film consists of crystallites with several different orientations, each with a different vacuum level in the range between 3 and 4 eV above the fermi level. These "anomalous" EDCs are presented because they provide evidence for possible fine structure in the d band density of states, as seen from the identification of peaks in the EDCs of Figs. 89a through 89c. All four of these d band peaks move in the manner of non-direct transitions, where $\Delta E_p = \Delta h\nu$, and correspond to the peaks labeled (2), (A), (B), and (C) in Fig. 85. Because of the abnormally low vacuum level, these peaks can be readily identified at energies as low as 4.5 eV above the fermi level. Except for the presence of the small peaks labeled (A), (B), and (C), the "anomalous" EDCs are consistent with the EDCs presented in Fig. 88.

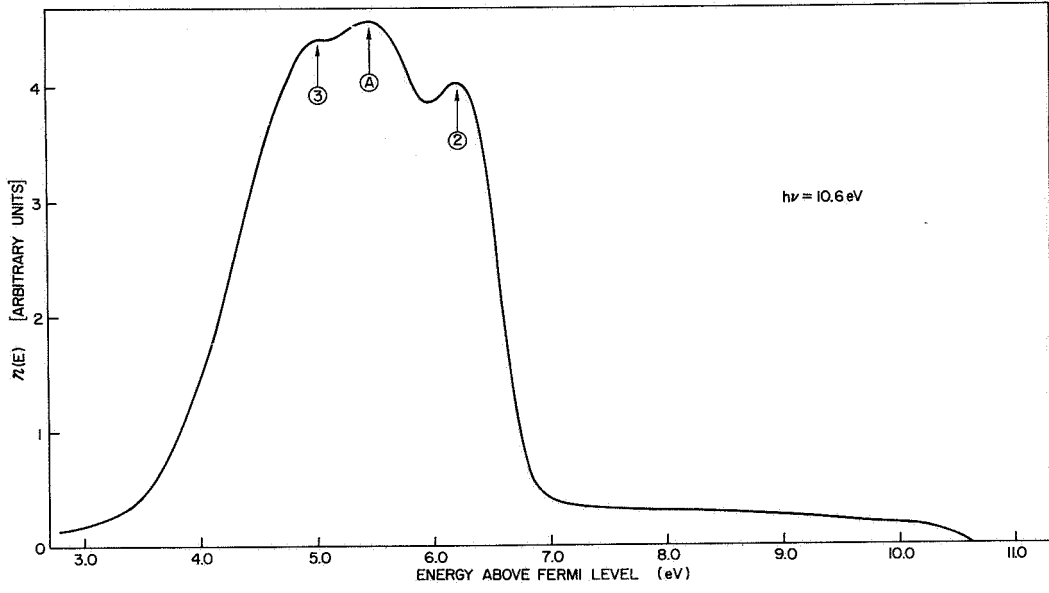


(a)

FIG. 89. ENERGY DISTRIBUTION CURVE FOR SILVER SAMPLE WITH AN ANOMALOUSLY LOW VACUUM LEVEL.

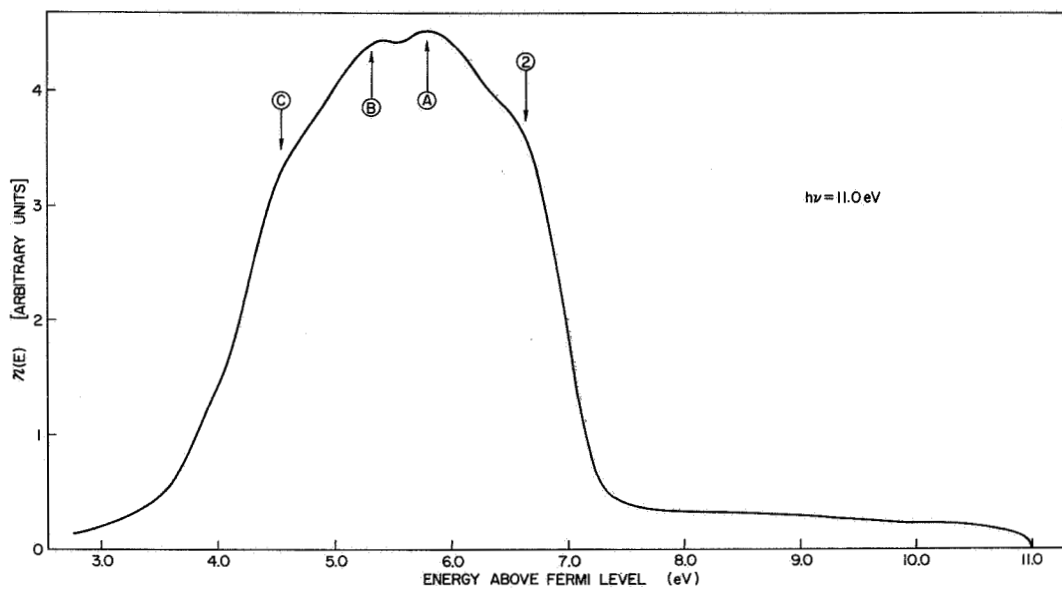


(b)

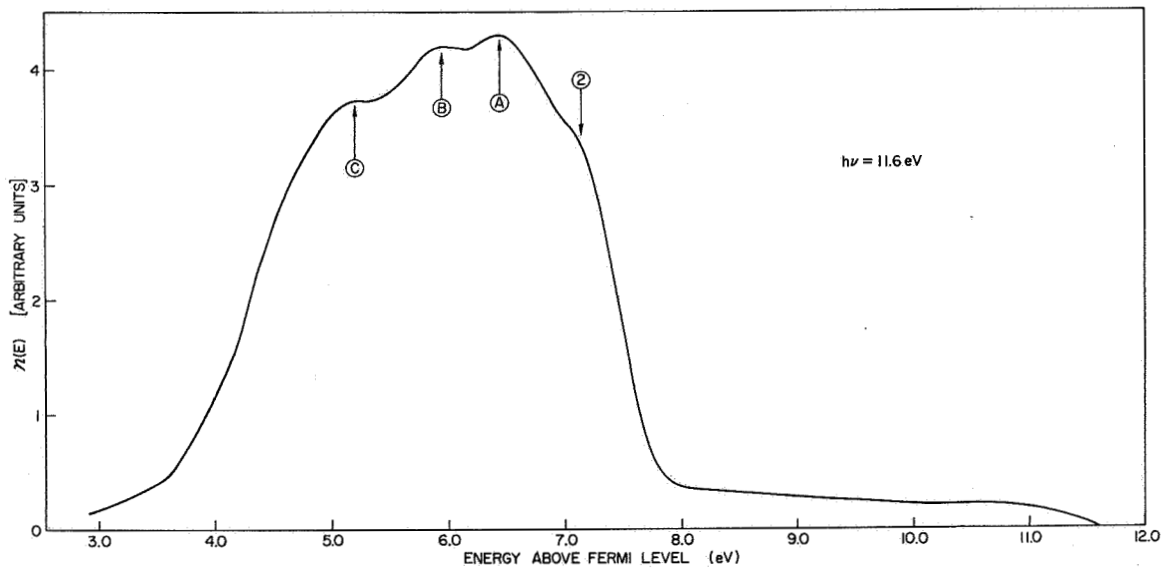


(c)

FIG. 89. CONTINUED.



(d)



(e)

FIG. 89. CONTINUED.

D. THE ELECTRON-ELECTRON SCATTERING LENGTH FOR SILVER

The calculated electron-electron scattering length $L(E)$ for silver is compared with several experimental data points in Fig. 90. The shape

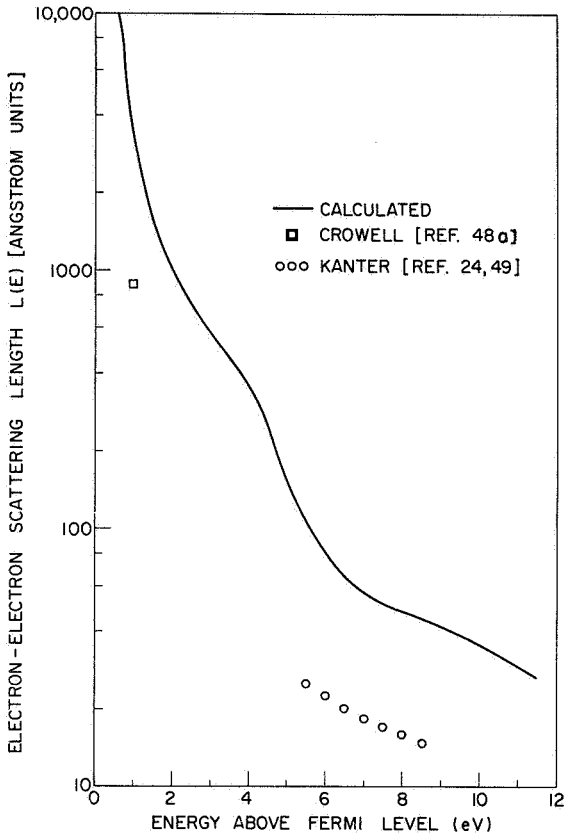


FIG. 90. CALCULATED ELECTRON-ELECTRON SCATTERING LENGTH FOR SILVER. Magnitude arbitrarily set equal to 44 \AA at 8.6 eV above the fermi level.

of the calculated $L(E)$ has been calculated from the optical density of states of Fig. 85, and the magnitude of the calculated $L(E)$ was arbitrarily set equal to 44 \AA at 8.6 eV above the fermi level. This value of 44 \AA was chosen so as to give good overall agreement between the calculated and the experimental quantum yield. The experimental data points of Crowell [Ref. 48a] and Kanter [Ref. 24] were obtained by the same techniques used for gold, and have been described in Chapter V. As can be seen from Fig. 90, the shape of the calculated $L(E)$ is in good agreement with the shape suggested by the experimental data points, but the calculated magnitude is too high by a factor of about 3.

This rather large discrepancy in magnitude is difficult to account for by any reasonable changes in the density of states of Fig. 85 or by errors in the quantum yield. Qualitatively, the density of states of Fig. 85 suggests that the electron-electron scattering length should be longer in silver than in either gold or copper, because the silver d bands are further below the fermi level than are the d bands in gold or copper, and consequently there are fewer possible scattering events in silver than in gold or copper. This qualitative reasoning concerning magnitude is borne out by the fact that in order to obtain agreement between the theoretical and experimental quantum yield, the magnitude of $L(E)$ for silver must be larger than the magnitude of $L(E)$ for either

gold or copper. Another possible explanation is that Kanter's [Ref. 24] experimental electron-electron scattering length for silver is somewhat too low. As seen in Chapter V, Kanter's experimental data for gold were in excellent agreement with the calculated results for gold. However, silver is considerably more susceptible to contamination than gold, and it is likely that any contamination would cause increased electron scattering, which could be interpreted as a shorter electron-electron scattering length. However, personal communication with Kanter indicates that his work has been done as carefully as possible, and his data for gold and silver are undoubtedly the best available at this time. Indeed, the author is indebted to Kanter for making available his gold and silver data prior to publication.

E. THE SPECIFIC HEAT FOR SILVER

If electron-phonon interaction is neglected, the density of states at the fermi surface can be calculated using Eq. (4.1) and the electronic specific heat for silver given in Ref. 95. The result is $N(E_f) = 0.275$ (electrons/eV-atom), and can be used as a qualitative check on the optical density of states of Fig. 85.

The outer electron configuration of silver is $4d^{10}5s^1$, so it can be assumed that the valence band of silver contains eleven electrons. Normalizing the valence band of Fig. 85 to hold eleven electrons, we obtain a value of $N(E_f) = 0.19$ (electrons/eV-atom) for the optical density of states at the fermi surface, as can be seen from the solid curve in Fig. 91. Thus the a priori optical density of states deduced solely from photoemission data is found to be in good agreement at the fermi surface with the value predicted from the specific heat.

The dashed curve in Fig. 91 shows how the valence band optical density of states can be adjusted near the fermi level to agree exactly with the value predicted by the electronic specific heat.

F. THE IMAGINARY PART OF THE DIELECTRIC CONSTANT $\epsilon_2(\omega)$ FOR SILVER

Using the theory of nondirect transitions and the optical density of states of Fig. 85, Eq. (3.98) can be used to calculate $\epsilon_2(\omega)$ for silver. The result is shown as the solid curve in Fig. 85, and is compared with

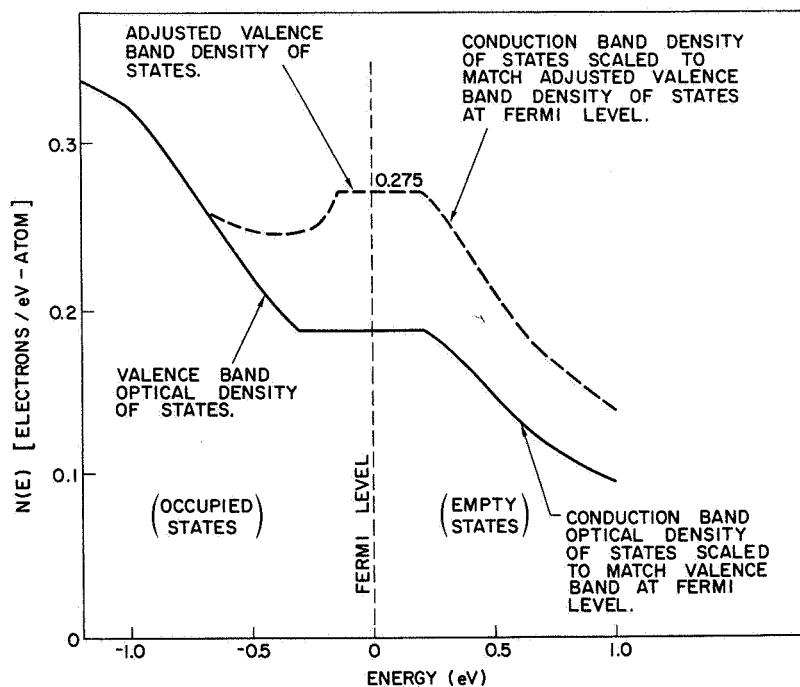


FIG. 91. ADJUSTMENT OF DENSITY OF STATES OF SILVER AT THE FERMI LEVEL TO AGREE WITH THE DENSITY OF STATES CALCULATED FROM THE SPECIFIC HEAT. The valence band of Fig. 85 is normalized to hold 11 electrons.

the "experimental" value of $\epsilon_2(\omega)$ that has been deduced from reflectivity measurements. The conduction band peak labeled (P) in the optical density of states of Fig. 85 has not been included in the calculation of $\epsilon_2(\omega)$. Table 4 identifies the initial and final states that are involved in the structure of the calculated $\epsilon_2(\omega)$, and it is found that the calculated $\epsilon_2(\omega)$ accounts very well for the experimental structure at energies of 3.3, 5.8, and 10.5 eV. However, the calculated $\epsilon_2(\omega)$ is not able to account for the strong, sharp peak in the experimental $\epsilon_2(\omega)$ at a photon energy of about 4.5 eV. [Including peak (P) of Fig. 85 in the calculated $\epsilon_2(\omega)$ would do little more than increase the strength of the calculated $\epsilon_2(\omega)$ in the region between 5 and 8 eV.]

The discrepancy between the calculated and the experimental $\epsilon_2(\omega)$ near 4 eV may be due to the very strong plasma resonance that occurs in silver at a photon energy of about 4.0 eV. As shown in Ref. 45, the energy loss function $\text{Im}[(-)\epsilon^{-1}]$ for silver peaks sharply at an energy of about

4.0 eV, strongly suggesting the presence of a many-body resonance. Hopfield [Ref. 65] has proposed a theory whereby phonon interaction enhances the coupling between the transverse electromagnetic wave and the longitudinal plasma resonance. Hopfield predicts that such a phonon-enhanced resonance should result in a sharp peak in the photoelectric EDCs and in a peak in $\epsilon_2(\omega)$ at photon energies in the vicinity of the plasma resonance. Berglund and Spicer [Ref. 37] have observed a very sharp peak in the experimental EDCs from cesiated silver at photon energies near the plasma resonance, and this sharp peak may very well be due to a plasma resonance.

As a particular example, Hopfield [Ref. 65] has incorporated phonon coupling to calculate the effect of the plasma resonance on $\epsilon_2(\omega)$ for the case of potassium, which has a plasma resonance at about 4.0 eV [Ref. 66]. Since silver also has a plasma resonance at this energy, one might expect that the plasma resonance in silver would affect $\epsilon_2(\omega)$ in qualitatively the same manner as the plasma resonance affects $\epsilon_2(\omega)$ in potassium. Thus, it is tempting to compare Hopfield's results for potassium with the discrepancy between the calculated and the experimental $\epsilon_2(\omega)$ in Fig. 92, since this discrepancy may be due to plasma resonance effects, which are not accounted for in the calculated curve of Fig. 92. Such a comparison is made in Fig. 93, where the magnitude of Hopfield's $\epsilon_2(\omega)$ has been scaled up by about an order of magnitude to match the peak height in the "discrepancy" curve. As seen in Fig. 93, the agreement in shape between Hopfield's theoretical $\epsilon_2(\omega)$ for potassium and the "discrepancy" curve for silver is remarkably good, indicating that the "discrepancy" between the calculated $\epsilon_2(\omega)$ and the experimental $\epsilon_2(\omega)$ for silver may very well be due to plasma oscillations enhanced by phonon coupling. A test of this possibility would be to experimentally measure the temperature dependence of $\epsilon_2(\omega)$ and the photoelectric EDCs of silver at photon energies in the vicinity of 4.0 eV, but these measurements have yet to be made.

G. THE PHOTOELECTRIC YIELD FROM CESIATED SILVER

The photoelectric yield and the EDCs for cesiated silver have been calculated using the optical density of states of Fig. 85 and the analysis described in Table 1 of Chapter III. The values for the absorption

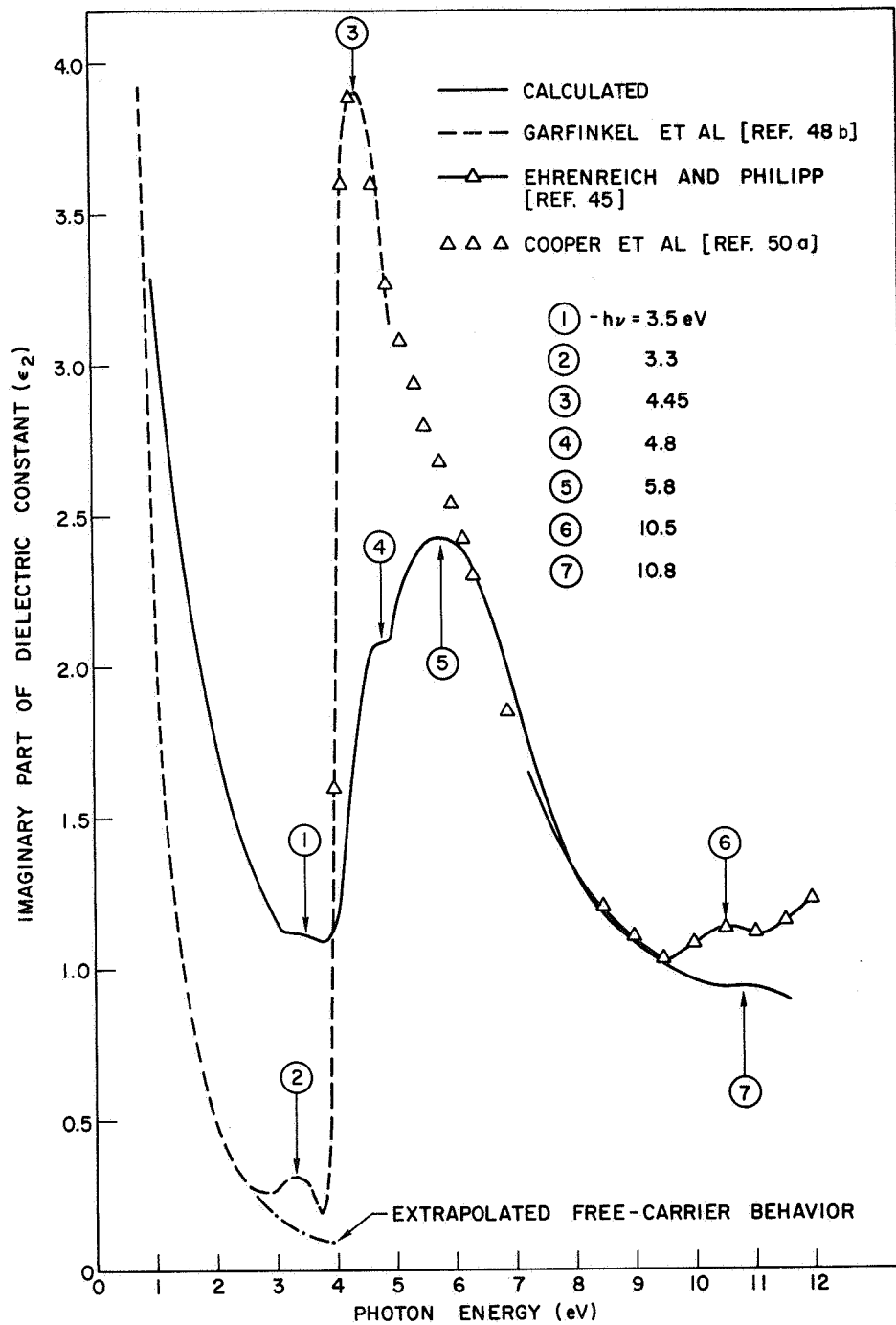


FIG. 92. COMPARISON OF CALCULATED ϵ_2 FOR SILVER WITH THE ϵ_2 OBTAINED FROM REFLECTIVITY MEASUREMENTS.

TABLE 4. IDENTIFICATION OF STRUCTURE IN $\epsilon_2(\omega)$ FOR SILVER (see Fig. 85)

Energy of Structure in the Experimental $\epsilon_2(\omega)$ (eV)	Energy of Structure in the Calculated $\epsilon_2(\omega)$ (eV)	Location of Initial State (Fig. 85)	Location of Final State (Fig. 85)
3.3	3.5	③	Empty states just above the fermi level
4.45 (very strong peak)	No strong peak observed	-	-
-	4.8	②	Empty states just above the fermi level
5.8 (shoulder)	5.8 (peak)	①	Empty states just above the fermi level
10.5	10.8	②	7

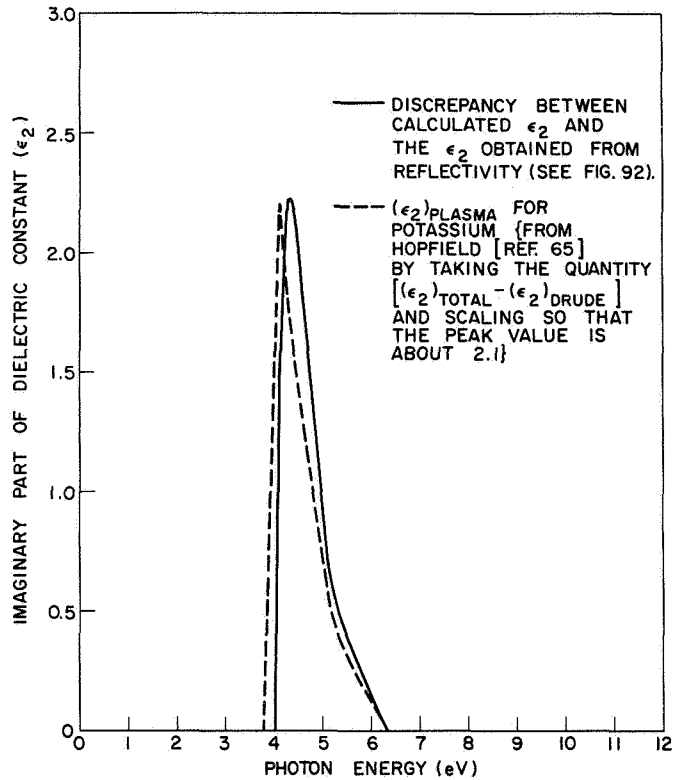


FIG. 93. DISCREPANCY IN ϵ_2 FOR SILVER ($h\nu > 4$ eV) COMPARED WITH $(\epsilon_2)_{\text{plasma}}$ FOR POTASSIUM, AS CALCULATED BY HOPFIELD [Ref. 65].

coefficient $\alpha(\omega)$ were taken from Ref. 45, and the magnitude of the electron-electron scattering length $L(E)$ was the same as that determined from the photoemission analysis of clean silver. The vacuum level was set to 1.6 eV, a value appropriate to silver covered with a surface monolayer of cesium. The calculated quantum yield is compared with the experimental results of Berglund and Spicer [Ref. 37] in Fig. 94. The agreement is seen to be excellent, both in shape and in magnitude, over nearly the entire range of energies between the vacuum level and the high energy cutoff of the LiF window.

In the region of energies between 1.6 and 3.8 eV, the reflectivity of silver is nearly 100 percent, and a small error in $R(\omega)$ could result in a large error in correcting the quantum yield for reflectivity. Thus, there may be a good deal of uncertainty in the experimental yield below

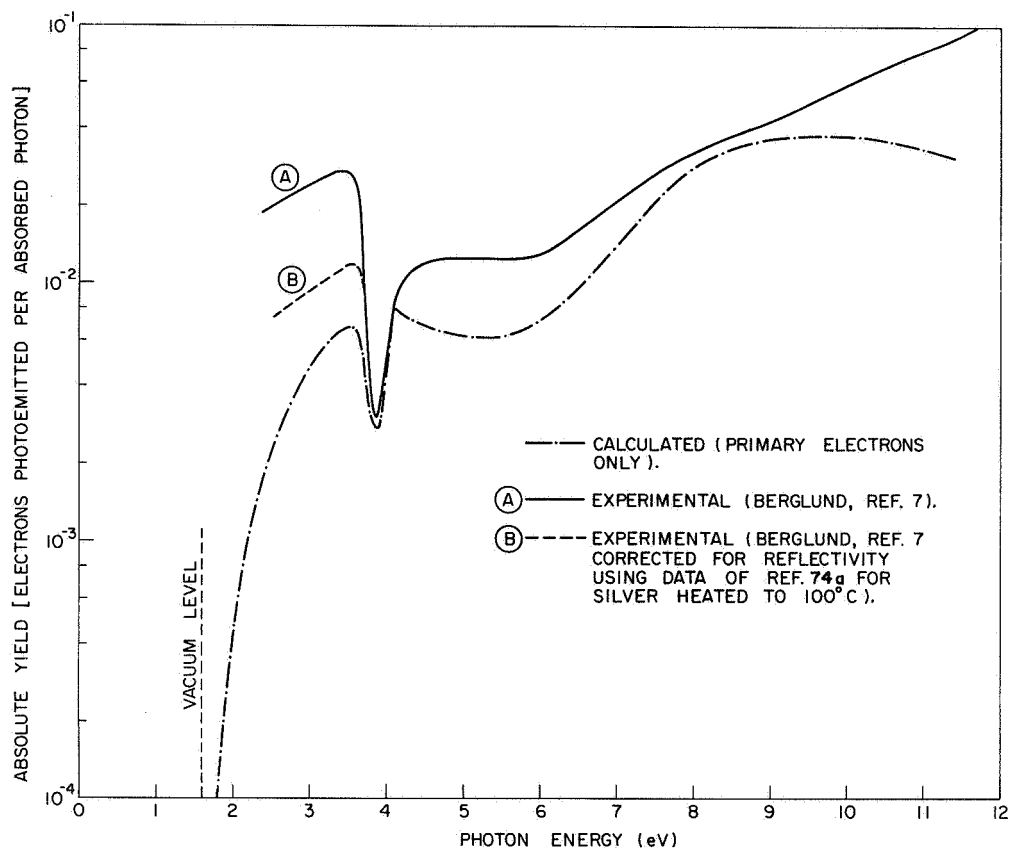


FIG. 94. COMPARISON OF CALCULATED YIELD WITH EXPERIMENTAL YIELD FOR SILVER WITH A SURFACE MONOLAYER OF CESIUM.

3.8 eV, since the reflectivity values used by Berglund and Spicer [Ref. 37] were taken from the literature, and not determined from the same silver samples that were used in measuring the quantum yield. In certain cases [Ref. 74a], it has been found that heating silver to only 100°C for a few hours can significantly change the reflectivity at photo energies below 3.8 eV. If the experimental quantum yield of Fig. 94 is corrected for reflectivity, using the values for silver that has been heated, curve B of Fig. 94 results. Curve B is somewhat closer to the calculated yield, and may be more appropriate to cesiated silver than curve A, since silver is heated to about 100°C during the cesiating process.

At photon energies above 3.5 eV, the calculated and the experimental quantum yields are in remarkably good agreement, when it is realized that the calculated curve accounts for only the primary (unscattered) electrons. Comparison of the calculated and the experimental EDCs (as shown in

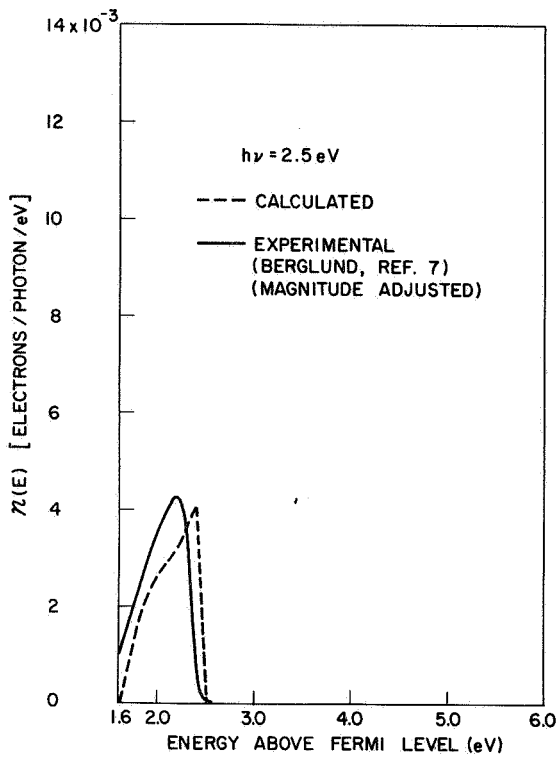
Section H of this chapter) indicates that the discrepancy in yield between 4 and 6 eV is probably due to Auger electrons, as described earlier by Berglund and Spicer [Ref. 37], and that the discrepancy above 9.5 eV is due to scattered electrons. In the range of photon energies between about 6.5 and 9 eV, the experimental EDCs are dominated by photoemission from primary d band electrons, and it would be expected that in this range of energies the magnitude of the calculated yield for primary electrons should be very close to the magnitude of the total experimental yield, since the primary d electrons dominate over the secondary scattered electrons and Auger electrons. This is indeed the case, as can be seen from the close agreement between the magnitudes of the calculated and the experimental quantum yield in the region between 6.5 and 9 eV.

A large dip in the quantum yield is seen to occur at a photon energy of about 3.9 eV, the energy of the plasma resonance in silver. The dip occurs because at the plasma resonance the absorption coefficient $\alpha(\omega)$ becomes very small, and the absorption depth becomes very long. Thus, a large fraction of the incident photons are absorbed deep in the crystal (far from the surface), and most of the photoexcited electrons cannot escape because the electron-electron scattering length is only about 350 \AA , much shorter than the absorption depth $[\alpha(\omega)]^{-1}$, which is more than 1000 \AA at the plasma resonance.

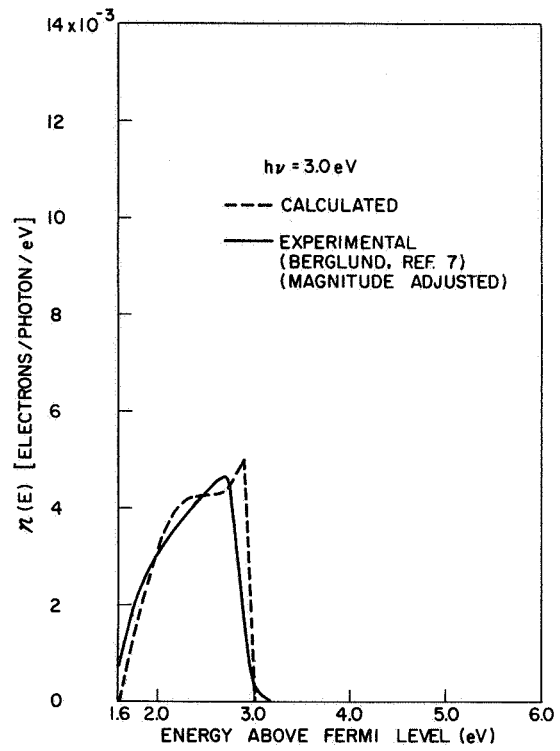
The excellent quantitative agreement between the experimental and the calculated quantum yield for cesiated silver indicates that there was no bulk reaction between the cesium and the silver in the earlier experiments of Berglund and Spicer [Ref. 37], and indicates that the photoemission data from cesiated silver are representative of bulk silver. Indeed, the photoemission data of Berglund and Spicer appear to be a superb example of the wealth of information that can be obtained in certain cases by lowering the vacuum level with a surface monolayer of cesium.

H. PHOTOELECTRIC ENERGY DISTRIBUTIONS FROM CESIATED SILVER

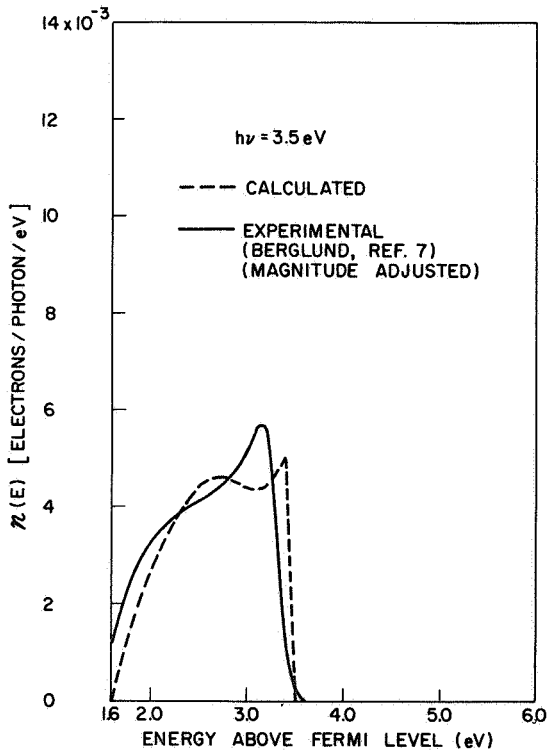
The calculated EDCs for cesiated silver are compared with the experimental EDCs of Berglund and Spicer [Ref. 37] in Figs. 95a through 95t. The experimental EDCs shown in Fig. 95 have been obtained by normalizing the raw data of Berglund and Spicer [Ref. 37] to their photoelectric yield.



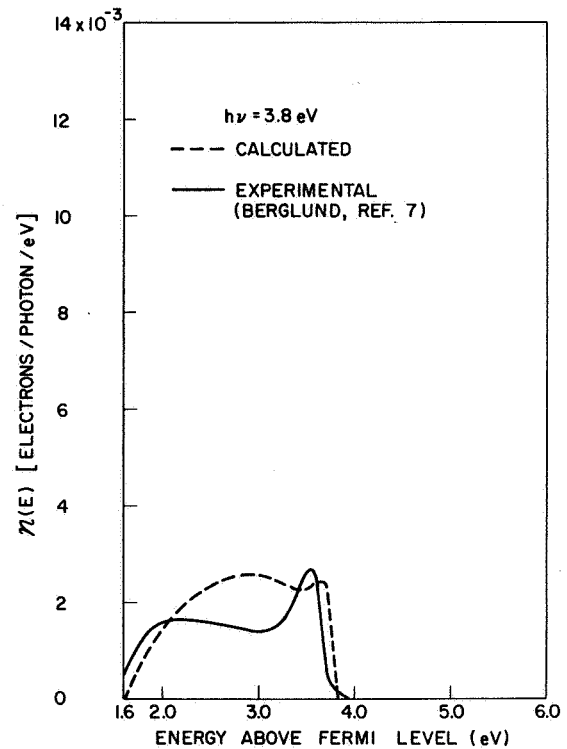
(a)



(b)

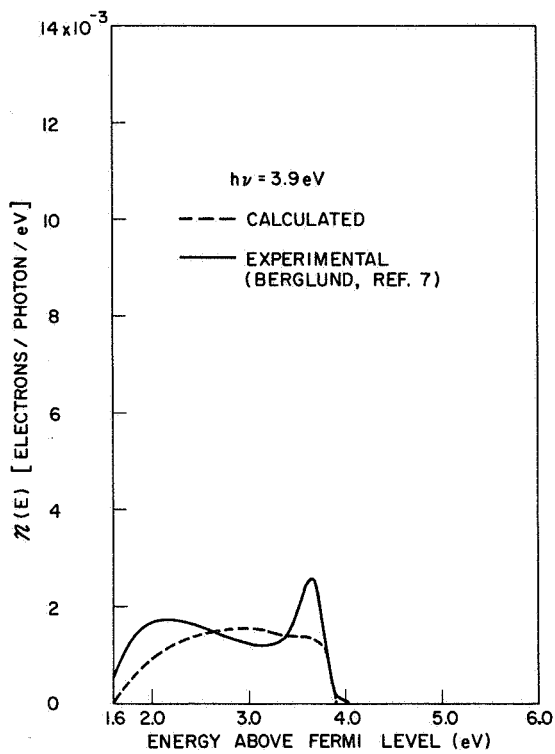


(c)

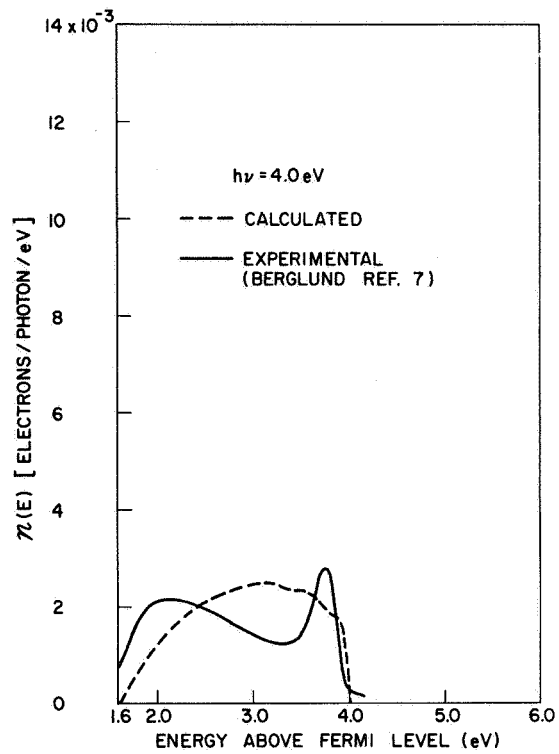


(d)

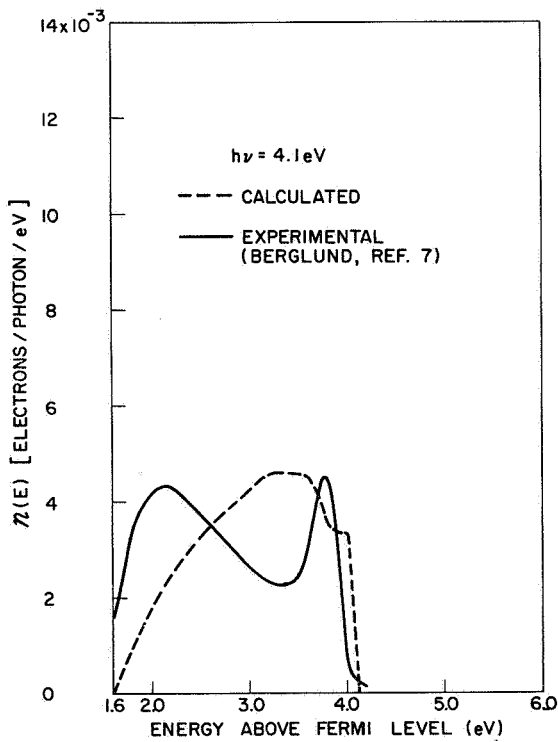
FIG. 95. PHOTOELECTRIC ENERGY DISTRIBUTION CURVES FOR CESIATED SILVER.



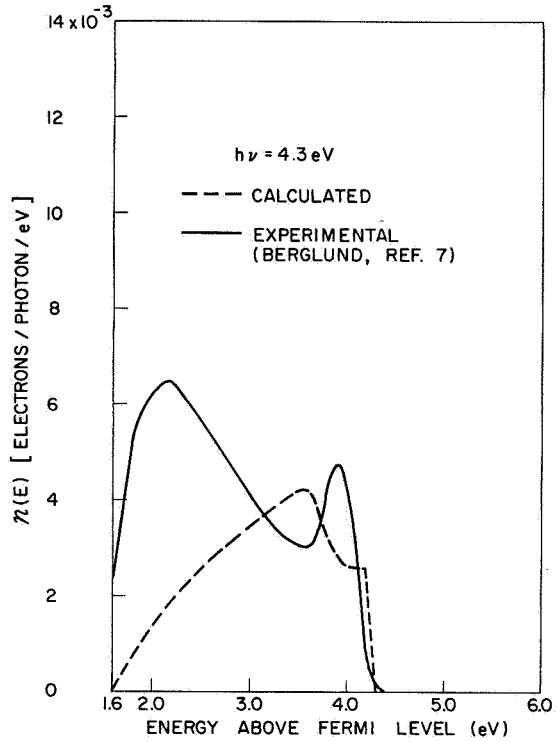
(e)



(f)

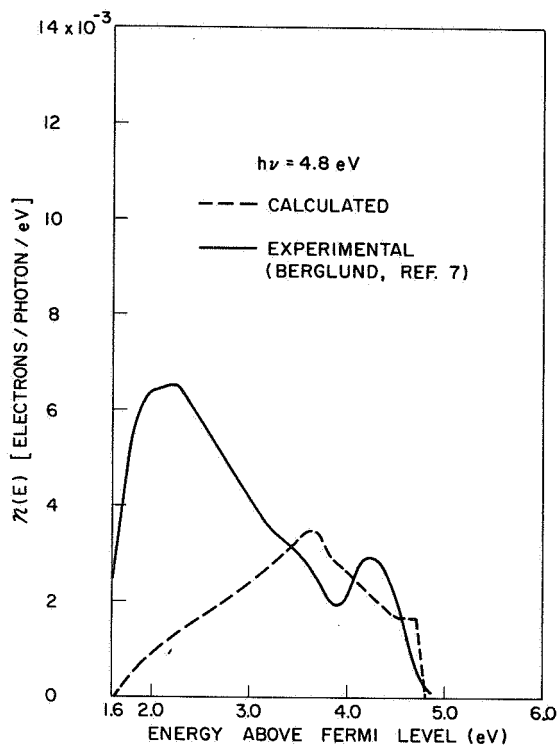


(g)

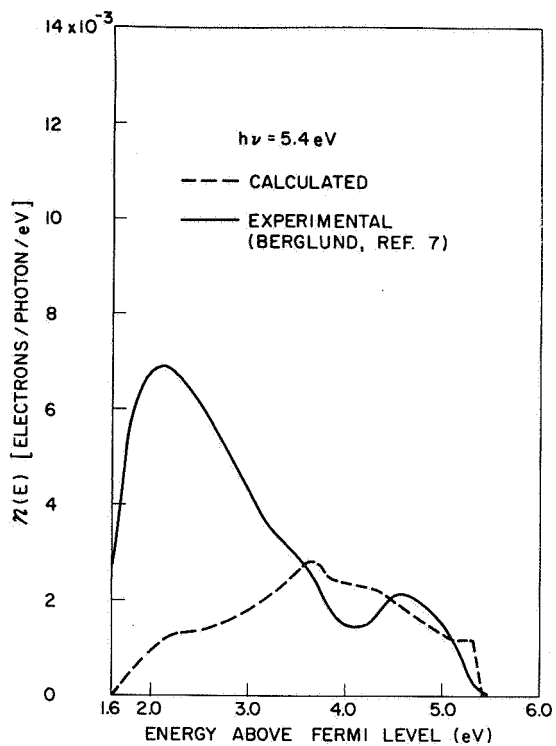


(h)

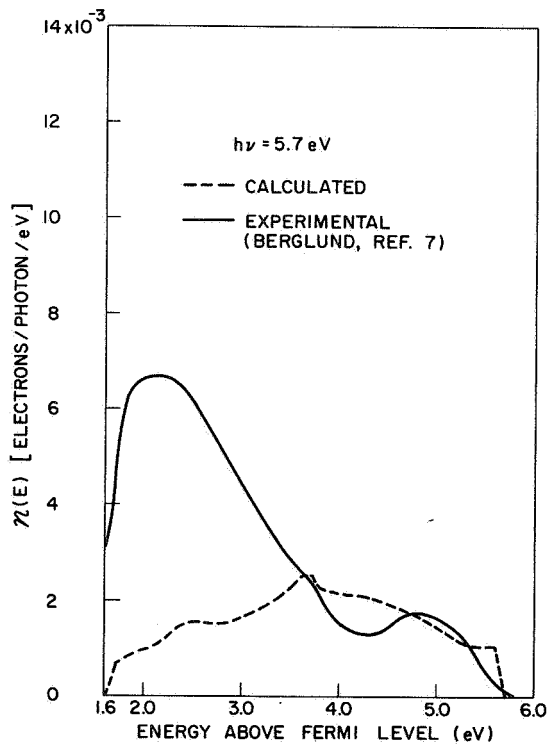
FIG. 95. CONTINUED.



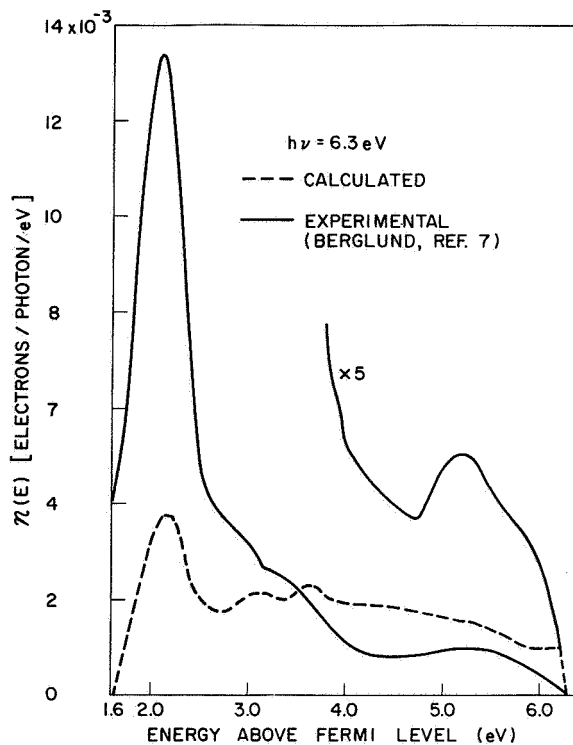
(i)



(j)

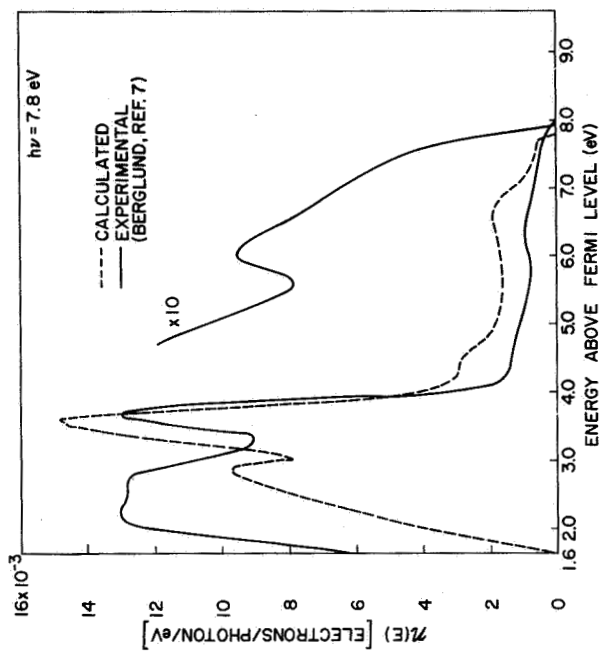


(k)

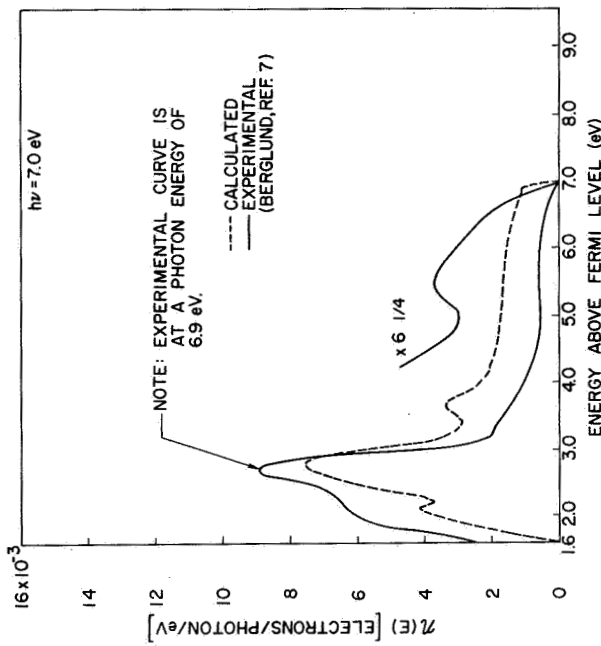


(l)

FIG. 95. CONTINUED.



(n)



(m)

FIG. 95. CONTINUED.

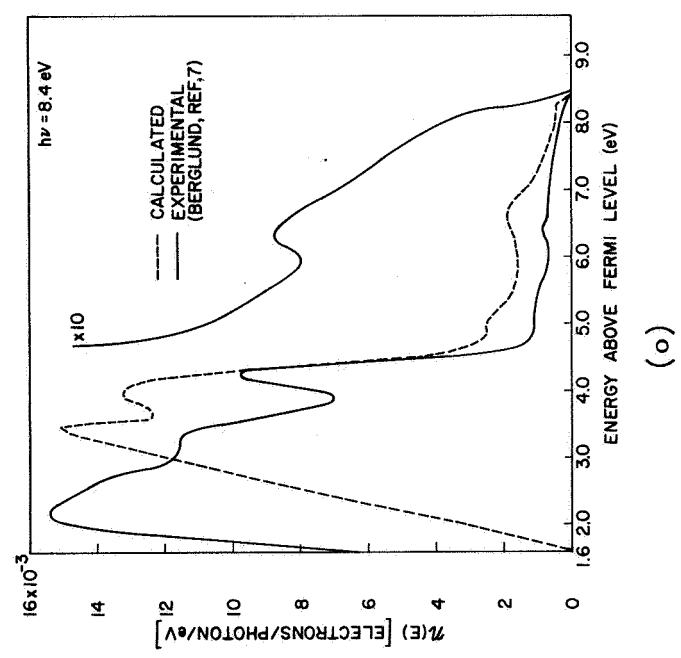
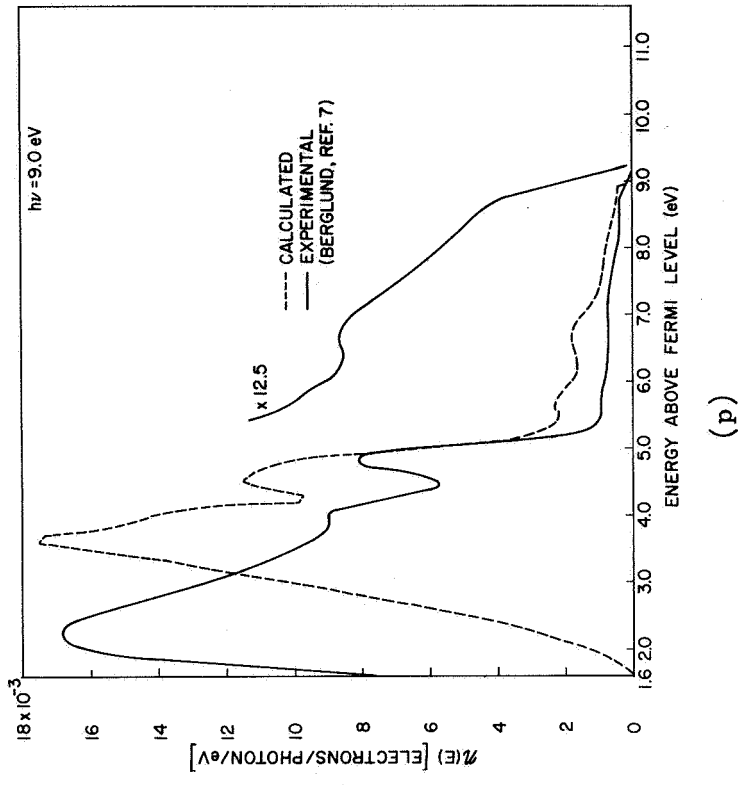


FIG. 95. CONTINUED.

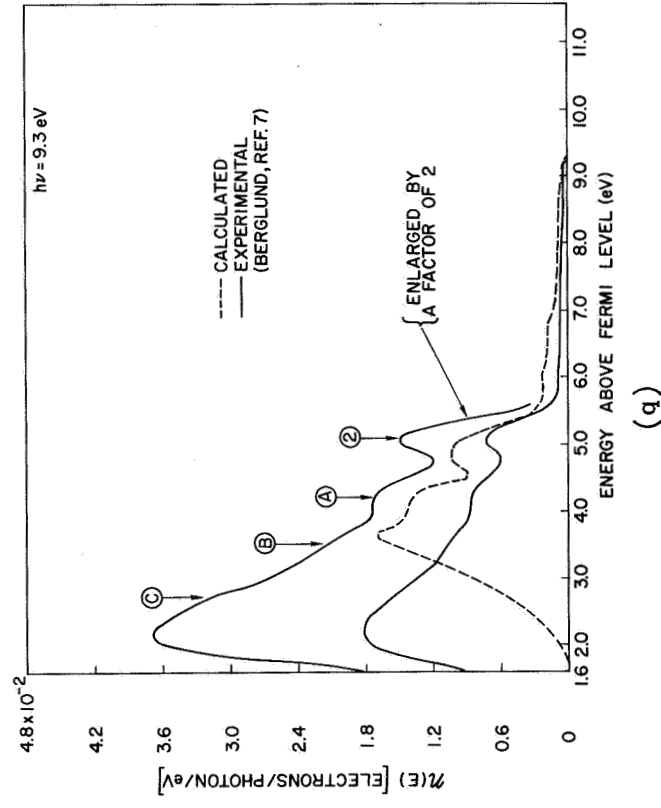
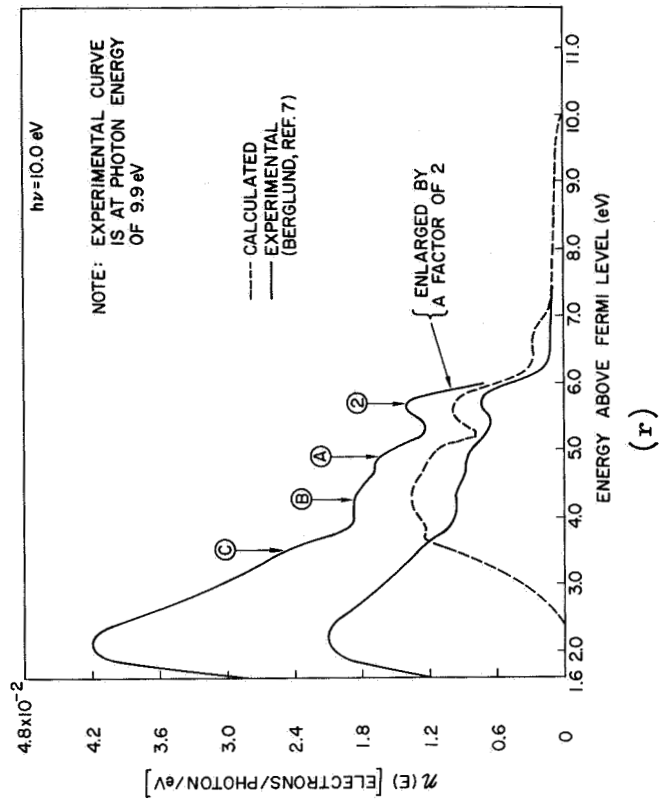


FIG. 95. CONTINUED.

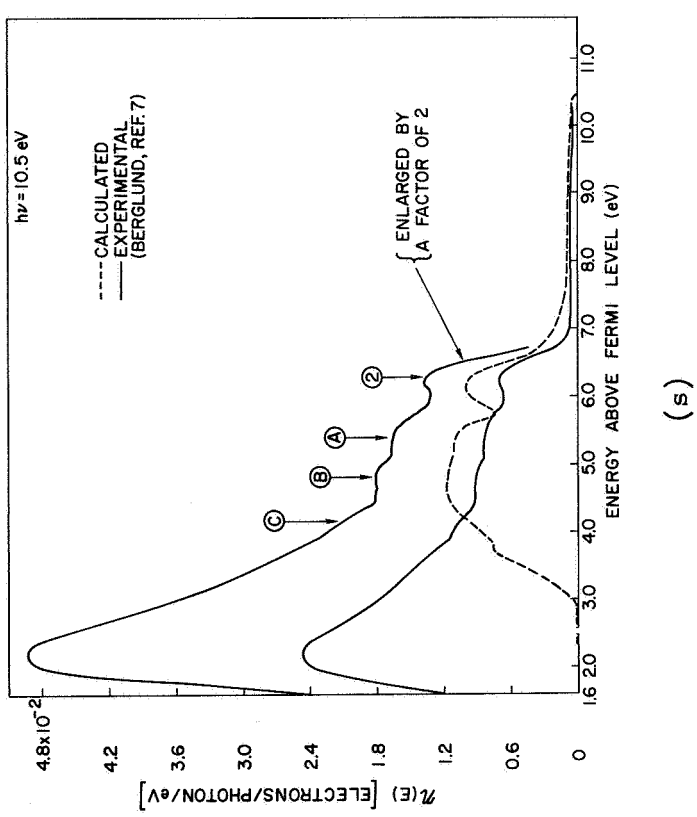
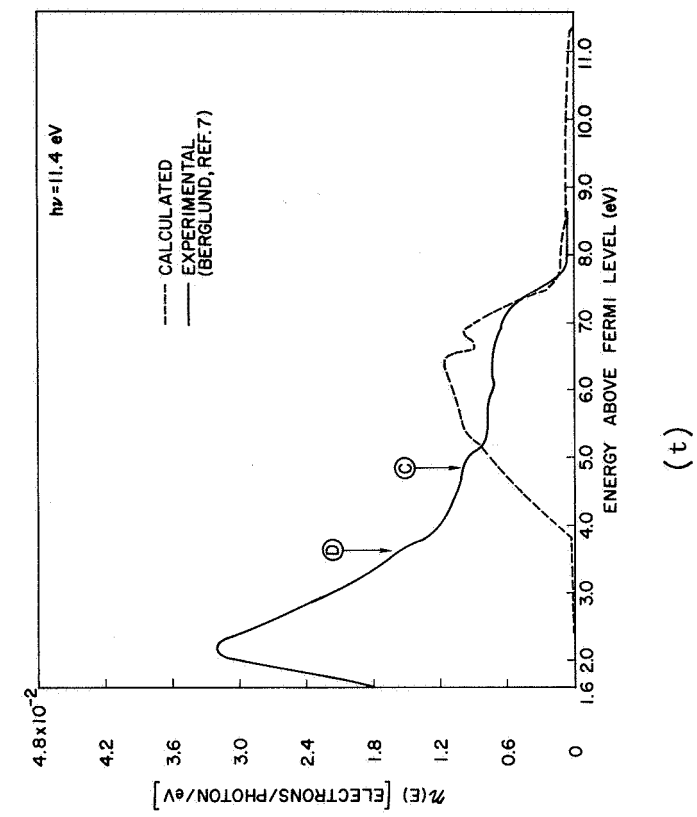


FIG. 95. CONTINUED.

Inspection of the curves in Fig. 95 shows that for all photon energies greater than about 4.3 eV, the calculated and experimental EDCs are in excellent agreement with respect to overall shape and magnitude. In making this comparison, one must realize that the calculated curves do not account for the Auger electrons and the scattered electrons, as discussed in Section G of this chapter.

The major discrepancy between the calculated EDCs and the experimental EDCs occurs in the range of photon energies between about 3.5 and 4.3 eV. This discrepancy is the large, sharp peak at the leading edge of the EDCs, which is seen to peak at a photon energy of about 4.0 eV, the energy of the plasma resonance in silver. In fact, Hopfield's [Ref. 65] theory predicts that a plasma resonance could cause such a prominent peak in the experimental EDCs. Thus, it is tempting to speculate that the unexplained peak in the silver EDCs is in some way intimately associated with the plasma resonance. According to Hopfield [Ref. 65], the strength of such a peak is dependent upon phonon coupling, and consequently is temperature-dependent. Spicer [Ref. 6] has suggested that Hopfield's theory can be tested by measuring the temperature-dependence of the photoelectric EDCs from cesiated silver at photon energies in the vicinity of 4.0 eV; however, such an experiment has not yet been done.

In addition to the plasma resonance, the calculated EDCs do not account for the direct transition that can be seen in the experimental EDCs in Fig. 95. The peak identifying the final states of the direct transition can be seen in the energy range between 4.0 and 6.5 eV above the fermi level, and will be discussed in detail in Section I of this chapter.

The fine structure peaks labeled (A), (B), and (C) in the d band optical density of states of Fig. 85 have not been included in the calculated EDCs shown in Fig. 95. As discussed earlier in this chapter, the locations of the peaks (A), (B), and (C) in Fig. 85 were deduced from a clean silver sample with an anomalously low vacuum level. This fine structure can also be seen in the experimental EDCs on cesiated silver in the range of photon energies between 7.8 and 11.6 eV. The fine structure has been labeled in Fig. 95, using the notation (A), (B), and (C) which corresponds to the notation used in the optical density of states of

Fig. 85. Thus, evidence for fine structure in the d bands of silver has been found in both clean silver and cesiated silver. This evidence strongly suggests that the peaks labeled (A), (B), and (C) in Fig. 85 are real and do indeed exist.

In addition to the fine structure discussed above, the experimental curve at 11.4 eV shows an additional unexplained "bump," which has been labeled (D). This "bump" could be due to structure deep in the valence band at an energy of about 8 eV below the fermi level. However, the existence of peak (D) in the experimental data is uncertain, and peak (D) must be verified by additional photoemission experiments on cesiated silver before it can be considered to be real.

A very interesting feature becomes apparent when the EDCs of Berglund and Spicer [Ref. 37] are normalized to yield and compared as shown in Figs. 96, 97, and 98. The significant feature of these EDCs is that the magnitude of the peaks in the EDCs decreases as the peaks move away from

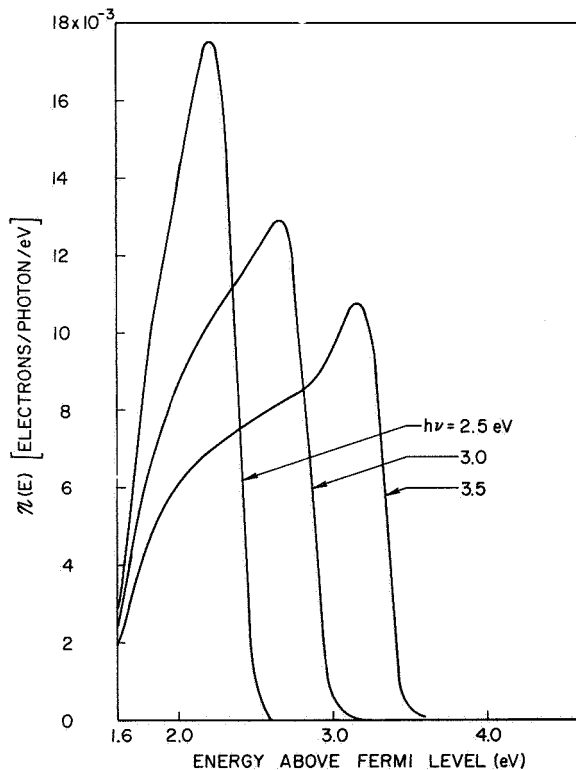


FIG. 96. EXPERIMENTAL ENERGY DISTRIBUTION CURVES OF CESIATED SILVER NORMALIZED TO BERGLUND'S YIELD [REF. 7].

the vacuum level, just as if there were a very strong peak in the conduction band density of states in the vicinity of 2.0 eV above the fermi level. The overall decrease in the magnitude of the EDCs in Figs. 96 and 97 does not appear to be readily explained by a peak in the conduction band density of states, but this would depend critically upon the shape of the conduction band peak and the shape of the valence band density of states just below the fermi level. It is also possible that strong direct transitions to states in the vicinity of 2 eV above the fermi level could cause the effect seen in Figs. 96, 97, and 98. Unfortunately, the data of Figs. 96, 97, and 98 do not provide enough information to enable us to determine

whether the strong "action" at 2.0 eV above the fermi level is due to direct transitions or to a high density of states in the conduction band. Nevertheless, these EDCs do provide direct

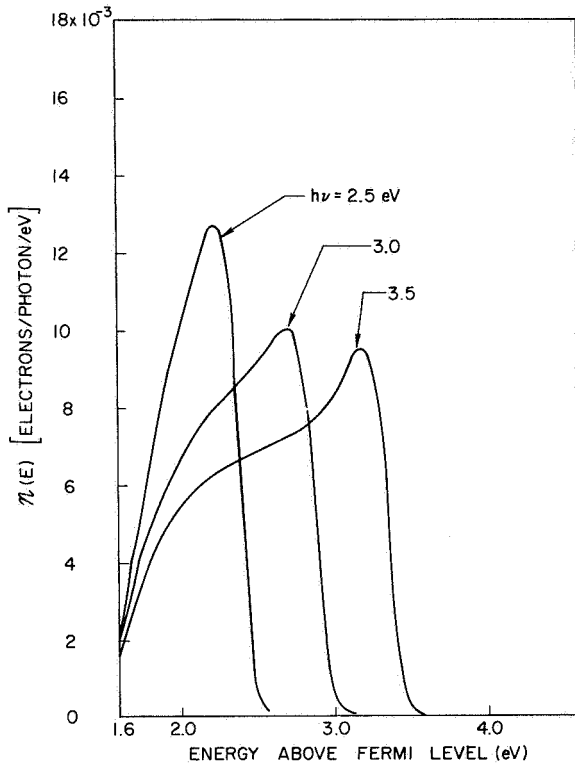


FIG. 97. EXPERIMENTAL ENERGY DISTRIBUTION CURVES OF CESIATED SILVER [REF. 7], NORMALIZED TO YIELD B OF FIG. 94.

experimental evidence of strong structure in the conduction band of silver in the vicinity of 2 eV above the fermi level. An interesting point is that the nature of the curves for silver in Fig. 96 is very similar to the nature of the corresponding curves for copper in Fig. 4 of Ref. 37, when the copper curves are normalized to yield.

Thus, the normalized EDCs of Figs. 96, 97, and 98 indicate that there is very likely to be structure in the conduction band density of states of silver in the vicinity of 1.7 to 2.0 eV above the fermi level, and this structure is indicated as peak (D) in the optical density of states of Fig. 85. Reference to the energy band diagram of Fig. 86 shows that the location of the X'_4 critical

point is at about 1.8 eV, just the same as the energy of peak (D) in Fig. 85. Thus, it would seem that the conduction band peak (D) is to be associated with the X'_4 critical point in the energy band diagram of silver. Consequently, if peak (D) does indeed exist, as is strongly suggested by the normalized EDCs of cesiated silver, it can be considered as experimental evidence that the X'_4 point in silver is at the same energy as the X'_4 point in copper, which has been identified earlier by Berglund and Spicer [Ref. 37].

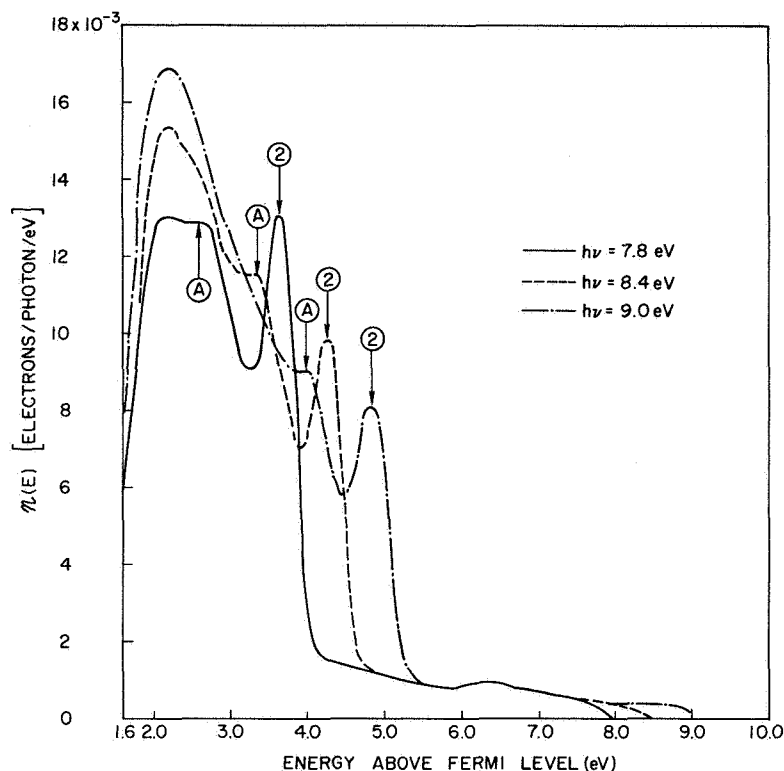


FIG. 98. EXPERIMENTAL ENERGY DISTRIBUTION CURVES OF CESIATED SILVER [REF. 7], NORMALIZED TO BERGLUND'S YIELD.

I. THE DIRECT TRANSITION IN SILVER

A direct transition is observed in the EDCs from clean silver at photon energies less than 8.6 eV, as shown in Fig. 99. In Fig. 99, a small circle is used to indicate the peak location that represents the energy of the final state in the direct transition. This direct transition is also clearly seen in the silver sample with the anomalously low vacuum level, as shown in Fig. 100.

The direct transition seen in the EDCs from clean silver is the same transition as the $L_2' \rightarrow L_1$ transition seen earlier by Berglund [Ref. 7] and Berglund and Spicer [Ref. 37] in the EDCs from cesiated silver, as can be seen from Fig. 101, where the peak energy E_p associated with the direct transition is plotted as a function of photon energy. The points corresponding to the direct transition in cesiated silver have been taken from the experimental EDCs of Fig. 95, and are seen to merge very closely

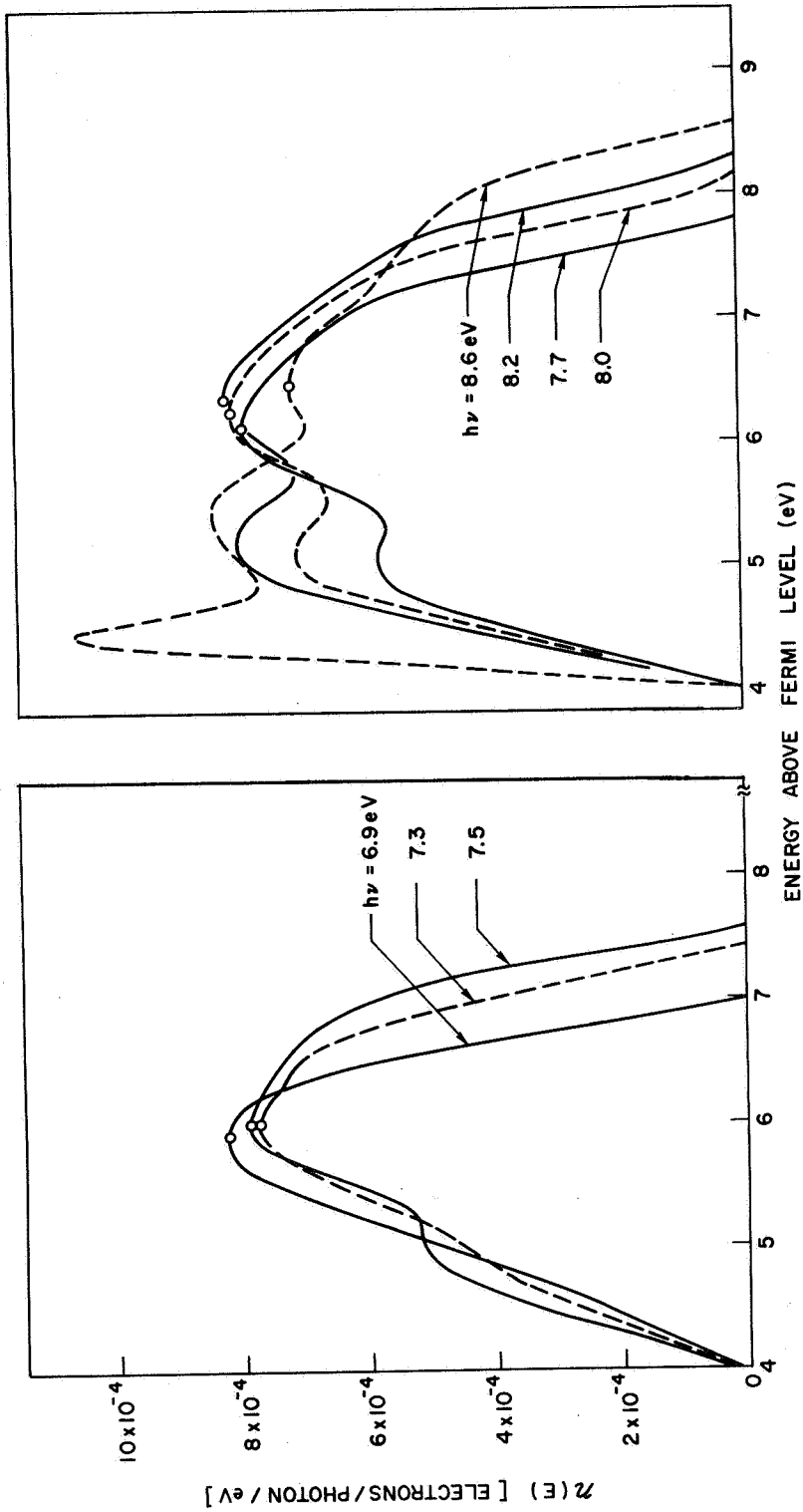


FIG. 99. EVIDENCE FOR DIRECT TRANSITIONS IN SILVER.

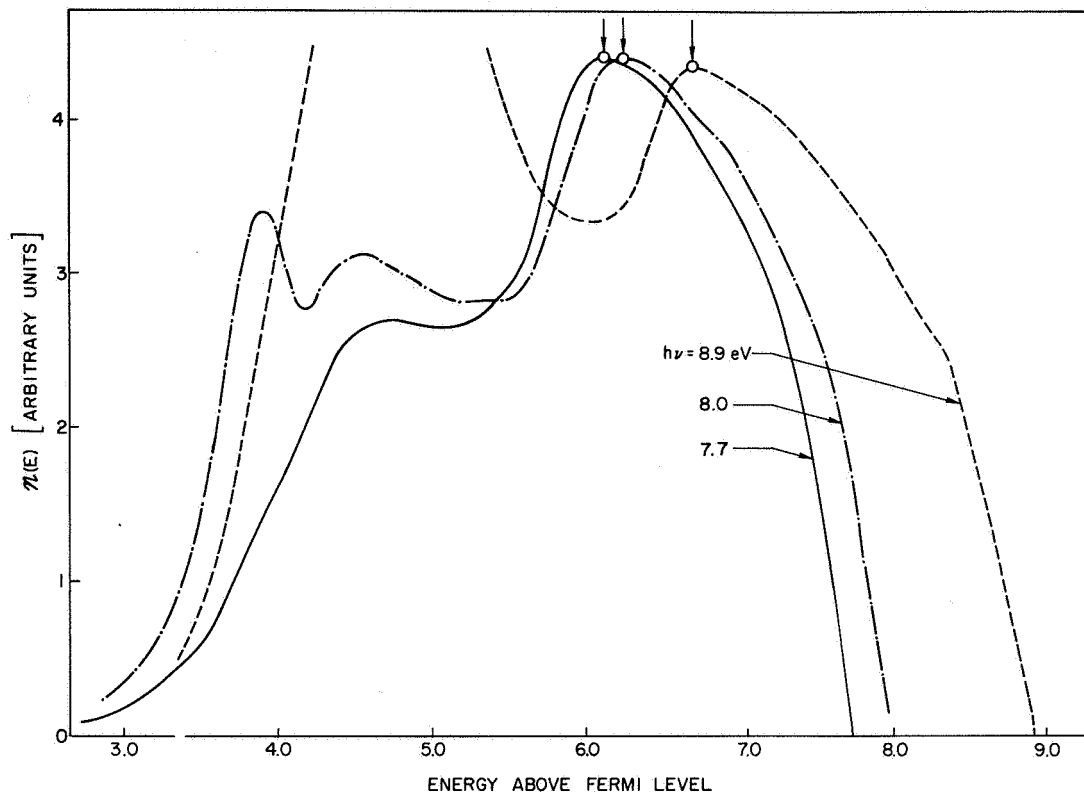


FIG. 100. EVIDENCE OF DIRECT TRANSITIONS IN A SILVER SAMPLE WITH AN ANOMALOUSLY LOW VACUUM LEVEL. Only the shapes of the curves are significant. The relative amplitudes are arbitrary.

with the points obtained from clean silver, thus identifying the direct transition in clean silver with the direct transition in cesiated silver.

As seen in Fig. 101, the direct transition in silver has been observed in the EDCs over a range of photon energies between 4.1 and 9.0 eV. At $h\nu = 4.1$ eV, the final energy of the direct transition is about 3.8 eV above the fermi level, and at $h\nu = 9.0$ eV, the final energy of the direct transition is at 6.5 eV above the fermi level. As seen in Fig. 85, there are peaks in the conduction band density of states at 3.5 and 6.5 eV above the fermi level, corresponding very closely to the lowest and highest energies at which the direct transition is observed. Thus, it is possible that the conduction band peaks at 3.5 and 6.5 eV are associated with critical points at the band edges of the conduction band that provides the final states for the direct transition, but this could be just a coincidence.

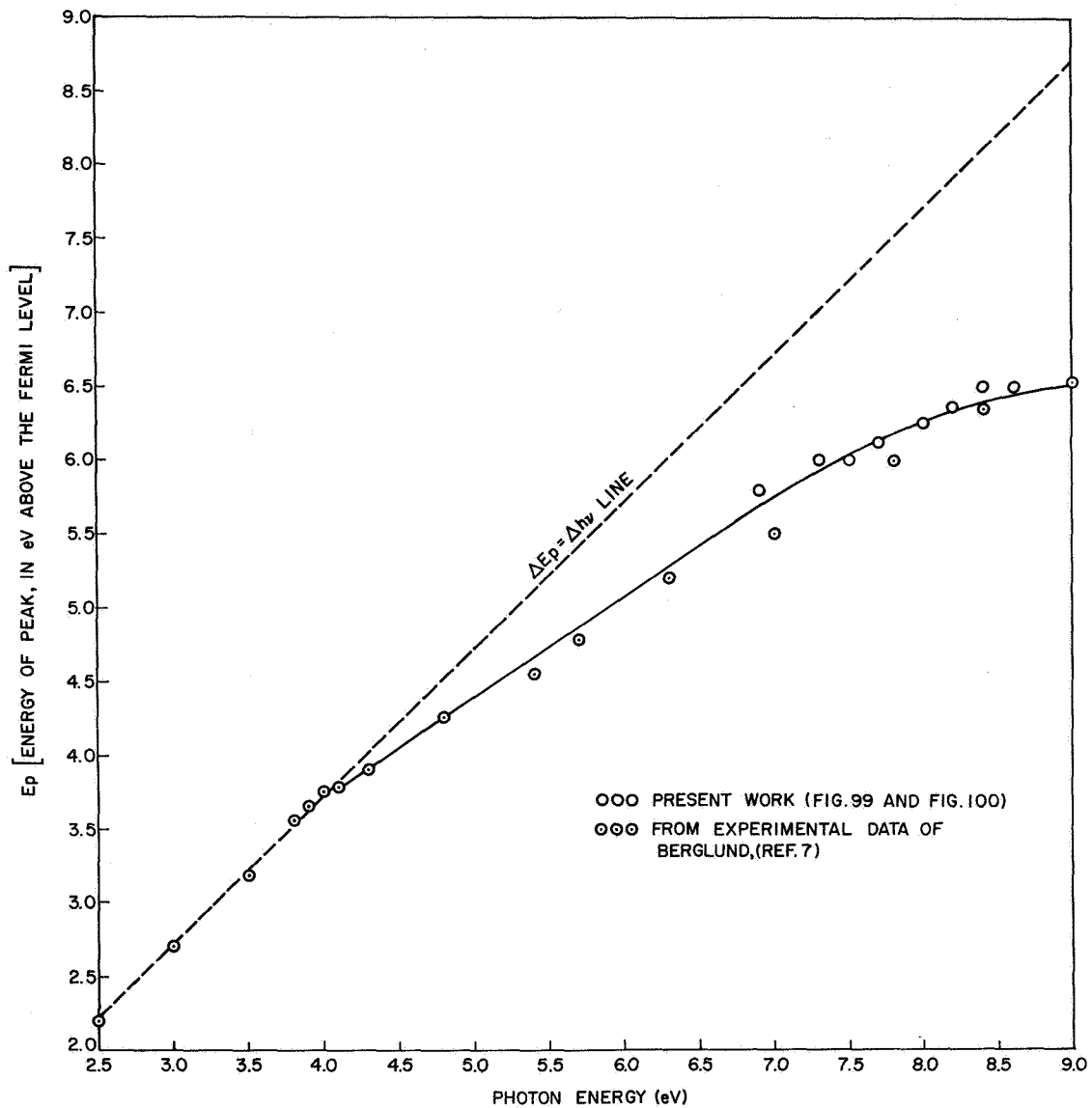


FIG. 101. DIRECT TRANSITIONS IN SILVER.

Since $E_{\text{initial}} = E_{\text{final}} - h\nu$, the energy of the initial state involved in the direct transition can be calculated as a function of photon energy from the values of E_{final} and $h\nu$ given in Fig. 101. The results of such a calculation are shown in Fig. 102. At photon energies between 2.5 and 4.0 eV, it is seen from Fig. 102 that the initial state is at 0.3 eV below the Fermi level, and that the transition is not a direct transition, but a nondirect transition where $(\Delta E_p)_{\text{final state}} = \Delta h\nu$. Berglund and Spicer [Ref. 37] have associated this initial state at 0.3 eV below the

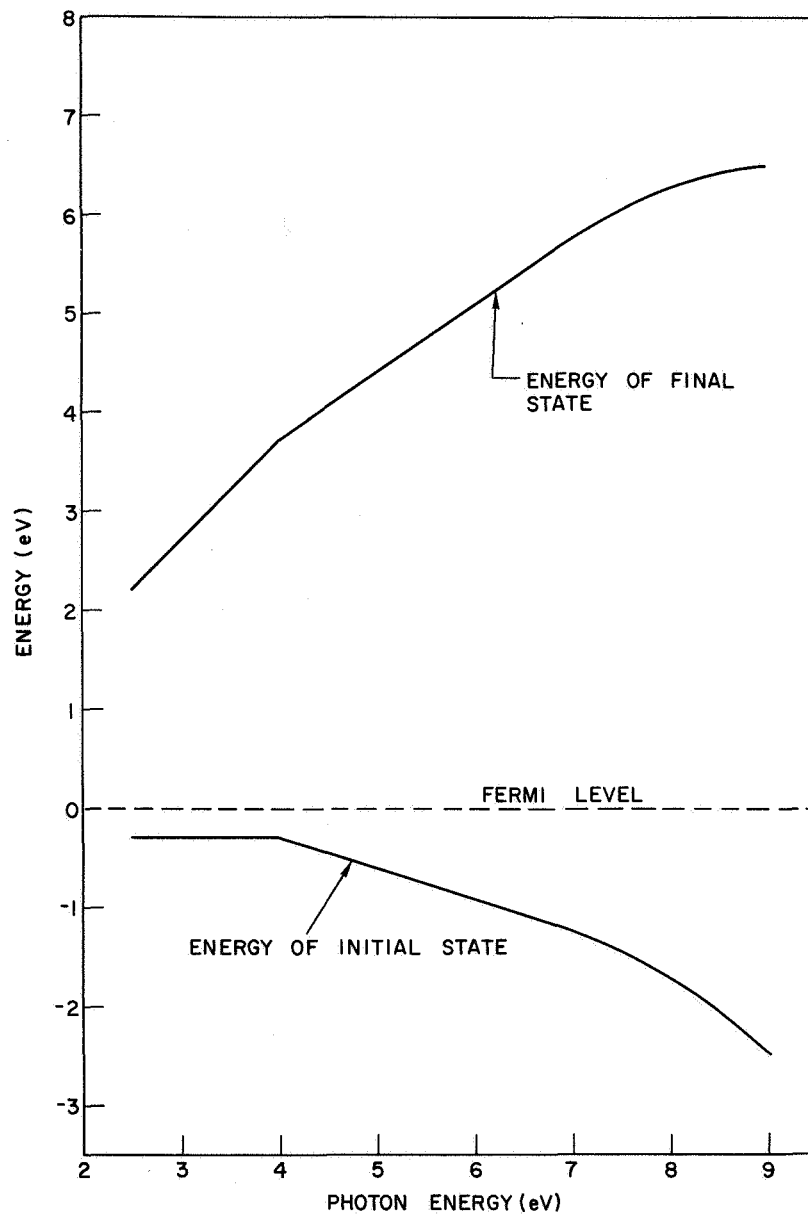


FIG. 102. ENERGY OF INITIAL AND FINAL STATES FOR THE DIRECT TRANSITION IN SILVER. The energy of the final state is taken as the smooth curve in Fig. 101.

fermi level with the L'_2 critical point in the energy band diagram of Fig. 86. In addition, they have associated the onset of direct transitions at 3.7 eV above the fermi level with the L_1 critical point in the conduction band of Fig. 86. Using the data of Fig. 102, we can obtain an estimate of the relative masses at L'_2 and L_1 in the following manner:

First, let us expand the conduction band at L_1 and the valence band at L_2' in a power series in k , where k is to be measured in some direction from the L point. Thus,

$$E_{\text{final}}^{L_1} = 3.7 + \frac{\hbar^2}{2m_{L_1}} \left(k^2 + A_3^{L_1} k^3 + \dots \right) \quad (6.1)$$

$$E_{\text{initial}}^{L_2'} = -0.3 + \frac{\hbar^2}{2m_{L_2'}} \left(k^2 + A_3^{L_2'} k^3 + \dots \right) \quad (6.2)$$

where the coefficient of the linear term has been set equal to zero. Near the L -point, the parabolic term will dominate, and

$$E_{\text{final}}^{L_1} \cong 3.7 + \frac{\hbar^2}{2m_{L_1}} k^2 \quad (6.3)$$

$$E_{\text{initial}}^{L_2'} \cong -0.3 + \frac{\hbar^2}{2m_{L_2'}} k^2 \quad (6.4)$$

From Eq. (6.3) and Eq. (6.4),

$$\frac{m_{L_2'}}{m_{L_1}} = \frac{E_{\text{final}}^{L_1} - 3.7}{E_{\text{initial}}^{L_2'} + 0.3} \quad (6.4)$$

The quantity

$$\left\{ (-) \left(\frac{E_{\text{final}}^{L_1} - 3.7}{E_{\text{initial}}^{L_2'} + 0.3} \right) \right\}$$

is plotted as a function of photon energy in Fig. 103, and is found to be a constant equal to 2.05 in the range of photon energies between 4 and 7 eV. Substituting the value into Eq. (6.4), the ratio of the masses is found to be

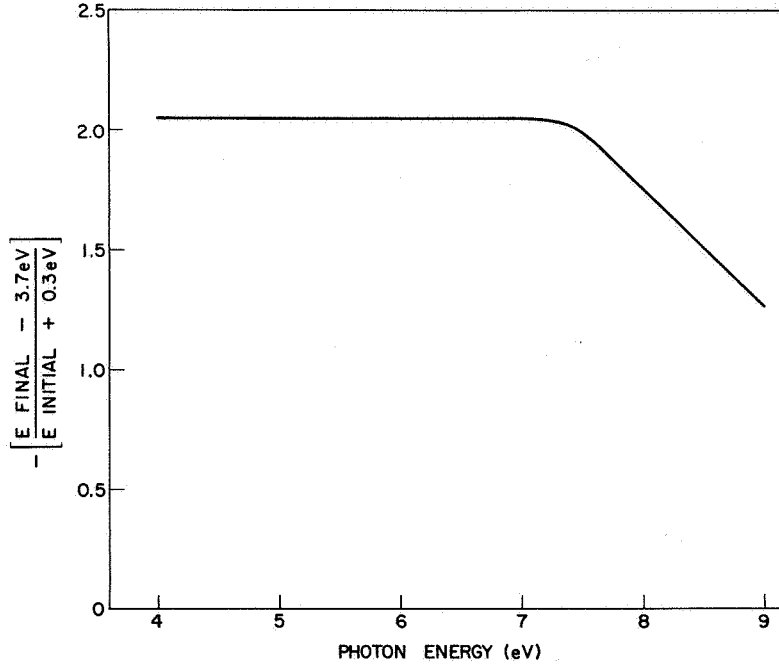


FIG. 103. DETERMINATION OF EFFECTIVE MASSES IN SILVER.

$$\frac{m_{L_2'}}{m_{L_1}} = 2.05 \quad (6.5)$$

An energy band diagram corresponding to the masses given in Eq. (6.5) is shown in Fig. 104. The band diagram of Fig. 104 explains the photoemission data in the entire range of photon energies between 4 and 7 eV, but is actually correct only when the parabolic approximations of Eq. (6.3) and Eq. (6.4) are valid.

Thus, we see that observation of a direct transition in the photoelectric EDCs in silver has led to experimental information concerning both the location and the masses of the L_2' and the L_1 critical points. This information should be of particular interest to theorists doing improved energy band calculations of silver.

J. CONCLUSIONS

New photoemission measurements on clean silver have been found to be consistent with the earlier work of Berglund and Spicer [Ref. 37], which

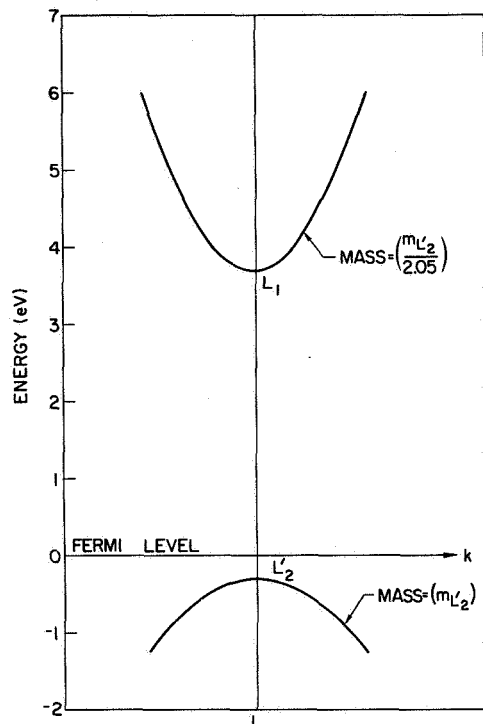


FIG. 104. PARABOLIC BANDS
EXPLAINING THE DIRECT TRANSITION
IN SILVER IN THE RANGE OF PHOTON
ENERGIES BETWEEN 4 AND 7 eV.

was done on cesiated silver. The experimental data from both clean silver and cesiated silver have been incorporated in constructing an optical density of states in the range of energies ± 11.6 eV above the fermi level. A number of new peaks in the optical density of states have been located, the most notable being possible fine structure in the d bands and the possible location of the X_4' critical point in the conduction band.

The bulk of the optical transitions are found to follow the theory of nondirect transitions, and an analysis based upon nondirect transitions has been successful in accounting for the shape and magnitude of the photoelectric EDCs and the quantum yield in both clean silver and cesiated silver. The imaginary part of

the dielectric constant $\epsilon_2(\omega)$ has been calculated solely from the optical density of states, using the theory of nondirect transitions and constant matrix elements. The calculated $\epsilon_2(\omega)$ is found to account for all of the major structure in the experimental $\epsilon_2(\omega)$ except for a sharp peak at the plasma frequency. This discrepancy in $\epsilon_2(\omega)$ has been related to Hopfield's [Ref. 65] theory involving phonon coupling, and future experiments testing Hopfield's theory have been suggested. A simple direct transition has been observed in the range of photon energies between 4.1 and 9.0 eV, and analysis of this direct transition has led to experimental values for the location and the relative masses at the L_2' and the L_1 critical points in the energy band structure of silver.



PRECEDING PAGE BLANK NOT FILMED.

VII. COMPARISON OF COPPER, SILVER, AND GOLD

Chapters IV, V, and VI have described in some detail the properties of copper, silver, and gold that have been deduced from the photoemission data of the present work and the earlier work of Berglund and Spicer [Ref. 37]. A number of these properties are remarkably similar in all three materials; for convenience in making comparisons, these properties are listed for all three materials in Table 5. In Table 5, a question mark is used to denote a value that is suggested by experimental evidence, but is not yet established.

Some of the entries in Table 5 should be particularly interesting to theorists doing future band calculations of copper, silver, and gold. A point of interest not emphasized before is that the mass ratio at the L point in copper is very different from the mass ratio at the L point in silver, as indicated in Section 2 of Table 5.

TABLE 5. COMPARISON OF CERTAIN PROPERTIES OF COPPER, SILVER, AND GOLD.
(All energies are in eV about the fermi level)

No.	Property	Copper	Silver	Gold
1	Location of d bands	(-) 2 to (-) 9	(-) 4 to (-) 7.5	(-) 2 to (-) 9
	Peaks in d bands	(-) 2.4 (major peak) (-) 2.8 (-) 3.7 (-) 5.55 (-) 7.1	(-) 4.4 (major peak) (-) 5.3 } fine structure (-) 5.65 } (-) 6.4 } on a large peak	(-) 3.0 (-) 3.8 (-) 6.1
2	Optical transitions from d-bands	Nondirect	Nondirect	Nondirect
	Optical transitions from s- and p-derived states located between the fermi level and the d bands	Bulk of transitions nondirect, except for one direct transition	Bulk of transitions nondirect, except for one direct transition	Bulk of transition nondirect, except for one direct transition
	Location of L_2' critical point	(-) 0.35	(-) 0.3	(-) 0.7 (?)
	Location of L_1 critical point	(+) 4.05	(+) 3.7	-
	$\left \frac{M_{L_2'}}{M_{L_1}} \right $	0.55 (deduced from Ref. 37)	2.0	-
	Location of X_4' critical point	(+) 1.8	(+) 1.8 (?)	[[+] 1.8] This hypothesized location would account for the peaks in $\epsilon_2(\omega)$ at 8.0 and 2.2 eV
3	High energy structure in the conduction band	+ 9.2 (?) (11.2 eV above top of d bands)	(+) 6.7 (10.7 eV above top of d bands)	(+) 8.5 (10.5 eV above top of d bands)
4	Vacuum level (typical)	(+) 4.5	(+) 4.0	(+) 4.9
5	Electron-electron scattering length at 8.0 eV above the fermi level	24 Å	47 Å	29 Å
6	Quantum yield at $h\nu = 11.0$ eV [elec/absorbed photon]	0.9×10^{-2}	1.4×10^{-2}	1.6×10^{-2}

VIII. THE CUPROUS HALIDES¹

A study of photoemission from the cuprous halides has been carried out in an attempt to shed light upon the role that the copper d-band plays in the energy band structure of the cuprous halides. Because copper and bromine are isoelectronic with germanium, there have been several attempts [Refs. 28 and 68] to identify peaks in the reflectivity spectrum of CuBr and the other cuprous halides with direct transitions between symmetry points in a germanium-like lattice. However, the photoemission studies presented in this chapter indicate that the copper d band lies only a few eV below the top of the valence band, and that certain major peaks in the reflectivity spectrum are due to transitions from the copper d band. Thus, the photoemission studies imply that the energy band structure of the cuprous halides cannot be obtained by simple modification of a germanium band structure, and that future band calculations of the cuprous halides must include the presence of the copper d levels in the valence band.

To provide a more coherent picture for the reader, an outline of the historical background involving the study of the cuprous halides and a tabulation of some of the pertinent physical properties will be presented as a prelude to the discussion of the photoemission data.

A. HISTORICAL BACKGROUND, SOME PHYSICAL PROPERTIES, AND A BONDING MODEL FOR THE CUPROUS HALIDES.

Table 6 lists some of the important properties of the cuprous halides. We note from Table 6 that at atmospheric pressure, the cuprous halides crystallize in the zincblende (diamond) structure. Since well known covalent materials such as Si and Ge also crystallize in the diamond structure, one might suspect that the bonding between the copper and halogen atoms in the cuprous halides is largely covalent. However, the relative ionicity (as determined by the Szigetti formula from the reststrahlen frequency and the atomic masses) is very high for the cuprous halides. On the Szigetti scale, zero indicates a completely covalent bond, and 1.0

¹Certain aspects of the work presented in this chapter have been reported upon earlier by Krolikowski and Spicer [Refs. 81-83].

TABLE 6. SOME PROPERTIES OF THE CUPROUS HALIDES.

Cuprous Halide	Outer Electron Configuration of Molecule	Relative Ionicity ¹ (Szigetti)	Lattice Constant (ZnS)	Crystal Structure ² (Atmospheric Pressure)		Sublimation Temperature ³ (pressure < 1×10^{-7} torr)
				Phase ⁴	Temperature (°K)	
CuCl	$(3d^{10})^+(3p^6)^-$	0.84	5.407 Å	γ β α	< 680 680 to melting -	550°K
CuBr	$(3d^{10})^+(4p^6)^-$	0.79	5.681 Å	γ β α	< 664 664 to 743 743 to melting	550°K
CuI	$(3d^{10})^+(5p^6)^-$	-	6.047 Å	γ β α	< 643 643 to 703 703 to melting	660°K

¹Ref. 69²Ref. 68³Present work⁴
 γ = zinblende
 β = Wurtzite
 α = Statistical bcc

indicates a completely ionic bond. From Table 6, we see that the ionicity of CuCl is 0.84, and that the ionicity of CuBr is 0.79; from such an ionicity scale, it would appear that the cuprous halides are as ionic as the alkali halides. However, ionic compounds are usually characterized by solubility in water, a NaCl crystal structure, and a large (~ 6 eV) energy gap. The cuprous halides are only slightly soluble in water, have a ZnS crystal structure, and have a relatively small (~ 3 eV) energy gap. Thus, the cuprous halides seem to be intermediate compounds, in that they possess some of the properties of both covalent and ionic materials. (See Ref. 69 for a more complete discussion of these properties.)

The outer electron configuration of the cuprous halides is $3d^{10}4s^1$, and the outer electron configuration of bromine is $4s^24p^5$. Since the one-electron ionization energy of the $4s^2$ electrons in the bromine atom is 24.5 eV [Ref. 84], it is likely that the $4s$ electrons of the halogen are too deep in the core to be involved in the valence bonding. If cuprous bromide is indeed ionic, as the Szigetti formula would have us believe, then the copper $4s$ electron must be tightly bound to the halogen atom, and the outer electron configuration of the CuBr "molecule" can be written $(3d^{10})^+(4p^6)^-$, as done in Table 6 for CuBr and the other cuprous halides.

According to the Unsöld theorem [Ref. 84], both the copper $(3d^{10})^+$ ion and the halide $(4p^6)^-$ ion would be spherically symmetric, and the physical configuration of the electron clouds would show no tendency to crystallize in a particular crystal structure.

The cuprous halides exhibit many of the properties of covalent materials, indicating that there must be a covalent bond between the copper atom and the halide atom. A possible explanation for the covalent bonding would be that there exists a considerable amount of p-d overlap between the copper d-levels and the halogen p-levels. Thus, it does not seem too unreasonable to speculate that the simultaneous ionic and covalent nature of the cuprous halides is due to the following phenomena:

- (1) The copper 4s electron is tightly bound to the halide atom.
- (2) There is strong p-d mixing between the copper d levels and the halogen p levels.

The nature of the bonding described by these speculations is illustrated in Fig. 105 for the case of cuprous bromide. It is to be noted

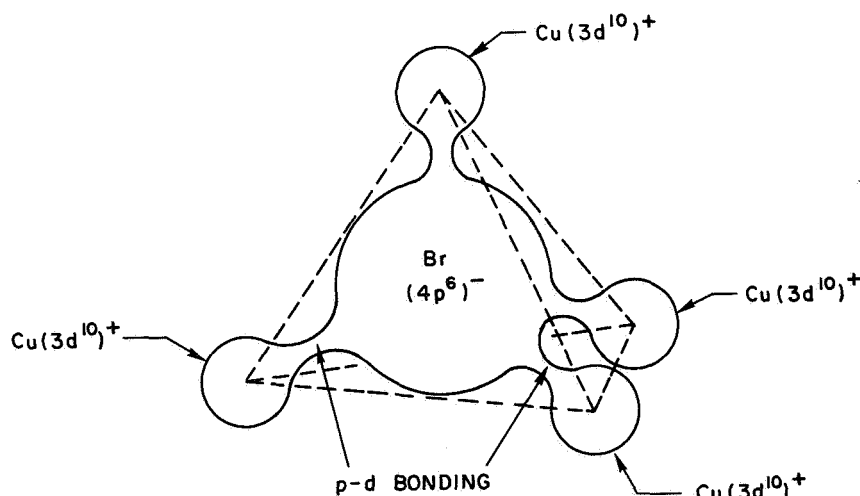


FIG. 105. PROPOSED MODEL OF THE CHEMICAL BONDING FOR THE ZINC SULFIDE PHASE OF CUPROUS BROMIDE.

that the radius of the bromine ion is drawn to be considerably larger than the radius of the copper ion. This has been done in accordance with

the Goldschmidt radii shown in Table 7 which have qualitative significance in the case of highly ionic materials.

TABLE 7. GOLDSCHMIDT'S IONIC RADII (Å) [REF. 29]

Ion	Radius
Cu ⁺	0.53
Cl ⁻	1.81
Br ⁻	1.96
I ⁻	2.20

Because of the spherical symmetry of the copper and halide ions, and because of the consequent lack of a preferred bonding direction, it might be expected that the cuprous halides could crystallize in several different crystal structures. This is indeed the case, as can be seen from Table 6. For example, CuBr has three phases: zincblende, hexagonal, and a complex body-centered cubic. Because covalent compounds tend to have the zincblende structure, and because ionic compounds tend to have the NaCl structure, it is tempting to speculate that the zincblende phase is dominated by the covalent p-d bonding, and that the bcc phase is dominated by the electrostatic interaction between the copper ions and the halide ions.

As seen from Table 6, the cuprous halides sublime at rather low temperatures for pressures less than 1×10^{-7} torr. Unfortunately, high vacuum conditions are essential for good photoemission studies of the cuprous halides, and at such low pressures, the cuprous halides tend to sublime before making the phase change from zincblende to hexagonal. Consequently, almost all of the photoemission data presented in this chapter is from the zincblende phase, and only a few attempts have been made to study the hexagonal phase.

X-ray powder patterns of evaporated films of CuBr show that the evaporated films consist of CuBr in the zincblende structure. This crystalline structure in the films indicates that the cuprous halides sublime in the form of Cu⁺(halide)⁻ molecules, and do not dissociate. Apparently, this type of sublimation is due to the ionic nature of the cuprous halides, since it is well known that covalent compounds tend to

dissociate upon sublimation, whereas ionic compounds tend to sublime as molecules.

Historically, the "unusual" nature of the energy gaps of the cuprous halides was first emphasized by Herman [Ref. 79] in his early "Speculations on the Energy Band Structure of Zinc-Blende-Type Crystals." Herman proposed that the energy gaps of horizontal sequences of zincblende-type semiconductors should be given by

$$(E_g)_{\text{polar}} = (E_g)_{\text{nonpolar}} + a\lambda^2 \quad (8.1)$$

In Eq. (8.1), $(E_g)_{\text{nonpolar}}$ is the energy gap of the corresponding isoelectronic semiconductor in the fourth column of the periodic table, (a) is a constant for each isoelectronic sequence, and $\lambda = 1$ for the III-V compounds, $\lambda = 2$ for the II-VI compounds, and $\lambda = 3$ for the I-VII compounds. For the diagonal sequences in the periodic table, Herman proposed that

$$(E_g)_{\text{polar}} = (E_g)_{\text{nonpolar}} + b\lambda \quad (8.2)$$

where (b) is a constant for each diagonal sequence. For the convenience of the reader, the portion of the periodic table pertinent to the present discussion is shown in Table 8.

TABLE 8. A PORTION OF THE PERIODIC TABLE

I	II	III	IV	V	VI	VII	VIII
		Al ¹³	Si ¹⁴	P ¹⁵	S ¹⁶	Cl ¹⁷	Ar ¹⁸
Cu ²⁹	Zn ³⁰	Ga ³¹	Ge ³²	As ³³	Se ³⁴	Br ³⁵	Kr ³⁶
Ag ⁴⁷	Cd ⁴⁸	In ⁴⁹	Sn ⁵⁰	Sb ⁵¹	Te ⁵²	I ⁵³	Xe ⁵⁴

As can be seen from Figs. 106 and 107, Herman's scheme is remarkably accurate in accounting for the energy gaps of the III-V and the II-VI compounds of both the horizontal and the diagonal sequences. However, as Herman pointed out, Figs. 106 and 107 show that the energy gaps of the cuprous halides do not follow the systematics of the other zincblende-type

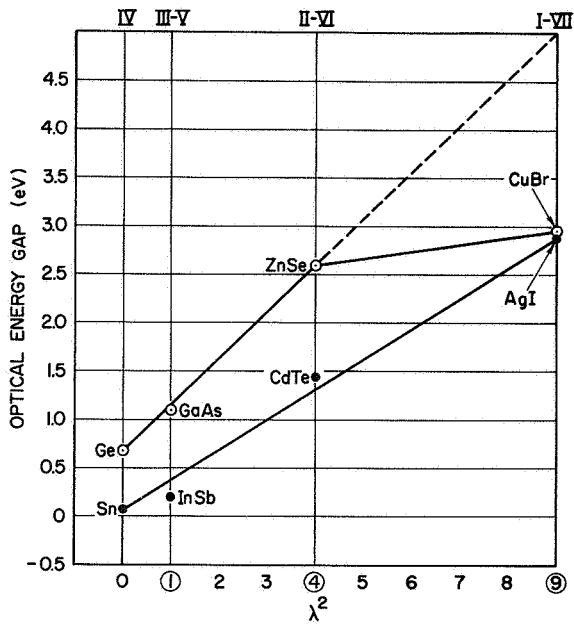
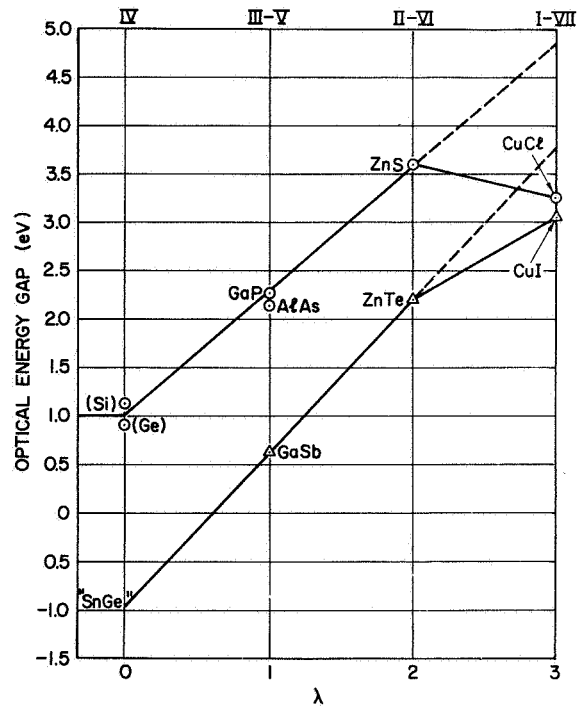


FIG. 106. OPTICAL ENERGY GAP VS λ^2 FOR HORIZONTAL SEQUENCES IN THE PERIODIC TABLE [REF. 79]. The energy gaps for the metal halides are from Cardona [Ref 68].

FIG. 107. OPTICAL ENERGY GAPS VS λ FOR THE DIAGONAL SEQUENCES IN THE PERIODIC TABLE [Ref. 79]. The energy gaps for the cuprous halides are from Ref. 68.



semiconductors, indicating that the cuprous halides might be different in some significant way from the rest of the zincblende-type compounds listed in Figs. 106 and 107.

As a possible explanation for this break in systematics, Herman and McClure [Ref. 67] proposed that the cuprous halides were very different from the III-V and the II-VI zincblende-type compounds in that the 3d electrons of the copper atom were involved in the valence band structure of the cuprous halides. Herman and McClure [Ref. 67] proposed the following energy band scheme to explain the optical spectrum of the cuprous halides:

With the aid of crystal field theory and energy band theory, we have interpreted the optical absorption spectra of CuCl, CuBr, and CuI. According to our interpretation, the weak absorption peak in the spectra of each of these compounds lying at about 3 eV is due to a $3d^{10}$ to $3d^9 4s$ transition within the Cu^+ ion; the strong absorption peak occurring in CuCl at 6.5 eV, in CuBr at 5.6 eV, and in CuI at 4.9 eV is due to the transfer of an electron from the halide to the Cu ion. In the language of energy band theory, the lowest conduction band and the highest valence band arise from the 4s and 3d states of the Cu^+ ion, respectively, while the next lowest valence band arises from the 3p Cl^- , 4p Br^- , and 5p I^- states. There are two forbidden bands, one between the 4s and 3d Cu^+ bands, and another between the 3d Cu^+ and the p halide bands; the optical energy gap is determined by the width of the former. It is now clear that our previous inability to reconcile the optical gap of CuBr with those of the other members of the isoelectronic sequence Ge-GaAs-ZnSe-CuBr results from the reversal in order of the cation 3d and anion 4p bands. (In Ge, GaAs, and AnSe, the 3d bands of Ge, Ga, and Zn appear to lie below the 4p bands of Ge, As, and Se.)

Thus, Herman and McClure [Ref. 67] suggested that the copper 3d band lies above the halogen p bands in the cuprous halides.

However, optical studies by Coehlo [Ref. 69] and by Cardona [Ref. 68] seem to identify the top of the valence band with the halogen p bands, and not with the copper d levels. As shown in Figs. 108 and 109 for the case of CuBr, the band edge absorption spectrum of the cuprous halides shows pronounced exciton structure. Cardona [Ref. 68] explained this excitonic structure in the following manner:

This exciton spectrum can be interpreted along the same lines as the absorption edge of other materials with wurtzite and zincblende structures. The strength of the exciton spectrum suggests direct allowed transitions which, by analogy with the other zincblende and wurtzite materials, should occur at $k = 0$. The top of the valence band (Γ_{15}) is triply degenerate without spin-orbit interaction in the zincblende structure. This degeneracy is reduced by spin-orbit splitting to a doubly degenerate state (Γ_8) and a singlet (Γ_6). The Γ_8 doublet gives the $Z_{1,2}$ peak whose degeneracy is lifted in strained samples.

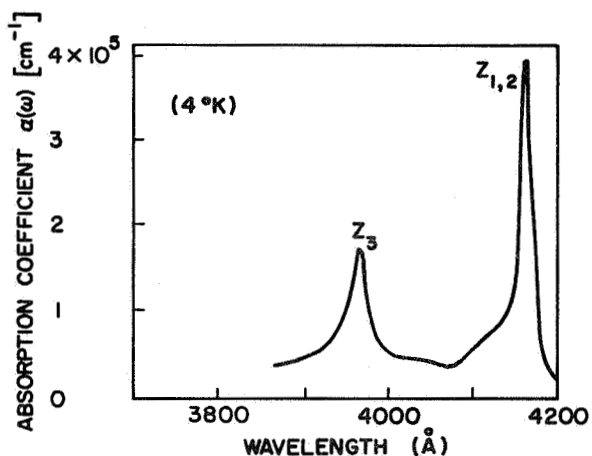


FIG. 108. EXCITON SPECTRUM OF CUPROUS BROMIDE [Ref. 68].

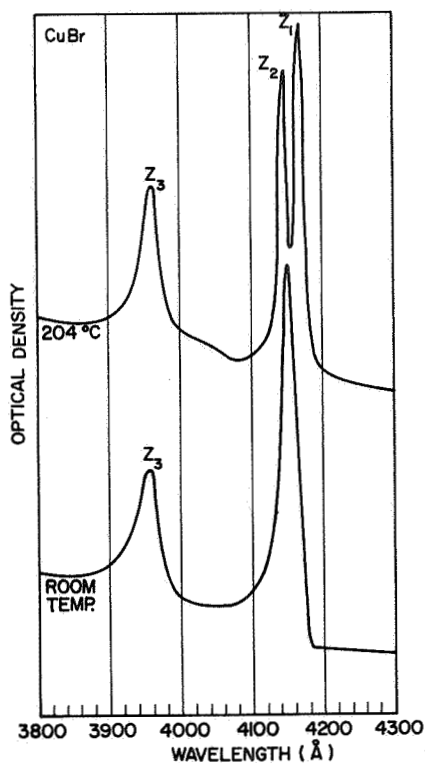


FIG. 109. EXCITON SPECTRUM OF A CUPROUS BROMIDE FILM EVAPORATED ON CLEAVED SODIUM CHLORIDE AND ANNEALED AT VARIOUS TEMPERATURES [Ref. 69].

Cardona pointed out a close correlation between the spin-orbit splitting between the $Z_{1,2}$ and the Z_3 peaks and the halogen spin-orbit splitting, as can be seen from Table 9. Note, however, that the experimental splittings are somewhat smaller than the halogen splittings. This phenomenon was explained by Cardona [Ref. 68] in the following manner:

The experimental splittings are considerably smaller than the halogen splittings; therefore, the valence band wavefunctions at $k = 0$ must, in the tight-binding approximation, be found from halogen wavefunctions with a large proportion of metal wavefunctions . . .

TABLE 9. EXCITON SPLITTINGS FOR THE CUPROUS AND SILVER HALIDES COMPARED TO THE HALOGEN SPIN-ORBIT SPLITTING [REF. 68]

Metal Halide	Energy difference between exciton peaks for the silver and copper halides (eV)	One-electron spin-orbit splitting parameters for the halogens (eV)	Halogen
CuCl	0.07	0.11	Cl
CuBr	0.15	0.45	Br
CuI	0.64	0.94	I
AgI	0.84		

Thus Cardona identified the top of the valence band as being derived mainly from the halogen states, but also pointed out that there is probably strong mixing between the copper d-levels and the halogen p levels. Nevertheless, because the high energy optical spectrum of the cuprous halides bears some resemblance to the spectra of Ge, Si, and other zincblende semiconductors, Cardona interpreted the spectra of the cuprous halides along the same lines as the other zincblende compounds. Thus, Cardona associated structure in the optical spectrum of the cuprous halides in the region of photon energies between 4 and 10 eV with direct transitions between symmetry points in a germanium-like lattice.

In the manner of Cardona, J. C. Phillips [Ref. 28] also associated peaks in the optical spectra between 4 and 10 eV with direct transitions

between symmetry points in a germanium-like lattice, and wrote that: "A wide range of experimental data now indicates that uv structure depends primarily upon crystal structure and only secondarily upon atomic composition . . ."

The photoemission data to be presented in this chapter indicate that the copper d band lies only a few eV below the halogen p bands, and that some of the major peaks in the optical spectrum of the cuprous halides are due to transitions from the copper d bands. Thus, the findings of the present photoemission studies show that Phillips' statement (above) does not apply to the cuprous halides, since the copper d bands account for some of the more important features of the optical spectrum. Since photoemission studies show that the copper d bands lie below the halogen p bands, the results of the present photoemission studies are consistent with the conclusions of Cardona [Ref. 68], who identified the copper part of the valence band with the halogen p levels.

B. PHOTOEMISSION AND OPTICAL STUDIES OF CUPROUS IODIDE

High vacuum photoelectric yield and energy distribution measurements have been made on three of the cuprous halides: CuCl, CuBr, and CuI. However, only the data on CuI have been analyzed in the manner of the quantitative analysis carried out on copper, silver, and gold because much of the data on the cuprous halides was taken in 1964 and in 1965, when the quantum yield could not be accurately measured in our laboratory. Thus, even though excellent EDCs had been measured for all three cuprous halides, the quantum yield data were not reliable enough to warrant a self-consistent quantitative analysis of the photoemission and optical data. When Koyama's quantum yield calibrations became available, the measurements on CuI were repeated, and reliable quantum yield was obtained for CuI. Since CuCl, CuBr, and CuI have similar optical and photoemission properties, the detailed analysis performed on CuI has been used to serve as a guide in analyzing the photoemission data from CuCl and CuBr.

1. The Optical Density of States for Cuprous Iodide

The optical density of states that has been deduced from photoemission and optical studies using a self-consistent analysis similar to

the analysis described in Table 1 is shown in Fig. 110. The shaded area of the minor peak labeled (7) was not included in the self-consistent analysis, because peak (7) appeared to have the nature of a direct transition, which cannot be accounted for by an analysis based upon nondirect transitions. The locations and the approximate relative heights¹ of the peaks (except peak (4)) were deduced directly from the experimental photoemission data in the following manner: The vacuum level of CuI is typically about 6.0 eV above the top of the valence band, and at photon energies between 10.5 and 11.8 eV, the shape of the of the experimental EDCs bears a very close resemblance to the valence band density of states in Fig. 110, with peak (1) being much larger than either peak (2) or peak (3). The relative strength of peak (1), compared with peaks (2) and (3), tends to identify peak (1) with the copper 3d bands, and peaks (2) and (3) with the halogen p bands. The energy location of peaks (1), (2), and (3) were determined quite accurately from the photoemission data. Having made the identification of peak (1) with the copper d bands and peaks (2) and (3) with the halogen p bands, the relative heights of peaks (1), (2), and (3) were adjusted so that the ratio of the area under peak (1) to the sum of the areas under peaks (2) and (3) was $\frac{10}{6}$, equal to the ratio of the number of 3d electrons (10) to the number of 4p electrons (6). The energy gap was estimated from the optical data of Coehlo [Ref. 69] and Cardona [Ref. 68], and the conduction band peaks labeled (5), (6), and (7) were located directly from the photoemission data.

The locations of the peaks labeled (1), (2), (3), (5), (6), and (7) in Fig. 110 have been deduced directly from the experimental photoemission data, and the uncertainty in the locations of these peaks is typically about ± 0.1 eV. The relative strengths of these peaks have been adjusted so as to give good overall agreement with the photoemission and optical data. However, the existence of peak (4) in the conduction band has not been observed directly by photoemission experiments; the relative strength and the location of peak (4) have been postulated in order to account for the major structure in the optical spectrum of CuI.

¹The entire conduction band optical density of states can be scaled by a single constant factor without affecting the results of the analysis, just as in the case of the analysis carried out on Cu, Ag, and Au.

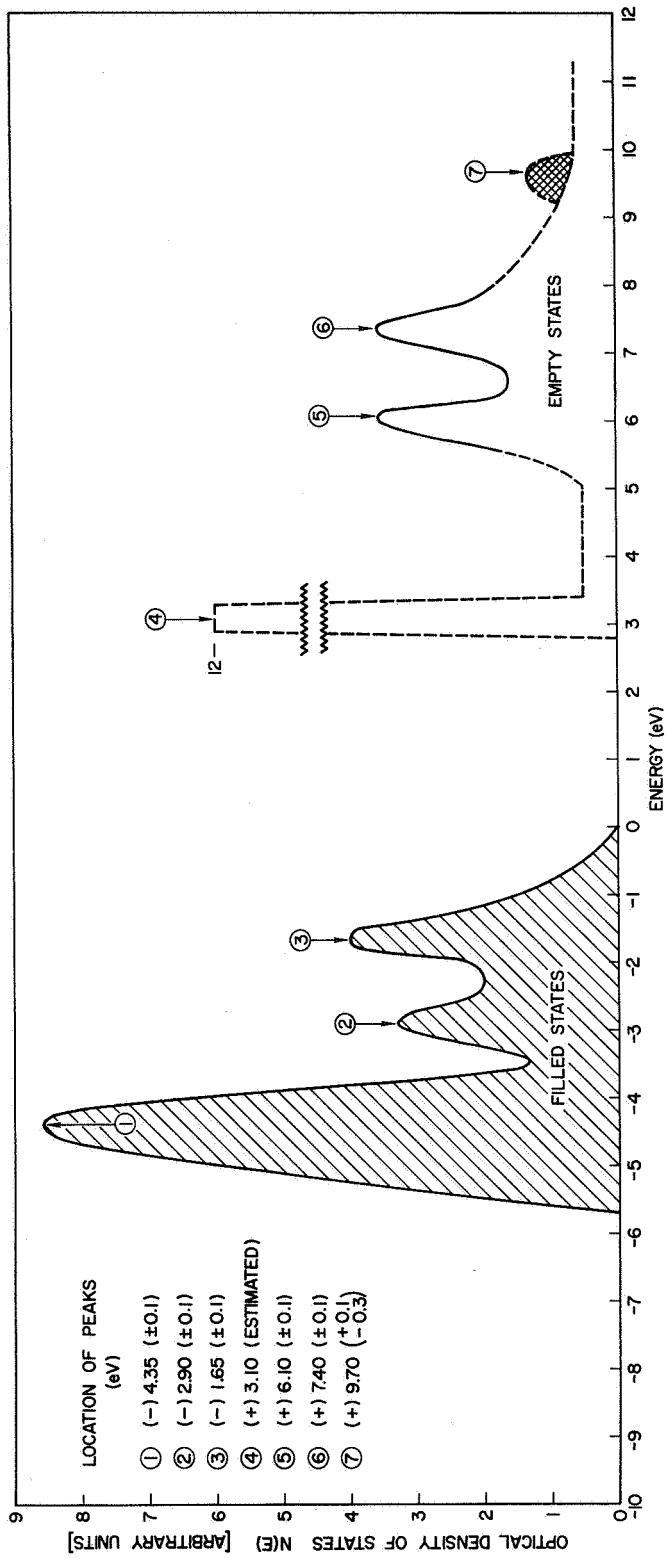


FIG. 110. ESTIMATED OPTICAL DENSITY OF STATES FOR CUPROUS IODIDE.

In the range of photon energies between 4 and 8 eV, there are three major peaks in the optical spectrum of CuI, and the energy separation of these peaks corresponds very closely to the energy separation between peaks (1), (2), and (3) in the valence band. Because of this remarkably close correspondence, it seems reasonable to assume that the three peaks in the optical spectrum are due to transitions from the three valence band peaks (1), (2), and (3) to the same final state in the conduction band. Following this reasoning, peak (4) was located at an energy of about 3.1 eV above the top of the valence band.

As will be shown later in this chapter, a detailed nondirect transition calculation of $\epsilon_2(\omega)$ from the optical density of states of Fig. 110 accounts remarkably well for the location of the structure in the optical spectrum of CuI, thereby justifying the location of peak (4) in the conduction band. However, to account properly for the strength of the peak in $\epsilon_2(\omega)$ due to optical transition from peak (1) to peak (4), the probability for this transition had to be assumed to be about one-third as strong as the probability for the rest of the optical transitions. The relatively smaller matrix element for the (1) \rightarrow (4) transition suggests that this transition might be dominated by direct transitions, and not by the total density of states, for the following reasons: If the d bands are quite flat over the entire Brillouin zone, and if the high density of states at peak (4) is derived largely from "flat" bands that extend only over a portion of the Brillouin zone, and if direct transitions govern the optical absorption process near the band edge, then only a fraction of the total number of d electrons in the valence band can make transitions to the bands of peak (4), and a reduced matrix element would result. However, if the d bands are quite flat, the wavefunctions describing the initial state of the electron have a distinct atomic character. Thus, it may be that atomic selection rules are more significant than "k-conservation" in determining the matrix element for the transition (1) \rightarrow (4), and that the reduced matrix element for this transition is due to the effect of atomic selection rules.

Because of the fact that all of the photoemission and optical data cannot be accounted for quantitatively by the assumption of constant matrix elements, there is some uncertainty in the relative peak heights

in the optical density of states of Fig. 110, especially in the strength of peak (4). However, an analysis based upon nondirect transitions and the optical density of states is able to account quite well for the bulk of the optical data, indicating that there is some real significance to the relative peak heights in Fig. 110.

The rest of the discussion to be presented on CuI in this chapter will be centered about the experimental data from which the optical density of states of Fig. 110 has been deduced, and the computer calculations of the quantum yield, the EDCs, $\epsilon_2(\omega)$, and $L(E)$ that are based upon the optical density of states. The computer calculations have been carried out by use of the optical density of states of Fig. 110 and the model of nondirect transitions. The computer calculations use the equations described in Table 1 with the following exceptions:

- (1) The hot electron group velocity v_g has been assumed to be constant, independent of energy because the conduction band of CuI is by no means free-electron-like; consequently, the free electron group velocity used in the analysis of Cu, Ag, and Au is inappropriate for CuI. Since no experimental or theoretical information is available on the energy dependence of the group velocity in the conduction band of CuI, there was no choice but to assume that $v_g = \text{constant}$.
- (2) The threshold function $T(E)$ was assumed to have approximately the form of a step-function, as shown in Fig. 111. The shape of the threshold function was dictated by the shape of the EDCs, and the limiting value of 0.5 has the physical meaning that an electron photoexcited at depth x from the surface must have a velocity component directed toward the surface if the electron is to have a chance of being photoexcited into the vacuum. Thus, the step-like threshold function is based on the assumption that any electron excited to an energy E above the vacuum level can escape if the electron can reach the surface before suffering an inelastic electron-electron collision and that electron-phonon collisions are improbable.

To account for the effects of electron-electron scattering, it has been assumed that the electrons photoexcited to energy E at depth x from the surface have a spherical velocity distribution, and the electron-electron scattering analysis has been carried out by use of the same basic equations used to calculate $L(E)$ for Cu, Ag, and Au, except that $v_g = \text{constant}$, and $T_f(E)$ is replaced in the equation by the $T(E)$ ¹ of Fig. 111. Of course, in order to conserve energy, no inelastic electron-electron collisions are possible in CuI at energies between the bottom of the conduction band and $E = 2E_g = (2)(2.9 \text{ eV}) = 5.8 \text{ eV}$ above the top of the valence band. Only unscattered electrons were included in the calculations of the quantum yield and the EDCs, since the experimental EDCs did not show evidence of a significant number of secondary (scattered) electrons.

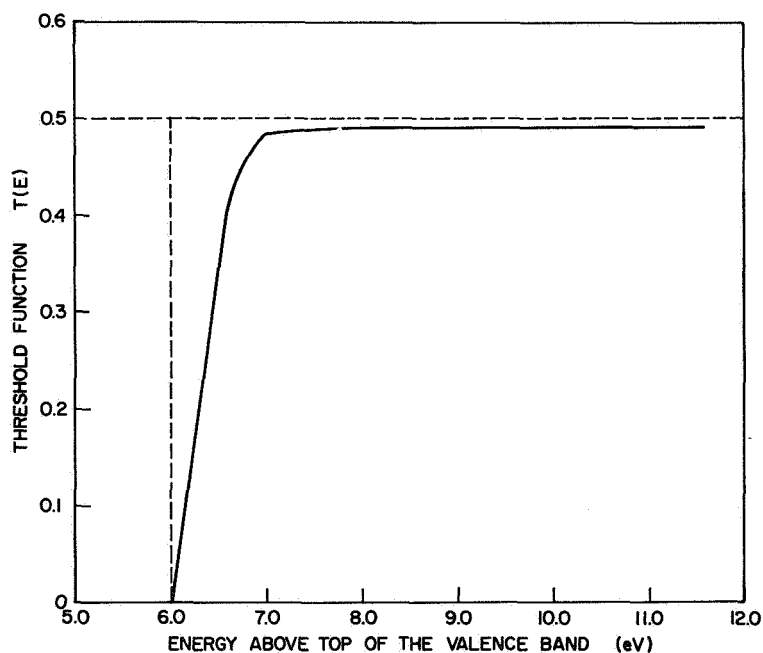


FIG. 111. THRESHOLD FUNCTION FOR CUPROUS IODIDE.

¹Replacing $T_f(E)$ by the $T(E)$ of Fig. 111 has the physical meaning of setting the escape cone equal to almost 90° for any energy E more than about 1 eV above the vacuum level.

2. Optical Data for Cuprous Iodide

Using the experimental methods described in Chapter II, the reflectivity of CuI was measured in the range of photon energies between 3 and 21.2 eV. Very good agreement was found between the high vacuum data and the windowless data, indicating that the reflectivity of CuI is quite insensitive to brief exposure to air. The experimental reflectivity data are compared with the data of Cardona [Ref. 68] in Fig. 112, where the agreement is seen to be quite good with regard to the location of structure. Note, however, that the magnitude of the reflectivity obtained in the present work is somewhat higher than the magnitude obtained by Cardona. At photon energies lower than 3 eV, new reflectivity measurements were not made, since the reflectivity data tabulated in Gmelin's Handbook seemed to match fairly well with the data of the present work.

The absorption coefficient $\alpha(\omega)$ and the imaginary part of the dielectric constant $\epsilon_2(\omega)$ were calculated from the reflectivity data, by use of the Kramers-Kronig analysis computer program written by Shay [Ref. 17]. For use in the computer program, the reflectivity data below 3 eV were taken from Gmelin; above 3 eV, the reflectivity data were taken from the curve labeled "present work" in Fig. 112.

The absorption coefficient $\alpha(\omega)$ obtained from the Kramers-Kronig analysis is compared in Fig. 113 to the results of the direct measurements of Cardona [Ref. 68], which were deduced from transmission measurements through thin films. The agreement with regard to location of structure is quite good, and the agreement with regard to magnitude is good, except for the magnitude of the absorption peak at about 7.9 eV. Note that at 80°K, Cardona's data resolve some fine splitting in the absorption peak at 6.2 eV, and make evident a distinct shoulder at about 7.2 eV. Due to the uncertainties in the reflectivity data below 3 eV, there is considerable uncertainty in the calculated absorption coefficient at energies below about 3 eV, as can be seen from the fact that the absorption coefficient is finite at photon energies smaller than the energy of the energy gap.

The "experimental" $\epsilon_2(\omega)$ that is calculated from the reflectivity data is shown in Fig. 114, where it is compared with the $\epsilon_2(\omega)$ that is calculated from the optical density of states of Fig. 110. Only

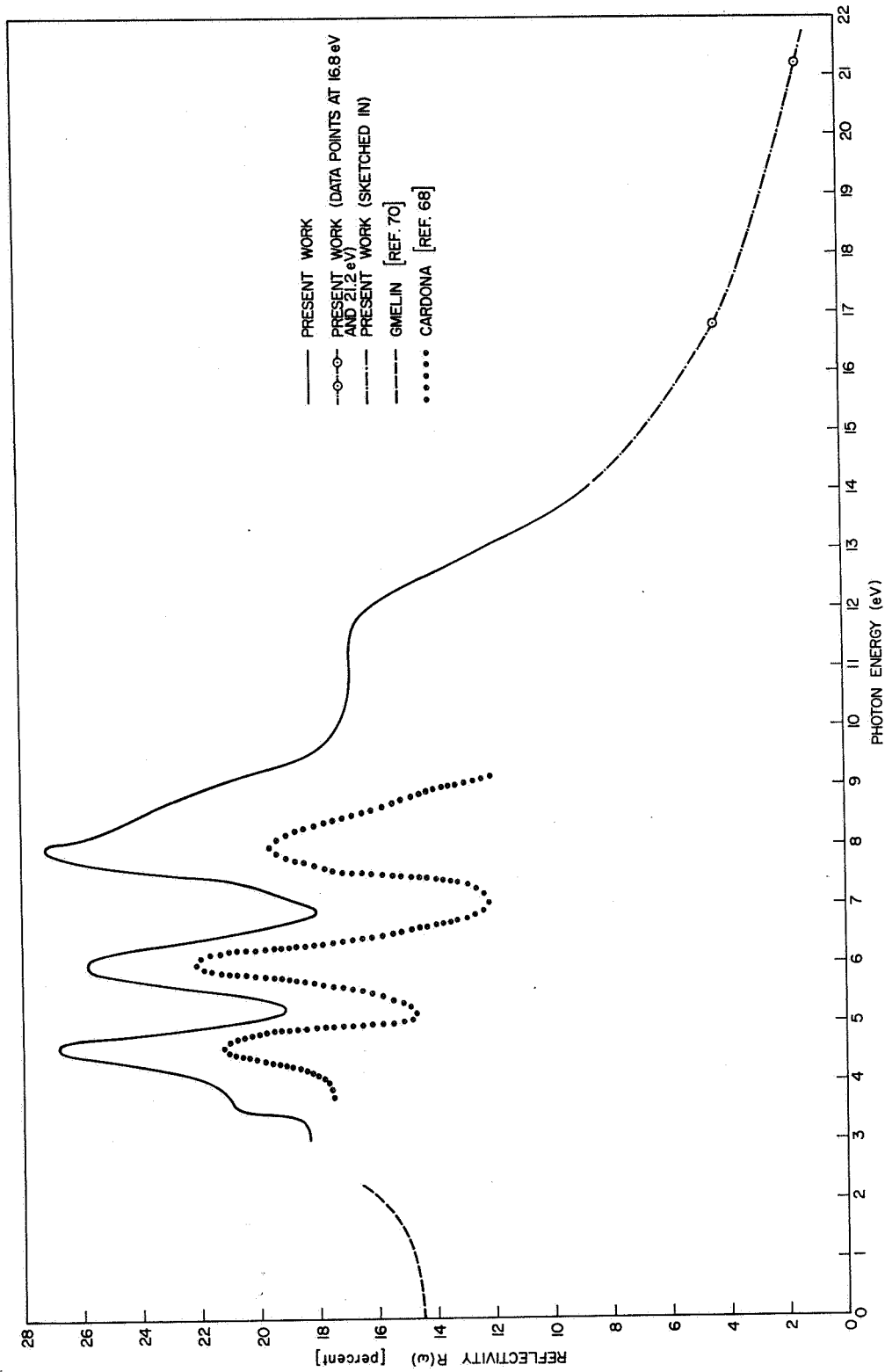


FIG. 112. REFLECTIVITY FOR CUPROUS IODIDE.

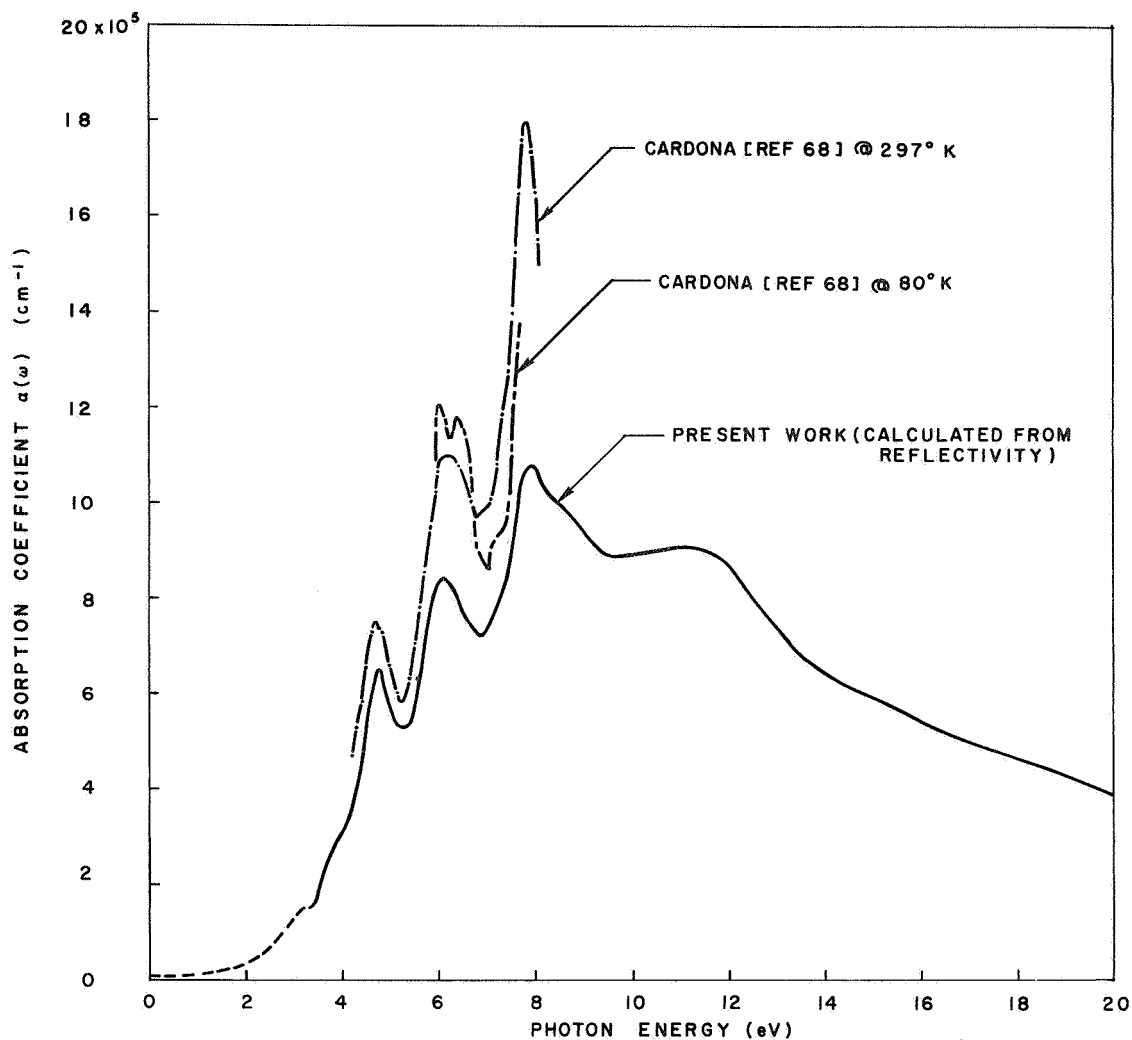


FIG. 113. ABSORPTION COEFFICIENT $\alpha(\omega)$ OF CUPROUS IODIDE.

the shape of $\epsilon_2(\omega)$ can be calculated from the optical density of states, and the "optical density of states" $\epsilon_2(\omega)$ has been fitted to the "experimental" $\epsilon_2(\omega)$ at 4.6 eV. Because of the uncertainty in the reflectivity data below 3 eV, there is considerable uncertainty in the "experimental" $\epsilon_2(\omega)$ at photon energies less than 3 eV.

As seen from Fig. 114, there is excellent agreement between the "calculated" and the "experimental" $\epsilon_2(\omega)$ with regard to the location of both major structure and detailed structure in the range of photon energies between 3 and 12 eV. One interesting feature in the "experimental" $\epsilon_2(\omega)$ is that there is a peak at 7.6 eV, and a shoulder at

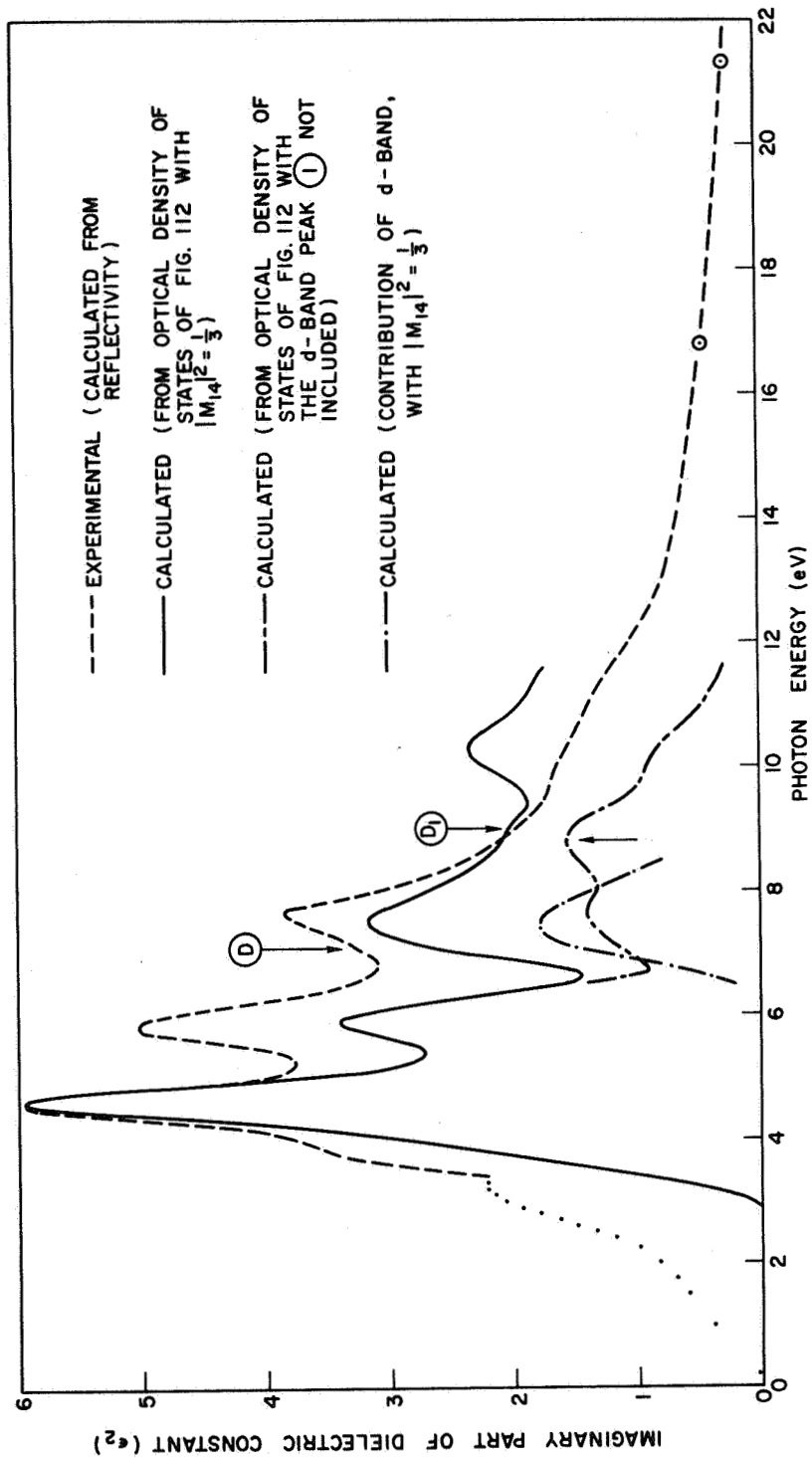


FIG. 114. COMPARISON OF CALCULATED AND EXPERIMENTAL VALUES OF $\epsilon_2(\omega)$ FOR CUPROUS IODIDE. The calculated curves are fitted at $h\nu = 4.6$ eV.

about 7.1 eV. In the calculated curve, the shoulder at 7.1 eV is not clearly evident, but decomposition of the calculated curve (as seen in Fig. 114) shows that the calculated peak at 7.5 eV is really composed of two distinct peaks: One peak is due to the transition (1) → (4), and the other peak is due to the transition (3) → (5), where the notation is appropriate to the peaks in Fig. 110. Because of the relative strengths of peaks (1) and (3), the transition (3) → (5) probably contributes strongly to the experimental shoulder at 7.1 eV, and the transition (1) → (4) has been associated¹ with the experimental peak at 7.6 eV. By such decomposition (easily done with a computer) details in the structure of $\epsilon_2(\omega)$ can be identified with transitions between certain peaks in the optical density of states of Fig. 110. The energies of the structure in the optical spectrum of CuI and the identification of this structure with peaks in the optical density of states are tabulated in Section E of this chapter, along with similar tabulations for CuCl and CuBr.

In calculating ϵ_2 from the optical density of states, it has been assumed that $|M_{14}|^2 = 1/3$ where $|M_{14}|^2$ is the square of the momentum matrix element joining peak (1) to peak (4). The quantity $|M_{ij}|^2$ gives the relative probability of transition between states *i* and *j*, and for all the other transitions, it has been assumed that $|M_{ij}|^2 = 1$, according to the model of direct transitions. Figure 115 shows that the transition (1) → (4) is much too strong [compared with the "experimental" $\epsilon_2(\omega)$] if $|M_{14}|^2 = 1$.

Because of the relative variation in the magnitudes involved, significant structure is sometimes more evident in the quantity $\omega^2 \epsilon_2(\omega) = \omega \sigma(\omega)$ than in the quantity $\epsilon_2(\omega)$. In addition, the quantity $\omega \sigma(\omega)$ is significant in that it is proportional to the total number of possible transitions in the model of nondirect transitions, and peaks in $\omega \sigma(\omega)$ tend to signify the onset of strong transitions at frequency ω .

¹ However, there is some uncertainty in these assignments, because the calculated quantum yield tends to be in better agreement with the experimental quantum yield if the strength of the (3) → (5) transition was increased, and the strength of the (1) → (4) transition decreased even lower than $|M_{14}|^2 = 1/3$. Thus the assignments describing the shoulder at 7.1 eV and the peak at 7.6 eV might be reversed.

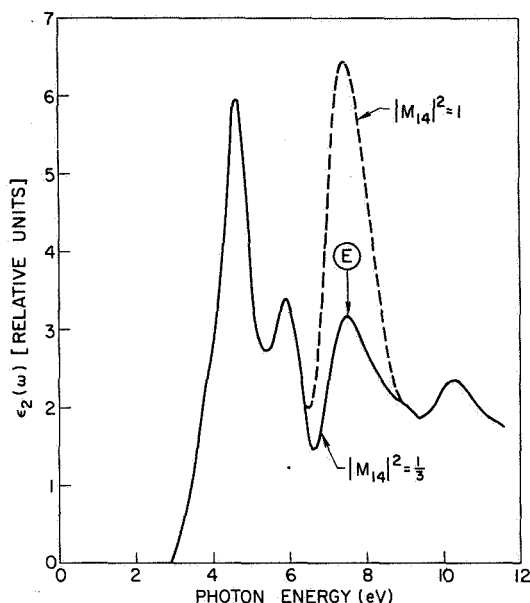


FIG. 115. EFFECT OF THE MATRIX ELEMENT $|M_{14}|^2$ ON $\epsilon_2(\omega)$ FOR CUPROUS IODIDE.

Consequently, the "calculated" $\omega\sigma(\omega)$ and the "experimental" $\omega\sigma(\omega)$ are compared in Fig. 116. In Fig. 116, the arrows pointing downward signify the location of structure in the "experimental" $\omega\sigma(\omega)$ and arrows pointing up signify the location of structure in the "calculated" $\omega\sigma(\omega)$.

In Fig. 117, the absorption coefficient of AgI is compared with the absorption coefficient of CuI. The remarkable similarity between the absorption coefficients of AgI and CuI indicates that the energy band structures of AgI and CuI are quite similar, with the location of the Ag d bands in AgI corresponding closely to the location of the Cu d bands in CuI. Both CuI and AgI have a zincblende crystal structure.

3. The Quantum Yield for Cuprous Iodide

The experimental and calculated quantum yields of CuI are compared in Fig. 118. The calculated quantum yield includes the effects of the electron-electron scattering length (Fig. 125). The agreement between the experimental and the calculated curves is quite good, and the calculated curve is seen to reproduce the major features of the experimental curve quite well. The most striking features of the quantum yield are the dip at about 9.8 eV, and the strong rise between 10 and 11 eV. The dip in the yield is caused by the strong transition $\textcircled{1} \rightarrow \textcircled{5}$, since

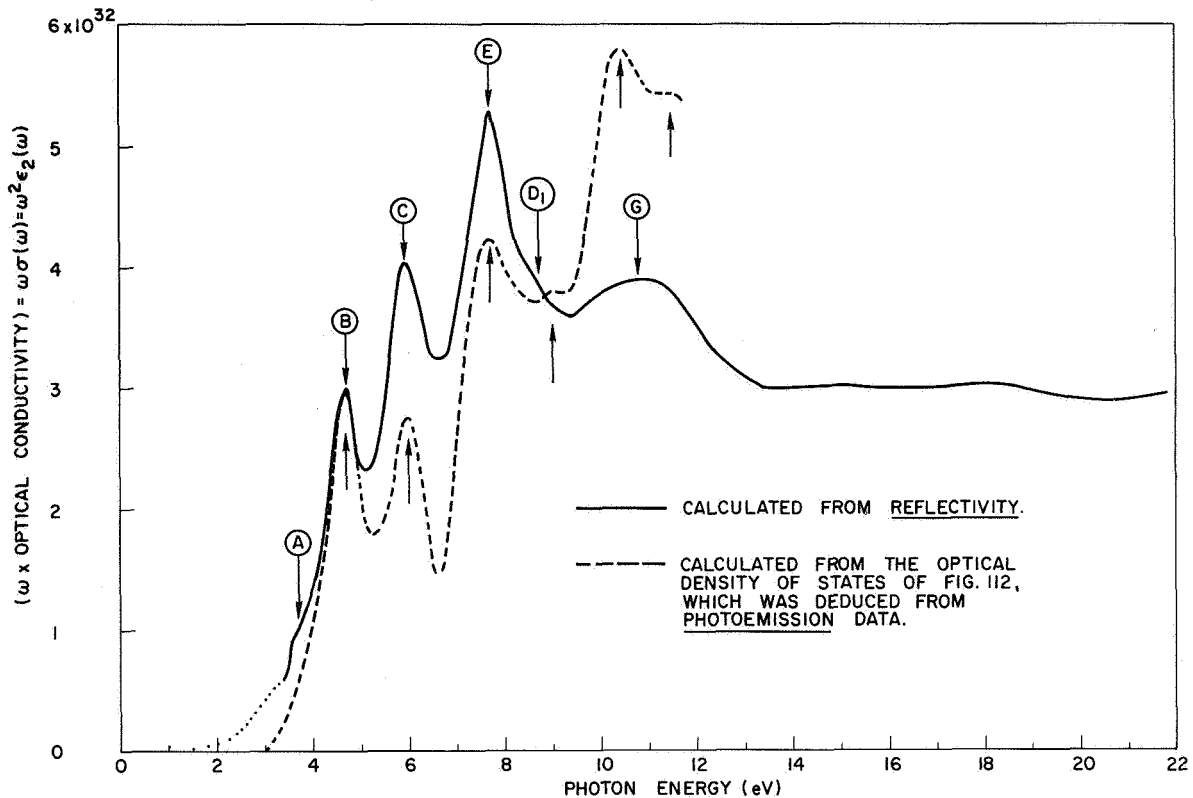


FIG. 116. THE QUANTITY $\omega\sigma(\omega) = \omega^2\epsilon_2(\omega)$ FOR CUPROUS IODIDE. The values of $\epsilon_2(\omega)$ are the same as in Fig. 114.

the final state (5) is located just below the vacuum level. The strong rise between 10 and 11 eV is caused by the onset of photoemission from valence band peak (1), which has been associated with the copper 3 d band.

Note that the calculated yield between 6.5 and 8 eV is somewhat lower than the experimental yield. As discussed in the previous section, the agreement between the calculated and the experimental yield would be better in this range of photon energies if the matrix element for the transition (3) → (5) was increased, and the matrix element for the transition (1) → (4) made even smaller than the value of one-third used in the present calculation.

The overall uncertainty in the experimental quantum yield is estimated to be about ±30 percent. This rather large uncertainty is due almost entirely to the uncertainty in the transmission of the LiF window. The transmission of the LiF window apparently changed during the course

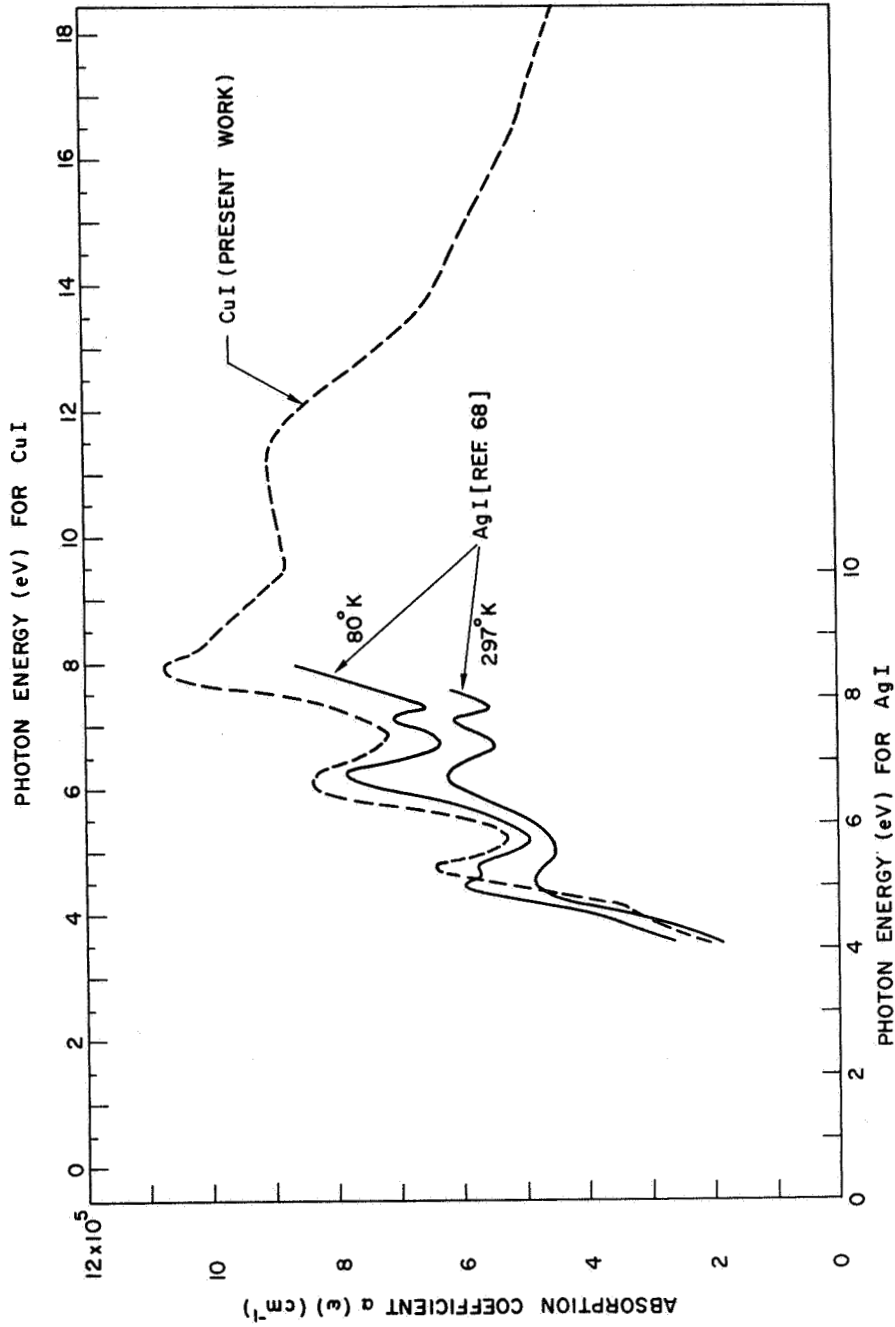


FIG. 117. COMPARISON OF ABSORPTION COEFFICIENT OF CUPROUS IODIDE AND SILVER IODIDE. Note that the curve for CuI is shifted by about 0.55 eV relative to the curve for AgI.

of the experiment, and the transmission used in calculating the quantum yield was taken to be the average of the LiF transmissions measured before and after the photoemission experiment. The ± 30 percent uncertainty in shape is gradual over the range of photon energies between 6 and 12 eV, and does not significantly affect the major features of the quantum yield in Fig. 118.

4. Photoelectric Energy Distribution Curves from Cuprous Iodide

The experimental EDCs normalized to the quantum yield of Fig. 118 are plotted in Figs. 119a through 119y. These experimental EDCs were obtained from CuI films prepared and measured at a vacuum of 2×10^{-9} torr, using the photoemission chamber described in Chapter II. In Figs. 119a through 119x, the experimental EDCs are compared with the EDCs calculated from the optical density of states of Fig. 110, using the threshold function of Fig. 111. The calculated EDCs are consistent with the calculated quantum yield in Fig. 118 and the calculated electron-electron scattering length (Fig. 125).

Except for the difference in magnitude for photon energies between 6.7 and 8 eV, Fig. 119 shows that there is very good agreement between the experimental EDCs and the calculated EDCs with regard to both shape and magnitude over the entire range of photon energies between 6.7 and 11.6 eV. This very good agreement attests to the validity of the optical density of states of Fig. 110, and to the application of the model of nondirect transitions to CuI. Note, however, that the agreement between the calculated EDCs and the experimental EDCs is not quite as good as the agreement obtained for copper, perhaps due to the matrix element variations that seem to exist in CuI.

The apparent coarseness of the calculated EDCs is due to the fact that the resolution of the computer program was only 0.1 eV. However the 0.1 eV resolution seems to adequately display the major features of the calculated curve, and the uncertainty in the input parameters to the computer calculation does not seem to warrant the use of resolution finer than 0.1 eV.

Figures 119p through 119y show the onset of photoemission from valence band peak (1) at photon energies greater than 10 eV. Because of

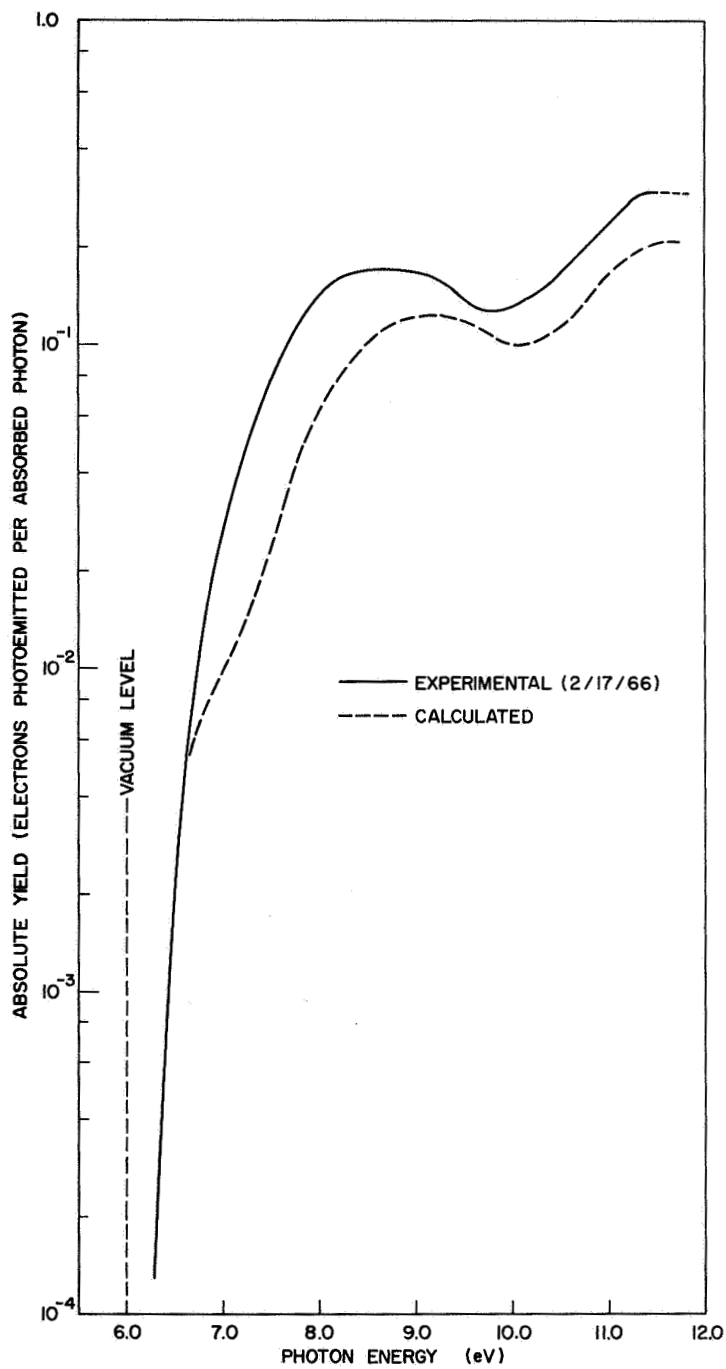
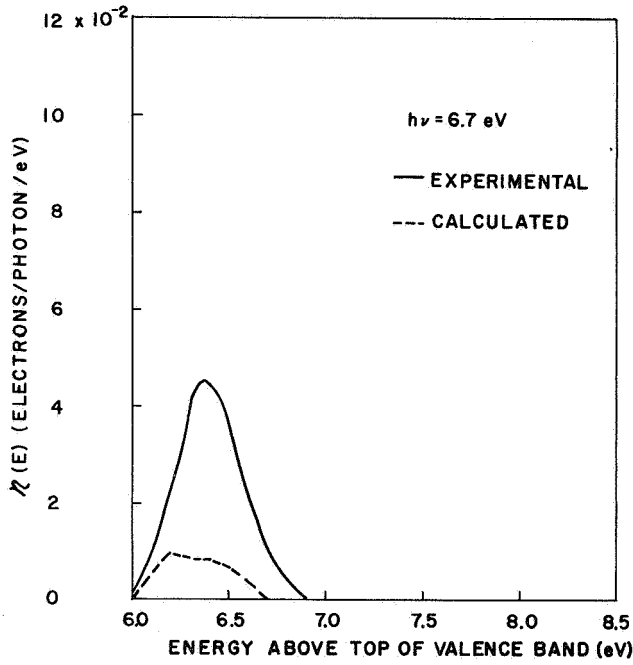
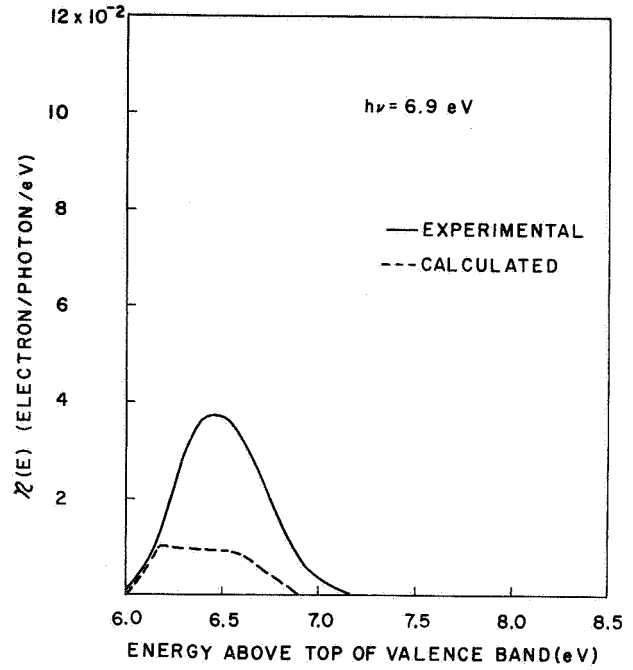


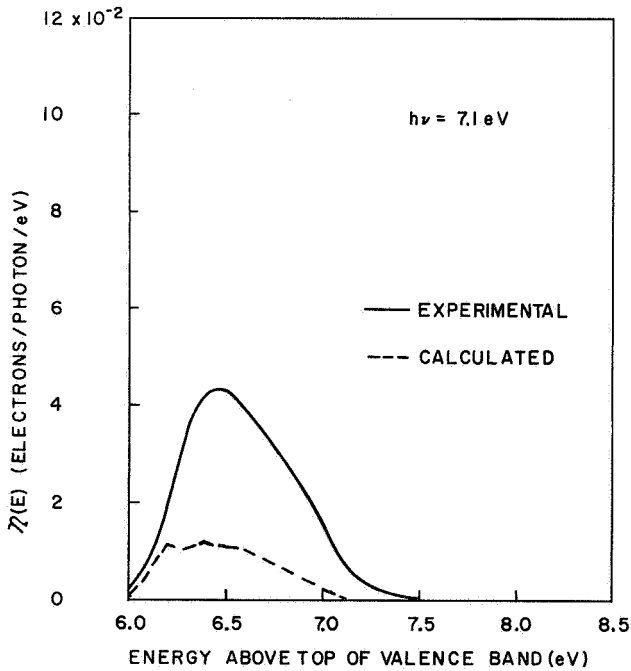
FIG. 118. PHOTOELECTRIC YIELD FOR CUPROUS IODIDE. The experimental curve has been obtained using the thermopile calibrations of Koyama [Ref. 16].



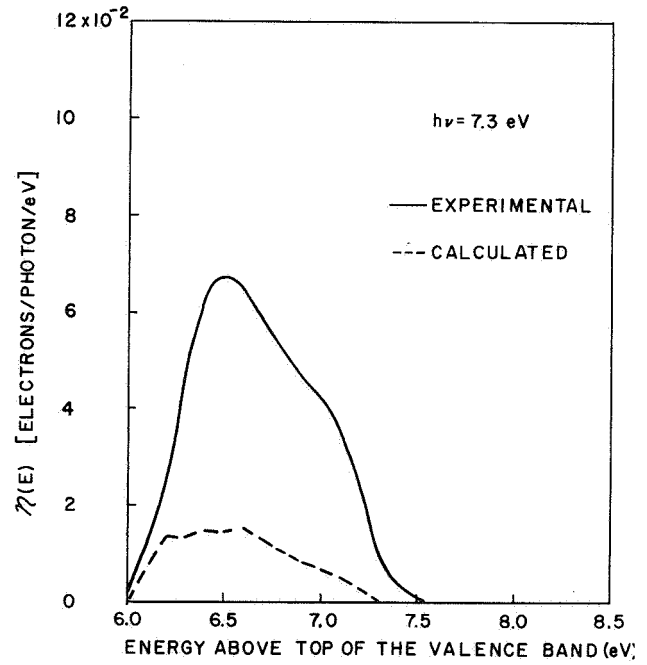
(a)



(b)

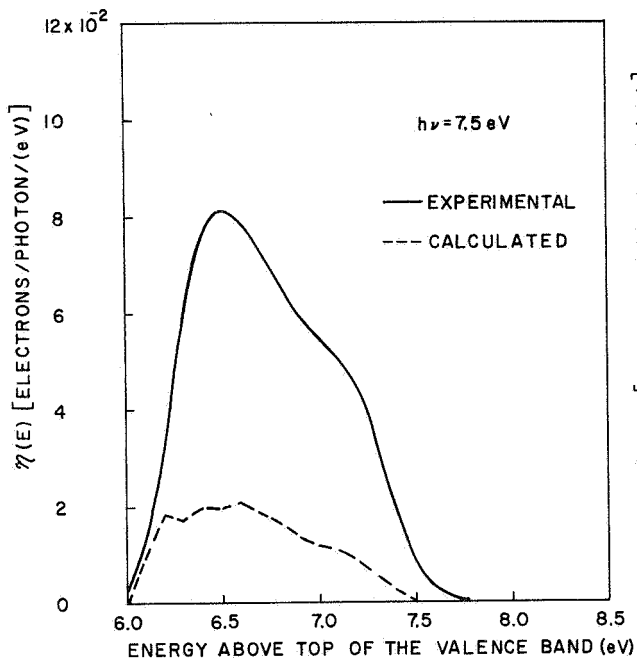


(c)

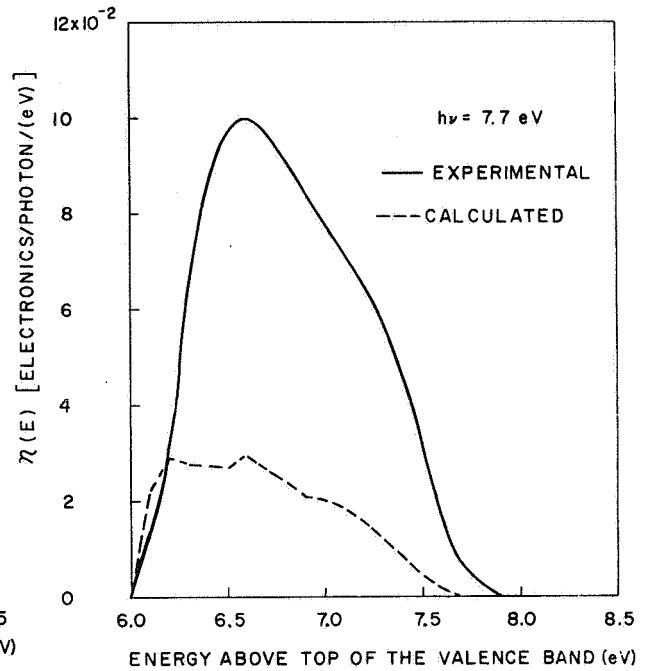


(d)

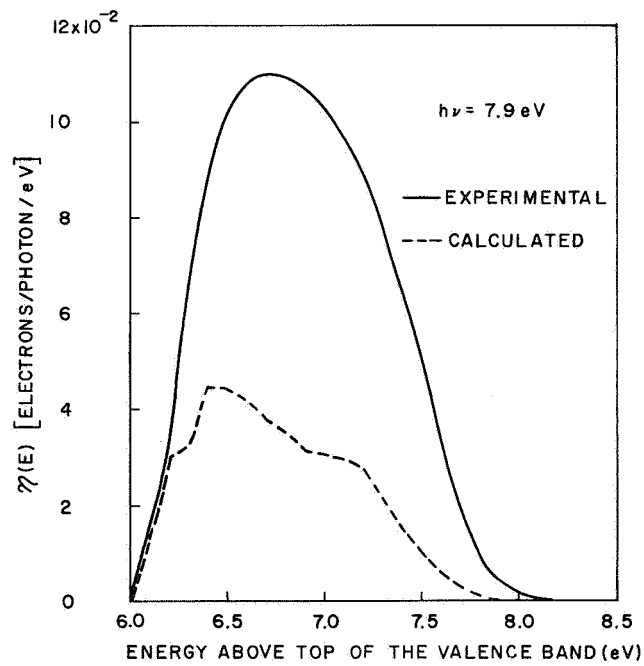
FIG. 119. COMPARISON OF EXPERIMENTAL AND CALCULATED ENERGY DISTRIBUTION CURVES FOR CUPROUS IODIDE.



(e)

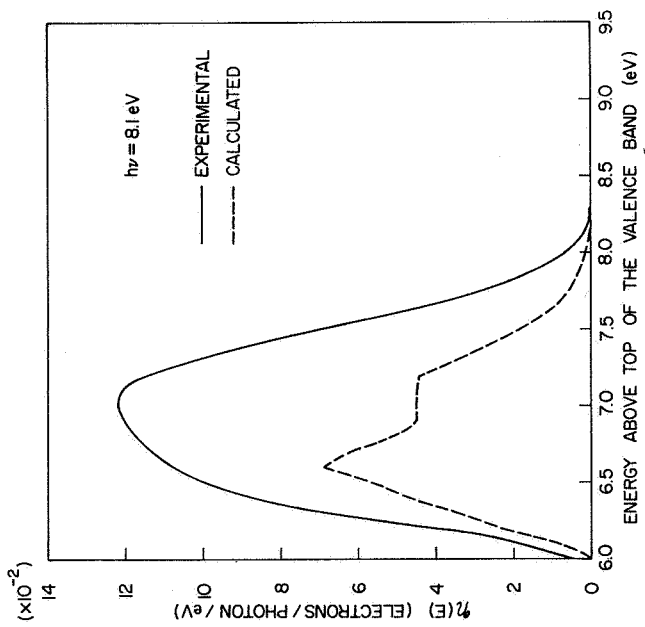


(f)

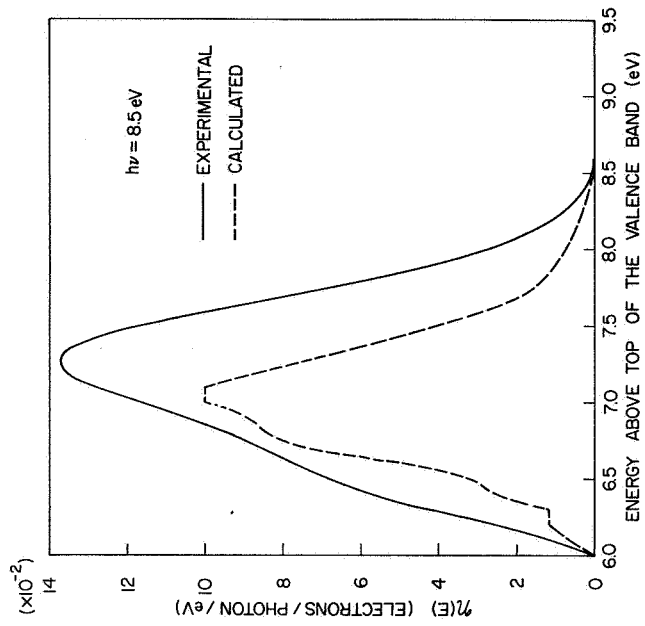


(g)

FIG. 119. CONTINUED.

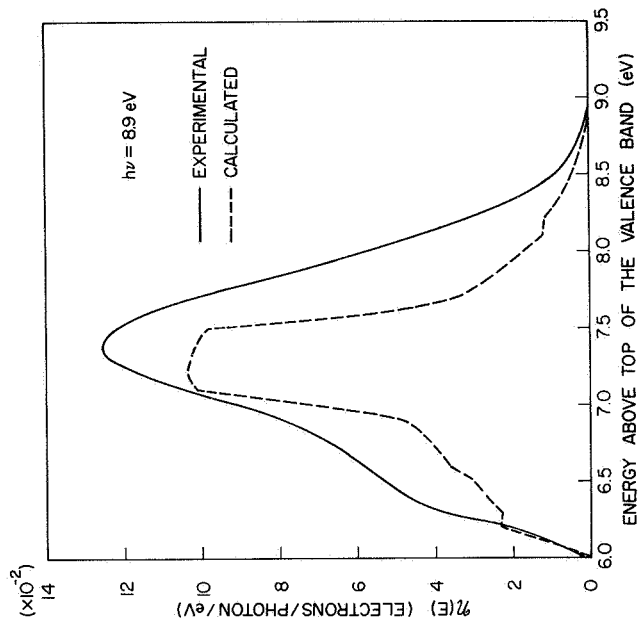


(h)

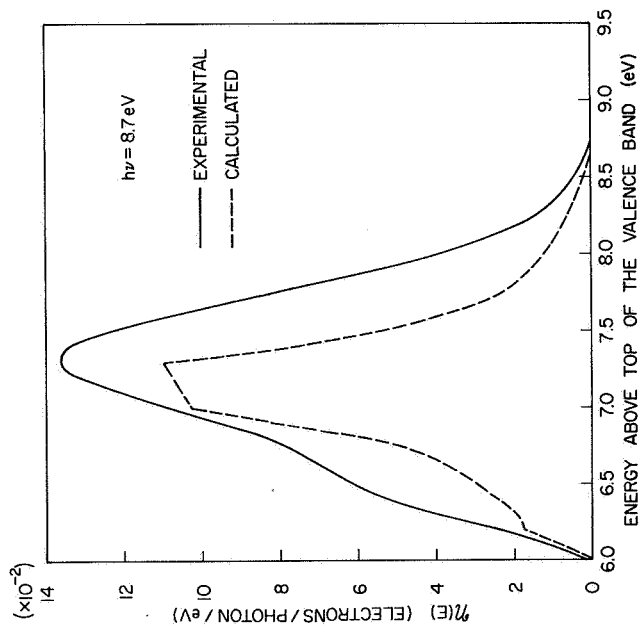


(i)

FIG. 119. CONTINUED.

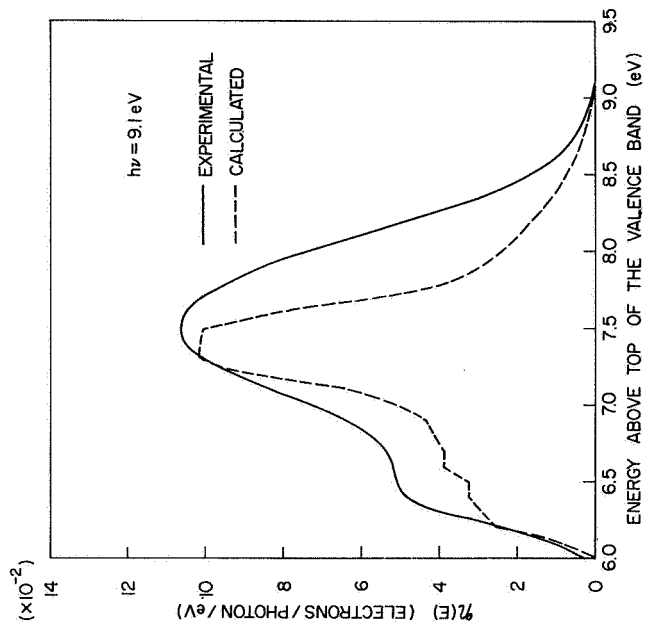


(j)

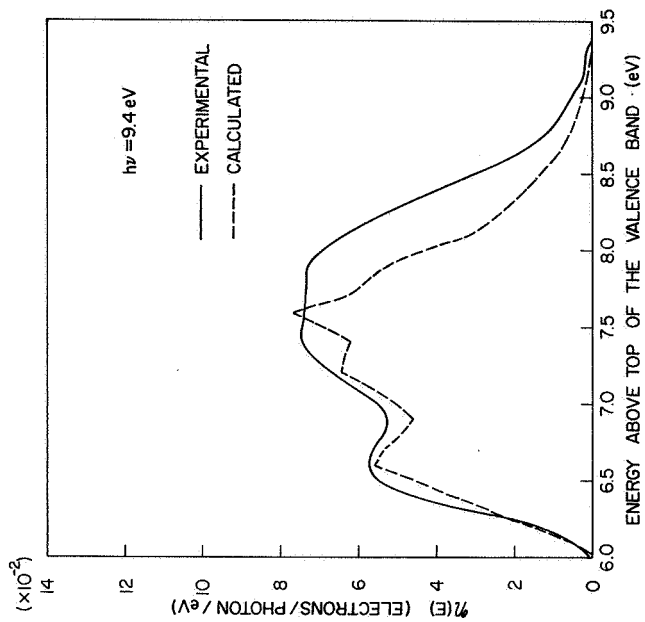


(k)

FIG. 119. CONTINUED.

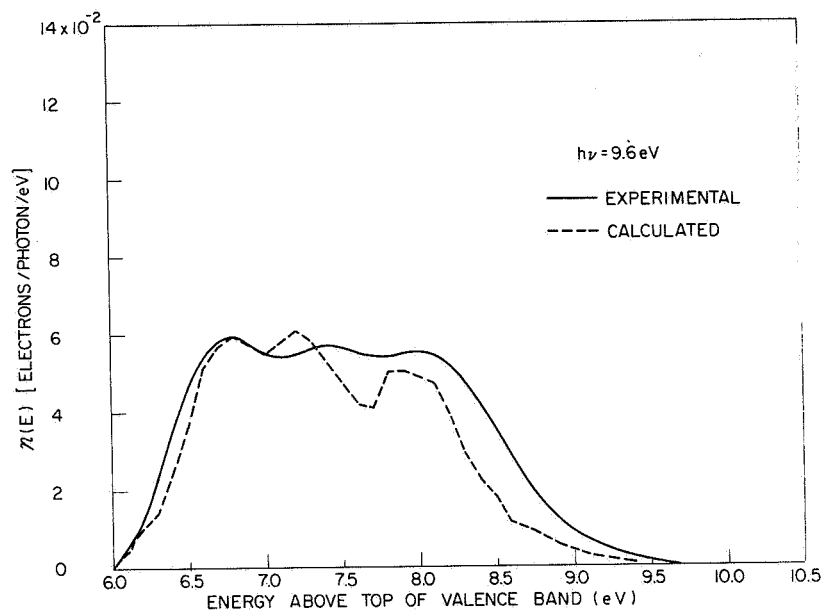


(1)

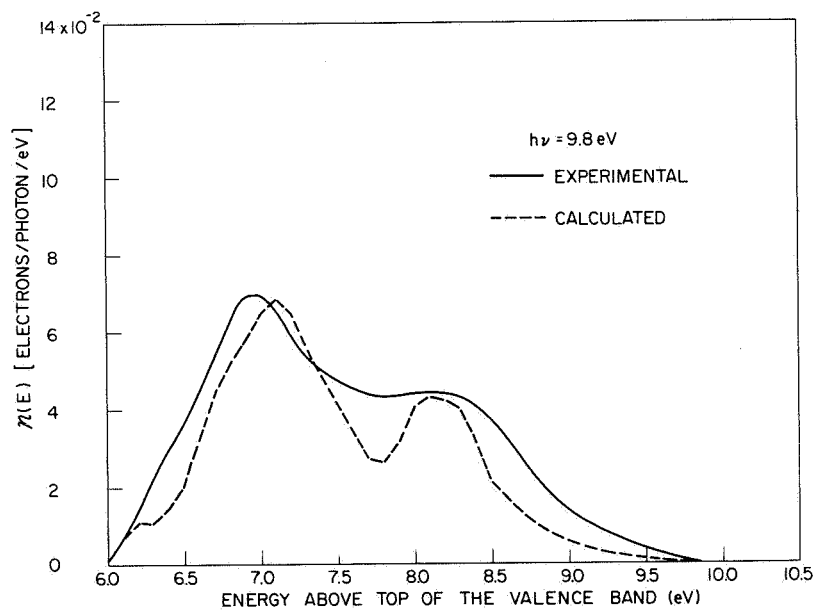


(m)

FIG. 119. CONTINUED.

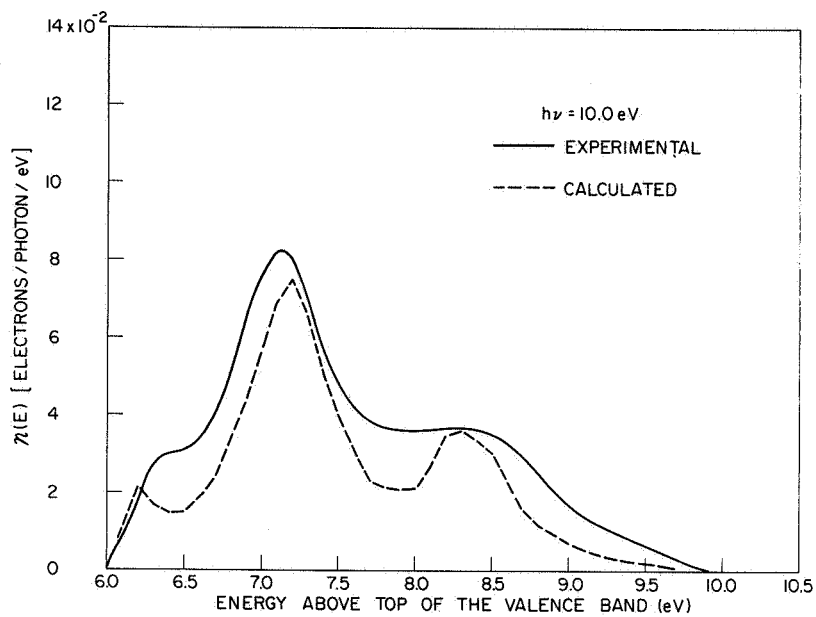


(n)

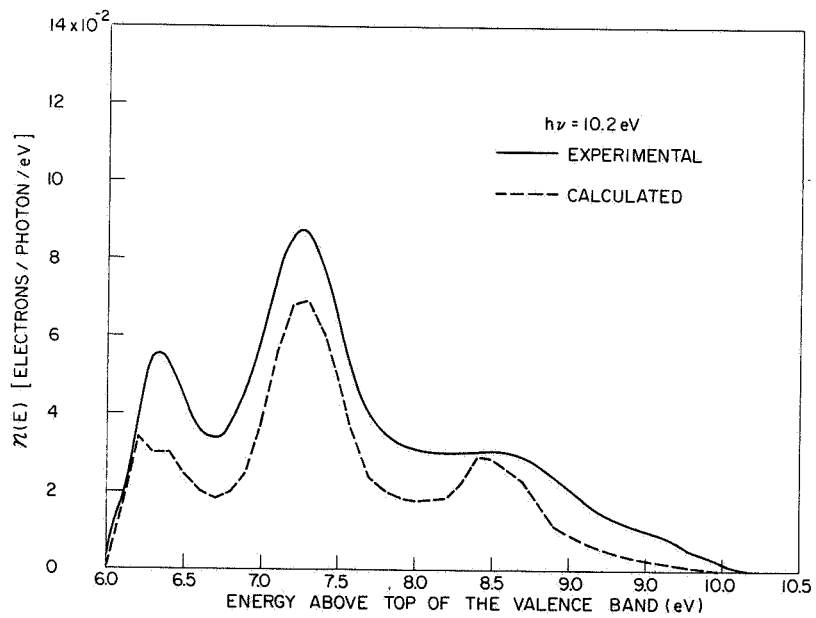


(o)

FIG. 119. CONTINUED.

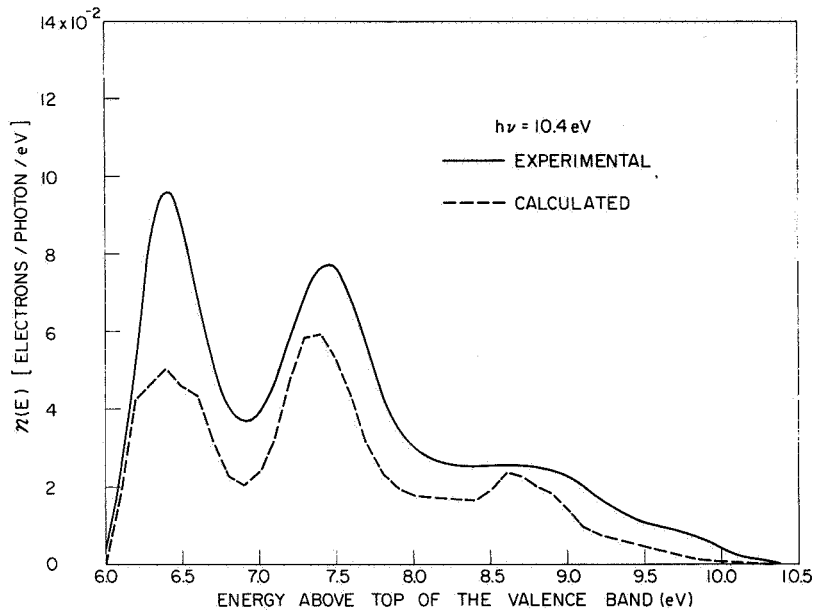


(p)

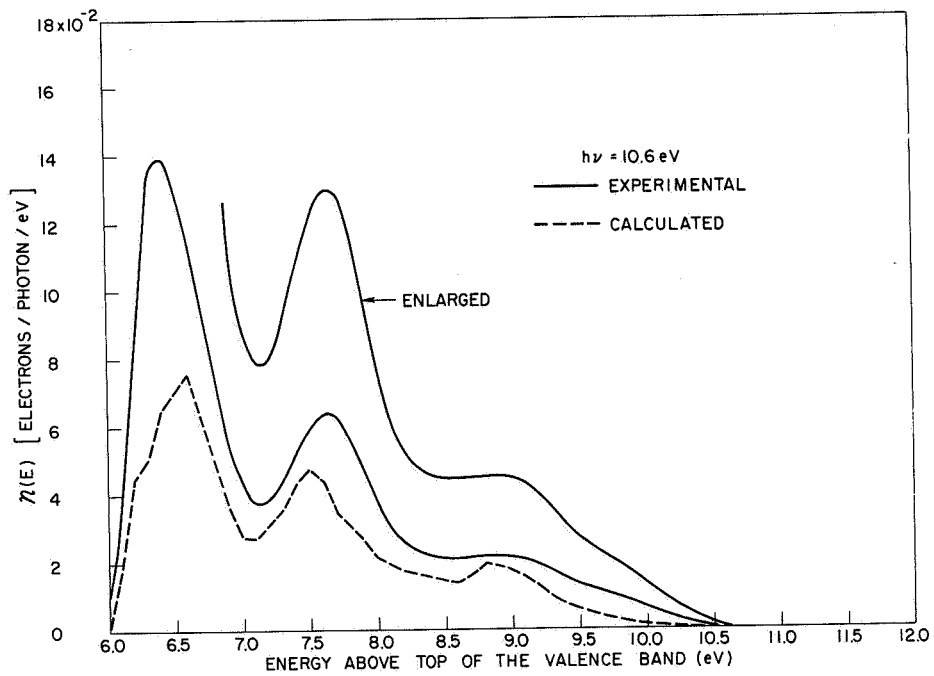


(q)

FIG. 119. CONTINUED.

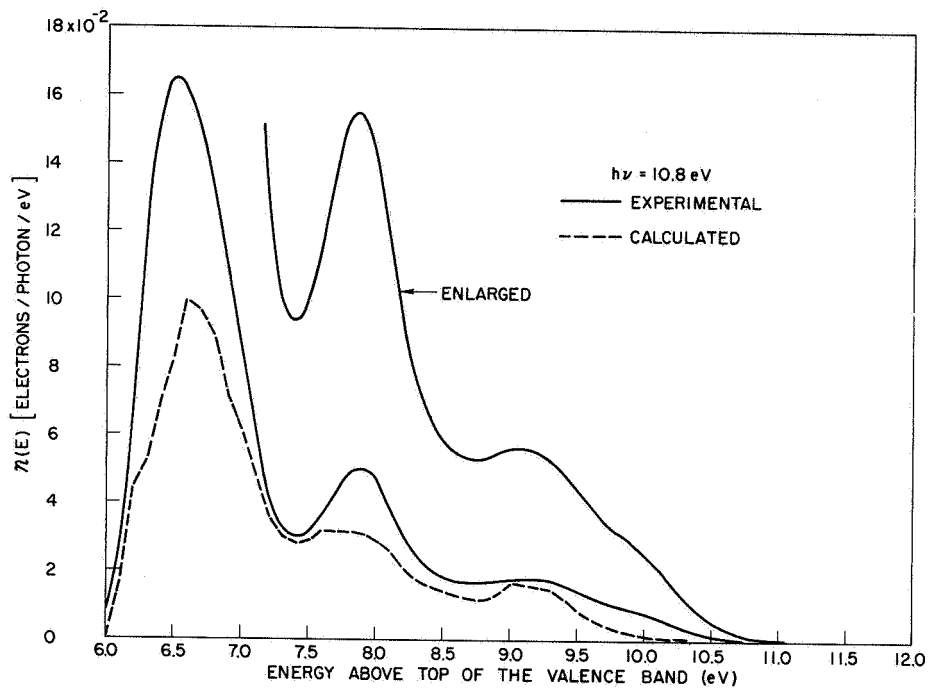


(r)

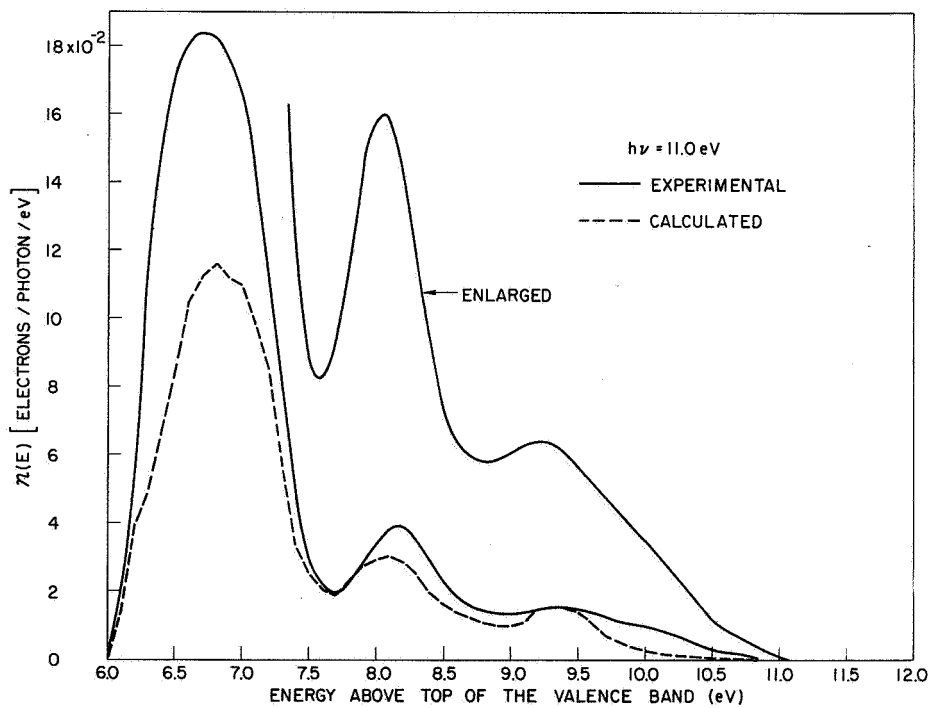


(s)

FIG. 119. CONTINUED.

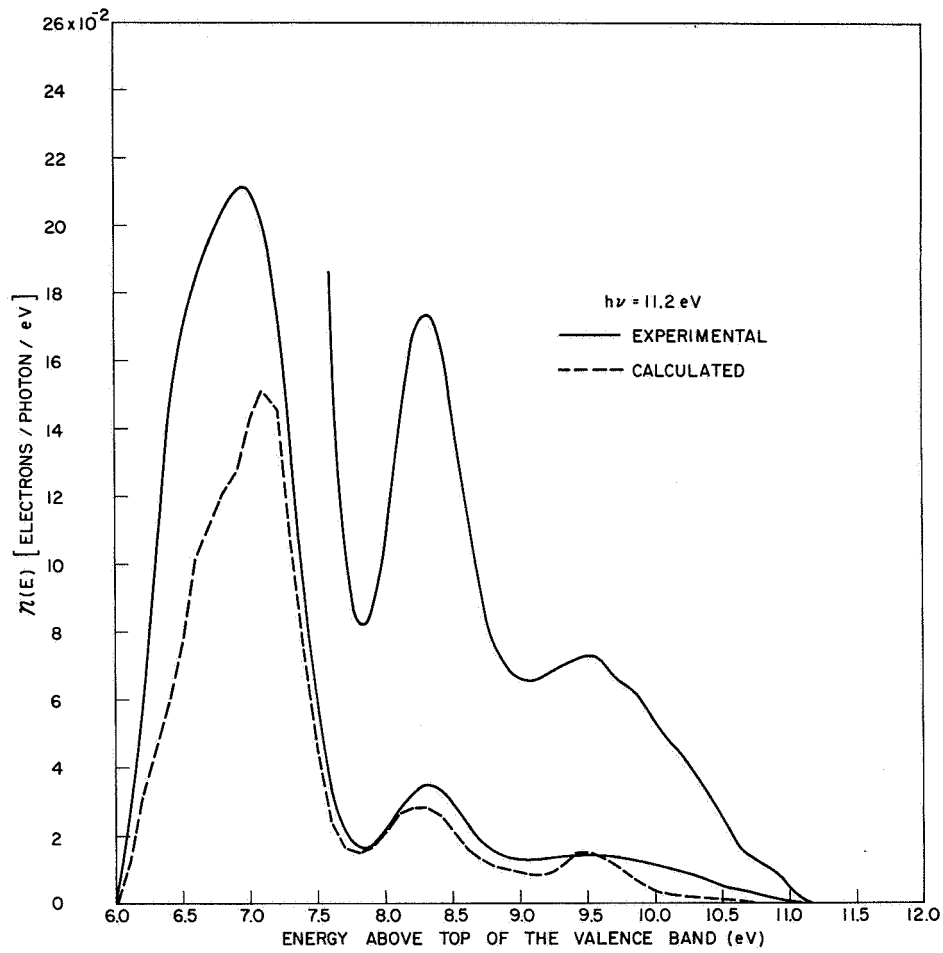


(t)



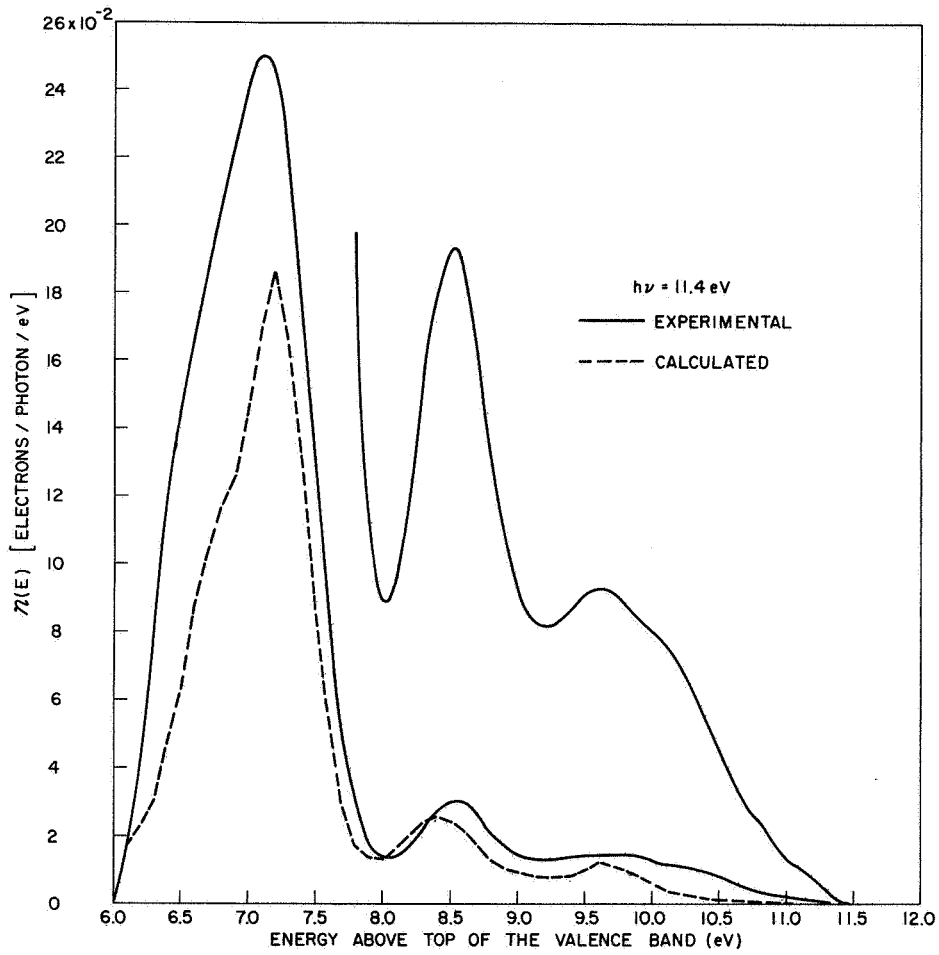
(u)

FIG. 119. CONTINUED.



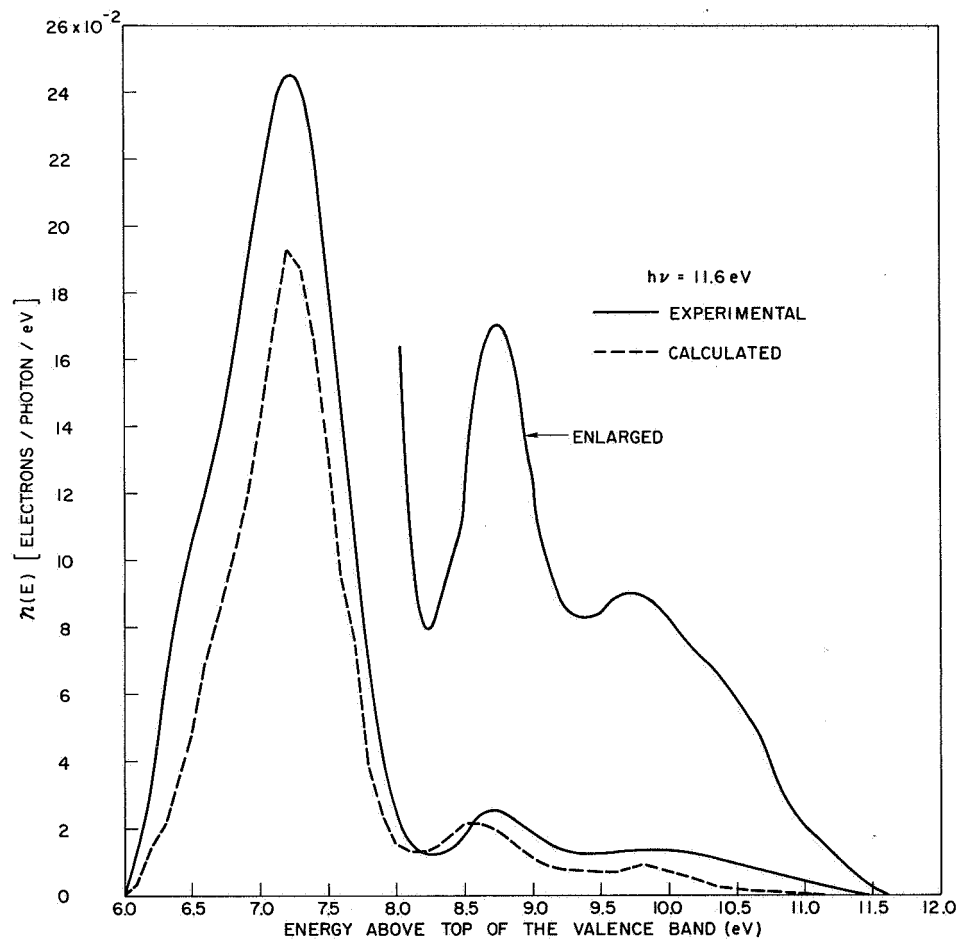
(v)

FIG. 119. CONTINUED.



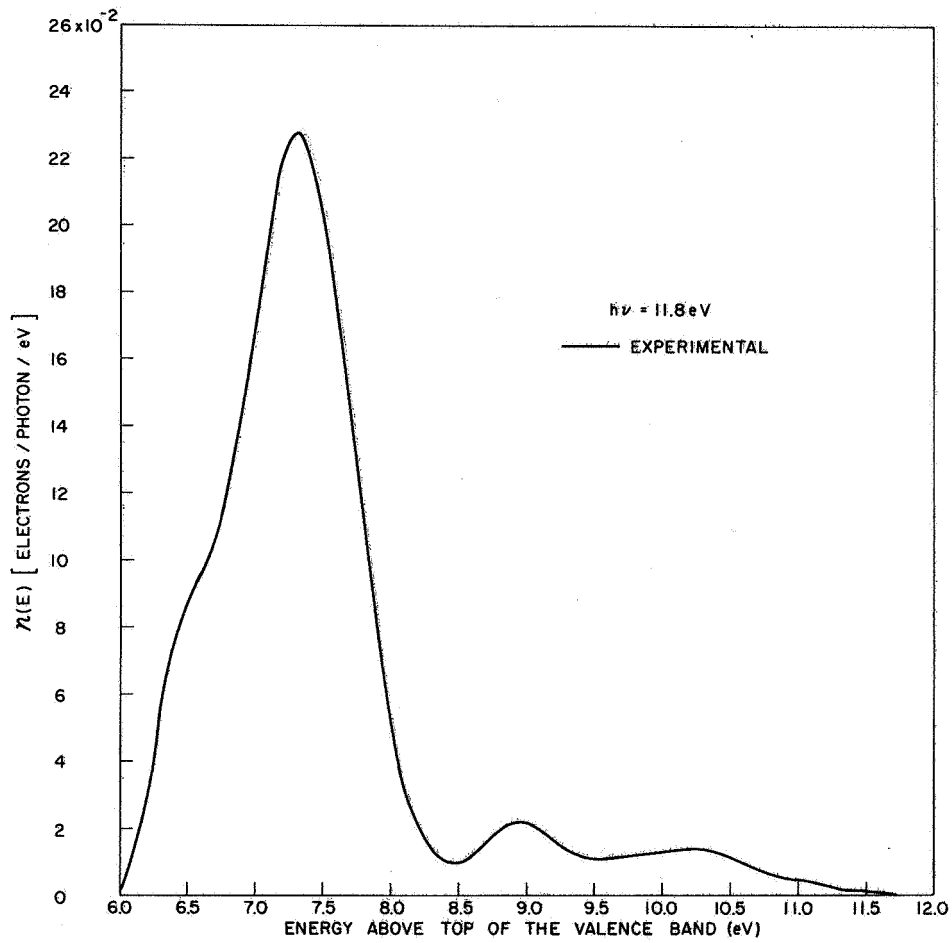
(w)

FIG. 119. CONTINUED.



(x)

FIG. 119. CONTINUED.



(y)

FIG. 119. CONTINUED.

the great strength of photoemission from valence band peak (1) compared with the photoemission from valence band peaks (2) and (3), valence band peak (1) has been associated with the copper 3d band, and valence band peaks (2) and (3) have been associated with the halogen 4p bands.

Even though valence band peak (3) is about equal in height to valence band peak (2) in the optical density of states of Fig. 110, the photoemission peaks originating from valence band peak (3) are smaller than the photoemission peaks originating from valence band peak (2) at photon energies greater than about 9.8 eV. This effect is due to modulation by the shape of the conduction band and to variations in the magnitude of the electron-electron scattering length $L(E)$.

The modulation of the EDCs due to peak (6) in the conduction band optical density of states has a rather pronounced effect upon the shape of many of the EDCs in Figs. 119. However, due to the rather complicated structure in the valence band density of states, the exact location of peak (6) is not obvious in most of the experimental EDCs. However, the location of peak (6) is clearly resolved at photon energies in the vicinity of 9.5 eV, as seen in Figs. 119m and 119n.

From the shape of the experimental EDCs in Figs. 119 near the vacuum level, there is a strong suggestion of a high density of states peak in the conduction band somewhere in the vicinity of the vacuum level. However, the threshold function obscures the exact location of the conduction band peak. Fortunately, the vacuum level was only about 5.0 eV in one sample of CuI, and the location of the conduction band peak became evident, as seen from the EDCs in Figs. 120 and 121. The EDCs of Figs. 120 and 121 provide direct experimental evidence for the conduction band peak labeled (5) in the optical density of states of Fig. 110. However, even with the low vacuum level shown in Figs. 120 and 121, the exact location of conduction band peak (5) is slightly obscured by the modulation of the threshold function. Consequently, peak (5) has been located at 6.1 eV above the top of the valence band in the optical density of states of Fig. 110, rather than 6.2 eV as might be expected from the location of the arrows in Figs. 120 and 121.

The EDCs from several different samples of CuI are compared in Fig. 122 for a photon energy of 10.4 eV. The shapes of the EDCs for all

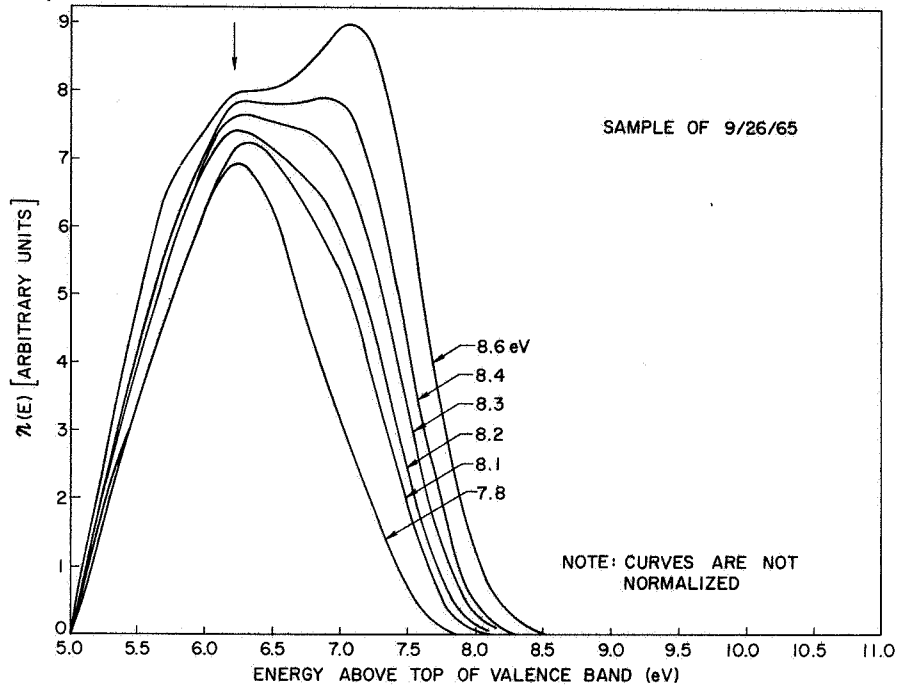


FIG. 120. EXPERIMENTAL ENERGY DISTRIBUTION CURVES FOR CUPROUS IODIDE IN THE RANGE OF PHOTON ENERGIES BETWEEN 7.8 AND 8.6 eV.

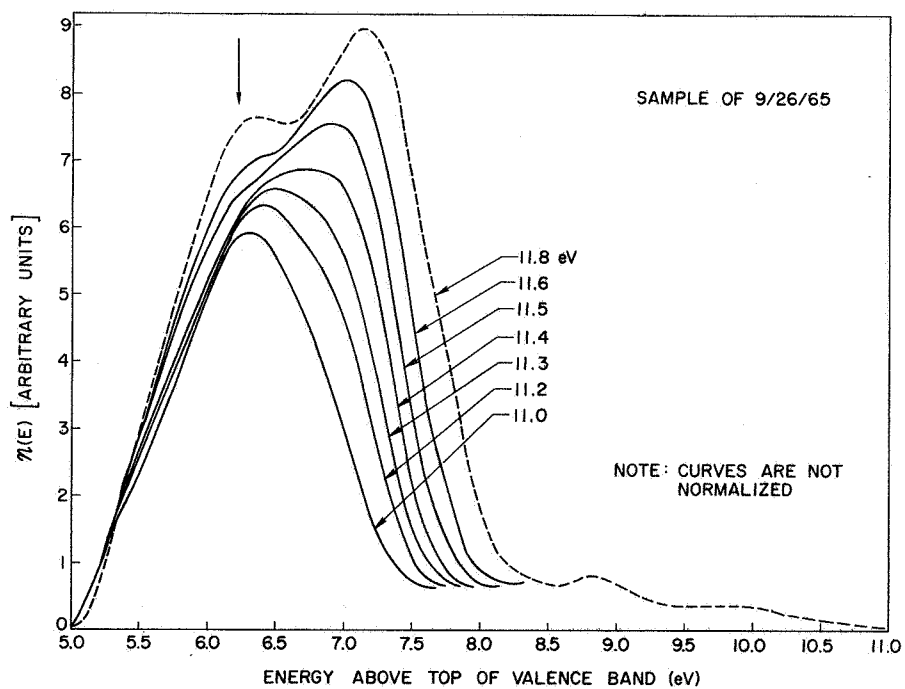


FIG. 121. EXPERIMENTAL ENERGY DISTRIBUTION CURVES FOR CUPROUS IODIDE IN THE RANGE OF PHOTON ENERGIES BETWEEN 11.0 AND 11.8 eV.

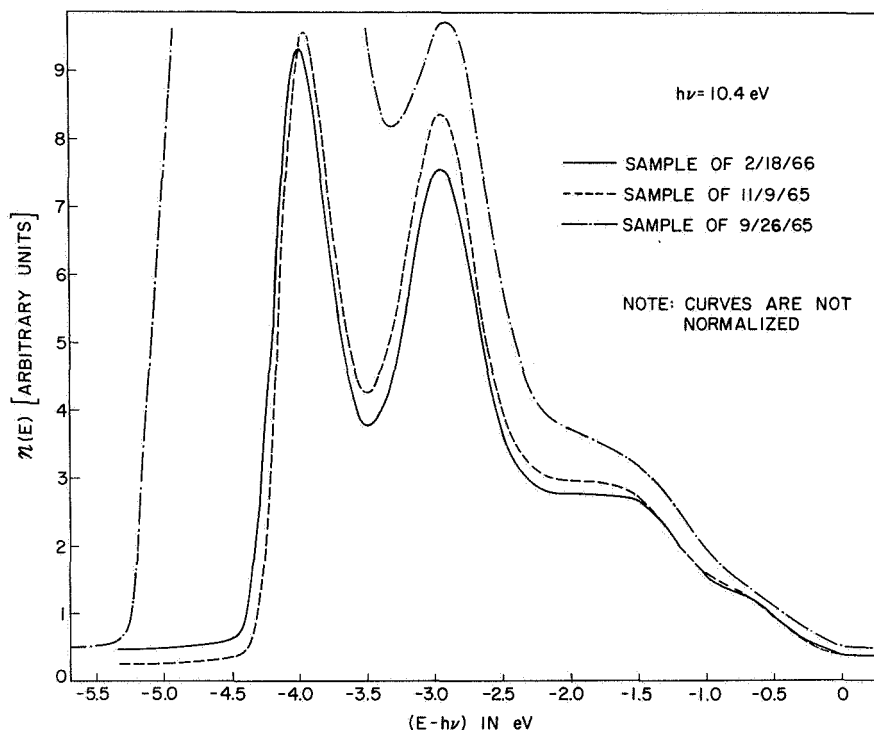


FIG. 122. COMPARISON OF EXPERIMENTAL ENERGY DISTRIBUTION CURVES FOR SEVERAL SAMPLES OF CUPROUS IODIDE. The quantity "E" labeling the energy axis is the energy of the photo-emitted electrons measured from the top of the valence band.

three samples are remarkably alike with respect to detailed structure, except for the fact that one sample has a vacuum level of about 5.0 eV, whereas the other two samples have a vacuum level of about 6.0 eV.

The sample dated 9-26-65 in Fig. 122 has essentially the same shaped structure as the other two samples in Fig. 122. However, when the sample was freshly evaporated, the structure was not as sharp, as seen from the comparison shown in Fig. 123. The EDC from the freshly evaporated sample has much broader structure than the EDC measured on the same sample two weeks later. A possible explanation would be that the freshly evaporated film was amorphous, and that the two-week interval between measurements allowed enough time for small crystallites to grow in the film. The sharp-structured EDC dated 9-26-65 would then be associated with the polycrystalline film, and the broad structured EDC dated 9-12-65 would be associated with the amorphous film. If this explanation is correct, then it is likely that the sharp structure in the optical data of CuI is also

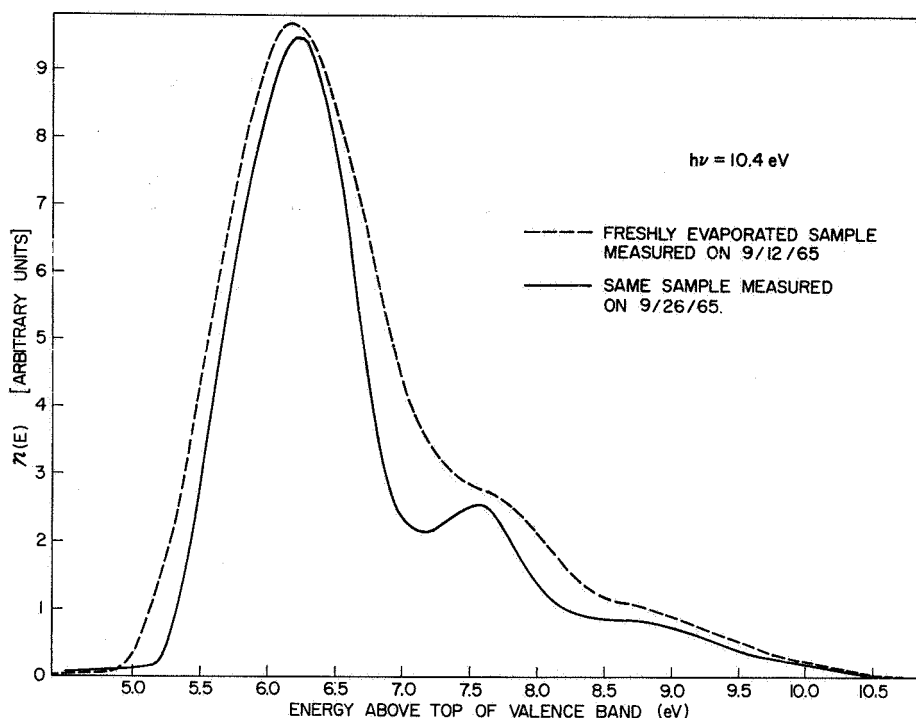


FIG. 123. EXPERIMENTAL ENERGY DISTRIBUTION CURVES FOR ONE CUPROUS IODIDE SAMPLE THAT HAD NO PRONOUNCED STRUCTURE WHEN FRESHLY EVAPORATED, BUT DID SHOW PRONOUNCED STRUCTURE UPON AGING. (The detailed structure in the aged curve can be seen more clearly in Fig. 122.)

dependent upon the existence of crystalline order. However, the extent of the crystalline order necessary for sharp optical structure cannot be easily inferred from only the data of Fig. 123, and it may be that only nearest neighbor crystalline order is necessary for the existence of sharp structure in the EDCs and the optical spectrum of CuI.

Sometimes (as in the case of CuI), modulation due to structure in the conduction band makes interpretation of the EDCs quite confusing, and it is often helpful to use an E_p vs $h\nu$ plot to aid in analyzing the experimental EDCs. Such a plot is shown in Fig. 124 for CuI. Note that the photoemission peaks due to valence band peaks (1), (2), and (3) tend to follow the law $\Delta E_p = \Delta h\nu$, i.e., the transitions are largely described by the model of nondirect transitions. Note also the severe modulation effects of conduction band peaks (5) and (6) upon the location of peaks and shoulders in the experimental EDCs. As seen in Fig. 124, a peak in

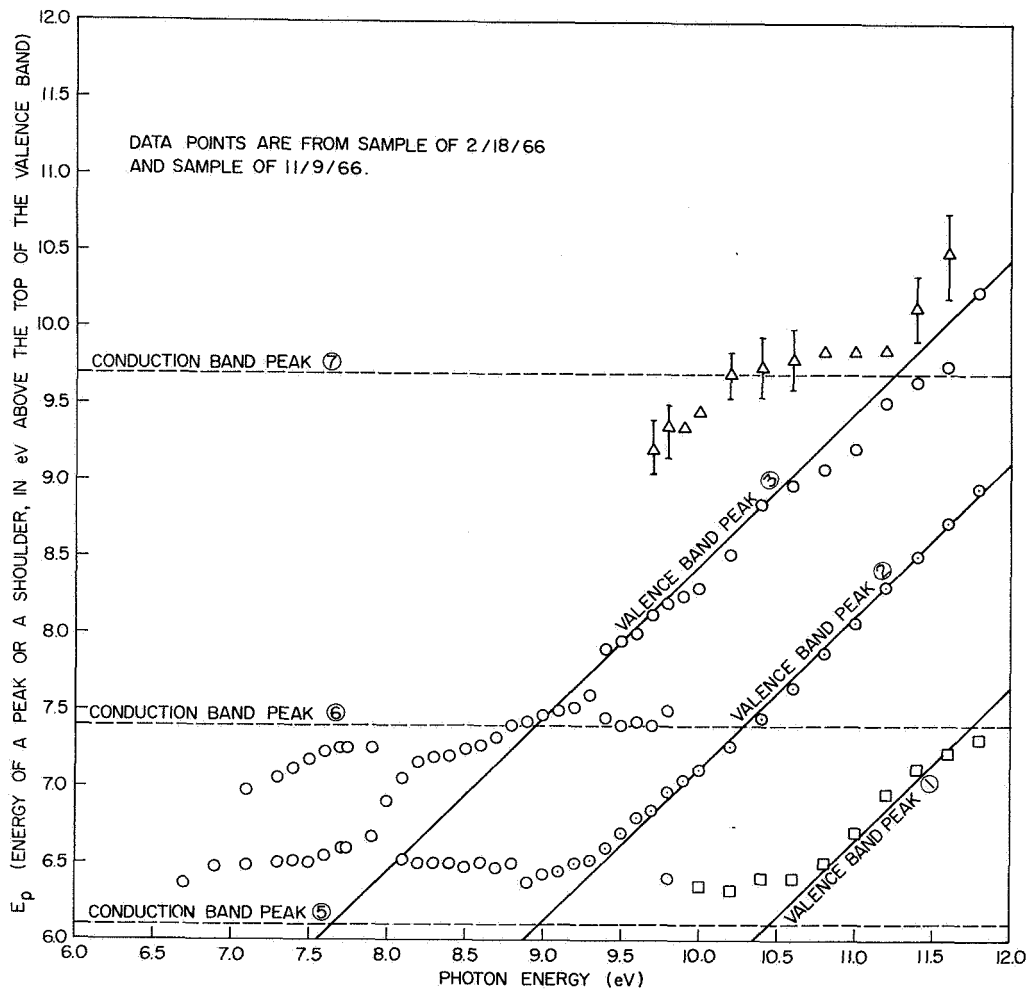


FIG. 124. E_p vs $h\nu$ PLOT FOR CUPROUS IODIDE.

conduction band density of states tends to result in a fixed peak in the EDCs. Apparently, the modulation effects of conduction band peak ⑥ seem to affect transitions from valence band peak ③ more severely than transitions from valence band peak ②; the transitions from valence band peak ② follow the law $\Delta E_p = \Delta h\nu$ more closely than the transitions from valence band peak ③. It may be that a portion of the transitions with initial states in the vicinity of peak ③ and final states in the vicinity of peak ⑥ have a considerable direct component, and are not solely non-direct transitions. In addition, the effects of group velocity and scattering may also be important [Ref. 23]. Thus, it is somewhat difficult to distinguish between direct and nondirect transitions in this rather

complicated case of severe conduction band modulation. Nevertheless, the nondirect model does seem to account for the bulk of the photoemission and optical data.

An E_p vs $h\nu$ plot such as shown in Fig. 124 can be used to locate the position of structure in the conduction band and valence band. Peaks due to conduction band structure tend to stay fixed in energy, peaks due to nondirect transitions from the valence band follow the law $\Delta E_p = \Delta h\nu$, and peaks due to direct transitions follow some intermediate curve where $\Delta E_p \neq \text{constant}$ and $\Delta E_p \neq \Delta h\nu$. If the distorting effects of conduction band modulation and electron-electron scattering are neglected, the location of a valence band peak involved in nondirect transitions can be found by merely extrapolating the $45^\circ \Delta E_p = \Delta h\nu$ lines back to zero photon energy, and reading the intercept on the E_p axis.

As seen from Fig. 124, conduction band peak (7) seems to modulate the experimental EDCs in a rather strange manner, indicating that there may be direct transitions between initial states near the top of the valence band to final states in the vicinity of peak (7). For this reason, peak (7) was not included in the computer analysis, which can account for only nondirect transitions.

5. The Electron-Electron Scattering Length $L(E)$ for Cuprous Iodide

The electron-electron scattering length $L(E)$ calculated from the optical density of states of Fig. 110 is shown in Fig. 125. Although there are no experimental electron-electron scattering length data on CuI, Pong [Ref. 71] has fortunately made experimental measurements on CuBr. Since the photoemission experiments of the present work indicate that CuBr is very similar to CuI, the magnitude of the calculated $L(E)$ for CuI was set by normalizing the calculated curve to agree with Pong's experimental data for CuBr in the range of energies between 10 and 11 eV. The magnitude of the resulting $L(E)$ curve for CuI is apparently not too far from being correct, since the magnitude of $L(E)$ helps to determine the magnitudes of the calculated quantum yield and EDCs, and the magnitudes of the calculated quantum yield and EDCs are in rather good agreement with the experimental photoemission data.

Note that the $L(E)$ curve for CuI does not monotonically decrease with increasing energy as do the $L(E)$ curves for Cu, Ag, and Au.

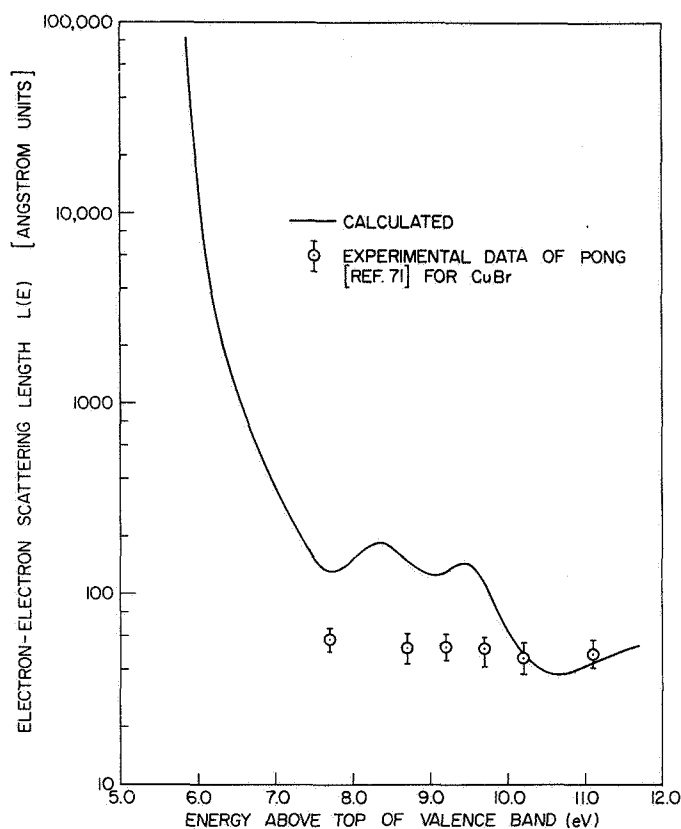


FIG. 125. CALCULATED $L(E)$ FOR CUPROUS IODIDE COMPARED WITH EXPERIMENTAL DATA OF PONG [REF. 71], WHICH IS FOR CUPROUS BROMIDE.

As a consequence of the sharp structure in the optical density of states of Fig. 110, the $L(E)$ curve for CuI has significant structure in the range of energies between 8 and 12 eV.

As seen in Fig. 125, $L(10.5 \text{ eV})$ is about a factor of three lower than $L(9.5 \text{ eV})$. Since this decrease in $L(E)$ occurs at about 10 eV, one might suspect that it is this decrease in $L(E)$ that causes the dip in the quantum yield of Fig. 118. However, this is not the case, since at a photon energy of 10 eV, very few electrons are excited to energies in the vicinity of 10 eV, as can be seen from the experimental EDCs of Figs. 119.

At energies less than $2E_g = 5.8 \text{ eV}$, there can be no inelastic electron-electron scattering if energy is to be conserved, so for $E \leq 5.8 \text{ eV}$, $L(E) = \infty$.

6. The Location of the Fermi Level in Cuprous Iodide

If the work function of the metal surface coating the collector can be known, the fermi level at the surface of a semiconducting photo-emitter can be deduced from the zero of energy in the photoelectric EDCs. The manner in which this is done is obvious from the diagrams of Fig. 126, where V_R is the retarding potential between the emitter and the collector, and ϕ_c is the contact potential between the emitter and the collector.

In the photoemission measurements carried out on CuI in the high vacuum photoemission chamber, the value of the collector work function was always well known, since two experiments were made on each pumpdown, the first experiment always being made on either Cu, Ag, or Au films which were evaporated inside the collector can in the manner described in Chapter II. From the first experiment on the metal substrate, the value of the collector can work function could be determined to within about ± 0.15 eV.

The three sets of data shown in Fig. 126 give values of 0.7, 0.8, and 1.0 eV for the energy of the fermi level above the top of the valence band. Since these values are all nearly the same, it seems reasonable to conclude that the fermi level at the surface of an evaporated film of CuI is typically about 0.8 eV above the top of the valence band. Since the (optical) energy gap of CuI is about 2.8 eV, it appears that the CuI film is p-type near the surface.

In all of the photoemission analyses presented thus far in this chapter, it has been tacitly assumed that there are no severe band-bending effects within an absorption length of the surface. Band-bending near the surface can have a significant effect upon the interpretation of the photoelectric EDCs, but band-bending can be accounted for if such factors as the bulk doping and the nature of the surface states are well understood.¹ Since no such information is presently available for the cuprous halides, the possible effects of band-bending will not be considered in the analysis of photoemission from the cuprous halides.

¹For an example in which band-bending effects are considered in analyzing photoemission data, see Ref. 80.

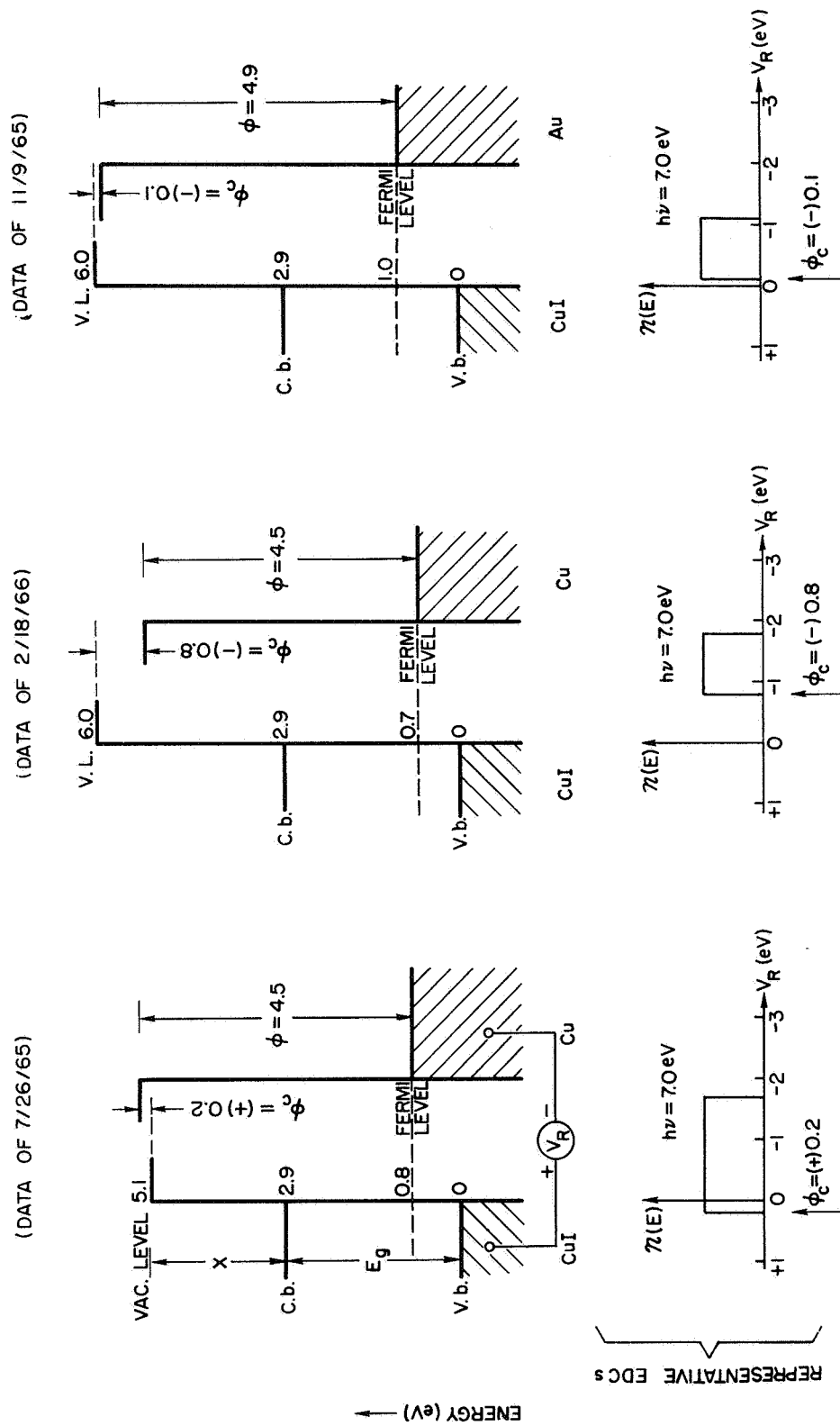


FIG. 126. LOCATION OF FERMI LEVEL FROM ENERGY DISTRIBUTION CURVES FOR CUPROUS IODIDE.

However, it seems likely that there are no severe band-bending effects near the surface of CuI, since the optical density of states deduced from the photoemission data accounts strikingly well for the detailed structure in the high energy optical data, which is independent of any band-bending effects.

7. Comparison with Energy-Band Calculations

Although no energy band calculations are presently available for the cuprous halides, energy band calculations do exist [Refs. 72, 73, and 78] for AgBr and AgCl, which are not too different from the cuprous halides. Since at least some qualitative insight might result from a comparison of these theoretical calculations with the photoemission results from the cuprous halides, the optical density of states for CuI is compared to Scop's [Ref. 72] APW energy band calculation for AgBr in Fig. 127. In Fig. 127, the valence band of Scop's AgBr calculation has been linearly stretched (by about 50 percent) so that the valence band width of the AgBr equals the experimental valence band width of CuI. The theoretical conduction band for AgBr has not been altered, except for a bodily shift of the entire conduction band relative to the top of the valence band.

A comparison of CuI with AgBr may at first seem to be unwarranted, for several reasons: (1) AgBr has a NaCl crystal structure whereas CuI has a ZnS crystal structure; (2) the metal and halogen atoms are different in the two materials. However, there is some justification in comparison, since the experimental photoemission data presented in this chapter show that CuCl, CuBr, and CuI have quite similar optical densities of states, indicating that the different halogen atoms do not have drastically different effects on the energy band structure of the cuprous halides. In addition, there is a close similarity between the absorption coefficients of AgI (ZnS lattice) and CuI (Zns lattice), as shown in Fig. 117. This close similarity suggests that the silver and copper atoms act in similar ways in the cuprous halides and the silver halides. To complete the analogy between the cuprous halides and the silver halides, it would be desirable to compare experimental EDCs from the cuprous halides with experimental photoelectric EDCs from the silver halides. Peterson [Ref. 77] has obtained EDCs for AgBr and AgCl.

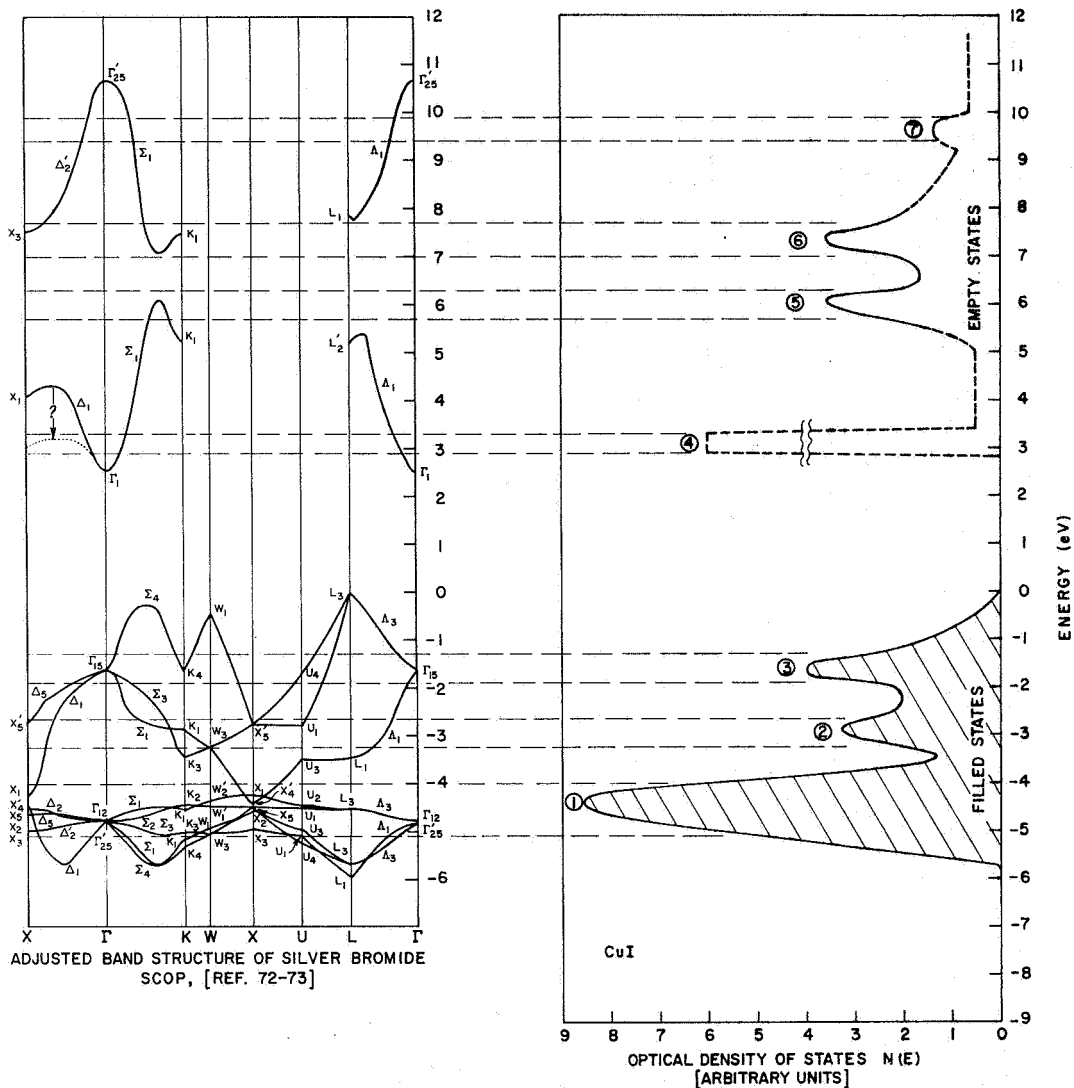


FIG. 127. COMPARISON OF OPTICAL DENSITY OF STATES FOR CUPROUS IODIDE WITH ADJUSTED BAND STRUCTURE OF SILVER BROMIDE. Scop's [Ref. 72,73] calculated valence bandwidth of 4.0 eV has been linearly scaled by about 50 percent to agree with the valence bandwidth of cuprous iodide.

Unfortunately, Peterson's experimental data suffer from problems of possible surface contamination,¹ and cannot be considered as definitive at this time.

In Fig. 127, a remarkable similarity exists between the adjusted band structure of CuI and the optical density of states of AgBr, in that there is a close correspondence between the peaks in CuI and "flat" bands in AgBr.

In the valence band, the most significant feature is the agreement between the location of the silver 4d bands and the location of CuI peak ①, which has been associated with the copper 3d bands. The CuI peak ② seems to correspond to the flat bands designated Σ_1 , and to the flat bands along the $X'_5 - U_1$ face. The CuI peak ③ seems to be associated with states near Γ_{15} , which are derived largely from the halogen 4p wavefunctions.

In the conduction band, the correspondence between CuI and AgBr is quite striking. As seen in Fig. 126, the conduction band of AgBr is actually composed of two conduction bands: The lower conduction band is derived largely from the silver 5s wavefunctions, and the upper conduction band is derived largely from the halogen 4d wavefunctions.² Cuprous iodide peak ④ corresponds closely to the flat bands at X_1 , CuI peak ⑤ corresponds to bands at the top of the lower conduction band, CuI peak ⑥ corresponds to the bands at the bottom of the upper conduction band, and CuI "peak" ⑦ corresponds to bands near the top of the second conduction band.

¹In Peterson's [Ref. 77] own words "...No special precautions with the surface were taken in sample preparation ...," and "...The bulk of external photoelectrons were found to emerge with a uniform distribution in energy between 0 and 2 eV for all incident energies...with the exception of a small tail which moves in proportion to increasing incident energy..." The photoemission characteristics described above by Peterson are often called "universal curves," because such characteristics are found in the photoemission data of many different types of materials, if the material is contaminated or has a poorly prepared surface.

²As discussed earlier, the character of the atomic wavefunctions from which the states are derived may be significant in determining the matrix element for the transition ① → ④.

Note that in the energy band calculation of AgBr, the top of the valence band is not at Γ , but at L. Bassani et al [Ref. 78] and Scop [Ref. 72] have pointed out that this effect is due to strong p-d mixing, and both authors have emphasized that there is strong covalent bonding between the silver d-wavefunctions and the halogen p-wavefunctions. This result is consistent with the results of the photoemission data, which are remarkably similar for CuCl, CuBr, and CuI; this similarity in the photoemission data of the cuprous halides indicates that the structure in the halogen bands is not determined primarily by the spin-orbit splitting, which is quite different for the different halogens. This covalent bonding in the silver halides also tends to substantiate the bonding scheme proposed for the cuprous halides earlier in this chapter.

Scop [Ref. 72] finds that for AgBr, the spin-orbit splitting at Γ_{15} is 0.58 eV, slightly more than the free ion value. However, Scop finds that the spin-orbit splitting at L_3 is less than 0.1 eV, due to the strong p-d mixing near the top of the valence band.

Note in Fig. 127 that there is an arrow suggesting that the X_1 point should be somewhat closer to the bottom of the conduction band in an iodine compound than in a bromine compound. As will be pointed out later in this chapter, the X_1 point in Scop's AgBr conduction band is closer to the bottom of the conduction band than is the X_1 point in Scop's AgCl calculations; this trend seems to correspond to the trend in the location of peak (4) in the cuprous halides.

C. PHOTOEMISSION STUDIES OF CUPROUS BROMIDE

As discussed earlier in this chapter, excellent photoelectric EDCs have been obtained for CuBr, but reliable quantum yield data corresponding to these EDCs could not be obtained due to the lack of an accurate calibration standard. However, the significant features of the quantum yield for CuBr can be obtained by noting the features common to a number of different sets of quantum yield data. Several sets of quantum yield data for CuBr are shown in Fig. 128; the feature common to all the sets of data is a dip at about 10 eV, followed by a rise at about 11 eV. Just as in the case of CuI, the dip is due to strong transitions from initial states in the copper d band to final states below the vacuum level,

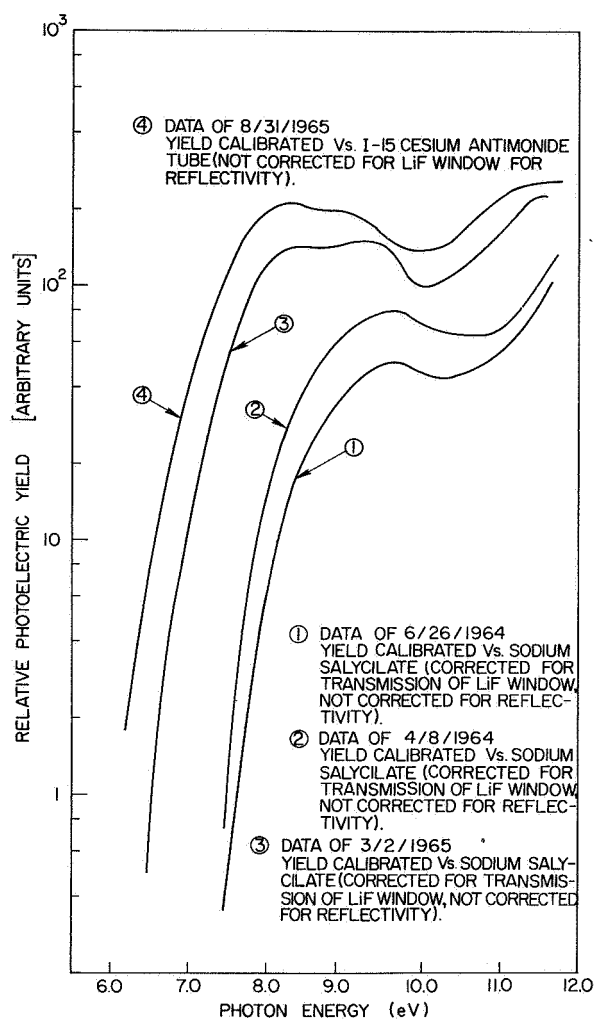
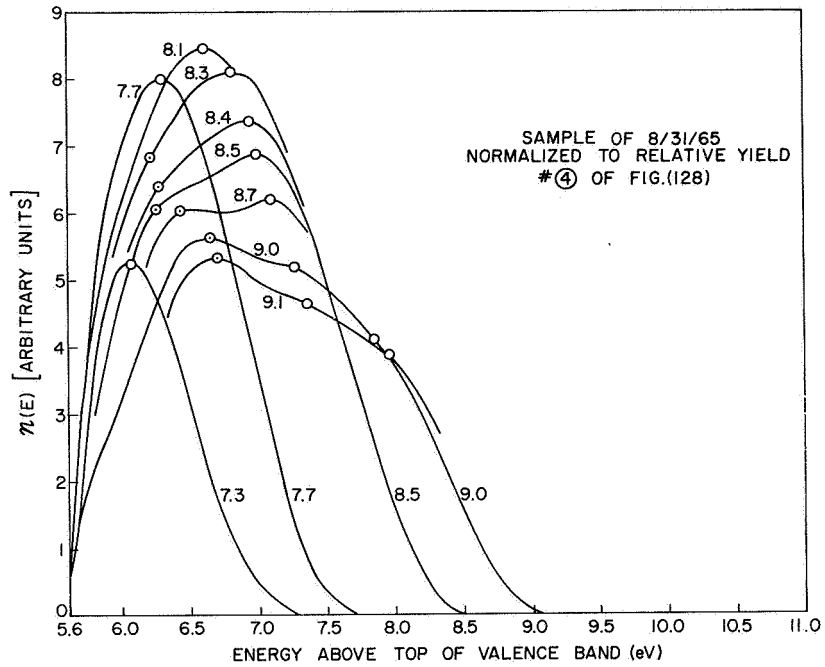


FIG. 128. PHOTOELECTRIC YIELD FOR CUPROUS BROMIDE.

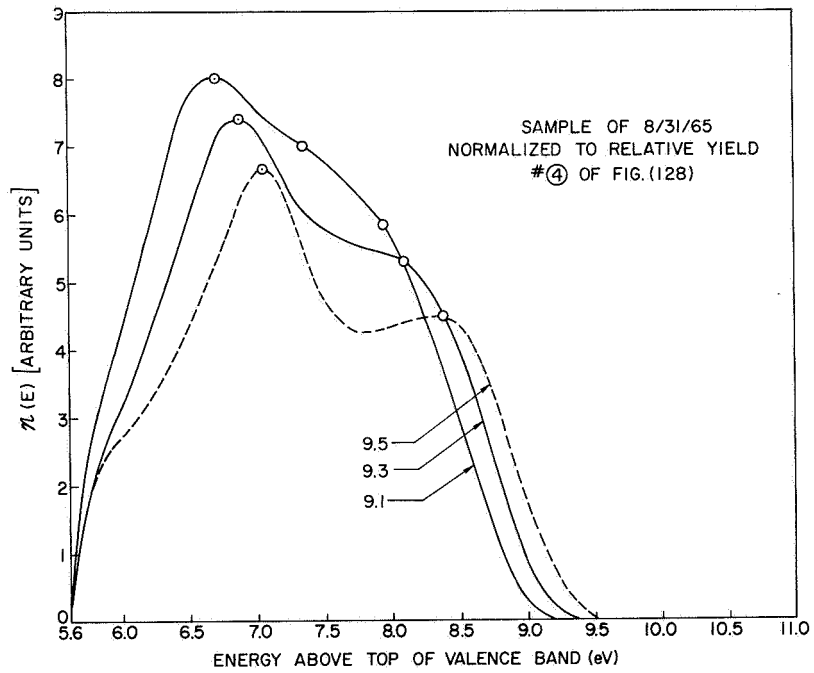
and the rise is due to the onset of photoemissions from the copper d band.

Although there is considerable uncertainty in the overall shapes of the yield curves of Fig. 128, the relative uncertainty is likely to be much smaller over small intervals in photon energy. Consequently, the normalized EDCs for values of $h\nu$ within about an eV of each other should give reliable information. In each of Figs. 129a through 129g, the EDCs are presented for a small enough range in energy so that the relative magnitudes of the EDCs are significant.

As seen in Fig. 129, the EDCs for CuBr have essentially the same features as the EDCs from CuI. In fact, the structure in the optical



(a)



(b)

FIG. 129. ENERGY DISTRIBUTION CURVES FOR CUPROUS BROMIDE.

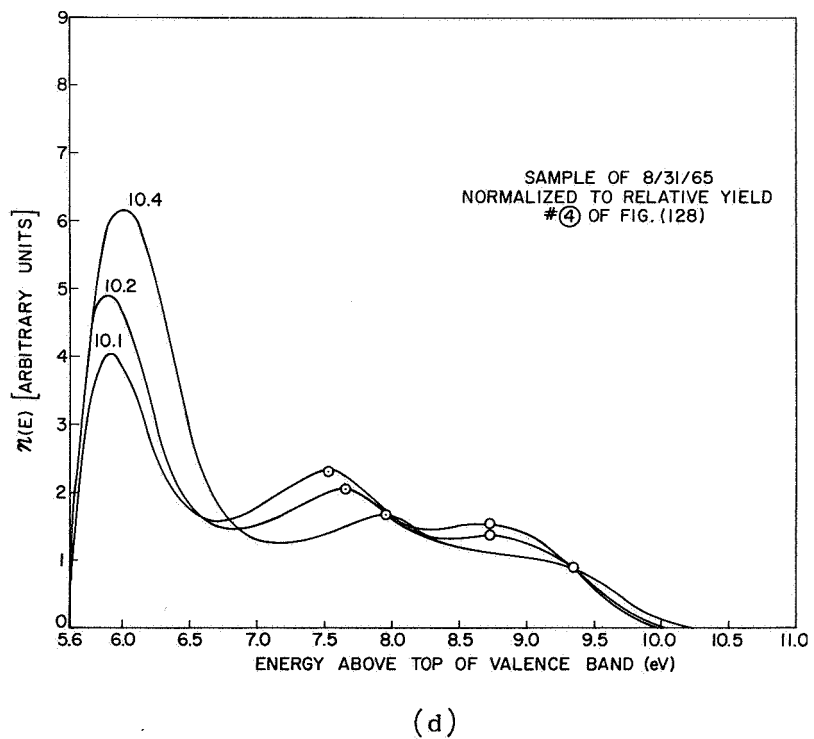
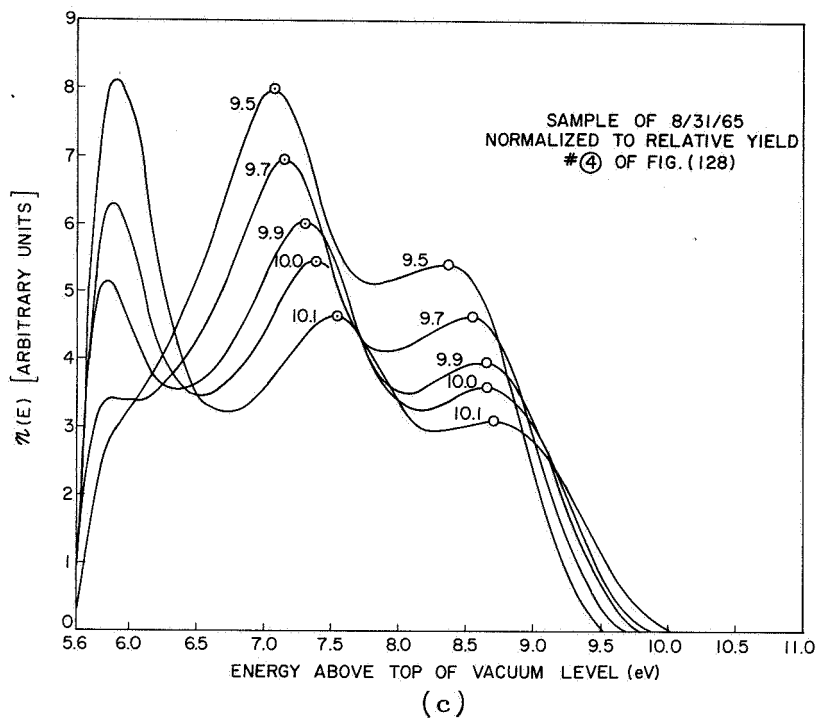
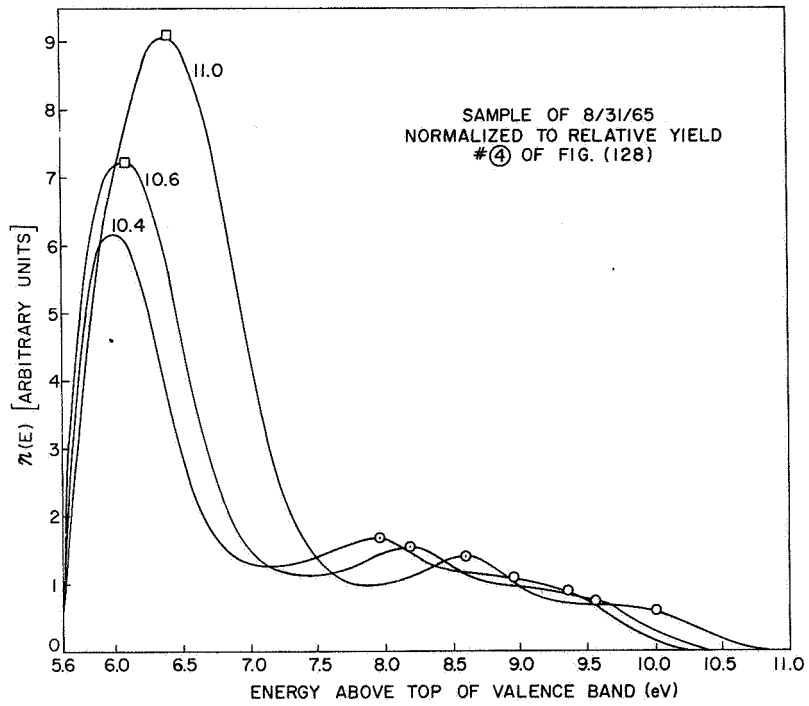
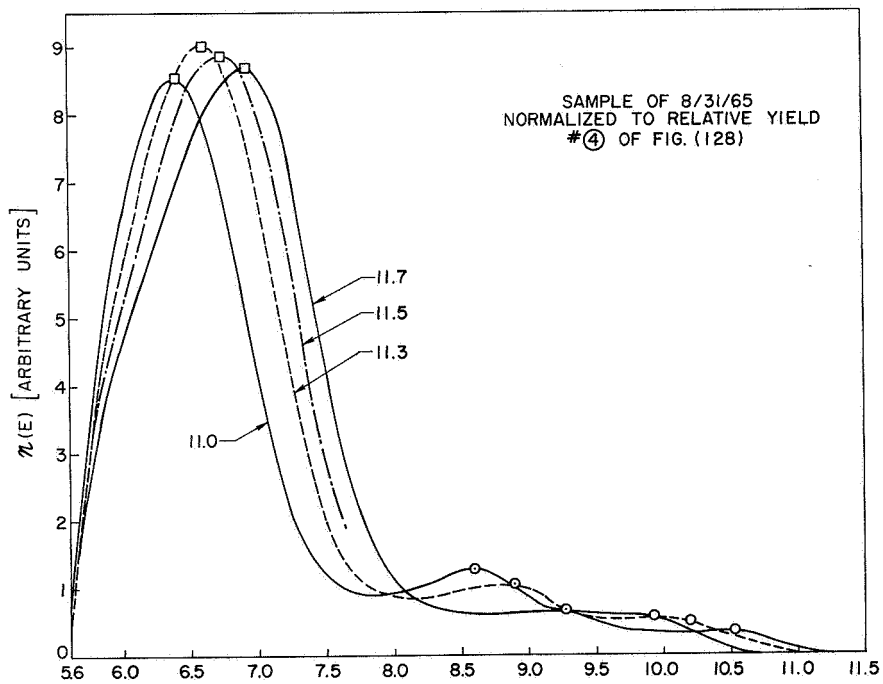


FIG. 129. CONTINUED.

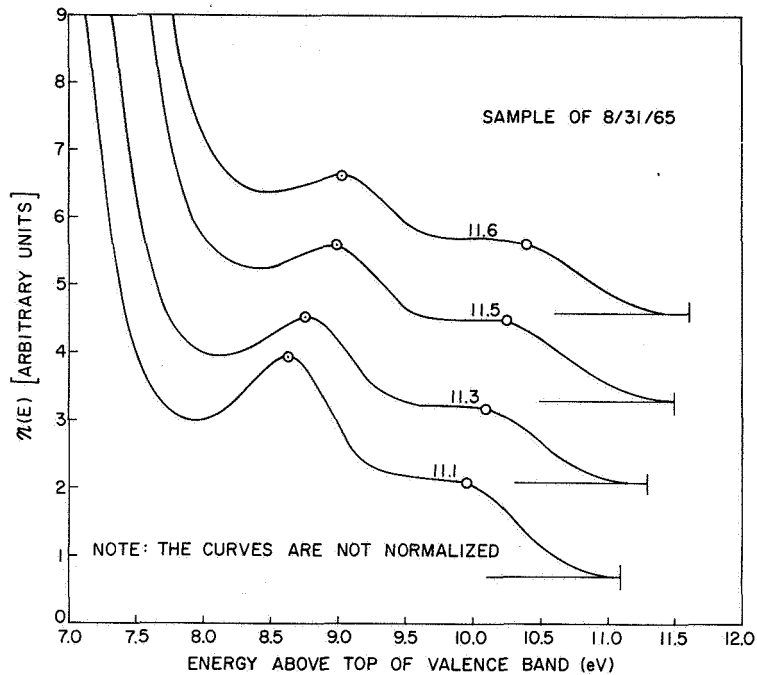


(e)



(f)

FIG. 129. CONTINUED.



(g)

FIG. 129. CONTINUED.

density of states of CuBr is found to correspond with the structure in the optical density of states of CuI. From Fig. 129, we see that the magnitudes of the EDCs tend to be large near the vacuum level, indicating a high density of states in the conduction band in the vicinity of the vacuum level. Unfortunately, the threshold function masks the exact location of this peak, which corresponds to peak (5) in the conduction band of CuI. The location of peak (5) in CuBr has been estimated to be at about 5.9 eV; this value is justified by the fact that it is consistent not only with the experimental EDCs, but also with the optical data and the dip in the photoelectric yield.¹

From the EDCs of Fig. 129, we see that there are three peaks that tend to follow the nondirect transition law $\Delta E_p = \Delta h\nu$. The location and size of these three peaks correspond very closely to the location and size of the three peaks seen in the EDCs for CuI, indicating that the valence

¹The dip in yield is caused by the transition (1) → (5).

band of AgBr is very similar to the valence band of CuI. Just as in CuI, the photoemission from the deepest of the three valence band peaks, indicating that in CuBr the deepest peak should be associated with the copper 3d bands, and that the other two peaks should be associated with the bromine 4p bands.

The locations of the conduction band peaks in CuBr that correspond to conduction band peaks (6) and (7) in CuI are identified somewhat more clearly in Figs. 130 and 131 than in Fig. 129. The fixed peak at about 7.3 eV in Fig. 130 locates conduction band peak (6), and the fixed peak at about 8.65 eV in Fig. 131 locates conduction band peak (7).

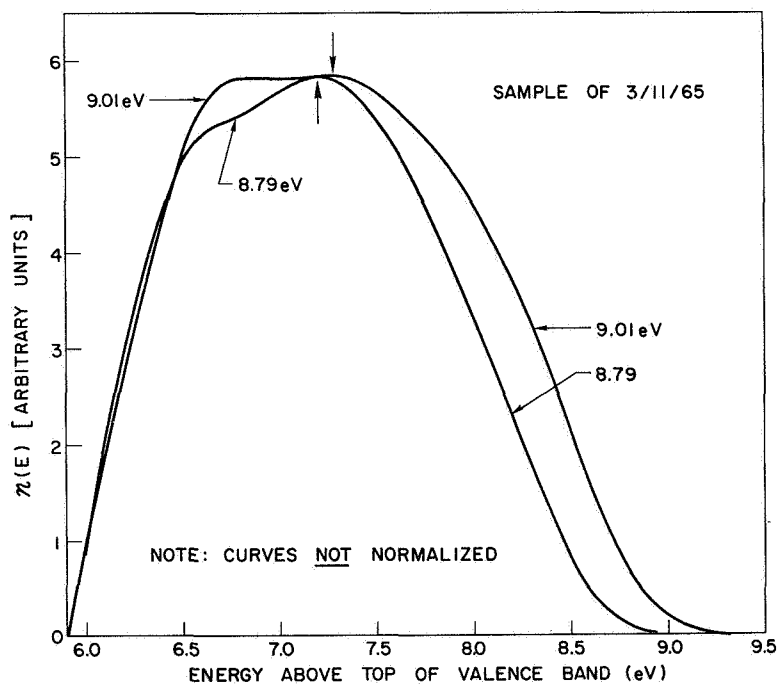


FIG. 130. ENERGY DISTRIBUTION CURVES FOR CUPROUS BROMIDE INDICATING STRUCTURE IN THE CONDUCTION BAND.

An E_p vs $h\nu$ plot for CuBr is shown in Fig. 132. In Fig. 132, the 45° line ($\Delta E_p = \Delta h\nu$) identifies the valence band peaks that obey the law of nondirect transitions, and the horizontal lines identify the location of fixed structure in the conduction band. Just as in the case of CuI, it appears that the conduction band structure modulates the transitions from valence band peak (3) more severely than the transitions

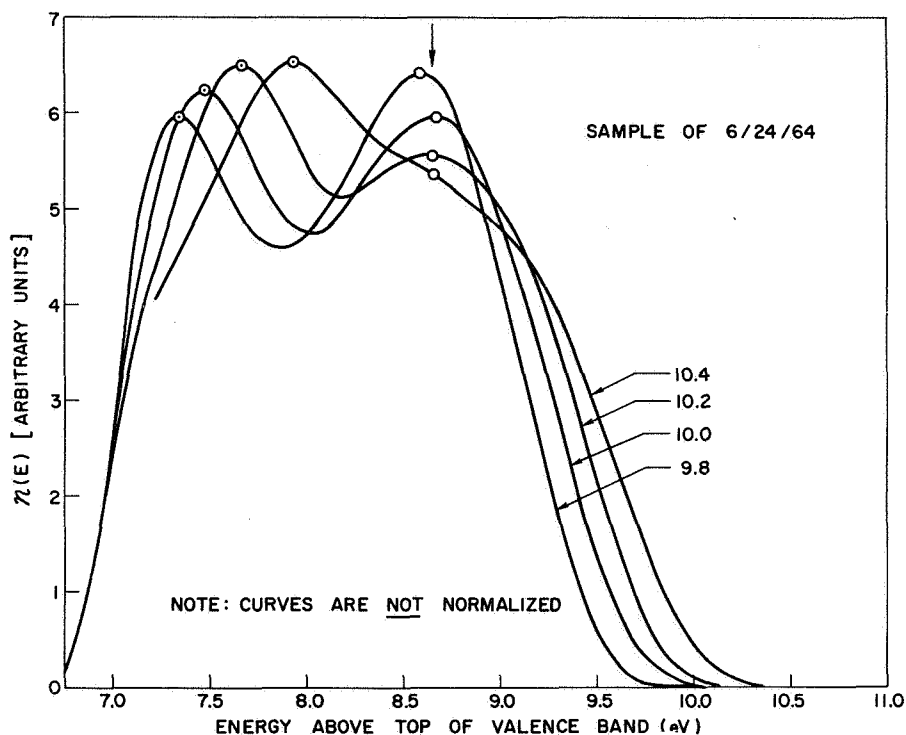


FIG. 131. ENERGY DISTRIBUTION CURVES FOR CUPROUS BROMIDE INDICATING STRUCTURE IN THE CONDUCTION BAND.

from valence band peak (2), indicating that a portion of the transitions from states near the top of the valence band are direct transitions, and not nondirect transitions. The optical density of states for CuBr that has been deduced from experimental photoemission and optical data is sketched in Fig. 133. In Fig. 133, the peaks (1), (2), (3), (6), and (7) have been located directly from the photoemission data. As discussed earlier, the location of peak (5) is strongly suggested by the experimental EDCs, and is consistent with structure in the optical data and the dip in the quantum yield. Just as in the case of CuI, the separation between the three major peaks in the optical data is the same as the separation between valence band peaks (1), (2), and (3), indicating that the three peaks in the optical data are due to transitions between the three valence band peaks and a single final state in the conduction band. The location of this final state is easily deduced from the optical data and the location of the valence band peaks, and is found to be about 4.0 eV

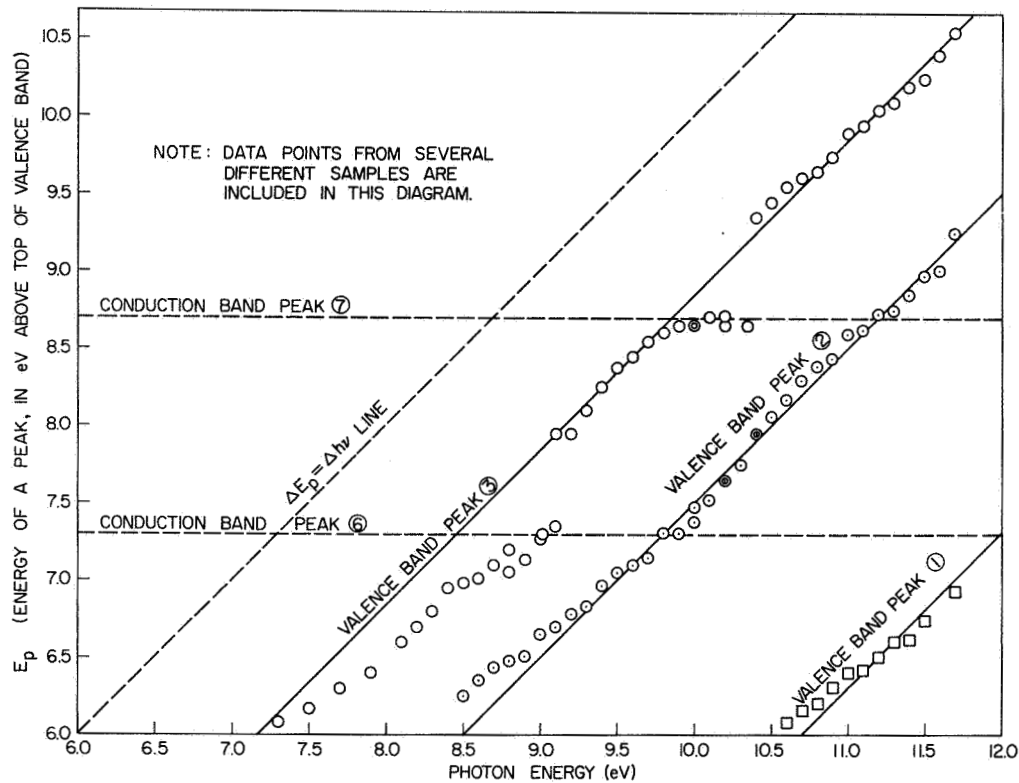


FIG. 132. ΔE_p vs $\Delta h\nu$ PLOT FOR CUPROUS BROMIDE.

above the top of the valence band. This final state is labeled state ④ in Fig. 133.

Having identified peak ① with the copper 3d band and peaks ② and ③ with the bromine 4p bands, the relative heights of peaks ①, ②, and ③ were adjusted so that the area under peak ① was 10/6 times the total area under peaks ② and ③, just as in the case of CuI. The relative peak heights in the conduction band were adjusted by analogy with the conduction band of CuI.

Note that there is a one-to-one correspondence between the structure in the optical density of states of CuBr (Fig. 133) and the structure in the optical density of states of CuI (Fig. 110). However, there are some small (but perhaps significant) differences in the locations of certain peaks. These differences will be discussed in more detail in Section E of this chapter.

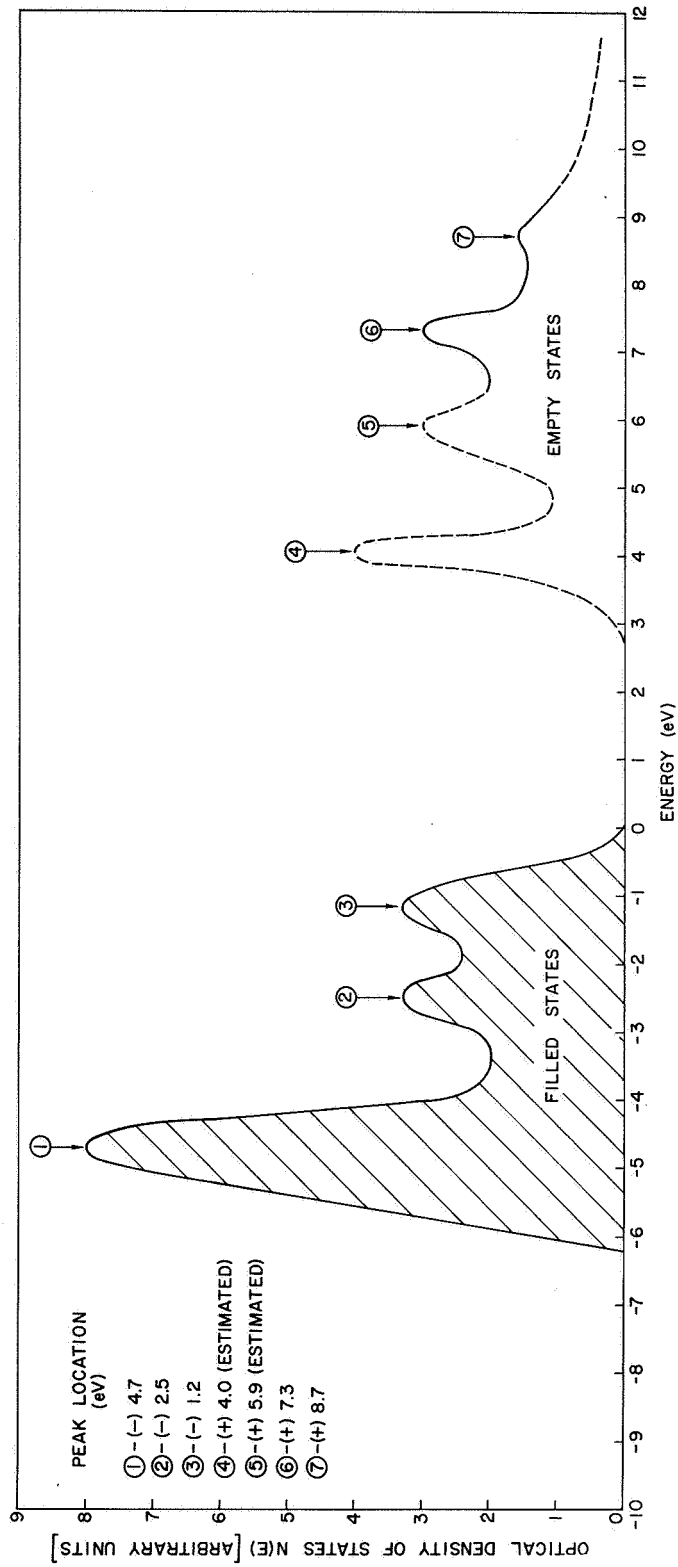


FIG. 133. ESTIMATED OPTICAL DENSITY OF STATES FOR CUPROUS BROMIDE.

Cardona's [Ref. 68] experimental data for the reflectivity and the absorption coefficient of CuBr are shown in Figs. 134 and 135; the arrows pointing downward indicate the location of experimental structure, and the arrows pointing upward correspond to the energy differences between valence band peaks and conduction band peaks in the optical density of states of Fig. 133. The three heavy arrows pointing upward indicate the energies of transitions to the final state (4), and it is seen that the energies of these heavy arrows correspond quite closely to the major structure labeled (B), (C), and (E) in Fig. 134. Except perhaps for the "predicted" peak at about 7.2 eV, there is very good correspondence between the structure in the experimental reflectivity, and the structure expected from the optical density of states of Fig. 133.

In Fig. 134, there is a rise in the experimental reflectivity at 7.2 eV, and it appears that this rise corresponds to the "predicted" peak at 7.2 eV. Much clear experimental verification of the "predicted" peak is evident in the 80°K absorption curve shown in Fig. 135, where a distinct shoulder is seen to appear in the experimental data at exactly 7.2 eV.

A more complete identification of the optical structure of CuBr will be presented in Section E of this chapter.

The optical density of states of CuBr is compared with Scop's adjusted band calculation of AgBr in Fig. 136. The adjusted band structure of AgBr shown in Fig. 136 is identical to the adjusted band structure presented earlier in Fig. 127, except that the energy gap is slightly different. Just as in the case of CuI, there is a surprising

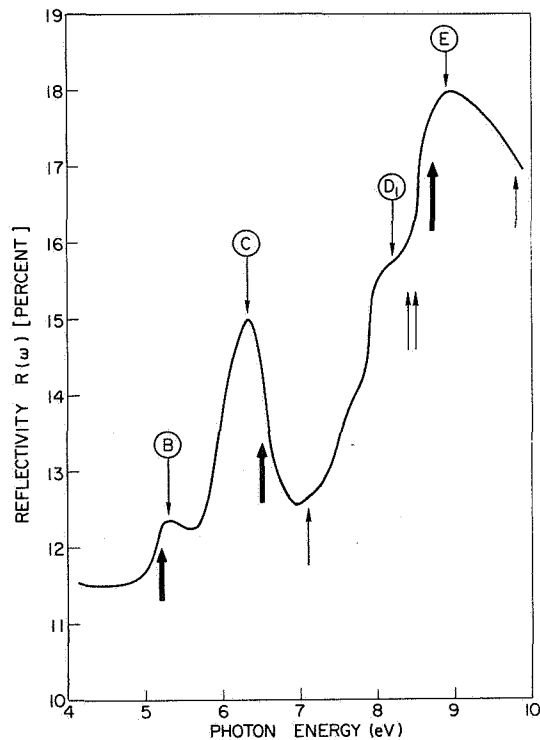


FIG. 134. REFLECTIVITY $R(\omega)$ FOR CUPROUS BROMIDE, FROM CARDONA [REF. 68].

correspondence between the peaks in the optical density of states of CuBr and the "flat" bands in the AgBr band diagram. Since the detailed corres-

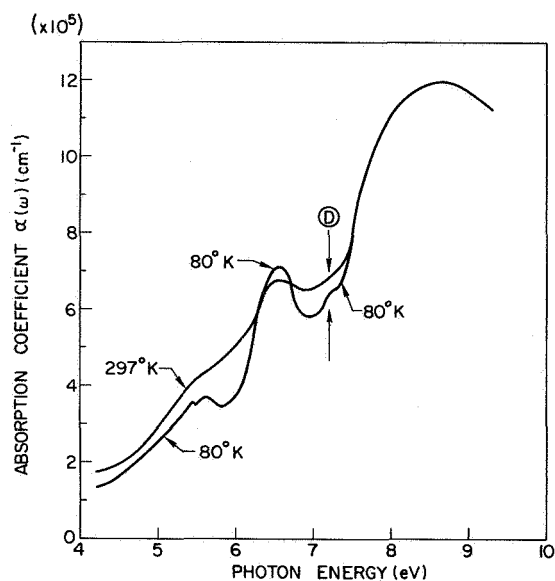


FIG. 135. ABSORPTION COEFFICIENT $\alpha(\omega)$ FOR CUPROUS BROMIDE, FROM CARDONA [REF. 68].

pondence pointed out earlier for the comparison between CuI and AgBr also applies to the comparison between CuBr and AgBr, the reader is referred to the earlier section on CuI for a detailed discussion of the relationship between the peaks in the optical density of states of CuBr and the "flat" bands in AgBr.

As discussed earlier in this chapter, the cuprous halides transform from the zinblende phase into the wurtzite phase at elevated temperatures. It was also pointed out that the phase change was difficult to study under high vacuum conditions, because the cuprous halides tend to

sublime at temperatures below the transition temperature. However, in the process of sublimating cuprous halide powders from a quartz boat onto a metal substrate, the color of the cuprous halide powder tends to change from white to yellow,¹ indicating that under high vacuum, at least a partial phase change may take place at temperatures lower than the transition temperatures listed in Table 6.

No serious attempt was made to study these phase changes during the course of this investigation,² but a few EDCs were obtained from CuBr at elevated temperatures when the effects of annealing were being studied.

¹This is especially true for CuI.

²Photoemission measurements can be readily made over the range of temperatures between 80°K and about 800°K using the photoemission chamber described in Chapter II, due to the limitations of time, nearly all of the photoemission data were taken at room temperature, and no effort was made to study photoemission as a function of temperature, even though the facility for making measurements at different temperatures was available during every photoemission experiment.

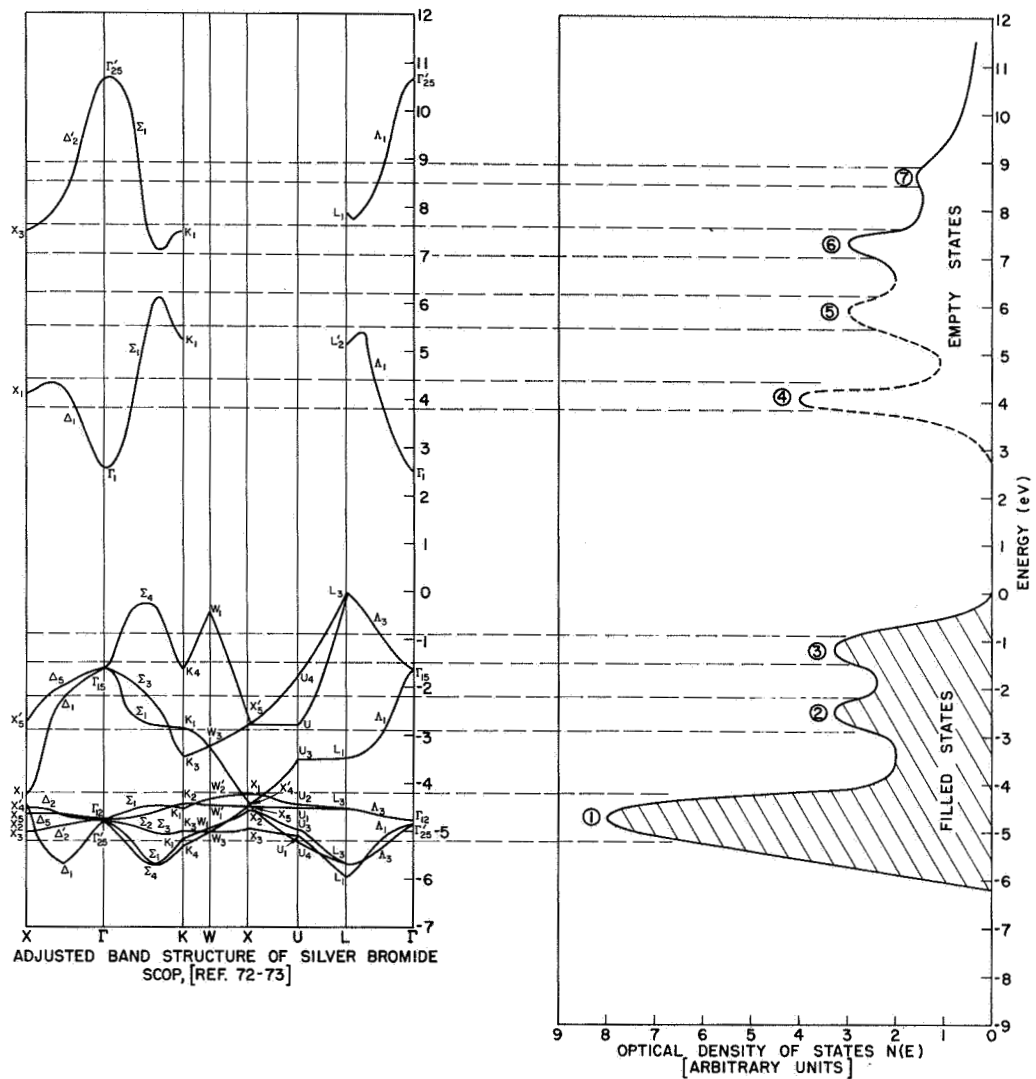


FIG. 136. COMPARISON OF OPTICAL DENSITY OF STATES FOR CUPROUS BROMIDE WITH ADJUSTED BAND STRUCTURE OF SILVER BROMIDE. Scop's calculated valence bandwidth of 4.0 eV has been linearly scaled by 50 percent to agree with the valence bandwidth of cuprous bromide.

These EDCs are shown in Figs. 137 and 138. At about 150°C, the photoemission peak originating from valence band peak (3) seems to merge with the photoemission peak originating from valence band peak (2), indicating that a phase change has taken place, and that the structure in the valence band of CuBr is sensitive to this change. This sensitivity to phase change implies that the detailed structure in the valence band of CuBr is quite sensitive to the nature of the crystal symmetry.

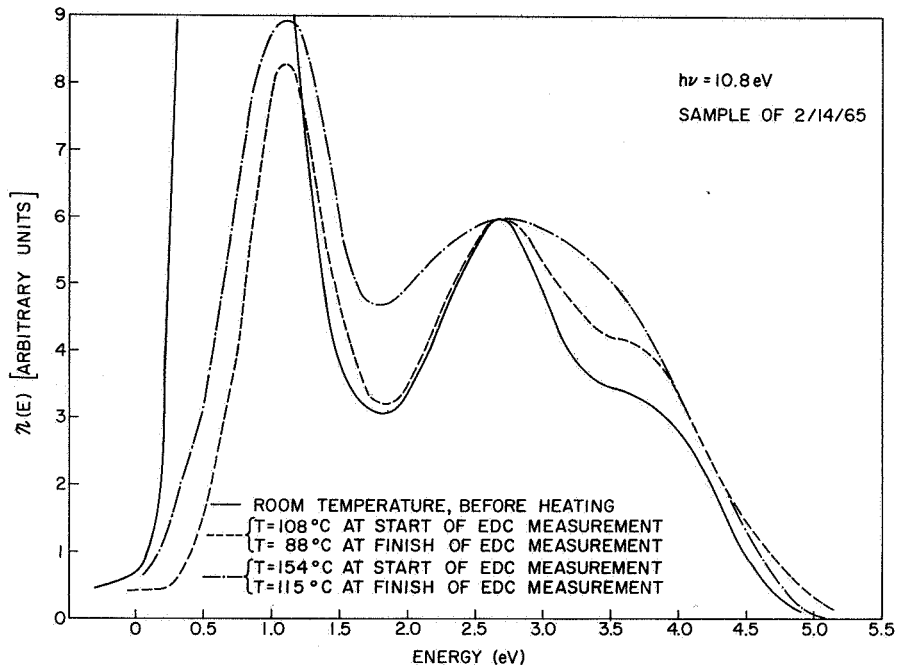


FIG. 137. EFFECT OF TEMPERATURE ON ENERGY DISTRIBUTION CURVES FROM CUPROUS BROMIDE. The curves are not normalized, but are fitted at 2.7 eV.

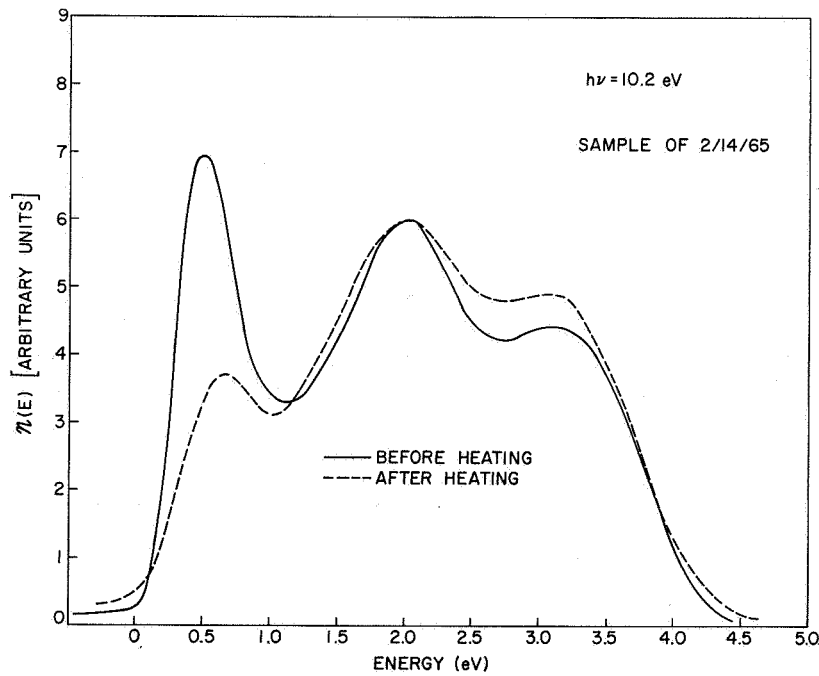


FIG. 138. ENERGY DISTRIBUTION CURVES FOR CUPROUS BROMIDE BEFORE AND AFTER HEATING. The curves are not normalized, but are fitted at 2.0 eV.

Although providing only very incomplete data, the EDCs of Figs. 137 and 138 indicate that phase changes in the cuprous halides can be studied by photoemission techniques, and that the photoemission data are sensitive to these changes. Consequently, it appears that photoemission studies can be a useful probe for obtaining information about the differences in the energy level structure of the zincblende and wurtzite phases of the cuprous halides. Such information might be very valuable to theorists doing future energy band calculations of the cuprous halides.

D. PHOTOEMISSION STUDIES OF CUPROUS CHLORIDE

Good EDCs have been obtained for CuCl, but there is some uncertainty in the quantum yield corresponding to these EDCs, because of the lack of an accurate calibration standard at the time the data were taken. What are probably the most reliable relative yield data taken for CuCl are shown in Fig. 139, where it is seen that the yield curve has the same characteristic features as the yield curves for CuI and CuBr. The characteristic dip at about 10 eV is due to transitions from the copper d band to states below the vacuum level, and the characteristic rise at about 11 eV is due to the onset of photoemission from the copper d band.

Because there is considerable uncertainty in the overall yield curve, the EDCs corresponding to the yield of Fig. 139 have been normalized to the relative yield only over small intervals in photon energy, just as was done for CuBr. These EDCs for CuCl are shown in Figs. 140a through 140h; in each of these, the relative magnitudes of the EDCs are significant.

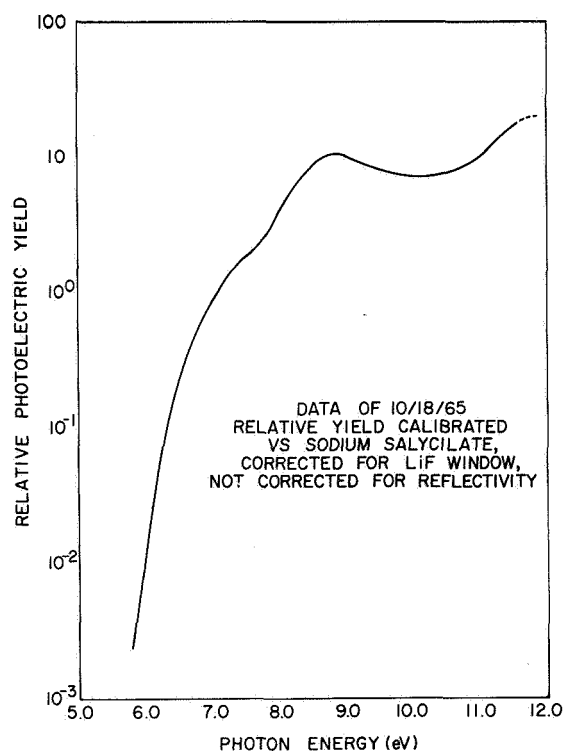
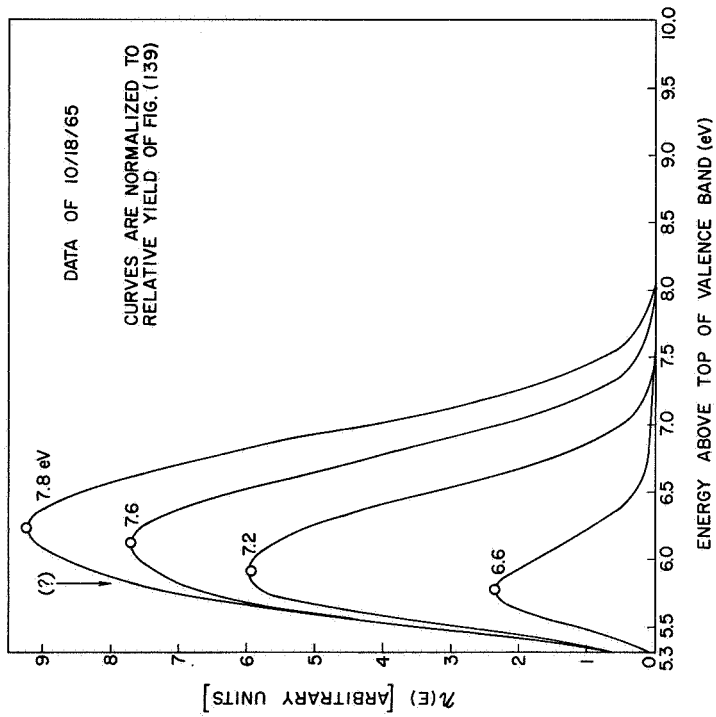
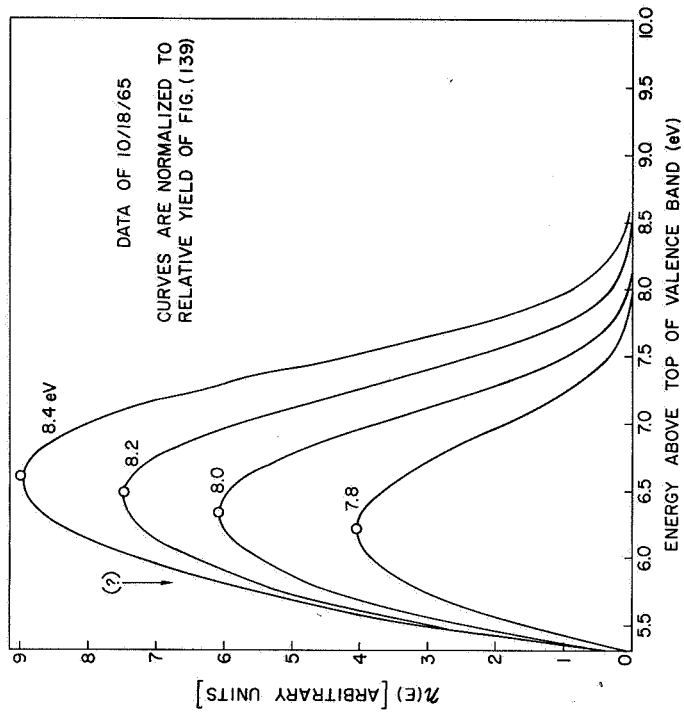


FIG. 139. RELATIVE PHOTOELECTRIC YIELD FOR CUPROUS CHLORIDE.

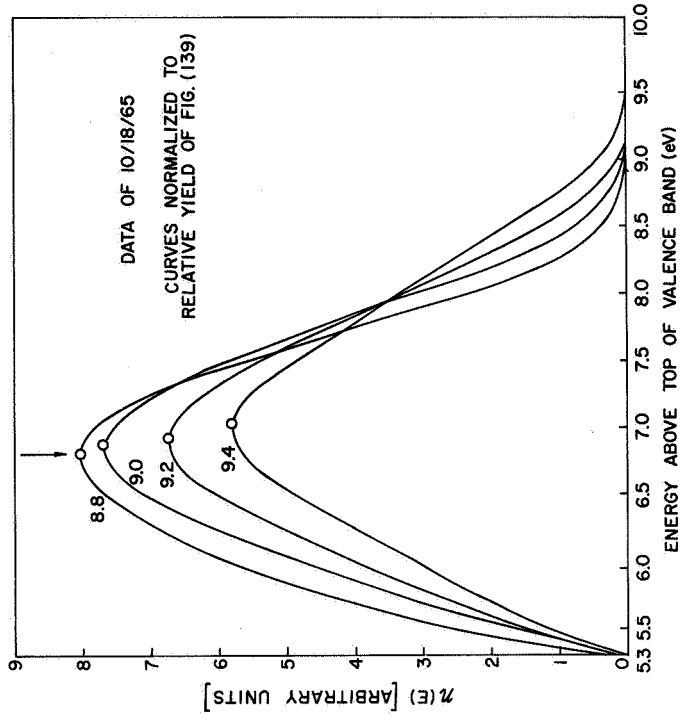


(a)

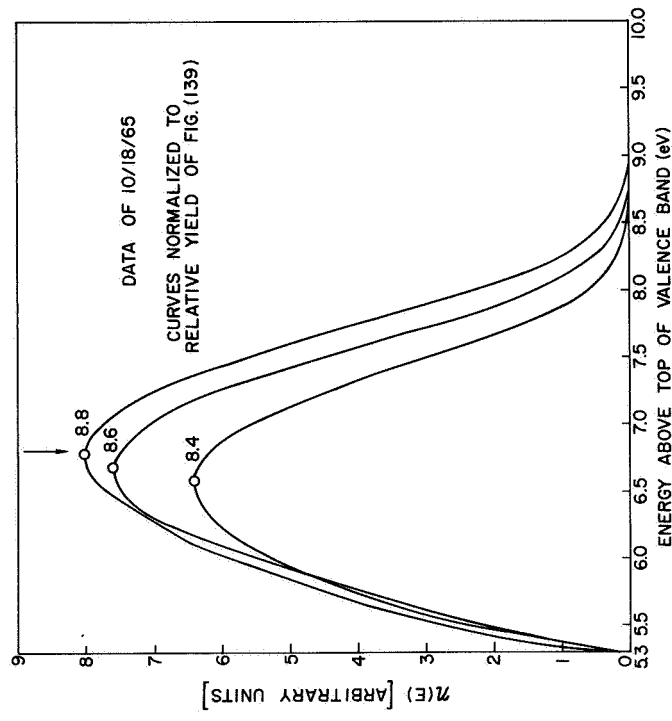


(b)

FIG. 140. EXPERIMENTAL ENERGY DISTRIBUTION CURVES FOR CUPROUS CHLORIDE.

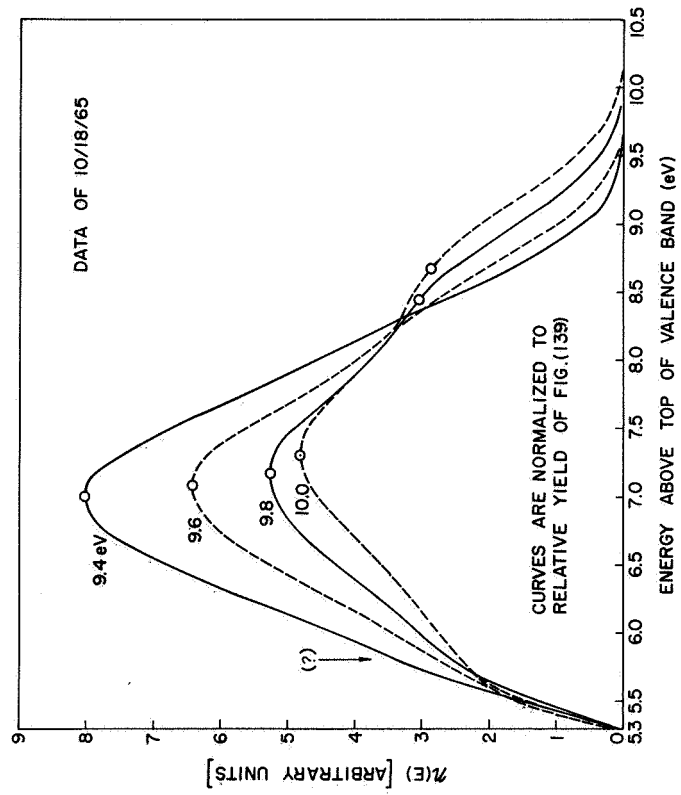


(c)

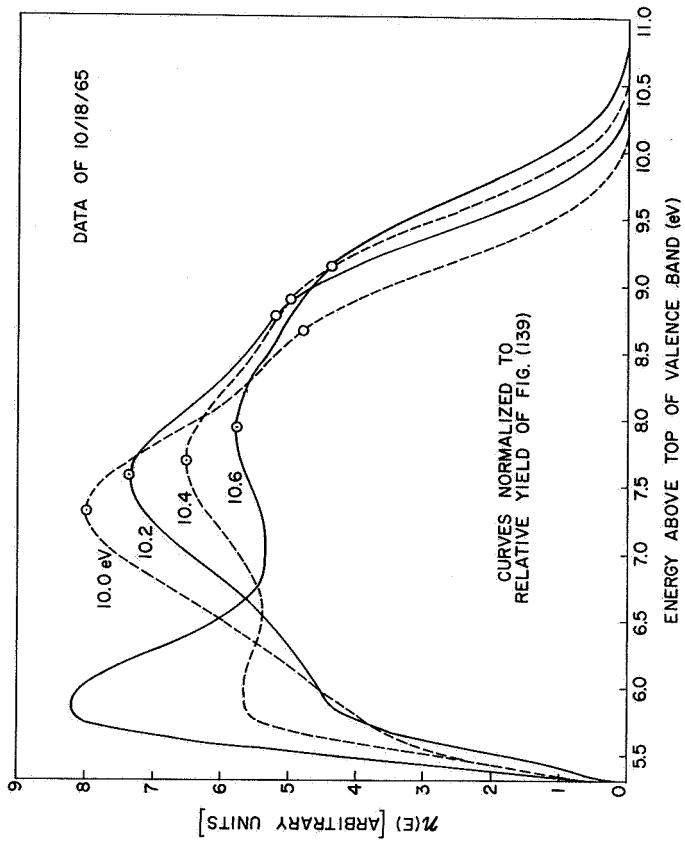


(d)

FIG. 140. CONTINUED.

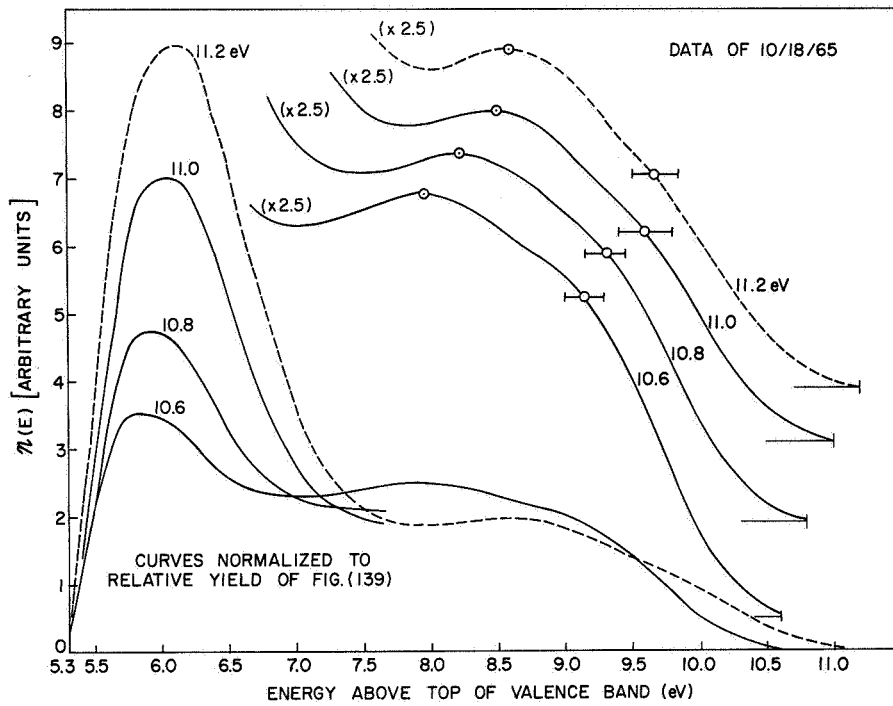


(e)

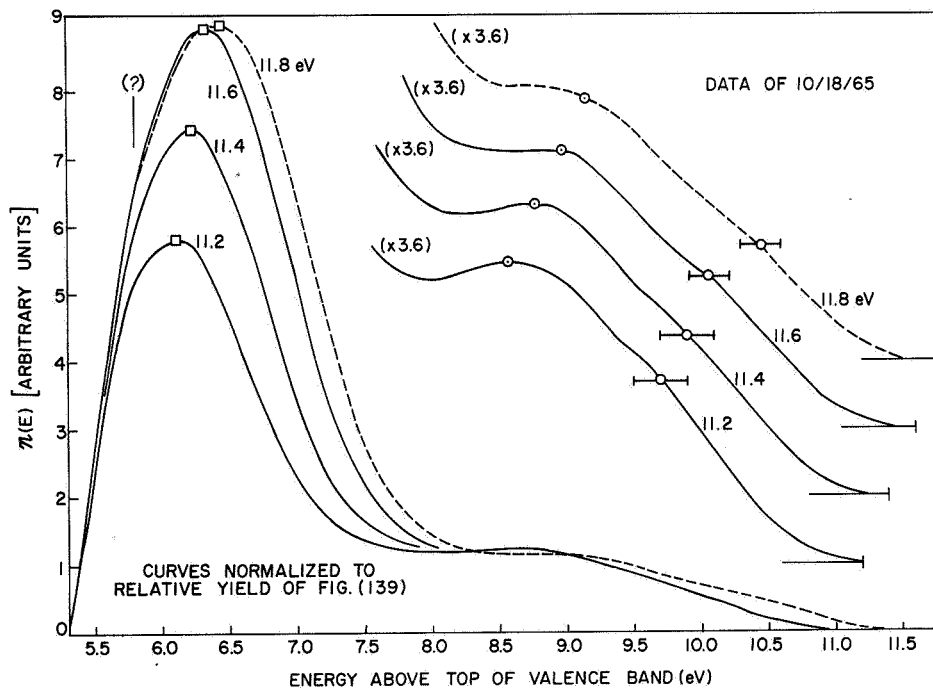


(f)

FIG. 140. CONTINUED.



(g)



(h)

FIG. 140. CONTINUED.

As seen from the EDCs of Fig. 140 and the E_p vs $h\nu$ plot in Fig. 141, the valence band of CuCl is quite similar to the valence bands of CuI and CuBr, except that the structure is not as "sharp." The 45° lines in Fig. 141 indicate that there are three peaks in the valence band of CuCl, all of which tend to follow the law of nondirect transitions, where $\Delta E_p = \Delta h\nu$. Just as in CuI and CuBr, photoemission from the deepest valence band peak is stronger than photoemission from the other two valence band peaks; thus, the deepest lying valence band peak has been identified with the copper d band, and the other two peaks have been identified with the halogen p bands.

Figure 140 and the E_p vs $h\nu$ plot of Fig. 141 show that valence band peak ③ is not clearly identified in the photoemission data until the peak is about 3 eV above the vacuum level (5.3 eV). Also, in the range of photon energies between 7.5 and about 9.8 eV, the E_p vs $h\nu$ plot identifies only one peak, which does not follow the law $\Delta E_p = \Delta h\nu$.

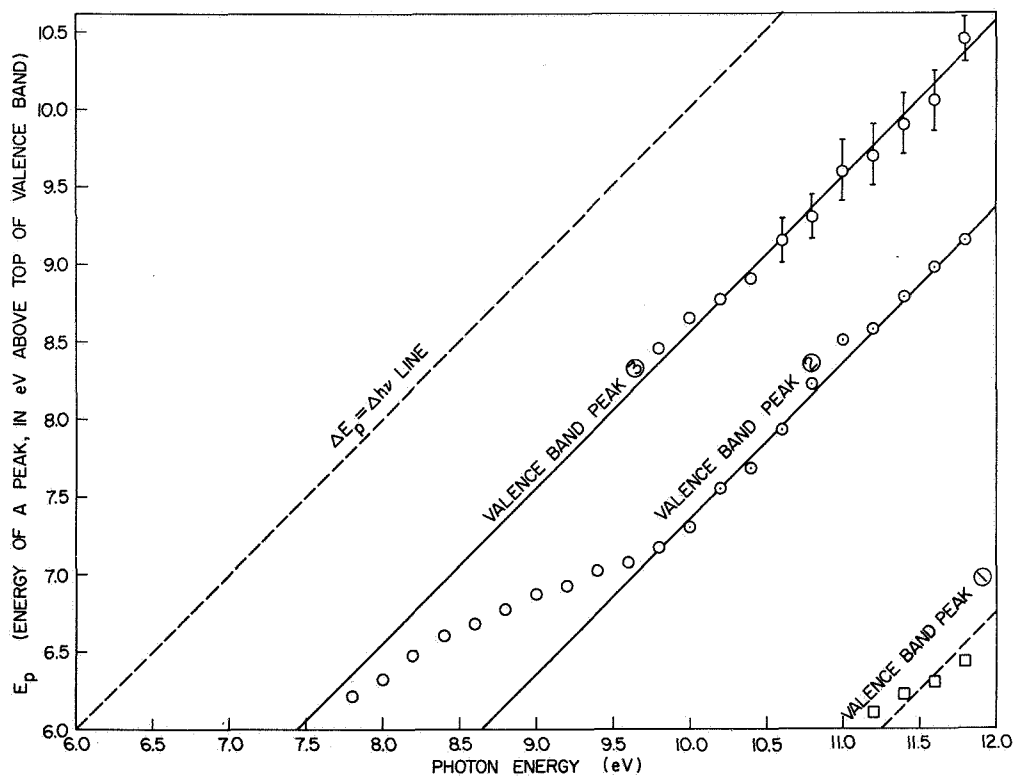


FIG. 141. ΔE_p vs $\Delta h\nu$ PLOT FOR CUPROUS CHLORIDE.

Interpreted in terms of nondirect transitions,¹ this experimental evidence suggests the existence of a broad "peak" in the conduction band density of states between 5.5 and 7.5 eV above the top of the valence band. The shapes of the EDCs of Fig. 140 near the vacuum level suggest (although rather vaguely) structure in the conduction band at about 5.8 eV. In addition, the rise and fall of the height of the EDCs of Figs. 140c and 140d indicate additional conduction band structure at about 6.8 eV. By analogy with CuI and CuBr, the tentative structure at 5.8 eV has been labeled "peak" (5), and the tentative structure at 6.8 eV has been labeled "peak" (6).

The optical density of states deduced from the photoemission and optical data of CuCl is shown in Fig. 142. In the valence band, peaks (1), (2), and (3) have been located by the experimental photoemission data, and the relative heights have been adjusted by association of peak (1) with the copper 3d band (containing 10 electrons), and by association of peaks (2) and (3) with the chlorine 3p bands (containing 6 electrons). The broad peak in the conduction band with labels (5) and (6) on the "corners" has been sketched in accordance with the previous discussion of the experimental photoemission data.

The location of peak (4) in the conduction band of CuCl has been estimated by relating structure in the optical density of states of Fig. 142 to structure in the reflectivity and absorption spectra shown in Figs. 143 and 144.

As seen from a comparison of Figs. 143 and 144 with the valence band of Fig. 142, the energy separations of the major peaks in the optical spectrum of CuCl do not correspond to the energy separation between the peaks in the valence band, as was the case for CuI and CuBr. However, the "broadness" of the peaks in the optical density of states of CuCl provides a "natural" explanation for this apparent discrepancy, as can be seen from the following explanations.

¹An alternative explanation might be direct transitions, or matrix element variation between initial states in the vicinity of valence band peak (3) and final states in the region between 5.5 and 7.5 eV above the top of the valence band. From the available data, it is difficult to distinguish between the several possible types of transitions. Whatever the cause, there is evidence of broad structure in the conduction band between 5.5 and 7.5 eV.

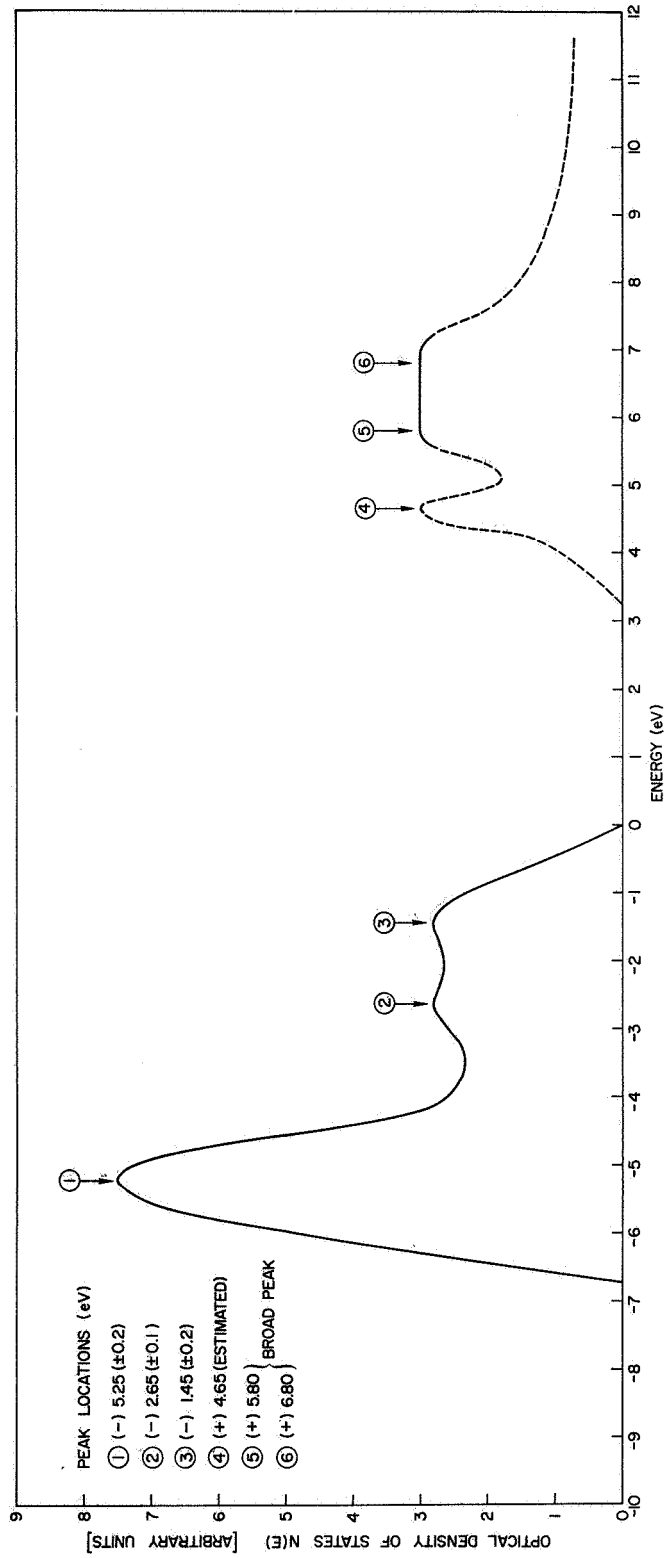


FIG. 142. ESTIMATED OPTICAL DENSITY OF STATES FOR CUPROUS CHLORIDE.

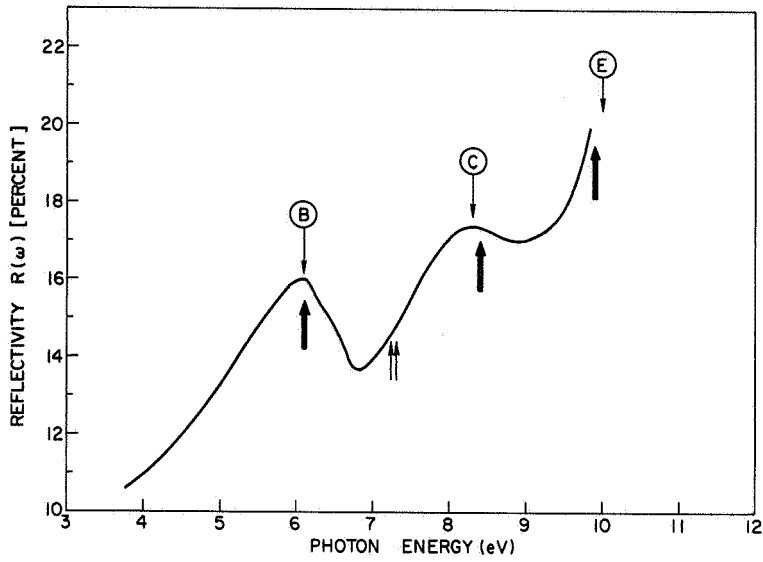


FIG. 143. REFLECTIVITY FOR CUPROUS CHLORIDE [Ref. 68].

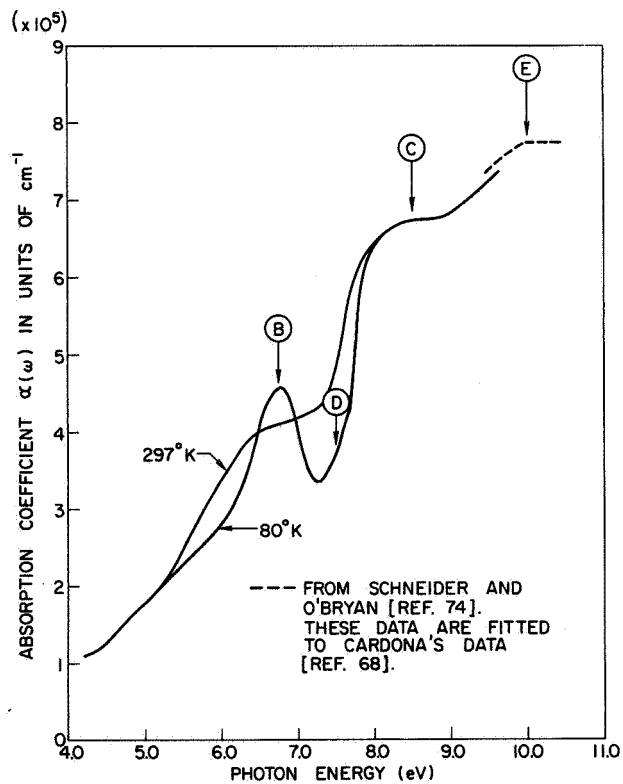


FIG. 144. ABSORPTION COEFFICIENT $\alpha(\omega)$ FOR CUPROUS CHLORIDE [REF. 68].

The difference in energy between the peaks labeled (B) and (E) in the experimental reflectivity is about 3.9 eV, and the energy difference between peaks (1) and (3) in the optical density of states is about 3.8 eV. Thus (neglecting for the moment valence band peak (2)), let us assume that reflectivity peaks (B) and (E) are due to transitions from valence band peaks (1) and (3) to the same final state in the conduction band; this locates conduction band peak (4) at about 4.65 eV above the top of the valence band, as shown in the optical density of states of Fig. 142.

Let us now compare the structure in the reflectivity spectrum of Fig. 143 with the structure that would be predicted from the energy differences between the valence band peaks and conduction band peaks in the optical density of states of Fig. 142. The arrows pointing upward in Fig. 143 indicate the locations of structure predicted from the optical density of states of Fig. 142. The heavy arrows locate expected strong structure. The arrows pointing downward in Figs. 143 and 144 locate structure in the experimental optical data. As shown in Fig. 143, the "predicted" peaks at 6.1 and 9.9 eV agree quite closely with the experimental reflectivity, thereby verifying the arbitrary location of peak (4) in the conduction band optical density of states. In addition, there is a predicted strong peak at 8.4 eV, corresponding very closely to the broad peak in the experimental reflectivity at 8.3 eV. This predicted peak at 8.4 eV is due to the strong coupling expected between the "center of gravity" of the broad valence band structure between peaks (2) and (3), and the "center of gravity" of the band structure between conduction band peaks (5) and (6). Thus, the existence of a broad conduction band structure in CuCl seems to explain in a very "natural" way the broad reflection peak labeled (C) in Fig. 143. Because of the relative strengths involved, this "center of gravity" coupling would be expected to be much stronger than the (2) → (4) transition, which is the transition that accounts for peak (C) in the reflectivity of CuI and CuBr.

The two weak peaks predicted at about 7.3 eV in Fig. 143 are due to the transitions (2) → (4) and (3) → (5), and seem to correspond to a rise in the experimental reflectivity; however, a rise in the experimental reflectivity is not sufficiently strong experimental evidence to conclude that the predicted transitions are in agreement with experiment.

Fortunately, Cardona [Ref. 68] has measured the absorption coefficient of CuCl at 80°K, and a distinct shoulder appears in these data at about 7.5 eV, as shown in Fig. 144. This shoulder corresponds quite closely to the predicted transition at about 7.3 eV. Thus, we see that the optical density of states of Fig. 142 does indeed account quite well for the experimental optical data of CuCl. The energies of the optical structures of CuCl and the identifications of this structure are tabulated in Section E of this chapter.

The optical density of states of CuCl is compared with Scop's [Refs. 72 and 73] theoretical energy band calculation of AgCl in Fig. 145. Scop's calculated valence bandwidth for AgCl is about 3.8 eV, and the optical density of states valence bandwidth for CuCl is about 6.5 eV. Thus, Scop's valence band for AgCl has been linearly stretched by about 70 percent in order to agree with the bandwidth of CuCl; the resulting "adjusted" valence band is shown in Fig. 145. Scop's conduction band for AgCl has not been altered, except for a bodily shift resulting in a change in the energy gap.

As seen from Fig. 145, there is a surprising correspondence between the peaks in the optical density of states of CuCl and "flat" bands in the adjusted band structure of AgCl. The most significant correspondence is that the "flat" bands derived largely from the silver 4d wavefunction correspond closely to peak (1), which has been associated with the copper d bands. In addition, the broad structure between peaks (2) and (3) correspond to the CuCl bands between the top of the valence band and 3 eV below the top of the valence band; since the theoretical bands in this region are largely derived from the chlorine 3p wavefunctions,¹ this correspondence tends to support the hypothesis that peaks (2) and (3) in the optical density of states are to be associated with the chlorine 3p bands.

In the conduction band, peak (4) seems to correspond to the X_1 point, peak (5) seems to correspond to the top of the lower conduction band, and peak (6) seems to correspond to the bottom of the lower conduction band.² A point of interest is that the X_1 point in the band

¹With considerable p-d mixing, as pointed out by Scop.

²It should be noted that Scop did not calculate the bands along the zone faces.

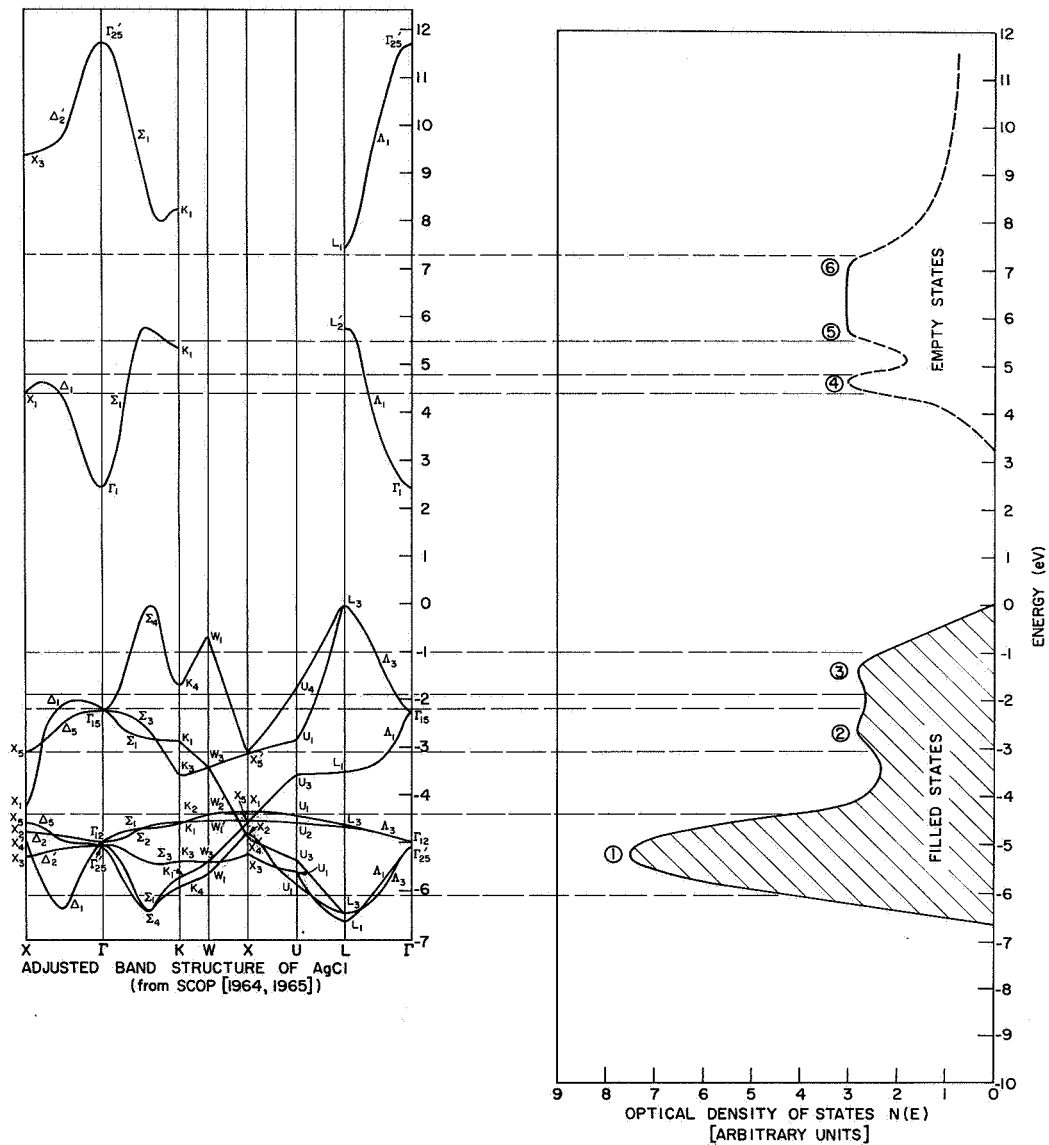


FIG. 145. COMPARISON OF OPTICAL DENSITY OF STATES FOR CUPROUS CHLORIDE WITH ADJUSTED BAND STRUCTURE OF SILVER CHLORIDE. (Scop's calculated valence bandwidth of 3.8 eV has been stretched linearly by about 70 percent to agree with the experimental bandwidth of CuCl.

calculation of AgCl is further from the bottom of the conduction band than in the band calculation of AgBr. As can be seen from the optical densities of states for CuCl, CuBr, and CuI, this trend in the location of the X_1 point corresponds to an apparent trend in the location of peak (4) in the optical density of states of the cuprous halides.

E. A COMPARISON OF CuCl, CuBr, AND CuI

As seen from the discussions of experimental data in this chapter, the location of structure in the optical density of states is very much the same for CuCl, CuBr, and CuI. For the convenience of the reader, the location of this structure is tabulated in Table 10. All of the peaks in Table 10 except peak (4) have been deduced directly from photoemission data; for all three cuprous halides, the location of peak (4) was chosen to obtain agreement with the optical data.

We have seen that the rather complex structure in the optical spectrum away from the band edge can be accounted for rather well in terms of the optical density of states. Table 11 lists the energies of structure in the optical data and the identification of this structure in terms of initial and final states in the optical density of states. The reader will note that in addition to accounting for all of the experimental structure that has been measured to date, Table 11 predicts structure in the cuprous halides at photon energies where experimental data has not yet been taken.

As discussed earlier in this chapter, Cardona [Ref. 68] has associated the major structure in the cuprous halides with direct transitions between symmetry points in a germanium-like lattice. Because of the importance of the copper d band in the optical spectra of the cuprous halides and because of the success of the nondirect model in accounting for both the photoemission and the optical data, Cardona's assignments must be considered to be quite erroneous.

In addition, the appearance of the copper d band in the photoemission and the optical data indicates that for the zincblende cuprous halides, the atomic nature of the constituent atoms is of primary importance, and that the crystal structure is of secondary importance. The above statement is in direct contradiction to J. C. Phillips [Ref. 28] who stated that

TABLE 10. LOCATION OF STRUCTURE IN THE ENERGY BANDS OF THE CUPROUS HALIDES¹

	Peak Number	CuCl	CuBr	CuI
Valence Band	①	(-)5.25 ±0.2	(-)4.7	(-)4.35
	②	(-)2.65	(-)2.5	(-)2.9
	③	(-)1.45 ±0.2	(-)1.2	(-)1.65
Conduction Band	④	(+)4.65 (Estimated)	(+)4.0 (Estimated)	(+)3.2 (Estimated)
	⑤	+5.8	} Broad Peak (+)5.9 (Estimated)	+0.1 (+)6.1 -0.3
	⑥	+6.8		(+)7.3
	⑦	-	(+)8.7	+0.1 (+)9.7 -0.3

¹All values are in electron volts, and all uncertainties are estimated to be ±0.1 eV, except where noted. The notation identifying the peaks is the same as that used in Figs. 110, 133, and 142. The zero of energy is at the top of the valence band.

"...A wide range of experimental data now indicates that uv structure depends primarily upon crystal structure and only secondarily on atomic composition... ." Because of the appearance of the copper d band in the experimental photoemission data, it must be concluded that Phillips' statement is erroneous, at least when applied to materials such as the cuprous halides.

The location of structure in the cuprous halides is pictured diagrammatically in Fig. 146 for the purpose of detecting any trends that might exist due to differences in the halogen atoms. Since the location of the first exciton peak is about 3 eV for all three cuprous halides, the direct gap has been estimated to be about 3 eV for all three cuprous halides. The absorption edge in Fig. 146 has been estimated from the

absorption data of Cardona [Ref. 68] and Coehlo [Ref. 69]. However, no good band edge data has yet been made on the cuprous halides, and the existence of an indirect gap is a distinct possibility.

As seen from Fig. 146, there are no strong systematic trends in the location of peaks (2), (3), (5), and (6). However, systematic trends are apparent for peaks (1) and (4).

- (1) The Cu d band peak labeled (1) is deepest in the valence band for CuCl, and shallowest for CuI.
- (2) Peak (4) is closest to the bottom of the conduction band in CuI, and furthest from the bottom of the conduction band in CuCl. This trend corresponds to the trend in the location of the X_1 point in Scop's band calculations of the silver halides, as can be seen in Figs. 136 and 145.

One of the most important results deduced from the photoemission data presented in this chapter is the identification of the copper 3d band. In the photoelectric EDCs from all three cuprous halides, the strength of the photoemission peaks due to transitions from valence band peak (1) is much stronger than the photoemission peaks due to transitions from valence band peaks (2) and (3); because of the relative difference in strength, valence band peak (1) has been associated with the copper 3d band, and valence band peaks (2) and (3) have been associated with the halogen p bands. Comparison of the cuprous halide optical densities of states with Scop's theoretical energy band calculations for AgBr and AgCl tends to confirm these peak associations, as seen in Figs. 136 and 145. However, Scop has pointed out that there is considerable p-d mixing in the silver halide valence bands; as discussed earlier in this chapter, it is also likely that there is strong p-d mixing in the valence bands of the cuprous halides. In accordance with the discussion above, we might suggest the following wavefunction identifications in the cuprous halides:

- (1) Energy bands in the vicinity of valence band peak (1) are derived largely from the copper d wavefunctions.

TABLE 11. EXPERIMENTAL OPTICAL DATA AND IDENTIFICATION OF STRUCTURE FOR THE CUPROUS HALIDES¹

Structure in Optical Data		CuCl	CuBr	CuI
Energy of first exciton peak		3.24	2.98	3.05
Absorption edge (estimated)		3.15	2.8	2.9
Ⓐ	Experimental	-	-	3.7 ($\omega\sigma$)
	Calculated	-	-	-
	Initial state	-	-	-
	Final state	-	-	-
Ⓑ Major Peak	Experimental	6.1 (R)	5.6 (R)	4.8 ($\omega\sigma$)
	Calculated	6.1 (d)	5.4 (d)	4.8 ($\omega\sigma$)
	Initial state	③	③	③
	Final state	④	④	④
Ⓒ Major Peak	Experimental	8.3 (R)	6.65 (R)	5.9 ($\omega\sigma$)
	Calculated	8.35 (d) 8.45 (d)	7.0 (d)	5.8 ($\omega\sigma$)
	Initial state	② ③	②	②
	Final state	⑤ ⑥	④	④
Ⓓ	Experimental	7.5 (α) (shoulder)	7.2 (α) (shoulder)	7.1 (ϵ_2) (shoulder)
	Calculated	7.3 (d) 7.35 (d)	7.2 (d)	7.6 (ϵ_2) (peak)
	Initial state	② ③	③	③
	Final state	④ ⑤	⑤	⑤
Ⓓ ₁	Experimental	-	8.2 (R) (shoulder)	8.7 ($\omega\sigma$) (shoulder)
	Calculated	-	8.4 (d) 8.5 (d)	9.0 ($\omega\sigma$) (peak) 9.0 (d) (weak)
	Initial state	-	② ③	② ③
	Final state	-	⑤ ⑥	⑤ ⑥

TABLE 11. CONTINUED.

Structure in Optical Data		CuCl	CuBr	CuI
Ⓔ Major Peak	Experimental	10.0 (α)	8.9 (R)	7.7 ($\omega\sigma$)
	Calculated	9.9 (d)	8.7 (d)	7.7 ($\omega\sigma$)
	Initial state	①	①	①
	Final state	④	④	④
Ⓕ	Experimental	Not Observed	9.5 to 10.0 (vague shoulder)	-
	Calculated	9.45 (d) (weak)	9.8 (d)	-
	Initial state	②	②	-
	Final state	⑥	⑥	-
Ⓖ	Experimental	No data	No data	10.8 ($\omega\sigma$) (Broad peak)
	Calculated	11.0 (d)	10.6 (d)	10.5 ($\omega\sigma$) 10.5 ($\omega\sigma$)
	Initial state	①	①	① ②
	Final state	⑤	⑤	⑤ ⑥
Ⓕ	Experimental	No data	No data	*
	Calculated	12.0 (d)	12.0 (d)	11.75 (d)
	Initial state	①	①	①
	Final state	⑥	⑥	⑥

¹The experimental data are taken from Cardona [Ref. 68], Coehlo [Ref. 69], and the present work. The energies of the initial and the final states involved in the optical transitions are given in Table 10. The notation (Ⓐ, Ⓑ, Ⓒ, etc.) identifying the experimental structure is the same as that used in Figs. 114, 115, 116, 134, 135, 143, and 144. Transitions to the minor peak ⑦ are not included in this table. The notation identifying the type of optical data is as follows:

R = from reflectivity
 $\omega\sigma$ = from $\omega\sigma(\omega)$
 ϵ_2 = from $\epsilon_2(\omega)$
 α = from absorption coefficient
d = energy difference between structure in the valence band and structure in the conduction band.

*There is evidence of a small peak in the experimental reflectivity data at 11.75 eV. However, not enough data points were taken in this region to definitively say that the peak was experimentally observed.

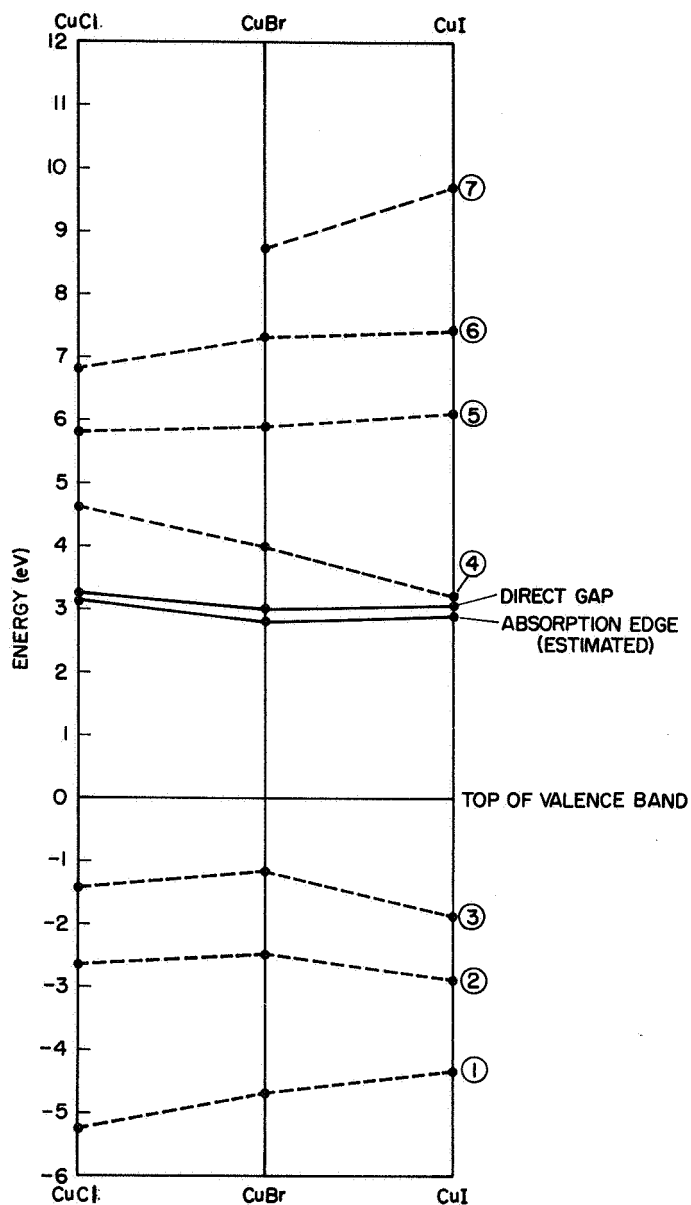


FIG. 146. LOCATION OF STRUCTURE IN THE ENERGY BANDS OF THE CUPROUS HALIDES. The labels ①, ②, ③, ④, ⑤, ⑥, and ⑦ denote structure that has been deduced from the present work. The direct gap has been taken to be equal to the energy of the first exciton peak (see also Tables 10 and 11).

- (2) Energy bands in the vicinity of valence band peak ② are derived largely from the halogen p wavefunction, but with considerable p-d mixing.
- (3) Energy bands in the vicinity of valence band peak ③ are derived largely from the halogen p wavefunctions, but with a small amount of p-d mixing.

As discussed earlier in this chapter, Cardona [Ref. 68] found a close correspondence between the experimental exciton splittings and the one-electron spin orbit splittings of the halogen atom. However, the observed splittings were somewhat smaller than the halogen splittings, and Cardona attributed this effect to strong p-d mixing. Because of the correspondence between the observed splittings and the halogen splittings, Cardona associated the top of the valence band with the halogen p levels. This conclusion is consistent with the findings of the photoemission studies presented in this chapter.

As seen in Fig. 147 and in Table 10, the experimental splitting between peaks ② and ③ in the optical density of states is roughly 1.0 eV for all three cuprous halides, indicating that the overall width of the halogen p bands is not due primarily to the spin-orbit splitting.¹ However, there does exist a trend in the manner in which peaks ② and ③ appear in the EDCs, as seen in Fig. 147: Peaks ② and ③ are "sharpest" in CuI, and "least sharp" in CuCl. Multiplying the spin-orbit splittings of Table 9 by 3/2 to obtain the splittings expected in a zincblende lattice,² we obtain spin-orbit splittings of 1.4 eV for CuI, 0.68 for CuBr, and 0.17 for CuCl. Note that there is a close correspondence between these spin-orbit splittings and the "sharpness" of peaks ② and ③ in the experimental EDCs of Fig. 147. A possible explanation for the relative "sharpness" of peaks 2 and 3 might be as follows:

¹All of the discussion in this chapter has tacitly assumed that one electron absorbs all the energy of a single photon, and that no energy is given to the lattice. However, there is a distinct possibility that some energy does to to the lattice in ionic materials.

²See Cardona [Ref. 68].

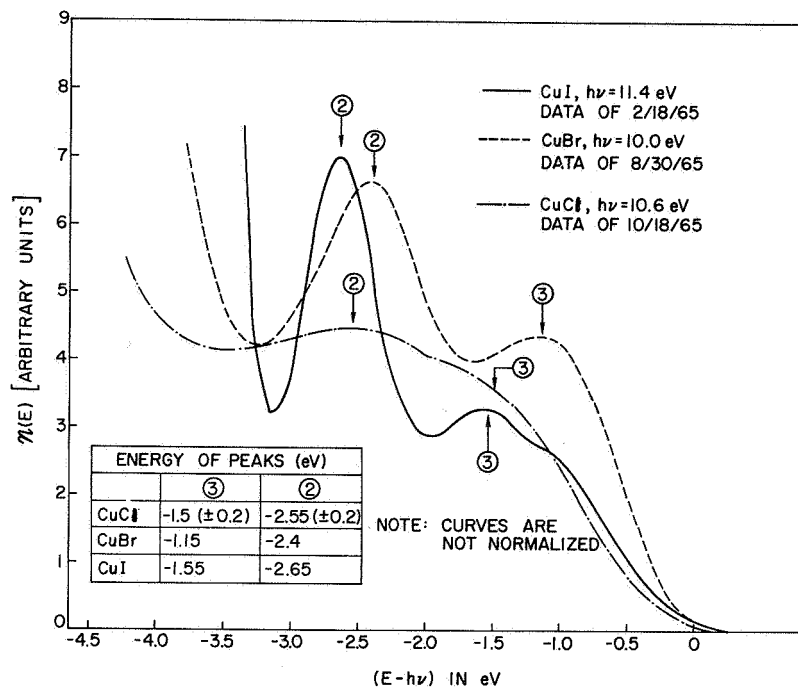


FIG. 147. COMPARISON OF EXPERIMENTAL ENERGY DISTRIBUTION CURVES FOR CUPROUS CHLORIDE, CUPROUS BROMIDE, AND CUPROUS IODIDE.

- (1) The 1.4 eV spin-orbit splitting of I significantly reinforces the "sharpness" of the "natural" 1.2 eV splitting of the valence band structure in CuI;
- (2) The 0.68 eV splitting of Br reinforces the "natural" 1.3 eV splitting in CuBr, but to a lesser extent than in CuI;
- (3) The 0.17 eV splitting in CuCl has little effect upon the "natural" 1.2 eV splitting in CuCl, which has broad structure.

As seen from the E_p vs $h\nu$ plots for CuCl and CuBr and from the success of the quantitative non-direct transition analysis done in CuI, the model of non-direct transitions seems to explain the bulk of the optical and photoemission data for the cuprous halides. However, as pointed out earlier in this chapter, certain features of the experimental photoemission and optical data do not follow the model of non-direct transitions, indicating the distinct possibility of matrix element variation and/or direct transitions in the cuprous halides.

As seen in the E_p vs $H\nu$ plots for CuCl, CuBr, and CuI, the transitions from valence band peak 2 tend to follow the model of non-direct transitions much more closely than the transitions from valence band peak ③. Since peak ③ is probably made up of mostly p-like wavefunctions, and since peak ② probably has considerably more p-d mixing than peak ③, one might deduce that the "direct"¹ transitions from bands in the vicinity of peak ③ are transitions from p-like wavefunctions, and that the more non-direct nature of the bands constituting peak ② is due to the greater p-d mixing. This association of p-like wavefunctions with "direct" transitions and d-like wavefunctions with non-direct transitions is consistent with the similar associations made with the wavefunctions of Cu, Ag, and Au, as discussed earlier in Chapters IV, V, and VI.

As a concluding remark, it should be pointed out that the experimental results and the interpretations made in this chapter should be of considerable interest to theorists making future energy band calculations of the cuprous halides.² In addition, it is hoped that the new information presented in this chapter will help lead to a better understanding of the "intermediate" nature of the zincblende cuprous halides.

¹A better description might be "unexplained."

²F. Herman is presently engaged in calculating the energy band structure of the cuprous halides (private communication).



IX. PHOTOEMISSION STUDIES OF CESIUM CHLORIDE,
CESIUM BROMIDE, CESIUM IODIDE, AND POTASSIUM IODIDE

Quantum yield and energy distribution measurements have been made from films of CsCl, CsBr, CsI, and KI prepared and tested in vacuum of typically 2×10^{-9} torr. These high vacuum measurements were made at photon energies up to 11.9 eV, the high energy cutoff of the LiF window. In the case of CsI, the measurements were extended to 16.8 eV, using the knock-off tube techniques described in Chapter II.

Although a considerable amount of photoemission data has been obtained from these alkali halides, the interpretation of these data appears to be somewhat more complex than was the case for the noble metals and the cuprous halides. As a result, an analysis as detailed as that made for the noble metals and the cuprous halides has not been carried out for the alkali halides. Nevertheless, the photoemission data have led to a great deal of new information concerning (1) the absolute energies of valence states and conduction states, and (2) the identification of the initial and final states responsible for structure in the optical absorption and reflectivity data.

A. PHOTOEMISSION STUDIES OF CESIUM BROMIDE

The relative quantum yield of CsBr is plotted in Fig. 148. The significant features to be noted therein are that (1) the threshold is at 6.0 eV or lower, and (2) there is a steep rise at about 7.4 eV. The experimental EDCs corresponding to the yield of Fig. 148 are shown in Figs. 149 through 158. As an aid in interpreting these EDCs the location of structure in the EDCs is plotted as a function of photon energy in Fig. 159. The optical density of states that has been deduced from the photoemission data is given in Fig. 160.

Figure 149 shows the EDCs in the range of photon energies between 6.6 and 7.4 eV; these EDCs are unusual in several ways: All have a width of about 1.5 eV, independent of the photon energy. Also, the leading edge of the EDCs does not move according to the law $(\Delta E)_{\text{leading edge}} = \Delta h\nu$, which was observed in the "normal" EDCs of the noble metals and the cuprous halides. Only for photon energies greater than about 8.5 eV does

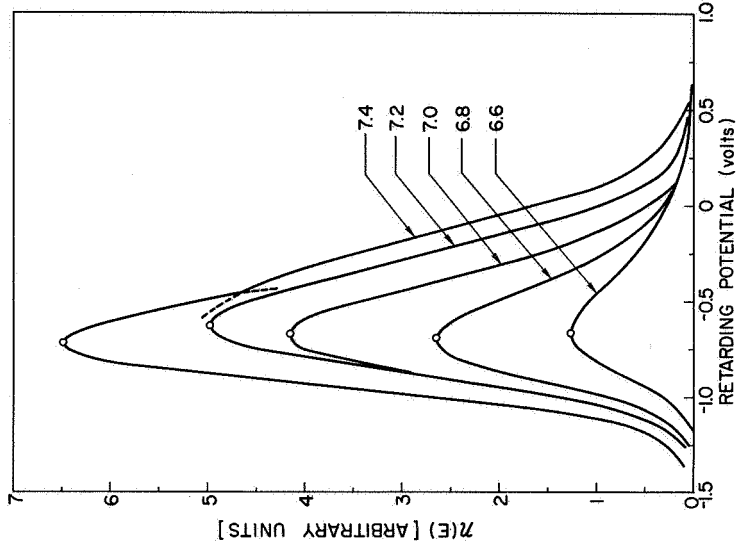


FIG. 149. ENERGY DISTRIBUTION CURVES FOR CESIUM BROMIDE IN THE RANGE OF PHOTON ENERGIES BETWEEN 7.2 AND 7.4 eV. The curves are normalized to the relative yield of Fig. 148.

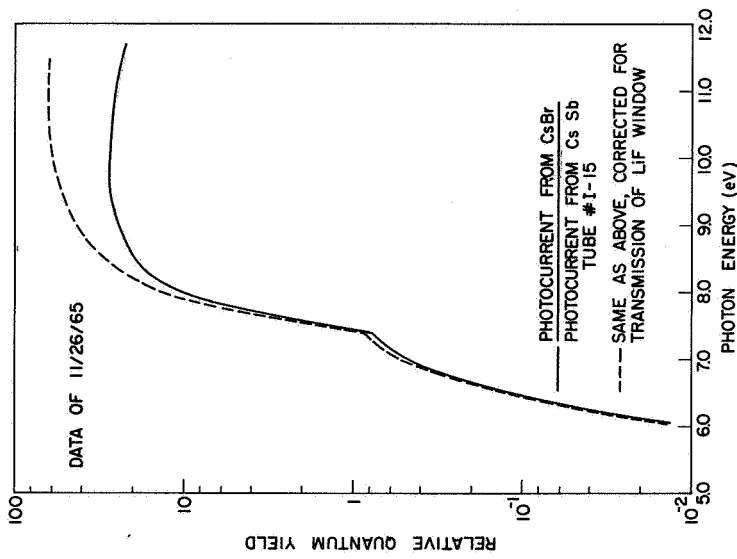


FIG. 148. RELATIVE QUANTUM YIELD FOR CESIUM BROMIDE.

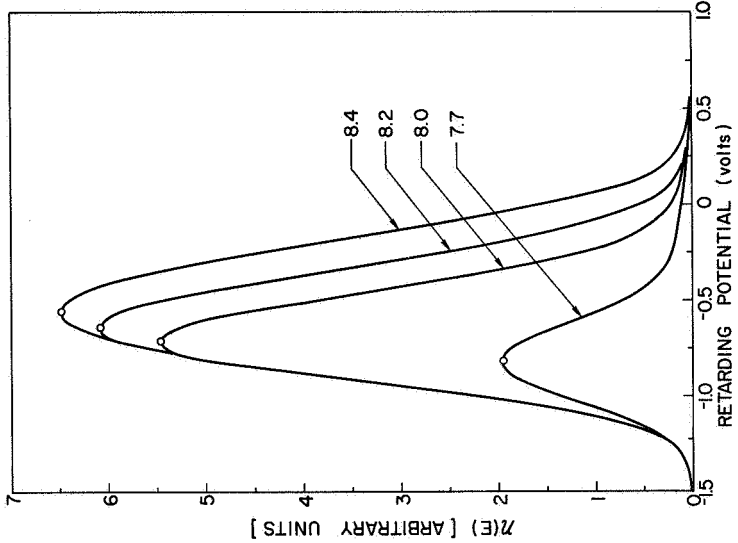


FIG. 151. ENERGY DISTRIBUTION CURVES FOR CESIUM BROMIDE IN THE RANGE OF PHOTON ENERGIES BETWEEN 7.7 AND 8.4 eV. The curves are normalized to the relative yield of Fig. 148.

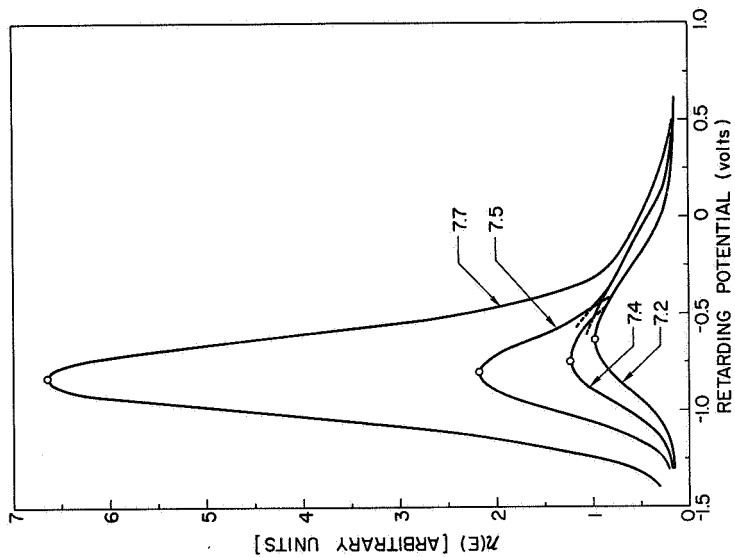


FIG. 150. ENERGY DISTRIBUTION CURVES FOR CESIUM BROMIDE IN THE RANGE OF PHOTON ENERGIES BETWEEN 7.2 AND 7.7 eV. The curves are normalized to the relative yield of Fig. 148. A quartz filter was used for all measurements except the curve at 7.7 eV.

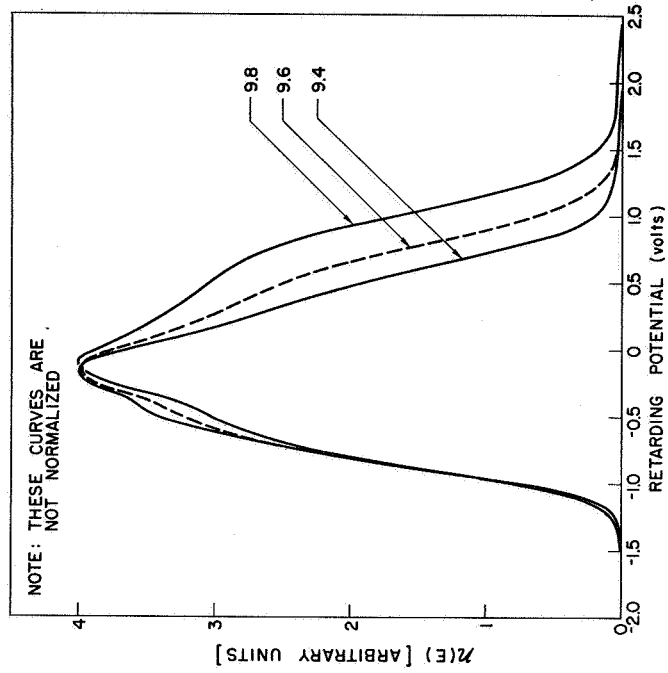


FIG. 153. ENERGY DISTRIBUTION CURVES FOR CESIUM BROMIDE IN THE RANGE OF PHOTON ENERGIES BETWEEN 8.4 AND 9.8 eV.

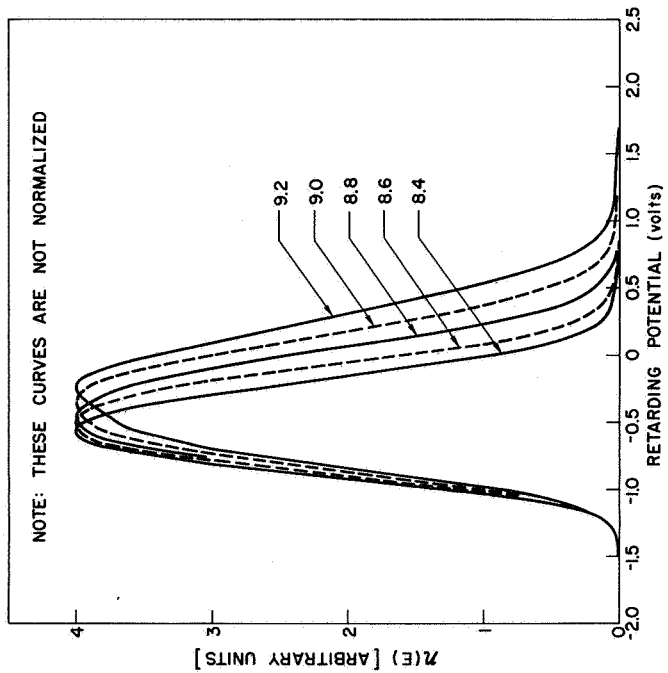


FIG. 152. ENERGY DISTRIBUTION CURVES FOR CESIUM BROMIDE IN THE RANGE OF PHOTON ENERGIES BETWEEN 8.4 AND 9.2 eV.

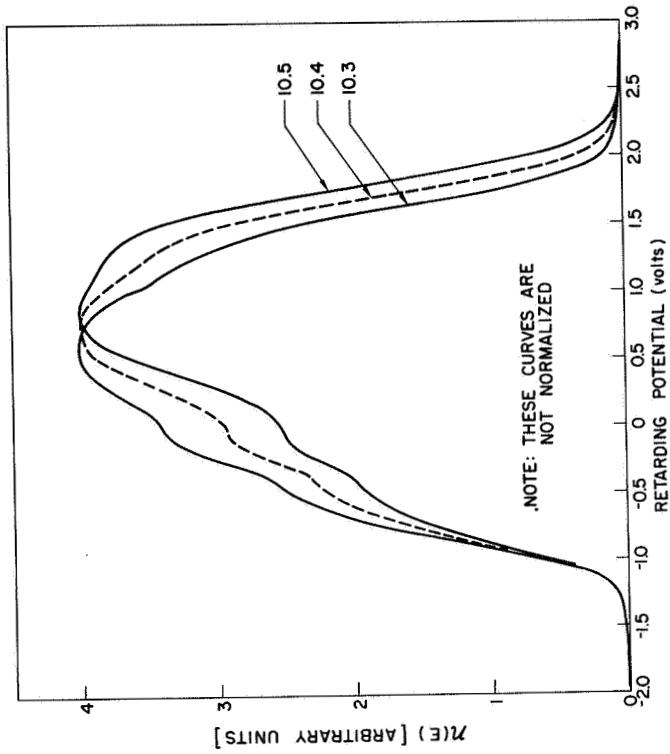


FIG. 155. ENERGY DISTRIBUTION CURVES FOR CESIUM BROMIDE IN THE RANGE OF PHOTON ENERGIES BETWEEN 10.3 AND 10.5 eV.

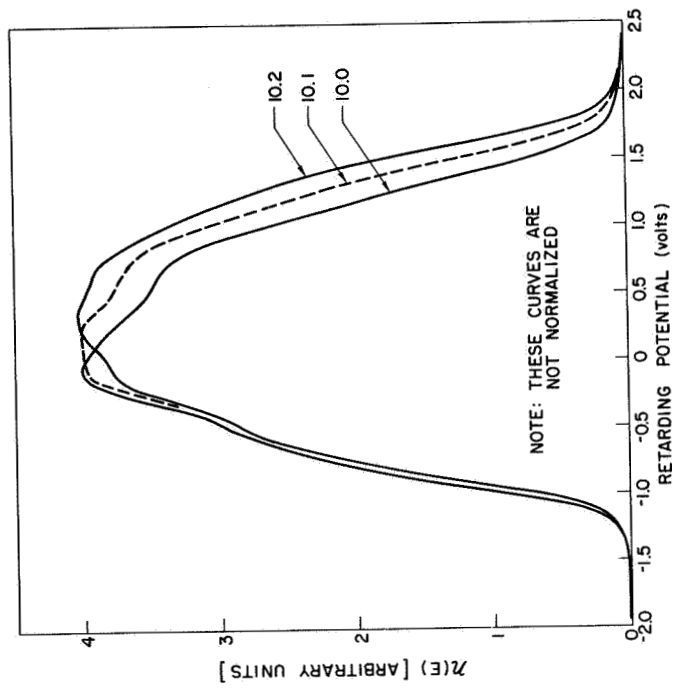


FIG. 154. ENERGY DISTRIBUTION CURVES FOR CESIUM BROMIDE IN THE RANGE OF PHOTON ENERGIES BETWEEN 10.0 AND 10.2 eV.

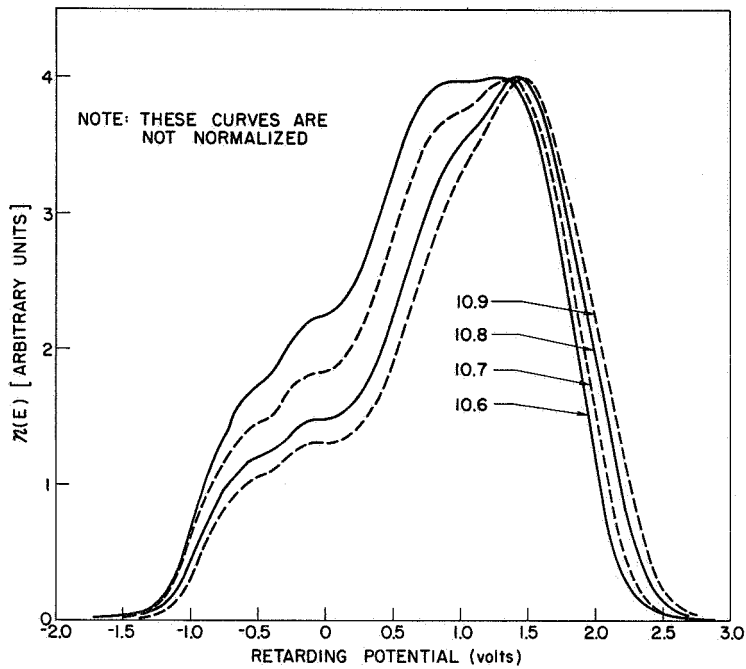


FIG. 156. ENERGY DISTRIBUTION CURVES FOR CESIUM BROMIDE IN THE RANGE OF PHOTON ENERGIES BETWEEN 10.6 AND 10.9 eV.

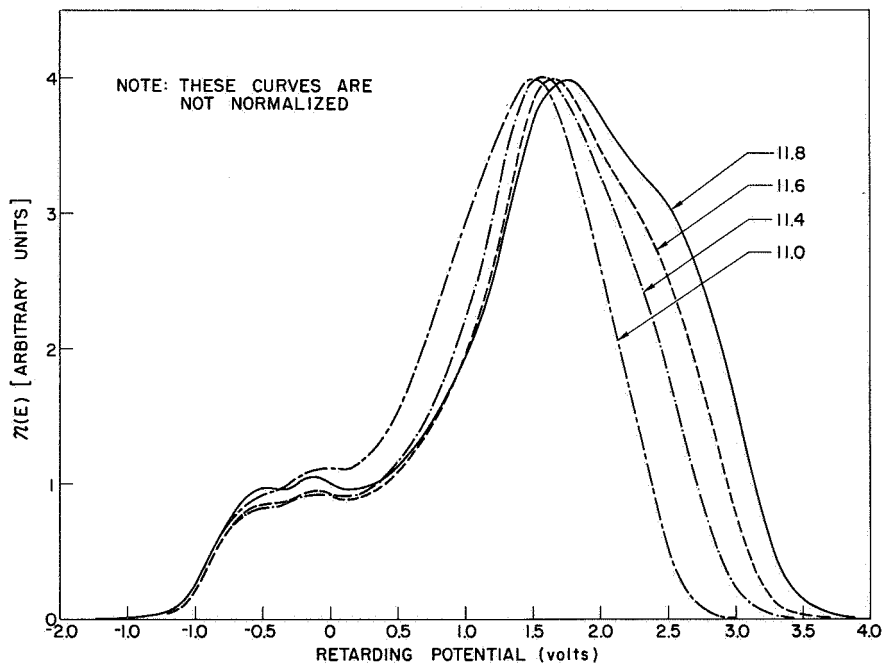


FIG. 157. ENERGY DISTRIBUTION CURVES FOR CESIUM BROMIDE IN THE RANGE OF PHOTON ENERGIES BETWEEN 11.0 AND 11.8 eV.

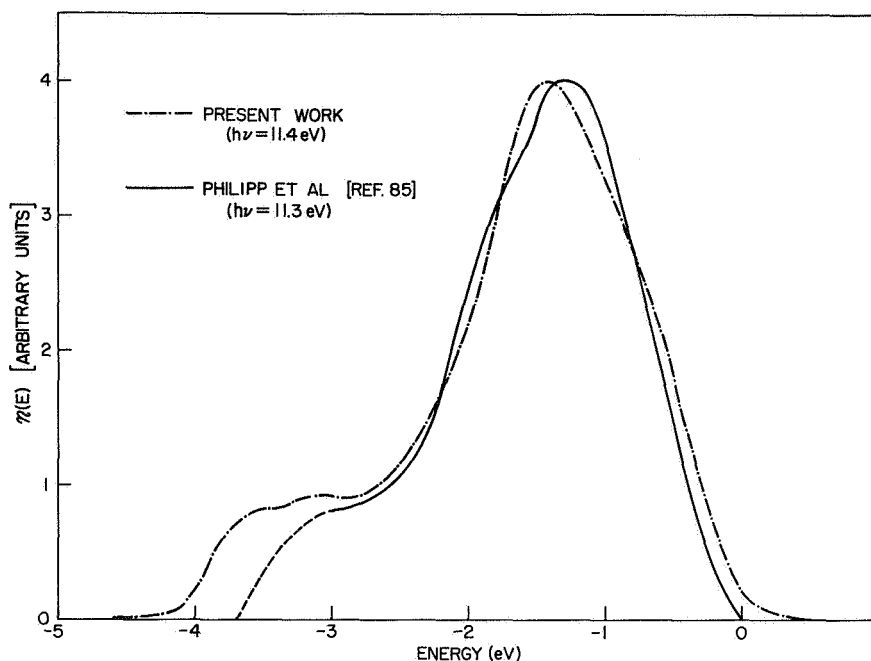


FIG. 158. COMPARISON OF THE PRESENT WORK WITH THE ENERGY DISTRIBUTION CURVE OBTAINED BY PHILIPP ET AL [REF. 85] FOR CsBr. The 11.3 eV curve is the only curve obtained by Philipp et al.

the leading edge of the EDCs follow the law $(\Delta E)_{\text{leading edge}} = \Delta h\nu$, as can be seen in Fig. 159. Note, however, that the 45° leading edge line indicates that the onset of photoemission from the top of the valence band to energies at $(-)\text{0.8 eV}^1$ begins at a photon energy of about 7.5 eV, which corresponds to the sharp rise in the quantum yield at 7.4 eV. Thus, it appears that the photoemission at photon energies less than 7.4 eV is due to some other effect than the "usual" photoemission from the valence band. This type of photoemission will be referred to as "threshold photoemission" in this chapter. As seen in Fig. 161 there is a strong exciton absorption at a photon energy of about 6.7 eV, and it might be possible that the EDCs of Fig. 149 are associated with this exciton. Apker and Taft [Ref. 91] discovered and studied extensively exciton-induced photoemission from F-centers, and the present "threshold photoemission"

¹ Referred to the retarding potential.

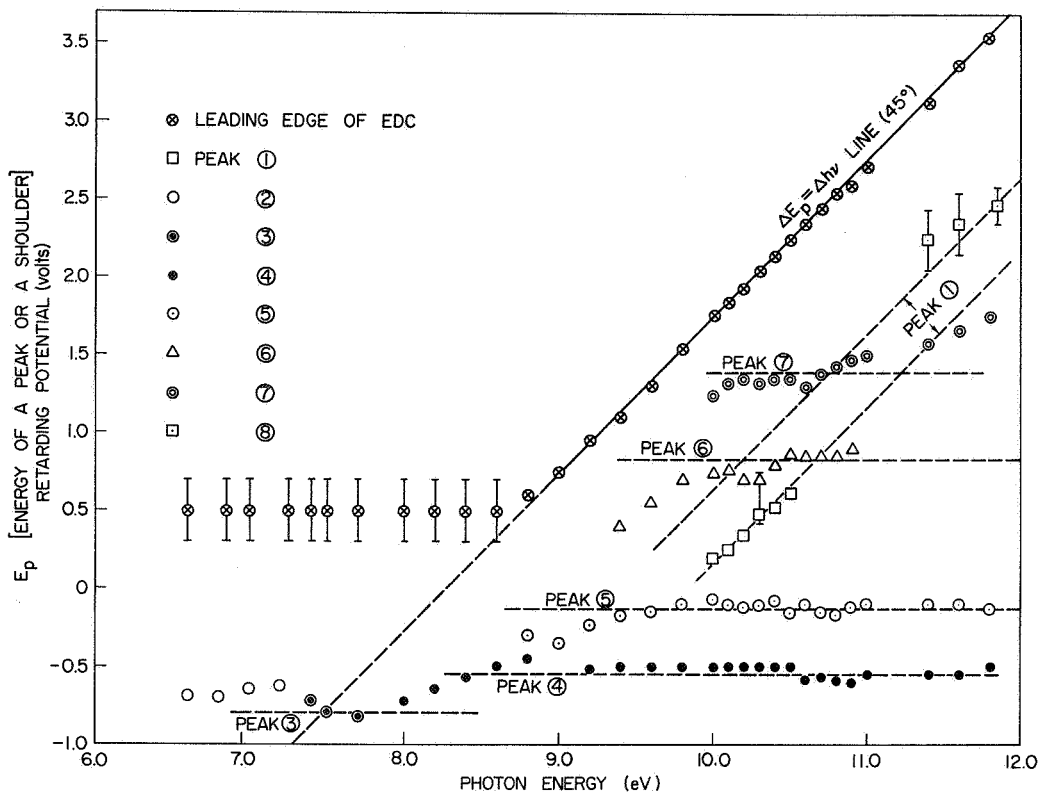


FIG. 159. E_p vs $h\nu$ FOR CESIUM BROMIDE.

may be due to this effect. However, the present studies (because of their emphasis on photoemission away from threshold) were not sufficiently extensive to establish definitively that this is the emission mechanism. In future work, this "threshold photoemission" should be studied more extensively. The possibility that it may be due to direct dissociation of an exciton should be recognized. For the sake of "keeping track" of this "threshold photoemission" in the discussions to follow, the final energy of the threshold photoemission has been designated by peak ② in the optical density of states of Fig. 160.

As seen in the EDCs at photon energies of 7.4, 7.5, and 7.7 eV, a very strong peak rises out of the threshold background. This peak is labeled peak ③ in Fig. 159. Note that the location of this peak is at about (-)0.8 eV, which is at a lower energy than the peak due to the "threshold photoemission." This very sharp rise at about 7.7 eV seems to correspond to the peak in the room temperature optical absorption that occurs at

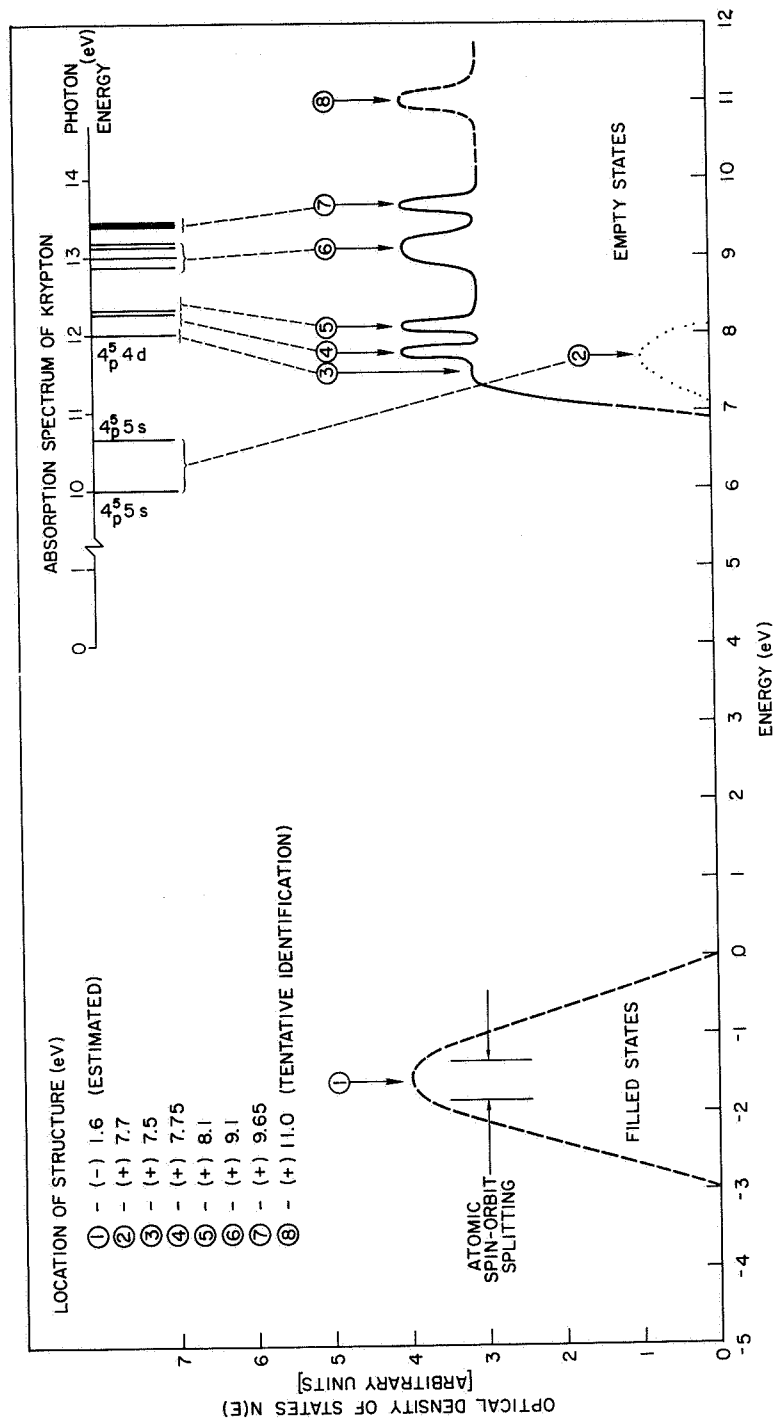


FIG. 160. ESTIMATED OPTICAL DENSITY OF CESIUM BROMIDE. The structure in the conduction band of cesium bromide is compared to the absorption spectrum of krypton [Ref. 86].

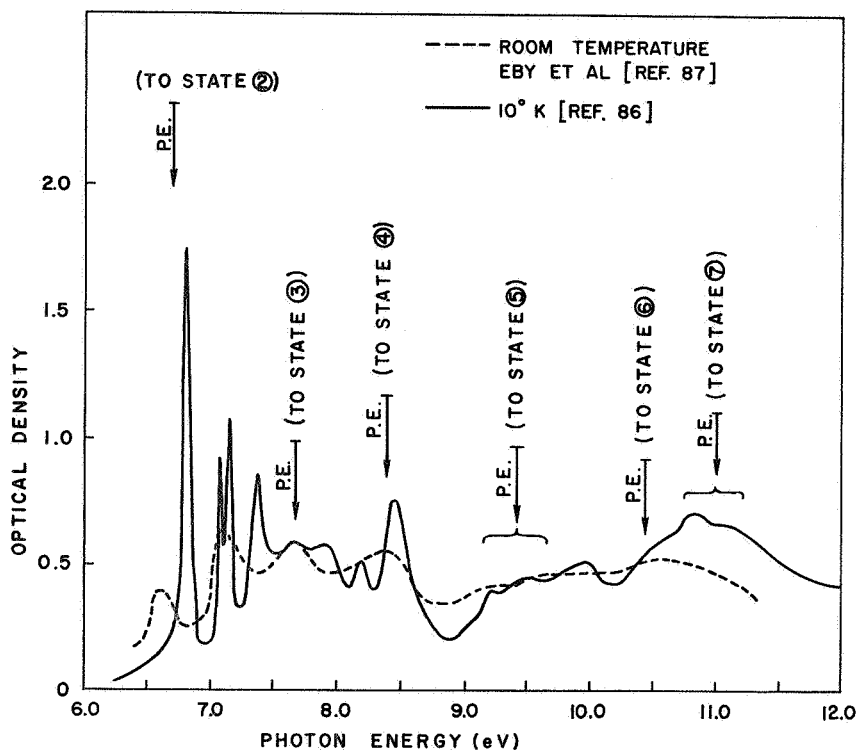


FIG. 161. OPTICAL DENSITY FOR CESIUM BROMIDE.

7.7 eV, as seen in Fig. 161. In addition, this sharp rise corresponds to the strong rise in the quantum yield at 7.4 eV, indicating that this transition is of the type normally associated with transitions between valence band states and conduction band states. This reasoning is supported by the fact that the 45° leading edge line in Fig. 159 intersects the location of peak ③ at $h\nu = 7.4$ eV, indicating that the sharp rise in the EDCs at photon energies of 7.4, 7.5, and 7.7 eV is due to strong transitions between the top of the valence band and states in the conduction band at 7.4 eV above the top of the valence band. This conduction band peak is labeled peak ③ in the optical density of states of Fig. 160.

The conduction band peaks ④, ⑤, ⑥, and ⑦ in Fig. 160 can be readily located from the experimental EDCs of Figs. 151 through 158 and by examination of Fig. 159. In order to understand how Fig. 160 was deduced, the reader will perhaps find it easiest to examine first Fig. 159, in which the position of structure in the EDCs is presented as a

function of $h\nu$. In CsBr, the conduction band structure modulates the energy distributions strongly as $h\nu$ is increased. Because of this strong modulation, structure tends to appear at the energy of the final state independent of photon energy. This produces points that lie along the horizontal lines in Fig. 159. These horizontal lines are intended to "average" the location of these points. The approximate position of the conduction band structure is given by the photon energy corresponding to the intersection of these horizontal lines with the 45° "leading edge" line. This value of the photon energy gives the location of the conduction band structure in terms of electron-volts above the top of the valence band. This deduction is possible because the 45° leading edge of the EDCs for $h\nu > 8.6$ eV must be due to electrons excited from the highest valence state. A more exact location for conduction band structure can sometimes be obtained by examining the EDCs and finding the energy for which the amplitude of the structure is largest.

Possible evidence of conduction band peak (8) is seen in the EDCs at photon energies between 11.4 and 11.8 eV. However, it is also possible that the shoulder labeled peak (8) is actually due to structure in the valence band. This ambiguity in the nature of peak (8) can be removed by future windowless measurements of the EDCs at photon energies greater than 11.8 eV.

Due to the severe modulation of the EDCs by structure in the conduction band, it has not been possible to identify any detailed structure in the valence band of CsBr. However, the gross characteristics of the valence band optical density of states can be obtained from inspection of the EDCs in Fig. 157, where the portions of the EDCs between 0.5 and 3.5 eV are probably a fair replica of the general shape of the valence band density of states. In accordance with the EDCs of Fig. 157, the valence band density of states in Fig. 160 has been sketched to have a maximum width of about 3.0 eV.

The magnitude of the quantum yield in Fig. 148 at a photon energy of 11.0 eV is very large, about 1.0 (electrons photoemitted per absorbed photon). However, there is a large uncertainty in the yield of CsBr due to the uncertainty in the yield of the standard tube No. (I-15) which

was used to calibrate the quantum yield. A quantum yield of unity indicates that all the photoexcited electrons are photoemitted, even those that have initial velocities directed away from the surface. Such a large quantum yield is perhaps not surprising, since CsBr has an energy gap of (roughly) 7.0 eV, and inelastic electron-electron collisions are impossible at energies less than twice the energy gap. Nearly unity quantum yield is possible if the photoexcited electrons that have initial velocities directed away from the surface are directed toward the surface. A possible mechanism for this phenomenon is electron-phonon scattering, in which the energy loss per collision is quite small (typically less than 0.1 eV), and where the direction change per collision could be quite large. The high quantum yield and the possible electron-phonon scattering seem to be consistent with the experimental EDCs of Fig. 157, where a peak of slow electrons characteristic of electron-electron scattering is conspicuously absent. In Fig. 157, the large structure within about 3.0 eV of the leading edge in each EDC is probably representative of the primary electrons initially directed toward the surface, and the small number of slow electrons are probably representative of those electrons that have encountered a large number of electron-phonon scattering events before reaching the surface and being photoemitted.

Figure 158 compares the present work with the earlier work of Phillip et al [Ref. 76], who measured only a single EDC from CsBr. As seen from Fig. 158, the agreement is quite good.

Figure 161 shows the optical density of CsBr at room temperature and at 10°K. The 10°K data have considerably more structure than the room temperature data, and there is a significant shift in the location of some structure with temperature. The arrows in Fig. 161 indicate the photon energies at which strong transitions are seen to occur in the experimental EDCs of Figs. 149 through 158. In Fig. 161, the abbreviation "P.E." signifies that the location of the arrow has been deduced from the photoelectric EDCs. The explanation beside each arrow in Fig. 161 identifies the conduction band state involved in the transition. As seen from Fig. 161, there is a very good correspondence between structure in the optical density and the photon energies at which strong transitions are evident in the experimental EDCs. This close correspondence indicates that the

peaks in the optical density of states of Fig. 160 are indeed representative of the final states to which the valence electrons are excited during the optical absorption process.

The large number of peaks in the conduction band of CsBr is reminiscent of the many absorption lines seen in the absorption spectra of gases. For this reason, the conduction band of CsBr has been compared with the absorption spectrum of krypton in Fig. 160. Krypton is an inert gas that lies next to bromine in the periodic table. The comparison between krypton and CsBr is justified because krypton has an outer electron configuration given by $(4s^2 4p^6)$, and the bromine ion in the very ionic CsBr has an outer electron configuration that is approximately¹ $(4s^2 4p^6)^-$. As seen in Fig. 160, there is apparently a close correspondence between the conduction band of CsBr and the absorption spectrum of krypton. For example, the exciton-derived peak (2) has been associated with the transition $(4p^5 5s)$, and the conduction band state (3) has been associated with the transition $(4p^5 4d)$. This close correspondence between CsBr and krypton may imply that at photon energies up to 10 eV, the fundamental absorption consists of atomic-like excitation between atomic-like levels of the $(Br)^-$ ion, and that the $(Cs)^+$ ion is not involved in the fundamental absorption.

B. PHOTOEMISSION STUDIES OF CESIUM CHLORIDE

The experimental quantum yield for CsCl is given in Fig. 162. One very important feature of CsCl is that the quantum yield is very high; at a photon energy of 11.3 eV, the yield (uncorrected for reflectivity) is about 0.88 (electrons photoemitted per absorbed photon). The error in the quantum yield of Fig. 162 is estimated to be about ± 15 percent. The large magnitude of the quantum yield seems to be in good agreement with the data of Metzger [Ref. 88], who finds that the quantum yield is

¹ However, it must be emphasized that the absorption spectrum of krypton represents the energy difference between states, and the peaks in the conduction band of CsBr represent absolute energies. Thus, the comparison of an absorption spectrum with an absolute energy scale is strictly correct only if there is a single initial state, which is not the case in CsBr. Nevertheless, there seems to exist a striking comparison between krypton and CsBr.

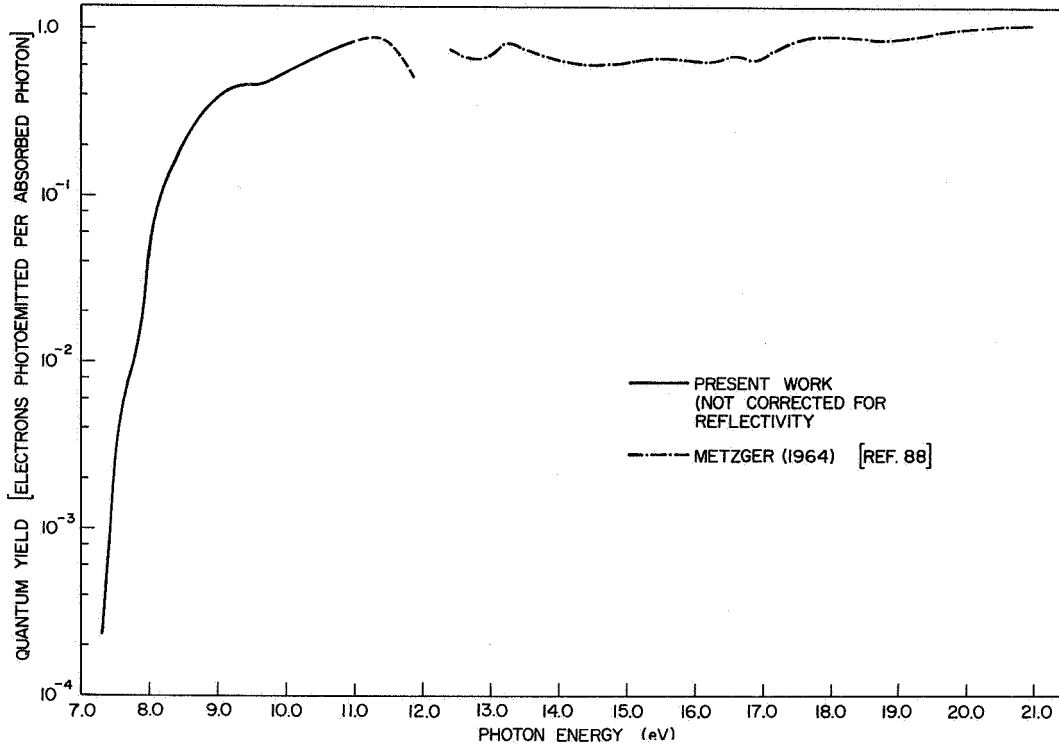


FIG. 162. QUANTUM YIELD FOR CESIUM CHLORIDE. The curve labeled "present work" was calibrated using Koyama's thermopile results dated 11-9-66.

about 0.7 (electrons photoemitted per absorbed photon) at a photon energy of 12.5 eV. Since the energy gap of CsCl is about 7.0 eV, a very high quantum yield would be expected for CsCl, and the earlier discussion explaining the nearly unity quantum yield in CsBr also applies to CsCl. Another interesting feature in the quantum yield is the inflection point that occurs at about 7.8 eV; this inflection point seems to correspond to the steep rise in the quantum yield of CsBr at 7.4 eV (Fig. 148).

The EDCs corresponding to the quantum yield of Fig. 162 are shown in Figs. 163 through 167. The E_p vs $h\nu$ plot used as an aid in interpreting the EDCs is given in Fig. 168, and the optical density of states deduced from the photoemission data is presented in Fig. 169.

The EDCs in Figs. 163 and 164 bear a resemblance to the EDCs for CsBr in Figs. 149 and 150, in that a strong peak appears to rise out of the threshold background, just as was observed in CsBr. A different photoemission mechanism for the threshold and for the higher $h\nu$ regions is

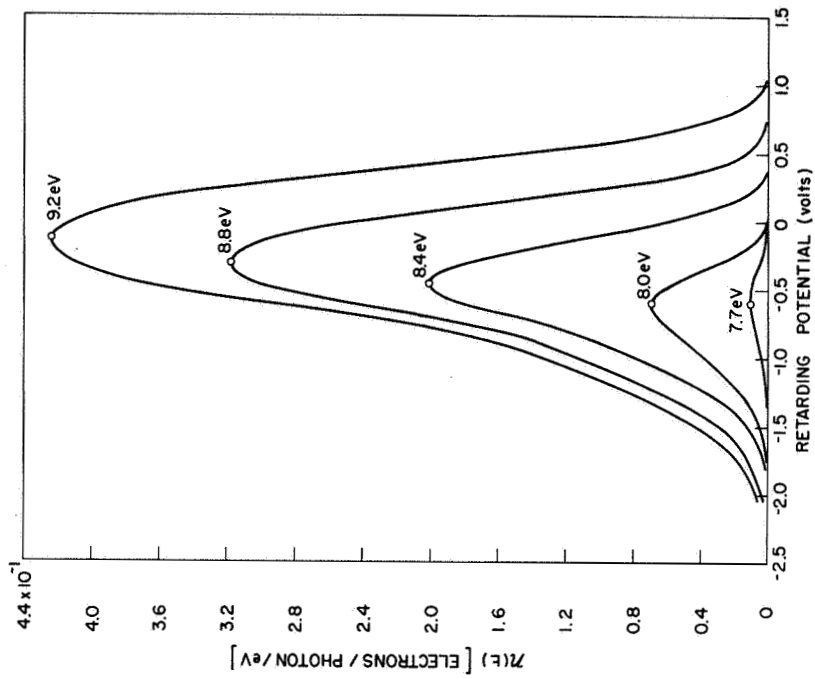


FIG. 164. ENERGY DISTRIBUTION CURVES FOR CESIUM CHLORIDE IN THE RANGE OF PHOTON ENERGIES BETWEEN 7.7 AND 9.2 eV.

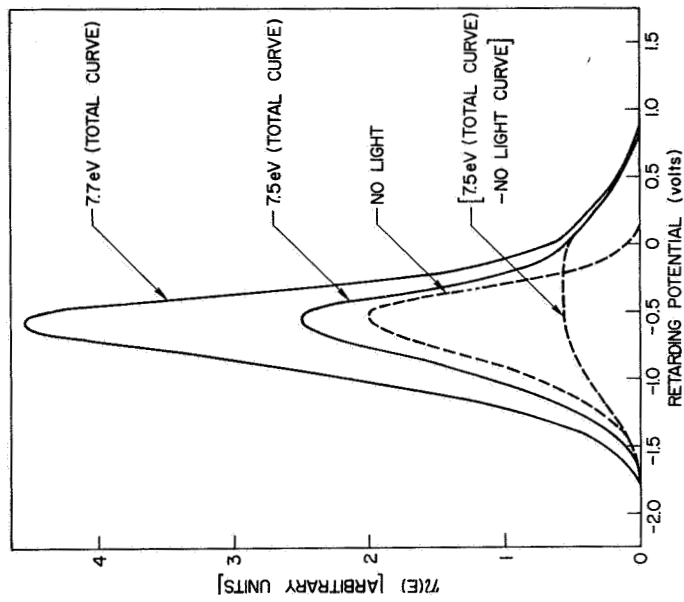


FIG. 163. ENERGY DISTRIBUTION CURVES FOR CESIUM CHLORIDE AT 7.5 AND 7.7 eV. The relative magnitudes of the EDCs are significant. The "no light" energy distribution curve was measured immediately after the 7.5 eV curve.

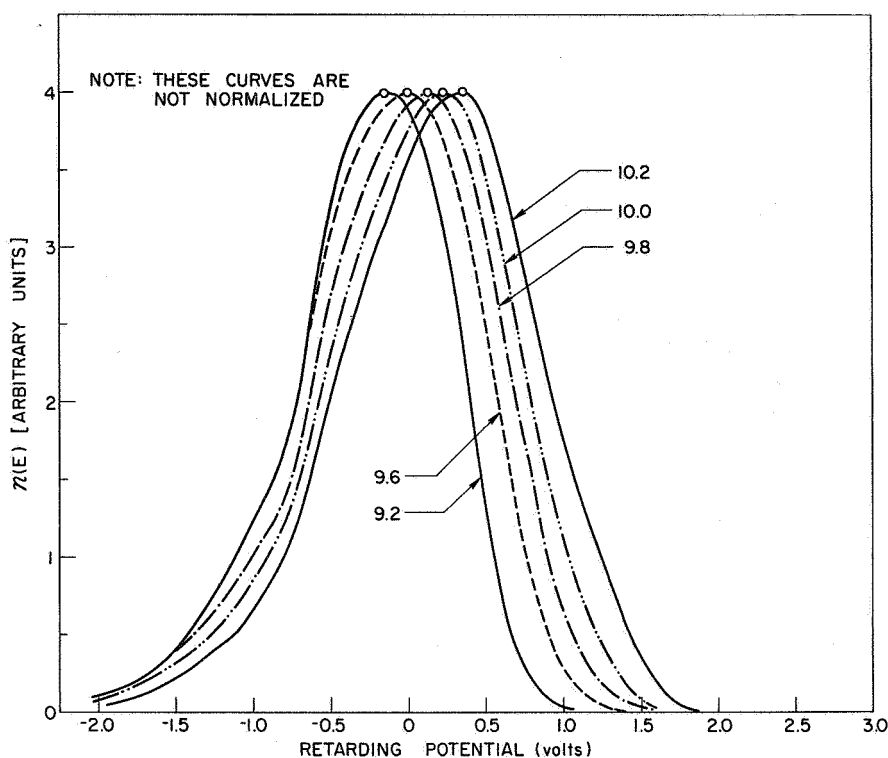


FIG. 165. ENERGY DISTRIBUTION CURVES IN THE RANGE OF PHOTON ENERGIES BETWEEN 9.2 AND 10.2 eV.

suggested by the inflection point of the quantum yield of CsCl at 7.8 eV, indicating that the quantum yield between 7.3 and about 7.6 eV might be due to exciton-induced photoemission, and that the quantum yield at photon energies above 7.8 eV is due to "normal" photoemission processes. The optical density of Fig. 170 indicates that there is a broad exciton absorption at about 7.6 eV, corresponding closely to the "background" photoemission evident in the EDCs of Fig. 163 for photon energies of 7.5 and 7.7 eV. The final energy of this threshold photoemission is represented as peak (2) in the optical density of states of Fig. 169.

An interesting and very strange feature shown in Fig. 163 is that an EDC was measured with no light incident upon the sample. This "no light" EDC was measured after the sample had been irradiated for several hours by a high intensity mercury arc (quartz jacket)¹ and after the quantum

¹This irradiation was part of an unsuccessful experiment to make CsCl conducting at temperatures of 80°K by the creation of F-centers. As will be discussed later in this chapter, the alkali halides tend to become insulating at 80°K, thus preventing the measurement of photoelectric EDCs from alkali halides at 80°K.

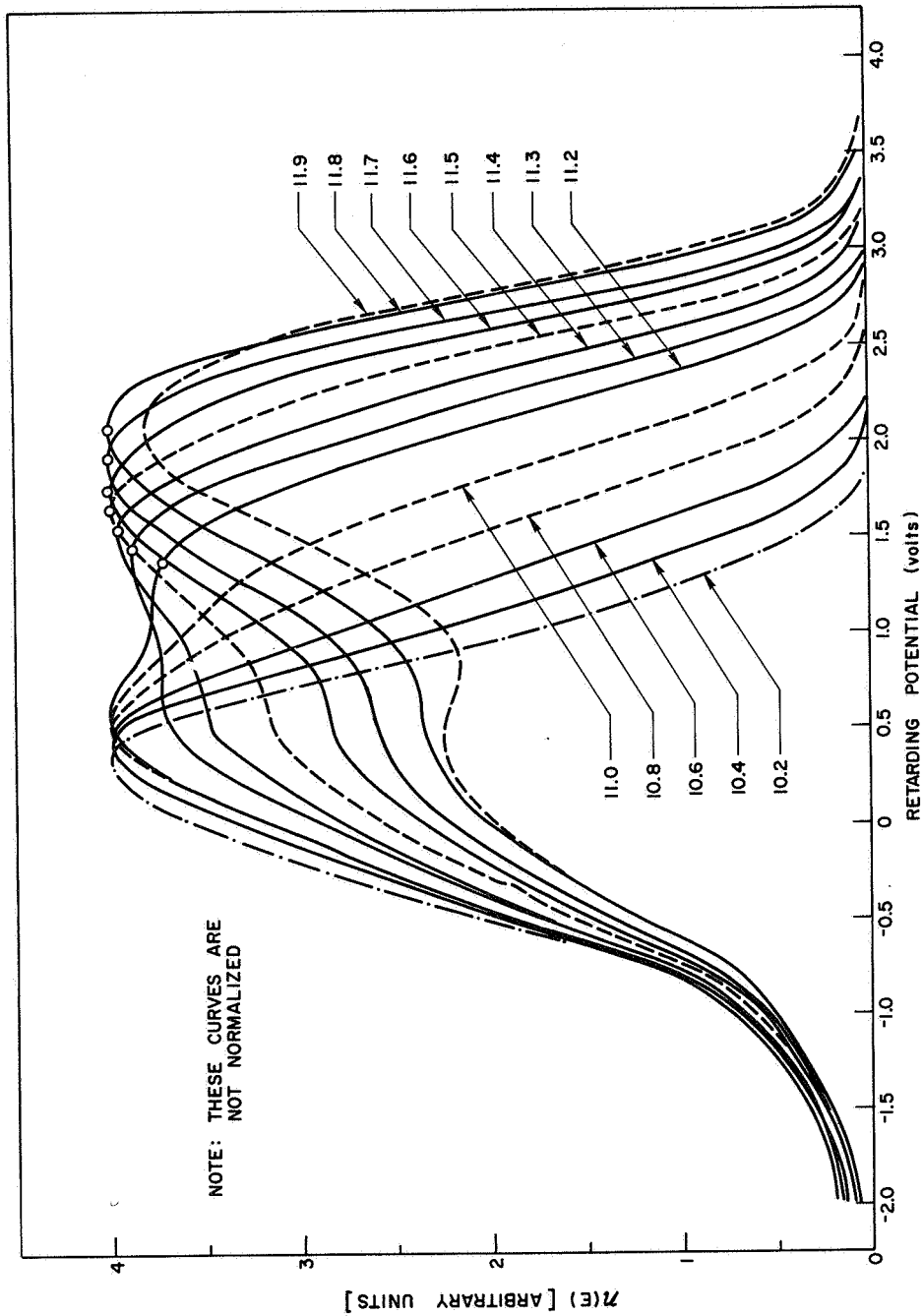


FIG. 166. ENERGY DISTRIBUTION CURVES FOR CESIUM CHLORIDE IN THE RANGE OF PHOTON ENERGIES BETWEEN 10.2 AND 11.9 eV.

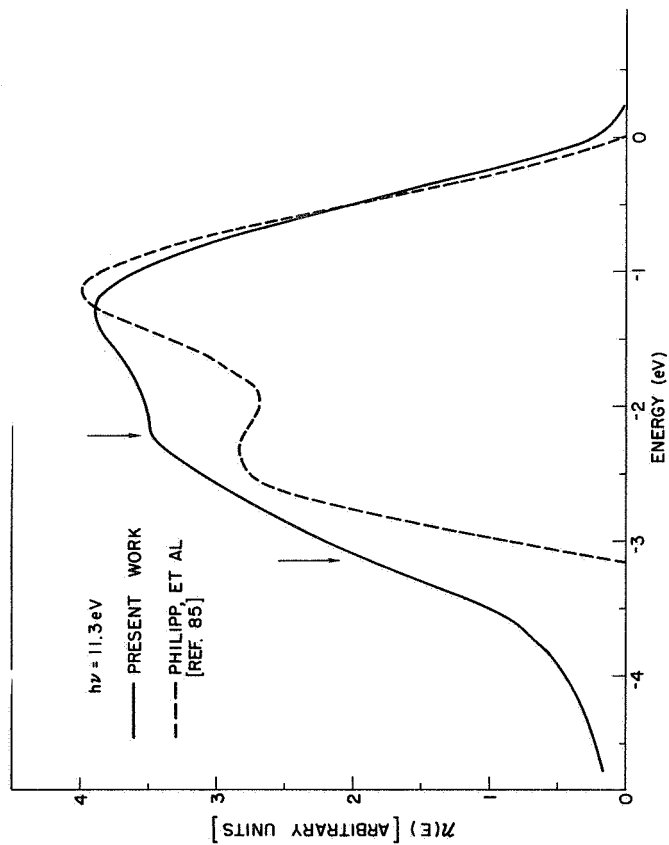


FIG. 167. COMPARISON OF SHAPES OF ENERGY DISTRIBUTION CURVES. The curve obtained by Phillip et al (1960) is the only curve obtained by these authors for cesium chloride.

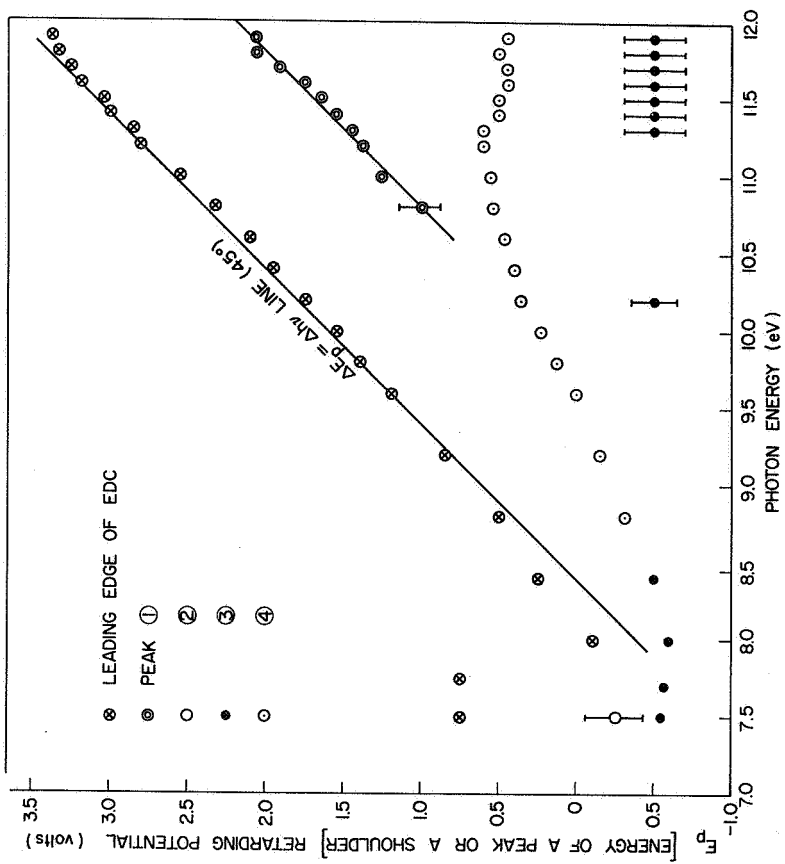


FIG. 168. E_p vs $h\nu$ FOR CESIUM CHLORIDE.

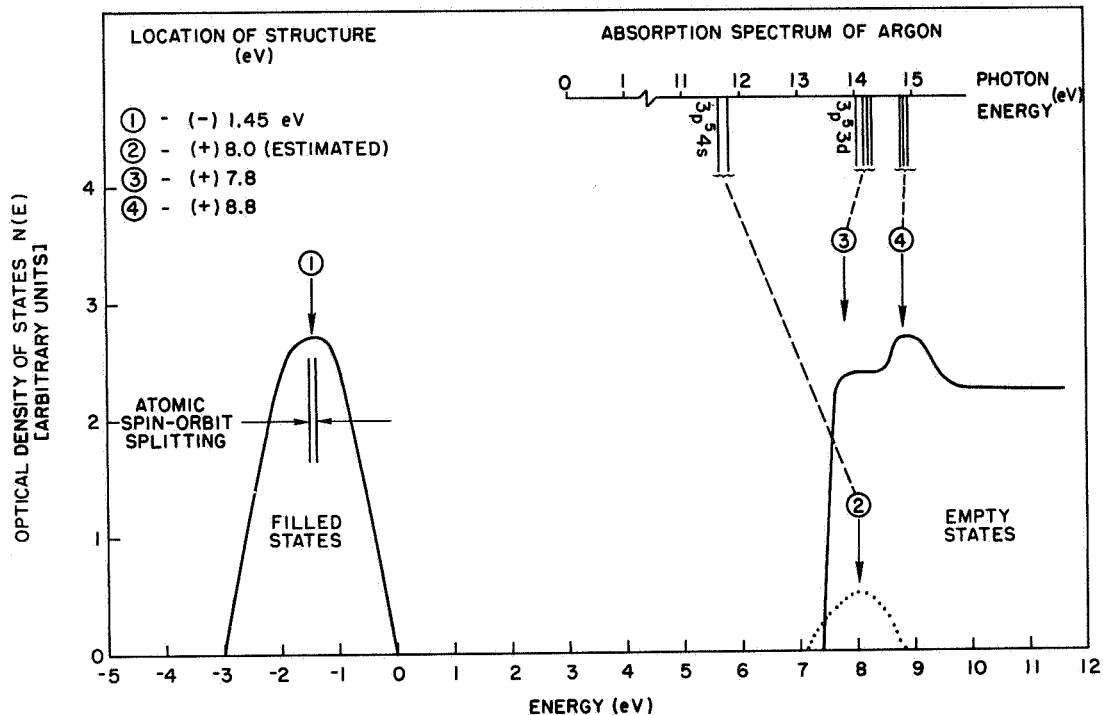


FIG. 169. ESTIMATED OPTICAL DENSITY OF STATES FOR CESIUM CHLORIDE. The conduction band of cesium chloride as compared with the absorption spectrum of argon (Teegarden and Baldini).

yield of Fig. 162 had been measured. The total current in the "no light" EDC was about 1.5×10^{-11} amperes.¹ The location of the peak in the "no light" curve corresponds closely to peak ③ in the optical density of states of Fig. 169, and was apparently due to electrons migrating exceedingly slowly toward the surface before being photoemitted. The times involved in this "delayed" photoemission were at least several minutes--the time required to measure an EDC. Unfortunately, the possible significance of the "no light" EDC was not appreciated at the time the data were being taken, and the time required for the "no light" EDC to disappear was not investigated.

¹This is a significant current, but it is small compared with the total currents of 5×10^{-10} amperes used in measuring most of the EDCs in Figs. 163 through 167.

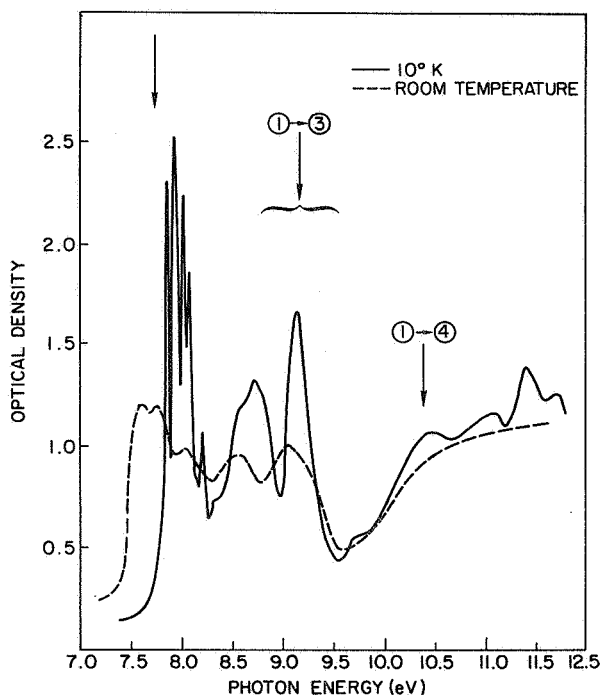


FIG. 170. OPTICAL DENSITY OF CESIUM CHLORIDE. The 10°K curve is from Ref. 86, and the room temperature curve corresponds to cesium chloride (II) in Ref. 87.

At photon energies greater than about 8 eV, the EDCs for CsCl seem to follow the "usual" photoemission law in which $(\Delta E)_{\text{leading edge}} = \Delta h\nu$, as can be seen in Fig. 168. Two "peaks" in the conduction band of CsCl can be identified in the EDCs of Figs. 163 through 167. One peak, labeled peak ④ in the optical density of states of Fig. 169, is a rather broad peak and is identified by the fixed peak at about (+)0.5 eV in the EDCs of Fig. 166. The other conduction band peak is obscured by the large number of curves drawn in Fig. 166; however, this second conduction band peak can be seen as a rather vague shoulder at (-)3.15 eV in Fig. 167. This second conduction band peak is labeled peak ③ in the optical density of states of Fig. 169. The valence band optical density of states of CsCl has been identified as the broad structure that appears between about (+)0.5 eV and (+)3.5 eV in the EDCs of Fig. 166 for photon energies greater than about 11.5 eV. This structure has a maximum width of about 3 eV, and appears to follow the law $\Delta E = \Delta h\nu$, which is characteristic of photoemission from the valence band of a material that is described by the model of nondirect transitions. For photon energies greater than about 11.5 eV, the slow electrons in the range of energies between (-)1.0 and (+)0.5 eV are probably electrons that have encountered many

electron-phonon scattering events, and the electrons in the range of energies between (+)0.5 and (+)3.5 eV are probably primary electrons that had initial velocities directed toward the surface.

In Fig. 167, data from the present work is compared with the data of Philipp et al [Ref. 76]; the EDC at 11.3 eV is the only data obtained by Philipp et al for CsCl. As seen from Fig. 167, the gross features of both EDCs are the same, except that the data of Philipp et al has noticeably sharper structure.

In Fig. 169, the conduction band of CsCl is compared with the absorption spectrum of argon, which is the inert gas that lies next to chlorine in the periodic table. The correspondence between krypton and CsCl seems to be quite good, implying that the fundamental absorption is largely due to excitation within the chlorine ion for photon energies less than about 10 eV.

The arrows in Fig. 170 denote the photon energies at which strong transitions are evident in the experimental EDCs. The arrow at 7.6 eV corresponds to the possible exciton-induced photoemission seen in the EDCs at 7.5 and 7.7 eV, and the arrow in the vicinity of 9.0 eV corresponds to the broad range of energies in which valence band peak (1) couples to conduction band peak (3). The strong transition at 10.5 eV is evident in the EDCs of Fig. 166. As observed from Fig. 170, the strong transitions seen in the EDCs correspond fairly well to the gross features in the optical density, but the EDCs do not account for the fine structure; this discrepancy may very well be due to the general broadness seen in the EDCs of the present work. Since Philipp et al [Ref. 85] have obtained EDCs with sharper structure than found in the EDCs presented here, it is possible that more information about the electronic structure of CsCl can be obtained by future photoemission measurements on CsCl samples that have been prepared in a manner different from that used in the present work. Since Eby et al [Ref. 87] have observed changes in the optical density of CsCl due to annealing, it is possible that the structure in the EDCs of CsCl might be "sharpened" by some annealing technique.

C. PHOTOEMISSION STUDIES OF CESIUM IODIDE

The experimental quantum yield for CsI is shown in Fig. 171. Just as in CsCl and CsBr, the quantum yield is very nearly unity in the vicinity of 11 eV. The uncertainty in the quantum yield labeled "present work" in Fig. 171 is estimated to be about ± 25 percent; this rather large uncertainty is due largely to the uncertainty in the transmission of the LiF window, which deteriorated somewhat during the experiment. The magnitude of the quantum yield obtained in the present work is in rather good agreement with the data of Metzger [Ref. 88], as can be seen in Fig. 171.

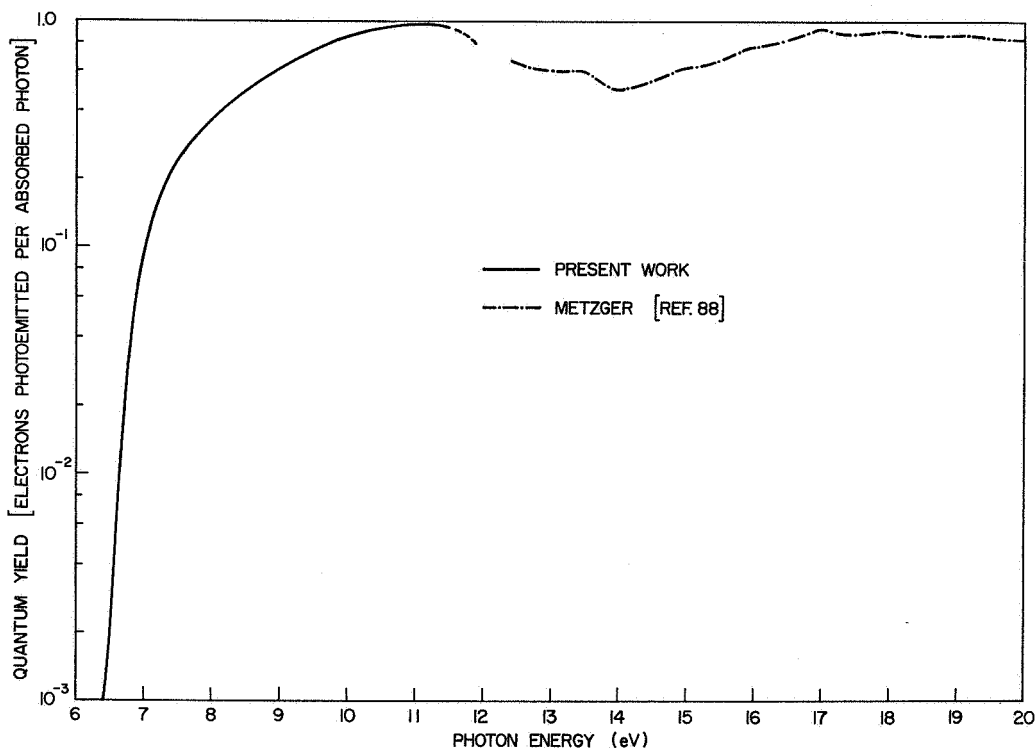


FIG. 171. QUANTUM YIELD FOR CESIUM IODIDE AT ROOM TEMPERATURE.

Note that there is a broad dip in the quantum yield in the vicinity of 14 eV, which is slightly more than twice the band gap of CsI. As will be discussed in more detail later in this section, the dip in the quantum yield is apparently caused by the onset of electron-electron scattering.

The relative quantum yield of CsI at a temperature of 80°K is shown in Fig. 172. At 80°K, the CsI films became insulating, and meaningful EDCs could not be obtained. However, the photocurrent from the insulating CsI did not saturate for collector voltages less than (+) 40 volts, and

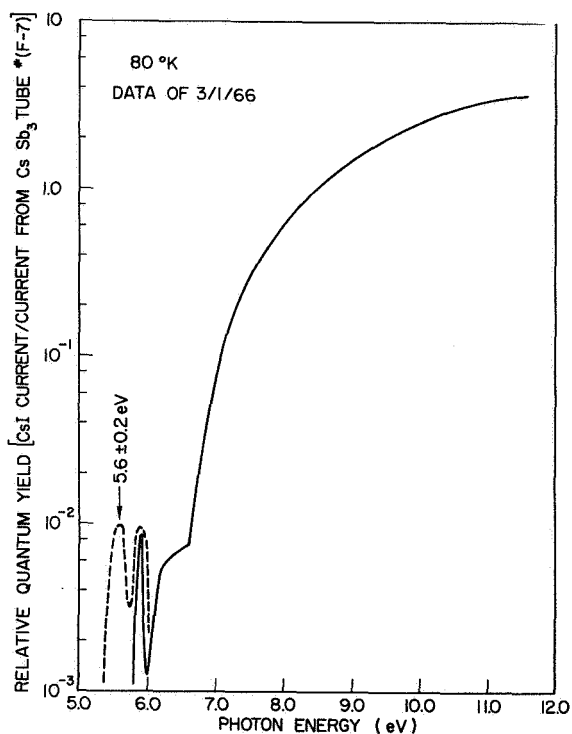


FIG. 172. RELATIVE QUANTUM YIELD OF CESIUM IODIDE AT 80°K.

the quantum yield data of Fig. 172 were obtained by using a collector voltage in excess of +40 volts. At photon energies greater than about 6.6 eV, the shape of the quantum yield has the same general character as the room temperature quantum yield; at both temperatures, there is a steep rise in the quantum yield at about 6.5 eV. However, at photon energies smaller than about 6.6 eV, there is structure in the 80°K quantum yield that is not present in the room temperature quantum yield. As seen in Fig. 172, the 80°K data have a shoulder at 6.3 eV, and a very sharp peak at 5.90 eV. Before detailed measurements of the quantum yield were made, the incident photon energy was scanned over the range between 5 and 6 eV, and the two dashed peaks in Fig. 172 were observed. However, after the peak at 5.90 eV had been carefully measured, the peak located at (approximately) 5.6 eV had disappeared. Structure in the threshold region of CsI has been observed earlier by Philipp and Taft [Ref. 92], who attributed the structure to exciton-induced photoemission from uncontrolled impurities and imperfections.

The experimental EDCs corresponding to the quantum yield of Fig. 171 are shown in Figs. 173 through 180. Just as in CsCl and CsBr, the EDCs at photon energies very close to the threshold for photoemission have a

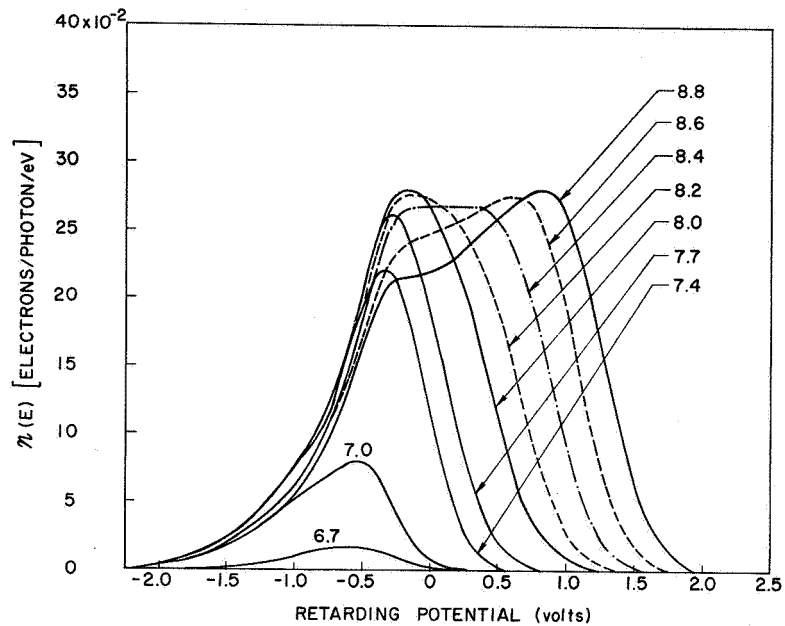


FIG. 173. ENERGY DISTRIBUTION CURVES FOR CESIUM IODIDE IN THE RANGE OF PHOTON ENERGIES BETWEEN 6.7 AND 8.8 eV.

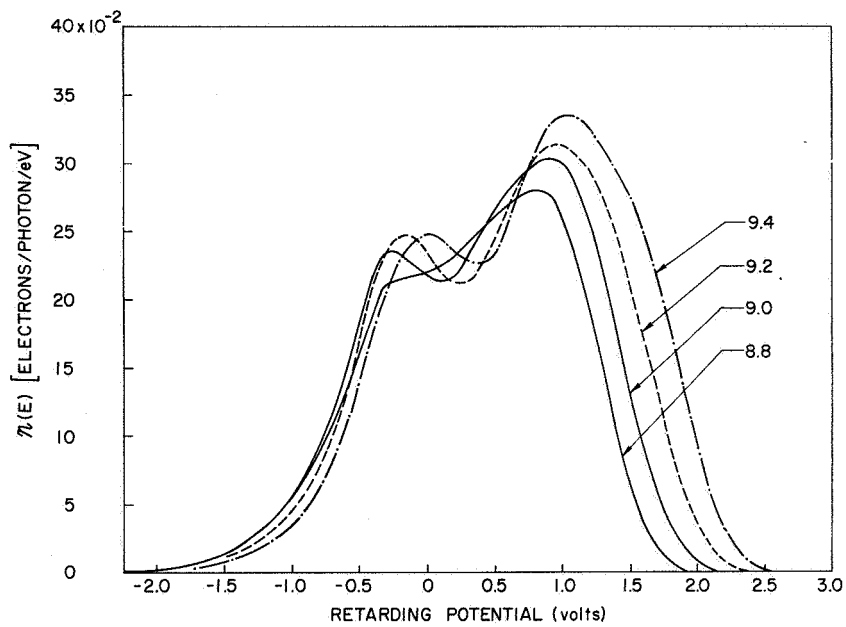


FIG. 174. ENERGY DISTRIBUTION CURVES FOR CESIUM IODIDE IN THE RANGE OF PHOTON ENERGIES BETWEEN 8.8 AND 9.4 eV.

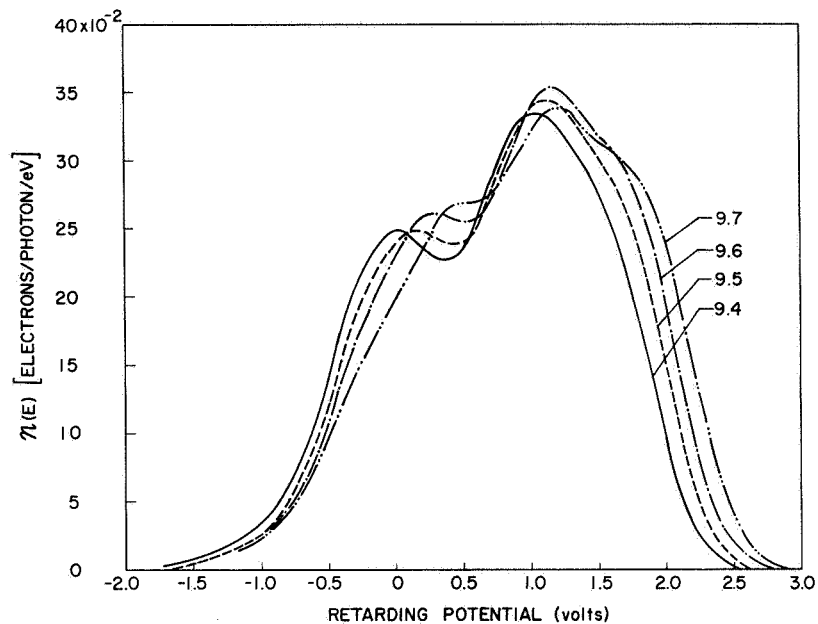


FIG. 175. ENERGY DISTRIBUTION CURVES FOR CESIUM IODIDE IN THE RANGE OF PHOTON ENERGIES BETWEEN 9.4 AND 9.7 eV.

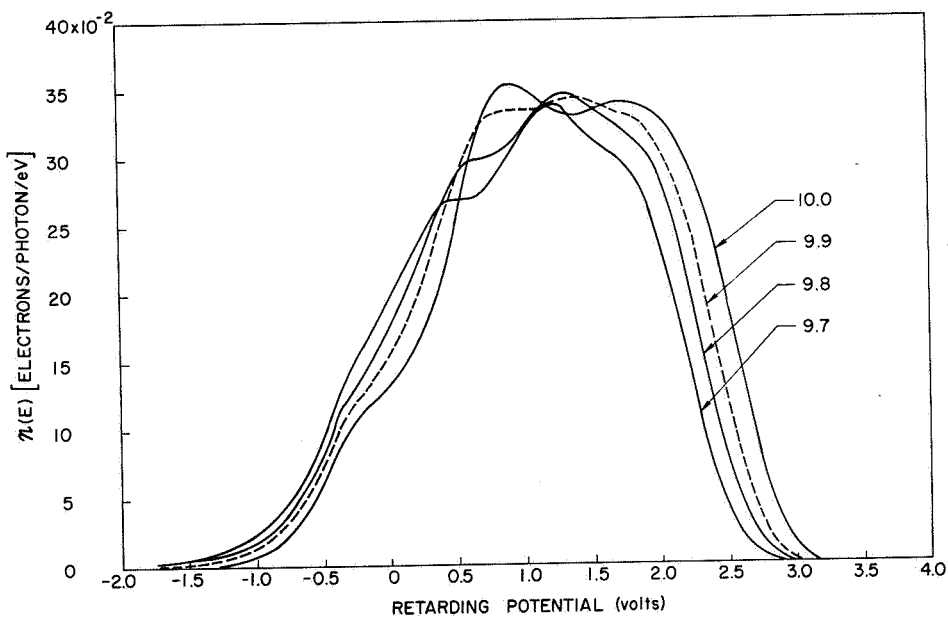


FIG. 176. ENERGY DISTRIBUTION CURVES FOR CESIUM IODIDE IN THE RANGE OF PHOTON ENERGIES BETWEEN 9.7 AND 10.0 eV.

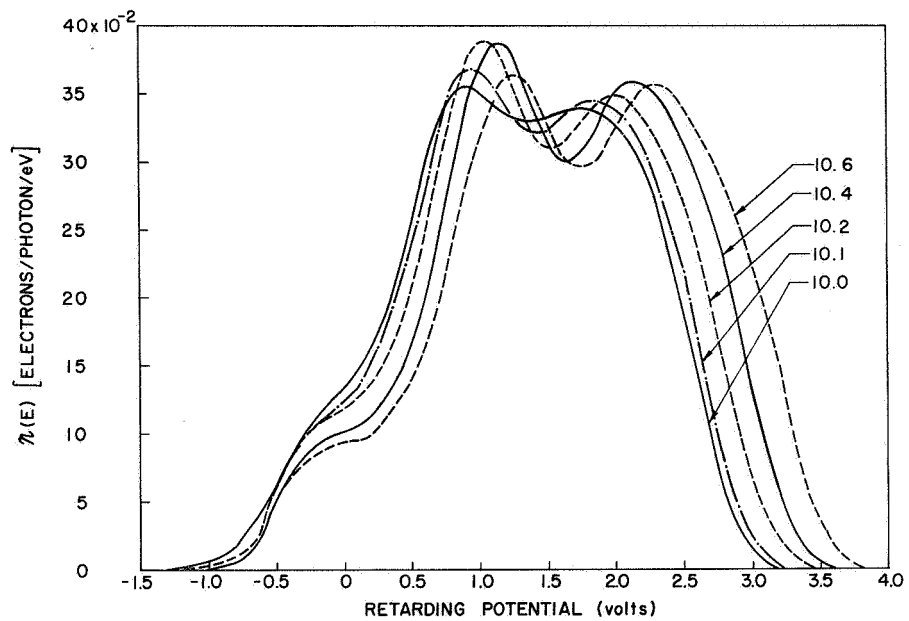


FIG. 177. ENERGY DISTRIBUTION CURVES FOR CESIUM IODIDE IN THE RANGE OF PHOTON ENERGIES BETWEEN 10.0 AND 10.6 eV.

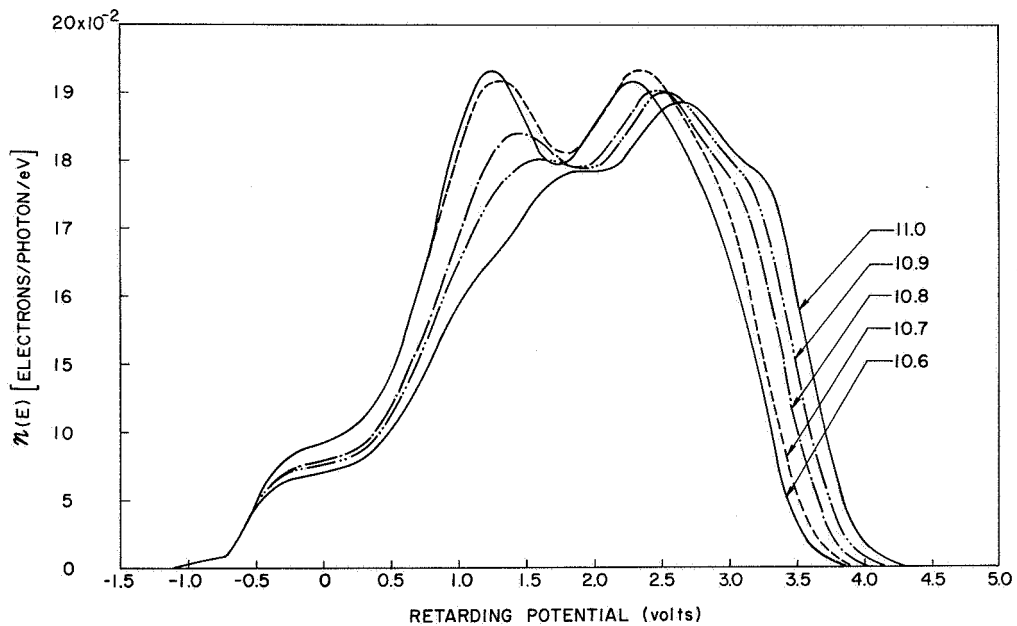


FIG. 178. ENERGY DISTRIBUTION CURVES FOR CESIUM IODIDE IN THE RANGE OF PHOTON ENERGIES BETWEEN 10.6 AND 11.0 eV.

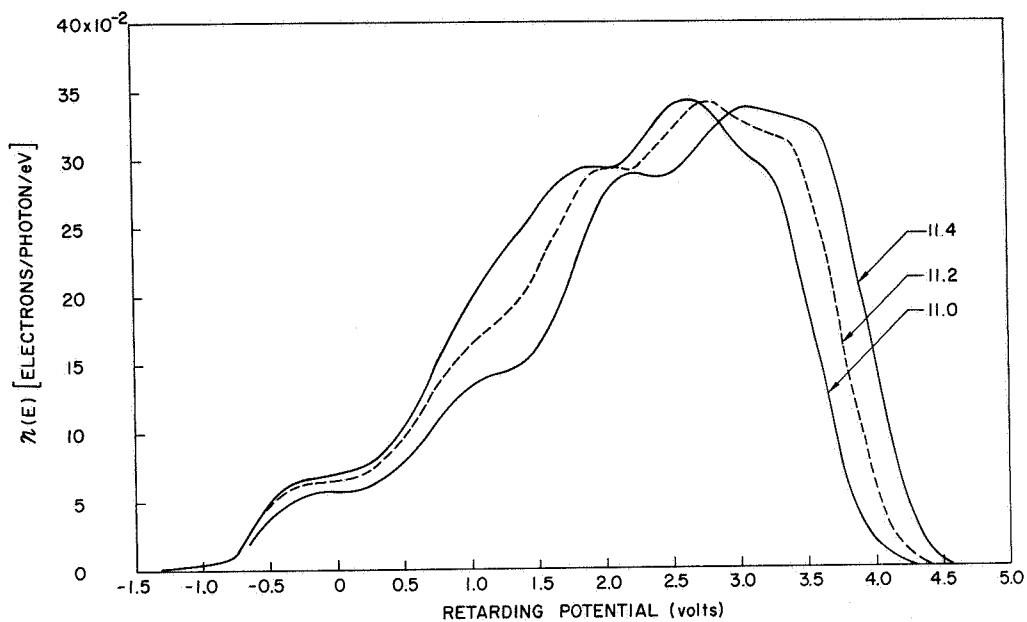


FIG. 179. ENERGY DISTRIBUTION CURVES FOR CESIUM IODIDE IN THE RANGE OF PHOTON ENERGIES BETWEEN 11.0 AND 11.4 eV.

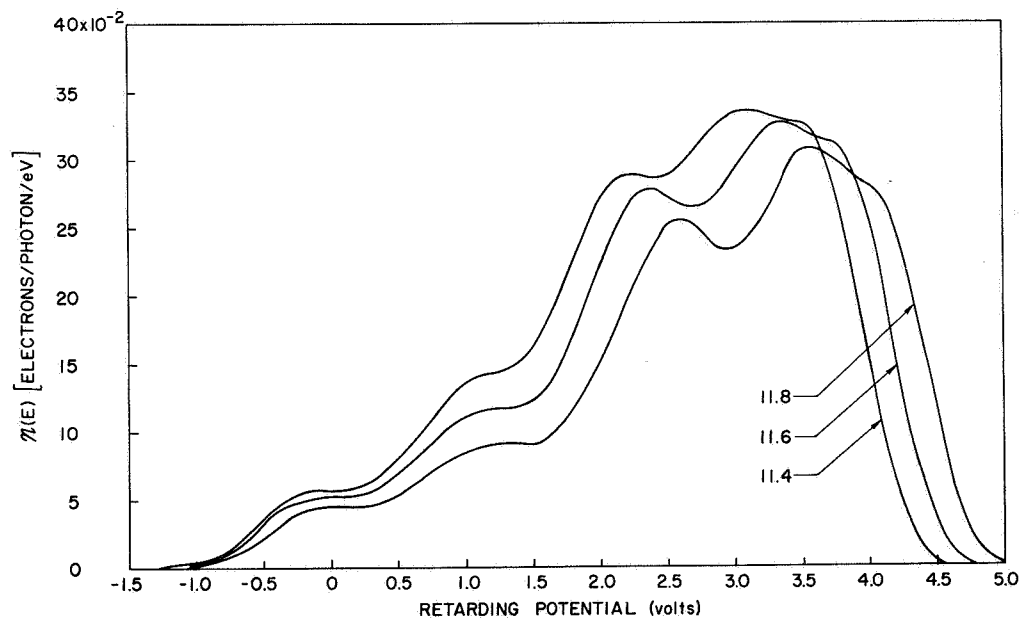


FIG. 180. ENERGY DISTRIBUTION CURVES FOR CESIUM IODIDE IN THE RANGE OF PHOTON ENERGIES BETWEEN 11.4 AND 11.8 eV.

width of about 1.5 eV, as seen from the EDC at 6.7 eV in Fig. 173. At photon energies greater than about 7.3 eV, the EDCs from CsI follow the "usual" law where $(\Delta E)_{\text{leading edge}} = \Delta h\nu$, as can be seen in the E_p vs $h\nu$ plot of Fig. 183. At photon energies below 11.8 eV, the EDCs from CsI show no evidence of inelastic electron-electron scattering, as indicated by the absence of a peak of slow electrons in the EDCs of Figs. 178, 179, and 180. EDCs from several samples of CsI are compared in Fig. 181, where it is seen that the EDCs are almost identical in shape, the only difference being that the structure is slightly "sharper" in some samples. Two EDCs from the present work are compared with the prior work of Philipp et al [Ref. 85] in Fig. 182, where the agreement between both sets of data is seen to be very good. The EDCs at 11.3 and 10.3 eV in Fig. 182 are the only EDCs obtained by Philipp et al for CsI.

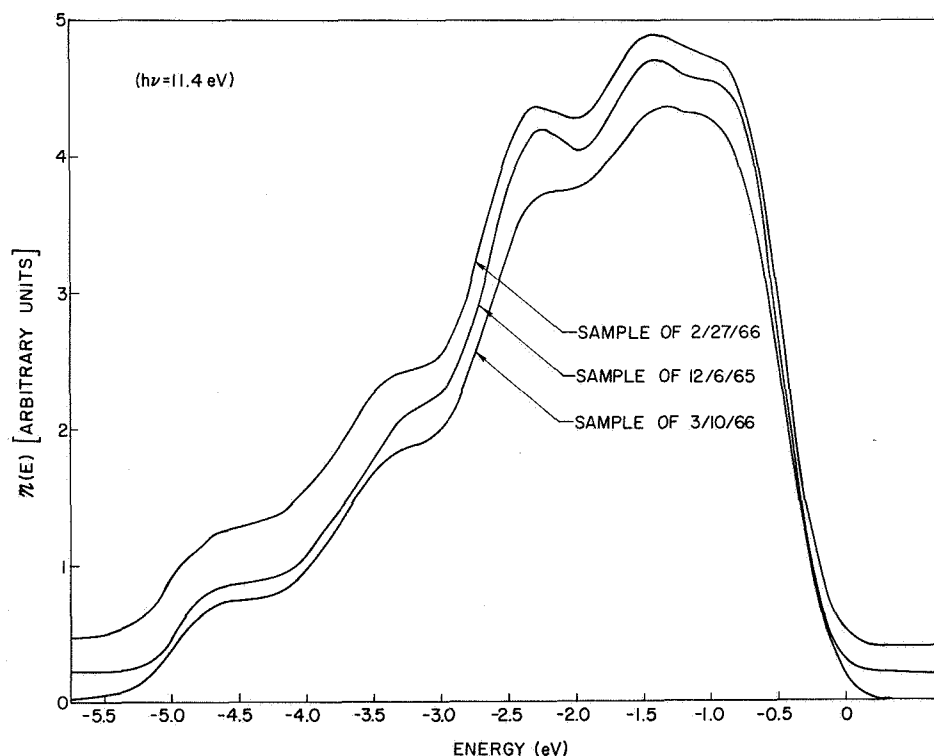


FIG. 181. COMPARISON OF THE SHAPES OF THE ENERGY DISTRIBUTION CURVES FROM SEVERAL SAMPLES OF CESIUM IODIDE.

The optical density of states for CsI is shown in Fig. 184. Except for peak (4), the optical density of states has been deduced from the photoelectric EDCs using the E_p vs $h\nu$ plot of Fig. 183 and the model

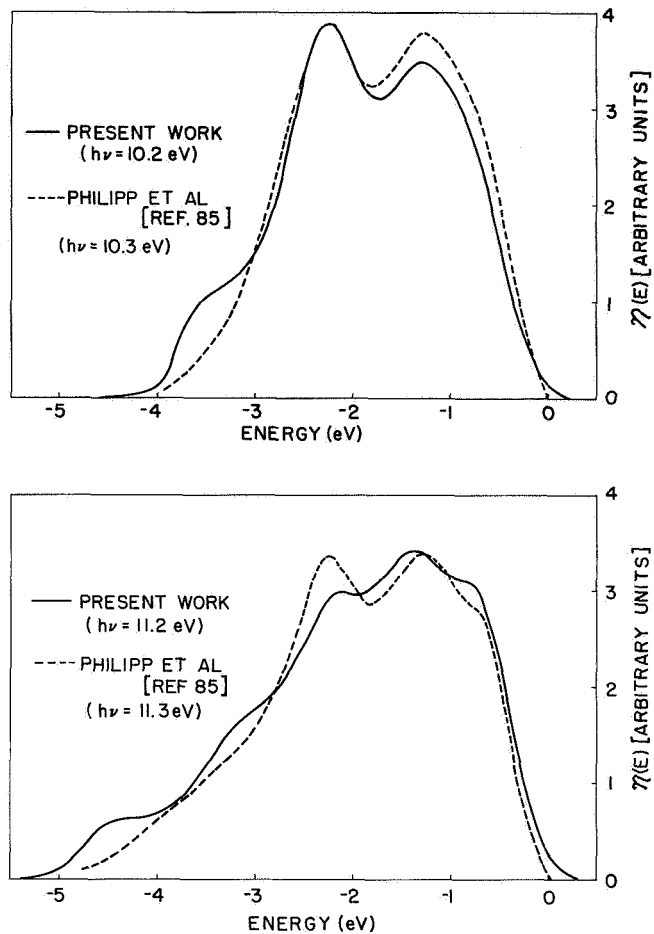


FIG. 182. COMPARISON OF SHAPES OF ENERGY DISTRIBUTION CURVES FOR CESIUM CHLORIDE. The curves at 10.3 and 11.3 eV are the only curves obtained by Philipp et al [Ref. 85] for cesium chloride.

of nondirect transitions. The location of peaks ④ in the conduction band of Fig. 184 is intended to represent the energy of the "threshold" EDCs that are observed at photon energies very close to the threshold for photoemission. The 45° lines labeled ①, ②, and ③ in Fig. 183 identify valence band peaks that follow the law $\Delta E_p = \Delta h\nu$. The valence band optical density of states in Fig. 184 is essentially a replica of the structure that follows the law $\Delta E = \Delta h\nu$ in the experimental EDCs at photon energies between 10.8 and 11.8 eV. The overall width of the valence band of CsI is about 3 eV, and the separation between peaks ① and ② corresponds closely to the atomic spin-orbit splitting, as seen

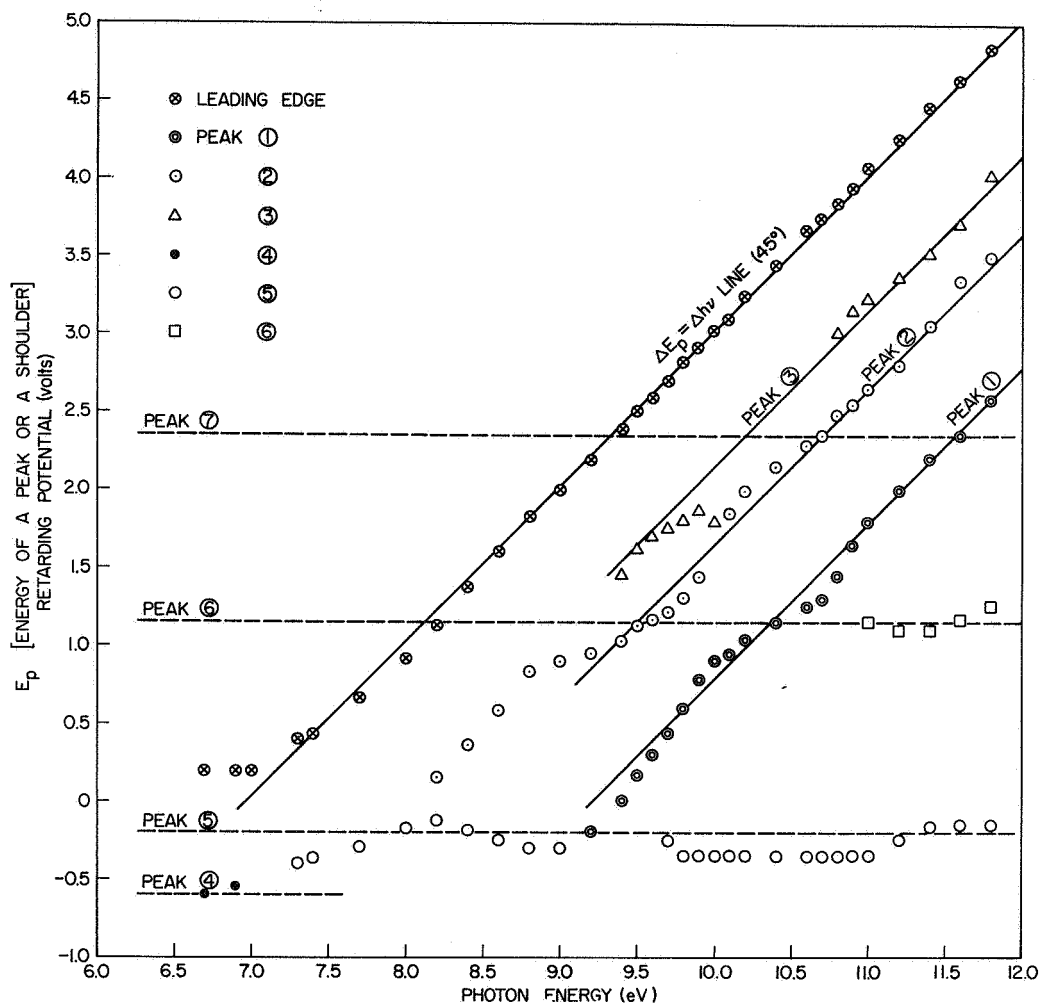


FIG. 183. E_p vs $h\nu$ PLOT FOR CUPROUS IODIDE.

in Fig. 184. In addition, it is tempting to speculate that peak (1) is associated with the nondegenerate split-off band, and that peaks (2) and (3) are associated with the doubly-degenerate split-off band.

Xenon is the inert gas that lies next to iodine in the periodic table, so the conduction band of CsI has been compared with the absorption spectrum of xenon in Fig. 184. Just as in the cases of CsCl and CsBr, there appears to be some correspondence between the absorption spectrum of the inert gas and the conduction band of the cesium halide, implying that the fundamental absorption in CsI at photon energies smaller than about 9 eV is due to excitation within the iodine ion. However, the correspondence between xenon and CsI is not as convincing as the correspondence between krypton and CsBr. In Fig. 184 the transitions

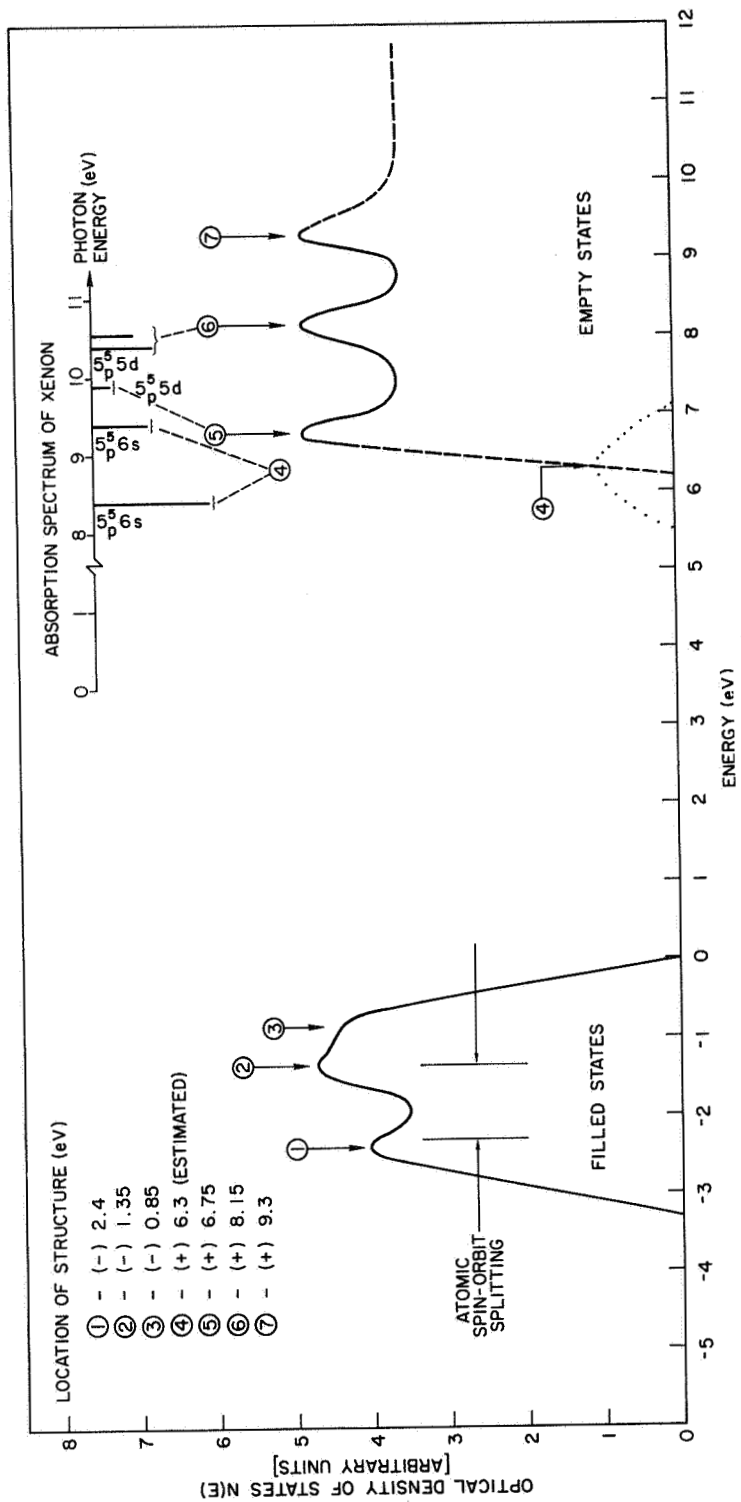


FIG. 184. ESTIMATED OPTICAL DENSITY OF STATES FOR CESIUM IODIDE.

($5p^5 6s$) have been associated with the exciton-derived states labeled (4), and a ($5p^5 5d$) transition has been associated with the strong conduction band peak (5), which is the lowest energy peak in the conduction band optical density of states.

The optical density and $\epsilon_2(\omega)$ for CsI are shown in Fig. 185. The arrows pointing upward designate the photon energies at which strong

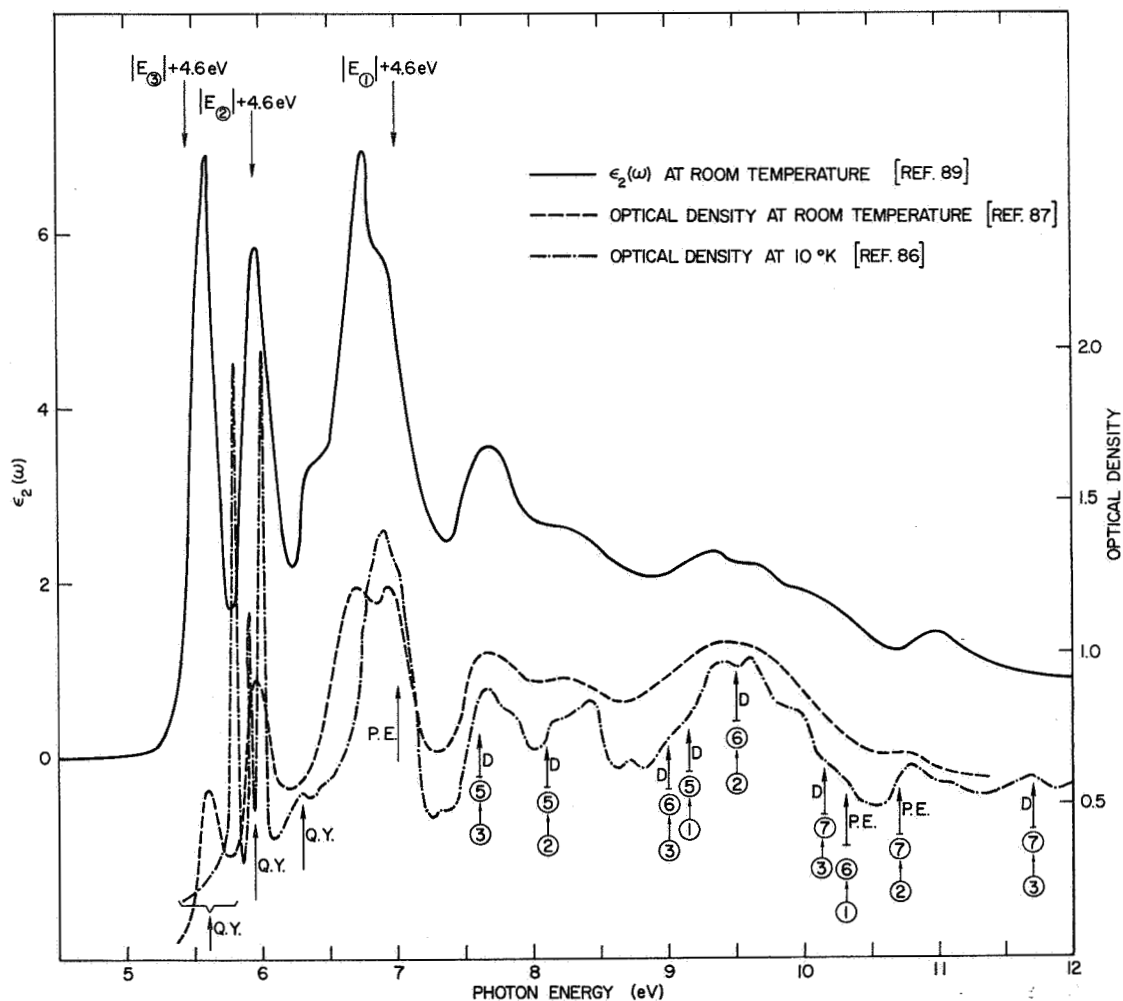


FIG. 185. OPTICAL DATA AND IDENTIFICATION OF STRUCTURE FOR CESIUM IODIDE.

transitions are evident in the experimental photoemission data. The symbols identifying the arrows are to be interpreted as follows: (1) "Q.Y." indicates structure that is evident in the quantum yield of Fig. 172; (2) "D" means that the energy of the arrow corresponds to the energy difference between structure in the valence band and structure in the conduction band of Fig. 184; (3) "P.E." means that strong transitions are evident in the photoelectric EDCs. As can be seen from Fig. 185, there is a close correspondence between the locations of the arrows deduced from photoemission data and the locations of structure in the optical data.

There appears to be an important inconsistency in the different types of optical data in Fig. 185, as can be seen by comparing Roessler's $\epsilon_2(\omega)$ with Teegarden's optical density: At a photon energy of about 6.75 eV, there is a sharp exciton-like peak in the $\epsilon_2(\omega)$ curve that is not evident in the optical density data. It is interesting to note that the energy spacings between the three exciton-like peaks in $\epsilon_2(\omega)$ correspond closely to the energy spacing between valence band peaks (1), (2), and (3), as indicated by the arrows that point downward in Fig. 185. This correspondence implies that the exciton peaks in $\epsilon_2(\omega)$ might be due to transitions from valence band peaks (1), (2), and (3) to the same final energy. This conclusion cannot be made using the optical density data, which appear to be inconsistent with the reflectivity data that were used to obtain $\epsilon_2(\omega)$.

If the work function of the metal collector is known, the location of the fermi level in the emitter can be deduced from the contact potential between the emitter and the collector, and from a knowledge of the threshold for photoemission. The contact potential is determined by inspection of the experimental EDCs, and the threshold is deduced from the quantum yield data. This has been done for one sample of CsI, and the results are shown in Fig. 186, where it is seen that the fermi level at the surface of the CsI is very close to the center of the energy gap.

Figure 187 through 189 show the EDCs measured from CsI during a knock-off tube experiment of the type described in Chapter II. Unfortunately, a copper pinch-off was not used for this experiment, and the pressure rose to about 1×10^{-5} torr when the glass stem on the knock-off

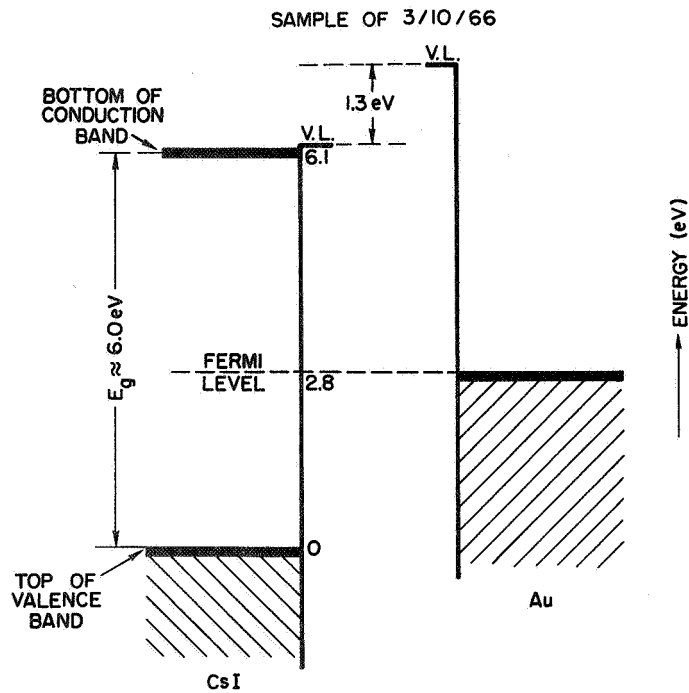


FIG. 186. LOCATION OF FERMI LEVEL IN CESIUM IODIDE.

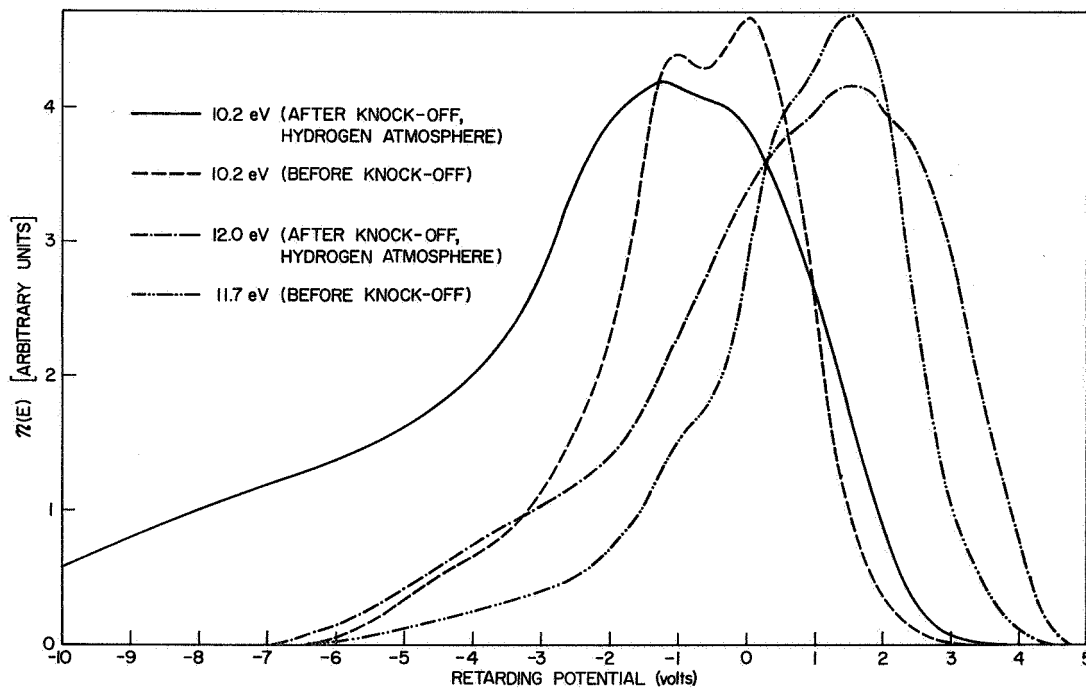


FIG. 187. ENERGY DISTRIBUTION CURVES FROM THE CESIUM IODIDE KNOCK-OFF-TUBE EXPERIMENT.

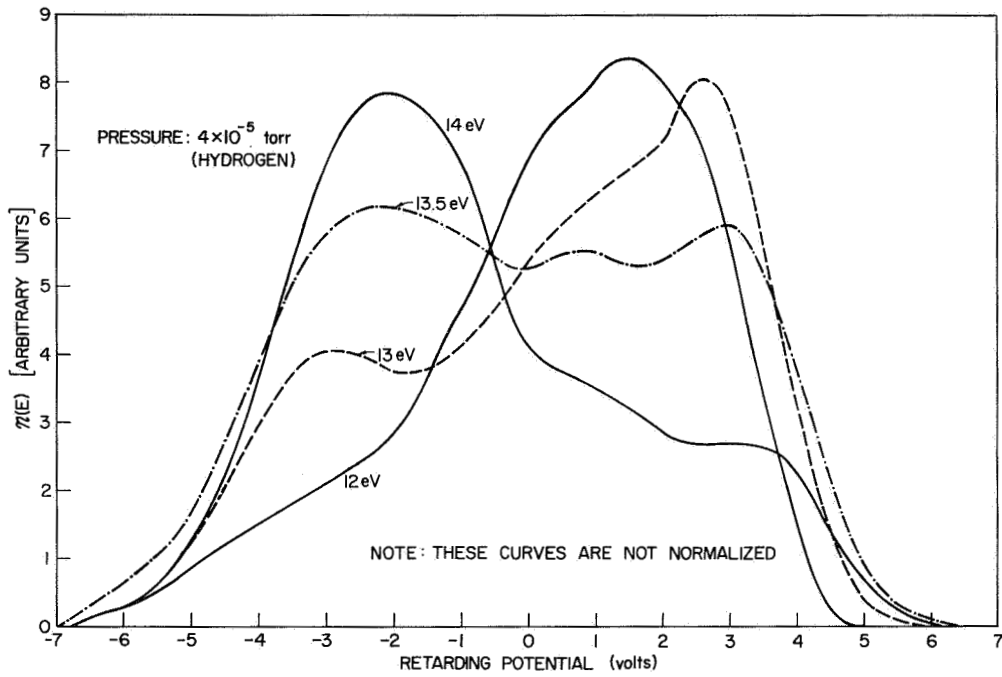


FIG. 188. ENERGY DISTRIBUTION CURVES FOR CESIUM IODIDE (KNOCK-OFF-TUBE EXPERIMENT).

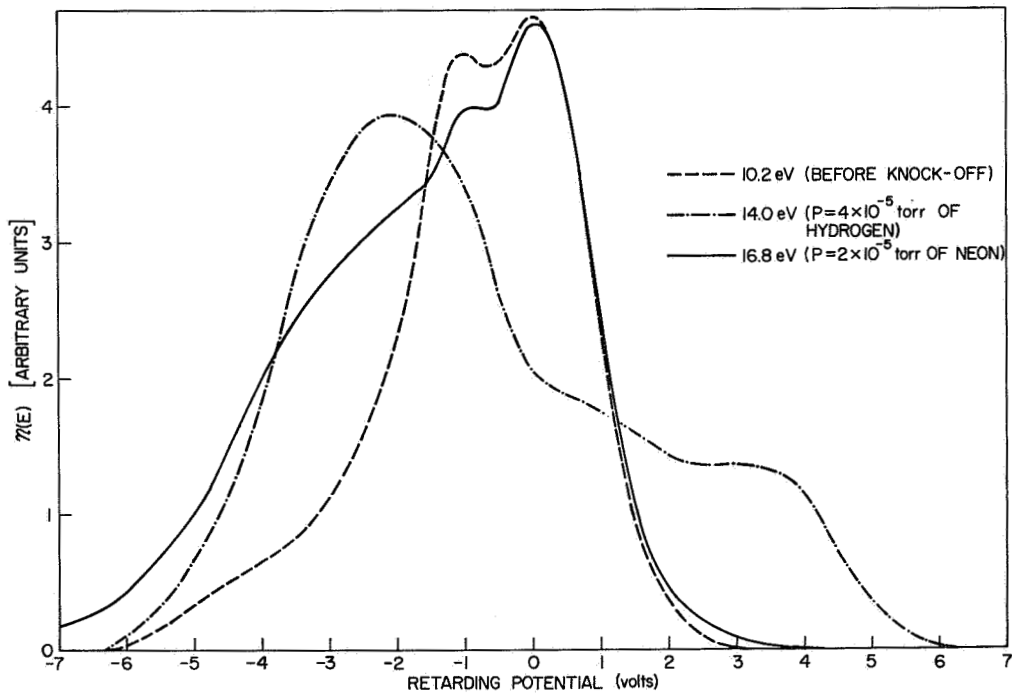


FIG. 189. ENERGY DISTRIBUTION CURVES FROM THE CESIUM IODIDE KNOCK-OFF-TUBE EXPERIMENT.

tube was sealed off with a torch. Consequently, the CsI film was somewhat contaminated, and the EDCs measured before the LiF window was knocked off, had a long, low energy tail, as shown in Fig. 187. In spite of the contaminations, some very interesting phenomena were observed during this experiment. As shown in Figs. 187 and 188, the "after knock-off" EDCs tended to follow the law $\Delta E_p = \Delta h\nu$ for photon energies up to about 13.0 eV. At 13.0 eV, a low energy peak of scattered electrons becomes evident in the EDCs, thus signifying the onset of inelastic scattering between the photoexcited electrons and the valence electrons. As seen from the sequence of EDCs between 13 and 14 eV in Fig. 188, the low energy peak of scattered electrons grows in amplitude at the expense of the high energy peak, as the photon energy increases from 13 to 14 eV. This evidence for severe electron-electron scattering at 14 eV is consistent with the quantum yield of Fig. 171, which has a dip at about 14 eV.

The "windowless" EDCs in Figs. 187 and 188 were measured in a hydrogen atmosphere, and do not seem to have the detailed structure that is seen in Fig. 189 for the EDC at 16.8 eV, which was measured in a neon atmosphere. Apparently the hydrogen diffuses into the CsI and scatters with the photoexcited electrons, resulting in a blurring of the detailed structure in the EDCs. The same effect was observed in a knock-off experiment on gold. In Fig. 189 it is important to note that no high energy electrons are evident in the EDCs, indicating that the electron-electron scattering length is very much smaller than the absorption depth. In addition, note that the structure in the EDC for $h\nu = 16.8$ eV seems to coincide almost exactly with the structure in the "before knock-off" EDC for $h\nu = 10.2$ eV. Thus it appears that the EDC at $h\nu = 16.8$ eV retains its shape after the inelastic electron-electron scattering takes place. (The structure in the EDC at $h\nu = 10.2$ eV is a fairly close representation of the valence band optical density of states.) The EDC at 16.8 eV can retain the shape of the valence band density of states after collision only if every photoexcited electron loses an energy equal to exactly $(16.8 - 10.2) = 6.6$ eV. The value of 6.6 eV is a good approximation to the energy gap of CsI, and also seems to correspond to the energy of a strong peak in the optical data, as seen in Fig. 185. Since all the photoexcited electrons appear to lose 6.6 eV, and the electron-

scattering length is very short, it is tempting to propose the following atomic-like mechanism for the electron-electron scattering event in CsI: Since the conduction band of CsI below 9 eV seems to correspond to the absorption spectrum of xenon, and since the peak in the optical data at 6.6 eV seems to correspond to a $(5p^5 6s^1)$ atomic transition, it may be that the preferential energy loss of 6.6 eV in the energy of the photo-excited electrons is due to the strong probability for the valence electrons to make the $(5p^5 6s^1)$ atomic-like transition. This mechanism would explain the apparent discrete loss of 6.6 eV, and the strength of the peak in the optical density at 6.6 eV would suggest a strong probability for the $(5p^5 6s^1)$ transition, which would result in a short lifetime and a short scattering length.

D. PHOTOEMISSION STUDIES OF POTASSIUM IODIDE

A film of KI was evaporated in a vacuum of 2×10^{-9} torr, and a complete set of EDCs and good quantum yield data were obtained within a few hours after the evaporation. During this time, the EDCs seemed to deteriorate in two ways: (1) The fermi level shifted several tenths of an eV; (2) a long, low energy "tail" began to appear in the EDCs. The shift in the fermi level is indicative of a charging effect, and the long, low energy tail is characteristic of a material that has a very high resistance. These effects might have been caused by such mechanisms as (1) diffusion of a foreign gas into the KI; (2) surface charging due to ultraviolet radiation; (3) bulk changes in the nature of the KI films. Fortunately, the deterioration of the EDCs was only slight during the period of measurement, and meaningful results were obtained from the photoemission data. During the several weeks following the original measurements, the experiment was discontinued due to the absence of the author. Several lengthy power shutdowns occurred during this period, and the vacuum in the photoemission chamber undoubtedly became quite poor. At the end of this time, the KI film had become highly insulating, and "normal" EDCs could not be measured. Interestingly enough, the quantum yield in the insulating state was somewhat higher than the quantum yield in the conducting state when a sufficiently large voltage (≈ 14 v) was applied. A possible explanation for this increase in quantum yield might

be that a foreign gas diffused into the KI and acted as a trap for carriers. Subsequent heating of the sample returned the KI to its original conducting state, perhaps because the heat drove the foreign gas out of the KI. The experimental data recorded during the sequence of events described above will be presented in this section.

The quantum yield for the conducting and insulating states of KI are shown in Fig. 190. The quantum yield for the insulating state reaches a

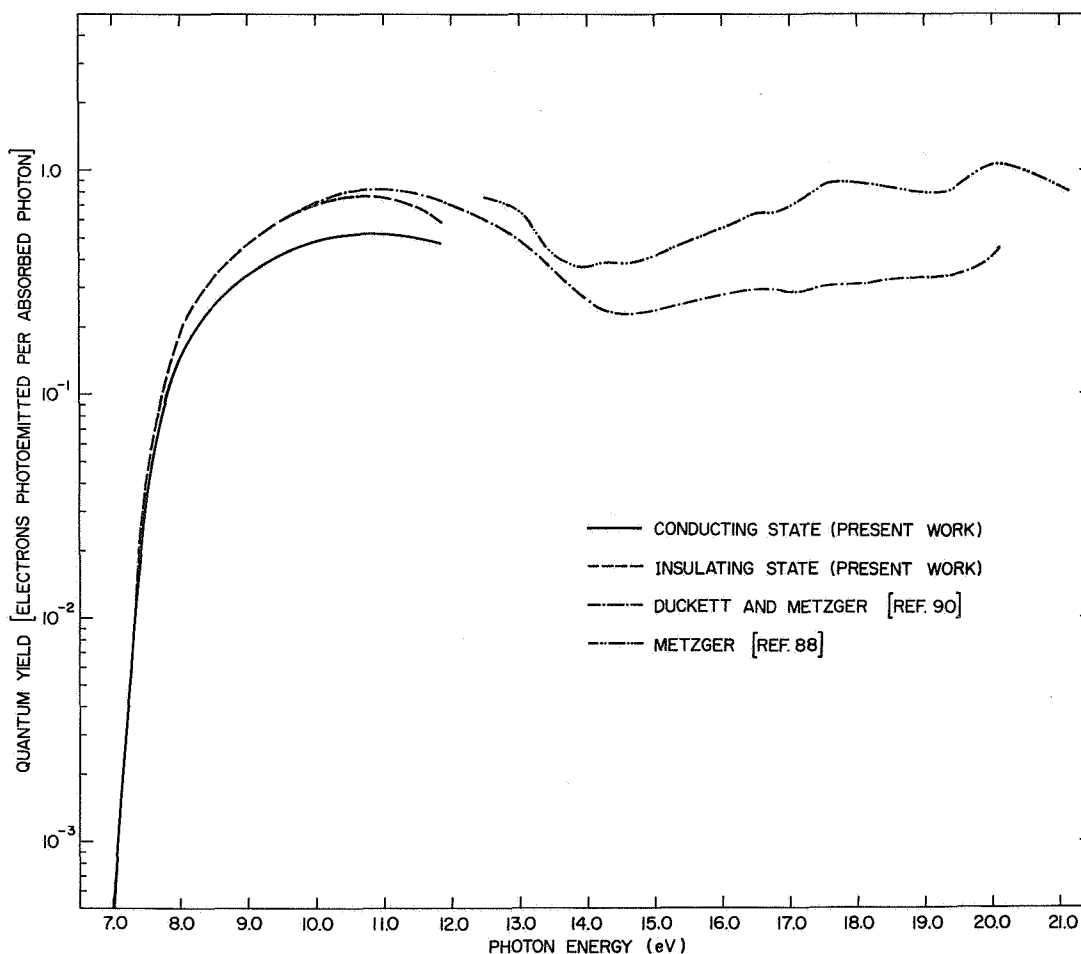


FIG. 190. QUANTUM YIELD FOR POTASSIUM IODIDE. The data labeled "present work" was obtained using R. Koyama's calibration curve dated 11-9-66. The "present work" curves were corrected for reflectivity using the data of Roessler.

maximum of 0.80 at 10 eV, and the quantum yield of the conducting state reaches a maximum of about 0.50 at 10 eV. The maximum yield of 0.50 for the conducting state suggests that the photoexcited electrons with initial velocities directed away from the surface did not suffer electron-phonon collisions, and consequently were not turned around before being collected by the metal substrate. The increased yield in the insulating state may be due to foreign gas atoms that trap the photoexcited electrons; the positive collector voltage then provides a strong enough field in the KI film to tear the photoexcited electrons away from the traps and cause the electrons to be photoemitted. The magnitude of the quantum yield of the insulating KI is in very good agreement with the data of Duckett and Metzger, as seen in Fig. 190. This close agreement suggests that Duckett and Metzger measured the quantum yield of insulating KI, and not the quantum yield of conducting KI.

The EDCs for the conducting KI film are shown in Figs. 191 through 195. As mentioned earlier, the fermi level of the KI film changed by

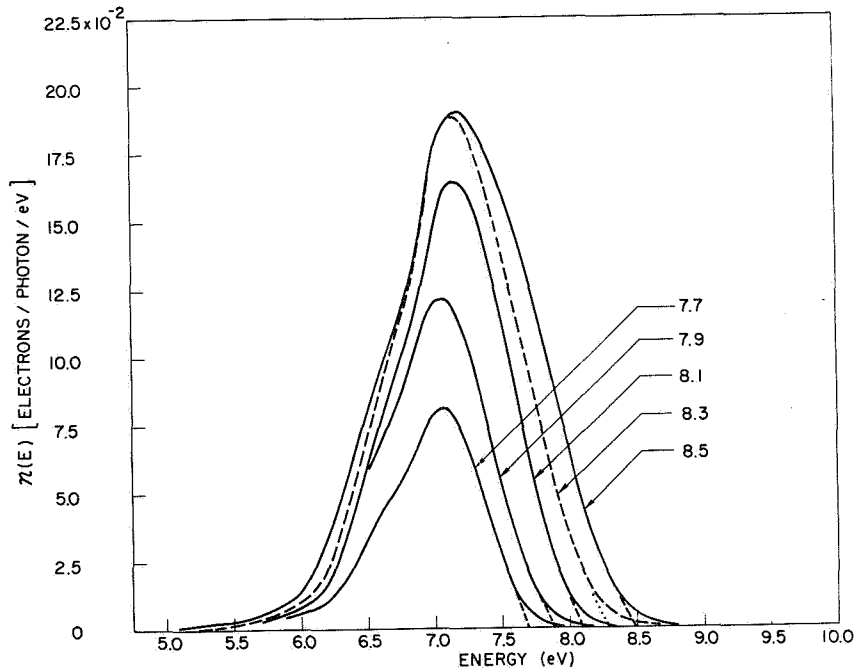


FIG. 191. ENERGY DISTRIBUTION CURVES FOR POTASSIUM IODIDE IN THE RANGE OF PHOTON ENERGIES BETWEEN 7.7 AND 8.5 eV.

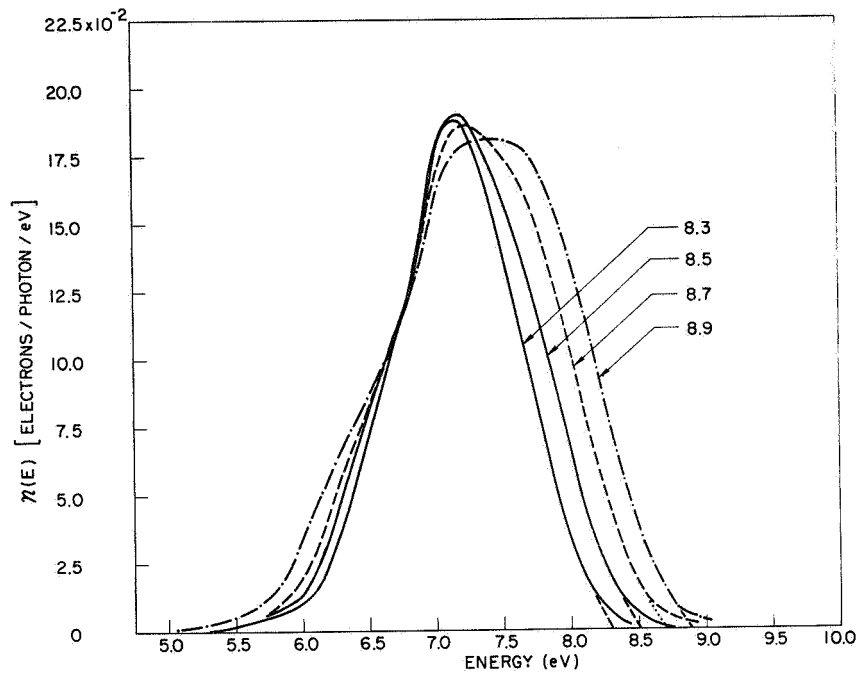


FIG. 192. ENERGY DISTRIBUTION CURVES FOR POTASSIUM IODIDE IN THE RANGE OF PHOTON ENERGIES BETWEEN 8.3 AND 8.9 eV.

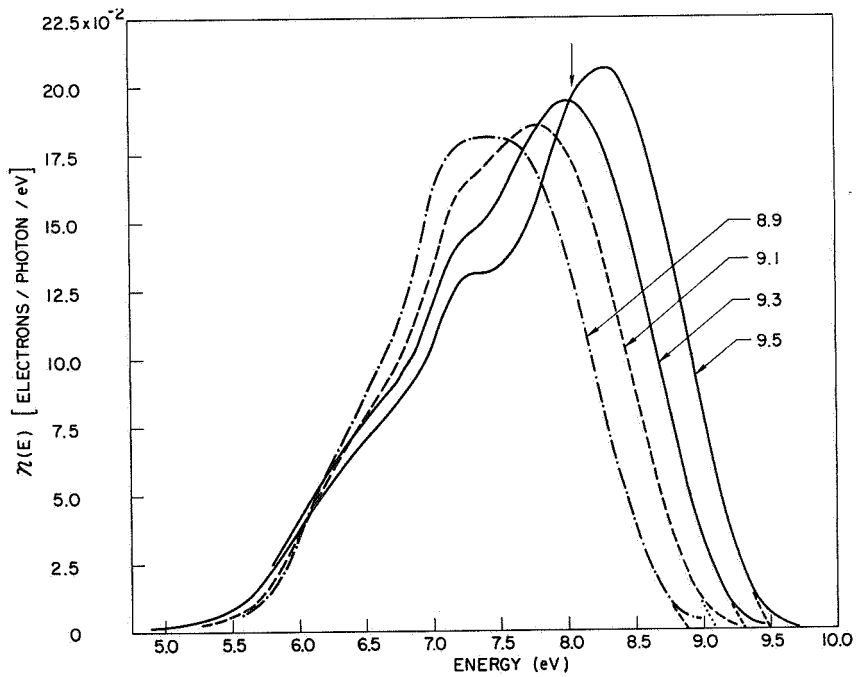


FIG. 193. ENERGY DISTRIBUTION CURVES FOR POTASSIUM IODIDE IN THE RANGE OF PHOTON ENERGIES BETWEEN 8.9 AND 9.5 eV.

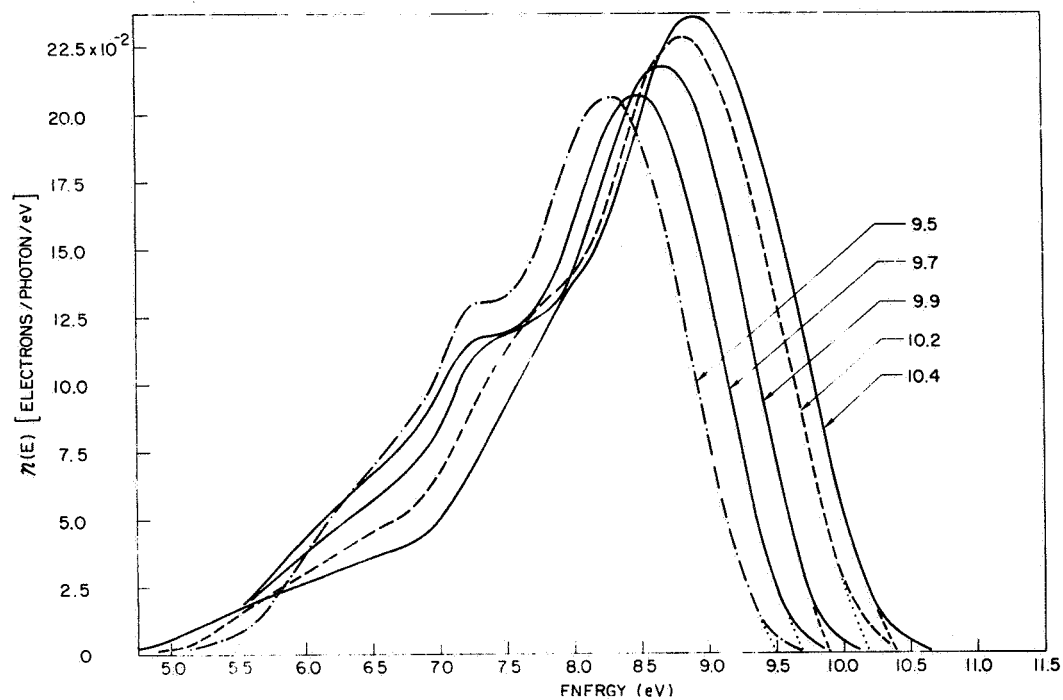


FIG. 194. ENERGY DISTRIBUTION CURVES FOR POTASSIUM IODIDE IN THE RANGE OF PHOTON ENERGIES BETWEEN 9.5 AND 10.4 eV.

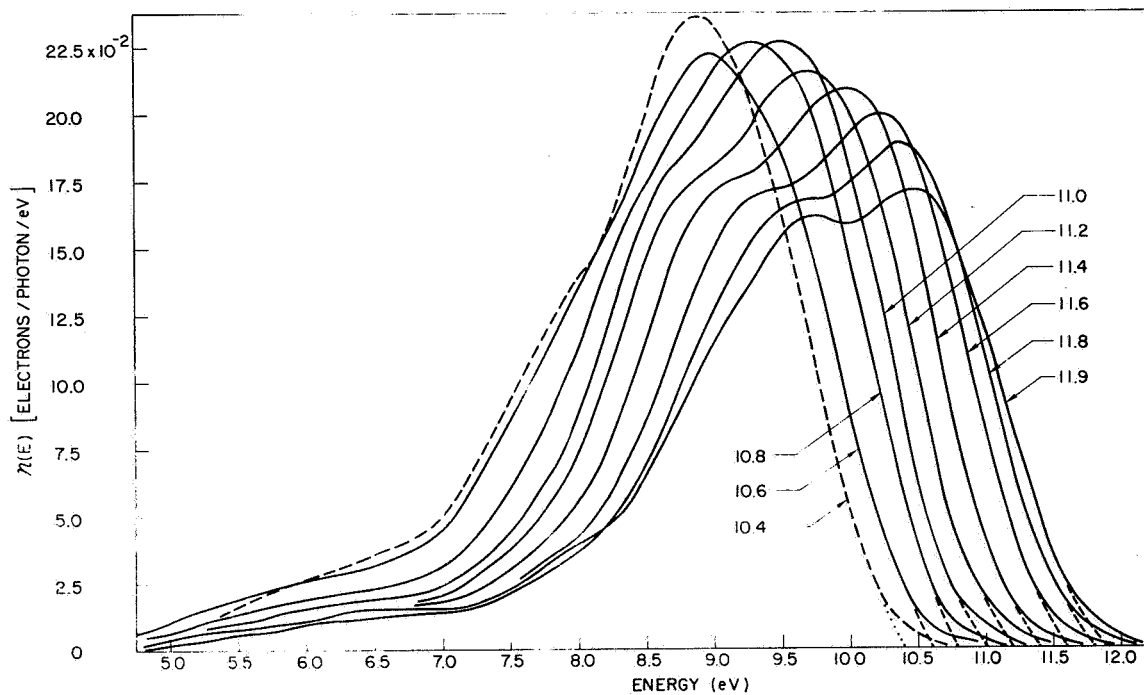


FIG. 195. ENERGY DISTRIBUTION CURVES FOR POTASSIUM IODIDE IN THE RANGE OF PHOTON ENERGIES BETWEEN 10.4 AND 11.9 eV.

several tenths of an eV during the course of measurements. Consequently, the energy of the EDCs relative to the collector was constantly changing. In order to circumvent this difficulty, it has been assumed that the EDCs in the range of photon energies between 7.7 and 11.9 eV follow the law $(\Delta E)_{\text{leading edge}} = (\Delta h\nu)$. Consequently, the EDCs have been put on the same energy scale in Figs. 191 through 195 by locating the leading edge of each EDC at an energy corresponding to the photon energy.

In Fig. 196 an EDC from the present work is compared with the only EDC obtained by Philipp et al [Ref. 85]; the agreement between the shapes of both curves is seen to be very good.

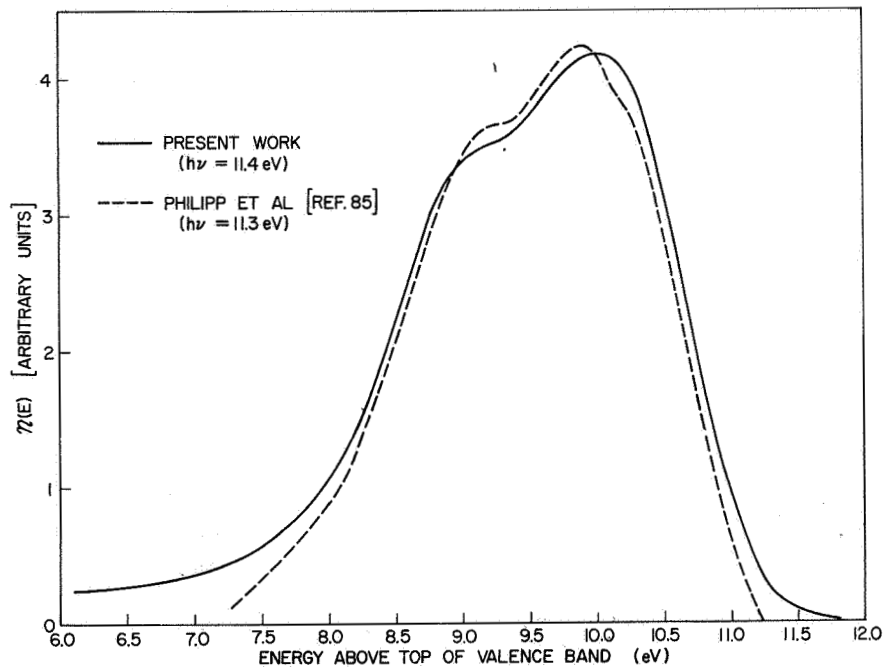


FIG. 196. COMPARISON OF PRESENT WORK WITH THE WORK OF PHILIPP, TAFT, AND APKER. The energy distribution curve at 11.3 eV is the only curve obtained by Philipp, Taft, and Apker. Only the shapes of the energy distribution curves are significant.

An E_p vs $\Delta h\nu$ plot for KI is shown in Fig. 197, and the optical density of states for KI is shown in Fig. 198. As seen from Figs. 195 and 197, there are two valence band peaks labeled ① and ② that follow the law $\Delta E_p = \Delta h\nu$. In addition to the valence band peaks, there are

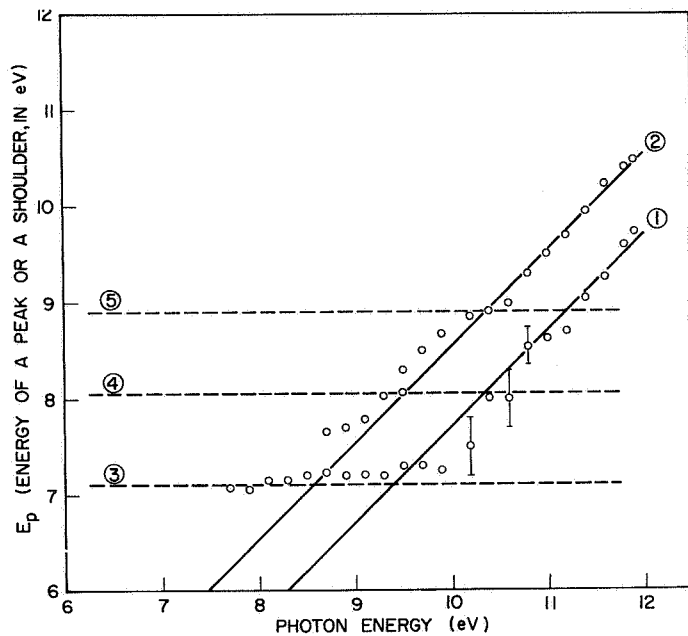


FIG. 197. E_p vs $h\nu$ FOR POTASSIUM IODIDE.

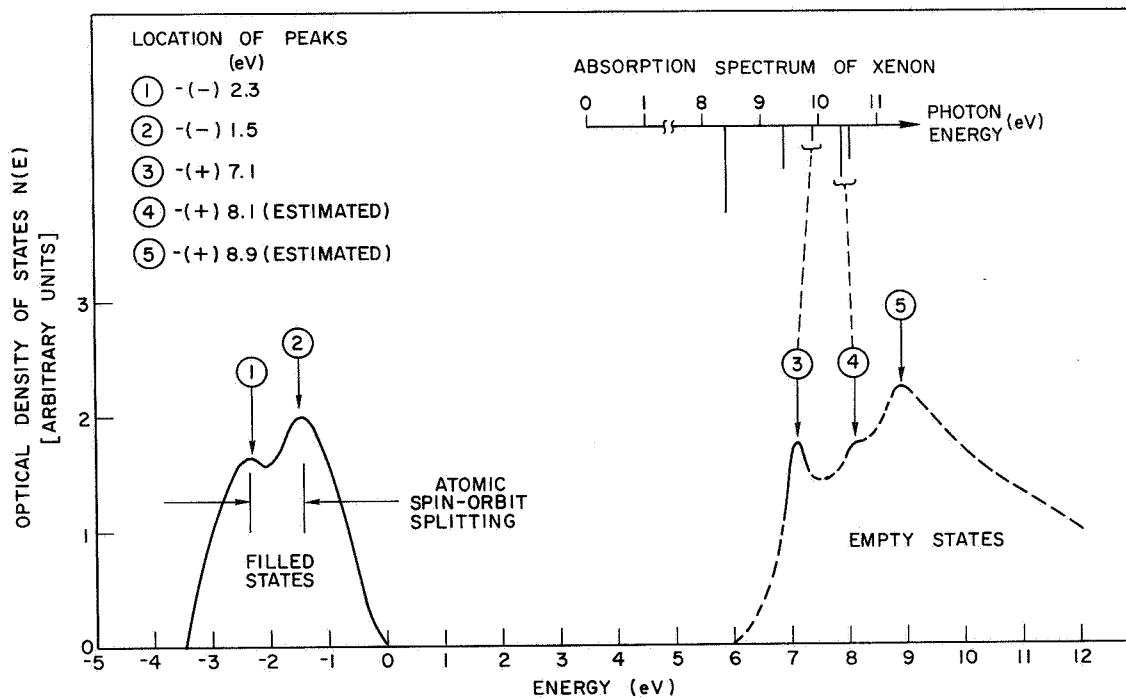


FIG. 198. ESTIMATED OPTICAL DENSITY OF STATES OF POTASSIUM IODIDE. The conduction band of potassium iodide is compared with the absorption spectrum of xenon (Teegarden and Baldini).

three conduction band peaks evident in the EDCs. Conduction band peak (3) is easily detected as the fixed peak at about 7.1 eV in Figs. 191, 192, and 193. Peak (5) is located at about 8.9 eV in Figs. 194 and 195; since the amplitudes of the EDCs tend to peak at 8.9 eV. Conduction band shoulder (4) is somewhat more difficult to locate, but can be readily identified as a shoulder at about 8.05 eV in the EDCs at $h\nu = 9.5$ eV, 9.7 eV, and 10.4 eV. In addition, the amplitudes of the EDCs tend to increase in magnitude in the vicinity of 8.05 eV, as seen in Figs. 193 and 194.

As shown in Fig. 198, the separation between valence band peaks (1) and (2) corresponds closely to the atomic spin-orbit splitting, just as in the case of CsI. Note that the conduction band structure in KI closely resembles the conduction band structure in CsI (Fig. 184), indicating that the conduction bands of both KI and CsI are due largely to the iodine ion, and not to the cesium ion or the potassium ion. The absorption spectrum of xenon is compared with the conduction band of KI in Fig. 197. Since the conduction band of KI is similar to the conduction band of CsI, the associations that were made between CsI and xenon have also been made between KI and xenon.

The optical density of KI is shown in Fig. 199 where the arrows indicate the photon energies at which strong transitions are seen in the photoelectric EDCs. The correspondence between the location of the arrows and structure in the optical density is quite good, indicating that the strong transitions seen in the EDCs are representative of the fundamental absorption process.

EDCs from the insulating state of KI are shown in Figs. 200, 201, and 202, where we see that positive collector voltages of more than 14 volts are required to collect all the photoexcited electrons in insulating KI. There is considerable structure in the "insulating" EDCs, and at photon energies greater than 11.0 eV, the EDCs from insulating KI bear a close resemblance to the EDCs from conducting KI, as seen in Fig. 202. Apparently, in "insulating" KI the electrons excited to low energies are somehow "trapped" and are not photoemitted, whereas the electrons excited to high energies are not as tightly bound by the traps and are photoemitted in the normal manner.

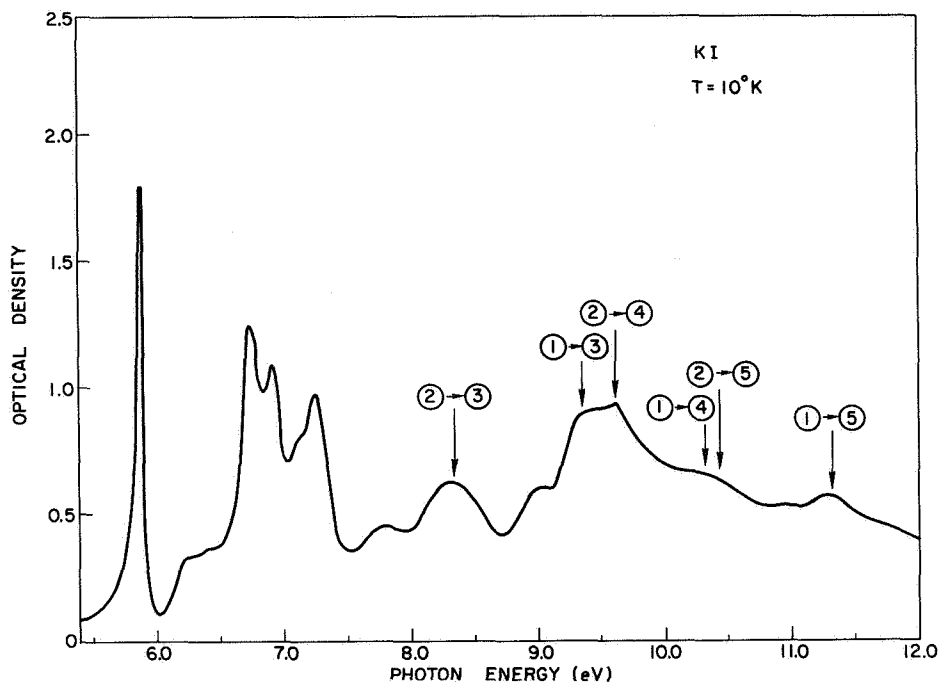


FIG. 199. OPTICAL DENSITY OF POTASSIUM IODIDE [TEEGARDEN AND BALDINI, REF. 86]. The arrows locate photon energies at which strong transitions are seen in the photoelectric energy distribution curves. The labels of the arrows identify the initial and final states involved in the transition (see Fig. 198).

Heating the insulating KI apparently drove the "traps" out of the KI, and the KI film returned to its normal conducting state. Figure 203 shows that after heating, the EDCs from the KI film were essentially identical to the EDCs measured from the freshly prepared KI film.

E. CONCLUSION

The photoemission data presented in this chapter have led to the construction of energy level diagrams locating the absolute energy of valence and conduction states in CsCl, CsBr, CsI, and KI. In addition, the photoemission data have led to the identification of the initial and final states involved in much of the structure in the optical spectra of these materials. The apparent correspondence between the conduction

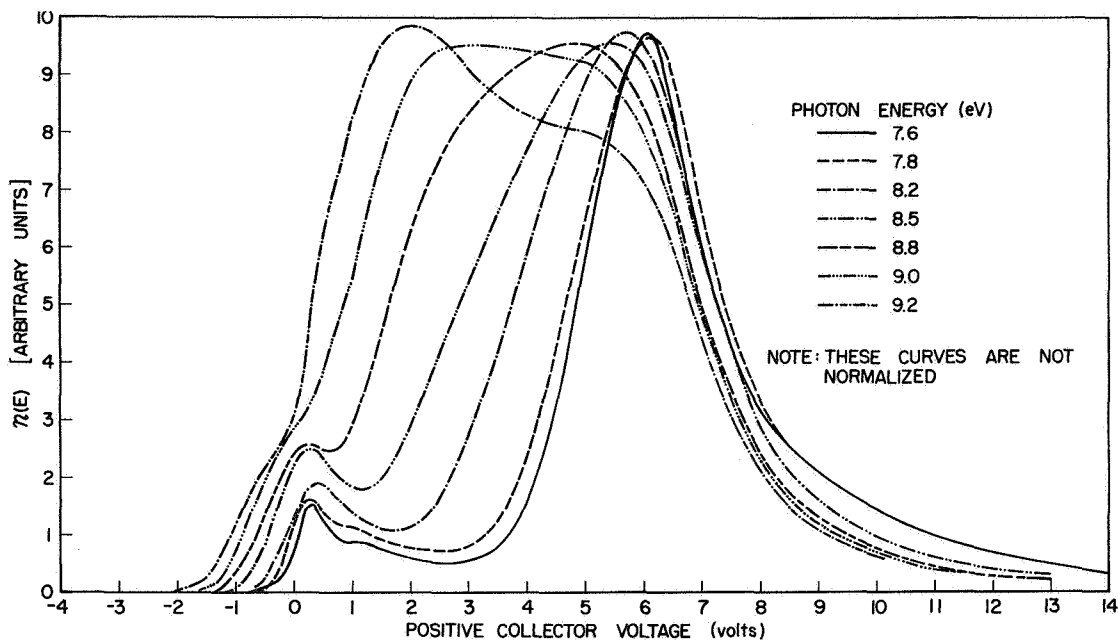


FIG. 200. ENERGY DISTRIBUTION CURVES FOR INSULATING POTASSIUM IODIDE IN THE RANGE OF PHOTON ENERGIES BETWEEN 7.6 AND 9.2 eV.

bands of these materials and the absorption spectra of the corresponding inert gases suggests that the fundamental absorption is due largely to excitation within the halogen ion. The observation that the conduction band of KI is similar to the conduction band of CsI supports the contention that the conduction bands in these materials are derived largely from the halogen states.

The results of this chapter indicate that photoemission is an excellent tool for investigating the electronic structure of the alkali halides, and it is hoped that the successes of the present study will stimulate future workers to undertake more complete and exhaustive photoemission studies of the alkali halides than has been possible during the present work.

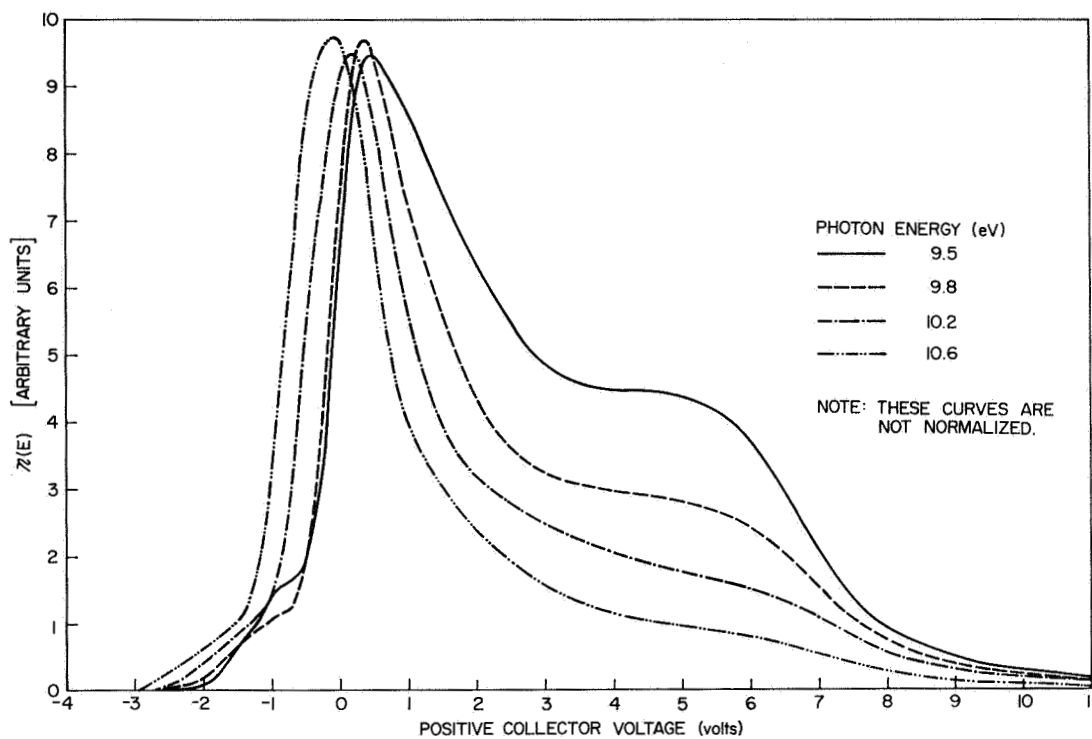


FIG. 201. ENERGY DISTRIBUTION CURVES FOR INSULATING POTASSIUM IODIDE IN THE RANGE OF PHOTON ENERGIES BETWEEN 9.5 AND 10.6 eV.

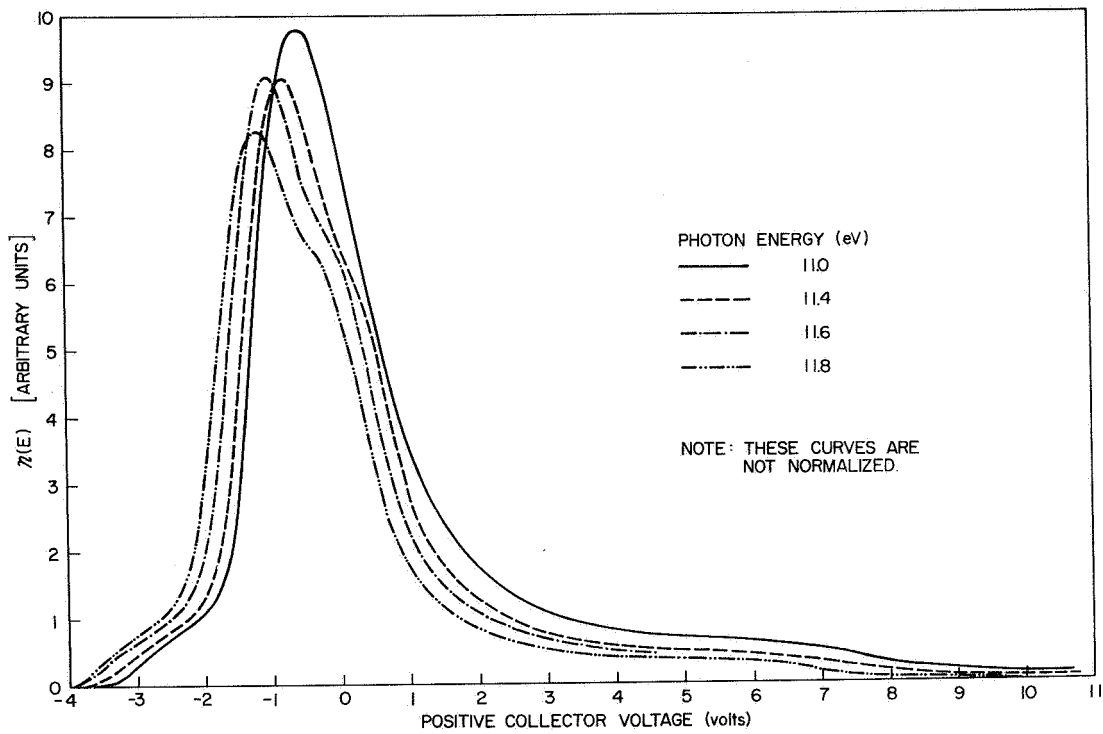


FIG. 202. ENERGY DISTRIBUTION CURVES FOR INSULATING POTASSIUM IODIDE IN THE RANGE OF PHOTON ENERGIES BETWEEN 11.0 AND 11.8 eV.

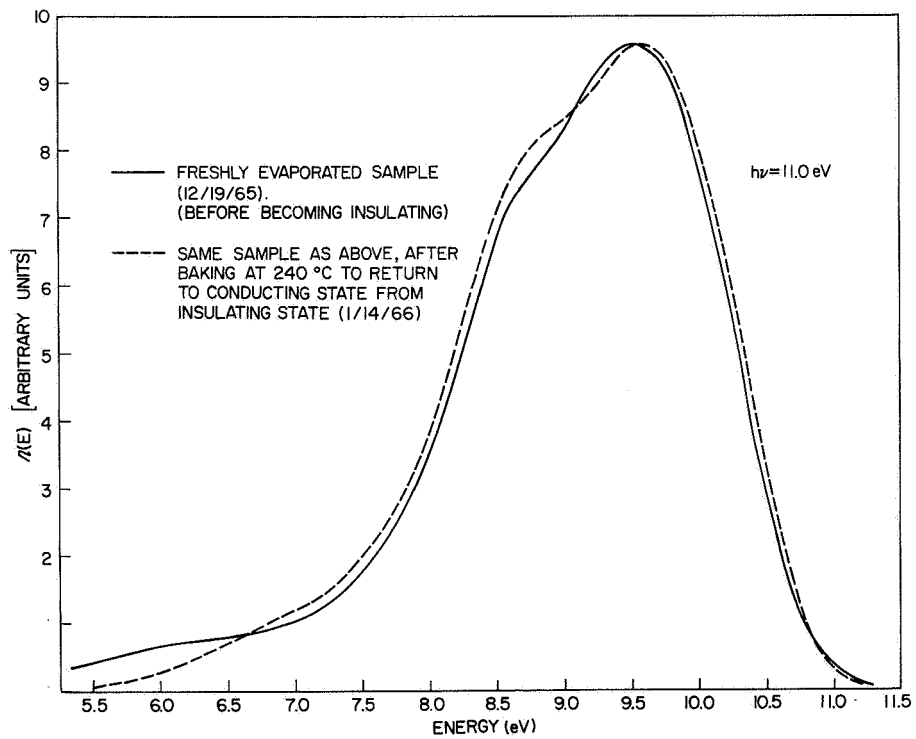


FIG. 203. COMPARISON OF ENERGY DISTRIBUTION CURVES BEFORE AND AFTER POTASSIUM IODIDE SAMPLE BECAME INSULATING. The curves are not normalized or fitted. Only the shapes are significant.



X. A COMPARISON OF THE NOBLE METALS, THE CUPROUS HALIDES, AND THE ALKALI HALIDES

The photoemission characteristics of the noble metals, the cuprous halides, and the alkali halides have a significant common property: In no case are the majority of the energy distributions characterized by the type of transition that would be expected from direct transitions between single Bloch states.

For the noble metals and the cuprous halides, the bulk of the EDCs are well described by nondirect transitions, in which $\Delta E = \Delta h\nu$. This appears to be especially true of transitions from the valence d bands, perhaps as a consequence of the localized nature of the d wavefunctions. Although nondirect transitions dominate in the noble metals, there is evidence of direct transitions between initial and final states derived largely from s- and p-like wavefunctions. In the noble metals, the initial states involved in direct transitions are located between the fermi level and about 2 eV below the fermi level. In the cuprous halides, the bulk of the EDCs are also well described by nondirect transitions, a notable exception being the transitions from the upper p band,¹ which seem to follow the law $\Delta E = \Delta h\nu$ only at high photon energies. Transitions from the deeper lying states in the cuprous halides seem to follow the model of nondirect transitions quite well at all photon energies; in the notation of Chapter VIII, these deeper lying states consist of the following structures: Peak (1), the deepest lying peak, which is due to states derived largely from d wavefunctions; and Peak (2), which is due to states derived largely from p wavefunctions, with the likelihood of considerable p-d mixing. Thus, in the noble metals and the cuprous halides, it appears that transitions from deep-lying states associated with d wavefunctions are almost always nondirect, whereas certain transitions from the higher lying s- and p-derived states² do not follow the

¹Labeled peak (3) in the notation of Chapter VIII.

²N. Smith [Ref. 93] has suggested that, because the relaxation time of the "hole" associated with the deeper lying valence state is likely to be shorter than the relaxation time of the hole associated with the higher lying valence states, the deeper lying levels are less likely to be well described by a single Bloch state than are the higher lying states. The relaxation time involved would be the relaxation time associated with the Auger process described earlier by Berglund [Ref. 7].

model of nondirect transitions at low photon energies. At high photon energies, all the transitions seem to be nondirect, even those from s- and p-derived states. The nondirect nature of the transitions from s- and p-derived states at high photon energies may be associated with the very short scattering lengths at energies well above the fermi level, since the very short lifetimes associated with these short scattering lengths require a more complex description of the final state than does a single Bloch state.

In the alkali halides studies in this report, the optical transitions and the EDCs seem to be much more complex than in the noble metals and the cuprous halides. One interesting feature is the strange "threshold photoemission" that may be associated in some way with excitons. In addition, there is considerable modulation of the EDCs due to conduction band structure, making interpretation of the EDCs quite difficult. As discussed in Chapter IX, a possible explanation of the complicated behavior of the alkali halides is that the fundamental absorption process in the alkali halides may be more governed by "atomic-like" selection rules than by "band-like" selection rules. Another point of possible significance is that the EDCs for the alkali halides tend to be more nondirect at high photon energies than at low photon energies, just as was found to be the case for direct transitions from s- and p-derived states in the noble metals and the cuprous halides.

In addition to trends in the optical absorption process, a comparison of the materials studied in this report reveals an interesting characteristic in the electronic structure of the cuprous halides [Ref. 81]. As a first approximation, the optical density of states for the cuprous halides can be constructed by simply adding the optical density of states of copper to the optical density of states of the appropriate cuprous halide. This additive feature suggests that for these materials, the nature of the constituent atom may be more important than the long range periodicity in determining the energy level structure. Justification for this statement can be seen in Fig. 204, where the optical densities of states of Cu, CuI, CsI, and KI are compared. As seen in Fig. 204, the strong peak ① in CuI corresponds to the strong 3d band peak in Cu, whereas the structure in the vicinity of peaks ② and ③ in CuI corresponds closely

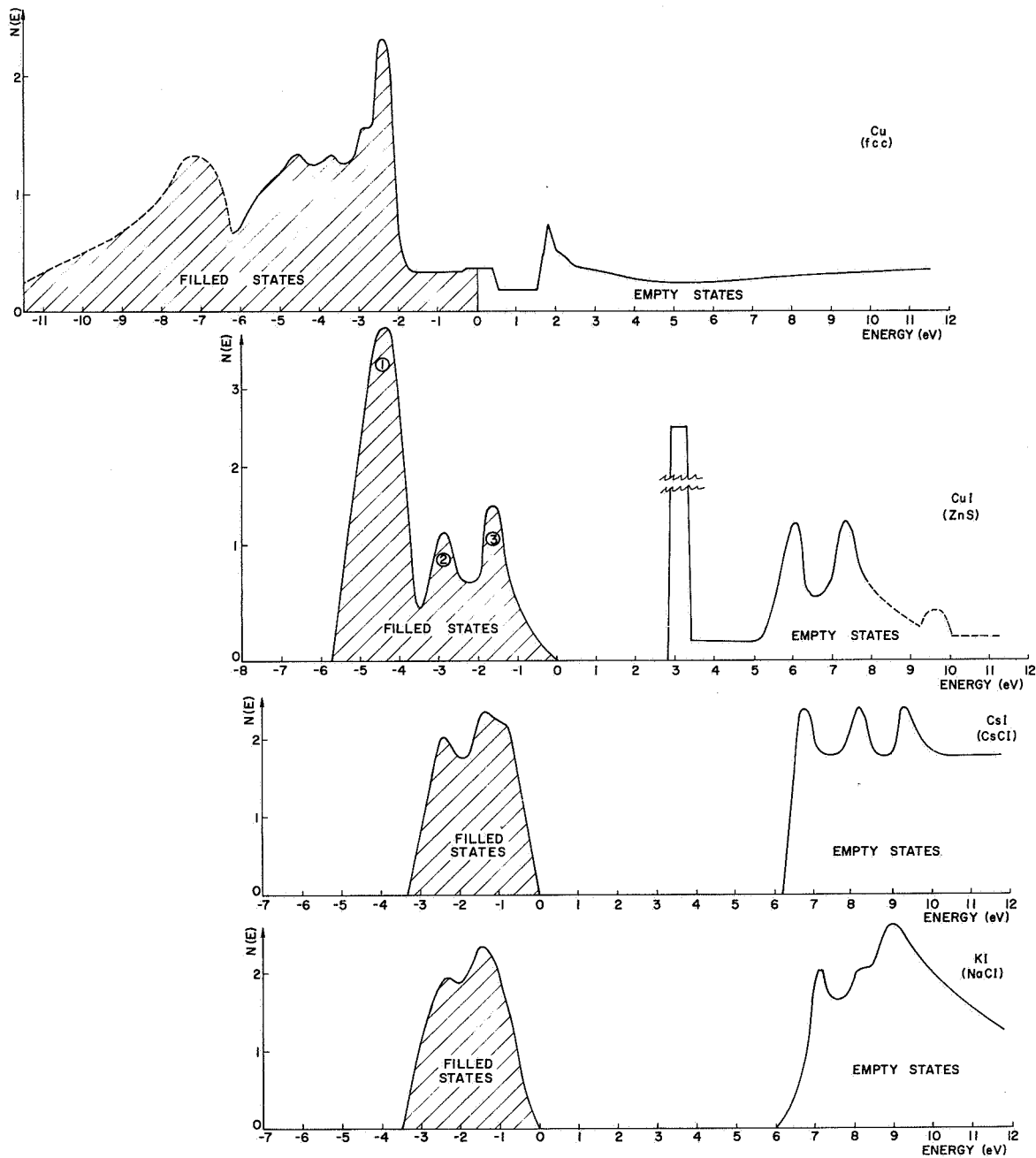


FIG. 204. A COMPARISON OF THE OPTICAL DENSITY OF STATES $N(E)$ FOR Cu, CuI, CsI, AND KI.

to the valence bands of CsI and KI, which are derived from the 5p wavefunctions of the iodine atom. In addition, there appears to be some correspondence between the conduction bands of CuI, CsI, and KI in the region between 6 and 10 eV above the top of the valence band, suggesting that these conduction band states may be associated with the iodine atom. The comparison between CuI, CsI, and KI seems to be quite remarkable, since all three materials have different crystal structures, as indicated in Fig. 204. Note, however, that the 3d band in CuI is significantly narrower than in Cu, suggesting that the d wavefunctions in CuI are considerably more localized than are the d wavefunctions in Cu.

Although the discussion above applies specifically to the case of CsI, the general statements also apply to the cases of CuBr and CuCl. It is worthwhile to note that in CuCl, CuBr, CuI, CsCl, CsBr, CsI, and KI, the valence band optical density of states derived from halogen wavefunctions is a structure about 3 eV wide. In the cesium halides, the separation of the peaks in the valence band seems to correspond to the spin-orbit splitting of the halogen atom:¹ In CsI, there are two major peaks separated by about 1 eV, the spin-orbit splitting of the iodine atom; in CsCl, only one peak is observed, corresponding to the very small (0.1 eV) splitting of the chlorine atom. All the cuprous halides, have two valence band peaks separated by about 1 eV; however the peaks are "sharpest" in CuI, and least "sharp" in CuCl, in correspondence with the spin-orbit splitting of the halogen atoms.

From the discussion above, it is apparent that, for the noble metals, the cuprous halides, and certain alkali halides, the bulk of the optical transitions are not well described by the "conventional" explanation of direct transitions between single Bloch states. In addition, there is strong evidence that in the cuprous halides and the alkali halides, the atomic nature of the constituent atoms may play a dominate role in the electronic structure and in the optical absorption process. It is hoped that this new experimental data, the analyses of these data, and the observations presented in this report will not only be of use to theorists making future energy band calculations, but will also be helpful in leading to a unified theory of the optical absorption process in solids.

¹As noted in Chapter IX, severe conduction band modulation prevented the positive identification of possible valence-band structure in CsBr in the range of photon energies below 11.9 eV.

APPENDIX A. UNIQUENESS OF THE PHOTOEMISSION ANALYSIS

In Chapter III, Section F, several methods were outlined by which the quantities $N_V(E)$, $N_C(E)$ and $T(E)$ could be calculated from the photoemission data. In this section we show that only in certain cases are these solutions unique. It is assumed, of course, that the calculated $N_V(E)$, $N_C(E)$ and $T(E)$ are in very good quantitative agreement with both the shape and the magnitude of the experimental EDCs.

In addition, we assume that the width of the valence band is greater than the difference between the vacuum level and the bottom of the conduction band. If this is not the case, a portion of the conduction band cannot be uniquely determined.

Case I.

$$[\alpha(\omega)L(E) \gg 1 ; \text{ ISOTROPIC CONDUCTION BAND}]$$

From Eq. (3.94), the experimental EDC is described by

$$\eta(E, \omega) = T(E) \frac{N_C(E) N_V(E - \hbar\omega)}{\int_{E_f}^{E_f + \hbar\omega} N_C(E) N_V(E - \hbar\omega) dE} \quad (\text{A.1})$$

where E_f is the energy at the top of the valence band. For convenience, we set $E_f = 0$. Let us assume that two sets of solutions exist, labeled by superscripts 1 and 2: $[N_V^1(E), N_C^1(E), T^1(E)]$; $[N_V^2(E), N_C^2(E), T^2(E)]$. If two such solutions exist, then they can be related in the following manner:

$$N_V^1(E) = g(E) N_V^2(E) \quad (\text{A.2})$$

$$N_C^1(E) = f(E) N_C^2(E) \quad (\text{A.3})$$

$$T^1(E) = z(E) T^2(E) \quad (\text{A.4})$$

If the two solutions exist, then we can write

$$\eta(E, \omega) = T^1(E) \frac{N_C^1(E) N_V^1(E - \hbar\omega)}{\int_0^{\hbar\omega} N_C^1(E) N_V^1(E - \hbar\omega) dE} = \frac{T^2(E) N_C^2(E) N_V^2(E - \hbar\omega)}{\int_0^{\hbar\omega} N_C^2(E) N_V^2(E - \hbar\omega) dE} \quad (A.5)$$

Using Eqs. (A.2), (A.3), and (A.4) in Eq. (A.5), we can cancel and rearrange to obtain

$$f(E) z(E) g(E - \hbar\omega) = \frac{\int_0^{\hbar\omega} f(E) N_C^2(E) g(E - \hbar\omega) N_V^2(E - \hbar\omega) dE}{\int_0^{\hbar\omega} N_C^2(E) N_V^2(E - \hbar\omega) dE} \quad (A.6)$$

The term on the right-hand side of Eq. (A.6) is just a function of $\hbar\omega$, which we shall call $\xi(\hbar\omega)$:

$$f(E) z(E) g(E - \hbar\omega) = \xi(\hbar\omega) \quad (A.7)$$

Equation (A.7) must hold for any $(\hbar\omega)$, at fixed (E) . So we can write

$$f(E) z(E) g(E - \hbar\omega_1) = \xi(\hbar\omega_1) \quad (A.8)$$

$$f(E) z(E) g(E - \hbar\omega_j) = \xi(\hbar\omega_j) \quad (A.9)$$

Taking the ratio of Eqs. (A.8) and (A.9),

$$\xi(\hbar\omega_j) g(E - \hbar\omega_1) = \xi(\hbar\omega_1) g(E - \hbar\omega_j) \quad (A.10)$$

We now solve Eq. (A.10) by the use of Fourier Transforms. Let the transform of $g(t)$ be $G(\gamma)$

$$g(t) \leftrightarrow G(\gamma) \quad (A.11)$$

From the "shifting" theorem [Ref. 98]

$$g(t - t_0) \leftrightarrow G(\gamma) e^{-j(\gamma t_0)} \quad (A.12)$$

Applying Eq. (A.12) to Eq. (A.10)

$$\xi(\hbar\omega_j) G(\gamma) e^{-j(\gamma\hbar\omega_i)} = \xi(\hbar\omega_i) G(\gamma) e^{-j(\gamma\hbar\omega_j)} \quad (\text{A.13})$$

so

$$\frac{\xi(\hbar\omega_j)}{e^{-j(\gamma\hbar\omega_j)}} = \frac{\xi(\hbar\omega_i)}{e^{-j(\gamma\hbar\omega_i)}} = K = \text{constant} \quad (\text{A.14})$$

since the left-hand side of Eq. (A.14) is a function of ω_j alone, and the right-hand side of Eq. (A.14) is a function of ω_i alone. Thus,

$$\xi(\hbar\omega_i) = K e^{-j(\gamma\hbar\omega_i)} \quad (\text{A.15})$$

for any ω_i . Applying Eq. (A.15) to Eq. (A.10),

$$\frac{g(E - \hbar\omega_i)}{g(E - \hbar\omega_j)} = e^{-j[\gamma(\hbar\omega_i - \hbar\omega_j)]} \quad (\text{A.16})$$

At $E = \hbar\omega_j$, Eq. (A.16) becomes

$$g(\hbar\omega_j - \hbar\omega_i) = g(0) e^{-j[\gamma(\hbar\omega_i - \hbar\omega_j)]} \quad (\text{A.17})$$

Since Eq. (A.17) is true for any $(\hbar\omega_i)$ and any $(\hbar\omega_j)$, we can write

$$g(E) = g(0) e^{j(\gamma E)} \quad (\text{A.18})$$

Since $g(E)$ is specified (by physical reasoning) to be real, γ must be imaginary. Thus,

$$\gamma = j(\beta) \quad (\text{A.19})$$

where β is real, and

$$\boxed{g(E) = g(0) e^{-\beta E}} \quad (\text{A.20})$$

If the effective number of electrons in the valence band is specified to be N_0 , then the quantity $g(0)$ can be determined from the normalizing relation.

$$N_0 = \int_{\text{v.b.}} N_V^1(E) dE = \int_{\text{v.b.}} N_V^2(E) dE = g(0) \int_{\text{v.b.}} N_V^1(E) e^{-\beta E} dE \quad (\text{A.21})$$

where (v.b.) indicates an integral over the valence band. Eq. (A.7) now becomes

$$\xi(\hbar\omega) = K e^{\beta\hbar\omega} = \frac{\int_0^{\hbar\omega} f(E) N_C^2(E) g(0) e^{-\beta(E - \hbar\omega)} N_V^2(E - \hbar\omega) dE}{\int_0^{\hbar\omega} N_C^2(E) N_V^2(E - \hbar\omega) dE} \quad (\text{A.22a})$$

or

$$\int_0^{\hbar\omega} [(K - f(E) g(0) e^{-\beta E}] N_C^2(E) N_V^2(E - \hbar\omega) dE = 0 \quad (\text{A.22b})$$

There is one solution for $f(E)$ that always satisfies Eq. (A.22):

$$f(E) = \frac{K}{g(0)} e^{+\beta E} \quad (\text{A.23})$$

Since Eq. (A.22) must be true for all ω , Eq. (A.23) is the only possible solution. This can be seen by rewriting Eq. (A.22) in the form

$$\frac{K}{g(0)} \int_0^{\hbar\omega} N_C^2(E) N_V^2(E - \hbar\omega) dE = \int_0^{\hbar\omega} f(E) e^{-\beta E} N_C^2(E) N_V^2(E - \hbar\omega) dE \quad (\text{A.24})$$

Since $N_C^2(E)$ and $N_V^2(E)$ are assumed to be known, the left-hand side of Eq. (A.24) is a known function of ω , and we can solve for $f(E)$ using the "unfolding" procedure of Eq. (3.99). Calling the left-hand side of Eq. (A.24) $N(\omega)$,

$$N(\Delta\omega) = \frac{K}{g(0)} \{N_c^2(\Delta\omega) N_v^2(-\Delta\omega)\} = \{f(\Delta\omega) e^{-\beta\hbar\Delta\omega} N_c^2(\Delta\omega) N_v^2(-\Delta\omega)\} \quad (\text{A.25a})$$

$$N(2\Delta\omega) = \frac{K}{g(0)} \{[N_c^2(2\Delta\omega) N_v^2(-\Delta\omega)] + [N_c^2(\Delta\omega) N_v^2(-2\Delta\omega)]\} = \{[f(2\Delta\omega) e^{-\beta\hbar 2\Delta\omega} N_c^2(2\Delta\omega) N_v^2(-\Delta\omega)] + [f(\Delta\omega) e^{-\beta\hbar\Delta\omega} N_c^2(\Delta\omega) N_v^2(-2\Delta\omega)]\} \quad (\text{A.25b})$$

$$N(3\Delta\omega) = \frac{K}{g(0)} \{[N_c^2(3\Delta\omega) N_v^2(-\Delta\omega)] + [N_c^2(2\Delta\omega) N_v^2(-2\Delta\omega)] + [N_c^2(\Delta\omega) N_v^2(-3\Delta\omega)]\} = \{[f(3\Delta\omega) e^{-\beta\hbar 3\Delta\omega} N_c^2(3\Delta\omega) N_v^2(-\Delta\omega)] + [f(2\Delta\omega) e^{-\beta\hbar 2\Delta\omega} N_c^2(2\Delta\omega) N_v^2(-2\Delta\omega)] + [f(\Delta\omega) e^{-\beta\hbar\Delta\omega} N_c^2(\Delta\omega) N_v^2(-3\Delta\omega)]\} \quad (\text{A.25c})$$

From Eq. (A.25a),

$$f(\Delta\omega) = \frac{K}{g(0)} e^{+\beta\hbar\Delta\omega} \quad (\text{A.26a})$$

Using Eq. (A.26a) in Eq. (A.25b),

$$f(2\Delta\omega) = \frac{K}{g(0)} e^{+\beta\hbar 2\Delta\omega} \quad (\text{A.26b})$$

Using Eqs. (A.26a) and (A.26b) in Eq. (A.25c),

$$f(3\Delta\omega) = \frac{K}{g(0)} e^{+\beta\hbar 3\Delta\omega} \quad (\text{A.26c})$$

In the limit $\Delta \rightarrow 0$, we obtain by induction

$$f(\omega) = \frac{K}{g(0)} e^{+\beta\hbar\omega} \quad (\text{A.27})$$

which is the same as Eq. (A.23). [In the case of a semiconductor, the "unfolding" in Eq. (A.25a) would start at $E = (E_g + \hbar\Delta\omega)$, rather than at $E = +\hbar\Delta\omega$.]

$$z(E) = \frac{\xi(\hbar\omega)}{f(E) g(E - \hbar\omega)} = 1 \quad (\text{A.28})$$

Thus we have shown that if a set of solutions $[N_c(E), N_v(E), T(E)]$ is found for Eq. (A.1), then there exists an infinite set of solutions that can be generated from the relations

$$N_V^\beta(E) = g(0) e^{-\beta E} N_V(E) \quad (\text{A.29})$$

$$N_C^\beta(E) = \frac{K}{g(0)} e^{+\beta E} N_C(E) \quad (\text{A.30})$$

$$T^\beta(E) = T(E) \quad (\text{A.31})$$

where $g(0)$ is found from Eq. (A.21), and where β is real (positive or negative). In the case for a metal, we require continuity of the conduction band and valence band at the fermi level ($E = 0$), so Eq. (A.29) through Eq. (A.31) become

$$N_V^\beta(E) = g(0) e^{-\beta E} N_V(E) \quad (\text{A.32})$$

$$N_C^\beta(E) = g(0) e^{+\beta E} N_C(E) \quad (\text{A.33})$$

$$T^\beta(E) = T(E) \quad (\text{A.34})$$

Thus, we see that the solutions to Eq. (A.1) are not unique, unless additional constraints are placed upon the solutions.

One additional constraint would be to require that the "optical density of states" satisfy Eq. (2.50),

$$\epsilon_2(\omega) = \frac{K}{\omega^2} |M(\omega)|^2 \int_0^{\hbar\omega} N_C(E) N_V(E - \hbar\omega) dE \quad (\text{A.35})$$

where K is a constant. Let us assume that the matrix element $|M^1(\omega)|^2$ corresponds to the set of solutions $[N_n^1(E), N_c^1(E), T^1(E)]$. Then,

$$\epsilon_2(\omega) = \frac{K}{\omega^2} |M^1(\omega)|^2 \int_0^{\hbar\omega} N_c^1(E) N_v^1(E - \hbar\omega) dE \quad (\text{A.36})$$

Let us ascertain if there exists another set of solutions such that

$$\epsilon_2(\omega) = \frac{K}{\omega} |M^2(\omega)|^2 \int_0^{\hbar\omega} N_c^2(E) N_v^2(E - \hbar\omega) dE \quad (\text{A.37})$$

where

$$|M^2(\omega)|^2 = m(\omega) |M^1(\omega)|^2 \quad (\text{A.38})$$

and Eq. (A.2) through Eq. (A.4) apply.

Using Eq. (A.29) and Eq. (A.30), Eq. (A.37) becomes

$$\epsilon_2(\omega) = \frac{K}{\omega} |M^2(\omega)|^2 \int_0^{\hbar\omega} \frac{K}{g(0)} e^{\beta E} N_c^1(E) g(0) e^{-\beta(E - \hbar\omega)} N_v(E - \hbar\omega) dE \quad (\text{A.39})$$

Comparing Eq. (A.39), Eq. (A.36), and Eq. (A.38), we find that

$$m^\beta(\omega) = K e^{+\beta\hbar\omega} \quad (\text{A.40})$$

so

$$|M^2(\omega)|^2 = \frac{1}{K} e^{-\beta\hbar\omega} |M^1(\omega)|^2 \quad (\text{A.41})$$

Thus, if a set of solutions $[N_c(E), N_v(E), T(E), |M(\omega)|]$ is found to satisfy Eq. (A.1) and Eq. (A.35), then there exists an infinite set of solutions

$$N_v^\beta(E) = g(0) e^{-\beta E} N_v(E) \quad \text{for } E \leq 0 \quad (\text{A.42})$$

$$N_c^\beta(E) = \frac{K}{g(0)} e^{+\beta E} N_c(E) \quad \text{for } E \geq 0 \quad (\text{A.43})$$

$$T^\beta(E) = T(E) \quad \text{for } E \geq 0 \quad (\text{A.44})$$

$$|M^\beta(\omega)|^2 = \frac{1}{K} e^{-\beta\hbar\omega} |M(\omega)|^2 \quad (\text{A.45})$$

where β is real (positive or negative).

If we require that $|M(\omega)|^2$ be a constant, then the

$$\beta = 0 \quad (\text{A.46})$$

and from Eq. (A.21),

$$g(0) = 1 \quad (\text{A.47})$$

Substituting Eq. (A.46) and Eq. (A.47) into Eq. (A.42) through Eq. (A.45), we find that

$$N^{\beta}(E) = N_V^{\beta}(E) \quad \text{for } E \leq 0 \quad (\text{A.48})$$

$$N_C^{\beta}(E) = KN_C(E) \quad \text{for } E \geq 0 \quad (\text{A.49})$$

$$T^{\beta}(E) = T(E) \quad \text{for } E \geq 0 \quad (\text{A.50})$$

$$|M^2(\omega)|^2 = \frac{1}{K} |M(\omega)|^2 \quad (\text{A.51})$$

In the case of a metal, we can require continuity of the valence band and the conduction band at $E = 0$, so $K = 1$, and there is only one solution.

Thus, we can see that unless we apply the constraint that $|M(\omega)|^2 = \text{constant}$, there is no unique solution to Eq. (A.1). However, the possible solutions are not arbitrary, but are specified by Eq. (A.42) through Eq. (A.44). In the case $|M(\omega)|^2 = \text{constant}$, Eq. (A.35) is found to put an additional constraint on the solutions of Eq. (A.1), and if a set of solutions $[N_C(E), N_V(E), T(E)]$ can be found to satisfy Eq. (A.1), then this set of solutions is unique (except for a constant scaling factor in the case of a semiconductor).

(The author wishes to thank A. Yu for his helpful discussions concerning the material presented in this section.)

Case II.

[$\alpha(\omega) L(E) \gg 1$; ISOTROPIC CONDUCTION BAND;
SMALL VELOCITY CONE]

From Eq. (3.103), the experimental EDC is given by

$$\eta(E, \omega) = \alpha(\omega) L(E) T(E) \frac{N_c(E) N_v(E - \hbar\omega)}{\int_{E_f}^{E_f + \hbar\omega} N_c(E) N_v(E - \hbar\omega) dE} \quad (\text{A.52})$$

The uniqueness argument proceeds in a manner identical to that used in Case I, and we obtain a unique solution only if $|M(\omega)|^2$ is a constant. In the case $|M(\omega)|^2 = \text{constant}$

$$N_v^\beta(E) = N_v(E) \quad (\text{A.53})$$

$$N_c^\beta(E) = K N_c(E) \quad (\text{A.54})$$

$$L^\beta(E) T^\beta(E) = L(E) T(E) \quad (\text{A.55})$$

$$|M^\beta(\omega)|^2 = \frac{1}{K} |M(\omega)|^2 \quad (\text{A.56})$$

Thus, we are not able to separate the functions $L(E)$ and $T(E)$. Only their product is unique. However, $L(E)$ can be obtained by independent experimental measurement. If the shape and magnitude of $L(E)$ were available, then the shape and magnitude of $T(E)$ could be obtained in a unique manner. By use of Eq. (3.18), and a knowledge of the appropriate group velocity $|v_g(E)|$, the shape of $L(E)$ can be calculated. If the shape of $L(E)$ is known, the shape of $T(E)$ can be calculated. If the calculated shape of $L(E)$ is normalized to an experimental point, both the shape and magnitude of $T(E)$ can be obtained.

Case III.

[FREE ELECTRON CONDUCTION BAND;
SEMICLASSICAL THRESHOLD FUNCTION]

The expression describing the experimental EDC is Eq. (3.83), or

$$\eta(E, \omega) = \left\{ C[\alpha(\omega) L(E), T_F(E)] \frac{[\frac{\alpha(\omega) L(E)}{\alpha(\omega) L(E)+1}]^2}{\int_{E_f}^{E_f + \hbar\omega} N_c(E) N_v(E - \hbar\omega) dE} \right\} \quad (A.57)$$

where T_F is the semiclassical threshold function, and the envelope of $N_c(E)$ has the free electron energy dependence of $(E)^{-1/2}$. $T_F(E)$ and the envelope of $N_c(E)$ are specified by one arbitrary parameter, the position of the bottom of the free electron band.

If $[\alpha(\omega) L(E)] \gg 1$, then uniqueness can be shown according to the arguments of Case I for $|M(\omega)|^2 = \text{constant}$. If $[\alpha(\omega) L(E)] \ll 1$, then the uniqueness arguments of Case II apply; in this case, the product $\{T_F(E) C[\alpha(\omega) L(E), T_F(E)]\}$ is specified within close limits by the limits imposed upon the selection of the position of the bottom of the conduction band. Thus, uniqueness of the product $\{C[\alpha(\omega) L(E), T_F(E) T_f(E) L(E)]\}$ would determine $L(E)$ and $T_F(E)$ within close limits, without having any experimental values for $L(E)$. The use of an experimental $L(E)$ would result in a unique solution for all the quantities of interest.

If the quantity $[\alpha(\omega) L(E)]$ is of the order of unity, and no experimental values are available for $L(E)$, then there is no assurance of uniqueness in Eq. (A.52) since $L(E)$ is arbitrary. However, the location of the bottom of the free electron band is dictated to within a restricted region by physical arguments, and this would severely restrict the possible values of $L(E)$.

Let us consider the case where the following restrictions hold:

- (1) $L(E)$ is calculated from Eq. (3.18), and normalized to one experimental point;
 - (2) the velocity cone is small, so the correction factor (c) is approximately unity.
- Under these conditions, $L(E)$ is specified, and Eq. (A.21) becomes

$$\eta(E, \hbar\omega) = \frac{\alpha(\omega) L(E)}{\alpha(\omega) L(E)+1} T_F(E) \frac{N_c(E) N_v(E - \hbar\omega)}{\int_{E_f}^{E_f + \hbar\omega} N_c(E) N_v(E - \hbar\omega) dE} \quad (\text{A.58})$$

In this case, the uniqueness of $N_c(E)$, $N_v(E)$, and $T_F(E)$ can be proved by following the procedure used in Case I.

Let us consider now the case where $L(E)$ is calculated from Eq. (3.18), but there are no experimental points for normalizations. Then there are three arbitrary parameters (see Table 1: (1) the magnitude of $L(E)$ at one point; (2) the relative peak heights in the valence and conduction bands; (3) the position of the bottom of the free electron band. In this case, it is not obvious that Eq. (A.58) has a unique solution, due to the complicated nature of the correction factor (C).

Thus, we see that in the region where $\alpha(\omega) L(E)$ is of the order of unity, we are not assured that Eq. (A.58) has a unique solution. However, if the calculated $L(E)$ can be normalized to experiment at one point, and the velocity cone is small, we are assured of uniqueness.

It is possible that the solutions of Eq. (A.58) are unique under conditions more general than those specified here. However, this remains to be shown.



APPENDIX B. COMPUTER PROGRAM FOR ANALYZING PHOTOEMISSION DATA

This section briefly describes a computer program written in ALGOL for the Burroughs B5500 computer at Stanford, and includes a copy of the program and a set of results obtained in the analysis of copper. The program incorporates Stanford Computation Center Library Program 159, which effects a plotting routine for the CalComp Plotter. The author of this investigation is indebted to Mr. Alan Maurer for incorporating library plot 159 into the program.

Given the proper input parameters, the program will cause the following parameters to be printed out:

- (I) $L(E)$, the electron-electron scattering length [calculated from Eq. (3.18), where the group velocity is given by $v_g \sim E + EB'$]
- (II) $T(E)$, the semiclassical threshold function [calculated from Eq. (3.11)]
- (III) $EFFTH(E)$, the effective value of the threshold function [calculated from Eq. (3.108)]
- (IV) $EPSILON[\hbar\omega] - \epsilon_2(\omega)$, the imaginary part of the dielectric constant [calculated from Eq. (3.98), with the momentum matrix $|M(\omega)|^2$ assumed constant]
- (V) ENERGY DISTRIBUTIONS - $\mathcal{N}(E, \omega)$ [calculated from Eq. (3.83)]
- (VI) ABSOLUTE YIELD - $Y(\hbar\omega)$ [calculated from Eq. (3.86)]

In addition to printing out the energy distributions $\mathcal{N}(E, \omega)$, in tabular form, the program will cause the energy distribution to be recorded on magnetic tape, and subsequently plotted on the CalComp Plotter. To save time (and expense), the axes have been suppressed in the plot routine, so the graphs (as plotted) do not have axes. The horizontal axis is one electron volt per inch, and the vertical scale is described later in this appendix.) The programmer will find it beneficial to write "PLOT 10 GRAPH PAPER" on the instruction card at the Stanford Computer, since the EDCs are difficult to read when plotted on plain paper.

If the reader wishes to use this program, he must change several punch cards, and put in the proper data cards, as indicated below. (The numbers at the left of the statements below correspond to circled numbers in the margin of the sample program included in this appendix.)

PUNCH CARDS IN THE BODY OF THE PROGRAM

① Change "copper" to the name of the material being studied.

①A Change the spelling "YEILD" to "YIELD."

② "EB" denotes the energy of the bottom of the free electron conduction band below the fermi level. The program requires that $(EB) \geq 0$, because the group velocity $v_g \sim E + EB$ must be calculated at all points in the conduction band. (The fermi level is defined to be the zero of energy.)

EXAMPLE: EB = 12 means that the bottom of the free electron band is 1.2 eV below the fermi level.

③ "EA" denotes the energy difference between the vacuum level and the fermi level.

EXAMPLE: EA = 45 means that the vacuum level is 4.5 eV above the fermi level.

④ "TMAX" denotes the number of different photon energies for which it is desired to plot EFFTH(E). $0 \leq TMAX \leq AMAX$ (see ⑭).

⑤ "AMAX" denotes the number of different photon energies for which it is desired to calculate EDCs. The maximum number of EDCs is 24, or $0 \leq AMAX \leq 24$.

⑥ SQRT(EFF + EB) defines the group velocity.

⑦ "NORM" normalizes the electron-electron scattering length at 8.6 eV above the fermi level.

EXAMPLE: NORM = [(24) × 1.0 @ -08/L(86)] sets the electron-electron scattering length L(E) equal to 27 Å at 8.6 eV above the fermi level.

⑧ This card sets the vertical scale for the CalComp Plotter.

EXAMPLE: MS[0] = 0.0045 means that 9 inches = 4.5×10^{-3} electrons/photon/eV, or that 1 inch = 0.5×10^{-3} electron/photon/eV.

⑨ Change "copper" to the name of the material being studied.

DATA CARDS AT END OF PROGRAM

- ⑩ Photon energies at which it is desired to have EDCs calculated.

EXAMPLE: "112" indicates a photon energy of 11.2 eV. There must be "AMAX" cards. The maximum photon energy is 11.6 eV.

- ⑪ $\alpha(\omega)$, the absorption coefficient. There must be "AMAX" numbers, and the n^{th} number corresponds to the n^{th} photon energy in ⑩.

EXAMPLE: (7.2 @ 05) means $(7.2 \times 10^5 \text{ cm}^{-1})$.

- ⑫ Numbers specifying the valence band density of states, starting at 0.1 eV below the fermi level and extending to 11.6 eV below the fermi level. There must be 116 cards.

- ⑬ Numbers specifying the conduction band density of states, starting at 0.1 eV above the fermi level and extending to 11.6 eV above the fermi level. There must be 116 cards.

- ⑭ Labels describing photon energies at which EFFTH(E) is to be plotted.

EXAMPLE: "8" indicates calculate and print EFFTH(E) for the photon energy given on the eighth number in cards ⑩. In the sample program, "8" corresponds to $\hbar\omega = 7.7 \text{ eV}$, and "16" corresponds to $\hbar\omega = 10.2 \text{ eV}$, as seen from the data cards giving the photon energies. Note that in the sample program, the photon energy is incorrectly labeled "8", rather than the corresponding photon energy "77." (The numbers in the table correspond to a photon energy of 7.7 eV only the labeling is incorrect - this can be easily corrected by the programmer.)

The sample program is presented below for convenience of the reader. It is highly recommended to anyone wishing to use this program that he add a "print statement" that would print out the data cards along with the calculations. The sample program does not do this, and the data listed below were obtained from a printer that directly read the punch cards in the computer deck. The sample program took about 5 minutes (including compilation time) on the B5500 computer.

0002 0151
0002 0151
0002 0152
0002 0152
0002 0158
0002 0158
0002 0165
0002 0166
0002 0166
0002 0168
0002 0168
0002 0171
0002 0172
0002 0174
0002 0179
0002 0179
0002 0182
0002 0185
0002 0187
0002 0190
0002 0193
0002 0196
0002 0211
0002 0214
0002 0217
0002 0220
0002 0223
0002 0237
0002 0241
0002 0241
0002 0242
0002 0247
0002 0247
0002 0251
0002 0257
0002 0265
0002 0267
0002 0275
0002 0277
0002 0278
0002 0278
0002 0284
0002 0284
0002 0287
0002 0290
0002 0304
0002 0307
0002 0312
0002 0312
0002 0328
0002 0328
0002 0333
0002 0333
0002 0335
0002 0335

⑥ ⑦

```

END;
IF BEE=1 THEN
  BEGIN
    FOR E+1 STEP 1 UNTIL ((E1-E0-1)/(2)) DO
      BEGIN
        D1[E0]+((CON[E]*CON[E1-E0-E]*V[E0])+D1[F0]);
      END;
    END;
    D2+(D2 + D1[E0]);
  END;
  L[EFF]+((SQRT(EFF+EB))/(D2));
END;
  NORM+(((22.0)*(1.08-08))/(L[86]));
  FOR EFF+3 STEP 1 UNTIL (EMAX + 1) DO
    BEGIN
      L[EFF]+((NORM) * (L[EFF]));
    END;
    WRITE((PAGE));
    WRITE((DBL),FMT5);
    WRITE((DBL),FMT11);
    WRITE((DBL),FMT12);
    WRITE(FMT8, FOR EFF+3 STEP 1 UNTIL (EMAX+ 1) DO [EFF,L[EFF]]);
    WRITE((PAGE));
    WRITE((DBL),FMT5);
    WRITE((DBL),FMT13);
    WRITE((DBL),FMT14);
    WRITE(FMT8, FOR E+EA STEP 1 UNTIL EMAX DO [E,T[E]]);
    FOR A+1 STEP 1 UNTIL TMAX DO
      BEGIN
        J+EM[A];
        FOR E+(EA+1) STEP 1 UNTIL EMAX DO
          BEGIN
            EFFTH[E,A]+T[E]*CON[E]*X
            ((ALP[J]*L[E])/((ALP[J]*L[E])+1))*
            ((ALP[J]*L[E])+1)/(ALP[J]*L[E])*X(1-((1)/(2*ALP[J]*L[E]*
            T[E]) *
            (LN(((ALP[J]*L[E])+1)/((ALP[J]*L[E]*SQRT((EA+ER)/(E+EB))))+
            1)))));
          END;
        END;
        WRITE((PAGE));
        WRITE((DBL),FMT5);
        WRITE((DBL),FMT15);
        WRITE((DBL),FMT15);
        WRITE(FMT2);
        WRITE(FMT3, FOR A+1 STEP 1 UNTIL TMAX DO EM[A]);
        WRITE((DBL));
        FOR E+(EA+1) STEP 1 UNTIL (H[AMAX]-1) DO
          BEGIN
            WRITE(FMT4,E, FOR A+1 STEP 1 UNTIL TMAX DO EFFTH[E,A]);
          END;
        FOR A+2 STEP 1 UNTIL (EMAX+1) DO
          BEGIN
            WCONDUCTIVITY[AJ+0];
            FOR E+1 STEP 1 UNTIL (A-1) DO
              BEGIN

```

```

0339 WCONDUCTIVITY[A]+WCONDUCTIVITY[A]+CONC[E]*V[A-E]]
0345 END;
0345 EPSILON[A]+WCONDUCTIVITY[A]]/(A*X);
0349 END;
0349 WRITE((PAGE));
0352 WRITE((DBLJ),FMT5);
0352 WRITE((DBLJ),FMT7);
0358 WRITE((DBLJ),FMT6);
0361 WRITE(FMT8, FOR A=2 STEP 1 UNTIL (EMAX+1) DO [A,EPSILON[A]]);
0376 BEGIN COMMENT CALCULATE AND PLOT EDC CURVES;
0009 SAVE FILE OUT PLOTTER 2(1,765);REAL ARRAY A[0:1022],A2[0:2,0:2];C[0:9];S,
0005 YMA[0:112];SYMB[=15:63],ABCD[0:2];REAL OLTH;
0014
0014 PROCEDURE PLOT(X,Y,IC);VALUE X,Y,IC;REAL X,Y;INTEGER IC;BEGIN STREAM PRO.
0000 CEDURE WRITE(FL,IFL,A);BEGIN SI+A;DI+IFL;I7(60(SI+SI-2;DS+6CHR));RELFASE.
0002 (FIL);END WRIT;OWN INTEGER IT,I,NPX,NPY,BA,T,WIDX,PEN;OWN BOOLEAN BOOL;I.
0002 NTEGER J,K,DX,DY,IY,NR,NT,NC,I12,NA;LABEL FINISH,ON,L1;FORMAT TORM(1022A6.
0002 )IF ABS(IC)>3 THEN BEGIN BA+0;WIDX+IF IC<=3 THEN 2*ELSE I*2;PEN+2;A[0]+.
0002 444444";A[1]+.444433";A[2]+.333332";GO TO FINISH;END;IF ABS(IC)PEN THEN.
0002 GO ON;PEN+5PEN;A[I]+C IF BOOL THEN.666661;ELSE IT+24955)+PEN+PEN;BOOL+TR.
0020 UE;FOR K+9PEN STEP=1 UNTIL 1500 BEGIN A[I+1]+.666666";IF I>1018 THEN RE.
0026 GIN A[1019]+.340000";WRIT(LOTTER,LOTTER(O),A[0]);I+3;GO ON;END;END;ON;
0034 NA+REAL(DX+NPX+(NPX+WIDX*X))>0);REAL(DX>0);IY+REAL(DY+NPY+(NPY+WIDX*Y))>.
0046 O)+REAL(DY>0);IF ABS(DY)>ABS(DY);THEN BEGIN NR+ABS(DY);NC+NT+ABS(DY);I12+.
0052 A2[NA,1]END ELSE BEGIN NR+ABS(COX);NC+NT+ABS(DY);I12+A2[1,IY]END;IY+A2[NA.
0059 ,IY];NA+NT DIV 2;NT+NR;L1:IF(NC+NC-1)>0 THEN BEGIN IF NA=NT THEN BEGIN.
0065 T+IY;NA+NA+NT;END ELSE BEGIN T+I12;NA+NA+NR END;IF BOOL+NOT BOOL THEN B.
0073 EGIN A[I]+T;IF(I+1)>1019 THEN BEGIN A[1019]+.340000";WRIT(LOTTER,PL.
0079 OTTER(O),A[0]);I+3;END;GO TO L1;END;IT+.005006"&T[15:33:9];GN TO L1;FND;
0085 IF IC<0 THEN BEGIN IF BOOL THEN I+1-ELSE A[I]+T+.000560";A[I+1]+.3400.
0095 00";WRITE(LOTTER,TORM,FOR K+0STEP UNTIL I DO A[K]);FINISH;WRITE(LOTTER.
0102 ,TORM,"444444","444433","333331","C(BA+(BA-1)MOD 100)MOD 10)&C(BA DIV 10.
0118 J[24:36:12],"133333","334444",FOR K+0STEP UNTIL 70 DO "444444");BOOL+TRUE.
0134 ;NPX+NPY+0;I+3;END;END;
0153
0014 PROCEDURE SYMROL(XO,YO,HGT,BCD,THETA,N);VALUE XO,YO,HGT,THETA,N;INTEGER.
0014 N;REAL XO,YO,HGT,THETA;ALPHA ARRAY BCD[0];BEGIN REAL BINX,AC,W,OSC,AINX,.
0014 I,OSTS,MOV1,HI,I,MOV2,W,C,CC,LP,XA,YA,XA6,YA6;OWN REAL CTH,STH,LABEL LOA.
0000 DB;DEFINE A=SYMA#,R=SYMB#;IF THETA+OLTH THEN BEGIN OLTH+THETA;CTH+COS(TH.
0000 ETA+THETA*.01745329251);STH+SIN(THETA);END;HI+HGT*.142857142857;XA+CTH*XH.
0002 I,YA+STH*HI;XA6+XA*6.0;YA6+YA*6.0;IF N<0 THEN BEGIN MOV1+IF N=-12 THEN 3EL.
0007 SE 2;XO+XO+MOV1*(XA-YA);YO+YO+MOV1*(XA+YA);BINX+N;GO TO LOADR;END;AC+W+C.
0014 CC+0;W+BCD[0];WHILE AC+AC+1<N DO BEGIN IF CC+CC+127 THEN BEGIN W+ACD(WC+W.
0025 C+1);CC+1;END;BINX+W.[12:6];W+0.8*W[12:18];30;LOADR;OSC+8*(RINX).[33:5];OSTS.
0032 +CAINX+R[3;NX].[39:19];LP+3;I+0;FOR I+1 STEP UNTIL OSC DO BEGIN IF I+.
0040 I+12 THEN BEGIN I+1;OSTS+CAINX+AINX+1;JEND;MOV1+OSTS.[6:3];MOV2+OSTS.[.
0048 9:3];OSTS+0;OSTS[6:12:36];IF MOV1=7 THEN LP+3;ELSE BEGIN PLOT(XO+MOV1*XA-W.
0054 OV2*YA,YO+MOV1*YA+MOV2*XA,LP);LP+2;END;END;XO+XO+XA6;YO+YO+YA6;END;END;
0061
0014 PROCEDURE NUMBER(X,Y,HGT,FLT,THETA,N);VALUE X,Y,HGT,FLT,THETA,N;INT FGR.
0014 N;REAL X,Y,HGT,FLT,THETA;BEGIN REAL FRAC;BOOLEAN B;LABEL SWORD;RPAF LABEL.
0014 AM PROCEDURE CV(XO);VALUE XO;BEGIN SI+LOC XO;DI+LOC CV;DI+2;DS+6DEC E.
0000 ND;REAL STREAM PROCEDURE LZRO(VN;B);VALUE VN,B;BEGIN LABEL M;SI+LOC VN;D.
0001 I+LOC LZRO;DS+WDS;SI+SI+6;DI+DI-6;5(IF SC=0 THEN BEGIN DS+LIT " ";SI+SI+.
0002 IEND ELSE JUMP OUT TO M);M;SI+LOC B;SKIP 4758;IF SB THEN BEGIN DI+DI-1;D.
0005

```



```

5230343000,DC10003436371706,DC13434000000000,DC104073746453404,DC10304,
143340000,DC142413010010617,DC137464500000000,DC100073746413000,DC147070,
434040040,DC147070434040000,DC133434130100106,DC11737464500000,DC100070,
444474000,DC110302027173700,DC10001110000000,DC14020274700000,DC136271,
706054031,DC1422010010131400,DC140312324364700,DC14503410000000,DC144041,
513040000,DC101452305410000,DC101103041470000,DC100070347254000,DC107004,
00000000,DC10007234740000,DC1000740700000,DC10304146377036,DC147703,
717060110,DC100073746453404,DC11001061737464,DC13010702240000,DC100073,
746453404,DC13443400000000,DC102324334140516,DC14626272000000,DC101452,
305412303,DC14323521000000,DC10343000000000,DC100112324160700,DC10212,
212112170,DC124251514240000,DC101417042044600,DC100000000000,DC100477,
00000000,DC101103041433414,DC105061737460000,DC12027074700000,DC107011,
030414700,DC10720470000000,DC10700244070000,DC10047700740000,DC107244,
724200000,DC107470040701434,DC10000000000000,DC110212313122200,DC100477,
016060717,DC116704131304041,DC102463545053513,DC13430000000000,DC1024270,
04440000,DC10727200000000,DC114167036340000,DC10040404000424,DC122000,
00000000,DC100442204402300,DC10040004404422,DC100400444002200,DC1243443,
41301001,DC13142422000000,DC12442202242200,DC120224422042200,DC12224220,
0000000,DC124014124220000,DC124024242202200,DC144331304131100,DC11131403,
1332200,DC110365004641070,DC12222000000000,DC102422220242200,DC10044044,
0220000,DC100442242202204,DC14022024220000,FILL SYMBOL WITH DC130157,DC,
T12156,DC114155,DC122153,DC132151,DC114150,DC112147,DC106146,DC114145,DC,
T14144,DC126142,DC114141,DC116140,DC114137,DC120135,DC122000,DC112002,DC,
T22003,DC132005,DC114007,DC122011,DC130013,DC112015,DC140016,DC130021,DC,
T34023,DC142025,DC132030,DC126032,DC106034,DC114035,DC112036,DC124037,DC,
T30041,DC124043,DC116045,DC116046,DC114047,DC126050,DC114052,DC114053,DC,
T12054,DC110055,DC132056,DC114060,DC106061,DC112062,DC112063,DC112064,DC,
T14065,DC106066,DC112067,DC110070,DC134071,DC116073,DC130074,DC124076,DC,
T26100,DC126102,DC104104,DC114105,DC130106,DC114110,DC100111,DC104112,DC,
T30113,DC110115,DC114116,DC106117,DC112120,DC112121,DC112122,DC116123,DC,
T14125,DC134126,DC122130,DC112132,DC110133,DC112134,DLTH#E10;
PLOT( 0.0, 0.0, 1019 ) ; COMMENT INITIALIZE PLOT ROUTINE. ;
BEGIN
FOR I=0 STEP 1 UNTIL (EMAX-1) DO
BEGIN
XAXIS(I)+I/10;
END;
SCALE( XAXIS, 116, 1, 11.5, XMIN, DX );
FOR J=1 STEP 1 UNTIL AMAX DO
BEGIN
Y(J)=0;
FOR E=(EA+1) STEP 1 UNTIL (H(J)-1) DO
BEGIN
M(E,J)+ (T(E)*CONJ(XV[H(J)-E]*ALP[J]*L[E])/((ALP[J]*L[F])+
1)*WCNDUCTIVITY[H(J)*X(O,1)]) *
((ALP[J]*L[E])+1)/(ALP[J]*L[E])*X(1-((1)/(2*XALP[J]*L[E]*
T(E))) *
(LN((ALP[J]*L[E])+1)/((ALP[J]*L[E]*SQRT((FA+ER)))+(EA+ER)))+
1)))));
Y(J)+(O,1)*X(M(E,J))+Y(J);
END;
IF J<AMAX THEN
BEGIN
FOR E=H(J) STEP 1 UNTIL (H[AMAX]-1) DO
BEGIN

```



```

WRITE((DBL1));
FOR E←(EA+1) STEP 1 UNTIL (H[AMAX]-1) DO
  BEGIN
    WRITE(FMT4,E,FOR A←9 STEP 1 UNTIL 16 DO M(E,A));
  END;
WRITE((PAGE1));
WRITE((DBL1),FMT5);
WRITE((DBL1),FMT1);
WRITE(FMT2);
WRITE(FMT3, FOR A←17 STEP 1 UNTIL AMAX DO H(A));
WRITE((DBL1));
FOR E←(EA+1) STEP 1 UNTIL (H[AMAX]-1) DO
  BEGIN
    WRITE(FMT4,E,FOR A←17 STEP 1 UNTIL AMAX DO M(E,A));
  END;
END;

```

```

0002 0684
0002 0687
0002 0692
0002 0692
0002 0707
0002 0707
0002 0710
0002 0713
0002 0716
0002 0719
0002 0733
0002 0736
0002 0741
0002 0741
0002 0756
0002 0756
0002 0756

```

```

SIN IS SEGMENT 023, PRT 123
BLK CTR IS SEGMENT 026, PRT 005
FILE IN IS SEGMENT 029, PRT 013

```

```

LN IS SFGMENT 022, PRT 092
WRITE IS SFGMENT 025, PRT 089
FILEOUT IS SEGMENT 028, PRT 012

```

```

COS IS SEGMENT 021, PRT 122
SORT IS SEGMENT 024, PRT 088
READ IS SEGMENT 027, PRT 083
SELECT IS SEGMENT 030, PRT 014
PRT SIZE=0147; NO. SEGS.=031; TOTAL SEGMENT SIZE=01885; DISK STORAGE REQ.=01885; EST. CORE REQ.=06865.
NO ERRORS DETECTED. ELAPSED COMPILATION TIME = 059 SECONDS.

```

```

WRITE([DBL]);
FOR E+(EA+1) STEP 1 UNTIL (H[AMAX]-1) DO
  BEGIN
    WRITE(FMT4,E,FOR A+9 STEP 1 UNTIL 16 DO M[E,A]);
  END;
WRITE([PAGE]);
WRITE([DBL],FMT5);
WRITE([DBL],FMT1);
WRITE(FMT2);
WRITE(FMT3, FOR A+17 STEP 1 UNTIL AMAX DO H[A]);
WRITE([DBL]);
FOR E+(EA+1) STEP 1 UNTIL (H[AMAX]-1) DO
  BEGIN
    WRITE(FMT4,E,FOR A+17 STEP 1 UNTIL AMAX DO M[E,A]);
  END;
END;

```

END.

232 PRECEDES B5000 AND IBJOB DATA CARDS

(10) { 50 55 60 65 68
71 74 77 81 84 87 90 93 96 99 102 105 108 112 116
9.0e+05 9.5e+05 9.1e+05 8.3e+05 7.8e+05
(11) { 7.2e+05 7.2e+05 7.2e+05 7.2e+05 7.2e+05
7.2e+05 7.2e+05 7.2e+05 7.2e+05 7.2e+05
7.2e+05 7.2e+05 7.2e+05 7.2e+05 7.2e+05
1.1 1.1 1.1
1 1 1 1 1 1 1 1 1 1 1 1 1.04 1.2 1.5 2.25 5.0 6.5 6.9
6.95 6.7 5.25 4.7 4.7 4.7 4.35 4.0 3.83 3.75 3.76 3.85 3.95 4.0 3.95
3.87 3.78 3.75 3.77 3.81 3.9 4.0 4.0 3.95 3.82 3.65 3.5 3.43 3.37 3.25
(12) { 3.15 3.0 2.87 2.7 2.53 2.37 2.1 2.05 2.0
2.6 3.05 3.3 3.5 3.75 3.85 3.9 3.95 4.0 4.0 3.95 3.9 3.8 3.6 3.4 3.2
3.08 2.95 2.85 2.73 2.62 2.52 2.43 2.35 2.28 2.17 2.10 2.00 1.95 1.90
1.85 1.80 1.75 1.70 1.65 1.60 1.55 1.50 1.45 1.40 1.35 1.30 1.25 1.20
1.15 1.10 1.05 1.00 0.95 0.90 0.85 0.80 0.75 0.70
1.8 1.8 1.8 1.8 0.85 .85 .85 .85 .85 .85 .85 .85 .85 .85 .85 1.8 2.7 3.6
2.92 2.47 2.35
2.25 2.10 1.97 1.85 1.80 1.75 1.71 1.68 1.65
1.62 1.59 1.56 1.53 1.50 1.47 1.44 1.41 1.38 1.36 1.34 1.32 1.30 1.28
(13) { 1.26 1.24 1.23 1.21 1.20 1.20
1.20 1.20 1.20
1.2 1.21 1.22 1.23 1.24 1.25 1.26 1.27 1.28 1.29 1.3 1.31 1.32 1.33 1.34 1.35
1.36 1.37 1.38 1.39 1.4 1.41 1.42 1.43 1.44 1.45 1.46 1.47 1.48 1.49 1.5 1.51
1.52 1.53 1.53 1.54 1.55 1.56 1.57 1.58 1.58 1.59 1.6 1.61 1.62 1.62 1.63 1.64
1.65 1.66 1.66 1.67 1.68 1.69 1.7 1.7 1.71 1.72 1.73 1.74 1.74 1.75 1.76
(14) { 1 3 5 8 11 16 18 20

APPENDIX C. A PRACTICAL METHOD FOR NORMALIZING
ENERGY DISTRIBUTION CURVES (EDCs)

The single most important type of data in this investigation is the photoelectric energy distribution curve, or EDC. During the photoemission experiment, these curves are traced by an x-y recorder on a sheet of graph paper (see Fig. C-1); the horizontal scale is in electron volts, but the vertical scale is arbitrary. In the analysis of photoemission data, it is imperative that the vertical scale be specific in (electrons photoemitted per absorbed photon per eV), so that the area of the "normalized" EDC equals the absolute photoelectric yield at that photon energy. The absolute yield is given in (electrons photoemitted/absorbed photon). Typically, EDCs are taken at (0.2) eV increments in photon energy, so that in the range from 4 to 12 eV, a single set of data may consist of 35 or more EDCs. Because of this large number of curves, it was necessary to devise a rapid, accurate method of scaling the vertical axis of the EDCs. A number of different "normalization" techniques were tried (including optical line followers and hard calculation), but the technique shown in Fig. C-1 has proved to be the most successful. This method is described below.

The original raw data curve is placed on the x-y recorder in the upper right-hand corner of Fig. C-1. This x-y recorder has "retransmitting potentiometers" on the x and y axis, so that any position on the x-y plane corresponds to a unique position on the x and y potentiometers. When a voltage is placed across the potentiometers, each point has coordinates (V_x, V_y) . Thus, the vertical (or "y") axis can be scaled by putting (V_x) into the vertical input of another x-y recorder (upper left-hand corner of Fig. C-1), and adjusting the vertical gain to the desired scale factor. Thus, there is a one-to-one mapping between the original curve and the "normalized" curve, except that the vertical scale is multiplied by a constant scale factor (S_y) . The horizontal axis can be scaled independently in the same manner. (Because an x-y recorder with retransmitting potentiometers was not always available, an equivalent "trace" was made with a moving slidewire and smooth rolling linear ball bearings. This inexpensive machine was adequate, but not as "smooth" as the costly x-y recorder mechanism.)

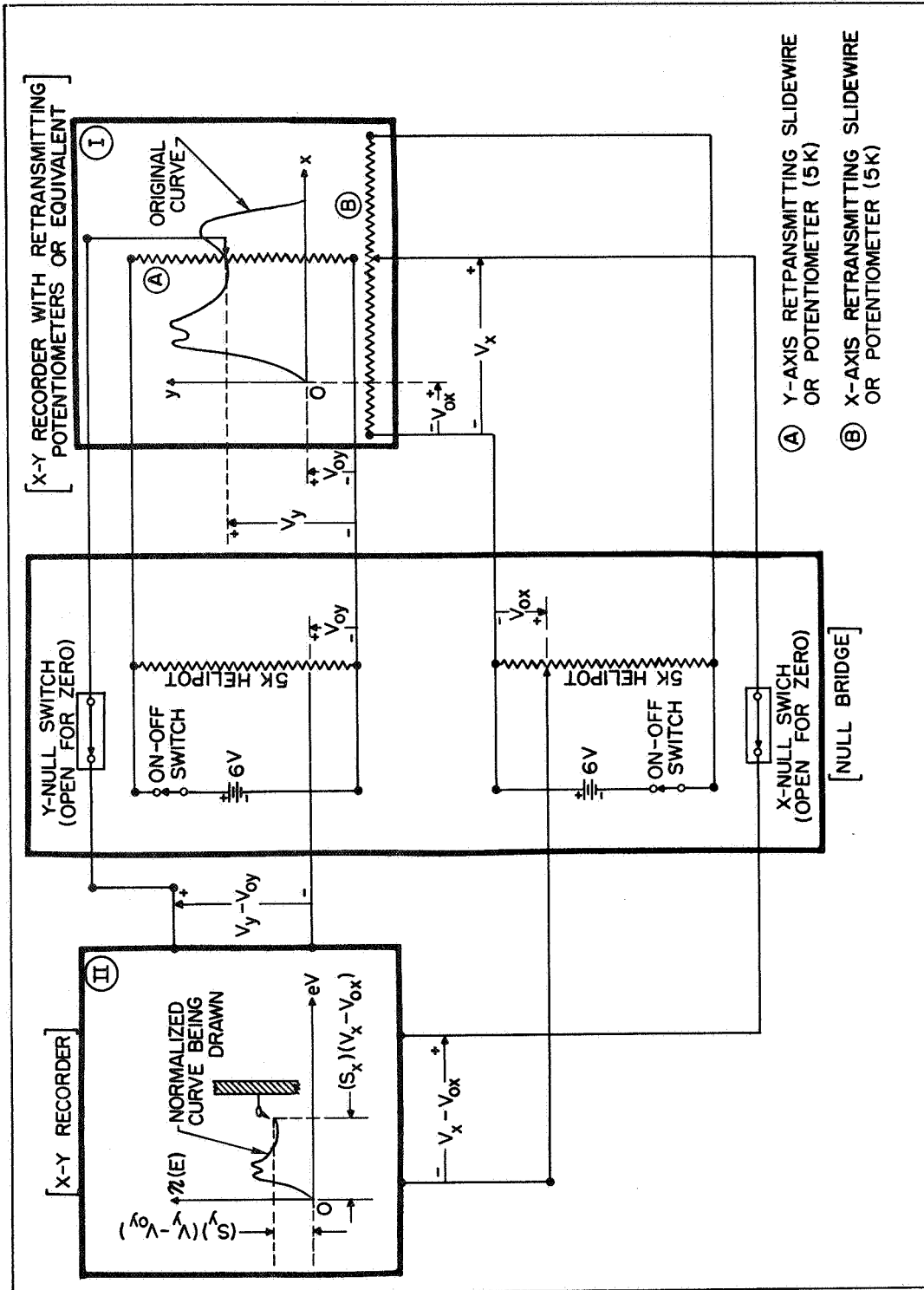


FIG. C-1. SCHEMATIC OF NORMALIZING APPARATUS.

Unfortunately, the "zero" on the raw data curve does not correspond to zero volts, but to the coordinates (V_{x_0}, V_{y_0}) . Thus, scaling the y-axis with the y-gain controls of the second recorder, scales the quantity (V_x) and not the quantity $(V_x - V_{x_0})$, which is the voltage that represents the "true" coordinates of the original curve, as seen from Fig. C-1. The null bridge in Fig. C-1 solves this problem by nulling out the "zero" voltage (V_{x_0}, V_{y_0}) , so that when the pointer is set at (V_{x_0}, V_{y_0}) on the original curve, the voltage into the second recorder is $(0,0)$. Thus, we can now use the vertical and horizontal gain controls of the second recorder to scale the voltages $(V_x - V_{x_0})$ and $(V_y - V_{y_0})$, which are the "true" coordinates of a point on the original curve.

The scale factor (S_y) is obtained by first using a Keuffel and Esser "Compensating Polar Planimeter" to find the area A (in square inches) of the original curve. Let us say that the scales on the "normalized" curve are to be η_y (electrons photoemitted per absorbed photon per eV per inch) and E_x (eV per inch). Thus, if the original horizontal scale is E_x^0 (eV per inch), then

$$S_x = \frac{E_x^0}{E_x} \quad (C.1)$$

The photoelectric yield Y (electrons photoemitted per absorbed photon) is known and corresponds to A_n square inches on the normalized axes where

$$A_n = \frac{Y}{(\eta_y)(E_x)} \quad (C.2)$$

The scaled curve must have an area (in square inches) equal to A_n , so

$$A_n = \frac{Y}{(\eta_y)(E_x)} \sum_i (S_y y_i)(S_x \Delta x_i) = S_y S_x \sum_i y_i \Delta x_i \quad (C.3)$$

where the y_i are the ordinates of the original curve, and the Δx_i are arbitrarily small increments in the abscissa of the original curve,

so that the measured area A (square inches) is given by

$$A = \sum_i y_i \Delta x_i \quad (C.4)$$

Using Eqs. (C.1), (C.3), and (C.4), we obtain for the the scale factor S_y

$$S_y(h\omega) = \frac{Y(h\omega)}{(n_y)(E_x^0)(A)} \quad (C.5)$$

The scale factor $S_y(h\omega)$ must be calculated for every EDC.

In practice, the normalization is carried out in the following manner (spelled out for future undergraduates who will be doing the "normalizing!").

1. Place the original data curve on x-y recorder (I) in the upper right-hand corner of Fig. C-1, and a blank piece of graph paper on x-y recorder (II).
2. Set the pointer of (I) (no ink!) to the coordinate (0,0) of the original curve.
3. Null out the voltages V_{x0} and V_{y0} by adjusting the helipots on the null bridge, and using x-y recorder (2) as a null meter. (At proper null, no deflection should be observed when the y-null switch or the x-null switch are depressed, i.e., opened.
4. Set the pointer of x-y recorder (II) to the origin desired for the normalized curve. EXAMPLE: $E_x^0 = 0.5$ eV/inch, $N = 12$, $N E_{x0} = 6$ in.
5. Move the pointer of x-y recorder (I) to $(N E_x^0)$ inches. Adjust the gain of x-y recorder (II) to $(N' = N E_x^0 S_x)$. EXAMPLE: $S_x = 0.5$, $N' = N E_x^0 S_x = (12)(0.5)(0.5) = 3$ in.
6. Set the pointer of x-y recorder (I) onto a point on the curve at height (h). Adjust the y-gain of x-y recorder (II) to height (hS_y) . EXAMPLE: $h = 6$ in., $S_y = 0.6$ $(hS_y) = 0.36$ in.

7. Scaling adjustments are complete. Move the pointer of x-y recorder (I) along the original curve; the ink pen of x-y recorder (II) will trace out the normalized curve.



REFERENCES

1. N. B. Kindig, Band Structure and Surface Effects in Cadmium Sulfide Photoemission Studies, TR No. 5201-1, SEL-64-095, Stanford Electronics Laboratories, Stanford, Calif., 1964.
2. G. Lewin, Fundamentals of Vacuum Science and Technology, McGraw-Hill Book Company, New York, 1965.
3. B. Schechtman, private communication.
4. L. Apker, E. A. Taft, and J. Dickey, J. Opt. Soc. Am. 43, 78 (1953)
5. W. E. Spicer, J. Phys. Chem. Solids, 22, 365 (1961).
6. W. E. Spicer, private communication, 1966.
7. C. N. Berglund, Band Structure and Electron-Electron Interactions in Copper and Silver--Photoemission Studies, TR No. 5205-1, SEL-64-053, Stanford Electronics Laboratories, Stanford, Calif., 1964.
8. R. C. Eden, private communication, 1966.
9. A. Y-C. Yu, Photoemission and Optical Studies of Cobalt, Palladium, Platinum, and Gadolinium, TR No. 5215-1, SEL-67-045, Stanford Electronics Laboratories, Stanford, Calif., May 1967.
10. R. Madden, National Bureau of Standards, lecture at Stanford University, 1966.
11. S. Tolansky, Surface Microtopography, Interscience Publishers, Inc., New York, 1960.
12. J. W. Beck, Multiple-Beam Interferometry for Small-Step Measurement, TR No. 1659-1, Stanford Electronics Laboratories, Stanford, Calif., 1961.
13. A. J. Blodgett, Band Structure and Ferromagnetism in Nickel, Iron, and Gadolinium, TR No. 5205-2, SEL-65-050, Stanford Electronics Laboratories, Stanford, Calif., 1965.
14. W. E. Spicer and C. N. Berglund, Rev. Sci. Inst., 35, 1665 (1964).
15. L. B. Leder and J. A. Simpson, Rev. Sci. Inst., 29, 571 (1958).
16. R. Koyama, dissertation in preparation.
17. J. Shay, Photoemission Studies of the Electronic Structure of CdTe, CdSe, and CdS, TR No. 5216-1, SEL-66-112, Stanford Electronics Laboratories, Stanford, Calif., 1966.

18. A. J. Dekker, Solid State Physics, Prentice Hall, 1959.
19. W. E. Spicer, F. Wooten, and R. Stuart, Monte Carlo Calculations Pertaining to the Transport of Hot Electrons in Metals, Rept. 7626, Lawrence Radiation Laboratory, Livermore, Calif., 1964.
20. C. N. Berglund and W. E. Spicer, Phys. Rev., 136, A1030 (1964).
21. E. O. Kane, lecture at Stanford University, 1967.
22. R. S. Burington, Handbook of Mathematical Tables and Formulas, Handbook Publishers, Inc., 1956.
23. E. O. Kane, J. Phys. Soc. Japan, 21 (Suppl.), 37 (1966).
24. H. Kanter, J. Appl. Phys. Letters, 1 Feb 1967.
25. J. Callaway, Energy Band Theory, Academic Press, New York, 1964.
26. Handbook of Chemistry and Physics, 44th ed., Chemical Rubber Publishing Co., 1963.
27. W. E. Spicer, class notes, Course EE 258, Stanford University, 1966.
28. J. C. Phillips, Phys. Rev., 133, A452 (1964).
29. F. Seitz, Modern Theory of Solids, McGraw-Hill Book Company, New York, 1940.
30. J. C. Phillips, The Fundamental Optical Spectra of Solids, Solid State Phys., 18 (Seitz and Turnbull, Eds.) (1966).
31. D. Brust, Phys. Rev., 134, A1337 (1964).
32. W. E. Spicer, Phys. Rev. Letters, 11, 243 (1963).
33. M. Sachs, Solid State Theory, McGraw-Hill Book Company, New York, 1963.
34. R. A. Smith, Wave Mechanics of Crystalline Solids, Chapman and Hall, 1961.
35. W. E. Spicer, Possible Non-One Electron Effects in the Fundamental Optical Excitation Spectra of Solids, unpublished paper, 1966.
36. J. Dickey, Phys. Rev., 81, 612 (1951).
37. C. N. Berglund and W. E. Spicer, Phys. Rev., 136, A1044 (1964).
38. J. C. Phillips, Phys. Rev., 137, A1836 (1965).
39. J. C. Phillips, Phys. Rev., 140, A1254 (1965).

40. H. D. Hagstrum, private communication.
41. H. D. Hagstrum, Phys. Rev., 150, 495 (1966).
42. J. Clift, C. Curry, and B. J. Thompson, Phil. Mag., 8, 593 (1963).
43. J. C. Phillips and F. M. Mueller, private communication.
44. L. Hodges, H. Ehrenreich, and N. D. Lang, Phys. Rev., 152, 505 (1966).
45. H. Ehrenreich and H. R. Philipp, Phys. Rev., 128, 1622 (1962).
46. B. R. Cooper, H. Ehrenreich, and H. R. Philipp, Phys. Rev., 138, A494 (1965).
47. D. Beaglehole, Proc. Phys. Soc. (London), 85, 1007 (1965).
- 48a. C. R. Crowell, private communication, University of Southern California.
- 48b. M. Garfinkel, J. J. Tiemann, and W. E. Engeler, Phys. Rev., 148, 695 (1966).
49. H. Kanter, private communication.
- 50a. B. R. Cooper, H. Ehrenreich, and H. R. Philipp, Phys. Rev., 138, A494 (1965).
- 50b. S. M. Sze, J. L. Moll, and T. Sugano, Solid-State Electron., 7, 509 (1964).
51. J. R. Cuthill, A. J. McAlister, and M. L. Williams, Phys. Rev. Letters, 16, 933 (1966).
52. F. M. Mueller, Phys. Rev., 153, 659 (1967).
53. G. A. Burdick, Phys. Rev., 129, 138 (1963).
54. J. C. Phillips, Phys. Rev., 153, 669 (1967).
55. V. Heine, Phys. Rev., 153, 673 (1967).
56. C. A. W. Marshall, Proc. Phys. Soc. (London), to be published. Private communication via W. E. Spicer, Stanford University.
57. J. Wood, private communication via W. E. Spicer and J. C. Slater, Stanford University.
58. B. Segall, Phys. Rev., 125, 109 (1962).
59. N. F. Mott and H. Jones, The Theory of the Properties of Metals and Alloys, Dover Publications, New York, 1958.

60. T. D. Stefano, private communication.
61. L. R. Canfield, G. Hass, and W. R. Hunter, *Le Journal de Physique*, Tome 25, 124 (1964).
62. American Institute of Physics Handbook, 1963, Chapter 6, p. 119.
63. C. R. Crowell and S. M. Sze, *J. Appl. Phys. Japan*, 37, 2683 (1966).
64. S. M. Sze et al, *J. Appl. Phys.*, 37, 2690 (1966).
65. J. J. Hopfield, *Phys. Rev.*, 139, A419 (1965).
66. D. Pines, *Rev. Mod. Phys.*, 28, 184 (1956).
67. F. Herman and D. S. McClure, *Bull. Am. Phys. Soc.*, 5, 48 (1960).
68. M. Cardona, *Phys. Rev.*, 129, 69 (1963).
69. R. Coehlo, Ph.D. Thesis, M.I.T., unpublished, Jun 1959.
70. Gimelins Handbuch der Anorganischen Chemie, System-Nummer 60, Kupfer Bl, 1958.
71. W. Pong, *J. Appl. Phys.*, 37, 3033 (1966).
72. P. M. Scop, *Phys. Rev.*, 139, A934 (1965).
73. P. M. Scop, M.I.T. Solid State and Molecular Theory Group, Quarterly Progress Report No. 54, unpublished, Oct 1964.
- 74a. T. Donovan, private communication.
- 74b. E. G. Schneider and H. M. O'Bryan, *Phys. Rev.*, 51, 293 (1937).
75. W. F. Krolikowski and W. E. Spicer, *Bull. Am. Phys. Soc.*, 11, 916 (1966).
76. H. Philipp, E. A. Taft, and L. Apker, *Phys. Rev.*, 120, 49 (1960).
77. C. W. Peterson, *Phys. Rev.*, 148, 335 (1966).
78. F. Bassani, R. S. Knox, and W. B. Fowler, *Phys. Rev.*, 137, A1217 (1965).
79. F. Herman, *J. Electronics*, 1, 103 (1955).
80. R. C. Eden, Photoemission Studies of the Electronic Band Structures of Gallium Arsenide, Gallium Phosphide, and Silicon, TR No. 5221-1, SEL-67-038, Stanford Electronics Laboratories, Stanford, Calif. 1967.
81. W. F. Krolikowski and W. E. Spicer, *Bull. Am. Phys. Soc.*, 11, 196 (1966).

82. W. F. Krolikowski and W. E. Spicer, *Bull. Am. Phys. Soc.* 9, 735 (1964).
83. W. F. Krolikowski and W. E. Spicer, *Bull. Am. Phys. Soc.* 10, 1186 (1965).
84. J. C. Slater, Quantum Theory of Atomic Structure, Vol. 1, McGraw-Hill, 1960.
85. H. Philipp, E. A. Taft, and L. Apker, *Phys. Rev.* 120, 49 (1960).
86. K. Teegarden and G. Baldini, *Phys. Rev.* 155, 896 (1967).
87. J. E. Eby, K. J. Teegarden, and D. B. Dutton, *Phys. Rev.* 116, 1099 (1959).
88. P. G. Metzger, Private communication.
89. Roessler, Ph.D. Dissertation, Cambridge University.
90. S. W. Duckett and P. G. Metzger, *Phys. Rev.* 137, A 953 (1965).
91. L. Apker and E. Taft, *Phys. Rev.* 82, 814 (1951).
92. H. R. Philipp and E. A. Taft, *J. Phys. Chem. Soc.* 1, 159 (1956).
93. N. Smith, Private communication.
95. C. Kittel, Introduction to Solid State Physics, John Wiley & Sons, 1956.
96. J. C. Slater, Quantum Theory of Molecules and Solids, Vol. 2, McGraw Hill, 1962.
98. A. Papoulis, The Fourier Integral and Its Applications, McGraw-Hill, 1962.
99. H. R. Philipp and H. Ehrenreich, *Phys. Rev.* 129, 1550 (1963).



DOCUMENT CONTROL DATA - R & D

(Security classification of title, body of abstract and indexing annotation must be entered when the overall report is classified)

1. ORIGINATING ACTIVITY (Corporate author) Stanford Electronics Laboratories Stanford, California	2a. REPORT SECURITY CLASSIFICATION Unclassified
	2b. GROUP

3. REPORT TITLE
PHOTOEMISSION STUDIES OF THE NOBLE METALS, THE CUPROUS HALIDES, AND SELECTED ALKALI HALIDES

4. DESCRIPTIVE NOTES (Type of report and inclusive dates)
Technical Report No. 5218-1

5. AUTHOR(S) (First name, middle initial, last name)
Walter F. Krolikowski

6. REPORT DATE May 1967	7a. TOTAL NO. OF PAGES 404	7b. NO. OF REFS 81
-----------------------------------	--------------------------------------	------------------------------

8a. CONTRACT OR GRANT NO. NGR-05-020-066	9a. ORIGINATOR'S REPORT NUMBER(S) SEL-67-039
b. PROJECT NO.	
c.	9b. OTHER REPORT NO(S) (Any other numbers that may be assigned this report)
d.	

10. DISTRIBUTION STATEMENT
Qualified requesters may obtain copies from DDC. Foreign announcement and dissemination is limited.

11. SUPPLEMENTARY NOTES	12. SPONSORING MILITARY ACTIVITY National Aeronautics and Space Admin. Center for Materials Research National Science Foundation
-------------------------	--

13. ABSTRACT

The possible presence of the copper d band in the valence band of the cuprous halides has been largely ignored in the recent literature, and structure in the optical spectrum of the cuprous halides has been associated with direct transitions between symmetry points in a germanium-like band structure. In order to test the validity of these explanations for the optical spectrum of the cuprous halides, the electronic properties of the cuprous halides have been investigated in detail by use of experimental photoemission techniques. The quantum yield and photoemission data resulting from these photoemission measurements have been interpreted in terms of the electronic structure of the cuprous halides, and it is found that the copper d band plays a significant role in the valence band of the cuprous halides.

In order to distinguish the copper d band from the halogen p bands in the cuprous halides, it was found useful to extend the photoemission studies to the noble metals and the alkali halides. Consequently, this report includes not only studies of the cuprous halides (CuCl, CuBr, CuI), but also detailed studies of the noble metals (Cu, Ag, Au) and certain alkali halides (CsCl, CsBr, CsI, and KI). Some of the most important results of this work are summarized below:

(1) The experimental quantum yield and photoelectric energy distributions have been measured for all the materials in the range of photon energies below 11.6 eV. In several cases, the measurements have been extended to photon energies as high as 21.2eV

(2) For nearly all of the materials, the optical density of states has been determined in the range of energies between 11.6 eV below the fermi level and 11.6 eV above the fermi level.



14. KEY WORDS	LINK A		LINK B		LINK C	
	ROLE	WT	ROLE	WT	ROLE	WT
<p>PHOTOELECTRIC EFFECT CUPROUS HALIDES COPPER SILVER GOLD ALKALI HALIDES OPTICAL PROPERTIES</p>						
<p>(Abstract Continued)</p> <p>(3) Nondirect transitions are found to dominate the optical absorption process in the noble metals and the cuprous halides. Direct transitions are found to have secondary importance compared with nondirect transitions.</p> <p>(4) For the noble metals and the cuprous halides, a simple mathematical model is found to account quantitatively for the quantum yield, the photoelectric energy distributions, the electron-electron scattering length, and $\epsilon_2(\omega)$. This mathematical model is based upon the model of nondirect transitions.</p> <p>The new information presented in this report should be useful to theorists making future energy band calculations, and may be helpful in leading to a unified theory for the optical absorption process in solids.</p>						